

# Sheffield Hallam University

*Stress generation during the processing of epoxy-carbon composites.*

OAKESHOTT, Jennifer L.

Available from the Sheffield Hallam University Research Archive (SHURA) at:

<http://shura.shu.ac.uk/20131/>

## A Sheffield Hallam University thesis

This thesis is protected by copyright which belongs to the author.

The content must not be changed in any way or sold commercially in any format or medium without the formal permission of the author.

When referring to this work, full bibliographic details including the author, title, awarding institution and date of the thesis must be given.

Please visit <http://shura.shu.ac.uk/20131/> and <http://shura.shu.ac.uk/information.html> for further details about copyright and re-use permissions.



255724

**Sheffield City Polytechnic Library**

**REFERENCE ONLY**

ProQuest Number: 10697438

All rights reserved

INFORMATION TO ALL USERS

The quality of this reproduction is dependent upon the quality of the copy submitted.

In the unlikely event that the author did not send a complete manuscript and there are missing pages, these will be noted. Also, if material had to be removed, a note will indicate the deletion.



ProQuest 10697438

Published by ProQuest LLC (2017). Copyright of the Dissertation is held by the Author.

All rights reserved.

This work is protected against unauthorized copying under Title 17, United States Code  
Microform Edition © ProQuest LLC.

ProQuest LLC.  
789 East Eisenhower Parkway  
P.O. Box 1346  
Ann Arbor, MI 48106 – 1346

STRESS GENERATION DURING THE PROCESSING OF EPOXY-CARBON  
COMPOSITES

JENNIFER LUCY OAKESHOTT

A thesis submitted in partial fulfilment of the requirements of  
the Council for National Academic Awards for the degree of  
Doctor of Philosophy

July 1992

Sponsoring Establishment:

School of Engineering,  
Sheffield City Polytechnic,  
Sheffield, S1 1WB,  
United Kingdom.

Collaborating establishment:

Rolls-Royce plc,  
PO Box 31,  
Derby, DE2 8BJ,  
United Kingdom.

## PREFACE

The work presented in this thesis was carried out in the School of Engineering at Sheffield City Polytechnic between June 1989 and May 1992 when the candidate was registered with the Council for Academic Awards for a higher degree. During this period the candidate has not been registered for any other CNAA award or university degree. The research was supervised by Dr. A. J. Fletcher of Sheffield City Polytechnic and Mr. J. Spence of Rolls-Royce plc., Derby.

In support of the program of work post-graduate courses were attended at Sheffield City Polytechnic in, finite element analysis, stress, numerical analysis and computer programing (Fortran 77), as was a conference (2-10 April 1990) entitled residual stress generation.

The research reported here is, as far as can be ascertained original except where due reference has been made to previous work.

## ACKNOWLEDGEMENT

First and foremost I would like to thank Dr. A. J. Fletcher who's advice, encouragement and constructive criticism have proved invaluable during my period as a PhD student.

I also wish to acknowledge Rolls-Royce plc (the collaborating establishment), and in particular Mr. J. Spence, for our regular meetings concerning the course of the research. The supply of samples and information regarding relevant literature, material properties, and manufacturing techniques have been gratefully received.

Special mention must also be made of the staff at Sheffield City Polytechnic: To Mr R. Hines and his library staff for their help in searching for the literature, to the graphics department for the reproduction of the colour prints, to fellow CAD/CAM users for their assistance with the computing and to various technicians for their help with the optical microscopy, electron microscopy and photography work (and also for the use of their fridge).

Thanks are due to Dr. A. Pugh for his help with the computer programing of random fibre arrays.

Funding from, Sheffield City Polytechnic through the National Advisory Board, and Rolls-Royce plc is gratefully acknowledged.

Finally I wish to express my gratitude to my parents for their moral support and understanding during the last three years.

## ABSTRACT

The stresses generated during the processing of carbon fibre/epoxy resin composite materials are predicted using the finite element method and classical lamination theory. Elastic material behaviour is assumed. Emphasis is placed on the residual microstresses which have been less-extensively studied than other aspects of the stress generation process.

Temperature and stress distributions are modelled through the thickness of laminates assuming cooling from the cure temperature of 190°C. At the microlevel the effect of varying fibre volume fraction, interfibre distance, packing geometry and fibre diameter are studied. Random and regular fibre arrays are considered.

It is found that the residual stresses are generated almost entirely due to the differing properties of the fibre and the matrix and the anisotropy of the fibres, rather than any temperature gradients within the materials. At the macrolevel maximum stresses (10-100 MPa) are calculated in the transverse layers of multidirectional laminates. At the microlevel maximum stresses (10-100 MPa) are predicted at the fibre/matrix interface. The exact values depend on the assumed laminate stacking sequence and distribution of fibres, respectively. The maximum values of the microstresses are found to be approximately inversely proportional to the minimum interfibre distance and proportional to the fibre diameter. This implies that, at the shorter minimum interfibre distances typical of more realistic random arrays, the maximum stress values are greater. When the macrostress and microstress fields are superimposed it is predicted that cracks will form at some of the fibre/matrix interfaces and propagate outwards into the matrix.

Observations of laminate samples under the electron microscope show no such cracking to occur, rather in a few localised regions, cracking around the fibre/matrix interface is apparent. It is suggested that in these regions the interface is weak and fails due to the weaker radial stress. Otherwise it is suggested that cracking is not observed due to a visco-elastic/visco-plastic behaviour of the matrix, the presence of an interlayer at the fibre/matrix interface with properties different to that in the matrix away from the interface and a crack suppressing mechanism resulting from the interaction of adjacent plies. The latter effect is most significant for thin plies.

It is proposed that regular packing of the fibres, which precludes low interfibre distances, will prevent microcracking. Hexagonal packing is preferred since this achieves the highest volume fraction and thus the highest strengths. Sizings applied to the fibres which improve the fibre/matrix adhesion, and react/diffuse into the matrix to produce a flexible interlayer, will improve the strength and impact resistance of these composites. In multidirectional laminates thin transverse layers, less than 0.5 mm are advised.

## NOMENCLATURE

Where symbols have not been defined in the text of the thesis the following terminology applies. Terms not included, or different from, those defined below are given in the text.

- A - In-plane modulus of a symmetric laminate (relates strains to stress resultant)
- B - Coupling modulus of asymmetric laminates (relates curvatures to stress resultant)
- C - Stiffness
- D - Flexural modulus of symmetric laminate (relates curvatures to moment resultant)
- E - Young's modulus
- G - Shear modulus
- M - Moment resultant
- N - Stress resultant
- Q - Reduced stiffness
- S - Compliance
- SH - Shear compliance
- T - temperature
- V - Volume fraction
  
- a - In-plane compliance of a symmetric laminate
- h - thickness (laminate, ply, element)
- $h_0$  - Unit ply thickness
- t - time

$\alpha$  - Thermal expansion coefficient  
 $\beta$  - Coefficient of moisture expansion  
 $\gamma$  - Shear strain  
 $\epsilon$  - Strain  
 $\epsilon^0$  - In-plane strain  
 $\eta$  - Coefficient of viscosity,  
 $\theta$  - Angle (ply orientation) or temperature  
 $\kappa$  - Curvature  
 $\lambda$  - Thermal conductivity  
 $\mu$  - displacement  
 $\nu$  - Poisson's ratio  
 $\rho$  - density or resistivity  
 $\sigma$  - stress  
 $\tau$  - Shear stress

Subscripts and Superscripts:

FPF - First ply-failure  
M - Mechanical (due to applied stress)  
L - Longitudinal direction (laminate axis or fibre axis)  
N - Non-mechanical (due to thermal/moisture expansion)  
R - Residual stress/strain  
T - Transverse direction (perpendicular to fibre axis or perpendicular to laminate axis and in the plane of the laminate).  
f - Fibre  
m - Matrix  
z - through the thickness of the laminate or along the fibre axis.  
r - radial direction, origin at fibre centre

$\theta$  - angular direction, origin at fibre centre

0 - In the 0° plies

45 - In the 45° plies

90 - In the 90° plies

Indicial notation is used for vector and tensor quantities throughout. The co-ordinate system referred to may be Cartesian (ijk, 123, LTz), polar-cylindrical (r,  $\theta$ , z) or curvilinear ( $\xi\eta\zeta$ ). Generally the contracted form with single indices has been used rather than the full tensor notation. The former is appropriate to situations where the stress and strain tensors are symmetric and the order of the indices is immaterial.

Laminate code:

Throughout the thesis the orientation of the plies in multidirectional laminates have been expressed according to a laminate code. This is illustrated below for a typical laminate.

$[0/90/+45/-45_2]_s$

The code shows the stacking sequence of the unidirectional ply groups within the laminate. The sequence is given in ascending order from the bottom ply. The numbers contained within the obliques indicate the orientation of the fibres within the plies when measured from the laminate axis. The subscripts to the numbers within the obliques denote the number of plies at the specified orientation and the subscript s outside the brackets indicates a laminate which is symmetric about the mid-plane. That is the stacking sequence of the

upper half is the same as the lower half except that the sequence is reversed. If no subscript is given outside the brackets the stacking sequence is for the whole laminate.

## CONTENTS

	Page
NOMENCLATURE	5
1 INTRODUCTION	30
2 LITERATURE SURVEY	32
2.1 General Introduction	32
2.2 Materials	33
2.2.1 Carbon Fibres	33
2.2.1.2 PAN Fibres	33
2.2.1.2 Structure	34
2.2.1.3 Properties	37
2.2.2 Resin Matrix	38
2.2.2.1. Epoxy Resin Matrix	38
2.2.2.2. Thermoplastic Resin Matrix	39
2.3 Manufacture	43
2.3.1 Fibre Tows and Yarns	43
2.3.2 Prepregs and Preforms	43
2.3.2.1 Tow Prepreg	43
2.3.2.2 Unidirectional Tape Prepregs	44
2.3.2.3 Multidirectional Tape Prepregs	45
2.3.2.4 Woven Fabric Prepregs	45
2.3.2.5 Non-Woven Fabric Prepregs	46

	Page
2.3.2.6 <i>Prepreg Properties</i>	46
2.3.2.7 <i>Multidirectional Reinforced Fabrics and Preforms</i>	47
2.3.2.8 <i>Knitted Structures</i>	48
2.3.2.9 <i>Hybridization</i>	49
2.3.3 <i>Processing</i>	50
2.3.3.1 <i>Open Moulding Techniques</i>	50
2.3.3.2 <i>Closed Moulding Techniques</i>	50
2.3.3.3 <i>Filament Winding</i>	51
2.3.3.4 <i>Braiding</i>	51
2.3.3.5 <i>Pultrusion</i>	52
2.4 <i>The Cure Process</i>	52
2.4.1 <i>Model of Loos and Springer</i>	52
2.4.2 <i>Effect of Ply Stacking Sequence and Laminate Geometry           on Resin Flow</i>	54
2.4.3 <i>Resin Flow Assuming Time Dependent Pressure/Viscosity           and a Visco-Elastic Prepreg</i>	54
2.4.4 <i>Three-Dimensional Resin-Flow Models</i>	55
2.5 <i>Residual Stress</i>	57
2.5.1 <i>Macrostress</i>	57
2.5.1.1 <i>Classical Lamination Theory</i>	62
2.5.1.2 <i>Moisture Effects</i>	65
2.5.1.3 <i>Effect of Curing Stress on First Ply-Failure</i>	71
2.5.1.4 <i>Geometric Non-Linearities</i>	76

	Page
2.5.1.5 <i>Edge Effects</i>	80
2.5.1.6 <i>Non-Linear Stress-Strain Response</i>	95
2.5.1.7 <i>Finite Element Modelling of Complex Geometries</i>	96
<b>2.6 Microstresses</b>	<b>97</b>
2.6.1 <i>Mechanics of Materials Methods</i>	97
2.6.2 <i>Elasticity Methods</i>	99
2.6.3 <i>Distribution of Fibres</i>	100
2.6.3.1 <i>Regular Fibre Arrays</i>	100
2.6.3.2 <i>Random Fibre Arrays</i>	108
2.6.4 <i>Photoelastic Determination of the Microstresses</i>	109
<b>2.7 Properties</b>	<b>110</b>
2.7.1 <i>Thermal Expansion Coefficients</i>	110
2.7.2 <i>Young's Modulus</i>	125
<b>2.8 Failure</b>	<b>129</b>
2.8.1 <i>First-Ply Failure</i>	129
2.8.2 <i>Failure due to Interply Load Transfer</i>	130
2.8.3 <i>The Energy Method</i>	131
2.8.4 <i>Fibre Failure</i>	134
2.8.5 <i>Visco-Elastic Behaviour</i>	137
<b>2.9 PAFEC</b>	<b>139</b>
<b>2.10 Resumé</b>	<b>140</b>

	Page
3 PROCEDURE	141
3.1 Theory	141
3.1.1 The Finite Element Method	141
3.1.2 Finite Difference Methods	142
3.1.3 Temperature Distributions	143
3.1.4 Stress Distributions	145
3.2 The PAFEC Finite Element Software	148
3.3 Finite Difference Modelling of the Temperature Distribution through the Thickness of a Prepreg	149
3.4 Finite Element Modelling of the Macrostressses	151
3.5 Finite Element Modelling of the Microstressses - Regular Hexagonal Fibre Array	154
3.5.1 Incorporation of Temperature Dependent Epoxy resin Properties	156
3.6 Finite Element Modelling of the Microstressses - Other Regular Fibre Arrays	157
3.6.1 Incorporation of Anisotropic Carbon Fibre Properties	160
3.7 Finite Element Modelling of Random Fibre Arrays	162
3.8 Generation of Random Fibre Arrays	164
3.9 Finite Element Modelling of Voronoi Cell from Random Fibre Array with 50% Fibre in the Section	165
3.10 Accuracy	165
3.11 Optical Microscopy	165

	Page
3.12 Electron Microscopy	166
3.13 Modelling of the Macrostressess using Classical Lamination Theory	166
4 RESULTS	170
4.1 Macromodelling	172
4.1.1 Temperature Distribution	172
4.1.2 Deformation and Stress Distributions	172
4.1.2.1 <i>Single Mesh</i>	172
4.1.2.2 <i>Double Mesh</i>	177
4.2 Micromodelling - Regular Fibre Arrays	180
4.2.1 Typical Hexagonal Fibre Array	180
4.2.1.1 <i>Deformation</i>	181
4.2.1.2 <i>Stresses</i>	182
4.2.1.3 <i>Accuracy</i>	187
4.2.2 Incorporation of Anisotropic Carbon Fibre Properties and Modelling of Other Regular Fibre Distributions	187
4.2.2.1 <i>Twelve Nearest Neighbours/15° Co-Ordination angle</i>	188
4.2.2.2 <i>Six Nearest Neighbours/30° Co-Ordination angle</i>	189
4.2.2.3 <i>Four Nearest Neighbours/45° Co-Ordination angle</i>	190
4.2.2.4 <i>Three Nearest Neighbours/60° Co-Ordination angle</i>	191
4.2.2.5 <i>Effect of Varying Poisson's Ratio</i>	192

	Page
4.3 Micromodelling - Random Fibre Arrays	192
4.3.1 Hypothetical Voronoi Cell	192
4.3.2 Generation of Random Fibre Arrays	194
4.3.3 Voronoi Cell from Random Fibre Array with 50% Fibre in the Section	195
4.4 Optical Microscopy	196
4.5 Electron Microscopy	198
4.6 Modelling of the Macrostressses using Classical Lamination Theory	198
4.6.1 Calculation of Laminate Mid-Plane Strains	199
4.6.2 Calculation of Ply Stressses	200
5 DISCUSSION	202
5.1 Literature Survey	202
5.1.1 Macrostressses	202
5.1.2 Microstressses	205
5.2 Microstress Models	211
5.2.1 Effect of Varying Interfibre Distance on the Maximum Stress Value	212
5.2.2 Effect of Varying Fibre Diameter on the Maximum Stress Value	213
5.2.3 Effect of Varying Fibre Volume Fraction on the Maximum Stress Value	214

	Page
5.2.4 Effect of Varying Fibre Diameter/Interfibre Distance on the Maximum Stress Value	215
5.2.5 Effect of Co-Ordination Angle on the Stress Distributions	216
5.2.6 Stress Distributions in the Carbon Fibres	217
5.2.7 Hypothetical Voronoi Cell	218
5.2.8 Computer Modelling of Random Fibre Arrays	220
5.2.9 Voronoi Cell from Random Fibre Array with 50% Fibre in the Section	222
5.3 Optical Microscopy	225
5.4 Electron Microscopy	226
5.5 Macromodelling	229
5.5.1 Single and Double Meshes	229
5.5.2 Results Obtained using Classical Lamination Theory	229
5.6 Combined Effects of Macro- and Micro-Models	232
5.7 Effect of Incipient Cracks on Composite Failure	234
5.8 Effect of Moisture Absorption	236
5.9 Strength of the Fibre/Matrix Interface	237
5.10 Interlayer Properties	238
5.11 Sizing Agents	238
6 CONCLUSION	240
7 FURTHER WORK	248
LIST OF REFERENCES	250

	Page
Summary of Programs given in the Results	262
TABLES	264
FIGURES	277
APPENDIX 1 - FIBDIST Program	A1
APPENDIX 2 - Modelling of Interlayer	A2

## List of Tables

Table	Page
1. Calculated fibre volume fractions.....	264
2. Program coding for regular fibre arrays.....	266
3. Maximum displacements.....	267
4. 30° co-ordination angle/six nearest neighbours - stresses in epoxy resin.....	268
5. 30° co-ordination angle/six nearest neighbours - stresses in carbon fibre.....	269
6. 45° co-ordination angle/four nearest neighbours - stresses in epoxy resin.....	270
7. 45° co-ordination angle/four nearest neighbours - stresses in carbon fibre.....	271
8. 60° co-ordination angle/three nearest neighbours - stresses in epoxy resin.....	272
9. 60° co-ordination angle/three nearest neighbours - stresses in carbon fibre.....	273
10. 15° co-ordination angle/twelve nearest neighbours - stresses in epoxy resin.....	274
11. 15° co-ordination angle/twelve nearest neighbours - stresses in carbon fibre.....	275

Table	Page
12. Random fibre arrays, Voronoi cells - stresses in epoxy resin.....	276
13. Random fibre arrays, Voronoi cells - stresses in carbon fibre resin.....	276

List of Figures

Figure	Page
1. Kelvin or Voigt unit .....	277
2. a) Curing strains of $[0_2/\pm\theta]_s$ graphite/plastic laminates.....	278
b) Curing stresses in $0^\circ$ plies of $[0_2/\pm\theta]_s$ graphite/plastic laminates.....	278
3. Residual octahedral shear stress state.....	279
4. a) Distribution of shrinkage stresses along ligament centre line, $\Delta/R = 0.5$ .....	280
b) Distribution of shrinkage stresses across section between fibres, $\Delta/R = 0.5$ .....	280
5. Probability density function, $g(x)$ in two dimensions of half-interparticle distance, $X$ , for intensity $\lambda$ and volume fraction $p$ ranging from 0 to 0.3.....	281
6. Regular hexagonal array and corresponding representative unit cell.....	282
7. Regular square array and corresponding representative unit cell.....	283
8. Regular array for fibre having three nearest neighbours and corresponding representative unit cell.....	284
9. Representative unit cell for fibre having twelve nearest neighbours.....	285

Figure	Page
10. Temperature distribution: cooling of the top surface from 190°C to 20°C over 2 hours. Given at the end of cooling, time $t = 7200$ seconds - model MATH (single mesh).....	286
11. Deformation: cooling of the top surface through 170°C over 2 hours. Given at the end of cooling, time $t = 7200$ seconds - model MASI (single mesh).....	287
12. Mesh, centre elements - model MASI (single mesh, $t = 7200$ s).	288
13. $\sigma_{xx}$ stress, centre - model MASI (single mesh, $t = 7200$ s)....	289
14. $\sigma_{xx}$ stress, top - model MASI (single mesh, $t = 7200$ s).....	290
15. $\sigma_{xx}$ stress, bottom - model MASI (single mesh, $t = 7200$ s)....	291
16. $\sigma_{yy}$ stress, centre - model MASI (single mesh, $t = 7200$ s)....	292
17. $\sigma_{yy}$ stress, top - model MASI (single mesh, $t = 7200$ s).....	293
18. $\sigma_{yy}$ stress, bottom - model MASI (single mesh, $t = 7200$ s)....	294
19. $\sigma_{zz}$ stress, centre - model MASI (single mesh, $t = 7200$ s)....	295
20. $\sigma_{zz}$ stress, top - model MASI (single mesh, $t = 7200$ s).....	296
21. $\sigma_{zz}$ stress, bottom - model MASI (single mesh, $t = 7200$ s)....	297
22. $\sigma_{xy}$ stress, centre - model MASI (single mesh, $t = 7200$ s)....	298
23. $\sigma_{xy}$ stress, top - model MASI (single mesh, $t = 7200$ s).....	299
24. $\sigma_{xy}$ stress, bottom - model MASI (single mesh, $t = 7200$ s)....	300

Figure	Page
25. $\sigma_{yz}$ stress, centre - model MASI (single mesh, $t = 7200$ s)....	301
26. $\sigma_{zx}$ stress, centre - model MASI (single mesh, $t = 7200$ s)....	302
27. Maximum principal stress, centre - model MASI (single mesh, $t = 7200$ s).....	303
28. Maximum principal stress vectors, centre - model MASI (single mesh, $t = 7200$ s).....	304
29. Maximum principal stress, top - model MASI (single mesh, $t = 7200$ s).....	305
30. Maximum principal stress, bottom - model MASI (single mesh, $t = 7200$ s).....	306
31. Minimum principal stress, centre - model MASI (single mesh, $t = 7200$ s).....	307
32. Minimum principal stress vectors, centre - model MASI (single mesh, $t = 7200$ s).....	308
33. Minimum principal stress, top - model MASI (single mesh, $t = 7200$ s).....	309
34. Minimum principal stress, bottom - model MASI (single mesh, $t = 7200$ s).....	310
35. Von Mises stress, centre - model MASI (single mesh, $t = 7200$ s).....	311
36. Von Mises stress, top - model MASI (single mesh, $t = 7200$ s).	312

Figure	Page
37. Von Mises stress, bottom - model MASI (single mesh, t = 7200 s).....	313
38. Maximum shear stress, centre - model MASI (single mesh, t = 7200 s).....	314
39. Tresca stress, centre - model MASI (single mesh, t = 7200 s).	315
40. Deformation: uniform cooling through 170°C - model ASI2 (double mesh).....	316
41. Mesh, centre elements - model ASI2 (double mesh).....	317
42. $\sigma_{xx}$ stress, centre - model ASI2 (double mesh).....	318
43. $\sigma_{xx}$ stress, unaveraged, centre - model ASI2 (double mesh)....	319
44. $\sigma_{xx}$ stress, top - model ASI2 (double mesh).....	320
45. $\sigma_{xx}$ stress, bottom - model ASI2 (double mesh).....	321
46. $\sigma_{yy}$ stress, centre - model ASI2 (double mesh).....	322
47. $\sigma_{yy}$ stress, unaveraged, centre - model ASI2 (double mesh)....	323
48. $\sigma_{yy}$ stress, top - model ASI2 (double mesh).....	324
49. $\sigma_{yy}$ stress, bottom - model ASI2 (double mesh).....	325
50. $\sigma_{zz}$ stress, centre - model ASI2 (double mesh).....	326
51. $\sigma_{zz}$ stress, unaveraged, centre - model ASI2 (double mesh)....	327
52. $\sigma_{zz}$ stress, top - model ASI2 (double mesh).....	328

Figure	Page
53. $\sigma_{zz}$ stress, bottom - model ASI2 (double mesh).....	329
54. $\sigma_{xy}$ stress, centre - model ASI2 (double mesh).....	330
55. $\sigma_{xy}$ stress, unaveraged, centre - model ASI2 (double mesh)....	331
56. $\sigma_{xy}$ stress, top - model ASI2 (double mesh).....	332
57. $\sigma_{xy}$ stress, bottom - model ASI2 (double mesh).....	333
58. $\sigma_{yz}$ stress, centre - model ASI2 (double mesh).....	334
59. $\sigma_{zx}$ stress, centre - model ASI2 (double mesh).....	335
60. Maximum principal stress, centre - model ASI2 (double mesh)..	336
61. Maximum principal stress vectors, centre - model ASI2 (double mesh).....	337
62. Max. principal stress, unaveraged, centre - model ASI2 (double mesh).....	338
63. Maximum principal stress, top - model ASI2 (double mesh).....	339
64. Maximum principal stress, bottom - model ASI2 (double mesh)..	340
65. Minimum principal stress, centre - model ASI2 (double mesh)..	341
66. Minimum principal stress vectors, centre - model ASI2 (double mesh).....	342
67. Minimum principal stress, unaveraged, centre - model ASI2 (double mesh).....	343

Figure	Page
68. Minimum principal stress, top - model ASI2 (double mesh).....	344
69. Minimum principal stress, bottom - model ASI2 (double mesh)..	345
70. Von Mises stress, centre - model ASI2 (double mesh).....	346
71. Von Mises stress, unaveraged, centre - model ASI2 (double mesh).....	347
72. Von Mises stress, top - model ASI2 (double mesh).....	348
73. Von Mises stress, bottom - model ASI2 (double mesh).....	349
74. Maximum shear stress, centre - model ASI2 (double mesh).....	350
75. Tresca stress, centre - model ASI2 (double mesh).....	351
76. Deformation on cooling through 170°C - model ES04.....	352
77. Maximum principal stress - model ES04.....	353
78. Maximum principal stress, vectors - model ES04.....	354
79. Maximum principal stress, unaveraged - model ES04.....	355
80. Minimum principal stress - model ES04.....	356
81. Minimum principal stress, vectors - model ES04.....	357
82. Minimum principal stress, unaveraged - model ES04.....	358
83. Von Mises stress - model ES04.....	359
84. Von Mises stress, unaveraged - model ES04.....	360

Figure	Page
85. Tresca stress - model ES04.....	361
86. Tresca stress, unaveraged - model ES04.....	362
87. Maximum shear stress - model ES04.....	363
88. Maximum shear stress, unaveraged - model ES04.....	364
89. Deformation on cooling through 170°C - model D15C.....	365
90. Maximum principal stress - model D15C.....	366
91. Maximum principal stress, vectors - model D15C.....	367
92. Von Mises stress - model D15C.....	368
93. Deformation on cooling through 170°C - model B03C.....	369
94. Maximum principal stress - model B03C.....	370
95. Maximum principal stress, vectors - model B03C.....	371
96. Von Mises stress - model B03C.....	372
97. Deformation on cooling through 170°C - model F03B.....	373
98. Maximum principal stress - model F03B.....	374
99. Maximum principal stress, vectors - model F03B.....	375
100. Von Mises stress - model F03B.....	376
101. Deformation on cooling through 170°C - model C54C.....	377
102. Maximum principal stress - model C54C.....	378

Figure	Page
103. Maximum principal stress, vectors - model C54C.....	379
104. Von Mises stress - model C54C.....	380
105. Deformation on cooling through 170°C - model E54A.....	381
106. Maximum principal stress - model E54A.....	382
107. Maximum principal stress, vectors - model E54A.....	383
108. Von Mises stress - model E54A.....	384
109. Deformation on cooling through 170°C - model C06B.....	385
110. Maximum principal stress - model C06B.....	386
111. Maximum principal stress, vectors - model C06B.....	387
112. Von Mises stress - model C06B.....	388
113. Deformation on cooling through 170°C - model F06A.....	389
114. Maximum principal stress - model F06A.....	390
115. Maximum principal stress, vectors - model F06A.....	391
116. Von Mises stress - model F06A.....	392
117. Deformation on cooling through 170°C - model B13C.....	393
118. Maximum principal stress - model B13C.....	394
119. Maximum principal stress, vectors - model B13C.....	395
120. Von Mises stress - model B13C.....	396

Figure	Page
121. Deformation on cooling through 170°C - model V001.....	397
122. Maximum principal stress - model V001.....	398
123. Maximum principal stress, vectors - model V001.....	399
124. Von Mises stress - model V001.....	400
125. 30% fibre volume fraction random fibre array.....	401
126. 50% fibre volume fraction random fibre array.....	402
127. Deformation on cooling through 170°C - model V053.....	403
128. Maximum principal stress - model V053.....	404
129. Maximum principal stress, vectors - model V053.....	405
130. Von Mises stress, model V053.....	406
131. Max. principal stress, high stress region - model V053.....	407
132. Max. principal stress, high stress region, vectors - model V053.....	408
133. Von Mises stress, high stress region - model V053.....	409
134. Centre plies of laminate sample - Mag x 60.....	410
135. Outer plies of laminate sample - Mag x 116:.....	411
a) View 1	
b) View 2	

Figure	Page
136. Cross sections through transverse layer - Mag x 365:.....	412
a) View 1	
b) View 2	
137. Cross sections through transverse layer - Mag x 590:.....	413
a) View 1	
b) View 2	
138. Ply interface - Mag x 590:.....	414
a) View 1 - no epoxy rich region	
b) View 2 - with epoxy rich region	
139. Epoxy rich regions between tows - Mag x 590:.....	415
a) View 1 -at ply interface.	
b) View 2 - in the centre of a transverse ply.	
140. Cracking at fibre/matrix interface, view 1:.....	416
a) Mag x 1440	
b) Mag x 2880	
141. Cracking at fibre/matrix interface, view 2:.....	417
a) Mag x 1360	
b) Mag x 2720, top	
continued c) Mag x 2720, bottom.....	418
142. Cracking at fibre/matrix interface, view 3:.....	419
a) Mag x 1360	
b) Mag x 2720	
143. Cracking at fibre/matrix interface, view 4 - Mag x 2880.....	420

Figure	Page
144. Cracking at fibre matrix interface, view 5 - Mag x 2880.....	420
145. Sectioning artifact:.....	421
a) Mag x 720	
b) Mag x 1440	
146. Polishing/sectioning artifacts:.....	422
a) View 1 - Mag x 1440	
b) View 2 - Mag x 720	
147. The greatest value of the maximum principal stress versus half-interfibre distance (XA) for varying co-ordination angle, $\theta$ ..	423
148. The greatest value of the maximum principal stress versus fibre radius showing the effect of variation in half-interfibre distance, XA.....	424
149. The greatest value of the maximum principal stress versus fibre volume fraction showing the effect of variation in co- ordination angle, $\theta$ .....	425
150. The greatest value of the maximum principal stress versus fibre radius to half-interfibre distance ratio, OX/XA.....	426

## 1 INTRODUCTION

Carbon fibre/epoxy resin composites are high strength, high modulus, low density materials having major applications in the aerospace, and to a lesser extent the automotive, marine and sports industries. Their high specific strength makes them a preferable material to denser high strength/modulus materials such as steel or aluminium in situations where weight is at a premium. Hence their use as a structural materials in the aerospace industry.

The composites are generally supplied in the form of prepreg tapes which consist of layers of continuous collimated bundles of carbon fibres or tows. These are pre-impregnated with epoxy resin and partially cured. The individual layers may have common or variant orientations to the axis of the prepreg tape when they are termed unidirectional or multidirectional, respectively. In unidirectional prepregs the fibres reinforce primarily in the direction parallel to the tape axis whereas in multidirectional prepregs improved properties are obtained transverse to the prepreg axis but at the expense of the on-axis properties. The tapes are applied to moulds in this pliable form and cure is completed at elevated temperatures and pressures in an autoclave oven. Other fibre preforms exist including various pre-impregnated woven and knitted fabrics, filament windings, braidings and more complex three-dimensional weaves.

The carbon fibres are anisotropic and have thermal expansion and mechanical properties very different from those of the epoxy resin. As a result on cooling the cured parts residual microstresses are generated in the fibres and the matrix. In addition properties in the

transverse direction of the unidirectional plies differ from those in the longitudinal, fibre direction. Hence for multidirectional laminates consisting of successive unidirectional plies at various orientations to the laminate axis residual macrostresses are generated due to the restraint of adjacent laminae on the free thermal expansion. Residual macrostresses can also be generated due to the geometry of the manufactured part.

Apart from the residual thermal stresses a literature survey has shown residual stresses to be generated due to the different moisture expansion coefficients of the epoxy resin and the carbon fibres. In this respect absorption of moisture by the prepregs after cure is important, in particular the associated moisture diffusion profiles.

The residual stresses are to the detriment of the mechanical properties of the material leading to microcracking and delamination with failure at lower applied stress levels. Distortion of the cured part can also result limiting precision in manufacture.

The thermal residual stresses developed on cooling cured unidirectional and multidirectional carbon fibre/epoxy resin laminates are studied using finite element analysis and classical lamination theory. First a literature review of the residual stresses in carbon fibre/epoxy resin composites is given including a summary of their manufacture, properties and uses.

## 2 LITERATURE SURVEY

### 2.1 General introduction

There is a considerable amount of literature concerning the manufacture, properties and uses of fibre-reinforced plastics as summarized below.

Manufacture      - open moulding techniques  
                    - closed moulding techniques  
                    - filament winding  
                    - pultrusion

Properties        - fibre  
                    - matrix  
                    - composite

Uses             - aerospace  
                    - automotive  
                    - marine  
                    - sports

There are many excellent general sources of reference [1 - 10]

In this survey particular attention is given to the curing stresses generated in carbon fibre/epoxy resin laminates as developed for the manufacture of structural components in the aerospace industry.

Processing techniques typically involves the autoclave moulding of pre-impregnated tapes.

## 2.2 Materials

Carbon fibre/epoxy resin composites have been developed as a high modulus, low density material having particular application in the aerospace and also the automotive, marine and sports industry. They have largely replaced structural metals such as steel and aluminium in situations where their high specific modulus and specific strength are to an advantage. In addition they offer superior fatigue resistance, lower thermal expansion with retention of properties at high temperatures and environmental resistance.

### 2.2.1 Carbon Fibres

Commercial carbon and graphite fibres are derived from organic precursors such as polyacrylonitrile (PAN) and rayon or by the extrusion of pitch. The fibres are produced by thermally decomposing the precursors under controlled conditions of heating and environment.

#### 2.2.1.2 PAN Fibres

Rolls-Royce discovered in 1963 that a high Young's modulus, around 600 GPa could be obtained by stretching PAN based carbon fibres and they have become the most important source of carbon/graphite fibres.

Manufacture involves an initial stabilization of the stretched fibre precursor by oxidation up to 250°C. This prevents melting in the subsequent processing and axially aligns the polymer molecules as they transform into a rigid ladder polymer structure. Carbonization follows without stretching in an inert atmosphere at 250-1500°C as most of the non-carbon elements are evolved and the remaining carbon atoms form a network of extended hexagonal ribbons, known as turbostratic graphite.

These ribbons align parallel to the fibre axis but the degree of order of one ribbon with respect to another is relatively low. A final heat treatment of short duration at 1500-2500°C known as graphitization with hot stretching above 2000°C improves the degree of order and plastically deforms the fibres. There is a consequent improvement in properties.

The single fibre filaments are usually sized to improve handling qualities and may be coated with compatible resins to facilitate impregnation in subsequent processing.

#### 2.2.1.2 Structure

Transmission electron microscopy and x-ray diffraction have shown carbon fibres to consist of many graphitic lamellar ribbons orientated roughly parallel to the fibre axis with a complex interlinking of layer planes both longitudinally and laterally [11-14]. The ribbons are composed of crystallites. The crystallites have the hexagonal layer structure of graphite but no three-dimensional order. They are known formerly as turbostratic graphite or more recently as graphene. The structure is typically defined in terms of crystallite dimensions,  $L_c$  and  $L_a$ , perpendicular to the fibre axis.  $L_c$  is the thickness of the crystallite perpendicular to the graphite layers and  $L_a$  is the width of the crystallite in the plane of the graphite layers.

It has been observed using transmission electron microscopy that the microstructure of the fibre precursor is largely retained such that a fibrillar structure is apparent in PAN fibres [11]. With increasing heat treatment temperature the orientation of the crystallites and

crystallite dimensions,  $L_c$  and  $L_a$  are noted to increase. For high Young's modulus fibres, typically greater than 400 GPa a sheath-core structure has been seen to develop [14] with highly aligned circumferentially orientated crystallites in the fibre outer layers combined with radially orientated crystallites having a lower degree of alignment in the fibre centre. The crystallites at the fibre surface were also noted to be larger.

Johnson and Watt [11] observed using transmission electron microscopy that the internal structure of 414 GPa carbon fibres graphitized at 2500°C consists of graphite crystallites about 100 Angstroms across with a preferred orientation of the basal planes parallel to the fibre axis. X-ray diffraction was reported to have shown similar turbostratic crystallites having  $L_c$  at least twelve layer planes and of the size 60-120 Angstroms across. Fibres heat treated to 1000°C showed a network of 800-1000 Angstrom fibrils running the full length of the fibre with  $L_a$  equal to 30 Angstroms. It was noted that Bacon and Tang [12] had observed long primary structures in rayon fibres and it was proposed that the strength of the fibre was a function of the interfibrillar bonding whereas the Young's modulus depended on the degree of orientation of the crystallites.

Badami, Joiner and Jones [13] also studied carbon fibres heat treated to 2600°C. X-ray diffraction/transmission electron microscopy showed the fibres to consist of graphite crystallites approximately 50 Angstroms in size with the basal planes highly orientated along the fibre axis, having a spread of about  $\pm 10^\circ$ . A d spacing of 3.39 Angstroms was calculated compared with 3.35 Angstroms for natural graphite, although no three-dimensional reflections were observed. The

crystallites were found to form chains up to a micron in length along the fibre axis. 250-1000 Angstrom diameter fibrils were observed parallel to the fibre axis and it was suggested that the observation of Bacon and Tang that the morphology of the original fibre structure is largely retained was correct.

Johnson [14] studied PAN fibres heat treated to 2500°C (type 1), 1500°C (type 2) and 1000°C (type A). X-ray diffraction showed the crystallites to be turbostratic and their size to increase with increasing heat treatment temperature. The crystallite preferred orientation and interlayer spacing were observed to decrease as the temperature increased.

Transmission electron microscopy showed the structures to be uniform apart from a thin 150-250 nm skin of circumferentially orientated crystallites in the type 1 fibres. A higher degree of axial preferred orientation of 14° and larger crystallite size,  $L_c$  of 10.0 nm was apparent in the skin compared with 26° and 3.3 nm in the core, respectively. Otherwise the crystallite orientations in the transverse sections were observed to be random. A higher stacking disorder was noted in the type 2 and type A fibres.

A non-uniform oxidation treatment given to the type 1 fibres resulted in sheath-core heterogeneity in the longitudinal and transverse sections. The sheath was approximately 1  $\mu\text{m}$  in width, more crystalline and surrounded by a highly crystalline skin. The transverse section showed more extensive layer planes than the core. For uniform oxidation the time and temperature of oxidation is such that the process is reaction controlled, whereas with non uniform oxidation the

process is diffusion controlled. Hence in the latter case the surface materials see a different oxidizing environment to the core and a more highly organized structure results in the oxygen rich outer layers.

Carbon fibres manufactured from mesophase pitch are noted for their higher density and larger crystallite size than PAN-based fibres [15]. This is due to their liquid crystal origin. The resulting fibres are of high modulus but intermediate strength due to strength limiting defects such as interfilament fusing, voids, foreign particle inclusions, surface defects and irregular shapes in cross-section.

#### 2.2.1.3 Properties

The high strength, stiffness and hardness of diamond is a direct consequence of the strong  $sp^3$  covalent bonding between the carbon atoms. Graphite has similar strong  $sp^2$  covalent bonding within the hexagonal-layer planes but weak dispersive Van der Waals' bonding between planes. The properties of graphite are therefore highly anisotropic having high Young's modulus and strength parallel to the planes and low values perpendicular to the planes. It also has a low shear modulus between planes.

The Young's modulus of carbon fibres is found to increase with alignment of the crystallites and therefore with graphitization temperature. Such an increase is not however apparent for tensile strength [16] since after an initial increase the tensile strength is observed to decrease. This is thought to be due to the development of the sheath-core structure and misaligned crystallites at flaws in the fibre surface. Residual stresses are generated on cooling due to the

differences in thermal expansion between the highly orientated outer layers and the less highly orientated core. The misaligned crystallites at flaws will produce regions of lower local modulus and therefore initiate failure.

### 2.2.2 Resin Matrix

#### 2.2.2.1 Epoxy Resin Matrix

The most commonly used matrix material used in advanced carbon fibre reinforced composite materials are the epoxy resins. They offer superior moisture and environmental resistance than the polyester and vinyl ester resins used in less demanding composite material applications. They have also good handling characteristics and processing flexibility at an acceptable cost. Their strain to failure is however relatively low.

They are characterized by the epoxide, oxirane or ethoxylene group consisting of two carbon atoms single bonded to an oxygen atom. There are two types of epoxy, those made by a reaction with epichlorohydrin known as glycidyls and those made by peroxidizing olefins known as cycloaliphatics. The most commercially important resins are the epoxidized phenols or phenyl glycidyls ethers, particularly epoxidized bisphenol A known as the diglycidyl ether of bisphenol A (DGEBA). These have applications in sporting goods, automotive accessories and pipes. Curing agents include aromatic and aliphatic amines or anhydrides.

For high performance aerospace applications speciality epoxy resins and curing agents are used giving excellent elevated temperature

resistance and good mechanical properties. Most frequently used is tetraglycidyl methylene dianiline (TGMDA) cured with diamino diphenyl sulphone with or without a borontrifluoride amine catalyst.

Moisture absorption lowers the glass transition temperature limiting their in service temperature to 120°C or 80°C for toughened epoxy resins.

#### 2.2.2.2 Thermoplastic Resin Matrices

A limited use has been made of newly developed thermoplastic resin matrices in order to improve hot/wet properties and impact resistance. They also have higher strains to failure than the epoxies allowing the strain potential of the carbon fibres to be used to their full. They include materials such as polyetheretherketone (PEEK), polyphenylene sulphide (PPS), polyetherimide (PEI) and polyamideimide (PAI) which has partial thermosetting characteristics.

They do not absorb significant amounts of water but when non-crystalline may not be resistant to organic solvents. They can be remoulded by application of heat and pressure although this can cause thermal degradation and have potentially low fabrication costs.

A discussion of the development of suitable resin matrices for glass and carbon fibre reinforced plastics used in aircraft structures was given by Johnson [17] as summarized below.

Performance requirements were listed as a high glass transition temperature, moisture/environmental fluid resistance, good mechanical properties and smoke, fire, toxicity considerations. Manufacturing requirements included sufficient shelf life, sufficient although not

excessive tack - stickiness for self adherence of the prepreg layers, low emission of volatiles due to solvents or chemical reactions, adequate although not excessive flow under pressure, easy/economic cure cycles and health hazard considerations.

The controllable viscosity, low cure shrinkage, easy cure, high glass transition temperature, high mechanical properties and good chemical resistance of epoxy resins were stated to have led to their predomination as a suitable matrix material. High glass transition temperature thermoplastic materials such as polycarbonate, polyethersulphone and polyphenylene sulphide were said to suffer from low creep resistance, solvent sensitivity and processing problems although useful when blended with epoxies. For high temperature uses phenolic resins and polyimide resins were stated to be preferable although more difficult to process.

For effective cure with an absence of voids it was stated that the viscosity of the resin is required to be sufficient for flow whilst simultaneously permitting the application of pressure during moulding. Gelation or bleeding of the excess resin must not occur in advance of forming. A high void content was shown to be detrimental to the interlaminar shear strength.

Water absorption by the resin, at pores or along exposed fibre surfaces was stated to have a plasticizing effect with a decrease in the glass transition temperature, resin stiffness, interlaminar shear and compressive strengths and overall high temperature performance. The hydrothermal stability was given to be dependent on the choice of resin and hardener, highly cross-linked structures such as cyclo-

aliphatic resins and polyfunctional epoxides based on aromatic amines being particularly satisfactory.

Diglycidyl ether of bisphenol A or DGEBA epoxide was stated to be the standard matrix for many applications whereas the basis of virtually all aerospace matrices was given as tetraglycidyl 4,4' diamino diphenyl methane. When cured with diaminodiphenyl sulphone, DDS or dicydiamide, DICY a highly cross linked structure which has a high glass transition temperature is obtained. The resulting resin is more reactive with the fibre surface, more resistant to water attack and tougher than DGEBA. In the case of a DDS cure a boron trifluoride amine complex catalyst is generally added for a more manageable cure cycle.

For low modulus matrices failure of the matrix to sustain compressive loads results in microbuckling of the fibres on bending. This was found to be apparent for low modulus thermoplastic matrix matrices but not for higher modulus DGEBA matrices where stable tensile failure utilized the strength of the fibres.

In addition to the requirements of hydrothermal stability, high glass transition temperature and high modulus a high matrix tensile strength was shown to be important. This was found to determine failure in the short beam shear test with cracks initiated and generated through the cross plies and subsequently along the lamina interfaces. Failure, however, also depends on the presence of flaws and a better measure of performance was thought to be a toughness criterion or resistance to microcrack propagation. For example in low modulus matrices some deformation and flow occurs and there is a certain resistance to

interfacial crack propagation when compared to the rapid interfacial crack propagation of brittle matrices.

Examples of commercial resin systems were given as BSL 314, a DGEBA with polysulphone additive and catalytic hardener with later development to BSL 914, a polyfunctional epoxide resin blended with polyethersulphone thermoplastic to control flow during gelation and crystalline DICY as a latent curing agent. This gave a matrix with a high stiffness, high glass transition temperature, excellent shelf life and tack (stickiness) with a rapid tool time.

DDS cured DGEBA was shown to have a low viscosity at temperatures too low for rapid cure whereas a DICY hardened epoxy/thermoplastic blend produced a flat trend of viscosity with temperature at higher overall levels necessary to sustain the applied pressure without excessive flow. The latent DICY hardener produces rapid cure above its solution temperature in the epoxide of 135°C.

An examination of the BSL 913/914 microstructures showed how phase separation of the polysulphone occurred during gelation. Problems were also encountered with the DICY hardener crystals which were filtered out of the matrix by the fibres such that there was incomplete cure of the flash and excess crystals in the body of the composite. The partially dissolved DICY crystals were found to be surrounded by the polysulphone phase. The DICY crystals were observed to react exothermically to form melamine with evolution of ammonia at 205-210°C. The melamine undergoes a phase transformation in this range.

These microstructural effects were stated to be to the detriment of

the mechanical properties of the composite with cracks propagated in the polysulphone phase. In addition poor temperature control or small exotherms during post cure often led to blisters and delamination in satisfactorily moulded components due to the reactions of the undissolved DICY crystals. Uniformly dispersed DICY crystals 3-6  $\mu\text{m}$  across rather than the 1-150  $\mu\text{m}$  across used previously eliminated to a large extent the problems of hardener crystal filtration. In addition the undissolved crystals produced phase separation on a finer scale.

### 2.3 Manufacture

#### 2.3.1 Fibre Tows and Yarns

Continuous carbon fibre for the manufacture of structural composites is available in the form of bundles of single carbon fibre filaments, known as yarns or rovings and tows. The yarns typically consist of 10,000 filaments or less which may be twisted to enhance bundle integrity while the tows contain 10,000-160,000 filaments with generally no twist. The fibres are supplied on spools for further processing.

#### 2.3.2 Prepregs and Preforms

Prepregs and preforms are the fibre structure with or without prior resin impregnation respectively used as the starting material for further processing into the finished part.

##### 2.3.2.1 Tow Prepreg

This is a low cost form of prepreg consisting of a single tow or strand of fibre impregnated with matrix resin. It <sup>is</sup> suitable for low

cost manufacturing methods such as filament winding.

#### 2.3.2.2 Unidirectional Tape Prepregs

The most commonly used form of composite material for structural applications is the unidirectional prepreg tape. A number of carbon fibre tows are collimated and hot pressed into a substrate paper or release film onto which softened and partially cured thermosetting epoxy resin has been cast. The prepreg is calendered for uniform thickness and consolidation of the individual fibres.

Alternatively the thermosetting resin may be applied in the form of a solution with subsequent solvent removal.

The substrate paper or release film typically consists of a calendered paper coated with nontransferable, cured silicone coating. The tape is supplied in the form of spooled tapes, 25-1525 mm wide and 0.08-0.25 mm thick depending on the number of filaments incorporated.

Processing of the unidirectional tape prepregs is by hand lay-up, machine cut-pattern or automatic machine lay-up. The tapes are placed onto moulds at specific orientations required for the desired mechanical properties. The markedly anisotropic nature of the individual prepreg layers enables the component properties to be controlled through lamination of successive layers at various orientations. Automatic machine lay-up using robots provides the most efficient method having a low scrap rate, short processing time and consistent results. The aerospace industry is therefore investing in automatic tape layers in a switch from its hand-laying operations.

#### 2.3.2.3 Multidirectional Tape Prepregs

As an alternative to the unidirectional tape prepreg, multidirectional tape prepregs are available in which multiple plies of unidirectional tape are orientated to the designer's choice. This allows controlled anisotropy but at increased cost. Typical uses are for applications requiring neither exceptional drape nor formability but repeated fibre orientations where there would otherwise be substantial lay-up costs.

#### 2.3.2.4 Woven Fabric Prepregs

Woven fabric prepregs are one of the most widely used fibre reinforced resin forms. They offer flexibility in fabrication technique but at higher cost than other prepreg forms. However structures manufactured using woven fibre fabrics offer significant savings in labour costs due to a reduction in the time required to position the fibre-reinforced material.

Unidirectional, plain, basket, twill and satin weaves exist with plain weave the most common, consisting of one warp yarn interlaced with one fill yarn. It has a very stable construction due to the tightness of the weave and uniform properties in both directions. It is particularly resistant to shear movement. In unidirectional weaves heavy warp yarns interlaced with fine filling yarns cause the carrier weaves to vanish which enables a high density of strong unidirectional fibres to be obtained. The weave is obviously very unbalanced.

From basket weave in which the single yarn of the plain weave is replaced by two or more yarns through diagonal twill weaves to satin weaves in which one warp yarn interlaces over several and under one

filling yarn a decrease in stability but an increase in drapeability of the fabric is produced. Thus for the moulding of compound curves, as is often required in the aerospace industry, the satin weaves are particularly suitable.

#### 2.3.2.5 Non-Woven Fabric Prepregs

As an alternative to woven fabric prepregs non-woven fabrics with the warp and fill yarns chemically bonded are produced. The fabrics are stable due to the chemical bonding but do not easily conform to complex mould shapes.

#### 2.3.2.6 Prepreg Properties

Tack: This is a measure of the adhesion of a prepreg to tool surfaces or other prepregs. It is dependent on the apparent viscosity of the resin and controlled in order to facilitate lay-up operations. This involves monitoring the resin and resin volatiles contents, the advancement of the resin cure and the room temperature and humidity of lay-up.

Prepregs with excessive tack are difficult to handle and have uncontrollable amounts of resin removed when the release film is separated. Too little tack due to prepreg ageing, cure advancement or inappropriate inherent properties prevents the prepreg curing effectively.

Flow: Flow indicates the capability of the resin to consolidate the laminate plies and expel volatiles and reaction gases. It is measured as the amount of resin bled from a prepreg as it cures and depends on prepreg age, cure advancement, resin content and viscosity. Thickening

or thixotropic additives can be added in order to control flow.

**Gel Time:** Gel time is the time taken for the resin to gel or reach high viscosities when a prepreg is placed between heated platens. It depends on prepreg advancement.

**Drape:** Drape is a measure of the formability of a prepreg around contours. Tapes are typically less drapeable than fabric forms of prepreg.

#### 2.3.2.7 Multidirectional Reinforced Fabrics and Preforms

The mechanical properties of two directional reinforced fabrics are satisfactory in the direction of fibre reinforcement only. To overcome this problem multidirectional fabrics and preforms have been developed with additional fibre reinforcement in directions where the properties are otherwise dominated by the matrix. The aim is to achieve isotropic characteristics approaching that of metals.

A large variety of different multidirectional preforms exist. Three commonly used types are described below.

**Polar weave:** These preforms have radial, circumferential and longitudinal reinforcement. Geometries of near-net configuration are produced such as cylinders, cones and convergent/divergent sections. For non-axisymmetric shapes the preforms may be deformed, and if necessary slit prior to deformation, on metal dies which allows rectangular or leading edge configurations to be produced. The preforms are impregnated with resin for geometric stability. Typically the structures contain 50% volume fraction of fibre with equal

reinforcement in each of the three directions. If improved load carrying ability is required in any given direction then the reinforcement in that direction can be increased.

Orthogonal Weave: Reinforcement is in three mutually perpendicular directions producing 45-55% volume fraction structures. The reinforcement may be balanced or unbalanced for anisotropic properties and rather than the net configurations obtained using a polar weave blocks of the material are generally machined to shape. The weave pattern has a fine unit cell resulting in superior mechanical properties and erosion resistance to that obtained from polar weave structures.

Angle/Warp Interlock: These are thick two dimensional fabric structures consisting of up to eight fill yarn layers held together by warp yarns running diagonally from one surface to another. Warp stuffer yarns can be introduced for higher in-plane strength. For closed structures the fabric is joined resulting in a plane of weakness not found in their polar weave counterparts.

It should be noted that stitched fabric and needled felt as a class of three dimensional preform fabric have only marginally improved cross ply properties over two dimensional structures, due to the small volume fraction of fibre in this direction.

#### 2.3.2.8 Knitted Structures

Two dimensional and three dimensional knitted preforms can be produced achieving fibre volume fractions up to 40% [18]. Advantages are improved shear properties due to a substantial amount of fibre lying

at 90° to the fabric surface and a continuous flow of fibre with no fibre discontinuities and associated weakness at joints in the structure.

A substantial amount of the fibre lies in a loop configuration and the orientation of fibres can be compared to that of a random mat. However for use in composite parts it is possible to achieve as much as 50% of the fibres in a straight configuration.

Complex integral shapes are possible which can be converted to rigid structures using matched die moulds either with prior resin impregnation or resin injection into the mould. Young's modulus properties are comparable to, whilst tensile strengths are less than, that of a random mat. The tensile strengths are, however more variable in the former case.

#### 2.3.2.9 Hybridization

In any of the preceding prepregs and preforms the carbon fibres can be hybridized with other fibres such as aramid, glass and boron. This overcomes the inherent disadvantages of the carbon fibres and produces a lower cost composite. For example the aramid fibre, Kevlar 49 is used in conjunction with carbon fibres to improve fracture strength and impact resistance whilst decreasing the specific gravity. In general aramid and glass fibres have high strengths with greater strain-to-failures than graphite fibres at reduced cost. They are therefore often used in situations where improved impact resistance and vibrational damping characteristics are required.

### 2.3.3 Processing

#### 2.3.3.1 Open Moulding Techniques

Wet Lay-Up: The fibre form is laid on an open mould and the polymer resin worked in by hand.

Vacuum Bag Moulding: The mould is sealed from the atmosphere by a plastic sheet, evacuated to consolidate the material onto the mould and heat applied. As the temperature increases the viscosity of the resin decreases sufficiently to flow and wet the fibres prior to cure at higher temperatures. The method produces good quality flat and curved sheets and sandwich panels.

Pressure Bag Moulding: This method utilizes a female mould to which pressure is applied from outside by steam or air.

Autoclave Moulding: The vacuum bag and pressure bag techniques are combined by vacuum sealing an open mould with a plastic sheet and transferring the mould assembly to an autoclave for curing. The prepreg is cured under vacuum with carefully controlled externally applied temperature and pressure.

High quality parts with a low void content can be achieved. If a suitably sized pressure vessel is used such components can be very large. It is typically used for the processing of advanced composites for the aerospace industry.

#### 2.3.3.2 Closed Moulding Techniques

Matched Die or Compression Moulding: pressure and temperature are applied to a closed mould.

Resin Injection or Resin Transfer Moulding: the fibre preform is placed into a closed mould and low viscosity resin injected at various locations under pressure. The assembly is then heated to cure the resin.

Closed moulding techniques enable high fibre loadings, close dimensional tolerances and high surface finish.

#### 2.3.3.3 Filament Winding

Resin coated fibres are wound onto a rotating mandrel having dimensions matching those of the inside of the part to be made. The fibres are coated by passing them through resin baths prior to winding or by using pre-impregnated bundles of fibres. Cure is achieved by heating the mandrel.

Filament winding is predominately used for the manufacture of composite tubes, pipes and pressure vessels producing consistent quality parts at a low scrap rate and low capital cost.

#### 2.3.3.4 Braiding

Braiding involves the intertwining of two or more systems of yarns in the bias direction. In a similar manner to filament winding dry or prepreg yarns, tapes or tows are braided over a rotating mandrel. Lower volume fractions are achievable than with filament winding but the braiding is more conformable and shapes having more complex contours can be produced. The wound parts are noted for their ease of handling, joining, torsional stability, structural integrity and damage resistance. Two dimensional and three dimensional braiding

processes produce components that show less interlaminar failure than filament wound and tape-laid composites. In addition improved intralaminar properties are obtained to that of laminated composites.

#### 2.3.3.5 Pultrusion

Resin coated fibre bundles are pulled through a heated die to produce a partially or fully cured product of constant cross sectional area. Capital and labour costs are low and there is a low scrap rate as with filament winding. The parts have high strength and stiffness in the fibre direction.

#### 2.4 The Cure Process

Various studies of the cure process in these composites have been made by Loos and Springer [19-22]; Loos and Freeman [23]; Gutowski [24,25]; Dave, Kardos and Dudukovic [26,27], and Lindt [28].

##### 2.4.1 Model of Loos and Springer

Loos and Springer developed a model [9-11] describing the temperature distribution, degree of cure of resin, resin viscosity, void size, temperature and pressure inside voids and the residual stress distribution after cure. A computer code CURE based on this model predicted the resin flow during cure. Results were verified experimentally using Hercules AS/3501-6, and latterly [12] Fiberite T300/976 and T300/934 graphite epoxy prepreg tape.

The thermochemical model related the temperature distribution in the prepreg to degree of cure of resin and resin viscosity. Heat generated by cure reactions was included in the conservation of energy

equations and heat transfer by conduction was assumed.

The resin flow model considered flow parallel and normal to the plane of the composite separately. The normal flow was described by Darcy's Law for flow in a porous medium and the parallel flow, along the fibres, by a channel equation for viscous flow between parallel plates. Linear pressure gradients were assumed throughout.

The stress model used the generally accepted principles of classical lamination theory [9, 10] for calculating residual stresses and was based, in particular on the method of Tsai and Hahn. This assumes linear elastic material behaviour and for a symmetric laminate a constant in-plane curing strain,  $\epsilon_j^0$  given by

$$\epsilon_j^0 = a_{ij} \int_0^L Q_{ij} \epsilon_{ij} dz$$

In this equation  $a_{ij}$  is the in-plane compliance of the laminate,  $Q_{ij}$  and  $\epsilon_{ij}$  are the reduced stiffness matrix and the strains, respectively of the individual plies and  $L$  is the laminate thickness measured in the  $z$ -direction.

The residual stresses,  $\sigma_i$  in each ply then follow from,

$$\sigma_i = Q_{ij} (\epsilon_j^0 - \epsilon_j)$$

where the reduction in the strain due to the thermal expansion,  $\epsilon_j$  is given by

$$\epsilon_j = \alpha_j (T - T_a)$$

$T$  is the temperature in the ply at the end of cure and  $T_a$  is the

ambient temperature. A more complete definition of the various terms can be found in the text of Tsai and Hahn [9].

Finally the void model described the void pressures and void size distribution resulting from, changes in prepreg temperature and pressure, and vapour transport through the void/prepreg interface. Vapour transport was assumed by Fickian diffusion.

#### 2.4.2 Effect of Ply Stacking Sequence and Laminate Geometry on Resin Flow

Loos and Freeman [23] measured resin mass flow, both parallel and perpendicular to the tool plate for Hercules AS/3501-6 prepregs. The effect of prepreg dimensions and ply stacking sequence on resin flow was examined. Using these results and those of Loos and Springer it was concluded that ply stacking sequence has no significant effect on resin flow whereas increasing length to thickness ratio causes an increase in the ratio of resin flow parallel to the flow perpendicular to the tool plate. The resin flow model of Loos and Springer was stated to give accurate predictions of resin mass flow although further experiments were thought necessary to determine the accuracy of the of resin mass flow measurements.

#### 2.4.3 Resin Flow Assuming Time Dependent Pressure/Viscosity and a Visco-Elastic Prepreg

The model developed by Gutowski [24,25] investigated the resin flow during cure assuming time dependent pressure and viscosity as well as a visco-elastic prepreg. Springer considered viscous flow of the resin alone with no load carried by the fibres. However, at high fibre

volume fractions this predicted unsatisfactory pressure distributions [22].

More accurate results were obtained using the analysis of Gutowski which included an elastic response due to fibre-fibre interactions. Hence the prepreg was assumed to behave visco-elastically as modelled by a parallel, nonlinear spring/damper set. Such a set, known as a Kelvin or Voigt unit, is represented diagrammatically in Figure 1.

The resin is assumed to show a viscous response typical of a dashpot and the fibres an elastic response typical of a spring. In combination the applied stress,  $\sigma_{app}$  is given by

$$\sigma_{app} = G\epsilon + \eta\dot{\epsilon}$$

where,

$\sigma_{app}$  = applied stress (applied pressure)

G = elastic modulus of the spring

$\eta$  = viscosity constant of the dashpot

$\epsilon$  = strain in the spring

$\dot{\epsilon}$  = strain rate of the dashpot

#### 2.4.4 Three-Dimensional Resin-Flow Models

More recently Dave, Kardos and Dudukovic [26,27] developed a three-dimensional resin-flow model which does not decouple the flows in the different directions, as is the case in the Loos and Springer model. It is based on soil consolidation theory used to predict the compaction of, and flow of liquid in, a porous medium under an externally applied stress. The porous medium is assumed to behave as a

linear elastic spring and flow occurs due to escape of fluid across the sample boundaries. Non-linear pressure gradients are predicted in the vertical and horizontal directions.

Using Gutowski's data three regions of stress-strain behaviour were defined as follows:

- i) an initial linear region of immediate settlement.
- ii) an intermediate region of primary compression analogous to a rapidly stiffening spring.
- iii) a final region of secondary compression due to plastic flow and gradual adjustment.

All the above models assume the fluid flow to be described by Darcy's Law for flow in a porous medium. This ~~is~~ applies to laminar flow, that is for small flow rates with a low Reynolds' Number, as would be expected with the flow of epoxy resin through a fibre composite laminate. The fluid velocity,  $V$  is then given by the relation

$$V = - \frac{S}{\mu} \frac{dP}{dz}$$

where,

$S$  = apparent permeability of the medium

$\mu$  = viscosity of the fluid

$dP/dz$  = the pressure gradient

Consolidation of the plies is predicted from the top down. An approach of Lindt [28] models a "squeezing" flow based on lubrication theory.

Consolidation is then predicted about the horizontal mid-plane.

Experimental evidence supports the Darcy Law approach.

## 2.5 Residual Stress

There are a number of causes of residual stress during the processing of carbon fibre epoxy resin composite materials. There are two thermal effects. One is due to the temperature gradients generated within the manufactured part on cooling from the cure temperature. The second occurs as a result of the differential thermal expansion or contraction of the matrix and the fibre. There is also a moisture dilation effect caused by the absorption of water by the matrix and a matrix shrinkage effect which accompanies the cure reactions. The latter occurs as a result of the cross linking process and is irreversible. Here we are mainly concerned with the thermal effect.

Various methods have been used to analyse these residual stresses. Classical lamination theory is important at the macrolevel although it is restricted to elastic behaviour. Finite element modelling is often used and many mathematical models have been derived. A cross section of these different methods are reviewed below which for convenience has been divided into the macrostresses and the microstresses.

### 2.5.1 Macrostresses

Much of the investigations into the residual stresses occurring in carbon fibre reinforced plastics has been on a macroscopic level. Thus each ply in a laminate is taken as having homogeneous, although anisotropic properties. The residual stress distribution then depends

on the particular stacking sequence as adjacent plies at differing orientations restrain each other.

An early work of Novak and DeCrescente [29] considered the thermal residual stresses in  $[\pm 45_n/0_{2n}/\pm 45_n]$  flexibilized resin matrix and  $[0_n/90_{2n}0_n]$  unflexibilized resin matrix laminates (see nomenclature for laminate coding). A simple theory calculated the elastic deformations on cooling from a stress-free temperature (T) assuming anisotropic layer properties and strong bonding between layers, such that the contraction in each layer was constant.

By balancing the layer forces the thermal stress equation,

$$\sigma_1 = \frac{(\alpha_1 - \alpha_2) \Delta T E_1}{1 + E_1 V_1 / E_2 V_2}$$

was obtained where,

$\sigma$  = thermal prestress

$\alpha$  = thermal expansion coefficient

E = modulus of elasticity

V = volume fraction

$\Delta T$  = temperature change

and subscripts denote layer numbers. Poisson's effects, that is the strain response transverse to the direction of the prestress, were considered negligible.

The temperature dependence of the mechanical properties of the two laminate systems was measured experimentally. Thermomechanical behaviour typical of epoxy resin materials was observed. Glass

transition was apparent as a sharp decrease in transverse tensile modulus at approximately 165°F (74°C) for the flexibilized resin matrix laminate and 300°F (149°C) for the unflexibilized resin matrix laminate. A change in the transverse thermal expansion coefficient was also noted in this region.

The flexibilized resin matrix laminate was found to yield at temperatures in excess of 74°C (165°F) corresponding to a sharp decrease in the ultimate strength.

Average values were obtained of the properties taken below the glass transition temperature which were then used in the thermal strain equation. The properties of the cross plies were assumed constant with temperature as they were expected to be less temperature sensitive and to have a relatively insignificant effect.

The relevant <sup>0 & 45°</sup> ~~cross~~ ply properties were

$$\alpha_{45} = 6 \times 10^{-6} / ^\circ\text{F} \quad (11 \times 10^{-6} / ^\circ\text{C})$$

$$\alpha_0 = 0$$

$$E_{45} = 3 \times 10^6 \text{ p.s.i.} \quad (21 \text{ GPa})$$

$$E_0 = 25 \times 10^6 \text{ p.s.i.} \quad (172 \text{ GPa})$$

The flexibilized resin matrix laminates were cured at 350°F (177°C) and the unflexibilized resin laminates at 300°F (149°C). Fabrication stresses in the transverse (90 degree) direction were calculated, this being the direction in which the strength of the layers is lowest and the thermal expansion highest.

For the flexibilized resin matrix laminates a maximum value of the

yield stress of 120 p.s.i. (0.8 MPa) added to 1150 p.s.i. (7.9 MPa) obtained using the thermal strain equation and assuming cooling from 165°F (74°C) to room temperature produced a figure for the transverse stresses of 1270 p.s.i. (8.8 MPa).

Measurements were not obtained for the yield strength and ultimate strength of the unflexibilized resin matrix laminates but a change in the measured value of the thermal expansion coefficient at around 260°F (127°C) was thought to indicate the onset of plastic flow. The deviation from linearity between 260°F (127°C) and 300°F (149°C) was however considered insignificant and the transverse stresses were therefore calculated at 3080 p.s.i. (21.2 MPa) using the thermal strain equation, noting that this might be a slight overestimate.

The greater restraint of the 0 degree plies in the  $[0_n/90_{2n}/0_n]$  laminate configuration and the higher glass transition temperature of the matrix were thought to explain the higher prestress calculated in the case of the unflexibilized resin matrix system to that calculated for the flexibilized resin matrix system. It was noted that a high temperature resin matrix would require the composite to have higher transverse strengths so as to withstand the thermal stresses generated during cure.

Experimental values of thermal prestress in the flexibilized resin system were obtained by comparing the stress-strain curves for a  $[\pm 45_4/0_8/\pm 45_4]$  laminate and a stress-free unidirectional laminate. In both cases the tensile stress was applied 90° to the fibre direction of the 0° plies. The difference in the strains at which the two laminates failed would give the thermal prestrain in the 0° plies of

the  $[\pm 45_4/0_8/\pm 45_4]$  laminate. The thermal prestress was obtained by multiplication of the thermal prestrain by the transverse Young's modulus.

Failure of the unidirectional laminate occurred at a composite strain of  $3.4 \times 10^{-3}$  whereas a knee in the stress-strain curve of the multidirectional laminate at a composite strain of  $1.9 \times 10^{-3}$  indicated the onset of cracking in the  $0^\circ$  plies. Assuming equal strains in the  $0^\circ$  and  $45^\circ$  plies the difference of  $1.5 \times 10^{-3}$  would represent the thermal prestrain in the  $0^\circ$  plies. When multiplied by the transverse modulus a prestress of 1230 p.s.i. (8.5 MPa) was obtained compared with the 1270 p.s.i. (8.8 MPa) calculated.

Cracking in the flexibilized resin matrix system due to the calculated thermal prestress of 1270 p.s.i. (8.8 MPa) was unexpected when compared to the transverse tensile strength of 3000 p.s.i. (20.7 MPa). However results showing a reduction in transverse tensile strength with gauge length indicated it to be a defect sensitive property and at gauge lengths of 6 in. the transverse tensile strength was shown to fall to 1200 p.s.i. (8.3 MPa). This would explain the cracking observed in the flexibilized resin matrix laminates at measured prestresses of only 1230 p.s.i. (8.5 MPa). The higher thermal prestresses of 3080 p.s.i. (21.2 MPa) calculated for the unflexibilized  $[0_n/90_{2n}/0_n]$  laminates would make cracking more likely. It was noted that such cracking has been observed.

In conclusion it was suggested that to prevent thermal cracking either a flexible resin matrix be used or the transverse strength of the laminate increased. A flexible resin matrix has a lower glass

transition temperature and stresses are relieved through plastic deformation. However they can not be used at high temperatures, 165°F (74°C) being the upper limit of application for the laminates investigated by the authors. Alternatively an increase in the transverse tensile strength has been observed to eliminate thermal cracking. Treated rayon-based fibres manufactured by United Aircraft Research Laboratories have been strengthened in this way by improving the fibre resin bond.

#### 2.5.1.1 Classical Lamination Theory

Classical lamination theory [9,10] assumes the laminate to consist of perfectly bonded laminae with the bonds infinitesimally thin and non-deformable by shear. Displacements are then continuous across lamina boundaries and the laminate acts as a single layer of material.

According to the Kirchoff hypothesis for thin plates the shearing strains,  $\gamma_{xz}$  and  $\gamma_{yz}$  in the planes perpendicular to, and the direct strain,  $\epsilon_z$  in a direction perpendicular to, the middle surface of a thin laminate are assumed to be negligible.

For small strains deformations can be assumed to be linear elastic and an expression derived for the stresses in the kth ply, obtained, viz,

$$\{\sigma\}_k = [Q_{ij}]_k \{(\epsilon^0) + z(\kappa)\}$$

where,

$\{\sigma\}_k$  = the in-plane normal or shear stresses of the kth ply

$[Q_{ij}]$  = the transformed reduced stiffnesses of the kth ply

$\{\epsilon^0\}$  = the in-plane normal or shear strains of the laminate mid-plane

$z$  = co-ordinate in the thickness direction, measured from the

laminates mid-plane

$(\kappa)$  = the bending and twisting curvatures of the laminate mid-plane

By integrating the layer stresses through the laminate thickness expressions can be derived for the resultant laminate forces and moments.

Hahn and Pagano [30] analysed the curing stresses in unidirectional boron/epoxy laminates using classical lamination theory. A total stress-strain-temperature relation was formulated in which the thermal strains and stress-strain relations were required at the final temperature of interest only. The mechanical behaviour was assumed temperature dependent and elastic with the total strain separated into mechanical and thermal parts.

The total strain method when compared to ~~the~~ previously used incremental methods showed the latter to result in the omission of important interaction terms, namely coupling expansion, which is a function of both temperature and stress. This determines how the mechanical strain is dependent on temperature even at the same stress level such that compliances can vary with temperature. Examples were given showing a 35% increase in the prediction of curing stresses due to the inclusion of coupling expansion.

The analytical results using both the total strain method and the incremental method were compared to available experimental data for  $[0_2/45]_s$  and  $[0/60]_s$  laminates of Narmco 5505 boron/epoxy composite. These were tested using two different thermal cycles. The total strain method was found to be in better agreement with experimental results,

predicting higher values than were obtained using the incremental method. The difference was largely attributed to the coupling expansion term.

A later paper by Pagano and Hahn [31] similarly assumed elastic material behaviour and temperature dependent properties applied under the assumptions of classical lamination theory. With the introduction of the concept of a stress free temperature their predictions were compared to deflection measurements in unsymmetric angle-ply T300/5208 graphite/epoxy and glass/epoxy laminates.

The stress free temperature,  $T_0$  was defined as the highest temperature at which the material behaviour is elastic. Above this temperature the stresses developed in the constrained composite layers were assumed negligible as the matrix softens and becomes inelastic. An estimated value of  $T_0$  of 250°F was tested experimentally by monitoring the temperature dependent deflections and comparing predicted strains with those obtained using strain gauges. 250°F was found to be a reasonable estimate.

It was shown that for graphite/epoxy unidirectional composites the strain components,  $\epsilon_T$  and  $\epsilon_L$  could be approximated as follows

$$\epsilon_T(T) = (T - T_0)\alpha_T(T) \qquad \epsilon_L = 0$$

where,

$\alpha$  = coefficient of thermal expansion

and the suffixes T and L denote directions transverse to and parallel to the fibres, respectively.

The predictions compared favourably to deflection measurements obtained experimentally. Predictions were also made of stresses at first ply failure using maximum stress and maximum strain failure criterion with and without curing stress. Curing stress was calculated to reduce the laminate initial failure stress by a factor of approximately two.

Little evidence of such reduced failure levels was in part thought to be due to moisture absorption prior to mechanical testing. Dilation resulting from moisture contents of 0.27 wt% was found to nullify curing stresses and for lengthy periods of moisture absorption a beneficial prestress was implied.

#### 2.5.1.2 Moisture Effects

Hahn [32] considered the residual stresses due to moisture absorption by replacing the thermal strain term in the curing stress equations formulated by Hahn and Pagano [30] by a nonmechanical strain comprised of thermal and swelling parts. In this way the residual stresses due to moisture expansion were included. The predictions were compared to experimental results for  $[0_2/\pm 45]_s$  laminates in various material systems.

In the individual plies uniform distributions of the strain in the longitudinal direction were assumed as was the stress in the transverse direction. Rather than the simple relations used previously the strains were calculated using to the equations

$$\epsilon_L^N = (V_m E_{mL} \epsilon_{mL}^N + V_f E_{fL} \epsilon_{fL}^N) / (V_m E_{mL} + V_f E_{fL})$$

$$\begin{aligned} \epsilon_T^N &= V_m \epsilon_{mT}^N + V_f \epsilon_{fT}^N + V_m \nu_{mLT} \epsilon_{mL}^N + V_f \nu_{fLT} \epsilon_{fL}^N \\ &\quad - (V_m \nu_{mLT} + V_f \nu_{fLT}) \epsilon_L^N \end{aligned}$$

The superscript N denotes nonmechanical effects whilst the subscripts, f, m, L, and T denote - of the fibre, of the matrix, parallel to the fibres and transverse to the fibres, respectively. The equations assume transverse isotropy. The longitudinal (average) residual stress,  $\sigma_L^R$  was the only non-vanishing stress component where,

$$\begin{aligned} \sigma_{mL}^R &= V_f E_{fL} E_{mL} (\epsilon_{fL}^N - \epsilon_{mL}^N) / (V_m E_{mL} + V_f E_{fL}) \\ \sigma_{fL}^R &= - V_m \sigma_{mL}^R / V_f \end{aligned}$$

Close agreement was found with more sophisticated solutions [33], additional experimental data [34] and residual fringe patterns in glass\polyester composites [35].

Equations derived for predicting the strain due to moisture expansion made the assumption that swelling occurred when the moisture concentration exceeded a critical amount,  $H_o$ . Thereafter the swelling was assumed to increase in proportion to the additional moisture concentration. Limited data on the swelling of epoxies supported this.

Moisture absorption by the fibres was assumed negligible.

Experimental results obtained for the variation of strain with temperature for T300/5208 Graphite/Epoxy when thermally cycled twice gave marginally higher values of the transverse strain than predicted.

The shrinkage observed at the end of the first thermal cycle was thought to be due to moisture desorption. No further shrinkage was observed at the end of the second thermal cycle, which indicated this

to be representative of the true thermal expansion.

An initial moisture concentration of 0.29% was estimated from the observed shrinkage and equations for moisture loss compared favourably with their results.

Under-prediction of the transverse strain was thought to be due to an incorrect assumption that  $H_0 = 0$ , and indeed the equations for weight loss showed one third of the total moisture loss to occur during the second thermal cycle.

For the multidirectional laminate the residual stresses,  $\sigma_i^R$  were calculated according to the equation

$$\sigma_i^R = Q_{ij}(\epsilon_j^{oN} + z\kappa_j^N - \epsilon_j^N)$$

where,

$\sigma_i^N$  = ply residual stress

$Q_{ij}$  = ply stiffness matrix

$\epsilon_j^{oN}$  = central plane strain

$\kappa_j^N$  = central plane curvature

$z$  = co-ordinate in the thickness direction

$\epsilon_j^N$  = ply strain

Analyses were made and compared to experimental results for  $[0_2/\pm 45]_S$  laminates of boron/epoxy, boron/plastic, graphite/epoxy, graphite/plastic and glass/epoxy. The relevant graphite/epoxy properties were as follows

Fibre Volume fraction,  $V_f = 0.45$

Specific gravity,  $s = 1.54$

Cure temperature,  $T_o = 445^\circ\text{K}$

Longitudinal Young's modulus,  $E_L = 190 \text{ GNm}^{-2}$

Transverse Young's modulus,  $E_T = 7.10 \text{ GNm}^{-2}$

Shear modulus,  $G_{LT} = 6.2 \text{ GNm}^{-2}$

Major Poisson's ratio,  $\nu_{LT} = 0.10$

Longitudinal strength,  $X_L = 1115 \text{ MNm}^{-2}$

Transverse strength,  $X_T = 41.9 \text{ MNm}^{-2}$

Shear strength,  $X_{LT} = 61.5 \text{ MNm}^{-2}$

The corresponding curing stresses and curing strains were as detailed below, where the superscript T denotes a temperature effect.

In-plane curing strain, $-\epsilon^{oT} \%$	Experimental	Calculated
- $0^\circ$ direction	-0.018	-0.019
- $90^\circ$ direction	0.104	0.122
- $45^\circ$ direction	0.036	0.052
Normalised curing stresses ( $45^\circ$ plies)		
- transverse, $\sigma_T^R/X_T$		1.09
- shear, $\sigma_{LT}^R/X_{LT}$		0.11

These assumed a stress-free temperature equivalent to the curing temperature. Normalized curing stresses in the  $0^\circ$  plies were not as great as those shown in the  $45^\circ$  plies.

~~Over~~-prediction of the strains in the  $90^\circ$  direction for all composite systems except the boron/plastic was thought due to an actual stress-free temperature,  $T_o$  that was lower than the cure temperature. The

transverse and shear moduli at  $T_0$  were significantly lower than at room temperature.

Greater observed transverse strains than the calculated values for the boron/plastic system were thought due to the significantly higher value of the normalized transverse stress,  $\sigma_T^R/X_T = 4.09$ . This it was suggested could lead to microcracking and thus effect the macroscopic response.

The effect of ply orientation was also investigated for  $[0_2/\pm\theta]_s$  graphite/plastic laminates. Graphs of stresses and strains versus angle,  $\theta$  were presented as reproduced in Figures 2, a) and b). As before higher calculated stresses were obtained than those observed.

Assuming a stress free temperature of 177°C equivalent to the cure temperature these show that transverse failure is expected for  $\theta > 35^\circ$ . However a suggested value for  $T_0$  of 121°C [31] would imply failure at higher  $\theta$  values.

The results for all material systems indicated high transverse curing stresses greater than 50% of the transverse strength. However for the  $[0_2/\pm 45]_s$  laminates investigated failure of the 45° plies was found to have little effect on the properties in the 0° direction. More significant changes were noted on failure of the 90° plies in  $[(\pm 45)_2/90_4]_s$  and  $[0/90]$  laminates.

Acoustic emission studies of two  $[0/\pm 45/90]_s$  graphite/epoxy laminates preloaded at room temperature and 182°C, respectively showed delayed acoustic emission activity on subsequent loading.

For the room temperature sample this was apparent as the "Kaiser

effect" with acoustic emission negligible until the preload level was exceeded. The acoustic emission shown by the laminate tested at 182°C occurred at higher stress levels which when later tested at room temperature decreased to lower stress levels. This was thought to be due to the recovery of curing stresses absent at 182°C.

Finally it was noted that moisture contents as low as 0.4% to 0.5%, which are typical of laboratory conditions can eliminate curing stresses in graphite/epoxy laminates and thus effect ply failure.

Previously Pipes, Vinson and Chou [36] investigated the hygrothermal response of fibre-reinforced polymeric composites. Analyses were made for Thornel 300/Narmco 5208 graphite-epoxy laminates with  $[0/+45/-45]_s$  configurations. Simultaneous solution of the classical diffusion equation

$$D \frac{\partial^2 M}{\partial z^2} - \frac{\partial M}{\partial t} = 0$$

where

D = diffusion constant

M(z,t) = moisture concentration

and the point stress laminated plate equations predicted moisture concentration,  $\sigma_x$ ,  $\sigma_y$  and  $\tau_{xy}$  distributions through the laminate thickness assuming symmetric absorption, symmetric desorption and single surface absorption.

Material properties were used as follows

$$E_1 = 1.43 \times 10^{11} \text{ Pa (} 2.08 \times 10^7 \text{ p.s.i.)}$$

$$E_2 = 1.01 \times 10^{10} \text{ Pa (} 1.46 \times 10^6 \text{ p.s.i.)}$$

$$\nu_{12} = 0.31$$

$$G_{12} = 4.14 \times 10^9 \text{ Pa (} 6.00 \times 10^5 \text{ p.s.i.)}$$

$$\beta_1 = 0.00$$

$$\beta_2 = 6.67 \times 10^{-3} / \text{wt\%}$$

$$h_0 = 0.1397 \text{ mm (} 0.0055 \text{ in.)}$$

It was noted that their analysis was limited to infinite thin plate geometries and to cases where moisture diffusion is adequately described by the classical diffusion equation, although alternative diffusion solutions could be incorporated. The diffusion rate was assumed stress independent and no account was made for the degradation in matrix properties brought about by a reduction in the glass transition temperature associated with moisture absorption. This it was noted would cause a reduction in composite strength properties dominated by matrix characteristics for example shear, transverse tension and longitudinal compression.

#### 2.5.1.3 Effect of Curing Stresses on First Ply-Failure

The first ply-failure in T300/5208 graphite/epoxy laminates having  $[0/90_3]_s$ ,  $[\pm 45/90_2]_s$  and  $[0/\pm 45/90]_s$  orientations was monitored by Kim and Hahn [37] using strain gauge and acoustic emission techniques.

Cracks were also observed using photomicrography. Experimental data ~~was~~ <sup>was</sup> compared to analytical predictions obtained with and without residual stress present. The effect of residual stresses on first ply-failure was discussed.

First ply-failure was defined as the first occurrence of a crack

within a laminate subjected to, usually a tensile load. It was noted that residual stresses can lead to premature matrix cracking. The analytical predictions were based on the maximum stress criterion and scatter in data was analysed using a Weibull distribution.

To investigate the effect of residual stress two groups of laminates were examined. One group was completely dry and the other had a moisture content of 1.3%. Moisture dilation would be effective in relieving the thermal residual stresses. The following conclusions were made from their results. Acoustic emission has proved to be a very reliable method for detecting ply failures within composite laminates. Continuous monitoring enables accurate predictions of first ply-failure stresses. The strain gauge technique is only effective in detecting cracks occurring immediately under the gauge and the size of the strain gauge determines its sensitivity.

Predicted first ply-failure stresses were found to be smaller than those experimentally determined for the  $[0/90_3]_S$  and  $[0/\pm 45/90]_S$  laminates but larger for the  $[\pm 45/ ]_S$  laminates. This was irrespective of moisture content. However the in situ transverse strength determined from the calculated first ply-failure stresses of all the laminates was found to have a Weibull distribution comparable to that of the strength of a  $[90_8]$  laminate. It was surmised that barring any size effects the theory correctly predicts the curing stresses when the laminates are considered collectively.

Moisture absorption was observed to increase both the first ply-failure stress and the ultimate tensile strength of the laminates for which failure is fibre controlled, that is in the  $[0/90_3]_S$  and

$[0/\pm 45/90]_s$  configurations. The deleterious effect of ply-failures on laminate ultimate failure was noted.

The analysis used the model of Hahn and Pagano [30,31] for determining residual cure stresses in symmetric laminates. Elastic material behaviour was assumed throughout. The laminates were assumed <sup>to be</sup> in uniaxial tension having a load,  $N_x$  applied in the 0-degree direction. Stresses were then calculated in the 90-degree plies, these being the weakest.

The maximum stress failure criterion states that a unidirectional ply fails whenever any one stress component reaches the corresponding uniaxial strength. No interactions are taken to occur between the different stress components, these effects only being significant for stress fields in which all the stress components are close to their respective ultimate values.

For the 90° plies investigated failure was predicted when  $\sigma_2$  reached the transverse strength,  $X_T$  producing a stress resultant

$$N_x^{FPF} = \frac{A_{xx}A_{yy} - A_{xy}^2}{Q_{22}A_{yy} - Q_{12}A_{xy}} (X_T - \sigma_2^R)$$

where,

$N_x^{FPF}$  = laminate stress resultant due to applied load at first ply-failure

$\sigma_2^R$  = the tensile curing stress

Q = reduced ply stiffness

A = laminate stiffness

- 1 denotes the fibre direction in the 90° plies
- 2 denotes the transverse direction in the 90° plies
- x denotes the loading direction
- y denotes the direction perpendicular to loading

Laminates were fabricated according to the manufacturers recommended cure cycle and tested under constant uniaxial tensile loading of 9 N/sec. using strain gauge and acoustic emission techniques. 5.08 cm and 0.635 cm long strain gauges were used. The axial strain and acoustic emission counts were plotted against the applied load and for large increases the specimens were unloaded and examined under a microscope for cracks. Increasing load levels were applied until several cracks were found. The specimens were subsequently tested to ultimate failure.

The following thermo-elastic properties for the lamina were used in the analysis. A stress-free temperature of 121°C was assumed as opposed to the cure temperature of 177°C.

Longitudinal Modulus, $E_L$ (GPa)	152.8
Transverse Modulus, $E_T$ (GPa)	11.24
Shear Modulus, $G_{LT}$ (GPa)	7.10
Major Poisson's Ratio, $\nu_{LT}$	0.33
Longitudinal Curing Strain	$0.267 \times 10^{-3}$
Transverse Curing Strain	$-2.167 \times 10^{-3}$

Photomicrographs showed typical 90° cracks to occur through the entire thickness of these plies although they were not observed to be straight. The residual stress,  $\sigma_2^R$  in the wet laminates was assumed to be zero and for the dry laminates was calculated according to the

equation,

$$\sigma_i^R = Q_{ij} A_{jkl}^{-1} N_k^T - Q_{ij} \epsilon_j^T$$

and the data above.  $N_k^T$  are the stress resultants due to the thermal strains,  $\epsilon_j^T$  (as measured from the stress-free state) and the superscript  $^{-1}$  denotes matrix inversion.

The underestimate of the first ply-failure stresses for the dry laminates could not be accounted for, although in the case of the wet laminates it was thought to be due to the presence of compressive residual stresses at the employed moisture content of 1.3%. This conclusion was not supported by the results for the  $[\pm 45/90_2]_S$  laminate in which case the theory overestimated the first ply-failure stresses. Indeed lower experimental first ply-failure stresses were observed for the wet specimens than the dry.

These conflicting results were resolved by converting the first ply-failure stresses to stresses within the  $90^\circ$  plies using the equation.

$$\sigma_2 = \frac{Q_{22} A_{yy} - Q_{12} A_{xy}}{A_{xx} A_{yy} - A_{xy}^2} N_x \sigma_2^R$$

The resulting in situ strengths of the  $90^\circ$  ply,  $\sigma_2$  were combined and fitted by a Weibull distribution of the form

$$R_{(X)} = \exp [-(X/X_0)]^\alpha$$

where,

$$R_{(X)} = \text{probability of the strength being greater than or equal to } X$$

$X_0$  = a scale parameter

$\alpha$  = a shape parameter

This compared well with results obtained for the  $[90_8]$  laminate irrespective of moisture content. Both the shape parameter and the scale parameter were observed to decrease in the presence of moisture corresponding to a reduction in transverse strength.

From the results it was concluded that absorbed moisture increases the first ply-failure stresses through relaxation of residual stresses and although the matrix controlled properties are degraded this delayed first ply failure leads to an increase in ultimate tensile strength for those laminates in which ultimate failure is fibre controlled.

The decrease in first ply-failure stress for the  $[\pm 45/90_2]_s$  laminate remained unexplained although the reduction in ultimate tensile strength was expected since ultimate failure is matrix controlled. Finally it was noted that the failed dry specimens showed more extensive cracking than the wet and gave noisier acoustic emission counts.

#### 2.5.1.4 Geometric Non-Linearities

Hyer [38,39] investigated the warping of graphite-epoxy (T300/5208) unsymmetric laminates. Numerical results were based on the following material properties.

$$E_1 = 181 \text{ GPa } (26.2 \times 10^6 \text{ p.s.i.})$$

$$E_2 = 10.3 \text{ GPa } (1.49 \times 10^6 \text{ p.s.i.})$$

$$\nu_{12} = 0.28$$

$$G_{12} = 7.17 \text{ GPa } (1.04 \times 10^6 \text{ p.s.i.})$$

$$\alpha_1 = -0.106 \times 10^{-6}/^{\circ}\text{C } (-0.059 \times 10^{-6}/^{\circ}\text{F})$$

$$\alpha_2 = 25.6 \times 10^{-6}/^{\circ}\text{C } (14.2 \times 10^{-6}/^{\circ}\text{F})$$

Classical lamination theory was extended to include geometric non-linearities and it was shown how in thin laminates (relative to their in-plane dimensions) deviations from classical lamination, could be accounted for.

The results showed that below a critical thickness to in-plane dimension ratio a unique saddle shape as predicted by classical lamination theory was found to be valid. However above this critical value a triple solution consisting of an unstable saddle shape and two stable cylindrical shapes was obtained. This explained much of the anomalous behaviour observed in thin laminates. In later work [40] Hyer developed the theory by using more sophisticated polynomials particularly for approximating the in-plane displacements. Although the original theory accurately predicted the warping due to out of plane deformation the later theory was thought to be more realistic in modelling the in-plane displacements not apparent in observations of warping.

Following on from the work of Hyer, Hahn and Hwang [41,42] examined the warping of unsymmetric graphite-epoxy (T300/5208) and Kevlar 49-epoxy laminates.

T300/5208 laminate material properties were used as follows

$$E = 0.0569 \qquad \nu = 0.28 \qquad h = 1 \text{ mm}$$

$$\epsilon_T = -3.994 \times 10^{-3} \qquad \epsilon_L = 0.0165 \times 10^{-3}$$

$E$  and  $\nu$  are the transverse-to-longitudinal modulus ratio and the major Poisson's ratio, respectively. The  $\epsilon$ 's are the nonmechanical strains and  $h$  is the laminate thickness. The strains in the transverse and longitudinal directions are denoted by the subscripts, T and L, respectively.

Warping generally as predicted by Hyer was observed although measured curvatures were somewhat greater, most noticeably in the case of the small panels. This was suggested to be due to boundary effects not allowed for in the theory. For the small panels it was <sup>noted</sup> ~~shown~~ that the predictions of Hyer reduce to classical lamination theory and how by setting one curvature to zero in classical lamination theory a good approximation for the deformation of large panels is obtained.

In addition the effect of surface adsorption, postcure, long-term exposure and cure-cycle on warping were investigated together with the effect of residual stress on ply-failure. Their findings are summarized below.

Measurements of the weight gain occurring during the first 30 minutes after taking the samples from the autoclave showed the uptake of moisture to stabilize more quickly than would be predicted by Fickian diffusion. This led to the conclusion that the moisture was being adsorbed onto the sample surfaces.

Postcure of the samples at 177°C for 1 hour and 2-5 hours caused the curvatures in the larger panels to be reversed. The samples were thought to flatten at the cure temperature and subsequently on cooling to flip over into the other unstable configuration. This is in

agreement with the predictions of Hyer. The small samples showed no significant change in the larger curvatures but the smaller curvatures were observed to increase. This was thought to be due to moisture desorption. Measurements of the weight loss supported this conclusion.

Conditioning of the samples at 75°C in a vacuum for 220 days caused no significant change in the deflections indicating that there was no relaxation of the residual stresses at this temperature. Samples stored in the laboratory for a period of eight months showed changes in deflection which were dependent on the ambient relative humidity.

Comparison of the curvatures obtained using various cure cycles showed a prolonged gelation <sup>below</sup> the cure temperature to reduce the residual stresses.

The residual stress in the transverse direction of  $[0/90/0/90]_s$  Kevlar 49/epoxy panels was calculated using laminated plate theory to be 15.9 MPa. This it was observed is significantly higher than the transverse tensile strength of 8.9 MPa and cracking would be expected. The average crack densities in the surface plies of actual  $[0/90/0/90]_s$  Kevlar 49/epoxy laminates were measured experimentally. The samples were initially left in the laboratory and then dried in a vacuum at 75°C with the crack density and weight loss measured intermittently. The crack density was found to increase with the general trend of the weight loss. However the fact that the samples were originally dry on leaving the autoclave led to the conclusion that some of the residual stress generation was time dependent. This it was proposed was as a result of visco-elastic behaviour and/or additional cure reactions subsequent to processing.

### 2.5.1.5 Edge Effects

At laminate free edges the assumptions of classical lamination theory imply boundary tractions which cannot exist. Alternative methods of analysis have shown that the stresses are non-uniform and significant interlaminar shear stresses develop in a region an order of the laminate thickness from the free edge.

Puppo and Evensen [43] investigated the interlaminar shear stresses in laminates under conditions of generalized plane stress. The laminate was considered comprised of two anisotropic layers separated by a single isotropic adhesive layer. Generalized plane stress was assumed for the anisotropic layers with interlaminar shear stresses developed in the isotropic layers due to the differing thermomechanical behaviour of the adjacent anisotropic layers.

Differential equations of equilibrium were solved for an infinite and finite laminate under uniform deformation in the x-direction. For the finite laminate the stresses,  $\sigma_x$ ,  $\sigma_y$  and  $\tau_{xy}$  were found to be proportional to the specific deformation and the interlaminar shear stresses,  $\tau_{zx}$  and  $\tau_{zy}$  identically zero. More complex expressions were derived for the finite laminate and a value was obtained of the interlaminar shear stress,  $\tau_{zx}$  ~~proportional to~~ <sup>which was dependent on</sup> the strip length,  $b$ , and approaching <sup>ed</sup> a finite value as  $b$  tended to infinity.  $\tau_{zy}$  was found to be zero.

The results differed from those of classical lamination theory in the prediction of interlaminar shear stresses in the finite laminate and non uniform stresses in each layer.

Pipes and Pagano [44] examined the stresses developed in symmetric graphite-epoxy resin laminates under uniform axial extension. Reduced elasticity field equations were derived and solved using a finite difference technique in four layer, finite width,  $\pm\theta$  angle ply laminates. Results were obtained showing differences from the predictions of classical lamination theory at the laminate free edge and in the prediction of interlaminar shear stresses.

Typical high modulus graphite-epoxy unidirectional material properties were used as follows

$$E_L = 20 \times 10^6 \text{ p.s.i. (138 GPa)}$$

$$E_T = E_Z = 2.1 \times 10^6 \text{ p.s.i. (14.5 GPa)}$$

$$G_{LT} = G_{TZ} = G_{LZ} = 0.85 \times 10^6 \text{ p.s.i. (5.9 GPa)}$$

$$\nu_{LT} = \nu_{TZ} = \nu_{LZ} = 0.21$$

Classical lamination theory assumes a state of plane stress. However for layers at different orientations boundary tractions on the free edge are implied which cannot exist. By drawing a free body diagram for each layer it was shown that to balance the non-zero couple resulting from the in plane shear stresses an equilibrating couple supplied by the interlaminar shear stress was required.

Results were also compared to those of Puppo and Evensen [43]. This proved favourable for  $\sigma_x$  and  $\tau_{xy}$  but, rather than the singularity in the interlaminar shear stress distribution,  $\tau_{zx}$  predicted at the free edge, the approximate Puppo and Evensen formulation predicted a finite interlaminar shear stress.

Pagano and Pipes [45] examined the influence of stacking sequence on

boundary layer effects and their significance to laminate strength. Examples were given in  $[\pm 15/\pm 45]$  boron-epoxy [46],  $[0/90]$  glass-epoxy [47] and quasi-isotropic glass and boron-epoxy laminates and coupons [48]. Free body diagrams were considered for angle ply laminates with  $15^\circ$  and  $45^\circ$  layer orientations. The stress distributions predicted by classical lamination theory are independent of stacking sequence and therefore do not explain their observations.

Results were calculated for boron-epoxy laminates under uniform axial extension with a constant temperature rise  $\Delta T$ . At the free edge interlaminar normal stresses and to a lesser extent interlaminar shear stresses were shown to be instrumental in precipitating delamination. As a result there is a degradation in strength under static and fatigue loading. For optimum protection against delamination it was suggested that stacking sequences should be chosen in order to satisfy one or other of the following considerations. That is either those resulting in the smallest values of both the interlaminar shear stresses (whilst avoiding the introduction of interlaminar normal tension) or those producing the highest values of interlaminar normal compression. The latter minimizes the detrimental effect of high interlaminar shear stresses.

The predictions are dependent on the lamination theory solution for  $\sigma_y$  and therefore the residual thermal stresses have a significant effect on the resulting interlaminar stress distributions. The results were found to be in agreement with the observations of Foye and Baker [46] and Kaminski [47].

Another mechanism thought to explain the dependence of strength on

stacking sequence was the constraining influence of adjacent layers on the propagation of a crack in a given layer or at a given interface. This has been studied in more detail by Chen and Sih [49] who examined the stress field local to a finite crack within a laminate under conditions of anti-plane strain, that is for displacements in the out-of-plane direction only. For these conditions there are only two non-vanishing stress components, namely  $\tau_{xz}$  and  $\tau_{yz}$ . Previous analyses of cracks at interfaces assuming conditions of plane strain were thought to be inadequate in that no estimate was made of the energy release rate due to debonding and that the theory could not be extended to multilayered systems. Under conditions of anti-plane shear no allowance needs to be made for this energy release rate. The stress singularity was proportional to  $1/\sqrt{r}$ , where  $r$  is the radius from the crack tip.

A model was developed for a crack within a four-layer composite the outer layers of which were assumed to have average properties of the composite as a whole. Solutions were obtained for identical inner layer properties and identical properties in every other layer. For the former problem limiting cases of a free edge and a clamped edge at the interface between the dissimilar materials were considered as well as a inner layer height approaching zero, thus modelling an adhesive layer. Results were given showing the variation of the normalized stress intensity factor,  $\phi(l)$  with the ratio of the two shear moduli and the inner layer height to half crack length ratio,  $h/a$ . In the case of the identical inner layer problem softer and harder outer layers caused  $\phi(l)$  to increase and decrease, respectively the effect being less apparent as the  $h/a$  ratio increased.

For the dissimilar inner layers problem the results showed the lamination to lower the intensity of the stress field which would in part explain why a layered composite can sustain higher loads. The normalized stress intensity factor decreased sharply from 1 to a minimum at  $h/a$  approximately equal to  $1/3$  and thereafter increased more gradually approaching a value of 1 the value for a single phase material again. This applied for all ratios of the shear moduli and the greater the ratio the more apparent the effect. It would suggest that the growth of an interface crack can be stable or unstable depending on the size of the crack relative to the layer thickness.

Following on from the work of Puppo and Evensen [43] and Pipes and Pagano [44] Isakson and Levy [50] determined the elastic behaviour of a four-ply  $\pm 45^\circ$  laminate under conditions of generalized plane strain. A finite element method considered triangular membrane and finite thickness shear elements representing the fibre-bearing layers and interlayers, respectively. The stiffness matrices assumed uniform *axial* strains with  $\sigma_x$ ,  $\sigma_y$  and  $\tau_{xy}$  stresses being generated in the fibre layers and  $\tau_{zy}$  stresses in the interlayers.

The method was applied to a flat rectangular plate loaded in uniaxial tension with mesh refinement along the loaded and side edges. Calculated stress distributions were given for  $\sigma_y$ ,  $\tau_{xy}$  and  $\tau_{zy}$  using the following material properties

$$E_{11} = 30.7 \times 10^6 \text{ p.s.i. (212 GPa)}$$

$$E_{22} = 3.5 \times 10^6 \text{ p.s.i. (24 GPa)}$$

$$\nu_{12} = 0.283$$

$$G = 1.0 \times 10^6 \text{ p.s.i. (6.9 GPa)}$$

$$h_o = 0.005 \text{ inch (0.127 mm)}$$

A good fit was obtained with the results of Pipes and Pagano [44].

Latterly [51] Pipes and Pagano developed an approximate solution to their previously derived displacement-equilibrium equations for finite-width laminates under uniform axial strain. The approximate solutions were found to correspond well with the exact solutions already obtained for four layer angle-ply symmetric laminates which, due to the economy of the method of solution were then extended to eight layer laminates. The approximation was as a result of a violation of equilibrium in the y- and z-directions on the assumption that the stresses  $\sigma_y$  and  $\sigma_z$  are negligible, as found in the exact solutions. Otherwise the six equations of compatibility were complied with.

The results showed that the interlaminar stress distribution for the eight layer laminates could be predicted from the results of the four layer problem. The approximate solution indicated singularities in  $\tau_{xz}$  at the free edge whereas the exact solution attained a finite value. In the case of the 45 degree angle ply laminates the boundary-layer thickness was found to be equal to the laminate thickness.

Wang and Crossman [52] investigated the thermally induced stresses in finite width, symmetric laminates resulting from uniform temperature changes. In particular the singular nature of the stresses at the interface near the free edge region were examined. How these edge effects influence laminate response under thermal loading was discussed. The work followed on from a previous paper [53] in which

the authors considered the stresses developed under uniaxial tension. This analysis used the finite element technique for conditions of generalized plane strain and assumed classical elasticity theory. The stresses were calculated according to the equation

$$\sigma_i = C_{ij} (\epsilon_j - \alpha_j \Delta T - \beta_j \Delta H) \quad i, j = 1, 6$$

where  $C_{ij}$  is the stiffness matrix,  $\Delta T$  is a change in temperature and  $\Delta H$  is a change in water content.

Stresses were modelled in high modulus graphite-epoxy  $[0/90]_s$ ,  $[90/0]_s$  and  $[\pm 45]_s$  laminates using 392 constant strain elements having 226 nodes and comprising the first quadrant of the laminate cross section. Refinement of the mesh at the interface edge region was by 224 triangular elements equivalent to 15% of the total field. The model had the capability of modelling the effects of both a constant hygrothermal exposure, as defined by the temperature difference,  $\Delta T(y, z)$  and a water content difference,  $\Delta H(y, z)$ , and an axial tensile force,  $F_x$ .

Results were given for a temperature increase of  $1^\circ F$  <sup>(1.8°C)</sup> assuming no applied force or hygrothermal exposure. Transversely isotropic material properties were used as given by Pipes and Pagano [44] together with longitudinal and transverse thermal expansion coefficients of  $0.2 \times 10^{-6}/^\circ F$  ( $0.36 \times 10^{-6}/^\circ C$ ) and  $16 \times 10^{-6}/^\circ F$  ( $28.8 \times 10^{-6}/^\circ C$ ), respectively. The thickness to width ratio of the laminates was 1:4. An edge effect was found to exist to a greater depth than that predicted under uniaxial tension.

At the centre of the laminates stress values closely approximated

those predicted by classical lamination theory. For the cross-ply laminates equal but opposite in-plane normal stresses,  $\sigma_x$  and  $\sigma_y$  are predicted in successive layers, these being tensile in the fibre direction and compressive transverse to this direction. There were no in-plane shear stresses. For the angle-ply laminate equal but opposite in-plane shear stresses,  $\tau_{xy}$  are predicted in successive layers and no in-plane normal stresses. Since the laminates are balanced equal strains,  $\alpha_x$  and  $\alpha_y$  are predicted in the x- and y-directions.

Profiles of stresses calculated across the width of the laminate at the cross-ply laminate mid-planes showed, at the free edge the  $\sigma_x$  stresses to increase to values 20% and 43% greater in the  $[0/90]_s$  and  $[90/0]_s$  laminates, respectively than predicted by classical lamination theory.  $\sigma_y$  decreased to zero at the free edge as required by the boundary conditions.

Significant interlaminar stresses were found to develop towards the free edge. At the  $[0/90]_s$  laminate mid-plane the interlaminar normal stress,  $\sigma_z$  increased from zero at the centre of the laminate and after a initial tensile region away from the laminate centre, developed significant compressive stresses at the free edge. Interlaminar shear stresses  <sup>$\tau_{yz}$</sup>  along the  $0^\circ - 90^\circ$  interface increased from zero at the centre of the laminate to a maximum close to the free edge and thereafter decreasing <sup>ed</sup> ~~ing~~ to zero as required by the boundary condition.

In the case of the cross-ply laminates graphs of the stresses through the laminate thicknesses, close to the free edge, also showed stress variations. The variation in  $\sigma_x$  was small within each layer whereas singularities were found to develop in  $\sigma_z$  and  $\tau_{yz}$  at the  $0^\circ - 90^\circ$

interface, these being compressive for  $\sigma_z$  in the  $[0/90]_s$  laminate and tensile for the  $[90/0]_s$  laminate.  $\sigma_z$  was generally tensile in the  $0^\circ$  layers, compressive in the  $90^\circ$  degree layers and zero at the laminate top surface as required by the boundary conditions. Their effect was most significant at the laminate mid-planes.  $\tau_{yz}$  was concentrated around the singularity at the ~~laminate mid-plane~~  <sup>$0-90^\circ$  interface</sup> with values approximately zero elsewhere. The singularities were evident to a depth of four times the laminate thickness. No singularities were calculated at the laminate mid-planes.

The profiles of the interface stresses for the two cross-ply laminates had a similar form although the stresses were of an opposite sign.

For the  $[\pm 45]_s$  angle-ply laminate the  $\tau_{xy}$  stresses decreased to zero along the laminate mid-plane whilst small compressive  $\sigma_x$  stresses and interlaminar tensile  $\sigma_z$  stresses were developed towards the free edge. Significant interlaminar shear stresses,  $\tau_{xz}$  and smaller interlaminar normal stresses ( $\sigma_z$  stresses), equivalent to the  $\sigma_x$  stresses at the laminate mid-plane, were developed towards the free edge along the upper interface. Maximum compressive and tensile values of  $\tau_{xy}$  and  $\sigma_x$  were evident close to the free edge  $\tau_{xy}$  attaining values 33% greater than those predicted by classical lamination theory.

Through thickness distributions close to the free edge showed the  $\tau_{xz}$  stresses to be concentrated at the upper interface where a singularity was thought to exist. Similar profiles of  $\sigma_x$  also indicated a tensile singularity at the upper interface and away from the interface compressive stresses.

The above stress distributions were shown to effect the predicted thermal expansion coefficients and displacements of the laminates. Significant differences were calculated at the free edge which decreased with increasing laminate width-to-thickness ratios.

Deviations of thermal strains from that predicted by lamination theory were determined by Titomanlio and Piccarolo [54] using estimates of the interlaminar shear stress distribution calculated on the basis of free body diagrams. Shear deformation in the thickness direction, which is neglected in lamination theory was shown to occur if the single laminae have different thermal expansion coefficients along their principal in-plane directions. The deformation occurs at the laminate edge where the normal stress component reduces to zero.

Considering the edge effects it was estimated using the results of others that tangential shear stresses,  $\tau_{zy}^n$  exist in a region an order of the laminate thickness from the free edge. On the basis of free body diagrams it was shown that the shear stresses when integrated over this region can be equated to the product of the classical lamination theory prediction of the normal stress and the lamina thickness. As a first approximation it was assumed that the shear stresses in this free edge zone had a constant value. The equations for  $\tau_{zy}^n$  determined through the free body diagrams were then related to the shear strain. Integration of the expression yielded an equation for the displacement of the external, free surface, edge with respect to the other edge of the lamina. These lamina displacements when referred to the sample width and summed over the laminate thickness produced an estimate of the surface strain deviation,  $\epsilon^d$ , (over that thickness) from the prediction of classical lamination theory.

A similar method was used to determine the effect of stacking sequence on the shear stress distribution. The shear strains are significantly influenced by the stacking sequence arrangement due to the anisotropy in the individual laminae. Variation of the shear strain with the coordinate in the thickness direction was presented qualitatively for  $[90/90/0/0]_s$  and  $[90/0/0/90]_s$  laminates. Zero surface strain deviation was predicted in the  $[90/0/0/90]_s$  laminate but significant amounts occurred in the  $[90/90/0/0]_s$  laminate.

Predictions were compared to experimental results for two quasi-isotropic carbon fibre reinforced epoxy resin laminates having the following stacking sequences: Laminate 1 -  $[\pm 18/\pm 72]_s$  and Laminate 2 -  $[0/90/0/90]_s$ . The agreement was reasonable with the correct order of magnitude for the strain deviation predicted in each case.

Stango and Wang [55] compared results obtained using classical lamination theory and a finite element method for a uniform temperature decrease,  $\Delta T$ . Numerical examples were given for quasi-isotropic  $[0/90/\pm 45]_s$  graphite epoxy laminates. The effect of laminate stacking sequence on the resulting stress distributions and their significance to the deformation and failure behaviour were examined, particular emphasis <sup>was</sup> ~~being~~ given to the interlaminar shear stress distribution.

The finite element analysis used a mesh of the first quadrant of the laminate cross section comprising 40 elements and material properties as given by Wang and Crossman [52]. Results obtained using classical lamination theory were first compared to the finite element results at

ply interfaces for the in-plane stresses,  $\sigma_x$ ,  $\sigma_z$  and  $\tau_{xz}$  assuming a  $[0/90/45/-45]_s$  laminate. Significant differences were noted, the stresses being non uniform across the laminate width with large stress gradients at the free edge. The interlaminar stresses,  $\sigma_y$ ,  $\tau_{zy}$  and  $\tau_{xy}$  not predicted by classical lamination theory were then investigated using the finite element method of solution in  $[0/90/45/-45]_s$  and  $[45/-45/0/90]_s$  laminates. Tensile interlaminar normal stresses,  $\sigma_y$  were noted at the free edge of all but the -45/0 interface.

Delamination occurring as a result of these tensile interlaminar stresses are detrimental to the strength of the laminates and it was suggested by careful laminate selection properties could be improved.

The effect of laminate stacking sequence on the interlaminar normal stress,  $\sigma_y$  was subsequently examined in  $[0/90/45/-45]_s$ ,  $[0/45/90/-45]_s$  and  $[45/0/90/-45]_s$  laminates. A change in direction of the interlaminar normal stresses was observed close to the free edge of the 45/0 and 0/45 interfaces of the  $[45/0/90/-45]_s$  and  $[0/45/90/-45]_s$  laminates, respectively producing a compressive value at the free edge of the former. Otherwise all values were tensile.

Investigations were made into the residual stresses in APC-2 cross-ply laminates by Jeronimidis and Parkyn [56]. Values were predicted according to classical lamination theory and compared to experimental results. The predictions were found to be accurate provided changes in the thermo-elastic properties with temperature were taken into account.

APC-2 is a pre-impregnated tape consisting of a thermoplastic PEEK matrix reinforced with continuous, unidirectional AS4 carbon fibres.

It is supplied by ICI plc. Thermoplastic matrices differ from thermosetting resin matrices requiring higher cure temperatures (in this case 380°C), and having well defined glass transition temperatures.

The laminate was cured under pressure according to the manufacturers recommended cure cycle. Slow cooling at 3°C/min. gave a crystallinity of 50% in the matrix. Thermo-elastic properties measured between room temperature and approximately 300°C were found to compare well with those published by ICI plc. Representative values, taken above and below the glass transition temperature of 143°C, were used in the analysis and a measured stress free temperature of 310°C was found to correspond to the peak recrystallization temperature of APC-2 cooled at 3°C/min.

Residual stresses and curvatures were predicted, incrementally for symmetric  $[90_2/0_4/90_2]$  and non-symmetric  $[0_n/90_n]$  laminates, step one being taken above the glass transition temperature between 310°C and 143°C and step two being taken below the glass transition temperature between 143°C and 20°C. The resulting stress distribution showed tension in the 90° plies and compression in the 0° plies. The predominating effect of the fibres in the 0° plies was to cause these layers to contract less and therefore restrain the adjacent 90° plies.

The transverse tension of 42 MPa predicted in the 90° plies of the  $[90_2/0_4/90_2]$  laminate was found to correspond to 50% of the transverse tensile strength. By comparison a value of 45 MPa measured by Flagg and Kural [57] in T300/934 carbon fibre/epoxy resin cross-ply laminate approximately equalled the transverse tensile strength. These high

transverse stresses were thought to explain the cracking observed by Nairn and Zoller [58] due to residual stress alone.

Residual stress measurement in the balanced laminates examined;  $[90/0_4/90]$ ,  $[90_2/0_4/90_2]$  and  $[90_6/0_4/90_6]$  was achieved using the first ply failure method of Kim and Hahn [37] and an indirect milling method. The first ply failure method predicts failure when the stress in any one ply reaches a value equal to the strength of the ply less the residual stress.

Failure stresses were measured for the  $90^\circ$  plies in three point bending using an Instron 1026 tensile test machine and in tension by the detection of audible emissions due to crack formation. Values were noted to correspond to changes in the slope of the load deflection graph and the audible emissions, respectively.

For the unbalanced laminates;  $[0/90]$ ,  $[0_2/90_2]$ ,  $[0_4/90_4]$  and  $[0_2/90_2/0_2/90_2]$ , measurements were made of curvature due to out of plane deformation. Values were compared to those obtained using classical lamination theory, an accurate prediction implying corresponding accuracy in the prediction of residual stress. The milling method used a similar approach except the surface of the balanced laminate was first milled away to produce an unbalanced laminate.

In three point bending an average over five specimens gave a measured stress to first ply failure of 73 MPa. This compared to a predicted stress to first ply failure of 65 MPa. These values were taken at room temperature ( $21^\circ\text{C}$ ). Tests repeated at  $-30^\circ\text{C}$  and  $-50^\circ\text{C}$  were thought to show less good agreement due to increased brittleness of the matrix.

In tension the average measured first ply failure was 39 MPa and agreed well with the predicted value of 38 MPa.

The milling method for a  $[90_2/0_4/90_2]$  laminate having the top two layers removed produced a radius of curvature equal to 375 mm. This when compared to a predicted value of 311 mm was considered a reasonable agreement in view of the difficulties of milling accurately.

Examination of the curvatures produced in the unbalanced laminates showed them to be bistable. This is a characteristic of thin laminates which show a cylindrical shape on cooling that can be inverted to form a second cylinder having a curvature of equal magnitude but of opposite sign to the first. Classical lamination theory predicts a simultaneous double curvature or saddle shape but Hyer [38-40] has shown that for laminates with sufficiently ~~large~~<sup>small</sup> thickness to in-plane dimension ratios the curvature of the cylinder is approximately equal to that predicted for the saddle shape. This approximation was found to be valid in the samples investigated.

Averages were taken over no less than three samples for each of the laminates investigated. A decrease in the room temperature curvatures with time was thought to be due to stress relaxation. This it was suggested would lead to an over prediction of residual stress which was not apparent in their results. Various reasons were put forward for this. To test their results a curved mould was constructed for a  $[0_4/90_4]$  cross-ply laminate. The laminate was predicted to flatten in the direction corresponding to the curvature of the mould which would therefore lose its bistability. Experiment confirmed their

predictions.

In conclusion the effect of the high transverse stresses was discussed. It was noted that although the first ply failure due to transverse cracking may not significantly reduce the strength and stiffness of cross-ply laminates, it may cause delamination at the interface between the 0° and 90° layers. This would result in a loss in integrity of the laminate and a consequent reduction in compressive strength. It was also noted that time effects may be significant when examining the residual stresses and strengths of thermoplastic materials. Further investigation of these relaxation effects was recommended.

#### 2.5.1.6 Non-Linear Stress-Strain Response

The assumption of linear elastic behaviour is not entirely correct as shown by Ditcher, Rhodes and Webber [59]. They proposed a analytical method to predict the non-linear stress-strain response of a carbon fibre reinforced plastic laminate. Experimental stress-strain curves were obtained for Ciba-Geigy 914-HTS-5 prepreg and a iterative secant modulus method used to predict the response of  $[0/\overset{\pm}{45}/0]$  16 layer laminates.

The predictions compared well with experimental results. The main non-linearities were noted in matrix shear and fibre compression.

Calculations of the residual stresses due to cooling from the cure temperature were found to be exaggerations thus predicting failure at too low a stress level. This was thought to be due to a stress free temperature lower than the assumed value of 150°C and an absence of

any allowance for matrix yielding which would redistribute the loads. At high temperatures yielding and creep effects at the laminae interface as opposed to the assumption of perfect bonding between layers were also thought to reduce the residual stresses. Otherwise the inclusion of thermal effects made little difference to the results.

#### 2.5.1.7 Finite Element Modelling of Complex Geometries

Finite element modelling is a useful method for analysing the mechanical behaviour of manufactured parts having complex geometries.

Two PhD theses are of particular interest. Radford [60] investigated the shape stability of moulded composites. Deformations occurring as a result of temperature changes, moisture absorption and cure shrinkage were considered. Initially the curvatures induced in asymmetric laminates by hygrothermal loadings, that is those occurring due to the combined effects of temperature changes and moisture absorption, were studied experimentally. This showed the as cured curvatures to decrease with temperature and increase with moisture absorption (but in an opposite sense), as would be expected. However there was also found to be a time dependent effect due to creep and consequent relaxation of the residual stresses. This produced a change in the stress free temperature to the test temperature and as a result larger room temperature curvatures. The greater the moisture absorption the greater the creep effect due to plastisization of the matrix (lowering of the glass transition temperature). Subsequently a closed form analytical model of the warping of a semi-cylindrical shell of unsymmetric geometry was developed together with a computer program,

PC-Laminate to calculate laminate curvatures using classical lamination theory. It was proposed that by using asymmetric laminates the warping could be balanced. The model predictions were compared to experimental and finite element results in carbon fibre prepregs when loaded thermally after cure.

Tsau [61] developed a three dimensional finite element computer program for fibre-reinforced laminates. An eight layer  $[0/\pm 45/90]_s$  laminate of SP-286T300 carbon fibre epoxy material with a central hole was modelled. Progressive failure of the elements to catastrophic failure was monitored using a failure criterion proposed by Hashin.

Dobie, Leavesley and Knight [62] applied a simple finite element program presented by Bathe and Wilson to predict the performance of filament wound parts. A state of residual strain and corresponding strength level in each element was calculated and loads applied. Performance was determined using a Weibull statistical failure theory.

Less is known about the residual microstresses which may be important in determining the failure mechanisms in these composites.

## 2.6 Microstresses

Jones [10] classified approaches for determining the micromechanical behaviour of composites into mechanics of material methods and elasticity methods.

### 2.6.1 Mechanics of Materials Methods

In mechanics of material methods simple rule of mixtures expressions are derived for engineering constants. For example those of Tsai and

Hahn given below using a representative volume element consisting of a fibre plate embedded in a matrix plate. Equivalent fibre and matrix strains are assumed in the fibre direction such that sections normal to the fibre direction remain plane.

Tsai and Hahn [9] explain how at an elementary level properties and stress-strain relationships of unidirectional fibre-reinforced composites can be predicted using an elementary rule of mixtures approach. The composite properties and stress and strain fields are derived assuming a uniaxially applied stress to a representative volume element consisting of a fibre plate embedded in a matrix plate. Subsequent modification of the boundary conditions was found necessary to allow for strain compatibility between the fibre and matrix. This resulted in a higher value for the transverse modulus directly as an effect of the imposed lateral constraint.

Results were given showing that although the rule of mixtures approach predicted accurate values for the longitudinal Young's modulus and Poisson's ratio the values predicted for the transverse Young's modulus and shear modulus were lower than those observed experimentally in glass/epoxy composites. A more realistic representative volume element was considered comprising a concentric composite cylinder of a fibre embedded in a matrix. The exact determination of stresses was not given. Instead a simpler semi-empirical approach was described in which stress partitioning parameters,  $\eta_y$  and  $\eta_s$  measured the relative magnitudes of the average matrix stresses to the average fibre stresses were applied. When  $\eta_y = \eta_s = 0.5$  rather than unity, <sup>as</sup>  $\lambda$  was assumed with the rule of mixtures approach much improved estimates of the moduli were obtained.

Decreasing stress partitioning parameters indicated increasing load carried by the fibres and since the fibres are stiffer than the matrix the composite moduli increase. The parameters are found to be independent of fibre volume fraction but related to the transverse shear modulus ratio,  $G_m/G_f$  and the Poisson's ratio of the matrix,  $\nu_m$ . However for values of  $G_f/G_m > 20$  as is the case for most structural composites where the fibres are significantly stiffer than the matrix, constant limiting values are approached.

### 2.6.2 Elasticity Methods

Elasticity methods use principles of elasticity for determining the micromechanical behaviour of composites. They can be solved using a variety of techniques. Bounding methods are used to place upper and lower bounds on the material properties. Exact solutions assume regular and random (hexagonal, square and cylindrical) arrays of fibres while self consistent models assume a single concentric fibre/matrix element embedded in material having properties of the composite as a whole. More realistically a contiguity approach utilizes a factor  $C$  as a measure of the separation of fibres.  $C = 0$  implies isolated fibres whereas  $C = 1$  implies that all fibres are in contact. A value of  $C$  is then determined experimentally. This has been found to be a true indication of fibre contiguity.

The exact elasticity solutions require advanced analytical or numerical methods and finite difference and finite element methods are used extensively.

A simple interpolation procedure developed by Halpin and Tsai was used

as a useful approximate representation of the more complex micromechanical results. The equations utilize a factor,  $\xi$  as a measure of fibre reinforcement, <sup>which</sup> depending ~~ing~~ on the fibre geometry, packing geometry and loading configuration and a factor,  $\eta$  as a measure of the reduction in the effectiveness of the fibres due to voids etc. These factors are also determined experimentally.

### 2.6.3 Distribution of Fibres

#### 2.6.3.1 Regular Fibre Arrays

Simple methods of modelling the microstresses assume the fibres to form regular arrays. Stresses then need only be modelled in a representative unit cell. It is generally assumed that the fibres form regular hexagonal or square arrays. Hexagonal arrays are close packed structures such that for cylindrical fibres packing fractions of up to 90.6% can be obtained. The highest packing achievable for a square array is 78.5%. It should be noted that the higher the packing fraction the more likely the fibres are to conform to a regular array.

Rohwer and Jiu [63] analysed the micromechanical curing stresses in carbon-fibre-reinforced (CFRP) using a three-dimensional finite element method. Linear elastic material behaviour was assumed for transversely isotropic fibres in square and hexagonal arrays. Material property ratios were used as follows

$$\begin{array}{lll}
 E_{Lf}/E_{Tf} = 15.00 & E_{Lf}/G_{LTf} = 27.59 & E_{Lf}/E_m = 685.7 \\
 \nu_{LTf}/\nu_{TTf} = 0.23 & \nu_m = 0.35 & \\
 \alpha_{Tf}/\alpha_{Lf} = -7.857 & \alpha_m/\alpha_{Lf} = -78.57 & 
 \end{array}$$

$\nu_{LTF}$  was assumed equal to  $\nu_{TTF}$ , measured values of  $\nu_{TTF}$  being unavailable. Fibre volume fraction,  $V_f$  was 0.6.

Displacements of pentahedral and hexahedral elements were restrained perpendicular to the radial symmetry planes and the end symmetry planes were constrained to remain plane with a normal stress resultant of zero. Conditions of generalized plane strain were assumed for the bottom surface.

The elements used quadratic distributions of the three displacements with the stresses being linear functions over the element volumes. Fine, medium and coarse element nets were created and refined at the fibre/matrix interface. A thin element layer at the free edge was to approximate the stress-free condition. A unit cell length equal to seven times the fibre radius ensured plane strain at the bottom surface.

A displacement pattern and contours for the related axial, radial, tangential and shear stresses were obtained using an unrealistically high value of  $\alpha_m \Delta T = 0.20$  to ensure a visible deformation. From the latter high stresses at the fibre/matrix interface and a rotationally symmetric state of stress was predicted.  $\Delta T$  was assumed negative to simulate cooling from the cure temperature.

**Axial Stresses:** These were approximately rotationally symmetric increasing from zero at the free edge. The compressive stresses in the fibre increased rapidly whereas the tensile matrix stresses increased gradually. A maximum compressive fibre stress much greater than the constant value at the bottom surface was apparent at a distance of 0.4 times the fibre radius from the free edge. The maximum was located

inside the fibre, close to the interface forming a ring around the circumference. The concentration was thought due to fibre anisotropy, in particular the high value of  $E_{Lf}/G_{LTf}$ . The matrix tensile stresses were close to the matrix failure stress and it was thought this could account for the reduced axial strength at low temperatures observed by Gadke [64].

Radial Stresses: Tensile stresses in the resin and compressive stresses in the fibre were explained in terms of compatibility. At the interface higher compressive stresses, caused by the Poisson's effect, were superimposed on the matrix tensile stresses. High stress gradients at the free edge near to the interface were thought to be due to a singularity. With stresses that the relatively weak matrix could not sustain this would indicate fibre/matrix debonding. However it was noted that material non-linearities would cause this peak to be substantially reduced.

Tangential Stresses: Tangential compression was predicted in the fibre and tangential tension in the matrix. This was due to the high value of  $\alpha_m/\alpha_f$  equal to  $\frac{\alpha_m}{\alpha_f} = \frac{10}{2.57}$ . Values increased rapidly from the low tensile values at the interface reaching a maximum approaching the matrix failure stress at the fibre surface. A singularity similar to that observed for the radial stresses was evident at the interface edge line.

Shear Stresses: Compatibility between the fibre and matrix led to a concentration of the shear stresses at the interface. These increased rapidly from zero at the free edge to a maximum at a distance of 0.01 times the fibre radius from the free edge. Along the interface the

shear stresses decreased more gradually. The stresses were approximately rotationally symmetric with a maximum at the resin surface equal to less than half the failure stress.

Radial-tangential and axial-tangential shear stresses were found to be one order of magnitude smaller than the axial-radial shear stresses. Values were necessarily zero at the symmetry planes. An increase in the radial tangential shear stresses between the radial symmetry planes at the interface were due to changes in radial stress.

In conclusion Rohwer and Jiu [63] suggested that the stress concentrations at the interface edge line for the radial and tangential stresses indicated the presence of singularities. The concentration of axial compressive stresses within the fibre and the rotational symmetry observed for all stresses except the radial and radial-tangential stresses were remarked upon. The latter were considered insignificant in determining the mechanical properties. More important were thought to be the high axial and tangential stresses approaching limit values at the free edge. These it was suggested were a likely cause of matrix failure and/or strength reduction.

Adams and Miller [65] presented a finite element analysis of the local stress state in unidirectional composites occurring as a result of temperature variation and moisture dilation. Elastic transversely isotropic fibres were assumed to be embedded in an inelastic isotropic matrix under conditions of generalized plane strain. Properties were assumed to be temperature and moisture dependent and the results were calculated for a typical graphite-epoxy composite.

Lack of experimental data led to the use of idealized stress-strain curves to model the mechanical behaviour of the epoxy resin. These were described using the curve-fit equation derived by Richard and Blacklock [66] as given below

$$\tau_o = \bar{E}\bar{\epsilon} / [1 + |\bar{E}\bar{\epsilon}/\bar{\sigma}_o|^n]^{1/n}$$

where,

$\tau_o$  = octahedral shear stress

$\bar{\epsilon}$  = octahedral shear strain

$\bar{E}$ ,  $\bar{\sigma}_o$ ,  $n$ , the yield strength and ultimate strength were calculated as linear functions of temperature and moisture content to fit these curves.

Otherwise the epoxy resin was assumed to have the constant material properties given below

coefficient of thermal expansion,  $\alpha = 45 \times 10^{-6} \text{ } ^\circ\text{C}^{-1}$

coefficient of moisture expansion,  $\beta = 2.68 \times 10^{-3} / \text{wt\% H}_2\text{O}$

Poisson's Ratio,  $\nu = 0.34$

Young's Modulus,  $E = 3.45 \text{ GPa } (0.5 \times 10^6 \text{ p.s.i.})$

The properties used for the graphite fibres were as follows

$E_T = 13.8 \text{ GPa } (2 \times 10^6 \text{ p.s.i.})$

$E_L = 276 \text{ GPa } (40 \times 10^6 \text{ p.s.i.})$

$\nu_T = 0.25$

$\nu_L = 0.20$

$\alpha_T = 21.6 \times 10^{-6} \text{ } ^\circ\text{C}^{-1} (12 \times 10^{-6} \text{ } ^\circ\text{F}^{-1})$

$$\alpha_L = -1.8 \times 10^{-6} \text{ } ^\circ\text{C}^{-1} (-1 \times 10^{-6} \text{ } ^\circ\text{F}^{-1})$$

Moisture dilation for the fibres was assumed to be zero.

A one quadrant unit cell based on a square periodic array of fibres and a fibre volume fraction of 40% was meshed into 230 triangular elements. Perfect bonding was assumed at the carbon fibre epoxy resin matrix interface where properties were assumed to be equal to that of the matrix.

The model was exposed to three different environmental states and stressed to failure under uniaxial transverse loading in the x-direction, corresponding to the direction in which the interfibre distance is shortest. Plots were obtained for contours of octahedral shear stress normalized by the octahedral shear yield strength when dry at room temperature. Failure was assumed to occur by one of two modes. That is, either when the octahedral shear stress in any element exceeded the octahedral shear strength of the material, or, when all three principal stresses in any element exceeded the uniaxial tensile strength (the hydrostatic tensile limit of the material). The former indicated failure by shear and the latter failure in tension. Loads were applied in 14 MPa (2000 p.s.i.) increments with material properties evaluated at the beginning of each increment.

The hygrothermal-stress-free initial condition assumed the composite to be stress-free at room temperature (21°C) with no moisture present. The matrix first yielded between the fibres, where the interfibre distance was shortest in the direction of the applied stress. The yielded region spread round the fibres and outwards. Failure occurred

hydrostatically in the interfibre region close to where the yield had initiated at an applied load of 110 MPa (16,000 p.s.i.).

The thermal residual stresses included condition assumed residual stresses generated on cooling from a stress-free temperature of 177°C (350°F) to room temperature to be present. Normalized contours of the residual octahedral shear stresses were obtained as reproduced in Figure 3. These were noted to be well below the yield value with the fibre in a relatively uniform axial compressive state of stress of approximately 32 MPa (4650 p.s.i.) and the matrix in a similar tensile state of stress but of slightly less magnitude. The radial normal stresses around the fibre interface were observed to be compressive.

Loading caused the following changes in the stress state of the matrix. The axial tensile stress increased and tensile in-plane principal stresses were generated in the shortest interfibre region in the direction of the applied stress: that is the compressive radial stresses in this region were dissipated. Failure was similar to the previous case at an average applied stress of 94 MPa (14,000 p.s.i.).

The thermal and moisture-induced residual stresses included condition assumed the thermal residual stresses to be generated as in the previous case but with a maximum saturated level of moisture (5.6 weight % in the matrix and 3.04 weight % in the composite). A reversal in the residual octahedral shear stresses was observed with the fibre elements in axial tension and the matrix elements in axial compression. The maximum principal stress was 33 MPa (4830 p.s.i.) being the axial stresses in the fibre elements.

Moisture dilation was enough to cause the matrix elements to yield in

the shortest interfibre region. Loading increased the yielded area and a maximum principal stress of 38 MPa (5450 p.s.i.) was observed in the fibre close to the interface in the direction of the applied stress. Failure occurred at an average applied stress of 90 MPa (13,000 p.s.i.) similarly to the previous case. Normalized contours were plotted for saturated moisture conditions.

From the results it was concluded that residual thermal curing stresses reduce the transverse normal strength of graphite epoxy composite materials. Moisture saturation reverses the residual microstresses and has a far greater effect than that due to temperature changes, as evident from the thermal expansion coefficient and moisture expansion coefficient of a typical epoxy resin given below,

$$\alpha_{\text{epoxy}} = 45 \times 10^{-6} \text{ } ^\circ\text{C}^{-1}$$
$$\beta_{\text{epoxy}} = 2.68 \times 10^{-3} / \text{wt\% H}_2\text{O}$$

with saturation corresponding to a 121°C temperature increase. However the residual stress reversal was found to have little effect on the predicted strength of the composite, that of the model with thermal residual stresses alone being reduced by 4 MPa.

The generalized plane strain condition assumed the x-y plane to remain plane and displacements in the z-axis direction to be linear functions of z, that is  $\epsilon_z$  to be constant. Also  $\gamma_{xz} = \gamma_{yz} = 0$ .

The solution procedure utilized a method of modifying the total stiffness matrix, described by Branca [57]. This permits any combination of external normal traction elements  $\Delta\sigma_x$ ,  $\Delta\sigma_y$  and  $\Delta\sigma_z$  and

temperature and moisture content increments  $\Delta T$  and or  $\Delta S$ , respectively, to be applied and solved simultaneously. It is a method successfully used by Karlak and Crossman [68].

In reality fibres form random arrays and modelling of regular arrays will give the mean stresses. Local variations in interfibre distance and packing arrangement are not considered nor the variation in the stress field associated with this. It would be expected for the stresses at these points to be the most extreme and therefore most critical with regard to performance and failure of the material.

#### 2.6.3.2 Random Fibre Arrays

Random distributions of points can be described using spatial or planar point processes [69]. The simplest is the Poisson point process whereby points are generated randomly within a volume  $B$  with intensity,  $\lambda$ . For point patterns of centres of non overlapping spheres the Poisson process is modified such that the distance between the centres of the spheres is not less than twice the sphere radius. Matern hard-core and simple sequential inhibition point processes exist. All the above assume uniform distributions. Non uniform distributions can be modelled using Matern cluster point processes. This is similar to a hard-core model in that points are Poisson distributed within a radius,  $R$  about an imaginary Poisson distribution of parent points.

Assuming no clustering of fibres planar hard-core models best represent the distribution of fibres in the transverse section of a unidirectional layer. Guild and Hogg [70] used such a distribution to

model the properties of these layers. They also used the concept of a Voronoi Cell - the region of a plane closer to one point than any other in describing the interparticle distance of the array.  $X$  was defined as the distance from the disc centre to the boundary of the Voronoi Cell.

In an earlier paper by Davy and Guild [71] it was shown how a size distribution of cylindrical cells mimicking the distribution of centre to boundary distances of the Voronoi cells could be established. An equation was derived relating the cylinder radii to the volume fraction such that the average volume of the cylinders was the same as if they filled space.

An approximation for the probability function  $g_x(x)$  of  $X$  for a planar Gibbs hard-core model was refined using a Taylor Series to allow for variation in cylinder size and used in finite element calculations of the properties.

#### 2.6.4 Photoelastic Determination of Microstresses

Experimental determination of the residual microstresses is very limited. Markoff and Daniel [72] mention photoelastic studies of the shrinkage stresses around inclusions and themselves conducted a three-dimensional analysis of the stress distribution in the epoxy matrix of a square array of polycarbonate rods subject to matrix shrinkage and transverse loading.  $\sigma_x$ ,  $\sigma_y$  and  $\sigma_z$  and the hoop stresses were calculated and expressed in a dimensionless form proportional to the shrinkage stresses present at the interface of an isolated fibre. The results are reproduced in Figures 4, a) and b).

## 2.7 Properties

### 2.7.1 Thermal Expansion Coefficients

A solving technique previously used by Ishikawa, Koyama and Kobayashi [73,74] for calculating the elastic moduli of unidirectional composites was modified and applied to the prediction of the thermal expansion behaviour of carbon and glass fibre/epoxy resin matrix composites.

An isotropic matrix, isotropic glass fibres or transversely isotropic carbon fibres and temperature dependent properties were assumed. The axial and transverse thermal expansion coefficients,  $\alpha_z$  and  $\alpha_x$  were determined using a modified version of a technique developed by the authors in an earlier paper for calculating the Young's modulus of unidirectional composites. Hexagonal and square arrays of fibres were assumed. The dependence of the composite thermal expansion coefficients on the constituent material properties was examined graphically.

Experimental work investigated the effect of temperature on fibre and epoxy resin thermal expansion coefficients,  $\alpha_f$  and  $\alpha_m$ , together with the influence of  $\alpha_m$  on  $\alpha_x$  and  $\alpha_z$ . Values of  $\alpha_{fr}$  and  $\alpha_{fz}$  for the carbon fibres were also estimated from their experimental results.

The thermo-elastic problem assumed a uniform temperature distribution with locally constant elastic moduli and thermal expansion coefficients. This enabled the Duhamel-Neumann law to be applied incrementally for small temperature differences  $\delta T$ . Other problems were described using an Airy stress function which after expansion

into a Fourier cosine series was solved using a collocation method.

The input data was analysed using a program, TEACOM (Thermo-elastic Analysis of Composites - Thermal Expansion Coefficients), collocation points for temperature increments of 5°C being chosen. The following material properties were assumed.

Carbon Fibres (estimated for Torayca T300):

$$\begin{aligned} E_{fz} &= 2.275 \times 10^4 \text{ kg/mm}^2 \quad (227.5 \text{ GPa}) \\ E_{fr}/E_{fz} &= 0.1 \\ \nu_{frz} &= 0.3 \\ \nu_{fr\theta} &= 0.42 \\ \alpha_{fz} &= -1.5 \times 10^{-6}/^\circ\text{C} \\ \alpha_{fr} &= 2.7 \times 10^{-5}/^\circ\text{C} \end{aligned}$$

Epoxy Resin Matrix (Epikote 828):

$$\begin{aligned} E_m &= 3.50 \times 10^2 \text{ kg/mm}^2 \quad (3.5 \text{ GPa}) \\ \nu_m &= 0.38 \\ \alpha_m &= 6.6 \times 10^{-5}/^\circ\text{C} \end{aligned}$$

Glass Fibres:

$$\begin{aligned} E_f &= 7.00 \times 10^3 \text{ kg/mm}^2 \quad (70 \text{ GPa}) \\ \nu_f &= 0.2 \\ \alpha_f &= 5.0 \times 10^{-6}/^\circ\text{C} \end{aligned}$$

Graphs of  $\alpha_z/\alpha_m$  and  $\alpha_x/\alpha_m$  versus the fibre volume fraction,  $V_f$  showed little difference in the results obtained using hexagonal and square fibre arrays. Values of  $\alpha_z$  for both the carbon fibre and glass fibre epoxy resin composites conformed to the modulus modified law of

mixture as given below

$$\alpha_z = (E_{fz} \alpha_{fz} V_f + E_m \alpha_m (1 - V_f)) / (E_{fz} V_f + E_m (1 - V_f))$$

whereas the law of mixture of Turner [75] was found to be less accurate when applied to the glass/epoxy composite.

The graph of  $\alpha_x/\alpha_m$  for the glass fibre epoxy resin composite was compared to the predictions of Wakashima et. al. [76], Greszczuk [77] and Schapery [78]. Values were found to be intermediate between that of the upper bound of Schapery and the lower bound of Wakashima et. al. Greszczuk predicted lower values than Wakashima et. al. It was noted that a maximum of  $\alpha_x$  occurs at very small values of  $V_f$ .

Further results considered the hexagonal array alone.  $\alpha_z/\alpha_m$  versus  $E_f/E_m$  was compared to the modulus modified law of mixture for the glass fibre epoxy resin composite at different volume fractions. The law of mixtures rule predicted marginally lower values the difference being greatest for small  $E_f/E_m$  when the secondary stresses induced by a temperature change and the difference between  $\nu_f$  and  $\nu_m$  are no longer negligibly small. Practical unidirectional composites however have large  $E_f/E_m$  ratios.  $\alpha_x$  was found to be practically independent of  $E_f/E_m$ .

Values of  $\alpha_x/\alpha_m$  versus  $\frac{\alpha}{\nu}_m$  at different volume fractions of the glass fibre/epoxy resin composite were compared to those predicted by the formula of Schapery as given below.

$$\alpha_x = (1 + \nu_m) \alpha_m (1 - V_f) + \alpha_f V_f$$

The law of mixture rule of Schapery predicted significantly higher

values, agreement only being good when both  $\nu_f$  and  $\alpha_m$  were large. It was noted that changes of  $\nu_m$  at high temperatures might therefore be significant. Finally  $\alpha_x$  versus  $\alpha_m$  was plotted for the carbon fibre epoxy resin composite at different fibre volume fractions, the carbon fibres being assumed anisotropic.  $\alpha_x$  was shown to be approximately linearly dependent on  $\alpha_m$ .

Thermal expansion coefficients were measured using an interferometric dilatometer at a heating rate of 1°C/min. between room temperature and 150°C. Averaged thermal expansion coefficients were calculated for Epikote 828 Epoxy, 3130 Epoxy and Epikote 828/T300 Carbon-Epoxy specimens. Off-axis and on-axis specimens were taken of the carbon/epoxy material.

Consistent results were obtained for  $\alpha_m$  below 60°C. Repeated readings from the same sample showed the first measurements to be inconsistent. This was considered to be due to the presence of absorbed moisture in the epoxy resin, the contraction resulting from moisture desorption on heating counteracting the thermal expansion characteristics. Consistency in subsequent readings would indicate slow reabsorption due to a small diffusion constant.

A comparison was made between the measurement of  $\alpha_x$  and numerical results for the composite. The carbon fibre properties were assumed to be temperature independent using values for  $\alpha_{fz}$  and  $\alpha_{fr}$  estimated experimentally. Measured temperature dependent properties were assumed for the epoxy resin. The agreement between experimental and numerical results was found to be good.

Similar comparisons of  $\alpha_z$  versus T proved difficult due to the very small values of  $\alpha_z$ . Experimental errors were relatively large. Taking this into account the agreement was considered good.

Off-axis  $\alpha(\phi)$  versus  $\phi$  for the composite samples averaged between 20°C and 60°C agreed well with results calculated using the formula

$$\alpha(\phi) = \alpha_z l_\phi^2 + \alpha_x m_\phi^2$$

where,

$$l_\phi = \cos \phi$$

$$m_\phi = \sin \phi$$

for  $\alpha_x = 3.0 \times 10^{-8}/^\circ\text{C}$  and  $\alpha_z = 3.62 \times 10^{-5}/^\circ\text{C}$

The thermal expansion coefficients of the Torayca-T300 carbon fibres were estimated graphically using the calculated  $\alpha_z/\alpha_m$  versus  $\alpha_{fz}$  and  $\alpha_{fr}$  relationships at different volume fractions. Values of  $\alpha_{fz}$  and  $\alpha_{fr}$  were read from the graphs using values of  $\alpha_z/\alpha_m$  measured at known volume fractions in 60% and 65%  $V_f$  samples. Two approximately equal values were obtained in this way producing averages of  $\alpha_{fz} = -7.8 \times 10^{-7}/^\circ\text{C}$  and  $\alpha_{fr} = 8.1 \times 10^{-6}/^\circ\text{C}$ . This was compared to the values used by Adams and Miller [65] of  $\alpha_{fr} = 21.6 \times 10^{-6}/^\circ\text{C}$  and  $\alpha_{fz} = 1.8 \times 10^{-6}/^\circ\text{C}$  which are comparable to the corresponding values for pyrographite.  $\alpha_{fz}$  was considered to be largely temperature independent due to the good agreement obtained between the experimental and numerical results on assuming these values. The temperature dependence of  $\alpha_{fz}$  could not therefore be decided.

In conclusion a summary of the analytical and experimental results was

given. The analysis showed  $\alpha_z$  to conform to the modulus modified law of mixture and  $\alpha_x$  values calculated for hexagonal and square arrays to be practically identical. Nearly linear relationships were predicted for  $\alpha_{fz}$  versus  $\alpha_z$ ,  $\alpha_{fr}$  versus  $\alpha_x$  and  $\alpha_m$  versus  $\alpha_x$ .  $\alpha_z$  was shown to be strongly dependent on  $E_f/E_m$  but  $\alpha_x$  little dependent on it.  $\nu_m$  was more influential in determining  $\alpha_x$ .

Experiment showed  $\alpha_z$  to be very small, fluctuating between negative and positive values, depending on the temperature and volume fraction of fibre. This was largely attributed to the small negative value of  $\alpha_{fz}$  associated with the carbon fibres. Considerably larger values for  $\alpha_x$  were observed having values nearly equal to  $\alpha_m/2$  at  $V_f = 65\%$ . The temperature dependency of  $\alpha_x$  was mainly due to that of  $\alpha_m$  and was therefore found to be influenced by moisture desorption at temperatures greater than  $60^\circ\text{C}$ .

The values of  $\alpha_{fr}$  and  $\alpha_{fz}$  predicted were quite different from the corresponding values for pyrographite. Values of  $\alpha_{fr}$  were taken as constant at temperatures below the glass transition point of the epoxy resin.

The off-axis properties were well described using the relation

$$\alpha(\phi) = l_{\phi} \alpha_z + m_{\phi} \alpha_x$$

Knibbs and Morris [79] investigated the angular dependence of the Young's modulus, conductivity and thermal expansion coefficient of unidirectional continuous carbon fibre/epoxy resin composite materials. In addition the effect of fibre misorientation, on Young's modulus and resistivity was examined. The composites were

assumed transversely isotropic and hexagonally symmetric.

Equations describing the angular dependence of properties were given based on the application of tensor theory to hexagonal symmetry. Misalignment effects were studied by means of a network model due to Cook [80], as well as a series averaging (Reuss, constant stress) and a Parallel averaging (Voigt, constant strain) model.

Experiments were carried out to test the theory and relevant properties were measured on a type 1, high modulus and type 2, high strength carbon fibre/epoxy resin (diglycidyl ether) composite. Fibre volume fractions of 50% with samples cured under pressure for 1 hour at 150°C plus 3 hours at 180°C were used. Void contents ranged from 1.7% to 6.0%. Electrical resistivity was measured to within ±7% and thermal expansion to within ±10% taken at 100°C as a mean over 80°C to 120°C.

The equations used for describing the angular dependence of properties were as follows

Stiffness:

$$S_{33}(\theta) = S_{11}\sin^4\theta + S_{33}\cos^4\theta + (2S_{13} + S_{44})\sin^2\cos^2\theta$$

where,

S = compliance

Conductivity:

$$\lambda_{33}(\theta) = \lambda_1\sin^2\theta + \lambda_3\cos^2\theta$$

$$\rho_{33}(\theta) = \rho_1\sin^2\theta + \rho_3\cos^2\theta$$

where,

$\lambda$  = conductivity

$\rho$  = resistivity

Thermal expansion:

$$\alpha_{33}(\theta) = \alpha_1 \sin^2 \theta + \alpha_3 \cos^2 \theta$$

where,

$\alpha$  = coefficient of thermal expansion.

The three misalignment models can be summarized as follows.

The network model of Cook for the Young's modulus assumes the fibres to be distributed over a range of angles,  $\theta$  with respect to the nominal axis such that the ratio of the observed to the ideal longitudinal composite modulus given by the rule of mixtures,  $E_O/E_L$  is calculated as a function of the root mean square, RMS misorientation angle.

By comparison the averaging models assume the composite to be composed of an aggregate of units of ideal composite each orientated at an angle,  $\theta$  to the longitudinal axis. The Young's modulus of each unit is then given by the law of mixtures. Averaging over all units according to a Reuss constant stress method for the series model or a Voigt constant strain method for the parallel model gives the Young's modulus of the aggregate for small misalignment angles,  $\theta$ . It was shown that the results obtained for a distribution with a range of misorientation angles approximates to that of a distribution with a

constant misorientation angle of the root mean square value.

Similar models were proposed for the electrical resistivity. The conductivity of the resin was assumed to be zero and contact resistance between fibres to be negligible. Equations derived using a network model were found to be identical to those obtained using a Parallel averaging method as given below.

$$\rho_3 = \rho_L \sec^2 \theta \quad (1)$$

$$\rho_1 = 2\rho_L \operatorname{cosec}^2 \theta \quad (2)$$

The series averaging method predicted zero conductivity for all composites having any misalignment and was therefore considered unrealistic.

The network model was also used to examine the thermal conductivity with the matrix conductivity assumed in parallel with the fibre terms. Equations (1) and (2) expressed in terms of conductivities then become

$$\lambda_3 = V_f \lambda_f \cos^2 \theta + V_m \lambda_m$$

$$\lambda_1 = 1/2 V_f \lambda_f \sin^2 \theta + V_m \lambda_m$$

Experimental results and the earlier work of Fahmy and Ragai [81] and Goggin [82] largely substantiated the angular dependence relations and of the three misalignment models the network model due to Cook gave the most consistent results.

Values of the misorientation angle,  $\theta$  predicted using the network model of approximately  $11^\circ$  were intermediate between those predicted by the Parallel model of approximately  $17^\circ$  and the series model of approximately  $6^\circ$ .

In deriving the network model for the electrical conductivity it was assumed that the interfibre contact resistance was negligible. However to predict misorientation angles comparable to those predicted by the network model for the Young's modulus fibre/fibre contacts needed to be 25% effective. The values of  $\theta$  predicted using the network model for thermal conductivity needed no corresponding modification for imperfect network geometry.

In summary the angular dependence relations were largely substantiated. The effect of fibre misalignment on the longitudinal properties was found to be small ( $\approx 4\%$ ) for the thermal and electrical conductivity but more significant ( $\approx 20\%$ ) for the Young's modulus. The converse was expected to apply for the transverse properties.

Uemura, Iyama and Yamaguchi [83] proposed simple algebraic expressions for predicting the thermal-expansion coefficients of unidirectional carbon-fibre-reinforced plastics (CFRP). Further analytical expressions for calculating the thermal expansion coefficients and curing stresses in filament-wound laminates were then derived and verified experimentally.

The unidirectional composite was modelled assuming a hexagonal array of fibres. The hexagonal unit cell being approximated by a concentric composite circle of outer radius  $r_m$  and inner radius  $r_f$ . Elastic deformations were predicted for a uniform temperature change assuming axisymmetric plane strain, temperature independent material properties and axisymmetrically orthotropic fibres.

Fundamental equations were obtained for the radial displacement,  $\mu$  in

terms of the matrix and fibre properties and fibre volume fraction by substitution of the appropriate stress-strain and strain-displacement relations into the equilibrium equation

$$\frac{d\sigma_{ri}}{dr} + \frac{\sigma_{ri} - \sigma_{r\theta}}{r} = 0$$

The subscript i could be either f or m, denoting the fibre or the matrix, respectively. Unknown constants were determined from the boundary conditions.

Expressions derived for the composite longitudinal and transverse thermal expansion coefficients showed that the thermal stresses predicted at the interface could significantly effect the interfacial bond strength. Curves of  $\alpha_L$  and  $\alpha_T$  versus  $V_f$  were predicted for a typical isotropic-glass-fibre-reinforced plastic and compared to the analytical results of others. A good agreement was obtained with the more rigorous approach of Ishikawa and Kobayashi in which an Airy stress function was applied.

Values were then calculated for an anisotropic-carbon-fibre-reinforced epoxy resin matrix having the following material properties.

High-tensile strength graphite fibre, Torayca T300:

$$\begin{aligned} E_{fL} &= 226 \text{ GNm}^{-2} & E_{fr} &= 15.8 \text{ GNm}^{-2} \\ \alpha_{fL} &= -0.7 \times 10^{-6}/^{\circ}\text{C} & \alpha_{fT} &= 8.0 \times 10^{-6}/^{\circ}\text{C} \end{aligned}$$

Epoxy resin matrix:

$$E_m = 3.4 \text{ GNm}^{-2} \quad \nu_m = 0.36 \quad \alpha_m = 62-70 \times 10^{-6}/^{\circ}\text{C}$$

The fibre thermal expansion coefficients are close to those calculated by Ishikawa and Kobayashi of  $-0.78 \times 10^{-6}/^{\circ}\text{C}$  and  $8.1 \times 10^{-6}/^{\circ}\text{C}$ .

As would be expected increasing volume fraction of fibre caused the expansion coefficient to decrease the effect being more significant and linear for  $\alpha_T$ .  $\alpha_T$  was also found to be a linear function of  $\alpha_{fT}/\alpha_m$  but independent of  $\alpha_{fL}/\alpha_m$ , whereas  $\alpha_L$  showed a linear relationship with  $\alpha_L/\alpha_m$  and no dependence on  $\alpha_{fT}/\alpha_m$ . Increasing  $E_{fL}/E_m$  caused the expansion coefficients to decrease the effect for  $\alpha_L$  diminishing with increasing  $V_f$ .

A graph of the interfacial microstresses in glass-fibre-reinforced plastics and carbon-fibre-reinforced plastics versus  $V_f$  showed significant tensile hoop stresses  $\sigma_{\theta m}$  to be generated in the matrix. These increased with increasing  $V_f$  and were calculated in the range of 15-25 MNm<sup>2</sup> for a temperature drop of 100°C. The remaining interfacial stresses  $\sigma_{rf}$ ,  $\sigma_{\theta f}$  and  $\sigma_{rm}$  were equal, compressive, of lower magnitude. They also decreased with increasing  $V_f$ .

Having derived expressions for the thermal expansion coefficients of a unidirectional composite it was shown how these could be used to predict the thermal expansion coefficients and thermal residual stresses in helical-wound and composite laminates. The equation

$$\begin{Bmatrix} \sigma_{hLi} \\ \sigma_{hTi} \\ \tau_{hLTi} \end{Bmatrix} = [C] \begin{Bmatrix} \epsilon_{hLi} \\ \epsilon_{hTi} \\ \gamma_{hLTi} \end{Bmatrix} - \begin{Bmatrix} \alpha_L \\ \alpha_T \\ 0 \end{Bmatrix} T$$

was given relating the principal stress and strain components in the helical windings, when measured relative to the fibre direction, through the stiffness matrix [C]. Transformation matrices [A] and [B]

converted these stress and strain components to and from, respectively an axis set, x-y at an angle  $\theta$  to the fibre direction

a) Helical-Wound Lamina:

A winding angle of  $\pm\theta$  to the longitudinal x-axis was assumed with a perpendicular and circumferential y-axis.

When laminated plate theory was assumed such that there is no slip between layers and a constant strain is predicted in each layer. Then with no externally applied force the principal stresses summed over both layers could be equated to zero. The unidirectional stress and strain relationships when applied within this framework gave a solution for the thermal expansion coefficient of a helical-wound lamina of the form given below.

$$\begin{Bmatrix} \alpha_{hx} \\ \alpha_{hy} \end{Bmatrix} = \begin{bmatrix} d_{11} & d_{12} \\ d_{21} & d_{22} \end{bmatrix} \begin{Bmatrix} \alpha_L \\ \alpha_T \end{Bmatrix}$$

Expressions were then derived for the thermal residual stresses when expressed relative to the fibre direction and the principal axes of the helix in terms of  $\alpha_L$  and  $\alpha_T$ . It is of interest to note that

$$\begin{aligned} \sigma_{hxi} &= 0 = \sigma_{hyi} \\ \sigma_{hLi} &= -\sigma_{hTi} \\ \tau_{hLTi} &= (l^2 - m^2) \tau_{hxyi} \\ \sigma_{hLi} (-\sigma_{hTi}) &= 2l\tau_{hxyi} \end{aligned} \quad \begin{aligned} l &= \cos\theta \\ m &= \sin\theta \end{aligned}$$

The predicted stresses are of equal magnitude in both layers but the shear stresses are of opposite sign.

Graphs, assuming a temperature increase, for the variation of  $\alpha_{hx}$  and the principal stress components expressed relative to the fibre direction with helical winding angle,  $\theta$  were given for anisotropic carbon fibres at volume fractions from 50% to 70%. The results for  $\alpha_{hx}$  showed a maximum negative value at approximately  $30^\circ$  decreasing from 0 at  $0^\circ$  and thereafter increasing. This contraction was thought to be due to internal residual stresses. A comparison made with experimental results proved favourable.

The residual thermal stresses showed a maximum value for  $\sigma_{hTi}$  ( $-\sigma_{hLi}$ ) at  $\theta = 45^\circ$ , this being <sup>tensile</sup> (compressive) for a temperature decrease. The shear stresses showed maxima of equal magnitude in the ranges  $20^\circ$ - $30^\circ$  and  $60^\circ$ - $70^\circ$  but of opposite sign. All residual stresses were zero at  $\theta = 0^\circ$  and  $\theta = 90^\circ$  as would be expected. A tensile curing stress,  $\sigma_{hTi}$  of  $30 \text{ MNm}^{-2}$  calculated for a temperature decrease of  $100^\circ\text{C}$  was thought significant in the formation of cracks during cure whilst shearing stresses,  $\tau_{LTi}$  were suggested to effect shear fracture along the fibres.

b) Composite Laminates:

These laminates were considered to be comprised of helical windings as before but with additional circumferential windings about the y-axis. A similar method based on laminated plate theory, but with coupling effects, that is shear stresses and shear strains, ignored, was used as in the helical analysis. The helical layer relationships were replaced by laminae relationships, and a constant strain assumed in each lamina. The stresses summed over all laminae in proportion to their thickness were equated to zero and the laminae stresses  $\{\sigma_j\}$

related to the laminae strains  $\{\epsilon_j\}$  through the equation

$$\{\sigma_j\} = [E_j](\{\epsilon\} - \{\alpha_j\}T)$$

Expressions for the composite thermal expansion coefficient were then derived in terms of the laminae thermal expansion coefficient and it was shown how the laminae thermal stresses could be determined using the equation

$$\{\sigma_j\} = [E_j](\alpha - \{\alpha_j\})T$$

It was noted that the residual stresses in the helical layers could be calculated either from the sum of those predicted for the helical lamina and the composite laminate or directly by substitution of the strain components of the composite laminate into the unidirectional stress-strain relationship.

Graphs were given showing the variation of  $\alpha_x$  and  $\alpha_y$  with helical winding angle,  $\theta$  at various helical winding thickness ratios,  $t_h$ . Graphs also showed the variation of  $\alpha_x$  with  $\alpha_{fT}$  at  $\theta = 0^\circ, 60^\circ$  and  $90^\circ$ ,  $V_f = 65\%$  and  $t_h = t_c = 0.5$  for various  $\alpha_{fL}$  and  $\alpha_m$  values. Thermal residual stresses expressed relative to the fibre direction for the helical lamina and the hoop lamina were plotted versus  $\theta$  at varying  $t_h$  values together with the combined thermal stresses in each layer of the helical lamina. Most significant were thought the  $\sigma_{hT}$  and  $\sigma_{cT}$  stresses occurring at winding angles,  $\theta$  of less than  $45^\circ$ . For a temperature decrease of  $100^\circ\text{C}$  these were shown to reach tensile values of approximately  $29 \text{ MNm}^{-2}$ . Such values are close to the fracture strength transverse to the fibres of  $40\text{-}50 \text{ MNm}^{-2}$ .

Experimentally the axial thermal expansion coefficient  $\alpha_x$  was measured for CFRP filament-wound laminated cylinders having circumferential and helical lamina in a balanced and symmetric lay-up. Variation of  $\alpha_x$  with temperature was attributed to the temperature dependence of the epoxy resin. Good agreement was obtained with theoretical values using  $\alpha_{fT} = 8 \times 10^{-6}/^{\circ}\text{C}$ . <sup>This</sup> ~~and~~ <sup>was</sup> ~~values~~ ~~were~~ noted to coincide with <sup>that</sup> ~~those~~ obtained by Ishikawa et.al.

In conclusion it was surmised that relationships had been derived to predict the thermal expansion coefficients and curing stresses in unidirectional fibre reinforced composites and a variety of filament-wound laminates. Favourable comparisons were made with experimental results using values of  $\alpha_{fL} = -0.7 \times 10^{-6}/^{\circ}\text{C}$  and  $\alpha_{fT} = 8.0 \times 10^{-6}/^{\circ}\text{C}$ .

Residual curing stresses transverse to the fibres were thought most relevant due to the low tensile strength in this direction. It was suggested that the temperature dependence of the constituent material properties could most effectively be introduced through the variation of  $\alpha_m$  with temperature

### 2.7.2 Young's Modulus

Guild and Hogg [70] developed a model to predict the stiffness of unidirectional fibre reinforced composites when loaded longitudinally and transversely. A finite element method together with spatial statistical techniques allowed real fibre distributions to be considered.

The stiffness in the longitudinal direction was thought adequately described by the classical rule of mixtures expression

$$E_L = E_f V_f + (1 - V_f) E_m$$

This assumes equal Poisson's ratios in the fibre and the matrix. Small errors arise due to differences in these values. In the transverse direction only the general trend of  $E_T$  versus  $V_f$  could be predicted assuming the fibres and matrix to be subject to the same stress. Poisson's ratio effects are more significant in this direction where they impinge on a soft (low modulus) part of the composite. The effects due to the differences between the fibre and matrix Poisson's ratios are therefore more apparent. Also, due to the high modulus of the fibre and the low modulus of the matrix, stress magnification would be expected in the matrix. That is rather than the constant stress assumption.

The finite element analysis used eight-noded axisymmetric elements as part of a LUSAS finite element package on a ICL 2988 computer. The material was modelled axisymmetrically as a collection of continuous cylinders, radius R containing a fibre, radius r at its centre. A grid of elements having length, L was created of a rectangular radial segment along the fibre axis. Longitudinal loading assumed the displacements in the fibre direction to be prescribed whereas to calculate the transverse modulus radial stresses were assumed with displacements prescribed at the cylinder outer surface. Glass fibre and resin matrix properties were used as follows

	Resin Matrix	Glass Fibres
Modulus (GPa)	3.5	76.0
Poisson's Ratio	0.35	0.21

The statistical analysis used Voronoi cells (the region of a plane closer to one point than to any other) to describe the interparticle distance,  $X$  in the transverse section of the composite. This was expressed in terms of the number of fibres per unit area,  $\lambda$  and the fibre volume fraction,  $p$  as follows

$$\bar{E}(X^2) = (\lambda\pi)^{-1} \quad \text{or} \quad \bar{E}(X^2/r^2) = p^{-1}$$

where  $\bar{E}$  denotes expected or average values over all directions and all fibre cross sections and  $r$  is the fibre radius.

An approximate probability density function,  $g_X(x)$  of the Gibbs hard-core model for which all non-overlapping configurations of fibres are equally likely was given, as found by the Davy and Guild in an earlier paper [71]. This function was plotted for distributions having one fibre per unit area and volume fractions ranging from 0 to 0.3 (Figure 5). The distributions were all markedly skewed with a preponderance of half-interparticle distance close to the minimum value of  $r = \sqrt{(p/\pi)}$ . The central tendency remained approximately constant with volume fraction whilst the spread reduced due to the regularity induced by the constraint of non-overlapping.

The earlier paper showed how a size distribution of cylindrical cells mimicking the distribution of centres of Voronoi cells could be established. An equation was derived relating the cylinder radii to the volume fraction such that the average volume of the cylinders was the same as if they filled space. That is the mean volume of the distribution of cylinders was equated to the reciprocal of the intensity of the distribution,  $\lambda^{-1}$ .

It was shown using the Voronoi cell relationship that the Young's modulus,  $E_L$  of a single cylinder when averaged over all cylinders in proportion to their cross sectional areas produces an expression for the Young's modulus of the material as follows

$$E_L = E_m + p(E_f - E_m)$$

This is consistent with the rule of mixtures expression and shows overall stiffness of the material to be independent of fibre distribution.

In the transverse direction a radial strain was applied to the finite element cylinder with a constant strain parallel to the fibres. Averaging over all cylinders in proportion to their cross sectional areas an estimate was made using a power series approximation for the transverse Young's modulus and longitudinal Poisson's ratio of the total material. A value was determined from the finite element grid for a cylinder radius equivalent to a fibre volume fraction of  $p$ . The properties were then expressed in terms of this value using a dispersion factor to adjust for the variability in  $R^2/r^2$ , a measure of the irregularity in fibre distribution. Results showed the fibre distribution to have no effect on the longitudinal modulus at all values of fibre volume fraction, from which it was concluded Poisson's ratio effects are insignificant.

The transverse modulus was shown to be dependent on the value of the longitudinal Poisson's ratio,  $\nu_{12}$  due to the assumption of generalized plane strain. For the random distribution of fibres considered the Poisson's ratio increased, by about 20% on the application of

dispersion factors. Similarly the resulting prediction of transverse Young's modulus showed a 20% increase on the application of dispersion factors. Experimental values of the transverse Young's modulus when compared to the predicted values were found to agree within the range introduced by the application of dispersion factors. This indicates that the randomness in fibre distribution has a significant effect on the transverse properties.

## 2.8 Failure

Failure in composite materials is a complex process. The material can be regarded as an anisotropic continuum with either overall measured and calculated strength characteristics or at a local level a predetermined resistance to fracture. If the material is further regarded as heterogeneous in its failure mechanisms, micromechanical effects which are important in the early stages of failure need to be considered.

### 2.8.1 First Ply-Failure

By the application of these concepts to the failure of a multidirectional laminate the first ply-failure can be determined from classical lamination theory using strength values of the individual plies. Maximum stress criterion, as discussed in section 2.5.1.3, and maximum strength potential methods also exist.

The maximum ~~strength~~<sup>stress</sup> criterion requires that no stress exceeds the compressive, tensile and shear strengths of an individual ply. This ignores interaction effects between the stresses which can cause a ply to fail at lower values. It is therefore primarily used for

predicting failure in plies where only one stress component predominates.

The strength potential theory incorporates these interaction effects by assuming an energy-like potential exists within the material which if exceeded will cause it to fail. It is defined in such a way that it is universally applicable to all stress states and can be determined from various strength measurements made on the individual plies.

To model the failure of a laminate once the first ply has failed a method known as the ply discount method can be used. This assumes the failed ply no longer carries any load which is redistributed to the remaining plies. The process is repeated with increasing load in an incremental linear relationship of applied load to laminate deformation until laminate failure occurs. The method is approximate as in practice some of the load is redistributed through the ply interface bonding. The high stiffness and interface strength of the adjacent plies will cause the failure to be localised. In addition similar redistribution mechanisms will take place at the fibre/matrix interface which are ignored due to the assumption of homogeneity. An alternative treatment considers the failed ply to be elastic/plastic which whilst mimicking the observed failure behaviour is not a true representation of the process.

### 2.8.2 Failure due to Interply Load Transfer

A fully three-dimensional stress analysis of laminates shows interlaminar,  $\sigma_z$ ,  $\tau_{zx}$  and  $\tau_{zy}$  stresses to exist at geometric discontinuities such as free edges, holes and other internal and

external flaws. These are the result of ply interface transfer mechanisms. The magnitude of these stresses are largely dependent on the laminate stacking arrangement.

If the interlaminar stresses are larger than the in-plane stresses then initial failure will be by delamination at the ply interfaces.

### 2.8.3 Energy Method

The initial stages of laminate failure are matrix cracking. As the matrix cracks the load is transferred to the fibres until the fibre breaking strain is exceeded and the laminate fails catastrophically.

Two modes of matrix cracking are observed [2]: fibre/matrix or interlaminar debonding and ply-to-ply or interlaminar debonding.

Interlaminar debonding is produced by the component of the in-plane stresses perpendicular to the fibres. The cracks form parallel to the fibres and perpendicular to the applied tension and are known as transverse cracks.

Intralaminar debonding occurs due to the intralaminar stresses. Plane cracks form parallel to the ply interface as a delamination.

These two modes of cracking are not independent since failure in one mode will lead to load transfer with redistribution of stresses and possible change in failure mode.

Failure is determined according to the theory of brittle fracture assuming a hypothetical distribution of effective flaws within a three-dimensional laminate stress field. These flaws are considered inherent properties of the material which do not effect the elastic

constitutive properties of the plies. However at a critical load these flaws will grow as determined by classical fracture mechanics into detectable cracks.

Crack growth occurs when the strain energy release rate reaches the material fracture toughness. This energy release is dependent on the initial crack (flaw) size and the magnitude of the applied stress. The crack will continue to propagate if the increase in strain energy release rate with crack length is positive.

The relationship between the crack (flaw) length and the strain energy release rate for a given applied laminate strain depends on the location of the crack (flaw), the ply stacking sequence and the ply elastic constants as well as the mode of failure. Residual thermal strains due to cooling from the stress free temperature if significant should also be included in the relationship.

From studying the constants in these relationships for interlaminar failure the free-edge effect has been found to be fully developed when a crack (flaw) reaches a value approximately the order of a couple of ply thicknesses. Delamination onset can therefore be determined by the minimum critical strain associated with the crack length greater than this value. It is also possible to determine at which ply interface delamination will initiate as well as the mode of failure.

For intralaminar failure studied in  $[0/90]_s$  coupons under uniaxial tension it has been found that the free-edge effects are relatively unimportant. Detectable cracks are thought to occur by coalescence of material microflaws lying in the thickness direction of a  $90^\circ$  layer. The cracks are noted to arrest a short distance from, or at the  $90^\circ/0^\circ$

interface where they may then propagate along the interface. This is consistent with the fact that the strain energy release rate coefficients are noted to reach a maximum at about three-fourths of the thickness of the  $90^\circ$  layer.

It has been found from the study of the acoustic emission behaviour of  $[0/90_n/0]$  coupons under uniaxial tension that the greater the thickness of the  $90^\circ$  plies, that is the greater the value of  $n$ , the ~~higher~~ <sup>lower</sup> the applied stress needs to be before such behaviour is recorded. The emissions show a characteristically distinct curve for each value of  $n$ . For  $n = 1$  failure occurs by breakage of fibres in the  $0^\circ$  plies with no prior acoustic emissions. The acoustic emissions are thought to be due to transverse cracking in the  $90^\circ$  plies.

Graphs of the strain energy release rate coefficients versus crack length for different values of  $n$  showed a single linear increase for all values of  $n$  up to a maximum at three quarters the thickness of the  $90^\circ$  layer, where they start to decrease toward the  $0^\circ/90^\circ$  interface. Hence any cracks propagating in the thinner  $90^\circ$  layers are likely to be arrested as they approach the interface, whereas cracks in the thicker  $90^\circ$  layers will continue to grow as the strain energy release rate coefficients increase. If the reduction in these coefficients past the maximum is not too great propagation may proceed to the interface.

For strong interfacial bonding an interfacial shear stress is developed at the end of a transverse crack as the load formerly carried by the  $90^\circ$  layer is transferred to the  $0^\circ$  layer. This stress decays exponentially a short distance from the crack tip in what is

known as a shear lag zone. The distance has been found to be proportional to the thickness of the 90° layer. Any subsequent cracks in the vicinity of the shear lag zone are effected by the shear stresses which must be incorporated in determinations of the strain energy release rate.

As the applied stress is increased more cracks form as the flaw that has the next highest strain energy release rate after incorporating shear lag effects propagates. Experiment has shown crack development to be essentially probabilistic in nature but for different 90° layer thicknesses the process is characteristically distinct. The thicker the 90° layer the lower the stress values at which cracks initiate such that for a single 90° layer failure is by fibre breakage in the 0° layers with no prior transverse cracking.

#### 2.8.4 Fibre Failure

The carbon fibres have a lower strain to failure than the epoxy resin matrix and assuming a uniform axial strain ultimate failure of a continuous fibre-reinforced composite will occur at the fibre breaking strain. For a unidirectional composite loaded in the fibre direction this leads to a prediction of a composite strength given by a rule of mixtures expression of the fibre tensile strength and the epoxy stress at a strain equal to the fibre failure strain.

This simplistic approach is inadequate since the individual fibres have a distribution of strengths due to the presence of imperfections, or Griffith flaws along the lengths of the fibres. The fibre strengths also decrease with increasing length of the fibres. Initial fibre

failure will not depend either on the sum of the fibre strengths or the average of the fibre strengths but on failure of the weakest fibre. This in turn causes a perturbation in the local stress field with high interfacial shear stresses developed at the fibre ends due to the vanishing axial stress. There will also be an increase in the stresses carried by the adjacent fibres.

At a fibre breakage the resulting damage will depend on the matrix and interfacial strengths. For a strong interface and brittle matrix the crack will continue to propagate through the matrix and adjacent fibres in a translaminar failure. This is not typical of polymer matrix composites. For a matrix having a low yield stress the crack will be blunted due to redistribution of the stresses and will not propagate further or, for an interface having a weak shear strength, the interface will fail and the crack will propagate along the fibre matrix interface. The latter mechanisms are more commonly observed in polymer matrix composites.

Various theories have been put forward to model the progression of the failure incorporating Weibull distributions of fibre strengths and statistical techniques. In uniaxial compression fibres have been observed to fail by microbuckling and kink-band formation.

Microbuckling of adjacent fibres may be in phase (shear mode) or out of phase (extension mode). Kink-band formation due to deformation along slip planes is seen in highly anisotropic fibres having a fibrillar structure and is attributed to their poor shear strength.

Marotzke [84] studied the local stress distributions around fibre ends under uniaxial loading using the finite element method. Glass fibres

in a thermoplastic matrix were considered. The high axial stresses in the fibre were shown to be transferred to the matrix around the fibre break through high interfacial shear stresses and to a lesser extent by a slight increase in the matrix axial stress. These matrix shear and axial stresses lead to either plastic yielding of the matrix with debonding of the fibre or matrix cracking and propagation along the fibre/matrix interface. The former results in a high energy fracture known as fibre pull-out and occurs in composites having a ductile matrix and high interfacial shear strength. The latter produces a low energy fracture and occurs in composites having a brittle matrix and low interfacial shear strength. Composites failing by fibre pull-out have good fatigue properties and impact resistance whilst the reverse is true for those failing by matrix cracking. The finite element model assumed the failure to be by the latter mechanism.

An algorithm was developed to monitor the effect of crack propagation along the interface. On the formation of a crack the axial stresses at the fibre end were reduced to zero. These increased linearly along the length of the crack and the slope of the line decreased as the crack propagated. The general level of the axial stresses in the fibre away from the fibre break were observed to decrease with increasing crack length. In addition as the crack propagated the maximum interfacial shear stresses decreased marginally and moved to the crack tip. Thus it is apparent that delamination of the fibre end leads to a transfer of the load from the fibre end to the crack tip for a brittle matrix and that total failure of the interface is probable.

Radial stresses were only apparent in the region of the broken fibre end where they reached high compressive values for the perfectly

bonded fibre, which decreased as the crack propagated. They have the effect of limiting the stress transfer through the debonded interface.

#### 2.8.5 Visco-Elastic Behaviour

Sato and Kurauchi [85] studied the deformation behaviour of a sheet moulding composite consisting of randomly dispersed chopped strands of glass fibres in a vinyl ester matrix. SEM observations of the microfailure under bending loads showed the behaviour to be dependent on the sizing agent. In one sample microfailure was seen to initiate as microvoiding around the fibre/matrix interface which then spread into the matrix region. Shear yielding of the matrix region between fibres followed with later microcracking at the interface. The microcracking grew into the matrix and to the interface of adjacent fibres resulting in a large crack which ultimately led to final failure of the composite.

A later sample in which the fibres had been treated with a different sizing agent showed brittle interfacial microfailure with no prior microvoiding or shear yielding. The former sample was found to have better fatigue properties, due to the toughening effect of the microvoiding and shear yielding.

Acoustic emission was found to precede ultimate failure and to be associated with the interfacial microcracking. By altering the sizing agent it was found that the acoustic emissions could be delayed to higher loads resulting in composites that had improved fatigue properties. The microvoiding and shear yielding was associated with increasing visco-elastic behaviour of the interphase.

Studies of sheet moulding composites made from carbon fibres showed acoustic emission to be produced on cooling from 200°C to room temperature. This was thought to be due to interfacial failure induced by the thermal residual microstresses. However such failure was not readily apparent using SEM. It was suggested that the interfacial microfailure was therefore very small. Further results showed that increasing amounts of sizing agents reduced the acoustic emission counts. It was thought that the sizing agent diffused into the matrix surrounding the fibre producing a layer between the matrix and the fibre of a different composition. This interlayer or interphase was thought to have a lower elastic modulus. Residual thermal stresses would therefore be relaxed in the region of the interphase and the microcracking suppressed.

Morgan and Mones [86] found localized plastic flow to have occurred during the deformation and failure process of epoxies. Fracture energies two or three times the theoretical estimates for purely brittle fracture having been reported. Studies of TGDDM-DDS and DGEBA-DETA epoxies showed deformation to be by a crazing process and to a lesser extent in TGDDM-DDS epoxies by shear banding. Fracture surfaces showed that cracks were more likely to propagate along the weak planes caused by these shear banding effects.

The modes of deformation/failure and mechanical properties of the epoxies were thought most highly influenced by the cross-linked network structures and the microvoid characteristics. It was proposed that regions of high cross-link density flow over regions of low cross-link density. DGEBA-DETA, TGDDM-DDS epoxies are not highly

cross linked and this would explain the high temperature ductility, thermal history and strain rate effects in the response of DGEBA-DETA epoxies.

Birefringence observed in TGDDM-DDS  $\text{BF}_3$  catalyzed epoxies was thought to be due to uneven catalyzation. Nodules, approximately 1 mm in size, and consisting of preferentially aligned macromolecules, were observed under polarized light. The nodules were thought to be associated with regions of high catalyst concentrations where the polymerization reaction proceeded at a faster rate. As a result of the chemical heterogeneity stresses would be generated during gelation and glass formation. Thus when observed under a polarizing microscope a birefringent network was be apparent. It was also noted that the TGDDM-DDS networks are not exclusively epoxide-amine reactions.

Microvoids were considered to form stress concentrations and sites for the accumulation of sorbed moisture, both deleterious to the mechanical behaviour of the epoxies. Causes of microvoids were given as trapped air and low molecular weight material during the curing process. The low molecular weight material for example crystals of DGEBA monomer and DDS crystallites are subsequently eliminated during the cure process.

## 2.9 PAFEC

In addition to the PAFEC manuals [87-90] two reports are worth mentioning regarding the use of the PAFEC finite element program. H. Watkins [91] studied heat transfer problems and applied them to the analysis of hot steel strip using an appropriate heat transfer coefficient to model a boundary layer. J. P. Stuart [92] analysed the

strains and stresses in a rectangular carbon fibre/epoxy resin laminate of dimensions 100 mm by 50 mm and thickness 5 mm under conditions of plane stress.

They give detailed descriptions and comments regarding the PAFEC method of analysis together with examples and recommendations for effective modelling.

#### 2.10 Resumé

This literature survey is by no means extensive since detailed descriptions of only some of the more relevant papers have been given. The search has shown that work so far has concentrated on the nature of the macrostresses in unidirectional composites and laminates. Deformations have largely been assumed to be elastic, which is a reasonable assumption for graphite-epoxy laminates.

Less literature is available concerning the residual microstresses within individual plies and effects due to visco-elastic or viscoplastic material behaviour. There is also little evidence of analyses of the stresses in more complex continuous carbon fibre structures, for example woven and knitted fabrics.

### 3 PROCEDURE

Stresses were determined using a finite element software package, PAFEC (Program for Automatic Finite Element Calculations) incorporating an interactive graphics system, PIGS for the pre- and post-processing of data using polychrome graphics terminals.

#### 3.1 Theory

There follows a summary of the theory of the finite element/finite difference techniques used in the modelling.

##### 3.1.1 The Finite Element Method

The finite element method provides an approximate solution to engineering problems that are expressed in terms of differential equations by requiring the value of a functional when calculated over the whole region to be minimized. The functional,  $\Pi$  is expressed as the integral of a function of an unknown function, over a volume,  $V$  and boundary,  $S$ . That is in general terms

$$\Pi = \int_V f(\phi), \frac{\partial}{\partial x}(\phi) \dots dV + \int_S g(\phi), \frac{\partial}{\partial x}(\phi) \dots dS$$

where  $\phi$  is the unknown function. It is necessary that some variational principle is presumed valid over the region.

The differential Euler equations required to solve the problem then represent a state of equilibrium as follows

$$\frac{\partial f}{\partial \phi} - \frac{\partial}{\partial x} \frac{\partial f}{\partial \phi_x} \dots = 0$$

within the region V, and

$$\frac{\partial g}{\partial \phi} - \frac{\partial}{\partial x} \frac{\partial g}{\partial \phi_x} \dots = 0$$

on the boundary S, where  $\phi_x = \partial\phi/\partial x$ .

The structure being analysed is divided into a mesh of elements and the functional evaluated for each element. Summation of the functional over all elements, when minimized and assuming connectivity at the element nodes, yields a solution to the problem.

### 3.1.2 Finite Difference Methods

Finite difference methods also provide solutions to engineering problems governed by differential equations but approximate to these in a discrete manner over a typical infinitesimal region.

Various methods of solution exist, the simplest being the explicit method. For a differential equation, say where temperature is expressed in terms of space and time, as in transient heat flow, and the temperatures are required at a later point in time, a forward value is used for the time derivative but backward known values are used for the calculation of the space derivative. Stability of the solution however requires that a quantity known as the Fourier number which is expressed in terms of the space and time step is less than or equal to 0.5. This imposes limitations on the time and space steps that can be used in the construction of the mesh.

More complex fully implicit methods are stable for any value of the Fourier number. These represent the second order space derivative in

terms of forward unknown values at the next time step. Each equation contains three unknowns and the solution is obtained by solving a system of equations. The method has the disadvantage that there is a larger truncation error and the accuracy which increases with the choice of time step is reduced.

General implicit methods resolve these limitations on the accuracy and time step by evaluating the second-order space derivative at a point intermediate between the two time steps, applying a weighting,  $\lambda$  and  $1 - \lambda$  to each of these values, respectively. The accuracy of the method decreases with increasing  $\lambda$  and is stable for all time steps and Fourier numbers provided  $\lambda$  is in the range 0.5 to 1.0. For  $\lambda = 0.5$ . The most accurate solution is obtained for a system that is stable for all time steps and Fourier numbers. The method is then known as the Crank-Nicolson method.

### 3.1.3 Temperature Distributions

The PAFEC analysis assumes a temperature distribution  $\{\theta\}$  governed by the Poisson equation

$$\frac{\delta^2 \theta}{\delta x^2} + \frac{\delta^2 \theta}{\delta y^2} + \frac{\delta^2 \theta}{\delta z^2} = \alpha \frac{\delta \theta}{\delta t}$$

A finite element solution can be obtained from the minimum value of the functional.

$$[S]\{\theta\} + [M]\{\dot{\theta}\} = [Q]$$

where,

- $\dot{\theta}$  = the derivatives of temperature with respect to time
- [S] = the square symmetric thermal conductivity matrix
- [M] = the square symmetric thermal mass matrix
- [Q] = the vector of heat fluxes which enter the structure at the nodes

Knowing  $\theta$  at a particular instant in time, PAFEC calculates the temperature gradients at that instant in time and rather than a finite element method uses a finite difference, Crank-Nicolson method to predict the transient temperature distribution at a later point in time,  $(t + \delta t)$ . Although the Crank-Nicolson method is stable for all time steps and Fourier numbers it does exhibit an oscillatory behaviour which does not decay. This is most severe at points where a large thermal shock is applied and in such cases it is important that the Fourier number has a value close to unity.

For steady state problems  $\dot{\theta} = 0$  the Poisson equation reduces to the Laplace equation,

$$\frac{\delta^2 \theta}{\delta x^2} + \frac{\delta^2 \theta}{\delta y^2} = 0$$

The minimum of the functional,

$$[S]\{\theta\} = [Q]$$

can then be solved provided at any one node either the temperature or the heat flux at that node is known. For such steady state problems PAFEC uses a finite element method of solution.

Temperature calculation elements are used in the analysis having one

degree of freedom at each node, viz temperature.

#### 3.1.4 Stress Distributions

For stress analyses various variational functions exist depending on which of the displacements, strains and stresses are unknown. The more complex of these have all of the stresses, strains and displacements unknown. By imposing certain conditions simpler variational functions are obtained. For example the condition that specified stress-strain relations are always satisfied.

The simplest situations use the principle of minimum potential energy, having only the displacements unknown and the strain displacement relations imposed; for example a linear elastic solid deforming according to Hooke's law, and the principle of minimum complementary energy having only the stresses unknown and the condition that the stresses are in equilibrium imposed.

For the case of minimum potential energy the variational function is given by the strain energy stored internally less the work done by externally applied loads. The structure is divided into a mesh of elements, the strain energy calculated for each element and summed over all elements. One dimensional, linear, two dimensional, triangular and rectangular and three dimensional, tetrahedral and brick elements exist.

The type of element used in the analysis depends on the deformations permissible, the degree of accuracy and the economy of computing required. Each type of element has a characteristic polynomial shape function,  $[N]$  expressed as a function of position and used to

describe the displacements at a general point within the element,  $\{\mu\}$  in terms of the nodal displacements of that element,  $\{\mu_e\}$ . The resulting pattern of displacements is known as the interpolation function,

$$\{\mu\} = [N] \{\mu_e\}$$

The shape functions are chosen to give the appropriate nodal displacements when the co-ordinates of the appropriate node are inserted. They have to satisfy certain convergence criteria, one of which is that continuity of the displacements (and their derivatives) occurs across the element boundaries. This ensures that finite integral values are obtained in the solution.

Shape functions are also used to describe the variation of the unknown function across the element.

The number of degrees of freedom or unknowns in the displacements and unknown function are dependent on the order of the shape function. Obviously the greater the number of nodes on an element the higher the degrees of freedom and the higher the order of the shape function. For a given degree of accuracy elements having higher order shape functions will require fewer but more complex elements. The effect this has on computing efficiency is relevant.

This is the situation for simple triangular and rectangular elements. For elements with more arbitrary shapes perhaps with curved sides it is necessary to define a local co-ordinate system. The elements are transformed into a simple shape in the  $\xi, \eta, \zeta$  co-ordinate system using, a geometric shape function  $[N]$ . Thus the curvilinear co-

ordinates are expressed in terms of the nodal co-ordinates. The geometric shape function is generally the same as that used to calculate the displacements and unknown function when the elements are termed isoparametric but can be different as in super- and sub-parametric elements. These elements are of importance in the modelling of the complex geometries often met with in practice where simple element shapes are impractical.

For conditions of plane stress or plane strain translational displacements are considered in two mutually perpendicular directions. A commonly used element is the eight noded isoparametric curvilinear element for plane stress and plane strain.

Displacements are expressed as a quadratic function of the curvilinear co-ordinates  $\xi$  and  $\eta$ . Knowing the displacements at each node the displacements at a general point,  $(\xi, \eta)$  can be expressed in terms of the nodal displacements using the shape function. The normal and shear strains are then determined from the derivatives of the displacements and the stresses calculated by multiplying the strain vector by the elasticity matrix [D].

The element strain energy, S.E. given by

$$\text{S.E.} = \frac{1}{2} \int (\epsilon)^T (\sigma) h \, dA,$$

can then be expressed in terms of the nodal displacements. The superscript T indicates the transpose of the strain vector and h and A are the thickness and area of the element, respectively.

Inclusion of rotational degrees of freedom requires the use of other categories of element.

### 3.2 The PAFEC Finite Element Software

Information, such as node co-ordinates, material properties, temperature distributions, loadings and lamination sequence are input into PAFEC using data modules. These are appended to a control module which details the conditions and path of the calculations, for example; plain strain, axisymmetric and read temperature file, calculate transient temperatures, to form a data or .DAT file.

Information created interactively through PIGS, such as mesh geometry, loadings, restraints and material type can be automatically saved to a .DAT file. Execution of the .DAT file will produce the finite element or finite difference calculations in a series of phases. During this process binary backing store files, .BS and .SS are created to store the data modules, stiffness matrices and calculated stress or temperature distributions. Phases 1, 4, 6, 7 and 9 are used for the modelling in this thesis.

Phase 1 processes the data modules, checking for syntax errors, and places them on backing store. Phase 4 processes the constraints on the system. Phase 6 calculates the stiffness matrices and places them on backing store. Phase 7 solves the system equations for displacements/temperatures and Phase 9 calculates the stress distributions which are then saved to the .SS file.

The results can be extracted from the Phase files or output graphically as displacements, contours or vectors. Alternatively the

displacements/temperatures and stresses can be processed and viewed interactively in PIGS. The processing files are written in Fortran.

References 91 and 92 are good examples of the use of PAFEC for heat transfer calculations and the analysis of stresses in anisotropic laminated materials, respectively.

### 3.3 Finite Difference Modelling of the Temperature Distribution through the Thickness of a Prepreg

Initially the temperature distribution through the thickness of 0.100 mm wide, 1 m long section of an eighteen ply laminate originally at 190°C was modelled using finite difference techniques. A constant cooling rate of the top surface to 20° over 2 hours was assumed. This was to simulate cooling of a prepreg to room temperature after cure. The carbon fibre/epoxy resin layers were assumed separated by a thin film of epoxy resin with the carbon fibre/epoxy resin layer and epoxy resin layer thicknesses and properties estimated as follows

Layer	Epoxy Resin	Carbon Fibre /Epoxy Resin
Density, RO (kg/m <sup>3</sup> )	1200	1500
Thermal conductivity, KX, KY (Jm <sup>-1</sup> s <sup>-1</sup> °C <sup>-1</sup> )	0.2	26
Specific heat capacity, SH (Jkg <sup>-1</sup> °C <sup>-1</sup> )	800	712
Layer thickness, L (mm)	0.046	0.254

Values for the epoxy resin were obtained from PAFEC standard material properties for Araldite, a typical epoxy resin, and values for the carbon fibre/epoxy resin layer from PLASCAM, a data base for plastic materials, as properties of a typical carbon fibre/epoxy resin

laminate. PLASCAM values for the density of typical "general purpose", "high heat" and "flexible" epoxy resins gave a value for the specific gravity of 1.2 rather than the 1.23 used by PAFEC. This was therefore substituted for the value of 1.23. Since values for the thermal conductivity and specific gravity of a carbon fibre/epoxy resin laminate were unobtainable values were used based on those of the carbon fibre given in reference [19] of the literature survey.

The carbon fibre/epoxy resin layer thickness was based on a value of 10 thousandths of an inch [93]. The epoxy resin film thickness was estimated as no information was available regarding a suitable value. A film approximately one twentieth of a millimetre producing a total layer thickness of 0.3 mm was thought appropriate. A previous finite element analyses has modelled laminates as membrane fibre bearing layers separated by layers of finite thickness which develop only interlaminar shearing stresses [50].

A mesh was constructed using eight noded temperature calculation - 39215, elements. The elements have one degree of freedom at each node, viz temperature. The mesh was one element wide having a single element to represent each layer.

The above information was incorporated into a program MATA (macromodel/temperature/version A - cooling) which modelled cooling through 170°C of the top surface of a laminate originally at 190°C. The transient temperature distribution was calculated every 2 seconds and the resulting temperature distribution saved at 900 second intervals. Temperatures were calculated in a similar manner using a program MATD (macromodel/temperature/version D - heating). This

assumed heating through 170°C of the top surface of a laminate originally at 20°C. The latter program would give the temperature distribution generated on heating of the laminate to the cure temperature.

The saved temperature distributions were later used in the calculation of the macrostresses. Due to problems with the determination of thermal stresses using PAFEC in which the thermal expansions are calculated relative to a strain free temperature of 0°C the temperatures were expressed as differences from the assumed strain free temperature of 190°C. For a true representation of the temperatures programs MATH and MATG were created corresponding to programs MATA and MATD, respectively.

Results showed the temperature difference through the thickness of the laminate at the end of the 2 hours to be less than 1°C. This was thought insignificant and it was assumed that the temperature gradients generated in the laminate on cooling from the cure temperature were negligible.

#### 3.4 Finite Element Modelling of the Macro stresses

The deformation, the stresses -  $\sigma_{xx}$ ,  $\sigma_{yy}$ ,  $\sigma_{xy}$ , maximum principal, minimum principal, von Mises, absolute, maximum shear and maximum in-plane shear were calculated based on the saved temperature distributions at the end of the two hours using programs, MASA (macromodel/stresses/cooling) and MASD (heating), assuming conditions of plane stress and programs, MASI (cooling) and MASJ (heating), assuming conditions of plane strain. Eight noded isoparametric

curvilinear quadrilateral, 36215 elements replaced the temperature calculation elements. These assume constant stresses through the thickness of the element and negligible bending stresses. The elements have two degrees of freedom ( $\mu_x, \mu_y$ ) in their own plane at each node.

Material properties were used as follows

Layer	Epoxy Resin	Carbon Fibre /Epoxy Resin
Principal compliances, SXX, SYX ( $m^2N^{-1}$ )	290 x 10 <sup>-12</sup>	5 x 10 <sup>-12</sup>
Cross compliance, SXY ( $m^2N^{-1}$ )	-130 x 10 <sup>-12</sup>	-1.25 x 10 <sup>-12</sup>
Shear compliance, SHXY ( $m^2N^{-1}$ )	841 x 10 <sup>-12</sup>	12.5 x 10 <sup>-12</sup>
Thermal expansion coefficients		
ALX,ALY ( $^{\circ}C^{-1}$ )	60 x 10 <sup>-6</sup>	0.5 x 10 <sup>-6</sup>
Young's modulus, E (GPa)	3.45	200
Poisson's Ratio, NU	0.45	0.25
Shear modulus,G (GPa)	1.2	80

As previously the epoxy resin properties were taken from PAFEC standard material properties for araldite and the thermal expansion coefficient of the carbon fibre/epoxy resin layer from PLASCAM information for a typical carbon fibre laminate. It is noted in PAFEC that the actual value of the Poisson's ratio for a photoelastic material is 0.5. This is not programmed into the scheme because of the numerical difficulties that arise with NU = 0.5. Values for the Poisson's ratio and Young's modulus of the carbon fibre/epoxy resin layer were taken as representative values from a variety of sources [2, 4, 5, 6, 7, 8, 9, 10, 94]

The shear modulus,  $G$  and compliances,  $SHXY$ ,  $SXX$ ,  $SXY$  (used to obtain strain from stress and required by the PAFEC laminate module) were calculated as follows

$$\begin{aligned} G &= E/2(1 + \nu) & SHXY &= 1/G \\ SXX, SYY &= 1/E & SXY &= -\nu/E \end{aligned}$$

The mesh was restrained to remain plane along the left and bottom edges with the corner node restrained in all directions.

A state of plane stress exists in infinite thin plates where negligible stresses are generated in the thickness direction. Zero strain in the out of plane direction implies a state of plane strain, this is typically shown along the axis of infinitely long cylinders. 7  $\mu\text{m}$  diameter, 1 m long fibres would approximate this condition and the programs MATA and MASI modelling cooling through 170°C under conditions of plane strain were thought to best represent the stresses generated on cooling after cure.

To improve the accuracy a refined mesh consisting of two elements each 0.050 mm wide was constructed based on the program MASI. Since the calculated temperature gradients through the thickness of the laminate were so small rather than reading a saved temperature distribution a uniform temperature loading of -170°C was applied. The program was termed ASI2.

Although isotropic material properties were assumed orthotropic elements, indicated by five as the last digit of the element numbers, were used so that in any subsequent modelling orthotropic material

properties could be introduced.

### 3.5 Finite Element Modelling of the Microstresses - Regular Hexagonal Fibre Array

On the basis that the temperature gradients within the laminate are negligible and the resulting stresses not high enough to initiate failure of the materials it was decided to concentrate on the residual thermal microstresses, created as a result of the different thermal expansion coefficients of the epoxy resin and the carbon fibres.

Since the geometry in the longitudinal direction of the fibres is constant the stresses could be adequately modelled by analyzing the stresses in a transverse section. In addition assuming a regular array of fibres, that is a distribution in which a structure regularly repeats itself throughout the array, the modelling could involve a unit cell approach. The most highly packed structures conform to a regular hexagonal array - see Figure 6, with fibre volume fractions of up to 90.6%. By comparison the highest fibre volume fractions achievable in regular square arrays are 78.5% see Figure 7. It was decided to model the hexagonal array as being the more probable distribution at the high volume fractions obtained commercially of 65% [93] and as has been assumed in the majority of the literature.

A triangular unit cell of the transverse section of a regular hexagonal array of fibres in an epoxy resin matrix was modelled assuming a typical fibre diameter of 7  $\mu\text{m}$  and interfibre distance of 4  $\mu\text{m}$  [93] as shown in Figure 6. This gave a fibre volume fraction of 37%. Material properties were used based on those for Torayca T300 carbon fibres and Ciba-Geigy BSL 914 epoxy resin as given below.

Material	Carbon Fibre	Epoxy Resin
Young's modulus (GPa)	15.8	3.9
Poisson's ratio	0.42	0.41
Thermal expansion coefficient ( $^{\circ}\text{C}^{-1}$ )	$8.0 \times 10^{-6}$	$48 \times 10^{-6}$

These were obtained from characterization tests undertaken on the epoxy resin at  $23^{\circ}\text{C}$  by Ciba-Geigy for Rolls-Royce plc and transverse properties given for the fibres in the literature [73,83].

The unit cell was assumed to undergo a uniform temperature decrease of  $170^{\circ}\text{C}$  from  $190^{\circ}\text{C}$  to  $20^{\circ}\text{C}$ .

Two cases were considered: that of a "radially restrained" unit cell restrained along the lines OA and OB, in a direction perpendicular to these lines, programs ES01 (plane stress) and ES03 (plane strain), and that of a "totally restrained" unit cell restrained along the outside edges, OA, OB and AB, perpendicular to these lines, program ES02 (plane strain) - See Figure 6. The former "radially restrained" unit cells used absolute values for the thermal expansion coefficients of the fibre and the matrix and the latter "totally restrained" unit cells used thermal expansion coefficients of the fibre and the matrix expressed relative to a mean overall value for the unit cell. The mean value was calculated from those of the fibre and the matrix weighted in proportion to the volume fraction of the material as follows

$$\alpha_{\text{mean}} = V_{\text{carbon fibre}} \alpha_{\text{carbon fibre}} + V_{\text{epoxy resin}} \alpha_{\text{epoxy resin}}$$

The restraint applied to the radially restrained unit cell was so as to preserve the symmetry of the array. The use of expansion

coefficients relative to a mean value in the totally restrained unit cell required the condition that the cell as a whole underwent no overall deformation. The former calculated the stresses generated due to differences in displacement from the free displacements of the epoxy resin and the carbon fibre and the latter those due to differences in displacement from a mean free thermal expansion of the material as a whole. The deformation and stresses were calculated for conditions of plane strain and plane stress.

The relative thermal expansion coefficients used in the totally restrained model were calculated at

$$\begin{aligned}\alpha_{\text{carbon fibre}} &= -25 \times 10^{-6} \\ \alpha_{\text{epoxy resin}} &= 15 \times 10^{-6}\end{aligned}$$

from a mean value of  $33 \times 10^{-6}$ .

### 3.5.1 Incorporation of Temperature Dependent Epoxy Resin Properties

The Ciba-Geigy characterization tests showed the properties of Ciba-Geigy BSL 914 epoxy resin to vary appreciably with temperature. This temperature dependence has been incorporated into both the macro- and micro-modelling of the stress distributions. At the microlevel it was decided to concentrate on the radially restrained unit cell under conditions of plane strain. This provided the best approximation to conditions around long fibres surrounded by epoxy resin.

The epoxy resin properties were allowed to vary with temperature in a program, ES04, according to the Ciba-Geigy characterization tests as follows

Temperature (°C)	-20	23	85	140	175	200
Thermal Expansion						
Coeff.( x 10 <sup>-6</sup> °C <sup>-1</sup> )	-	48	53	65	81	104
Young's Modulus						
(GPa)	4.4	3.9	3.4	2.8	-	-
Poisson's Ratio	0.398	0.407	0.413	0.423	-	-

### 3.6 Finite Element Modelling of the Microstresses - Other Regular Fibre Arrays

The micromodelling so far had considered one specific distribution of fibres, that is hexagonal packing of 7  $\mu\text{m}$  diameter fibres separated by a distance of 4  $\mu\text{m}$ . To model alternative arrangements of fibres a similar right angled triangle was used for the mesh but allow but the acute angles of the triangle were allowed to vary in a way dependent on the proposed arrangement of fibres.

In addition the modelling employed a fibre volume fraction of 36.7%. Commercially fibre volume fractions of 65% are achievable and fibre diameters can range from 6  $\mu\text{m}$  to 11  $\mu\text{m}$ . By altering the dimensions of the micromesh it was proposed to study the effect of varying fibre volume fraction, fibre diameter and consequent variation in interfibre distance on the microstresses.

Triangular meshes with various "co-ordination angles",  $\theta$  subtended at the fibre centre were modelled. Angles of 30°, 45°, 60° and 15° were chosen since these represent arrangements in which the fibres have 6, 8, 3 and 12 nearest neighbours, respectively see Figures 5, 6,

7 and 8. The regular square array obtained for  $\theta = 45^\circ$  has been modelled in the literature [63,65,73] in addition to the hexagonal array. Less closely packed structures are achievable using a square array but at low volume fractions such structures are as equally realistic as hexagonal arrays.

It should be noted that the meshes with a  $15^\circ$  co-ordination angle do not represent unit cells since they can not be replicated to completely fill a transverse layer whilst maintaining the prescribed fibre co-ordination. They instead represent a region of regularity local to a single fibre. The calculated fibre volume fractions for these meshes are for this local region and not the composite as a whole. In the finite element modelling it was necessary to model two adjacent  $15^\circ$  triangles in order to produce an element angle at point O not less than  $30^\circ$ .

Volume fractions were calculated for interfibre distances of 0.5, 1.5, 2.5, 3.5, 4.5, 5.5 and fibre diameters of  $6 \mu\text{m}$ ,  $7 \mu\text{m}$ ,  $8 \mu\text{m}$ ,  $9 \mu\text{m}$ ,  $10 \mu\text{m}$  and  $11 \mu\text{m}$ . Meshes were constructed within the range 30% to 65% fibre volume fraction. The calculated volume fractions are detailed in Table 1.

To preserve the symmetry of the packings it is necessary that the end line, AB of the unit cell remains straight and the  $90^\circ$  OAB and acute  $30^\circ$ ,  $45^\circ$ ,  $60^\circ$  and  $15^\circ$  angles, OBA angles do not change - See Figures 6-9. In the former hexagonal array programs the line AB was noticed to have a slight incline away from the point A (Figure 76). This led to a modification to the restraints so that nodes on the end plane were constrained to move in the y-direction by an amount equal to that

moved in the y-direction by the node at A.

The various meshes and programs were identified using a four character name. The first character represented the fibre diameter with A, B, C, D and E equivalent to fibre ~~diameters~~ <sup>radii</sup> of 3.0, 3.5, 4.0, 4.5, 5.0 and 5.5  $\mu\text{m}$  respectively. The second two characters represented the co-ordination angle with 15, 30, 45 and 60 equivalent to co-ordination angles of  $15^\circ$ ,  $30^\circ$ ,  $45^\circ$  and  $60^\circ$ , respectively. The last character represented the interfibre distance with A, B, C, D, E, and F equivalent to interfibre distances of 0.5, 1.5, 2.5, 3.5, 4.5 and 5.5  $\mu\text{m}$ , respectively.

Later the meshes were refined for improved accuracy and, for simplicity, to identify these meshes and programs separately the order of the co-ordination angles was reversed. Hence 51, 03, 54 and 06 were equivalent to co-ordination angles of  $15^\circ$ ,  $30^\circ$ ,  $45^\circ$  and  $60^\circ$ , respectively. The program coding is detailed for ease of reference in Table 2.

It was observed that in the case of the meshes having a  $15^\circ$  co-ordination angle there was a limiting interfibre distance below which 12 fibres could not be arranged around one single fibre in a regular array. Arrangements below this minimum interfibre distance were however modelled provided they fell within the volume fraction range 30-65%. Such arrangements could well exist in random arrays and it was useful to observe the general trend. The volume fractions associated with the minimum interfibre distances were of the order 20-30% and although this was outside the volume fraction range considered it was found useful to model the first array associated with an interfibre

distance greater than this minimum.

The position of the maximum principal stress was located in the mesh and the effect of varying the fibre volume fraction, the interfibre distance, the angles within the triangle and the fibre diameter on the value and the location of the maximum stress point monitored. This high stress point would be the most probable place for crack initiation. It is particularly relevant when considered in combination with stress raisers. These might include; cracks, porosity, inclusions such as undissolved crystals and impurities and phase separation of the matrix. The stress concentrations associated with the defects, if occurring in an already highly stressed region, would make failure of the material that much more likely. The von Mises, Tresca, minimum principal and maximum shear stresses were also of interest due to the significance these have on the viscous/plastic flow of the epoxy resin.

There is no evidence in the literature of these effects having been studied in detail before. Nevertheless such variations in fibre density and arrangement do affect the microstress fields and are of practical interest.

### 3.6.1 Incorporation of Anisotropic Carbon Fibre Properties

The earlier modelling of the regular hexagonal array of fibres had made no allowance for anisotropic carbon fibre properties with transverse properties being used. Previous work [2,63,65,73,83,93] suggests that the carbon fibres are markedly anisotropic, with respect to, in particular, the Young's modulus and thermal expansion

coefficient. In the later model anisotropic (transversely isotropic) carbon fibre properties were introduced as follows.

Carbon Fibre	Transverse	Axial
Young's modulus (GPa)	15.8	226
Poisson's ratio	0.42	0.30
Thermal expansion coefficient ( $^{\circ}\text{C}^{-1}$ )	$8.0 \times 10^{-6}$	$-0.7 \times 10^{-6}$
Shear Modulus (GPa)	5.56	8.19

Again these values were obtained from properties given in the literature [73, 83]. A value for the transverse shear modulus was deduced from the ratio of  $E_{Lf}/G_{LTF} = 27.59$  given by Rohwer and Jiu [63]. There appears to be some doubt in previous publications concerning an appropriate value for the transverse Poisson's ratio of the carbon fibre. It is a difficult quantity to measure and is often estimated. There is a general consensus on the use of a value of 0.15, e.g. Zhang and Evans [95], Chen and Chang [96] and Whitney [97]. By comparison Goggin [98] assumed a value of 0.28 with an axial Poisson's ratio of 0.50, Hashin [99] a value of 0.30 with  $\nu_A = 0.20$  and Adams and Miller [65] a value of 0.25 with  $\nu_A = 0.20$ .

A typical program, B03C was copied and the transverse Poisson's ratio changed to 0.15. By running this program and comparing the results to those obtained using a Poisson's ratio of 0.42 the effect of the change on the deformations and stresses could be observed.

Subsequently the transverse Poisson's ratio was modified to 0.15 in all the programs and the original program B03C, having a Poisson's ratio of 0.42, renamed B13C.

### 3.7 Finite Element Modelling of Random Fibre Arrays

To model random arrays of fibres, more closely resembling the fibre arrays obtained in practice, the unit cell approach is no longer applicable. It is however possible to consider specific local arrangements of fibres.

There is little evidence in the literature of studies concerning the effect of local variations in fibre packing on the residual microstresses. The most closely packed structures are obtained assuming regular hexagonal arrays of fibres. As the fibre volume fraction decreases it would be expected that the fibre distribution would become increasingly random perhaps with clustering of the fibres. The shortest interfibre distance would then vary from location to location.

To model these random arrays similar right angled triangles were used as in the regular arrays but these were no longer assumed to repeat themselves regularly throughout the array. Instead a "hypothetical" Voronoi cell was assembled to model a proposed random arrangement of fibres, program V001. Two of each of the 15°, 30°, 45° and 60° triangular meshes for a fibre of diameter 7  $\mu\text{m}$  were incorporated. This gave a cell having five sides (five nearest neighbours) and a fibre volume fraction of 26.7%. It could therefore be regarded as intermediate between an hexagonal and a square array. The node at the fibre centre was totally restrained with no other restraints applied. The shortest interfibre distance was 1  $\mu\text{m}$  and the longest interfibre distance was 12  $\mu\text{m}$ . This array is not based on an observed distribution but is one that incorporates the various cells examined

in the regular arrays in a single model. It does therefore represent the range of possible geometries in a single model.

The effect of variation in fibre distribution, within the plies, on the generation of residual macrostresses in multidirectional laminates is of practical interest. If the microstructure is such that the transverse coefficient of thermal expansion and/or the transverse Young's modulus of a ply is large then the resulting residual macrostresses will be large. The restraint imposed on anisotropic plies in a multidirectional laminate is dependent upon the relative orientation of adjacent plies. The greater the anisotropy in the thermal expansion coefficient and Young's modulus the greater the stress generated in the ply will be. Similarly if the residual microstresses are large then the ply will be weaker and more likely to fail, thus affecting the properties of the lamina as a whole. Since cracks initiate at high stress points then the range of microstress values is relevant with regard to failure of the laminate.

It can be seen that by modelling regular fibre arrays an overall average view of the residual microstresses are obtained. However the full range and extremes of the microstresses found in truly random arrays is not evident in such regular arrangements. These extremes are of practical interest, since they will have a marked effect on the residual stress distribution.

To investigate such effects a model needed to be developed that would generate a random array of fibres at different volume fractions. It would then be possible to observe the effect of the variation in interfibre distance and consequent Voronoi cell arrangement on the

stress distributions created during cooling of an actual composite.

### 3.8 Generation of Random Fibre Arrays

A program - FIBDIST3 was developed using BASIC to model random fibre arrays at specified volume fractions. This has been listed in Appendix 1.

The number of fibres and fibre volume fraction to be modelled are specified and a random number generator locates this number of points within a rectangular area that possesses an aspect ratio of 2. Circles of radius,  $r$  having a scaled size appropriate to the required area and area fraction are then generated around these points. The program is such that the centres of the circles must lie within one radius of the edges of the rectangle.

The centres of the circles are tested to find if any are closer than two times the circle radii. If this is so then the circles are moved apart by the amount they overlap + 3 units ( $0.006 \times C$ , where  $C$  is the width of the rectangle) and the testing process repeated. Eventually no circles should overlap, although in cases where the volume fraction of fibre is high this is not achievable in a reasonable time.

The program was used to model two random arrays of 10 fibres at 30% and 50% volume fraction. Random arrays of 10 and 20 fibres at 65% volume fraction did not rearrange themselves satisfactorily with no overlapping. The coordinates of the 30% and 50% volume fraction arrays of fibres were scaled, assuming  $7\mu\text{m}$  diameter fibres, and transferred into PIGS.

### 3.9 Finite Element Modelling of Voronoi Cell from Random Fibre Array with 50% Fibre in the Section

A Voronoi cell arrangement was later constructed about the 50% array. It was obvious that no complete Voronoi cell was contained within the 30% fibre array. The only complete Voronoi cell in the 50 fibre array was enlarged and meshed for finite element analysis, program V053. A single total restraint of the node at the fibre centre was applied as for the hypothetical Voronoi cell.

### 3.10 Accuracy

To determine the accuracy of the finite element meshes plots of the unaveraged stresses were obtained. Continuity of these stresses across the element boundaries is a measure of the accuracy of the modelling. If necessary the meshes were further refined.

### 3.11 Optical Microscopy

Although all the models of the fibre distributions considered so far are theoretically possible, in the case of the randomly generated models, there was a perceived need to obtain information about actual distributions in the composites under consideration. A cured laminate sample, cut with a diamond saw and approximately 9 cm x 17 cm x 3.5 mm, was obtained from Rolls-Royce from which two 1cm x 1cm pieces were cut. The laminate surfaces showed the outer layers to consist of four-harness satin weaves at 45° orientations. The edges as cut by Rolls-Royce showed a smoother and straighter section through the thickness of the laminate.

The pieces were mounted in hardened epoxy resin. One piece was mounted

with the outside surface uppermost and the other with the inner surface uppermost. The samples were polished using 400  $\mu\text{m}$  and 600  $\mu\text{m}$  SiC and subsequently 6  $\mu\text{m}$  and 1  $\mu\text{m}$  diamond. The microstructures were observed with a Zeiss photomicroscope and the images recorded using a video copier. The arrangement of fibres was examined and the samples scanned for the presence of cracks.

The video prints were later photographed and developed for inclusion in the thesis.

### 3.12 Electron Microscopy

The samples examined using the optical microscope were later coated with a thin conducting layer of gold for observation under the electron microscope. The samples were scanned for the presence of microstructural defects.

### 3.13 Modelling of Macrostressess using Classical Lamination Theory

Standard prepreg tapes are of the order 300 mm wide and 5 mm deep. They can therefore be thought to approximate to an infinitely thin plate. According to The Saint Venant's Principle the stresses in thin plates conform to a state of plane stress except in a region of the order of the plate thickness from the free edge, where interlaminar stresses can be developed. This is due to a relaxation of the rigorous boundary conditions applicable at the edge in the centre of the plate. The width of the mesh used previously was insufficient to model this edge effect accurately.

The earlier macromodelling also assumed isotropic ply properties.

The literature has shown the carbon fibre/epoxy resin layers to be largely dependent on the axial carbon fibre properties in the longitudinal direction and the epoxy resin properties in the transverse direction. The carbon fibres are strong, have a high modulus and a small negative thermal expansion. In contrast the epoxy resin is weak, has a low modulus and large positive thermal expansion. Hence in the case of multidirectional laminates in which the successive unidirectional layers are stacked at various orientations to the prepreg length residual stresses are generated due to the mutual restraint of adjacent layers.

Classical lamination theory adequately calculates the stresses away from the edge the laminate whilst also allowing for the incorporation of orthotropic material properties. Thus the residual stresses in multidirectional laminates can be determined. Conditions of plane stress, continuity of the plies across the ply interfaces, and thus a uniform strain through the thickness, and stresses which are balanced through the thickness are assumed.

It was proposed to superimpose the previously obtained microstresses on the macrostress distributions. This would give an idea of the overall stress levels and maximum values. The effect the overall background stress distribution had on the local stress fluctuations would then be apparent.

The computer program, PC-Laminate developed by R Radford [60] was utilized to calculate the mid-plane strains,  $\epsilon^0$  and curvatures,  $\kappa$  together with the stress resultant, N and moment resultant, M in a typical laminate subject to a uniform temperature load of  $-170^\circ\text{C}$ . An

eighteen ply  $[0_4/90_{10}/0_4]$  symmetric laminate was chosen. That is a laminate having a central layer of 10 plies in which the fibre direction is transverse to the laminate axis sandwiched between two layers each of four plies in which the fibre direction is parallel to the laminate axis. The laminate was 4.572 mm thick and incorporated transversely isotropic material properties as used by Pagano and Pipes [44], Wang and Crossman [52] and Stango <sup>& Wang.</sup> [55] as follows.

Carbon Fibre/Epoxy Resin Lamina	Transverse	Longitudinal
Young's modulus (GPa)	14.5	138
Poisson's ratio	0.21	0.21
Shear modulus (GPa)	5.86	5.86
Thermal expansion coefficient ( $^{\circ}\text{C}^{-1}$ )	$28.8 \times 10^{-6}$	$0.045 \times 10^{-6}$

The mid-plane strains and curvatures and stress and moment resultants are calculated according to the classical lamination equation,

$$\begin{Bmatrix} \epsilon^0 \\ \kappa \end{Bmatrix} = \begin{bmatrix} A & B \\ B & D \end{bmatrix} \begin{Bmatrix} N \\ M \end{Bmatrix}$$

once the laminate in-plane, out-of-plane and coupling matrices, [A], [D] and [B], respectively have been determined.

The calculated mid-plane strains and curvatures were substituted into the classical lamination equation,

$$\sigma_k = Q_k (\epsilon^0 + z\kappa - \alpha_k \Delta T)$$

where,

$\sigma_k$  = the stresses in the kth ply

$Q_k$  = the stiffness matrix of the kth ply

$z$  = the location of the kth ply in the thickness of the  
laminar measured from the laminar mid-plane

$\alpha_k$  = the thermal expansion coefficients of the kth ply

$\Delta T$  = the applied temperature load

so as to determine the stresses in the  $0^\circ$  and  $90^\circ$  plies.

#### 4 RESULTS

A reference page is included at the beginning of the figures defining the various finite element programs for which the results have been given. For clarification of the regular fibre array models reference should be made to Table 2 - Program coding: regular fibre arrays.

Values extracted from the figures, such as maximum displacements and maximum stress values and location, have been summarized in Tables 3-13. Also included in the tables are calculated interfibre distance/fibre diameter ratios and fibre volume fractions.

The deformations and distributions of temperature and stress within the finite element models are given in the Figures 10-133. The more important results are presented in colour. The deformations are shown having a scaled maximum displacement of 1 cm. The actual displacement that this represents is detailed adjacent to the Figures and for comparison between models in Table 3.

Averaged temperatures and stresses are presented as shaded contours with line contours overlaid and unaveraged distributions as line contours. For the maximum and minimum principal stresses the average stress vectors are also shown. For these — represents an in-plane tensile stress,  $\left| \text{—} \right|$  represents an in-plane compressive stress,  $\Delta$  represents a tensile stress within  $30^\circ$  of the plane normal and  $\nabla$  represents a compressive stress within  $30^\circ$  of the plane normal. The maximum stress is indicated by a circle. With regard to averaged stresses it should be noted that averaging can not take place at material boundaries due to the different material properties. Stress values are therefore not continuous across the fibre/matrix

interfaces, XY, where two values of the stress vectors are obtained.

In addition to the obvious directional, direct and shear stresses definitions of the other stresses that can be calculated using PAFEC together with the associated failure criteria are detailed below.

Principal stresses are the normal stresses acting on principal planes having no associated shear stresses. Principal stresses,  $\sigma$  act on planes at  $90^\circ$  to each other such that for three dimensional stress states there are three principal stresses. On planes at  $45^\circ$  to these principal planes the maximum shear stresses,  $\tau_{\max}$  are obtained, where

$$\tau_{\max} = \frac{\sigma_{\max} - \sigma_{\min}}{2}$$

Theories to predict yielding of a material under complex stress conditions acknowledge that yielding is associated with shear actions. Two criteria fulfil this condition as described below.

Tresca's yield criteria predicts yielding to occur first when the maximum shear stress in a complex stress system equals the maximum shear stress in uniaxial tension,  $\sigma_Y/2$  or

$$\sigma_{\max} - \sigma_{\min} = \sigma_Y$$

where  $\sigma_Y$  is the yield strength in simple tension.

This is somewhat conservative but easy to use [99].

Von Mises yield criteria predicts yielding to first occur when the maximum shear strain energy in a complex stress system equals that in uniaxial tension. This gives

$$(\sigma_1 - \sigma_2)^2 + (\sigma_2 - \sigma_3)^2 + (\sigma_3 - \sigma_1)^2 = 2\sigma_Y^2$$

where  $\sigma_1$ ,  $\sigma_2$  and  $\sigma_3$  are the principal stresses in three dimensions.

This is well supported by experimental evidence [101].

#### 4.1 Macromodelling

##### 4.1.1 Temperature Distribution

The saved temperatures using the program MATH, modelling cooling of the top surface of the prepreg from 190°C to 20°C over 2 hours, show the temperature difference through the thickness of the laminate is 0.25°C at the end of the 2 hours (7200 secs) - see Figure 10. This confirms that the assumed uniform cooling generates negligible temperature gradients within the prepreg after cure. Since elastic material behaviour is assumed in the modelling, (that is there is a linear increase in stress with strain), these final temperatures can be used to determine the thermal residual stresses. For a corresponding plastic analysis, where the increase of stress with strain is non-linear, calculations incremental in strain would be required through the different temperature distributions.

##### 4.1.2 Deformation and Stress Distributions

###### 4.1.2.1 Single Mesh

Plots are given at the end of the cooling process, time  $t = 7200$  seconds of the, deformation (Figure 11), enlarged view of the centre of the mesh (Figure 12) and some of the stress contours (Figures 13-39) obtained for the program, MASI, modelling cooling of the top

surface of the prepreg through 170°C under conditions of plane strain.

The deformation (Figure 11) is given for a scaled maximum displacement of 1 cm representing an actual displacement of 20.8  $\mu\text{m}$ . The original undeformed mesh is indicated by the solid line and the subsequent deformed shape by the dashed line. The mesh is restrained in the x-direction along the left hand edge, AC and in the y-direction along the bottom edge, AB. The thinner layers represent the epoxy resin layers and the thicker layers the carbon fibre/epoxy resin layers.

The enlarged view of the centre of the mesh (Figure 12) shows the alternation of the thin epoxy resin layers with the thicker carbon fibre/epoxy resin layers. The interface between the epoxy resin layers and the carbon fibre/epoxy resin layers have been labelled XY, the restrained left hand edge AC and the free right hand edge BD. This is for ease of reference in describing the stresses.

The stress distributions are presented at the centre and for the more relevant stresses;  $\sigma_{xx}$ ,  $\sigma_{yy}$ ,  $\sigma_{xy}$ ,  $\sigma_{zz}$ , maximum principal, minimum principal and von Mises, also at the top and bottom of the mesh. Stress vectors are shown for the maximum and minimum principal stresses.

Stress variations are apparent across the width of the mesh implying that an edge effect exists at the free right edge, BD, as would be expected. The stresses are concentrated in the epoxy resin layers where their absolute values are higher than in the carbon fibre/epoxy resin layers. This is because the carbon fibre/epoxy resin layers are stiffer and therefore more resistant to deformation. Maximum values of

the different stresses in the epoxy resin occur in the range 10-100 MPa at the epoxy resin/carbon fibre-epoxy resin interface, XY. These decrease towards the centre of the layers. Different patterns of stresses are apparent at the top and bottom of the mesh due to the free edge at the top and the restraint applied to the bottom. These have been given in the figures for the more important stresses listed above. The temperature difference of 0.25°C through the thickness of the laminate, as expected, creates negligible stress gradients through the thickness of the prepreg. This can be seen by comparing the stress profiles close to the top and at the centre of the mesh. The differing values of the contours obtained immediately at the top and at the bottom of the mesh are thought to be due to the extremes in stress associated with the free top edge and bottom restraint, respectively. It should be noted that the;  $\sigma_{xx}$ ,  $\sigma_{zz}$ , maximum principal, von Mises and Tresca stresses exceeded the tensile strength of the epoxy resin of 47.7 MPa, having maximum tensile values of; 82 MPa, 47 MPa, 89 MPa, 76 MPa and 88 MPa, respectively.

The directional normal stresses,  $\sigma_{xx}$ ,  $\sigma_{yy}$  and  $\sigma_{zz}$  (Figures 13-21) are generally tensile in the epoxy resin layer and compressive in the carbon fibre/epoxy resin layer. This is due to the mutual restraint of the low thermal expansion carbon fibre/epoxy resin layers and the high thermal expansion epoxy resin layers. The values reach a maximum at the layer interfaces. The effect of the free edge is apparent as a further decrease in the stress, of the order of 10 MPa, in the x-direction. The typical section taken at the centre of the mesh shows maximum values of 75.6 MPa, 24.25 MPa and 44.6 MPa for the  $\sigma_{xx}$ ,  $\sigma_{yy}$  and  $\sigma_{zz}$  stresses, respectively along the unrestrained edge, AC at

point X on the interface in the epoxy resin layer. These reduce to 48.8 MPa, -35 MPa and 18.5 MPa, respectively along the restrained edge, BD at the centre of the epoxy resin layer. In the carbon fibre/epoxy resin layers the centre sections show at the intersection between the interface and the restrained edge, point X, maximum compressive values of -44.9 MPa, -17.66 MPa and -13.9 MPa. These reduce to values of +8.6 MPa, - 3.69 MPa and -0.9 MPa at the centre along the restrained edge. The  $\sigma_{xx}$  stresses become more compressive, of the order of -10 MPa, towards the mid-plane between the restrained and free edge about which plane they are approximately symmetrical. The  $\sigma_{yy}$  stresses become significantly more tensile towards the free edge, of the order 28 MPa. A similar increase in the tensile  $\sigma_{zz}$  stresses is apparent towards the free edge, but is less pronounced, of the order 6 MPa.

The directional shear stresses,  $\sigma_{xy}$  (Figures 22-24) show maximum values of  $\pm 29.51$  MPa at the free edge, BD, adjacent to the interface between the epoxy resin layer and carbon fibre/epoxy resin layer, XY. These have a positive sense (clockwise) adjacent to the top interface and a negative sense (anticlockwise) adjacent to the bottom interface. At the centre of the epoxy resin layer the shear stresses reduce to zero. Lesser values ranging from -3.27 MPa to 3.27 MPa are similarly seen, although in an opposite sense, through the thickness of the carbon fibre/epoxy resin layer. The out-of-plane  $\sigma_{yz}$  and  $\sigma_{zx}$  (Figures 25 and 26) stresses show negligible values, (of the order 0 Pa to 100 Pa), in comparison to the other directional stresses.

The maximum principal stress (Figures 27-30) shows a similar pattern

to the  $\sigma_{yy}$  and  $\sigma_{zz}$  stresses. The typical centre section in the epoxy layer gives maximum tensile values of 73.2 MPa at the interface along the restrained edge, point X, increasing to 84.1 MPa at the free edge, point Y. At the centre of the layer values range from 51.4 MPa at the restrained edge to 29.7 MPa at the free edge. Values in the carbon fibre/epoxy resin layers range along the restrained edge from -13.7 MPa at the interface to 7.9 MPa at the centre. Towards the free edge the stress becomes increasingly more tensile, of the order of +10 MPa. The maximum principal stress vectors (Figure 28) show these to act in the x-direction along the restrained edge changing to 30° to the x-direction toward the free edge. The centre section shows the minimum principal stress (Figure 31) to reach maximum compressive values of -48.2 MPa at the interface in the carbon fibre/epoxy resin layer decreasing toward the centre of the restrained edge to values of -2.2 MPa. These become increasingly more tensile reaching values of +13 MPa at the centre of the free edge. In the epoxy resin layer the minimum principal stress varies from a maximum tensile value of 20.7 MPa at the interface restrained edge junction, point X, to -2.2 MPa at the centre restrained edge junction and -9.9 MPa at the centre free edge intersection. The vectors (Figure 32) show the maximum values of the minimum principal stress at the interface to act approximately in the y-direction at the restrained edge changing to the x-direction away from this edge.

A similar pattern is apparent for the von Mises stresses (Figures 35-37), maximum shear (Figure 38) and Tresca (Figure 39) stresses with an increasing stress range from maximum shear, 5.9 MPa to 44 MPa, through von Mises, 10.8 MPa to 76 MPa, to Tresca, 11.9 MPa to 88 MPa. The

epoxy resin layers show a similar distribution to those of the  $\sigma_{xy}$  stresses with values ranging from 73.4 MPa at the interface free edge to 47.0 MPa at the centre restrained edge. The carbon fibre/epoxy resin layers show maximum positive values, of 47 MPa for the von Mises stresses, at the top and bottom free edge interfaces decreasing to 14.1 MPa toward the centre. Values decrease from the free edge towards the restrained edge except in the centre of the carbon fibre/epoxy resin layer where a minimum can be seen around the centre line. The more conservative estimate produced by the Tresca stress is apparent together with the relationship between the Tresca, maximum shear, maximum principal and minimum principal stresses.

PAFEC also has the capability of producing the absolute and maximum in-plane shear stresses. The absolute stresses are the greatest in magnitude of the principal stresses. The maximum in-plane shear stresses are given by half the difference between the maximum and minimum principal stresses. For the two dimensional elements used these act in the plane of the element. Values of the maximum in-plane shear stresses were therefore found equal to the maximum shear stresses.

#### 4.1.2.2 Double Mesh

The double mesh was created in order to model more accurately the variation in stresses across the width of the prepreg. It was obvious from the results obtained using the single mesh that an edge effect exists at the free edge, BD which had not been adequately modelled. This is because conditions change from free edge to central restraint in a single element. Using the single mesh the temperature gradient

through the thickness of the single mesh had been found to be negligible. For this reason a constant temperature loading of  $-170^{\circ}\text{C}$  was applied.

Similar plots to those obtained using the single mesh are given for the double mesh (Figures 40-75). Unaveraged stresses are also given of the  $\sigma_{xx}$ ,  $\sigma_{yy}$ ,  $\sigma_{zz}$ ,  $\sigma_{xy}$ , maximum principal, minimum principal and von Mises stresses as an indication of the accuracy achieved (Figures 43, 47, 51, 55, 62, 67 and 71). This check was not possible using the single mesh since there are no element boundaries across which to observe the discontinuities. Stresses are not averaged at boundaries between different materials due to the unequal material properties.

The deformation (Figure 40) is, as previously, shown for a scaled maximum displacement of 1 cm representing an actual deformation of  $20.6\ \mu\text{m}$ . This compares well with the value obtained using the single mesh of  $20.8\ \mu\text{m}$ .

The enlarged view of the centre of the mesh (Figure 41) shows the doubling of the width of the mesh in the x-direction and the refinement of the mesh in the carbon fibre/epoxy resin layers in the y-direction.

The stress distributions (Figures 42-75) follow a more detailed but similar pattern to those obtained using the single mesh. The stress ranges are generally marginally greater ( $< 5\ \text{MPa}$ ) although in several cases the minimum values are extended to significantly lower values ( $4\text{-}13\ \text{MPa}$ ). The stresses in the epoxy layer are noted to be more concentrated around the free edge, BD. In addition the stresses in the centre of the carbon fibre/epoxy resin layer are generally fairly

constant through the depth of the layer (the y-direction) only changing close to the interface. Using the single mesh a continuous variation is apparent through the depth of these layers.

Once again a different pattern of stresses is noted at the top and bottom edges. The  $\sigma_{xx}$ ,  $\sigma_{zz}$ , maximum principal, von Mises, maximum shear and Tresca stresses are all observed to exceed the tensile strength of the epoxy resin 47.7 MPa. These have maximum values of 83 MPa, 49 MPa, 95 MPa, 81 MPa, 47 MPa and 94 MPa, respectively. See Figures 42, 50, 60, 70, 74 and 75.

These stress distributions can be expected to be more accurate, compared to the original mesh, due to the mesh refinement. The unaveraged stresses show discontinuities in the range 0-10 MPa in the carbon fibre/epoxy resin layers and 0-30 MPa in the epoxy resin layers. Obviously the greater the variation in stress the less the accuracy.

The macromodelling shows the assumed uniform cooling of the prepreg after cure generates no significant temperature gradient through the thickness of the prepreg or the associated thermal residual stresses. Residual stresses are generated almost entirely due to the differing thermal expansion coefficients of the assumed epoxy resin film and the carbon fibre/epoxy resin lamina. These show a variation across the width of the prepreg due to an edge effect and a repeating pattern through the thickness of the laminate, which varies only close to the free top and restrained bottom edges.

The thermal residual stresses are due to the mismatch between the

carbon fibre properties which predominate in the carbon fibre/epoxy resin layers and the epoxy resin properties of the separating film. There is, in contrast no significant effect due to any temperature gradients present in the laminate. It appears therefore that in unidirectional laminates the residual microstresses are likely to be more significant than the residual macrostresses. No account had been taken of the anisotropic nature of the carbon fibre/epoxy resin laminae but this would not alter the reasoning. The residual stresses generated due to anisotropy in multidirectional laminates having plies at various off-axis orientations have been extensively studied, as apparent in the literature.

For these reasons in the later modelling it was decided to concentrate on the residual microstresses.

#### 4.2 Micromodelling - Regular Fibre Arrays

##### 4.2.1 Typical Hexagonal Fibre Array

Results from some of the earlier programs modelling a typical regular hexagonal array of 3.5  $\mu\text{m}$  diameter fibres at 37% fibre volume fraction are now summarized (Figure 6). These have been selected as the most informative. Models were originally developed to cover all the conditions of plane strain, plane stress, "radial restraint" and "total restraint". This was due to uncertainty concerning how best to represent the actual conditions.

ES01 ("radially restrained", plane stress) - This models a unit cell restrained along the lines, OA and OB in a direction perpendicular to these lines. Absolute thermal expansion coefficients under conditions

of plane stress are assumed.

ES03 ("radially restrained", plane strain) - This is as ES01 but with the conditions of plane stress changed to plane strain.

ES04 ("radially restrained", plane strain, temperature dependent, epoxy resin properties) - This is as ES03 but with temperature dependent epoxy resin properties.

ES02 ("totally restrained", plane strain) - This as ES03 but with the unit cell restrained along the lines, OA, OB and AB, in a direction perpendicular to these lines. Thermal expansion coefficients relative to a mean value for the unit cell are assumed.

Results are given in the Figures for the model which was selected as the most realistic, ES04. This represents a state of plane strain and incorporates "radial restraints" and temperature dependent properties. Labels, OXABY, where XY represents the undeformed fibre/matrix interface and OAB, represents the undeformed lines of symmetry of the unit cell, have been included on the figure representing the deformation (Figure 76). The presence of these lines permits ease of reference in discussing the results.

#### 4.2.1.1 Deformation

Figure 76: Deformations were produced (having scaled maximum displacements of 1 cm) for each of the programs, ES01, ES02, ES03 and ES04. These showed the desired restraints to be achieved. Figure 76 gives the result for the model ES04 with the deformed shape, OX'A'B'Y', superimposed on the undeformed shape, OXABY. Models ES01 and ES03 were similarly "radially restrained" along the lines, OA and

OB, perpendicular to these lines, with the end plane, AB remaining approximately parallel to the z axis (a small deviation from this parallel line led to modification of the restraints in the later programming). This is necessary to retain the hexagonal symmetry of the array. Maximum displacements occurred at the point B. In addition program ES02, representing the deformation relative to the overall average deformation of the unit cell was "totally restrained" along the outside edges, OA, OB and AB, perpendicular to these lines.

The magnitude of the maximum screen displacement, see Table 3, was noted to increase from conditions of plane stress - 35.5 nm (ES01) through conditions of plane strain - 51.8 nm (ES03) to conditions of plane strain with the incorporation of temperature dependent properties - 66.5 nm (ES04). Under conditions of longitudinal contraction the transverse displacement would be expected to increase as conditions change from plane stress to plane strain. Similarly with incorporation of the temperature dependent properties where the Young's modulus decreases with temperature further increases in displacements would be expected. The maximum relative displacement obtained for the "totally restrained" model, ES02 was at the fibre/matrix interface and was equal to 20.1 nm

#### 4.2.1.2 Stresses

i) "Radially Restrained" Models, ES01, ES03, ES04:

A similar pattern of stresses was apparent in all the calculations where the unit cell was radially restrained. The magnitude of the stresses however was noted to increase from conditions of plane

stress (ES01) through plane strain (ES03) to plane strain with temperature dependent properties (ES04). This can be explained by a similar reasoning as for the deformations.

Since the stress contours obtained for the three programs ES01, ES03 and ES04 follow approximately similar patterns although of slightly differing magnitudes it is simplest to examine the stresses of one program in detail. ES04 representing a state of plane strain as typified by long cylindrical fibres and incorporating temperature dependent properties is chosen as the most realistic of these models. Unaveraged stresses are included as a measure of the accuracy obtained.

a) Directional stresses:

The elements are meshed in the global y-z plane. Plots were obtained of the variation in the in-plane  $\sigma_{yy}$  and  $\sigma_{zz}$  normal stresses and the  $\sigma_{yz}$  shear stresses. These were difficult to interpret since they are based on a Cartesian geometry and bear no relation to the rotational symmetry of the fibres. They have therefore not been included in the results. It was however noted that the  $\sigma_{zz}$  stresses, were found to be more significant, having greater values. These reached a maximum tensile value of 40 MPa in the epoxy close to the interface at point X, decreasing to values of around 5.2 MPa at B, and an approximately constant compressive value of around -20.1 MPa in the fibre. By comparison the  $\sigma_{yy}$  stresses had approximately constant compressive values of around -17.64 MPa in the outer regions of the fibre, whilst in the epoxy resin, values ranged from around -15.45 MPa at point X on the interface decreasing to a maximum tensile value of

3.13 MPa on the line AB.

b) Maximum Principal Stress

Figure 77-79: A maximum tensile value of 40.0 MPa is obtained in the matrix at the fibre/matrix interface which decreases to values of around 2.2 MPa outwards into the epoxy at B. An approximately constant value of around -15.4 MPa is calculated in the fibre. The small fluctuations at the centre of the fibre are probably due to a meshing instability. The maximum values are noted to be less than the tensile strength of the epoxy (47.7 MPa). No details are available regarding the transverse strength of the carbon fibres but a longitudinal value of 3.5 GPa is specified, as measured in the impregnated strand test method, by Torayca for T300 fibres. It seems unlikely that stresses of the order of -15 MPa will exceed the transverse strength of the fibres.

The vectors for the maximum principal stress (Figure 7E) show that this stress acts in a direction parallel to the fibre/matrix interface, changing outwards from the interface to act along the line of symmetry, AB. In the fibre the pattern is less clear although it appears to change from a direction perpendicular to the line of symmetry OB to a direction parallel to the line, OA, from OB to OA. The maximum tensile stress in the epoxy of 40 MPa is located on the fibre/matrix interface at a point  $10^\circ$  from the line OA.

The anomalous distribution obtained of the unaveraged stresses (Figure 79) could not be explained.

### c) Minimum Principal Stress

Figures 80-82: A maximum compressive stress of -22.45 MPa is obtained in the carbon fibre close to O along the line OB. However it is likely that the stress fluctuations at the centre are due to an instability. Otherwise approximately constant compressive values of around -19.8 MPa to 17.1 MPa are observed in the fibre. In the epoxy this value decreases outwards from the point, Y on the fibre/matrix interface, to a maximum tensile value of 2.74 MPa close to B along the line, AB.

The pattern of vectors (Figure 81) shows that this stress acts radially in the epoxy resin. In the fibre away from the centre the vectors show the stress to change from acting, parallel to OB along the line OB, to, perpendicular to OA along the line OA. At the fibre centre the vectors show a tendency to act in the hoop direction although the direction is variable.

### d) Von Mises/Tresca

Figures 83-86: The von Mises stress (Figures 83-84) shows a maximum tensile value of 51 MPa in the epoxy at the fibre/matrix interface which decreases on moving outwards from the fibre to a minimum value of 3.40 MPa. An approximately constant value of around 15.4 to 20.3 MPa is obtained in the fibre. The maximum tensile stress of 51 MPa is noted to exceed the tensile strength of the epoxy of 47.7 MPa measured at 23°C.

The Tresca stress (Figure 85-86) shows a similar pattern to, but with values marginally greater than, the von Mises stress as would be expected. A maximum tensile value of 56.1 MPa decreasing to 6.4 MPa in

the epoxy resin was obtained with approximately constant values of between 17.4 MPa to 23 MPa in the fibre.

e) Maximum Shear Stresses

Figure 87-88: Since the modelling is in two dimensions, plots of the maximum shear stresses are equivalent to those of the maximum in-plane shear stresses. These show a similar pattern to the von Mises stresses although lesser in magnitude, as would be expected, having a maximum value of 29.4 MPa at the fibre interface decreasing to 1.85 MPa outwards into the epoxy at B. An approximately constant value of around 8.75 MPa to 11.50 MPa is evident in the fibre.

ii) "Totally Restrained" Model, ES02

The contour patterns for the "totally restrained" model - ES02 were found to differ marginally from those of the "radially restrained" models - ES01, ES03 and ES04. The latter allowed the unit cell to expand outwards from the centre of the fibre whilst maintaining the hexagonal symmetry of the packing. The former considered dimensional changes different from the overall average dimensional changes of the unit cell. The average contraction of the unit cell is effectively subtracted from the true thermal expansion such that the edges are restrained in all directions. The expansion coefficients of the epoxy and the fibre are expressed relative to this average contraction.

The similarity in the stress contours for the radially restrained and totally restrained models confirmed their approximate equivalence; although comparing programs ES03 and ES02 significant differences were observed in the magnitude of the directional, minimum principal,

maximum principal,  $\sigma_{yy}$   $\sigma_{zz}$  stresses. The shear;  $\sigma_{yz}$ , maximum shear, maximum in-plane shear and von Mises stresses showed little difference.

#### 4.2.1.3 Accuracy

Continuity of the unaveraged stresses for the model ES04 across the element boundaries show a reasonable degree of accuracy to be achieved, estimated at between 0 and 4 MPa. See Figures 82, 84, 86 and 88. This accuracy was improved in the later modelling by refinement of the finite element mesh.

#### 4.2.2 Incorporation of Anisotropic Carbon Fibre Properties and Modelling of Other Regular Fibre Distributions.

In the subsequent calculations refinements were made to model other regular fibre distributions and anisotropic fibre properties. Plots are given of the maximum principal stress contours and vectors and the von Mises stress contours. For ease of reference points O, A, X, B and Y marking the fibre centre, the points of symmetry and fibre/matrix interface along the straight and inclined edges, respectively are indicated on the undeformed structure at the beginning of each set of plots.

The results are summarized in Tables 4-11 and the trends discussed. Rather than include figures for all the results examples are given which illustrate the trends. For all models maximum stress values were noted at the fibre/matrix interface in the epoxy resin. In the case of the maximum principal stress this is tensile and generally acts in a direction tangential to the fibre/matrix interface. Tables 4, 6, 8 and

10 show the maximum values of the maximum principal stress and the von Mises stress to increase with decreasing interfibre distance and increasing fibre diameter.

The pattern of the stresses varies with co-ordination angle, that is the number of nearest neighbours in the packing.

#### 4.2.2.1 Twelve Nearest Neighbours/15° Co-Ordination Angle

Figures 90-93: One example is given, model D15C which is adequate to describe all the variations. The maximum principal and von Mises stresses can be seen to decrease radially outwards from the fibre/matrix interface into the epoxy resin such that a maximum occurs in the epoxy resin fairly uniformly around the fibre circumference. The rate of decrease in stress is marginally greater along the inclined edge, OB leading to low stresses in the region around point B. The maximum principal stress vectors show this to act tangentially to the fibre/matrix interface close to the interface with a gradual change in direction away from the interface to act along the line AB. Table 1 shows the maximum values of the maximum principal and von Mises stresses which can be seen to increase with decreasing interfibre distance and increasing fibre diameter.

The maximum principal and von Mises stresses in the fibre are noted to be small and in the case of the maximum principal stress generally slightly compressive, in the range -1 MPa to -20 MPa and 5 MPa to 15 MPa, respectively with little variation across the fibre. A slight decrease in the magnitude of the maximum principal stress and increase in the von Mises stresses at the fibre centre is probably due to a meshing instability. The magnitude of the values were noted to

increase with increasing interfibre distance and decreasing fibre diameter.

As the co-ordination angle, that is the number of nearest neighbours in a regular packing increases, the constant maximum value of the maximum principal stress around the fibre circumference is no longer observed as described below.

#### 4.2.2.2 Six Nearest Neighbours/30° Co-Ordination Angle

Figures 93-100: In the case of the programs modelling an hexagonal array of fibres, similar patterns of stresses are obtained to those calculated using the programs modelling twelve nearest neighbours. A greater rate of decrease in the stresses along the edges OB and OA is however observed in the former case. In addition the maximum values no longer occur uniformly around the fibre circumference. Instead they occur on the fibre/matrix interface close to the inclined edge, OA, in the case of the maximum principal stress, and on the fibre/matrix interface close to the straight edge, OB, in the case of the von Mises stress. These differences are more noticeable at short interfibre distances and to a lesser extent at large fibre diameters. The figures are given for the two extremes, model B03C and model F03B.

The pattern of stresses in the fibre is similar to that obtained using the programs modelling twelve nearest neighbours except that in a few cases the maximum principal stresses are noticed to fall off marginally at the fibre/matrix interface. Values range from -2 MPa to -19 MPa, in the case of the maximum principal stresses, and 4 MPa to 14 MPa in the case of the von Mises stresses. A similar trend, to

that observed in the 15° co-ordination models, is apparent of an increase in the magnitude of the values of the fibre stresses with increasing interfibre distance and decreasing fibre diameter.

#### 4.2.2.3 Four Nearest Neighbours/45° Co-Ordination Angle

Figures 101-108: The effects noted with the programs modelling hexagonal arrays of fibres (30° co-ordination angle) are exaggerated further when the co-ordination angle increases to 45° (square fibre arrays). For short interfibre distances/large fibre diameter there is an actual increase in the stresses along the edge, XA. Then the maximum principal stress in the epoxy at X can be equivalent to or even less than the maximum principal stress at B and the maximum value of the von Mises stress can move from point X to A. The maximum value of the maximum principal stress is located as before at the fibre/matrix interface close to the inclined edge, OB. In addition it is noted that for short interfibre distances the maximum principal stress close to the interface is observed to have a direction slightly off tangential to the fibre surface. Figures are given for two extremes showing the effect of large interfibre distance/small fibre - model C54C versus small interfibre distance/large fibre diameter - model E54A.

In the fibre the magnitude of the compressive maximum principal stresses decrease significantly towards the fibre/matrix interface whilst the von Mises stresses are observed to increase. This is most noticeable at short interfibre distances/large fibre diameters. Values range between -18 MPa and 11 MPa in the case of the maximum principal stresses and 4 MPa and 44 MPa in the case of the von Mises stresses.

At high interfibre distance to fibre diameter ratios the stress contours are axially symmetric about the fibre centre but at low interfibre distance to fibre diameter ratios maxima occur at point X in the case of the von Mises stresses. Further they have a tendency to form toward the inclined edge, OB in the case of the maximum principal stresses. The tensile values of the maximum principal stress and high values of the von Mises stresses are associated with these maxima. This causes the trend of increasing von Mises stress with decreasing fibre diameter to interfibre distance ratio to be reversed at short interfibre distances. A similar reversal in the trend of increasing compressive stresses (decreasing tensile stresses) with decreasing fibre diameter to interfibre distance ratio is observed in the case of the maximum principal stress (Table 6).

#### 4.2.2.4 Three Nearest Neighbours/60° Co-Ordination Angle

Figures 109-116: A further exaggeration of the changes in stress distribution with increasing co-ordination angle is observed with the programs modelling three nearest neighbours. The maximum values of the von Mises stress and maximum principal stress (maximum tensile/minimum compressive) in the epoxy resin are, as before, generally located at point X and close to the inclined edge, OB, respectively on the fibre/matrix interface. Again examples are given for the two extremes of short interfibre distance/large fibre diameter ratio - model C06B and large interfibre distance/small fibre diameter ratio - model F06A.

The fibre stresses range between -18 MPa and 8 MPa in the case of the maximum principal stresses and 7 MPa and 68 MPa in the case of the von Mises stresses. The distributions are similar to, but more

exaggerated, than those observed in the 45° co-ordination angle models. The magnitude of the stresses in all of the 60° models increases with decreasing interfibre distance and increasing fibre diameter.

#### 4.2.2.5 Effect of Varying Transverse Poisson's Ratio

Figures 117-120: The calculations presented in the previously described figures employ a transverse Poisson's ratio of 0.15. This is as opposed to the value of 0.42 used in the original programs. The example given (Figures 117-120) of one of the original models (B13C) when compared to its corresponding later model (B03C - Figure 93-96), (with a transverse Poisson's ratio of 0.15), shows the change to this more generally accepted value to have a marginal effect on the results. The uncertainty concerning the value to use is not therefore considered detrimental to the results.

### 4.3 Micromodelling - Random Fibre Arrays

Predictions of the deformations and stresses generated on cooling through 170°C in more realistic, random arrays were obtained first for a "hypothetical" Voronoi cell. This was constructed from a representative selection of the different types of unit cells used to model the regular arrays. Later random fibre arrays were generated using a computer program, FIBDIST3 from which a typical Voronoi cell was extracted and meshed for finite element analysis.

#### 4.3.1 "Hypothetical" Voronoi Cell

Figures 121-124 show the deformation, maximum principal stress and vectors and von Mises stress for the Voronoi cell modelling a

hypothetical random array of fibres. The central fibre has five nearest neighbours and can therefore be thought intermediate between an hexagonal and a square array. The cell is not based on any observed distribution of fibres but incorporates each of the types of unit cells used to model the different regular arrays of fibres. The fibre volume fraction in the cell is 26.7%.

The deformation (Figure 121) of the hypothetical Voronoi cell shows a slight deviation from the "radial restraints" applied in the regular fibre array models. In the latter case there is no movement of the lines, OA, OB, OC, OD, OE, OF, OG, OH, OI and OJ in a direction perpendicular to these lines, which is not exactly the case in the Voronoi cell.

The results from the hypothetical Voronoi cell show the maximum stress values (Figure 122) to be concentrated around the fibre/matrix interface except at the position of minimum interfibre distance, OA. Here the half-interfibre distance is  $0.5 \mu\text{m}$ . This occurs at the junction of the sections, JOA and AOB, corresponding to the  $45^\circ$  unit cell B54A and the  $60^\circ$  unit cell, respectively (see Figure 121). The maximum value is located a short distance,  $0.5 \mu\text{m}$ , away from the interface to the edge of the Voronoi cell where it reaches its greatest value of 68 MPa. The maximum principal stresses are tensile and act tangentially (Figure 123) to the fibre surface close to the interface, with a gradual change in direction away from the interface, to act along the lines of symmetry of the Voronoi cell between fibres.

The maximum principal stresses in the fibre show low values of between -17.6 MPa away from, and 21 MPa concentrated around, the maximum

stress region in the epoxy resin.

A significant area of the hypothetical Voronoi Cell is subject to a maximum principal stress greater than the tensile strength of the matrix (47.7 MPa) - (see the region bounded by the 46.8 MPa contour).

The von Mises stresses (Figure 124) show a pattern very similar to that of the maximum principal stresses. In the epoxy resin maximum values of 57-59 MPa are obtained on the line of shortest interfibre distance away from the fibre/matrix interface and minimum values of approximately 30 MPa at the edges of the Voronoi cell where the interfibre distance is large. The variation of the von Mises stress in the fibre is less pronounced than that observed for the maximum principal stresses, which possesses values ranging between 2.55 MPa and 20 MPa.

#### 4.3.2 Generation of Random Fibre Distributions

In order to determine the stresses in truly random fibre arrays it was necessary to be able to model this randomness. The computer program, FIBDIST3, developed for this purpose is described in the Procedure. Random fibre arrays were modelled using the program for 10 fibres at 30%, 50% and 60% fibre volume fractions. Unfortunately the means by which the program moves the randomly located fibres so that they do not overlap did not produce a satisfactory 60% fibre volume fraction array. The high volume fraction and the mechanics of the programming made this impossible within a reasonable time span. The resulting distribution would in any case have approximated closely to an hexagonal array. This arises because the flexibility in position of

the fibres falls as the amount of fibre increases. Hence even random arrays at 60% fibre volume fraction will be close to the regular hexagonal array appropriate to this volume fraction.

The random distributions obtained using 30% and 50% fibre volume fractions are given in Figures 125 and 126, respectively. The 50% fibre volume fraction array also shows the Voronoi cell arrangement including the only complete Voronoi cell which is used in the subsequent finite element calculations described below. No other complete Voronoi cell was available in the random arrays.

#### 4.3.3 Voronoi Cell From Random Fibre Array with 50% Fibre in the Section

The results obtained using the Voronoi cell from the 50% fibre volume fraction array are given in Figures 127-133. The deformation of the Voronoi Cell (Figure 127) shows that the cell rotates under the influence of the stress. This is of course associated with the uneven stress distribution created by the random fibre array.

Extremely high stresses are evident in the three regions where the fibres are closest, maximum values of, the maximum principal (Figure 128 and 129) and von Mises stresses (Figure 130) being, 320 MPa and 261 MPa, respectively. Enlarged views of the region where these maximum stresses occur (Figures 131-133) show them to be concentrated around a discontinuity in the geometry of the fibre surface, present due to the circular interface being approximated by a regular polygon of twelve sides. Minimum values of approximately, 30 MPa in the case of the maximum principal stresses and 15 MPa in the case of the von Mises stresses, are observed in the epoxy resin at the edges of the

Voronoi cell away from the fibre/matrix interface. The maximum principal stress vectors (Figure 129) show a pattern similar to that of the hypothetical Voronoi cell.

The stresses in the fibre have relatively constant values of between, -13.3 MPa and 4 MPa in the case of the maximum principal stress, and, 1.96 MPa and 15 MPa in the case of the von Mises stress, although the wide range of stresses in the model necessarily mean that some of the detail is lost. A marginal increase in these stresses is observed in the three regions where the interfibre distance is shortest.

#### 4.4 Optical Microscopy

Figures 134-139: No significant difference was noticed between the features observed in the micrographs taken from the edge and centre specimens except that the edge sample showed regions where material appeared to have been pulled out of the surface. This was thought to be due to the greater polishing required of the centre specimen (the as-cut surface was very uneven). It is proposed that the poorer surface quality was due to damage to the surface by the abrading particles. Minimal polishing was required of the edge sample since the surface was already very smooth due to the cutting with the diamond saw. Most of the micrographs given in the figures are therefore taken from the edge sample.

Optical micrographs are given showing the layered nature of the laminate with the fibres at various orientations in the different plies - see Figure 134 and 135. Nine distinct layers were apparent with the fibres alternating between transverse and longitudinal

orientations. The longitudinal layers had uniform thicknesses of approximately 0.42mm. The transverse plies were thinner (0.10 mm and 0.17 mm) except in the two surface layers. The laminate appeared to be symmetric. The individual tows making up the structure are evident with regions of epoxy rich material between tows. It is clear that no uniformly thin epoxy resin layer separates the fibre layers, as assumed in the earlier macromodelling. Rather the fibres are arranged in tows which may impinge directly on other tows/layers or be separated by small regions of epoxy resin.

The epoxy rich regions in the thinner centre plies (transverse) extended across the full width of the plies whilst in the thicker outer plies (transverse) widths of up to approximately 2 mm were obtained. In these outer plies they were located at the ply interface.

Further micrographs show magnified views of some transverse sections of the tows - Figures 136 and 137. These were examined for arrangement of fibres within tows and the presence of cracks. Magnified views were also obtained at a ply interface (Figure 138) and of some of the epoxy rich regions (Figure 139).

At these magnifications there was no evidence of cracking. Within the tows the fibres were fairly densely packed although random. The fibres formed rings, clusters and localised regions where the packing approximates to hexagonal and to a lesser extent square arrays. Fibres that had five nearest neighbours ~~was~~ <sup>were</sup> common. It was unusual to see fibres with three nearest neighbours but when they did occur they tended to be associated with the rings of fibres. There appeared also to be a random variation in half-interfibre distances. These possessed

values that range from zero to 7  $\mu\text{m}$ .

The Hypothetical Voronoi cell, which is composed of a cross section of the regular array unit cells, has five nearest neighbours and half-interfibre distances ranging from 0.5  $\mu\text{m}$  to 6.0  $\mu\text{m}$ . It seems, therefore that this was a good approximation to the actual fibre arrays observed within the tows. In addition it appears that the assumption of random fibre arrays in the computer modelling of the fibre distributions is correct.

#### 4.5 Electron Microscopy

Figures 140-146: When examined under the electron microscope the majority of the sample (estimated at between 95% and 90%) appeared to be crack free. However several interesting features were observed in localized regions. Generally two magnifications are given of each view so that both the detail and surrounding area are shown. In Figures 140-144 cracks are seen to occur close to and sometimes follow the line of the matrix/fibre interface. In one instance a crack or defect was observed to cross a fibre (Figure 142) but this was an exception. Linear defects made up of a series of hackles were also shown in the transverse sections (Figure 145). In other regions numerous small angular artifacts were apparent (Figures 146).

#### 4.6 Modelling of the Macrostressess using Classical Lamination Theory

Following on from the earlier macromodelling, calculations were made using classical lamination theory of the stresses in a typical multidirectional, prepreg tape. As before a uniform temperature decrease of 170°C was assumed. Anisotropic (transversely isotropic)

properties were incorporated. By the superposition of these macrostress fields on the microstress fields it was intended to determine the probable overall stress distributions. This assumes elastic material behaviour.

A  $[0_4/90_{10}/0_4]$  symmetric ply stacking sequence was chosen, consisting of an inner layer of 10 plies in which the fibre directions were transverse to the laminate axis. This inner layer was sandwiched between two layers, each of four plies, in which the fibre directions were parallel to the laminate axis.

First the equilibrium laminate mid-plane strains and stress resultants were determined using a the software package PC-Laminate [60] as described in the Procedure.

#### 4.6.1 Calculation of Laminate Mid-Plane Strains

The mid-plane strains and stress resultants for the  $[0_4/90_{10}/0_4]$  laminate were calculated using the computer program, PC-Laminate as follows

$$\begin{aligned} \epsilon_x &= -6.97 \times 10^{-4} & \epsilon_y &= -5.11 \times 10^{-4} \\ N_x &= 0.229 \text{ MPam} & N_y &= 0.205 \text{ MPam} \end{aligned}$$

where the x-direction is that of the laminate axis from which the orientation of the ply.  $\theta$  is measured. Values were also calculated for the laminate curvatures;  $\kappa_x$ ,  $\kappa_y$  and  $\kappa_{xy}$ ; stress resultant,  $N_{xy}$  and moment resultants;  $M_x$ ,  $M_y$  and  $M_{xy}$ , but at levels that were negligible in comparison to  $\epsilon_x$ ,  $\epsilon_y$ ,  $N_x$  and  $N_y$ , as would be expected for a symmetric laminate. Rounding errors can produce values of these quantities at the magnitude observed. These negligible values can be

regarded as zero.

#### 4.6.2 Calculation of Ply Stresses

Having obtained values for the extensional (as opposed to bending) mid-plane strains of the laminate the stresses in the 0° and 90° plies could be determined using the classical lamination equation for the stresses in the kth ply,  $\sigma_k$

$$\sigma_k = Q_k (\epsilon^0 + z\kappa - \alpha_k \Delta T)$$

where,

$Q_k$  = stiffness matrix of the kth ply

$\epsilon^0$  = laminate mid-plane strains (extensional)

$z$  = location of ply in the laminate thickness direction measured from the laminate mid-plane

$\kappa$  = laminate mid-plane curvatures

$\alpha_k$  = ply thermal expansion coefficients

$\Delta T$  = temperature load

Since the laminate under consideration was symmetric the curvature effects could be ignored.

The 0° and 90° ply stiffness matrices in the laminate axis were calculated as

$$Q_0 = \begin{bmatrix} 137 & 3.1 & - \\ 3.1 & 14.6 & - \\ - & - & 5.9 \end{bmatrix} \text{ GPa} \quad Q_{90} = \begin{bmatrix} 14.6 & 3.1 & - \\ 3.1 & 137 & - \\ - & - & 5.9 \end{bmatrix} \text{ GPa}$$

using the equations of Tsai and Hahn [9]. It was necessary to transform the on-axis stiffness matrix of the 90° plies, that is the stiffness matrix expressed relative to the longitudinal direction of the fibres, to one expressed relative to the laminate axis.

Inserting the appropriate values of the ply expansion coefficients the ply stresses were calculated as

$$\sigma_x = -73 \text{ MPa} \quad \text{and} \quad \sigma_y = 63 \text{ MPa}$$

in the 0° plies, and

$$\sigma_x = 60 \text{ MPa} \quad \text{and} \quad \sigma_y = -49 \text{ MPa}$$

in the 90° plies, where the x-direction is that of the laminate axis.

## 5 DISCUSSION

The findings of the literature survey, the micromodelling, the optical microscopy, the electron microscopy and the macromodelling are commented on and their significance to practical residual stress distributions discussed. The relevance of the residual stress distributions to the mechanical behaviour and failure of the composites is then detailed together with the effect of environmental and processing factors such as moisture absorption and fibre surface treatments.

### 5.1 Literature Survey

It was found convenient to summarize the findings from the literature survey in two sections; the macrostresses and the microstresses.

#### 5.1.1 Macrostresses

The literature survey has shown that classical lamination theory predicts adequately stress distributions at the centre of multidirectional carbon fibre/epoxy resin laminates [9,10,19-22]. The theory is based on the principle that although the free expansion of adjacent unidirectional plies are unequal, due to their anisotropy and differing orientation to the laminate axis, the fact that they are connected along the top and bottom surfaces results in a constant ply strain through the laminate thickness. This causes stresses to be generated in each ply that are unequal but which as a whole are in equilibrium across the laminate thickness. Hence in the case of thermal loads, whereas no stresses are generated in isotropic plates due to a free thermal expansion, residual thermal stresses are

generated within an anisotropic laminated material. The theory has been developed to calculate the strains, stresses, curvatures and moments for symmetric and unsymmetric laminates using laminate moduli and compliances. Material properties are assumed temperature independent.

Classical lamination theory also assumes that the laminate behaves with linear elastic characteristics. Experiment has shown that at least to a first approximation this is a valid assumption [30]. There may be some visco-elastic behaviour at the higher temperatures, experienced during the initial stages of cooling after cure, but these effects are expected to have only a marginal contribution to the generation of the thermal residual stresses. Further, due to lack of information they are difficult to quantify.

Total stress-strain-temperature relations [30] and incremental methods [56] have been applied to classical lamination theory to include the effect of temperature dependent material properties on the generation of the thermal residual stresses. The concept of a stress-free temperature, lower than the curing temperature has also been introduced [31]. This is the lowest temperature, once the epoxy is fully cured, that will give a completely stress free laminate. It indicates the temperature from which stresses are generated on cooling and can be found by heating deformed unsymmetric laminates to the temperature at which they flatten. Predictions have been found to agree with experimental observations in boron/epoxy, glass/epoxy, carbon/epoxy (T300/5208) carbon/thermoplastic - APC-2 (AS4/PEEK) laminates [32].

The expansion accompanying moisture absorption has been studied due to its effect on the resulting residual stress distribution. Division of the total strain into mechanical and non-mechanical components with the non-mechanical component comprised of swelling and thermal parts has allowed this effect to be included [32]. The mechanical strain is defined as that occurring directly as a result of an applied load/stress and the non-mechanical strain as that occurring due to non-mechanical effects such as temperature changes and moisture absorption. Various models for the diffusion and absorption of moisture have been put forward [32,36] dependent on the relative humidity of the environment. It has been noted that the moisture absorption in as much as it lowers the glass transition temperature and thus the stiffness of the polymeric matrix will have an adverse effect on the mechanical properties of the of the laminate. This is most noticeable in situations where it is required to sustain compressive loads. In particular a lowering of the interlaminar shear strength, the compression strength and the general high temperature properties is observed.

For thin unsymmetric laminates solution methods more complex than those of classical lamination theory have been derived [39,40]. The strain-displacement relationships in classical lamination theory are assumed linear. The out-of-plane deformations observed by Hyer [30-32] in unsymmetric laminates of the order of the laminate thickness indicated geometric non-linearities to have an important effect. These effects were then introduced through non linear strain-displacement relationships. An extension of the theory to include these geometric non-linearities predicts that as the thickness to side length ratio

decreases two stable cylindrical equilibrium states replace the single saddle shape solution of classical lamination theory. The critical side length at which this phenomenon is observed is found to increase with increasing thickness of the laminate. In addition the cylindrical shapes show a snap-through action whereby a slight application of force will cause the laminate to flip over to the other stable cylindrical shape. Observations of the warping of unsymmetric T300/5208 carbon fibre/epoxy resin laminates [30,41,42] and APC-2 (Hercules AS4 carbon fibres/PEEK thermoplastic matrix) [56] has largely confirmed these predictions.

At the free edge of a laminate the stress normal to the free surface necessarily reduces to zero and as a result, in a region of the order of the laminate thickness from the free edge, interlaminar normal and shear stresses are generated. The generalized plane stress assumption of classical lamination theory is no longer valid in this region. Good correlation has been found between the solutions obtained using approximate formulations [43], finite difference [44] and finite element methods [50].

The resulting stress distributions at the free edge are found to be dependent on the particular stacking sequence of the laminate [45,52,54,55].

For the complex geometries of manufactured parts finite element analysis offers the best method of solution [60-62].

### 5.1.2 Microstresses

The micromechanics of continuous fibre reinforced composites has been

studied using various techniques [6,7,9,10]. Mechanics of materials approaches make certain simplifying assumptions regarding the mechanical behaviour from which so called rule of mixtures expressions can be derived. These assumptions may depend on the loading conditions. For example the material properties of a unidirectional composite can be determined as follows. First for longitudinal loadings it is assumed that there are equal strains in the fibre axis direction in both the fibre and the matrix. Second for transverse or shear loadings it is assumed that there are equal transverse and shear stresses in both the fibre and the matrix. The former produces expressions for the longitudinal Young's modulus and the major Poisson's ratio and the latter expressions for the transverse Young's modulus and the in-plane shear modulus. Effectively models in series and parallel are assumed to represent the different loading situations. Unit cells containing laminar, rectangular, square and circular fibres have been considered in this type of analysis. The results are found to predict adequately responses in the longitudinal direction but to be less accurate in the transverse direction.

More rigorous solutions are derived using the principles of classical elasticity theory. That is by solving simultaneously the accepted equilibrium equations, Hooke's law and strain-displacement relations. Methods include bounding techniques, exact solutions and self-consistent models. In bounding techniques the principle of minimum complementary energy is applied to determine the lower bound and the principle of minimum potential energy to give the upper bound. This leads to a range of values between the transverse Young's modulus and the longitudinal Young's modulus as derived in the mechanics of

materials approach outlined above.

Exact methods have modelled circular and square fibres arranged in regular periodic, square, diamond and hexagonal arrays using representative volume elements. Methods of solution are complex and are often achieved using finite element and finite difference approaches. Self-consistent models consider a single fibre embedded in a concentric cylinder of matrix material which in turn may be embedded in a homogeneous material that possesses properties of the composite as a whole. The volume fraction of the fibre in the composite cylinder is the same as that in the composite as a whole. It is successful in being applicable to any regular or irregular array.

To allow for randomness in fibre distributions and the associated contact between fibres a so called contiguity factor,  $C$  has been applied to semi-empirical equations.  $C = 1$  indicating all the fibres in contact and  $C = 0$  indicating no fibres in contact. The value of  $C$  that gives the best fit to experimental results is then inserted into the equations.

To overcome the complexities of exact solutions a semi-empirical approach of Halpin and Tsai [10] uses simple generalized equations in terms of two variables,  $\xi$  and  $\eta$ , representing the degree of reinforcement by the fibres and the reduction in fibre volume fraction, respectively.  $\xi$  is dependent on the fibre geometry, the packing geometry and the loading conditions whereas  $\eta$  depends on the rigidity of the fibres and the presence of voids. These can be related to the exact solutions or experimental data through a curve fitting technique. For  $\xi = 0$  the lower bound series model is obtained and for

$\xi = \infty$  the upper bound parallel model is obtained.

The above methods are primarily concerned with the determination of the overall composite mechanical properties and stresses in terms of the individual matrix and fibre properties. For a complete knowledge of the state of stress or strain in the composite finite element or finite difference methods offer the best methods of solution. It is possible to allow for randomness in fibre distributions by incorporating statistical methods.

Analytical and finite element methods of solution to the residual microstresses have considered regular square and hexagonal arrays of fibres using square, triangular and cylindrical unit cells [63,65,83,70]. To model random arrays statistical analysis have been incorporated with the application of dispersion factors to the finite element results [70].

In the transverse direction a state of plane strain and transversely isotropic material properties have generally been assumed whereas in the longitudinal direction anisotropy in the carbon fibre properties has been allowed for.

For a detailed analysis of the properties and mechanical behaviour of fibre reinforced materials the report by Hashin [101] can be referred to. With regard to random arrays of fibres the papers discussed in the literature survey by Guild, Hogg and Davy [70,71] for the prediction of the Poisson's Ratio, longitudinal and transverse Young's moduli of unidirectional fibre reinforced composites are relevant. These papers incorporate a probability function,  $g_x(X)$  to describe the variation in interparticle distance at different volume

fractions. The interparticle distance,  $X$  is defined using the concept of Voronoi cells - the region of a plane closer to one point than any other, as the distance from the centre of a disc to the boundary of its Voronoi cell. The probability function,  $g_x(X)$  which is dependent on the dispersion of the fibres within the matrix is calculated assuming a Gibbs hard-core model in which all non-overlapping configurations of discs are equally likely. The function  $g_x(X)$  is given for volume fractions of 0, 0.1, 0.2 and 0.3, as reproduced in Figure 5.

It was difficult to incorporate the probability distribution of Guild, Hogg and Davy in the present analysis since the interparticle distance is measured in a randomly chosen direction to the boundary of its Voronoi cell and does not represent the shortest interfibre distance.

It is, however, of interest to consider the implications, qualitatively of the probability density function on the finite element results. An indication would be given of the probable range of interparticle distances for a given volume fraction together with the likelihood of a particular interfibre spacing. For example, consider the distribution, as calculated by Guild, Hogg and Davy, at a fibre volume fraction of 30%. Assuming  $\lambda = 1$  circle per unit area, that is one fibre occurs per unit area of the transverse section, it is possible to equate the fibre area per unit area to the fibre volume fraction as follows

$$\pi r^2/l = 0.30$$

where  $r$  is the radius of the fibres.

Thus a value of  $r$  appropriate to these conditions is calculated,

$$r = \sqrt{(0.30/\pi)} = 3.1$$

For a similar fibre volume fraction of 30% and assuming typical fibre radii of  $3.5 \mu\text{m}$  there would no longer be one fibre per unit area. However the same probability density function (Figure 5) can be used provided a scaling factor of  $3.5 \times 10^{-6}/3.1$  is applied to the values of half-interparticle distance. For 30% fibre volume fraction this gives half-interparticle distances (centre to centre) ranging from a minimum of  $3.5 \mu\text{m}$  to a most probable spacing of  $4.9 \mu\text{m}$  and a maximum spacing of  $10.5 \mu\text{m}$ .

It can be seen that the distributions are skewed with a preponderance of values at the lower interparticle spacings. In addition with increasing fibre volume fraction this skewedness is exaggerated. Hence at 30% fibre volume fraction there is a most probable half interparticle distance (surface to surface) of  $1.4 \mu\text{m}$ .

This calculated value is not equivalent to the half interparticle distance -  $XA$ , considered in the micromodelling since it is an average distance over all possible directions to the edge of the Voronoi cell. For fibres with six, four, three and twelve nearest neighbours it would equate to half interparticle distances,  $XA$  of  $1.0 \mu\text{m}$ ,  $0.9 \mu\text{m}$ ,  $0.86 \mu\text{m}$  and  $1.04 \mu\text{m}$ , respectively ( $1.4 \cos(\theta/2)$ ). Hence it can be seen that the finite element models corresponding to half interparticle distances, a of  $1.0 \mu\text{m}$  are typical and that as the fibre volume fraction increases half interparticle distances of  $0.5 \mu\text{m}$  will be more typical due to the increasing skewedness of the probability

density function. In addition there will be a considerable number of fibres closer than these half interparticle distances.

The literature survey shows that the area of the residual microstresses offers the greatest scope for further investigation. The macrostresses have been studied extensively and yet the microstresses play a crucial role in the mechanics of these materials. Studies of the residual microstresses have in general considered regular arrays of fibres and when random arrays have been modelled this has been in order to predict the properties of the composites as a whole. The local extremes of residual stress resulting from irregularities in the fibre distributions, however, are important inasmuch as they effect the micromechanical behaviour. The matrix is under severe load at high stress points and on subsequent loading cracking or maybe viscous flow can result depending on the properties of the matrix. This in turn effects the load transfer mechanism operating between the matrix and the fibre, leading ultimately, to failure of the composite.

## 5.2 Microstress Models

The results of the present analysis can be summarized using the graphs given in Figures 147-150. The results have been considered in terms of the maximum value of the maximum principal stress, which for conciseness will be termed the maximum stress value. The assumption that the yield stress is higher than the tensile strength of the epoxy resin and that the material behaviour is elastic implies that failure will be determined by this stress value.

### 5.2.1 Effect of Varying Interfibre Distance on the Maximum Stress Value

The most obvious relationship is the effect of interfibre distance on the maximum stress values - see Figure 147. In the range of half interparticle distances investigated, that is 0.5  $\mu\text{m}$  to 5.5  $\mu\text{m}$ , the maximum stress values are tensile and appear to have a relationship that is approximately inversely proportional to the interparticle distance. A polynomial regression line drawn through the points shows that the values can exceed the tensile strength of the epoxy resin at interfibre distances of 1  $\mu\text{m}$ . Assuming elastic behaviour of the matrix it would be expected, therefore that cracking would occur at fibre separations of less than or equal to 1  $\mu\text{m}$ .

A spread of values is observed about the regression line which is not random but dependent on fibre diameter. This is clear when models with equivalent interfibre distances and co-ordination angles but different fibre diameters are compared. These show a range of maximum stress values, as much as 7 MPa for the values obtained at a half interfibre distance of 0.5  $\mu\text{m}$ , which are highest for the larger fibre diameters and lowest for the smaller fibre diameters.

Due to the limited range of half interfibre distances modelled, (0.5  $\mu\text{m}$  to 5.5  $\mu\text{m}$ ) it is not possible to predict the maximum stress values outside this range; the trend observed is purely empirical. However in the limit as the interfibre distance reduces to zero the maximum stress would be expected to, if not increase to infinity, at least approach very high values. In practice these high stresses would probably be relieved by cracking and possibly plastic flow at the

microlevel. Plastic flow has not been allowed for in the finite element modelling since, in the temperature range under consideration, the epoxy resin is considered to show elastic material behaviour. Nonetheless, much as in the way that localised plastic flow occurs at the crack tip in brittle materials, it is possible that localised plastic flow will occur in these highly stressed regions. Similarly at the very high interfibre distances approximating to isolated fibres it would be expected that the maximum stress value would approach some low limiting value. The distribution of stresses would be symmetric about the fibre axis with maximum values at the fibre/matrix interface. Photoelastic results obtained for polycarbonate rods in an epoxy resin matrix when cooled from cure [72] support this prediction. It was also noted in the same publication that the shrinkage stresses obtained around an isolated circular inclusion can be thought equivalent to those present around a circular hole to which a boundary pressure,  $p$  is applied.

The graph of maximum stress value versus half interfibre distance appears to show that the greater the co-ordination angle the higher the maximum stress value. However by limiting the volume fraction range from 30% to 65% the lower the interfibre distance the higher the co-ordination angle must necessarily be. This trend is therefore thought to be largely due to the association of packing angle with interfibre distance.

### 5.2.2 Effect of Fibre Diameter on the Maximum Stress Value

Figure 148 shows the effect of fibre diameter more clearly. At each interfibre distance an increase in fibre diameter results in an

increased maximum stress value. The relationship is approximately linear, having an equal effect at all interfibre distances. The effect is much less significant than that of interfibre distance.

### 5.2.3 Effect of Varying Fibre Volume Fraction on the Maximum Stress Value

Figure 149 shows that the maximum stress value increases with increasing fibre volume fraction, although the exact relationship is dependent on the mesh angle. It is noted that decreasing interfibre distance and increasing fibre diameter necessarily result in an increased fibre volume fraction and therefore, from the preceding two graphs (Figures 147 and 148), it would be expected that the maximum stress value would increase. However, the graphs show no effect due to co-ordination angle. Figure 147 did show the low stress values to be concentrated in the 15°-30° meshes and the high stress values in the 45°-60° meshes but this was, as stated previously, largely due to the constraint that the volume fraction should lie between 30% and 65%. This then limits the possible interfibre distances.

The above would imply that the effect of fibre volume fraction on the maximum stress values are as a direct result of the associated changes in interfibre distance and fibre diameter. This is confirmed by a comparison of meshes with the same fibre diameter and interfibre distance but different meshing angles. For example meshes D51C, D03C and D54C. These are all found to have an equal maximum stress value of 34 GPa. Comparisons with other groups of meshes produces similar results (Tables 4, 6, 8 and 10).

Apparently the overall tensile stress in the contracting matrix is

increased by an increase in the proportion of fibre in the composite. however, this is not an explicit relationship since the change in fibre volume fraction is also associated with changes in both the interfibre distance and the fibre diameter. These two parameters have explicit relationships with the maximum value of the maximum principal stress (Tables 4, 6, 8 and 10) whereas there is no relationship between the maximum stress value and the fibre volume fraction at constant values of the fibre diameter/interfibre distance ratio. Hence larger fibre radii and smaller interfibre distances imply higher maximum stress values regardless of the packing density/co-ordination angle.

#### 5.2.4 Effect of Varying Fibre Diameter/Interfibre Distance Ratio on the Maximum Stress Value

Models that possessed equal fibre diameters and interfibre distances were found to have equal maximum stress values. This together with the approximate inverse proportionality of the maximum stress value to the interfibre distance (Figure 147) and direct proportionality of the maximum stress value to the fibre diameter (Figures 148), implied a relationship to exist between the maximum stress value and the fibre diameter/interfibre distance ratio,  $O_X/X_A$ . The graph of the maximum stress value versus fibre diameter/interfibre distance ratio (Figure 150) shows that the resulting points fall on a single line. However the relationship is not linear. Whether the calculated regression line is a correct interpretation of the correspondence is not clear. It may be that if values were calculated outside this range a different and possibly more approximate trend would be apparent. However, assuming

the regression line is a correct interpretation, it would seem that as the half-interfibre distance reduces to values less than  $0.5 \mu\text{m}$  the maximum stress value does not necessarily approach infinity. Rather some limiting value is approached.

Again it is interesting to consider the possible results in the limiting cases as the fibre diameter/interfibre diameter ratio approaches infinity and zero. The former would be approximated by two infinitely thick plates separated by a negligible distance and the latter as an isolated fibre of negligible cross sectional area. In these situations it would be expected that maximum stress values of infinity and zero would be obtained, respectively. Neither of these are particularly realistic representations of fibre distributions but they do give the bounds to the problem.

#### 5.2.5 Effect of Co-Ordination Angle on the Stress Distributions

The co-ordination angle is far more important with regard to the overall pattern of stresses in the epoxy resin and the location of the maximum stress value. The greater rate of decrease in the maximum principal stress observed along the inclined edge, OB (Figures 90, 94, 98, 102, 106, 110 and 114) is expected since there is a greater length of contracting epoxy resin along this side. Indeed at large packing angles, most noticeably at low interfibre distances, the difference is such that the maximum principal stress increases along the straight side, OA. It is interesting to note that modelling of two rigid cylindrical fibres in an infinite matrix when subject to in-plane loadings has shown a variation in maximum stress location with inclusion spacing [72]. For wide spacings, the maximum principal

stress occurred at the interface whilst for spacings less than one-fibre radius the maximum value was located at the mid-point between the fibres. This modelling is effectively of a situation in which a fibre has one nearest neighbour and a co-ordination angle of  $360^\circ$ .

The location of the greatest maximum principal stress value in the epoxy and the direction of the associated force vector tangential to the fibre/matrix interface would imply that any cracks would initiate at the fibre/matrix interface and propagate perpendicular to this surface.

In the  $15^\circ$  models the stress concentration occurs uniformly around the fibre circumference. It would be expected therefore equally probable that a crack would initiate anywhere on the fibre circumference. The movement of this maximum towards the inclined edge, OB as the packing angle increases means that the crack would then be more likely to initiate in the epoxy at the fibre/matrix interface close to the inclined edge, OB. In addition the change to an off tangential maximum force vector in the case of the larger  $60^\circ$  and  $45^\circ$  co-ordination angles at short interfibre distances would cause the crack to grow outwards towards the straight edge, OA.

#### 5.2.6 Stress Distributions in the Carbon Fibres

The maximum principal stresses in the carbon fibres were generally compressive and of magnitudes less than those observed in the epoxy resin. The stress distributions were also more uniform. Maximum absolute values were obtained of between -10 MPa and -20 MPa for the maximum principal stress and 10 MPa and 60 MPa for the von Mises stresses. Stress variations observed at the fibre centre in all of the

models were thought due to a meshing instability and therefore ignored. In the case of the models having 15° and 30° fibre co-ordination angles, that is the packings in which the fibres have twelve and six nearest neighbours, very uniform distributions were obtained with just a slight tendency in a few of the 30° co-ordination models for the maximum principal stresses to become less compressive and the von Mises stresses to increase at the fibre/matrix interface. In the case of the 45° and 60° co-ordination angle models the stress variations towards the interface became more pronounced with a gradual change from the fibre centre. As was observed in the case of the stresses in the epoxy resin, as the interfibre distances decreased the magnitude of the stresses became greater. In addition the maximum values of the von Mises stresses rather than occurring uniformly at the fibre/matrix interface showed maximum values at point X on the interface. A slight tendency was also shown for the minimum compressive/maximum tensile values of the maximum principal stress to occur at the fibre/matrix interface toward the inclined edge, OB at these shorter interfibre distances. These changes in stress distribution appeared to be associated with the changes in the location of the maximum values of the stresses in the epoxy resin.

Since the fibres are considerably stronger than the epoxy matrix, having axial tensile strengths in the range 2-7 GPa, and the stresses are lower in the fibre than in the weaker epoxy resin it can be assumed that failure is unlikely to be initiated in the fibre.

#### 5.2.7 Hypothetical Voronoi Cell

This refers to the finite element model used to model a "hypothetical"

random array of fibres. The mesh contains a representative selection of the meshes used to model the regular fibre arrays in a single Voronoi cell. The resulting cell contains a single fibre with five nearest neighbours and with the shortest interfibre distances in the range  $0.5 \mu\text{m}$  to  $6.0 \mu\text{m}$ .

The deformation of the hypothetical Voronoi cell shows the radial restraint assumption of the regular fibre array models is not strictly correct when random fibre distributions are considered although it is a good approximation.

The location of the greatest maximum principal stress at point A, mid-way between the two closest fibres on the line of shortest interfibre distance separating the  $45^\circ$ , JOA and  $60^\circ$ , AOB areas (Figures 121 and 122), can be explained by considering the corresponding regular array models discussed above (Tables 4,6 and 8). In particular the results obtained using the B54A, B06A, B03B and B03C unit cells and to which the Voronoi cell approximates in this region. From the B54A and B06A regular fibre array models it would be expected that the maximum stress value would occur at an angle of  $30-35^\circ$  to the line OA on the fibre/matrix interface (Tables 6 and 8/Figures 106 and 114). Instead the adjacent  $30^\circ$  regions where the stresses are significantly lower have the effect of suppressing the maximum along the fibre/matrix interface (Table 4/Figures 94 and 98). The increase in the maximum principal stress outwards along the straight edge, XA calculated using the regular B54A and B06A models then results in a maximum value at point A.

The maximum values of the maximum principal stress and the von Mises

stress are 68 MPa and 59 MPa, respectively. This is higher than would be expected from the regular fibre array models corresponding to the geometry in this region - see figure 150 for a fibre diameter/interfibre distance ratio of 7. Obviously the variable interfibre distances in this model, (that is the randomness in fibre distribution), cause the stresses to be distributed less uniformly. Hence greater extremes of stress result.

A crack would be expected to initiate at the most highly stressed point mid-way between the two closest fibres. Due to its action along the edge of the Voronoi cell it should propagate in the matrix toward the fibre centres.

#### 5.2.8 Computer Modelling of Random Fibre Arrays

The method used to model a random array of fibres required all the fibres to be totally enclosed within a prescribed rectangle having an aspect ratio of 2. This was in order to include only whole fibres within the rectangle thus facilitating the calculation of the volume fraction. In effect every fibre on the edge of the rectangle is moved to a position where its centre is at a distance  $R_m$  from the edge whilst the other co-ordinate remains unchanged. In reality, for truly random arrays, fibres would be located randomly on the edge of the rectangle. This results in the fibres only being strictly random in the area  $(2C - 2R)(C - 2R) \text{ m}^2$ , where  $C$  is the width of the rectangle in metres.

In addition a condition is applied such that overlapping fibres are moved apart by the distance they overlap plus  $0.006 \times C \text{ m}$ . As a result

many fibres are moved to a distance  $0.006 \times C$  m apart. This could be regarded as analogous to the compacting process as the prepreg is cured under pressure in an autoclave. That is fibres collide as the prepreg is compressed which reduces the final fibres separations to a thin membrane layer of epoxy resin. The thickness of the proposed layer is uncertain but values of  $0.15 \mu\text{m}$  ( $C = 25.3 \mu\text{m}$ ) and  $1.18 \mu\text{m}$  ( $C = 19.6 \mu\text{m}$ ) have been imposed in the 30% and 50% fibre volume fraction arrays, respectively. These values were not decided upon beforehand since the formulation of the program causes them to be dependent on the width of the rectangle. They do however appear to be of the right order of magnitude for the 30% array whilst the value of  $1.18 \mu\text{m}$  for the 50% array is probably too thick. Obviously the dependence of the thickness of the membrane layer on the width of the rectangle and thus the fibre volume fraction, due to the fact that a higher volume fraction for a given number of fibres will require a smaller rectangle, is erroneous. The membrane layer thickness is of course also dependent on the chosen number of fibres in the array as a larger number of fibres for a given volume fraction will require a larger rectangle.

An alternative interpretation of the specified movement,  $0.006 C$ , of the overlapping fibres is as a energy induced by the applied pressure. As the fibres collide some will push past each other to fill adjacent voids. Their ability to do this will depend on the applied pressure which can be thought analogous to the value of  $0.006 C$ .

The resulting fibre array is approximately random but has an excessive number of fibres located at a distance  $0.006 \times C$  m apart and with their centres at a distance  $R$  m from the edge of the rectangle.

### 5.2.9 Voronoi Cell From Random Fibre Array with 50% Fibre in the Section

The rotation of the Voronoi cell is unexpected. However the restraining influence of adjacent Voronoi Cells is not considered and no doubt would reduce this effect, while at the same time introducing an additional stress.

The extremely high stresses observed in the three regions where the interfibre distances are shortest are thought largely to be due to the discontinuous modelling of the geometry of the fibre surface. That is the approximation of the circular interface by a regular polygon having twelve sides. This is supported by the fact that the most highly stressed points occur at the corners of the polygon. Further refinement of the mesh in the fibre would be required to alleviate this effect. It is interesting to note however that discontinuities do cause such stress concentrations, as this is important with regard to defects on the fibre surface. Geometrical, structural and compositional flaws are observed in the fibres [14,15,16] and no doubt will effect the resulting stress distributions.

Nevertheless having explained these extremely high stresses the regions of maximum stress occur where the interfibre distance is small. In these regions values of between 49 MPa and 83 MPa are obtained for the maximum principal stress and 41 MPa and 67 MPa for the von Mises stress. When comparing this to the results obtained using the regular fibre array models it is in agreement with the general trend observed of high maximum principal and von Mises stresses at low interfibre distances and large fibre diameters in the

latter. This is apparent if the value of the fibre diameter/interfibre fibre distance ratio of 40 and maximum stress value of 83 MPa (Table 12) is compared to the results given in Figure 150.

However the exact location of the maximum stress regions is not explained. With the 45° and 60° co-ordination angle regular array models at short interfibre distances, to which the Voronoi cell approximates in the region of the shortest interfibre distance, the maximum principal stress occurs on the fibre/matrix interface at angles ranging between 25° and 40° to the line of shortest interfibre distance (Tables 6 and 8). One possible explanation is that, as for the hypothetical Voronoi cell, the relatively lower stresses in the adjacent regions with larger interfibre distances causes the interface to be less highly constrained. Thus these maxima would be suppressed. In addition, due to the wide range of stresses occurring in the Voronoi cell and the limit to the chosen number of contours of ten, such variations will be less apparent. It should also be noted that the distributions can only be regarded as approximate due to the angular modelling of the fibre surface.

To summarize the results obtained using both the Voronoi cells and regular fibre array models show maximum stress regions to be associated with short interfibre distances. Whether as the interfibre distances decrease to values less than 0.5  $\mu\text{m}$  further increases in stress occur is less certain. Such situations are not modelled in the regular arrays or "hypothetical" Voronoi cell and in the Voronoi cell from the 50% random fibre array angularities in the fibre geometry obscure the results. However the regular fibre arrays do seem to indicate that changes in interfibre distance are less significant at

low interfibre distances (Figure 150). This is in agreement with the results obtained from the Voronoi cell from the 50% fibre volume fraction random fibre array. In addition it is probable that all the fibres will be surrounded by a thin coating layer of epoxy resin. This is supposed because presumably the epoxy resin, inasmuch as it is required to wet the fibres, has a low angle of contact with the fibres. Thus below a certain thickness the epoxy resin would not readily separate from the fibre surface. A limit would then be imposed on the generation of the residual stresses.

In conclusion it appears from the micromodel results that high residual stresses occur in regions of low interfibre distance and that these are exacerbated by discontinuities on the fibre surface. To prevent high stresses it is proposed that the fibre packing should be as regular as is possible and that faults on the fibre surface should be avoided. It may be that a coating applied to the fibres prior to forming the prepreg would limit the interfibre distances.

With regard to the random fibre array models it seems that the variation in the distances between nearest neighbours is important. Comparing the ratio of the shortest interfibre distance to the longest interfibre distances, a value of 0.08 is obtained for the hypothetical Voronoi cell and, for that associated with the 50% fibre volume fraction random fibre array, a value of 0.03. The corresponding maximum values of the maximum principal stress (ignoring the effects due to the irregular geometry of fibre in the latter model) are 68 MPa for the hypothetical Voronoi cell and 83 MPa for the Voronoi cell from the 50% fibre volume fraction array. The hypothetical Voronoi cell has

a far greater minimum interfibre distance ( $0.5 \mu\text{m}$ ) than the Voronoi cell from the 50% fibre volume fraction array ( $0.09 \mu\text{m}$ ). However, the variation in interfibre distances or randomness in the former is greater than in the latter. It appears that the level of randomness of interfibre distance within a Voronoi cell may also affect the stress distribution and thus counteract the effect of interfibre distance. This would explain why the stresses calculated in the Voronoi cell from the 50% volume fraction array are not significantly greater than those in the hypothetical voronoi cell.

### 5.3 Optical Microscopy

In the earlier macromodelling with the single and double meshes the fibre bearing layers were assumed to be separated by thin ( $0.025\text{mm}$ ) layers of epoxy resin. The optical micrographs presented in the results showed no evidence of such epoxy resin layers, leading to the conclusion that the assumption was incorrect. Instead the individual tows making up the ply layers were seen to impinge directly on the adjacent plies with regions of epoxy resin rich material between tows.

For the purposes of modelling the fibre sections of primary concern are those taken transversely to the fibre direction. At higher magnifications there appears to be a random variation in interfibre distance and location of the fibres as would be expected. See Figures 136 and 137. The fibres are noted to touch, form rings, clusters and localised regions of close packing. The Voronoi cells obtained using the random number generator are realistic representations of those distributions obtained in actual composites. In the samples examined no cracking was observed under the optical microscope. Possible

reasons for this were thought that either the cracks are too small to be observed or there is microyielding in the matrix. This is supported by the observations of Sato and Kurauchi [85] who studied samples of a sheet moulding compound (consisting of randomly dispersed chopped-strands of glass fibres in a vinyl ester resin matrix) treated with various sizing agents. Samples were examined to failure in bending using electron microscopy. Some of the samples showed initial microvoiding of the matrix in the interfacial region. This later spread into the matrix region between fibres followed by shear yielding of this region and cracking at the fibre/matrix interface. Other samples treated with different sizing agents showed interfacial microcracking, but with no prior microvoiding and shear yielding. Measurements of the thermo-acoustic emission generated on the cooling of samples indicated interfacial cracking which was found to be suppressed with increasing quantities of sizing agent. However when examined under the electron microscope no cracking was apparent. It was proposed that the cracking was at the sub microlevel. Little information is available regarding the exact yield behaviour of the epoxy resin and therefore it is difficult to predict its response in these circumstances.

#### 5.4 Electron Microscopy

The results showed (Figures 140-144) in a few local regions many cracks around the fibre/matrix interface. These were probably formed as a consequence of the thermal stresses set up during cooling. At other locations different types of defect were noted which were thought due to the sample preparation (Figures 145 and 146). These were apparent as surface damage which was observed to be independent

of the microstructure. It was for this reason that the defects were thought due to sample preparation.

The crack paths indicate that the failure is due to the stresses exceeding the interfacial strength rather than the tensile strength of the epoxy resin. From the micromodel distributions obtained of the maximum principal stress it would be expected that if the interface was strong the cracks would initiate at the fibre/matrix interface and propagate outwards. Instead it appears that in certain instances where the interface is weak this is failing due to the lower radial stresses. Thus the cracks run parallel to the fibre/epoxy interface (Figures 140-144). In the modelling perfect bonding is assumed between the fibre and the matrix and no account is made for weak interfacial properties. There is an obvious discrepancy between the experimental observations and the results of the stress calculations. This is most probably due to relatively weak interfacial bonding.

The single case of a crack or defect crossing a fibre was atypical and had a different form to that of the interfacial cracks. Bader et al [102] also noticed cracks to run through fibres in one particular batch of prepreg they examined. In a later batch made from a fibre with a modified surface treatment, which reduced the interfacial strength, the effect was much less frequently observed.

The surface damage, as mentioned previously, was observed to be independent of the microstructure and was thought to be due to the sample preparation rather than inherent defects. That is the sectioning of the laminate with a saw and subsequent polishing. The damage took the form of linear hackle features, made up of a series of

indentations/pulled-out pieces of material (Figure 145), and more general irregular damage to the surface (Figure 146). The linear features were probably formed due to the sawing action and the numerous angular artifacts as a result of the abrading particles as the material had been pulled out of the surface. Such features have not therefore been discussed further.

No cracking was apparent in the sections through the longitudinal layers or at the ply interfaces although in these areas defects were more difficult to observe. Cracking at a ply interfaces was observed by Bader et al [102] where a transverse crack in a  $90^\circ$  ply meets a  $0^\circ$  ply. However this was typical of high loadings and thick  $90^\circ$  plies (4mm) not applicable to the samples examined here. In the same publication longitudinal splits were observed in glass fibre reinforced plastics (GFRP) due to the Poisson's effect: that is the mismatch between the Poisson's ratio of the longitudinal and the transverse laminae. These occurred with increasing load subsequent to the transverse cracking. No such phenomenon was observed in the carbon fibre reinforced plastics (CFRP) although in these materials the mismatch is greater. It was thought that this was because the ultimate failure strain of the CFRP is smaller than that of the GFRP and the laminate fractures before large Poisson's strains are developed. With respect to the micromodelling in this thesis the maximum principal stress vectors were observed to act within  $30^\circ$  of the transverse plane. It is therefore not surprising that no cracking was observed in these longitudinal fibre directions.

## 5.5 Macromodelling

### 5.5.1 Single and Double Meshes

The optical microscopy work has shown the assumption of a thin epoxy resin layer between the plies in a laminate to be incorrect. Nevertheless epoxy rich regions are observed between the individual tows making up the layers, particularly in woven prepregs. The single and double meshes show that in the epoxy rich regions high tensile stresses, in the range 10-110 MPa, are generated. Epoxy rich regions are therefore critical with regard to the stress distributions within the layers. Maximum principal stresses (70-110 MPa), greater than the tensile strength of the epoxy resin, 47.7 MPa were calculated in these regions. The calculations can only be regarded as approximate since the finite element meshes were coarse, and isotropic properties were assumed for the carbon fibre layers with temperature independent properties for the epoxy resin, but it is obvious that cracking is highly probable in epoxy rich regions.

### 5.5.2 Results Obtained using Classical Lamination Theory

The stresses occurring in the centre of the typical multidirectional laminate were determined using classical lamination theory as an estimate of the probable background stress distributions on which the microstresses are superimposed. The chosen symmetric  $[0_4/90_{10}/0_4]$  laminate has an inner layer consisting of ten plies in which the fibres are orientated at  $90^\circ$  to the laminate axis sandwiched between two outer layers each of four plies in which the fibres are orientated at  $0^\circ$  to the laminate axis. The classical lamination theory assumes elastic deformations only, with perfect bonding between plies. That is

there is a constant geometry through the thickness of the laminate, and no interlaminar stresses. Edge effects are therefore not accounted for, nor are effects due to plasticity or geometric non-linearities. The latter however is only important for laminates having a ply stacking sequence that is unsymmetric about the laminate mid-plane, which are not considered here.

The laminate mid-plane strains and stress and moment resultants were first determined after a uniform temperature decrease of 170°C. Compressive laminate mid-plane strains were calculated in both the x-direction parallel to the laminate axis and the y-direction transverse to the laminate axis. ~~This is because the directions transverse to the fibres having thermal expansion coefficients greater than those in the directions parallel to the fibres. When the assumption of perfect bonding between plies is applied the free deformations are necessarily increased in the directions parallel to the fibres and restrained in the directions transverse to the fibres. Balancing the stresses through the thickness of the laminate causes the former effect to predominate so an actual laminate mid-plane strain that is compressive is obtained.~~

As stated previously the lack of laminate curvature and moment resultants is due to the laminate ply stacking sequence being symmetric about the mid-plane axis. The laminate is also unbalanced, there being a greater number of 90° plies than 0° plies. The greater strain and stress resultant in the x-direction, the laminate axis, is therefore expected since the 90° plies have the predominating effect.

The compressive  $\sigma_x$  and  $\sigma_y$  stresses in the fibre directions of the 0°

and the 90° plies, respectively are due to the greater contraction in the transverse direction of the adjacent plies. Similarly the tensile  $\sigma_y$  and  $\sigma_x$  stresses in the transverse directions of the 90° and 0° plies, respectively can be explained as due to the restraining influence of the fibres in the adjacent plies. Again it is noted that the predominating effect of the 90° plies has led to these values being greatest in the 0° plies.

The macrostresses obtained in this way vary between -73 MPa and 63 MPa, which are of the same order of magnitude as the maximum values of the calculated microstresses (maximum principal) of between 30 MPa and 60 MPa, and greater than the epoxy tensile strength of 47.7 MPa. Only one specific ply stacking sequence has been considered and one set of material properties assumed, also no temperature dependence of these properties has been allowed for. However an alternative stacking sequence,  $[\pm 45/0/90]_s$  considered by Stango and Wang [55] using the same material properties yielded similar results as follows,

$$\begin{aligned} \sigma_y = -\sigma_x = 61 \text{ MPa}, \tau_{xy} = 0 & \quad \text{in } 0^\circ \text{ ply} \\ \sigma_y = -\sigma_x = -61 \text{ MPa}, \tau_{xy} = 0 & \quad \text{in } 90^\circ \text{ ply} \\ \sigma_y = \sigma_x = 0, \tau_{xy} = -61 \text{ MPa} & \quad \text{in } 45^\circ \text{ ply} \\ \sigma_y = \sigma_x = 0, \tau_{xy} = 61 \text{ MPa} & \quad \text{in } -45^\circ \text{ ply} \end{aligned}$$

Note that this laminate is balanced and therefore equal and opposite stresses are obtained in the adjacent layers. Also by including angle-ply,  $\pm 45^\circ$  plies in addition to the cross ply, 90° plies, ply shear stresses,  $\tau_{xy}$  have been introduced. These are due to the calculation of shear terms in the  $\pm 45^\circ$  stiffness matrices when transformed from the ply axis to the laminate axis.

In the above calculations of the macrostresses the mechanical behaviour has been assumed temperature independent, linear elastic. As discussed in the micromodelling the epoxy resin properties are in fact temperature dependent and it would be expected that the properties of the individual unidirectional plies would also be temperature dependent. In addition the material properties as given by Ciba-Geigy for the epoxy resin show the glass transition temperature of the epoxy resin to occur in the range 160-195°C. Hence some visco-elastic behaviour may be expected on cooling from the cure temperature of 190°. This latter effect was ignored in both the macro- and micro-modelling since the residual stresses generated in this temperature range were thought to be minimal. Nonetheless, when both the temperature dependence and possible visco-elastic behaviour of the epoxy resin are taken into account, it can be seen that the calculated residual macrostresses are <sup>probably over</sup> ~~conservative~~ estimates of the actual values.

#### 5.6 Combined Effects of Macrostress and Microstress Distributions

The macrostresses associated with multidirectional laminates and epoxy rich regions can be regarded as a background stress distribution on which the microstress fields are superimposed. The effect of the two types of stress in combination will of course depend upon the particular stacking arrangement of the plies. For example a transverse layer sandwiched between two longitudinal layers will produce a large tensile stress field superimposed on the transverse microstresses, making cracking highly probable. In contrast a transverse layer in a unidirectional laminate has no, or when sandwiched between two 45°

layers a much smaller, tensile stress field superimposed on the transverse microstress distribution.

The macrostress results presented for the  $[0_4/90_{10}/0_4]_S$  and  $[\pm 45/0/90]_S$  considered show compressive stresses to be developed in the fibre directions and tensile stresses in the transverse directions, as would be expected. Since it is the transverse directions that are the weakest, their properties being largely dependent on those of the epoxy resin, it is the stresses in these transverse directions that are the most critical with regard to the onset of cracking.

It is noted that the tensile macrostresses calculated in the transverse directions of the above laminates (63 MPa, 60 MPa and 61 MPa) already exceed the tensile strength of the epoxy resin (47.7 MPa). With the superposition of the randomly occurring microstresses, which have maximum tensile values of the maximum principal stress in the range 30 MPa to 60 MPa, these high macrostresses can only be aggravated. Thus it would be expected that microcracking in the transverse layers is highly probable.

Even for unidirectional laminates, where there are no superimposed macrostresses, the microstresses are at such a level that where the interfibre distance reduces below  $0.5 \mu\text{m}$  cracking would be expected. For multidirectional laminates the stresses in the transverse directions will always be tensile. However their magnitude will depend on the particular stacking sequence considered. Since the microstresses occur randomly there will be instances where the tensile macrostresses in the transverse direction and the direction of

the maximums (tensile) in the microstresses will coincide. Here the stresses can be added directly. In the case of the maximum microstresses (tensile) in other directions the combined stresses will not be as great, since it will be the resolved component of the macrostress that is added to the microstress. They will, however, be more than the microstress or macrostress considered in isolation. It is therefore deduced that cracking in the transverse directions of any multidirectional laminate is more probable than in a unidirectional laminate. The effect is obviously dependent on the particular stacking sequence under consideration.

#### 5.7 Effect of Incipient Cracks on Composite Failure

The presence of any microscopic cracks or microvoids constitute the incipient flaws that initiate transverse cracking and thus first ply failure. If the stress levels are such that there is no propagation then their presence will not be detrimental to the properties of the material. However on loading the residual stresses are the background stress on which the applied stresses are superimposed. Thus, when the load is applied in an appropriate direction, high residual stresses, will cause failure at lower applied loads. At stress levels causing these flaws to grow to detectable cracks their presence are highly significant particularly with regard to fatigue loadings. It is clear that these micromechanical effects are critical with regard to the overall mechanical behaviour of the composites. In particular the interfacial bond strength is highly significant with regard to failure of the transverse layers.

Concerning the propagation of cracks Bader, Bailey, Curtis and Parvizi

[102] have shown the thickness of the plies to be relevant. For crack propagation they proposed that this must be both mechanistically and energetically favourable. Mechanistically an equation was used to calculate the strain magnification in the matrix resulting from an externally applied strain. This gave a strain magnification factor, SMF, dependent on the interfibre distance,  $\Delta$  which tends to the ratio of the Young's modulus of the fibre to that of the matrix,  $E_f/E_m$  as  $\Delta$  tends to zero. Since for all fibre volume fractions regions exist where the fibres touch due to randomness in the arrays a constant value of 6 and 8-10 was calculated for the SMF in carbon fibre and glass epoxy systems, respectively. The dependence of the microstresses on the interfibre distance supports the finite element results obtained in this thesis.

The energetic considerations suggests the crack propagation to be dependent on the ply thicknesses. For thin plies the thermal strains in the longitudinal and transverse plies alter the energetics of the system. As a result propagation becomes less likely and any microcracks are suppressed. Good agreement was obtained between the theory and experimental results for glass/epoxy resin and reasonable agreement for carbon fibre/epoxy resin composites. In cross ply and multi-ply laminates constructed from thin plies ( $< 0.5$  mm) the cracking was energy controlled whilst for thicker plies the transverse cracking mechanism controlled the crack propagation.

In the thin transverse plies, estimated at between 0.1 mm and 0.5 mm, of the samples examined under the electron microscope the general absence of cracks suggests that such a crack suppressing mechanism is

in operation.

It is the nature of composites that cracks are blunted and stresses redistributed with total catastrophic failure delayed. Therefore whilst cracks are undesirable since they cause the properties to deteriorate the material may still be perfectly serviceable and their presence does not necessarily imply failure.

#### 5.8 Effect of Moisture Absorption

The effect of moisture absorption by the epoxy resin is relevant. As detailed in the literature survey this has been shown to cause significant expansion of the epoxy resin at levels causing relief and even reversal of the thermal residual stress [31,41,65]. Indeed the levels of moisture existing in graphite/epoxy laminates exposed to laboratory conditions has been observed to completely negate the transverse curing strain [32]. Using the figures of Adams and Miller the shrinkage resulting from a 170°C temperature decrease is equivalent to 4.2 weight percent loss in moisture of the epoxy resin and maximum saturation levels in the epoxy matrix correspond to 5.6 weight percent. The moisture gain is clearly dependent on the ambient conditions as indeed has been shown [31,32,41], and most probably occurs by initial adsorption of water onto the prepreg surface followed by diffusion into the prepreg [36,41]. Assuming the laminates are moisture free during cure it would be expected that cracks would form on cooling from the cure temperature. However it may be that subsequently, as moisture is absorbed from the atmosphere and diffuses inwards, there would be an expansion of the epoxy resin into these cracks.

With regard to moisture absorption it should also be remembered that it has the effect of lowering the glass transition temperature of the epoxy resin, resulting in a degradation of the mechanical properties. Hence there will be a decrease in the Young's modulus and strength of the matrix which will facilitate plastic flow.

### 5.9 Strength of the Fibre/Matrix Interface

The properties of the fibre/matrix interface are significant. In the finite element modelling it has been assumed that the fibre is perfectly bonded to the matrix and the properties of the matrix close to the interface are the same as that in the main body of the epoxy. In many cases this has been shown not to be so [84,85]. Weak interfaces result in laminates with poor shear strength due to loss of the fibre/matrix bond and the associated load transfer mechanism between the fibre and the matrix. Such laminates fail by interfacial failure and fibre pull-out. At the macrolevel this is apparent as poor interlaminar shear strength. For strong interfaces the failure is translaminar and occurs at considerably higher stress levels.

The factors influencing the interfacial bonding are mechanical, physical and chemical [103]. Mechanical adhesion is enhanced by carbon fibre of high surface area since a large region will then be in contact with the epoxy. Unfortunately the fibre surfaces are generally very smooth due to the alignment of the graphitic planes parallel to the fibre surface. Various oxidation treatments given to the fibres increase the surface area and are therefore desirable. It is also thought that the oxidation treatment has the effect of removing flaws in the fibre surface which would otherwise act as stress raisers.

Wetting of the fibre by the epoxy resin is also important with regard to mechanical adhesion since poor wettability will imply poor contact between the fibre and the matrix. In such cases increased surface area of the fibre will not enhance the mechanical adhesion.

Physical and chemical bonding between the fibre and the matrix are dependent on good contact and therefore again good wetting of the fibre by the matrix. Physical bonding is due to weak van der Waals forces such as London dispersive forces, dipolar interactions and hydrogen bonding. Chemical bonding occurs due to the adsorption of chemical groups and the formation of true covalent bonds between the fibre and the matrix. For oxidized carbon fibres in an epoxy resin matrix a reaction is thought to take place with surface carboxylic and phenolic groups and again oxidation of the fibres is thought to be beneficial.

#### 5.10 Interlayer Properties

The presence of a low modulus region or flexible interlayer in the matrix adjacent to the interface whilst not effecting the strength of the composite has been shown [103] to significantly increase the impact strength of the composite, or the energy of rupture. It has been proposed that the presence of the fibre may alter the polymerization reactions of the epoxy resins and thus produce an interfacial region with differing mechanical and rheological properties to that of the epoxy away from the interface.

#### 5.11 Sizing Agents

More recently the coating of the fibres with sizing agents to form a

thin flexible interlayer has been found to be beneficial [85]. In addition to improving the processing characteristics these can be chosen so as to improve the interfacial bonding and interlayer properties. It is thought that the low Young's modulus and/or viscous flow of the matrix close to interface causes the transverse cracking to be suppressed or even eliminated. On the loading of appropriately sized composites observations have shown microvoiding to occur in the matrix close to the interface with subsequent shear yielding of the matrix between fibres. This in turn produce a stress dependence of the visco-elastic behaviour. The resulting composites are stronger and more impact resistant. In particular acoustic emission counts, indicating the onset of transverse cracking, are delayed to higher stress levels and the composites are noted to have better fatigue properties. The effects are dependent on the type and quantity of sizing agent.

Sizing agents added to protect the fibres and improve handling during processing may adversely effect the interfacial properties. For example the commonly used film-forming polymers such as polyvinyl alcohol and polyvinyl acetate, due to their polar nature, readily absorb moisture. If not entirely removed during subsequent processing or incompletely reacted with the matrix they will attract moisture to the interphase region and reduce the bond strength between the matrix and the fibre.

## 6 CONCLUSIONS

6.1 The optical microscopy has shown the assumption of a thin epoxy resin film separating the epoxy impregnated fibre layers to be incorrect. More typically the epoxy impregnated fibre tows are found to be separated by epoxy-rich regions of irregular morphology.

6.2 The maximum principal stresses predicted by the macromodelling in the epoxy resin layers are tensile, in the range 10-120 MPa, and generally greater than the strength of the epoxy resin (47.7 MPa). The residual stresses are developed as a result of the high thermal expansion coefficient of the epoxy resin layers ( $60 \times 10^{-6} \text{ } ^\circ\text{C}^{-1}$ ) compared to that of the fibre rich layers ( $0.5 \times 10^{-6} \text{ } ^\circ\text{C}^{-1}$ ) together with the differing mechanical properties of the two materials. The maximum principal stresses are highest at the fibre/epoxy layer interface. It is obvious that a similar situation would develop in the epoxy resin regions between tows.

6.3 The literature has shown high residual macrostresses, in the range 10-100 MPa, to be developed in multidirectional laminates. The stresses are generated due to the anisotropic nature of the carbon fibres. The macrostress generation has been confirmed in the present work using a software package, PC-Laminate, in conjunction with classical lamination theory. The magnitude and sense of the stresses depend on the stacking sequence of the plies within the laminate. Most critical are those stresses in the plane of the laminate but transverse to the fibre axes. Here they are tensile due to the restraint of the lower thermal expansion longitudinal and off-transverse directions of the adjacent plies. The transverse directions

are the weakest since their properties are determined largely by the properties of the epoxy resin. In addition there is evidence in the literature that high interlaminar stresses are developed at ply interfaces, at faults and at the edges of multidirectional laminates. These interlaminar stresses also depend on the ply stacking sequence and can cause delamination of the composites.

6.4 Finite element micromodelling of regular fibre arrays has shown the maximum values of the maximum principal stresses to depend largely on the shortest distance between fibres and to a lesser extent on the fibre diameter. The maximum values for the fibre arrays considered are found to be approximately inversely proportional to the interfibre distance and proportional to the fibre diameter. No effect on the maximum values is observed for changes in the packing of the fibres, that is the number of nearest neighbours. Hence for a prescribed interfibre distance and fibre diameter changes in the density of the fibre packing or fibre volume fraction produces no significant change in the maximum value of the maximum principal stress.

6.5 The finite element micromodelling of the regular fibre arrays has shown the overall pattern of the stresses to be dependent on the assumed packing of the fibres, that is the number of nearest neighbours. This affects the location of the maximum value of the maximum principal stresses. For fibres with a large number of nearest neighbours, most noticeably at large interfibre distances, the maximum values occur uniformly around the fibre/matrix interface. As the number of nearest neighbours decreases, most noticeably at short interfibre distances and large fibre diameters (high fibre volume fractions) the maximum values of the maximum principal stress occur on

the fibre/matrix interface but at an angle of up to  $40^\circ$  away from the line of the shortest interfibre distance. In similar circumstances the maximum values of the von Mises stress occur away from the fibre/matrix interface on the line of the shortest interfibre distance.

6.6 For the regular fibre arrays with short interfibre distances/large fibre diameters and low fibre volume fractions, that is three to four nearest neighbours, the maximum principal stresses reach values greater than the tensile strength of the matrix (47.7 MPa). Assuming elastic behaviour in the epoxy resin, which is a reasonable assumption at room temperature, material failure would be by brittle fracture. Failure would then occur by crack initiation and growth once the maximum principal stress has exceeded the tensile strength of the epoxy resin. The maximum values are observed to act in the plane transverse to the fibres in a direction tangential to the fibre/matrix interface. Cracks would therefore be expected to form on the fibre/matrix interface and grow outwards into the epoxy. For fibre packings in which the fibres have six or fewer nearest neighbours the cracks would be most likely to initiate at a angle of between  $20^\circ$  and  $40^\circ$  to the line of shortest interfibre distance. The former angle refers to hexagonal packing (six nearest neighbours) and the latter to three nearest neighbours.

6.7 At the microlevel the assumption of a regular array of fibres has been shown to be incorrect. Within the tows the arrangement is random and in many instances the fibres touch. The extremes of stress shown by the micromodelling to be associated with negligible interfibre distances are therefore relevant.

6.8 A "hypothetical" Voronoi cell was analysed using the finite element method to model the stresses in a proposed random array of fibres. This combined a range of the unit cells used in the regular fibre arrays in a single model. Similar patterns of stress were obtained to those calculated using the regular fibre array models, with the maximum principal and von Mises stresses concentrated around the fibre/matrix interface. However rather than directed at an angle to the line of shortest interfibre distance, as would be expected from the regular array models, maximum values occurred along the line of the shortest interfibre distance. These were 68 MPa and 59 MPa in the case of the maximum principal and von Mises stresses respectively. The values were also higher than would be expected from the corresponding regular array models. Obviously the random arrangement of fibres has the effect of redistributing the stresses so that there are greater extremes of stress. The directions of the stresses were similar to those observed in the regular fibre array models.

6.9 A computer program, FIBDIST was developed in order to create a more realistic random array of fibres. Distributions of fibres were created for ten fibres at 30% and 50% fibre volume fractions. A fibre and its associated Voronoi cell were isolated from the 50% array and meshed for finite element analysis. A similar pattern of stresses was calculated as in the "hypothetical" Voronoi cell but with maximum values of the stresses much greater, 320 MPa for the maximum principal stress and 261 MPa for the von Mises stress. This was largely due to the approximation of the circular geometry of the fibre by a regular polygon. Ignoring this effect more realistic values of between 49 MPa and 83 MPa for the maximum principal stress and 41 MPa and 67 MPa for

the von Mises stress were evident, respectively. These were not very dissimilar to those maximum values obtained for the hypothetical Voronoi cell although the shortest interfibre distance was far smaller.

6.10 The modelling has shown that both the macro- and micro-stresses can exceed the tensile strength of the epoxy resin. If the two stress distributions are superimposed, assuming elastic material behaviour, cracking in the transverse layers of multidirectional laminates becomes highly probable.

6.11 In practice with or without loading initial microcracking is usually observed in the transverse sections around the fibre/matrix interface rather than as cracks which propagate out from the interface into the epoxy resin. This is thought due to weak interfacial properties. In the initial stages of failure these interfacial debonds coalesce to form transverse cracks. Later delamination may occur where the transverse cracks meet an adjacent longitudinal layer. Finally as the load is transferred to the longitudinal layers longitudinal splits form due to the mismatch between the Poisson's contractions of the adjacent layers. Finally the longitudinal layers fail.

In other cases failure can proceed without prior microcracking. This generally occurs when fibre treatments and sizings have been applied that strengthen the fibre/matrix bond and/or modify the properties of the epoxy resin close to the interface.

6.12 Observations under an optical microscope of a typical multidirectional laminate sample showed random arrangements of fibres

in the sections transverse to the fibre direction which were similar to those modelled using the computer program FIBDIST. That is fibres touching, forming clusters and rings with local regions of close packing. No cracking was observed at this magnification.

6.13 Electron microscopy showed in a few regions cracks running around the fibre/matrix interface. These were not apparent using the optical microscope. The cracks indicated interfacial failure rather than failure of the epoxy resin. From the micromodelling predictions it was expected that cracking in the epoxy resin would occur perpendicular to the fibres. This implies that in these regions the interface is weaker than the epoxy resin.

6.14 A general absence of cracking in the samples examined under the electron microscope was explained as follows.

a) Viscous/plastic flow in the matrix at the macrolevel. This would occur during the initial stages of cooling when the epoxy resin was at temperatures close to its glass transition temperature. Since the residual stresses generated at this stage would be small these effects were thought to be limited.

b) Viscous/plastic flow in the matrix at the microlevel. This was thought to be more significant, particularly if treatments applied to the fibre surface resulted in an interlayer with properties more flexible than that of the matrix away from the interface. It was noted that such effects, occurring as microvoiding and shear yielding, have been observed in the literature [85].

c) The thinness of the transverse layers causing the transverse

cracking to be suppressed. It has been proposed that for a crack to propagate it must be both mechanistically and energetically favourable [102]. As the thickness of the transverse layer decreases the energetics of propagation becomes less favourable.

6.15 To reduce the high residual stress concentrations associated with short interfibre distances it is proposed that the fibre arrays should be as regular as possible. In addition high fibre volume fractions will ensure that the strength and modulus potential of the fibres is utilized fully. For a given packing structure increasing the fibre volume fraction has the effect of reducing the interfibre distances and thus increasing the residual microstresses. Increases in volume fraction resulting from changes in packing arrangement, say from loose packings in which the fibres have less than six nearest neighbours to denser more closely packed structures, do not effect the residual microstresses in this way (provided there is no change in the minimum interfibre distance). It is suggested, therefore, that regular hexagonal and square fibre arrays are preferable. These achieve the highest fibre volume fractions, and thus the highest strengths of the composites, whilst precluding very short interfibre distances.

It may be that precoating of the fibres prior to forming the prepreg could set a limit to the minimum interfibre distance.

6.16 Benefits also result from good matrix/fibre bonding as this increases the fibre/matrix interfacial strength. Appropriate sizing agents or surface treatments applied to the fibres will produce this effect. Cracking at the fibre/matrix is suppressed producing composites having improved impact resistance and fatigue properties.

Similarly a flexible interlayer between the epoxy resin and the carbon fibre is beneficial.

6.17 Finally in multidirectional laminates the transverse layers should be thin,  $< 0.5$  mm. This has the effect of suppressing any transverse cracking, which is typical of the initial stages of failure.

## 7 FURTHER WORK

At the microlevel it would be of interest to create a mesh to replicate a small region of a photograph of an actual lamina cross section. A practical microstress distribution would then be obtained. Difficulties would be encountered, however, in the generation of the mesh in the regions where the fibres are closest. This has been found to be so in the construction of the Voronoi cells presented in this thesis. Here the mesh needs to be very fine in order to achieve reasonable accuracy and ensure the angles in elements adjacent to the interface are not too small. Refinement of the mesh within the fibres is also necessary if a shape more closely approximating a circle is to be obtained. The stress concentrations resulting from irregularities in the fibre surface would then be removed.

There is a need for the stresses to be modelled at very short interfibre distances,  $< 0.5 \mu\text{m}$ . As explained above the finite element mesh in these situations needs to be very fine for accurate modelling. This would indicate whether, as the interfibre distance decreases to zero, infinitely high stresses or some limiting value is approached.

It would be useful to introduce an interfacial bond strength into the micromodelling as cracking often initiates here rather than in the epoxy resin. Alternatively the effect of a flexible interlayer or transverse cracks could be modelled.

At the macrolevel further effects of the laminate stacking sequence could be studied, although much work has already been carried out in this area. As an alternative or in addition the effects of laminate geometry on the residual stresses associated with the other fibre

preforms mentioned in the literature survey could be investigated.

For example it has been shown [60] that symmetric laminates of unsymmetric geometry such as right angle stiffeners will distort on curing due to out of plane anisotropy. This is known as the spring-forward phenomenon [104]. The enclosed angle of a part is observed to decrease on forming. Relevant geometries include L-shaped cross sections, "top-hat" components and curved plates.

The stresses in other fibre preforms such as woven or knitted fabrics could be modelled. The properties of the individual tows would be assumed as the input parameters and a finite element mesh created to represent the structure of the material. For example a knitted loop or a basket weave could be analyzed.

It may also be of interest to introduce visco-elastic/visco-plastic material behaviour using finite element analysis. This would reproduce more accurately effects in the region of the glass transition temperature.

## LIST OF REFERENCES

1. Handbook of Composite Materials, Vol.1 - Strong Fibers; Elsevier Science Publ. 1985.
2. Engineered Materials Handbook, Vol. 1 - Composite; ASM International 1987.
3. Engineered Materials Handbook, Vol. 2 -Engineering Plastics; ASM International 1988.
4. The RAPRA Review Reports, Vol. 1, No. 1 - Advanced Composites; Thomas, D. K.; Pergamon Press. 1987
5. Delmonte, J; Technology of Carbon and Graphite Fiber Composites; Van Nostrand Reinhold 1981.
6. Chawla, K. K; Composite Materials, Science and Engineering; Springer Verlag 1987.
7. Agarwal, B. D. and Broutman L. J.; Analysis and Performance of Fiber Composites; John Wiley & Sons 1980.
8. Vinson, J. R. and Chou, T; Composite Materials and their use in Structures; Applied Science Publ. 1975.
9. Tsai, S. W. and Hahn, H. T.; Introduction to Composite Materials; Technomic Publ. 1980.
10. Jones, R. M.; Mechanics of Composite Materials; McGraw-Hill 1980.
11. Johnson, W. and Watt, W.; Structure of High Modulus Carbon Fibres, Nature, Vol. 215, July 22, 1967, pp. 384-386.

12. Bacon, R. and Tang, N. M.; Carbon, 2, 221 (1964).
13. Badami, D. V., Joiner, J. C. and Jones, G. A.; Microstructure of High Strength, High Modulus Carbon Fibres; Nature, Vol. 215, July 22, 1967, pp. 386-387.
14. Johnson, D. J.; Recent advances in studies of carbon fibre structure, Phil. Trans. R. Soc. London A, 294 (1980), pp. 443-449.
15. Bacon, R.; Carbon fibres from mesophase pitch, Phil. Trans. R. Soc. London A, 294 (1980) pp. 437-442.
16. Reynolds, W. N. and Moreton, R.; Some factors affecting the strengths of carbon fibres; Phil. Trans. R. Soc. London A, 294 (1980) pp. 451-461.
17. Johnson, J. W.; Resin matrices and their contribution to composite properties; Phil. Trans. R. Soc. London A, 294 (1980) pp. 487-494.
18. Williams, D.; New knitting methods offer continuous structures; Advanced Composite Engineering, June 1987, pp. 12-13.
19. Loos, A. C. and Springer, G. S.; Curing of Epoxy Matrix Composites; Journal of Composite Materials, Vol. 17, March 1983, pp. 135-169.
20. Springer, G. S.; A Model of the Curing Process of Epoxy Matrix Composites; Progress in Science and Engineering of Composites; Hayashi, T., Kawata, K. and Umekawa, S., Ed.; ICCM-IV, Tokyo 1982, pp. 23-35.

21. Loos, A. C. and Springer, G. S.; Curing of Graphite/Epoxy Composites; AFWAL-TR-83-4040 1983.
22. Springer, G. S., Tang, J. and Lee, W. I.; Effects of Cure Pressure on Resin Flow Voids, and Mechanical Properties; AFWAL-TR-87-4058 1987.
23. Loos, Alfred C. and Freeman, Jr. William T.; Resin Flow During Autoclave Cure of Graphite-Epoxy Composites; ASTM STP 873, 1985, pp. 119-130.
24. Gutowski, T. G.; A Resin Flow/Fibre Deformation Model for Composites; 30th National SAMPE Symposium, March 1985, pp. 925-934.
25. Gutowski, T. G., Wineman, S. J., Cai, Z.; Applications of the Resin Flow/Fibre Deformation Model; 31st International SAMPE Symposium, April 7-10, 1986, pp. 245-254.
26. Dave, R., Kardos, J. L. and Dudukovic, M. P.; A Model for Resin Flow During Composite Processing. Part 1: General Mathematical Development; Polymer Composites, Vol. 8, No. 1, February 1987, pp. 29-38.
27. Dave, R., Kardos, J. L. and Dudukovic, M. P.; A Model for Resin Flow During Composite Processing. Part 2: Numerical Analysis for Unidirectional Graphite/Epoxy Laminates; Polymer Composites, Vol. 8, No. 2, April 1987, pp. 123-132
28. Lindt, J. T.; SAMPE Quarterly, 16, 58, 1985
29. Novak, R. C. and DeCrescente, M. A.; Fabrication Stresses in Graphite-Resin Composites; Journal of Engineering for Power (Trans. ASME), October 1970, pp. 377-380.

30. Hahn, H. T. and Pagano, N. J.; Curing Stresses in Composite Laminates; Journal of Composite Materials, Vol. 9, January 1975, pp. 91-106.
31. Pagano, N. J. and Hahn, H. T.; Evaluation of Composite Curing Stresses; Proceedings of ASTM Conference on Composite Materials, May 1976, pp. 317-329.
32. Hahn, H. Thomas; Residual Stresses in Polymer Matrix Composite Laminates; Journal Composite Materials, Vol. 10, October 1976, pp. 266-278.
33. Schapery, R. A.; Thermal Expansion Coefficients of Composite Materials based on Energy Principles; Journal of Composite Materials, Vol. 2, 1968, p. 380.
34. Marom, G. and Weinberg, A.; The Effect of Fiber Critical Length on the Thermal Expansion of Composite Materials; Journal of Materials Science, Vol.10, 1975, p. 1005.
35. Hahn, H. T. and Morris, D. H.; Anisotropic Photoelasticity with Application to Composites; SESA Spring Meeting, May 1976
36. Pipes, R. Byron, Vinson, Jack R. and Chou, Tsu-Wei; On the Hygrothermal Response of Laminated Composite Systems; Journal of Composite Materials, Vol. 10, April 1976, pp. 129-148.
37. Kim, R. Y. and Hahn, H. T.; Effect of Curing Stresses on the First Ply-Failure in Composite Laminates; Journal of Composite Materials, Vol. 13, January 1979, pp. 2-16.

38. Hyer, M. W.; Some Observations on the Cured Shape of Thin Unsymmetric Laminates; Journal of Composites Materials, Vol. 15, March 1981, pp. 175-194.
39. Hyer, M. W.; Calculations of the Room-Temperature Shapes of Unsymmetric Laminates; Journal of Composite Materials, Vol. 15, July 1981, pp. 296-310.
40. Hyer, M. W.; The Room-Temperature Shapes of Four-Layer Unsymmetric Cross-Ply Laminates; Journal of Composite Materials, Vol. 16, July 1982, pp. 318-340.
41. Hahn, H. Thomas and Hwang, D. G.; Residual Stresses and Their Effects in Composite Laminates; Proceedings of NCKU/AAS International Symposium on Engineering Science and Mechanics, Taiwan, Dec 1981, pp. 1199-1214.
42. Hahn, H. T.; Warping of Unsymmetric Cross-Ply Graphite/Epoxy Laminates; Composite Technology Review, Vol. 3(3), 1981, pp. 114-117.
43. Puppo, A. H. and Evenson, H. A.; Interlaminar Shear in Laminated Composites Under Generalized Plane Strain, Journal of Composite Materials, Vol. 4, April 1970, pp. 204-220.
44. Pipes, R. Byron and Pagano, N. J.; Interlaminar Stresses in Composite Laminates Under Uniform Axial Extension; Journal of Composite Materials, Vol. 4, October 1970, pp. 538-548.
45. Pagano, N. J. and Pipes, R. Byron; The Influence of Stacking Sequence on Laminate Strength; Journal of Composite Materials, Vol. 5, January 1971, pp. 50-57.

46. Foye, R. L. and Baker, D. J.; Design of Orthotropic Laminates; 11th Annual AIAA Structures, Structural Dynamics, and Materials Conference, Denver, Colorado, April 1970.
47. Kaminski, B. E.; On the Determination of the Failure Surface for an Orthotropic Quasi-Homogeneous Material; Master's Thesis, Georgia Institute of Technology, June 1969.
48. Halpin, J. C. and Wu, E. M.; 1971
49. Chen, E. P. and Sih, G.C.; Interfacial Delamination of a Layered Composite Under Anti-Plane Strain; Journal of Composite Materials, Vol. 5, January 1971, pp. 12-23.
50. Isakson, G. and Levy, A.; Finite-Element Analysis of Interlaminar Shear in Fibrous Composites; Journal of Composite Materials, Vol. 5, April 1971, pp. 273-276.
51. Pipes, R. B. and Pagano, N. J.; Interlaminar Stresses in Composite Laminates - An Approximate Elasticity Solution; Journal of Applied Mechanics, September 1974, pp. 668-672.
52. Wang, A. S. D. and Crossman, Frank W.; Edge Effects on Thermally Induced Stresses in Composite Laminates; Journal of Composite Materials, Vol. 11, July 1977, pp. 300-312.
53. Wang, A. S. D. and Crossman, Frank W.; Some New Results on Edge Effects in Symmetric Composite Laminates; Journal of Composite Materials, Vol 2., 1977, p. 92.

54. Titomanlio, G. and Piccarolo; Thermal expansion behaviour of laminated composite - Evaluation of superficial deviation from lamination theory, *Composites*, Vol. 15, No. 1, January 1984, pp. 39-42.
55. Stango, R. J. and Wang, S.S.; Process Induced Thermal Stresses in Advanced Fiber-Reinforced Composite Laminates; *Polymer Processing, Proceedings of Design Conference*, Washington DC, Sept. 11-15, 1987.
56. Jeronimidis, G. and Parkyn, A. T.; Residual Stresses in Carbon Fibre-Thermoplastic Matrix Laminates; *Journal of Composite Materials*, Vol. 22, May 1988, pp. 401-415.
57. Flaggs, D. L. and Kural, M. H.; Experimental Determination of the In Situ Transverse Lamina Strength in Graphite/Epoxy Laminates; *Journal of Composite Materials*, 16: 103 (1982).
58. Nairn, J. A. and Zoller, P.; Residual Stresses in Amorphous and Semicrystalline Thermoplastic Matrix Composites; *ASTM Special Tech. Publ. 937 on Toughened Composites*. Philadelphia: ASTM (1986).
59. Ditcher, A. K., Rhodes, F. E. and Webber, J. P. H.; Non-Linear Stress-Strain Behaviour of Carbon Fibre Reinforced Plastic Laminates; *Journal of Strain Analysis*, Vol. 16, No. 1, 1981, pp. 43-51.
60. Radford, Donald W.; Shape stability in composites; PhD Thesis, Rensselaer Polytechnic Institute, 1987.
61. Tsau, Li-ren; Finite element analysis of composite laminates; PhD Thesis, University of Minnesota, 1987.

62. Dobie, M. J., Leavesley, P. J. and Knight, Jr., C. E.; Residual Strain and Strength Loss in Filament Wound Circular Rings; Final Report, Oct. 13, 1980 - September 30, 1981 for Oak Ridge Y-12 Plant, Virginia Polytechnic Institute and State University, Y/Sub/80-7733/1-01, Aug. 1982.

63. Rohwer, Klaus and Jiu, Xie Ming; Micromechanical Curing Stresses in CFRP; Composites Science and Technology, 25, 1986, pp. 169-186.

64. Gadke, M.; Evaluation of the influence of relative humidity and temperature on the mechanical properties and on failure of multidirectional laminates on the basis of measured single ply characteristic values; Entwicklung und Anwendung von CFK-Strukturen, DGLR-Bericht 84-02 (1984)

65. Adams, Donald F. and Miller, A. Keith; Hygrothermal Microstresses in a Unidirectional Composite Exhibiting Inelastic Material Behaviour; Journal of Composite Materials, Vol. 11, July 1977, pp. 285-299.

66. Richard, R. M. and Blacklock, J. R.; Finite Element Analysis of Inelastic Structures; AIAA Journal, Vol.7 (1969), p. 432.

67. Branca, T. R.; Creep of a Unidirectional Metal Matrix Composite Subjected to Axial and Normal Lateral Loads; TAM Report 341, Dept. of Theoretical and Applied Mechanics, University of Illinois, June 1971.

68. Karlak, R. F. and Crossman, F. W.; Failure Mechanisms in Composite Systems; Lockheed Palo Alto Research Laboratory, Palo Alto, California, Final Report to the U.S. Naval Air Systems Command under contract N00019-74-C-0339, August 1975.

69. Lorz, U.; Cell-area Distributions of Planar Sections of Spatial Voronoi Mosaics; *Materials Characterization*, 25, pp. 297-309 (1990)
70. Guild, F. J., Hogg, P. J. and Davy, P. J.; A Predictive Model for Fibre Reinforced Composites using Finite Element Analysis and Spatical Statistical Techniques.
71. Davy, P. J. and Guild, F. J.; the distribution of interparticle distance and its application in finite-element modelling of composite materials; *Proceedings of The Royal Society of London, A*, 418, pp. 95-112, 1988.
72. Marloff, R. H. and Daniel, I. M.; Three-dimensional Photoelastic Analysis of a Fiber-reinforced Composite Model; *Experimental Mechanics*, April 1969, pp. 156-162.
73. Ishikawa, Takashi and Koyama, Kazuo and Kobayashi, S Higeo; Thermal Expansion Coefficients of Unidirectional Composites, *Journal of Composite Materials*, Vol. 12, April 1978, pp. 153-168.
74. Ishikawa, T., Koyama, K. and Kobayashi, S.; Elastic moduli of Carbon-Epoxy Composites and Carbon Fibres; *Journal of Composite materials*, Vol. 11, 1977, p. 332.
75. PAFEC Data Preparation Manual, Level 2.1; PAFEC Ltd. 1978.
76. PAFEC 75 Theory, Results; PAFEC Ltd. 1975
77. PAFEC User Manual, Level 6.1; Pafec Ltd. 1984.
78. PIGS User Manual, Level 4.1; PAFEC Ltd.

79. Knibbs, R. H. and Morris, J. B.; The effects of fibre orientation on the physical properties of composites; Composites, September 1974.
80. Cook, J.; Journal of Applied Physics Series 2, 1, 1968, p. 799.
81. Fahmy, A. A. and Ragai, A. N.; Journal of Applied Physics , 41, 1970, p.5112.
82. Goggin, P. R.; Journal of Materials Science, 8, No. 2, 1973, p. 233.
83. Uemura, Masuji, Iyama, Hisashi and Yamaguchi, Yoshiko; Thermal Residual Stresses in Filament-Wound Carbon-Fibres-Reinforced Composites; Journal of Thermal Stresses, 2, 1979, pp. 393-412.
84. Marotzke, C. G.; Micromechanical Investigation of Fiber Reinforced Polymers; Mechanical Behaviour of Materials - VI, Proceedings of the Sixth International Conference, Kyoto, Japan, 29 July - 2 August, 1991, Vol. 3, pp. 67-72; Editors, Jono, M. and Inoue, T., 1991.
85. Sato, N. and Kurauchi, T.; Deformation Behaviour of Composite Interphase; Mechanical Behaviour of Materials - VI, Proceedings of the Sixth International Conference, Kyoto, Japan, 29 July - 2 August, 1991, Vol. 3, pp. 73-78; Editors, Jono, M. and Inoue, T., 1991.
86. Morgan, R. J. and Mones, E. T.; Structure-Property Relations of Composite Matrices; Resins for Aerospace; Editor, May, C. A., 1980.
91. Watkins, Howard; A study of the capabilities of a Finite Element Computer Program, when used for the purpose of Heat Transfer Analysis; BSc Report, Sheffield City Polytechnic, 8th May 1981.

92. Stuart, J. P.; The Analysis of Stresses and Strains in Laminate Materials using Finite Element Technique; BEng Report, Sheffield City Polytechnic, April 1988.
93. Rolls-Royce, private communication
94. King, J. E.; Failure in Composite Materials; Metals and Materials, Vol. 5, No. 12, December 1989, pp. 720-726.
95. Zhang, W. and Evans, K. E.; Numerical Prediction of the Mechanical Properties of Composites with Anisotropic Components, using Finite Element Methods; Computer Aided Design in Composite Material Technology, Editors, Brebbia, C. A., de Wilde, W. P. and Blain, W. R.; 1988, pp. 443-457.
96. Chen, C. H. and Cheng, S.; Mechanical Properties of Anisotropic Fiber-Reinforced Composites; Journal of Applied Mechanics, March 1970, pp. 186-189.
97. Whitney, J. M.; Elastic Moduli of Unidirectional Composites with Anisotropic Filaments; Journal of Composite Materials, Vol. 1, 1967, pp. 188-193.
98. Goggin, P. R.; The Elastic Constants of Carbon-Fibre Composites; Journal of Materials Science, 8, 1973, pp. 233-244.
99. Hashin, Z.; Analysis of Properties of Fiber Composites with Anisotropic Constituents; Journal of Applied Mechanics, September 1979, Vol. 46, pp. 543-550.
100. Iremonger, M. J.; Basic Stress Analysis; Butterworth Scientific 1982.

101. Hashin, Zvi; Theory of fiber reinforced materials; NASA CR-1974, University of Pennsylvania, March 1972.
102. Bader, M. G., Bailey, J.E., Curtis, P.T. and Parvizi, A.; The Mechanisms of Initiation and Development of Damage in Multi-Axial Fibre-Reinforced Plastics Laminates; Proceedings of 3rd International Symposium on Mechanical Behaviour of Materials, Cambridge UK, 1979, Vol 3, pp. 227-239.
103. Ehrburger, P. and Donnet, J. B.; Interface in Composite Materials; Phil. Trans. R. Soc. London A, 294 (1980), pp. 495-505.
104. Zahlan, N. and O'Neill, J. M.; Design and Fabrication of Composite Components; The Spring-Forward Phenomenon; Composites, Vol. 20, No. 1, January 1989.

## Summary of Programs Given in the Results

### Macromodelling

0.1 mm section through a 1m long, 5.4 mm thick isotropic laminate. Includes 0.046 mm thick epoxy resin films separating the laminate plies.

#### a) Single Mesh:

MATH - Temperature distribution: cooling of top surface from 190°C to 20°C over 2 hours. Given at the end of cooling,  $t = 7200$  secs.

MASI - Stress distribution: cooling of top surface through 170°C over 2 hours. Given for temperature distribution at 7200 secs.

#### b) Double Mesh:

ASI2 - Stress distribution: uniform cooling through 170°C.

### Initial Micromodelling

Regular fibre Arrays - Hexagonal packing, 3.5 $\mu$ m diameter fibres, % fibre volume fraction, isotropic fibre properties.

ES01 - Radial restraints, plane stress.

ES02 - Total restraints, plane strain.

ES03 - Radial restraints, plane strain.

ES04 - Radial restraints, plane strain, temperature dependent epoxy properties.

Later Micromodelling

Regular Fibre Arrays - Variable fibre packing, fibre diameter, interfibre distance, fibre volume fraction. Anisotropic fibre properties.

D51C	] See Table 2. Program coding for regular fibre arrays.
B03C	
F03B	
C54C	
E54A	
F06A	
C06B	

Random Fibre Arrays: 3.5 $\mu$ m diameter fibres, anisotropic fibre properties.

V001 - Hypothetical Voronoi cell.

V053 - Voronoi cell from 50% fibre volume fraction random fibre array.

Fibre Radius, OX ( $\mu\text{m}$ )	Unit Cell Length, OA ( $\mu\text{m}$ )	Fibre Volume Fraction (%)			
		Co-Ordination Angle ( $^{\circ}$ )			
		15	30	45	60
3.0	3.5	71	66	58	44
3.0	4.5	45	58	35	27
3.0	5.5	30	28	23	18
3.0	6.5	22	19	17	13
3.0	7.5	15	-	-	-
3.5	4.0	75	69	60	46
3.5	5.0	49	45	38	29
3.5	6.0	34	31	27	21
3.5	7.0	26	23	20	15
3.5	8.0	19	-	-	-
4.0	4.5	78	71	62	48
4.0	5.5	52	48	42	32
4.0	6.5	37	35	30	23
4.0	7.5	26	26	22	17
4.0	8.5	22	-	-	-
4.0	9.5	19	-	-	-
4.5	5.0	78	73	64	49
4.5	6.0	56	50	44	34
4.5	7.0	41	38	32	25
4.5	8.0	30	29	25	19
4.5	9.0	26	-	-	-
4.5	10.0	19	-	-	-

Table 1. Calculated fibre volume fractions.

Fibre Radius, OX ( $\mu\text{m}$ )	Unit Cell Length, OA ( $\mu\text{m}$ )	Fibre Volume Fraction (%)			
		Co-Ordination Angle ( $^{\circ}$ )			
		15	30	45	60
5.0	5.5	82	74	65	50
5.0	6.5	56	54	46	36
5.0	7.5	45	40	35	27
5.0	8.5	34	31	27	21
5.0	9.5	26	-	-	-
5.0	10.5	22	-	-	-
5.5	6.0	82	76	66	51
5.5	7.0	60	55	48	38
5.5	8.0	45	43	37	28
5.5	9.0	37	35	29	23
5.5	10.0	30	-	-	-
5.5	11.0	26	-	-	-

Table 1. - continued.

Co- Ordination Angle (°)	Unit Cell Length, XA (μm)	Fibre Radius (μm)					
		3.0	3.5	4.0	4.5	5.0	5.5
30	1.5	A03B	B03B	C03B	D03B	E03B	F03B
	2.5	-	B03C	C03C	D03C	E03C	F03C
	3.5	-	-	-	-	E03D	F03D
45	0.5	A54A	B54A	C54A	D54A	E54A	-
	1.5	A54B	B54B	C54B	D54B	E54B	F54B
	2.5	-	-	C54C	D54C	E54C	F54C
60	0.5	A06A	B06A	C06A	D06A	E06A	F06A
	1.5	-	-	C06B	D06B	E06B	F06B
15	1.5	A51B	B51B	C51B	D51B	E51B	F51B
	2.5	A51C	B51C	C51C	D51C	E51C	F51C
	3.5	A51D	B51D	C51D	D51C	E51D	F51D
	4.5	-	-	C51E	D51E	E51E	F51E
	5.5	-	-	-	-	E51F	F51F

Table 2. Program coding for regular fibre arrays.

Program	Maximum Displacement ( $\mu\text{m}$ )
MASI	20.8
ASI2	20.6
ES01	.0355
ES02	.0201
ES03	.0518
ES04	.0665
D51C	.0531
B03C (B13C)	.0575 (.0569)
F03B	.0463
C54C	.0774
E54A	.0374
C06B	.0900
F06A	.0746
VO01	.106
VO53	.293

B13C - Poisson's Ratio 0.42 compared to 0.15 in the other programs.

Table 3. Maximum displacements.

Program	Stresses in Epoxy Resin (MPa)				Ratio, OX/XA	Fibre Volume Fraction (%)
	Maximum Principal		Von Mises			
	Max. *	Min.	Max.	Min.		
A03B	35 (22.5)	-15.1	52	5.7	2.00	40
B03B	36 (26.3)	-14.1	52	5.3	2.33	45
B03C	32 (26.3)	-17.6	52	6.7	1.40	31
B13C	33 (26.3)	-18.2	53	6.8	1.40	31
C03B	37 (26.3)	-13.2	52	5.0	2.67	48
C03C	33 (26.3)	-16.6	52	6.3	1.60	35
D03B	38 (26.3)	-12.4	53	4.7	3.00	50
D03C	34 (26.3)	-15.8	52	6.0	1.80	38
E03B	39 (26.3)	-11.7	53	4.4	3.33	54
E03C	34 (26.3)	-15.1	52	5.7	2.00	40
E03D	32 (30.0)	-17.4	52	6.6	1.43	31
F03B	39 (26.3)	-11.1	53	4.2	3.67	55
F03C	35 (26.3)	-14.5	52	5.5	2.20	43
F03D	33 (26.3)	-16.8	52	6.4	1.57	35

\* Location of the maximum principal stress at the fibre matrix interface in degrees from the y-axis given in brackets.

Table 4. 30° co-ordination angle/six nearest neighbours - stresses in epoxy resin.

Stresses in Carbon Fibres (MPa)				
Program	Maximum Principal		Von Mises	
	Centre *	Interface	Centre *	Interface
A03B	-3	-15	13	6
B03B	-7	-14	12	5
B03C	-5	-18	14	7
B13C	-5	-18	14	7
C03B	-6	-13	12	5
C03C	-4	-17	13	6
D03B	-5 (-12)	-5	7 (5)	7
D03C	-3	-16	13	6
E03B	-4 (-12)	-9	7 (4)	7
E03C	-3	-15	13	6
E03D	-5	-17	13	7
F03B	-4 (-11)	-9	7 (4)	7
F03C	-7	-15	12	6
F03D	-4	-17	13	6

\* Minimum values away from the centre given in brackets

Table 5. 30° co-ordination angle/six nearest neighbours - stresses in carbon fibre.

Stresses in Epoxy Resin (MPa)						
Program	Maximum Principal		Von Mises		Ratio, OX/XA	Fibre Volume Fraction (%)
	Max. *	Min.	Max.	Min.		
A54A	47 (28.1)	-11.9	71	4.9	6.00	58
A54B	35 (39.4)	-16.5	54	6.3	2.00	35
B54A	47 (30.9)	-11.7	72	4.7	7.00	60
B54B	36 (42.2)	-15.7	55	6.0	2.33	38
C54A	49 (30.9)	-11.5	74	4.6	8.00	62
C54B	37 (42.2)	-15.0	56	5.7	2.67	42
C54C	33 (42.2)	-17.7	54	6.8	1.60	30
D54A	50 (30.9)	-11.3	75	4.5	9.00	64
D54B	38 (42.2)	-14.2	67	5.4	3.00	44
D54C	34 (42.2)	-17.1	54	6.5	1.80	32
E54A	51 (30.9)	-11.3	75	4.4	10.00	65
E54B	39 (42.2)	-13.9	58	5.3	3.33	46
E54C	34 (42.2)	-16.5	54	6.3	2.00	35
F54B	40 (42.2)	-13.5	59	5.2	3.67	48
F54C	35 (42.2)	-16.0	54	6.1	2.20	37

\* Location of the maximum principal stress at the fibre matrix interface in degrees from the y-axis given in brackets.

Table 6. 45° co-ordination angle/four nearest neighbours - stresses in epoxy resin.

Stresses in Carbon Fibres (MPa)				
Program	Maximum Principal		Von Mises	
	Centre *	Interface	Centre *	Interface
A54A	-3 (-12)	3	8 (5)	22
A54B	-4 (-17)	-9	14 (6)	9
B54A	-3 (-12)	3	8 (5)	28
B54B	-3 (-16)	-8	13 (6)	8
C54A	-3 (-12)	4	8 (4)	36
C54B	-2 (-15)	-7	13 (6)	13
C54C	-5 (-18)	-10	14 (7)	9
D54A	-2 (-11)	10	8 (5)	43
D54B	-7 (-14)	-7	8 (5)	13
D54C	-4 (-17)	-9	14 (7)	9
E54A	-2 (-11)	10	8 (4)	44
E54B	-5 (-14)	-5	8 (5)	19
E54C	-4 (-17)	-9	14 (6)	9
E54D	-5 (-14)	-5	8 (5)	19
F54C	-3 (-16)	-8	13 (6)	9

\* Minimum values away from the centre given in brackets

Table 7. 45° co-ordination angle/four nearest neighbours - stresses in carbon fibre.

Stresses in Epoxy Resin (MPa)						
Program	Maximum Principal		Von Mises		Ratio, OX/XA	Fibre Volume Fraction (%)
	Max. *	Min.	Max.	Min.		
A06A	45 (37.5)	-15.2	84	7.4	6.00	44
B06A	47 (33.8)	-15.3	84	7.5	7.00	46
C06A	49 (33.8)	-15.5	86	7.6	8.00	48
C06B	36 (41.3)	-17.0	64	7.4	2.67	32
D06A	49 (37.5)	-15.6	87	7.8	9.00	49
F06A	51 (33.8)	-15.8	87	8.0	11.00	51
D06B	37 (41.3)	-17.0	64	7.4	3.00	34
E06A	50 (33.8)	-15.7	87	7.9	10.00	50
E06B	38 (41.3)	-16.8	67	7.4	3.33	36
F06A	51 (33.8)	-15.8	87	8.0	11.00	51
F06B	39 (41.3)	-16.7	70	7.4	3.67	38

\* Location of the maximum principal stress at the fibre matrix interface in degrees from the y-axis given in brackets.

Table 8. 60° co-ordination angle/three nearest neighbours - stresses in epoxy resin.

Program	Stresses in Carbon Fibres (MPa)			
	Maximum Principal		Von Mises	
	Centre *	Interface	Centre *	Interface
A06A	-8 (-15)	1	11 (7)	34
B06A	-6 (-15)	7	11 (8)	58
C06A	-6 (-16)	7	12 (8)	59
C06B	-9 (-17)	-9	10 (7)	21
D06A	-6 (-16)	7	12 (8)	60
D06B	-9 (-17)	-3	10 (7)	28
E06A	-6 (-16)	8	12 (8)	68
E06B	-9 (-17)	-3	10 (7)	29
F06A	-6 (-16)	8	12 (8)	68
F06B	-8 (-17)	-3	11 (7)	36

\* Minimum values away from the centre given in brackets

Table 9. 60° co-ordination angle/three nearest neighbours - stresses in carbon fibre.

Stresses in Epoxy Resin (MPa)						
Prog.	Maximum Principal		Von Mises		Ratio, OX/XA	Fibre Volume Fraction (%)
	Max. *	Min.	Max.	Min.		
A51B	35 (0.0)	-14.3	51	5.4	2.00	45
A51C	32 (0.0)	-18.0	51	6.8	1.20	30
A51D	30.1 (7.5)	-20.2	52	7.7	0.86	22
B51B	36 (11.3)	-13.2	51	5.0	2.33	49
B51C	32 (3.8)	-17.0	51	6.4	1.40	34
B51D	30.8 (3.8)	-19.2	52	7.3	1.00	26
C51C	33 (3.8)	-16.0	51	6.1	1.60	52
C51D	31.5 (3.8)	-18.4	51	7.0	1.14	37
C51E	30 (3.8)	-20.0	52	7.6	0.89	26
D51C	34 (11.3)	-15.1	51	5.7	1.80	41
D51D	32 (3.8)	-17.6	51	6.7	1.29	30
D51E	30.6 (3.8)	-19.2	52	7.3	1.00	26
E51C	35 (11.3)	-14.3	51	5.4	2.00	56
E51D	32 (3.8)	-16.8	51	6.4	1.43	45
E51E	31.2 (3.8)	-18.6	52	7.0	1.11	34
E51F	30.0 (3.8)	-19.8	52	7.5	0.91	26
F51C	35 (11.3)	-13.6	51	5.2	2.20	60
F51D	33 (11.3)	-16.1	51	6.1	1.57	45
F51E	31 (11.3)	-17.9	52	6.8	1.22	37
F51F	30.5 (11.3)	-19.2	52	7.3	1.00	30

\* Location of the maximum principal stress at the fibre matrix interface in degrees from the y-axis given in brackets.

Table 10. 15° co-ordination angle/twelve nearest neighbours - stresses in epoxy resin.

Stresses in Carbon Fibres (MPa)				
Program	Maximum Principal		Von Mises	
	Centre *	Interface	Centre *	Interface
A15B	-2	-14	12	5
A51C	-6	-18	14	7
A13D	-8	-20	14	8
B51B	-6	-13	12	5
B51C	-5	-17	13	6
B51D	-7	-19	14	7
C51C	-4	-16	13	6
C51D	-6	-18	14	7
C51E	-8	-20	14	8
D51C	-3	-15	13	6
D51D	-5	-18	13	7
D51E	-7	-19	14	7
E51C	-2	-14	12	5
E51D	-4	-17	13	6
E51E	-6	-19	14	7
E51F	-7	-20	14	8
F51C	-6	-14	12	5
F51D	-4	-16	13	6
F51E	-6	-18	14	7
F51F	-7	-19	14	7

\* Minimum values away from the centre given in brackets

Table 11. 15° co-ordination angle/twelve nearest neighbours - stresses in carbon fibre.

Stress in Epoxy Resin (MPa)							
		Maximum Principal		Von Mises		Ratio,	Fibre Volume
Program	Max.	Min.	Max.	Min.	OX/XA	Fraction (%)	
V001	68	-17.6	59	2.55	7	27	
V053 *	49-83	-13.3	41-67	1.96	40	65	

\* Maximum values of 320 MPa for the maximum principal stress and of 261 MPa for the von Mises stress are not included. These occurred at angularities in the modelled fibre surface and were thought unrealistic.

Table 12. Random fibre arrays, Voronoi cells - stresses in epoxy resin

Stresses in Carbon Fibres (MPa)					
		Maximum Principal		Von Mises	
Program	Maximum	Minimum	Maximum	Minimum	
V001	21	-18	17	2.5	
V053	4	-13	4	2	

Table 13. Random fibre arrays, Voronoi cells - stresses in carbon fibre.

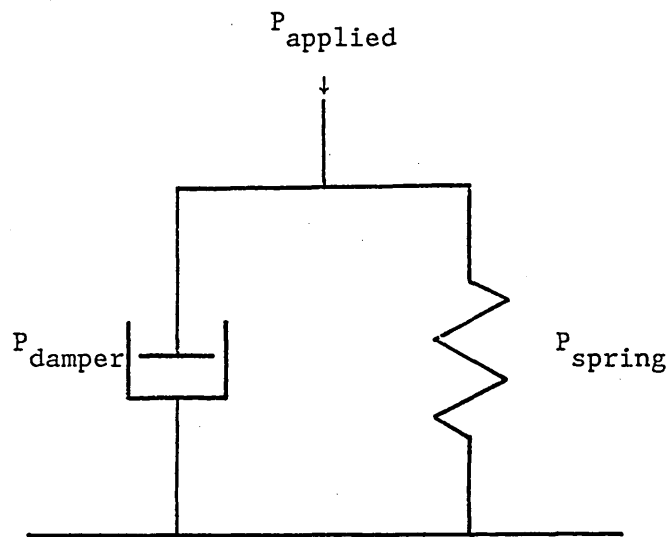


Figure 1. Kelvin or Voigt unit.

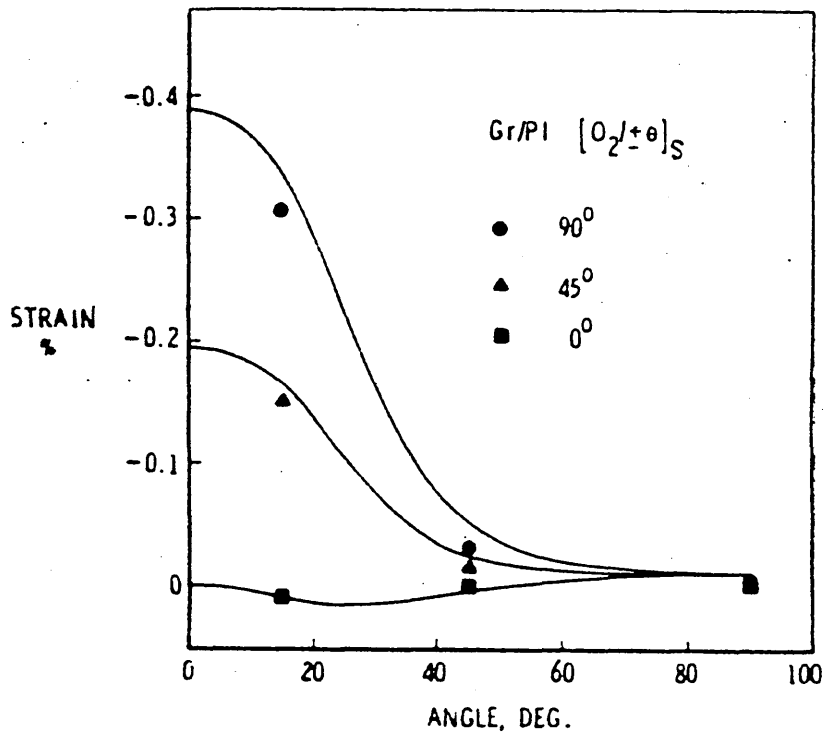


Figure 2, a) Curing strains of  $[0_2/\pm\theta]_S$  graphite/plastic laminates.

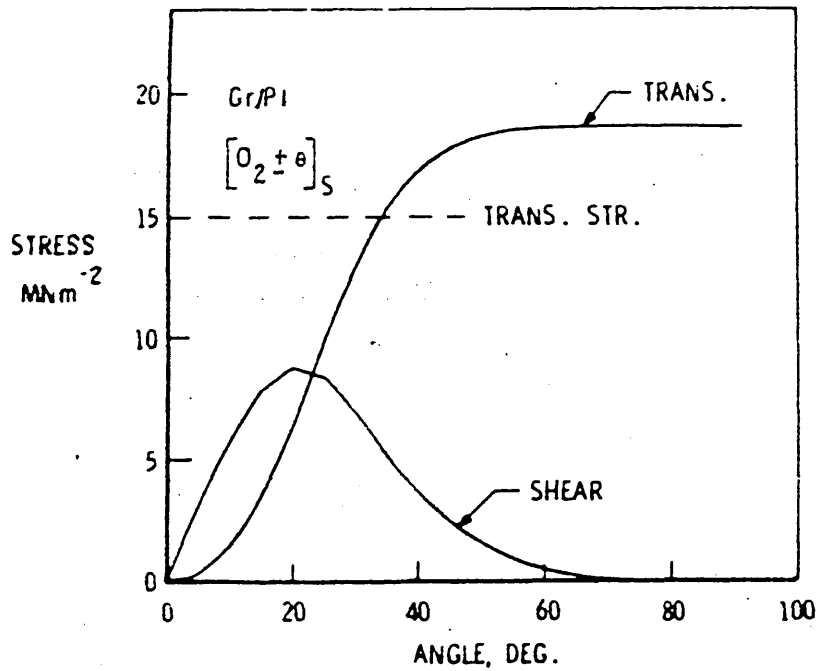


Figure 2, b) Curing stresses in  $0^\circ$  plies of  $[0_2/\pm\theta]_S$  graphite/plastic laminates.

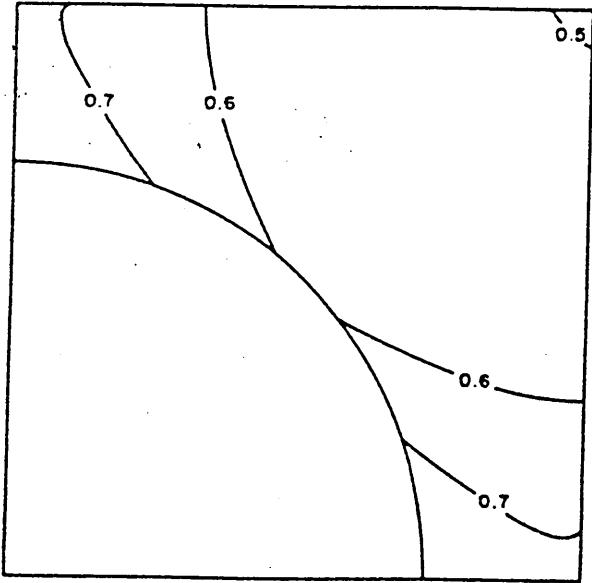


Figure 3. Residual octahedral shear stress state

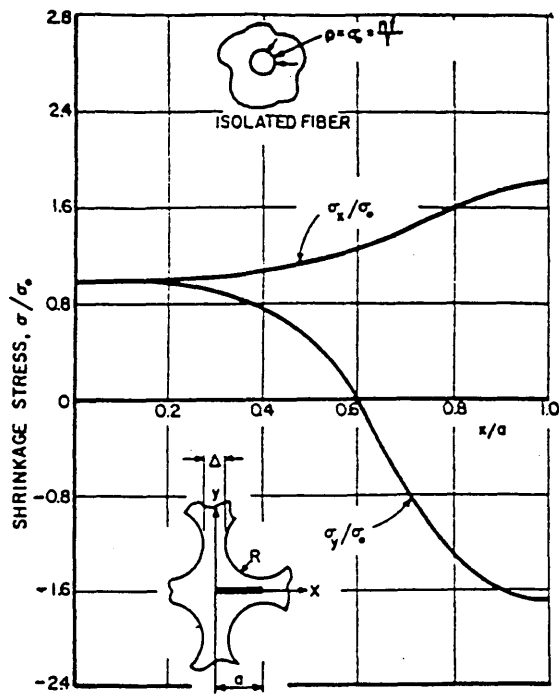


Figure 4, a) Distribution of shrinkage stresses along ligament centre line,  $\Delta/R = 0.5$ .

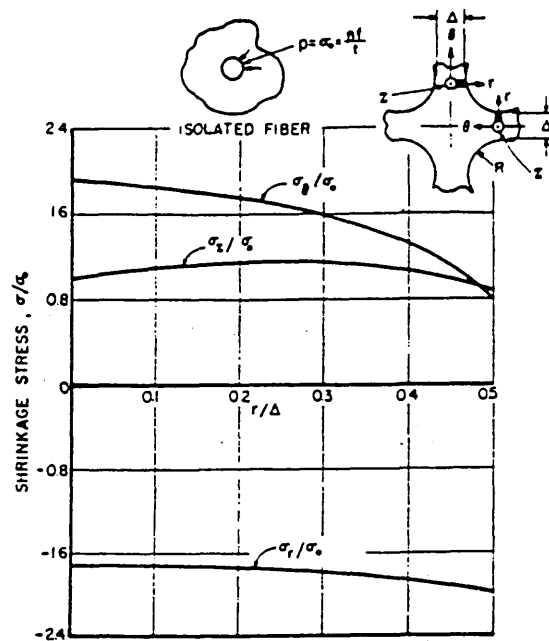


Figure 4, b) Distribution of shrinkage stresses across section between fibres,  $\Delta/R = 0.5$

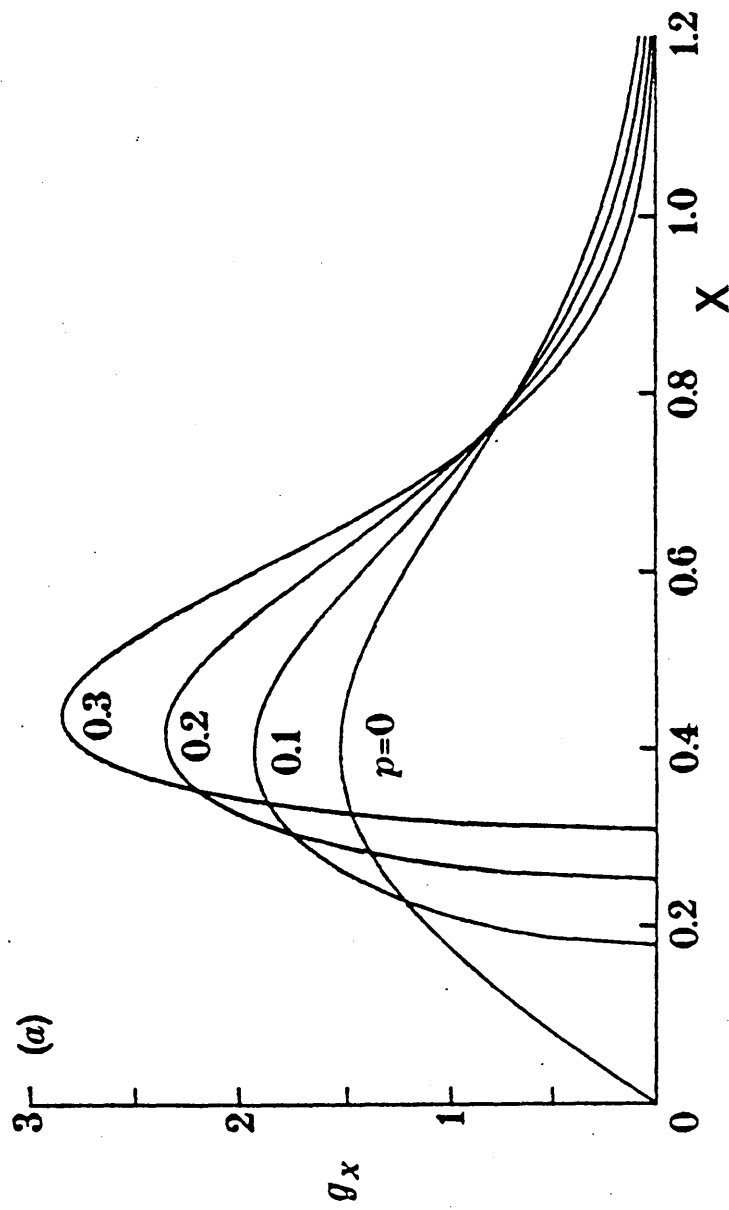


Figure 5. Probability density function,  $g(x)$  in two dimensions of half-interparticle distance,  $x$ , for intensity

$\lambda = 1$  and volume fraction  $p$  ranging from 0 to 0.3

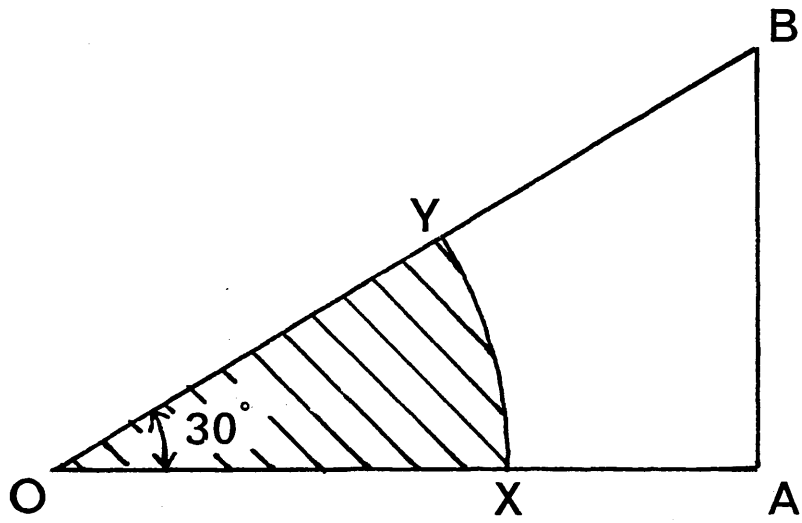
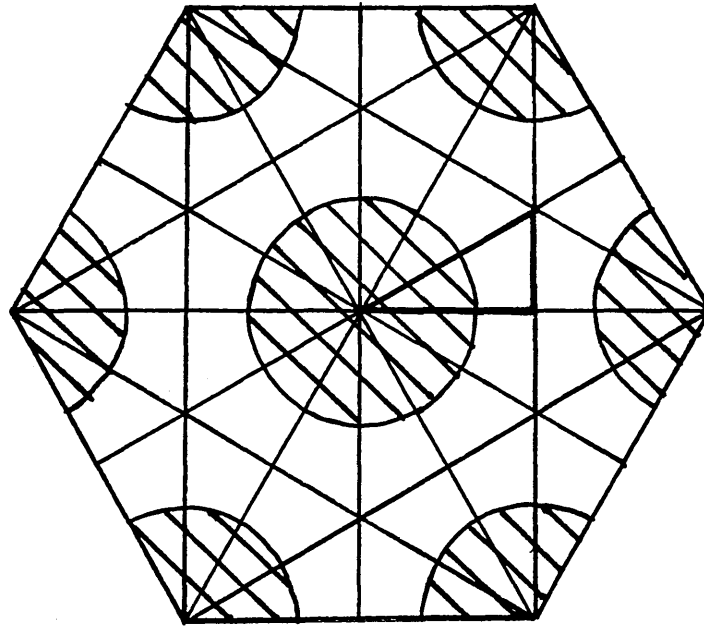


Figure 6. Regular hexagonal array and corresponding representative unit cell

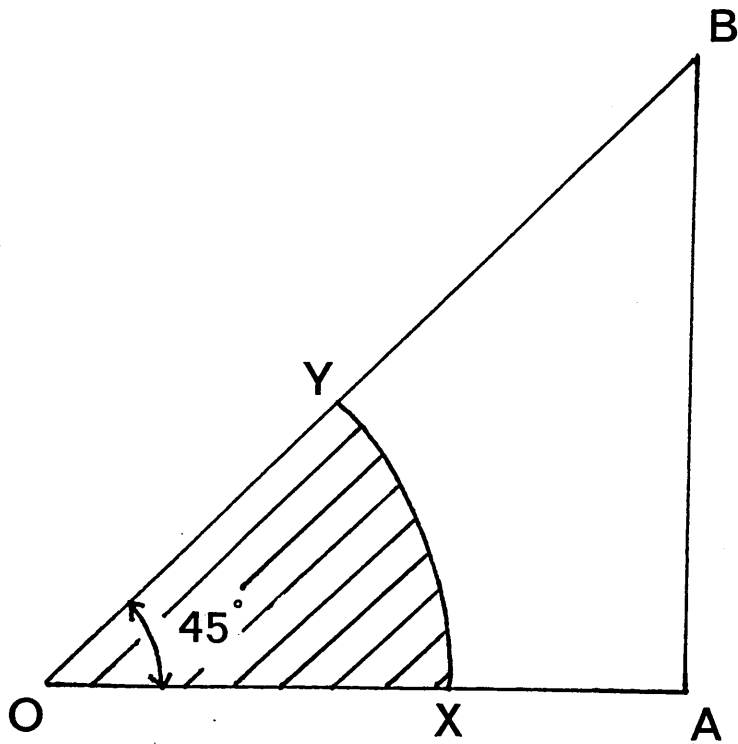
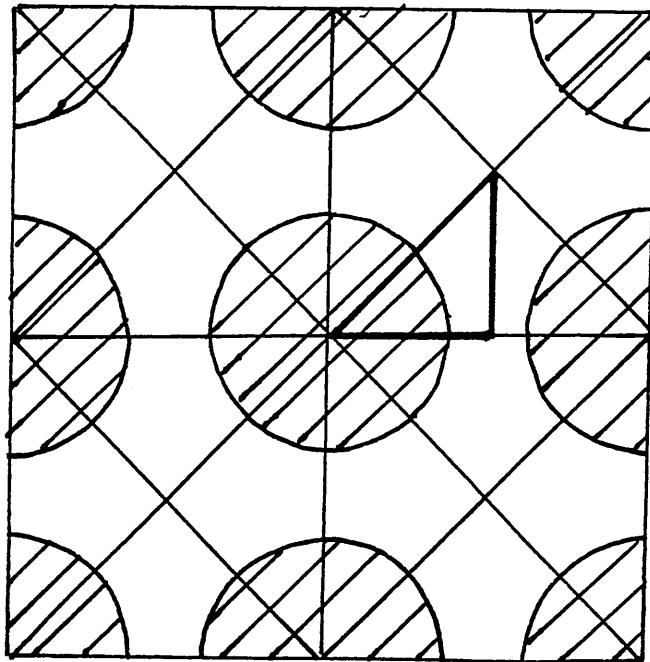


Figure 7. Regular square array and corresponding representative unit cell

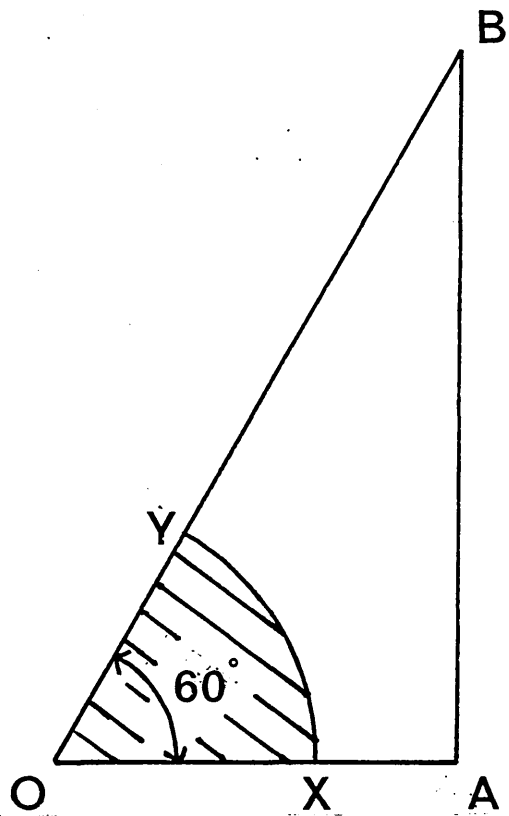
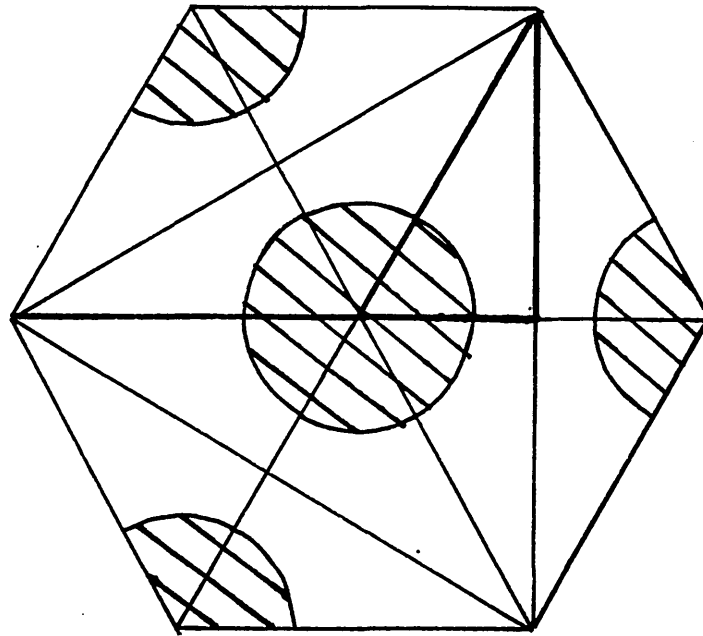


Figure 8. Regular array for fibre having three nearest neighbours and corresponding representative unit cell

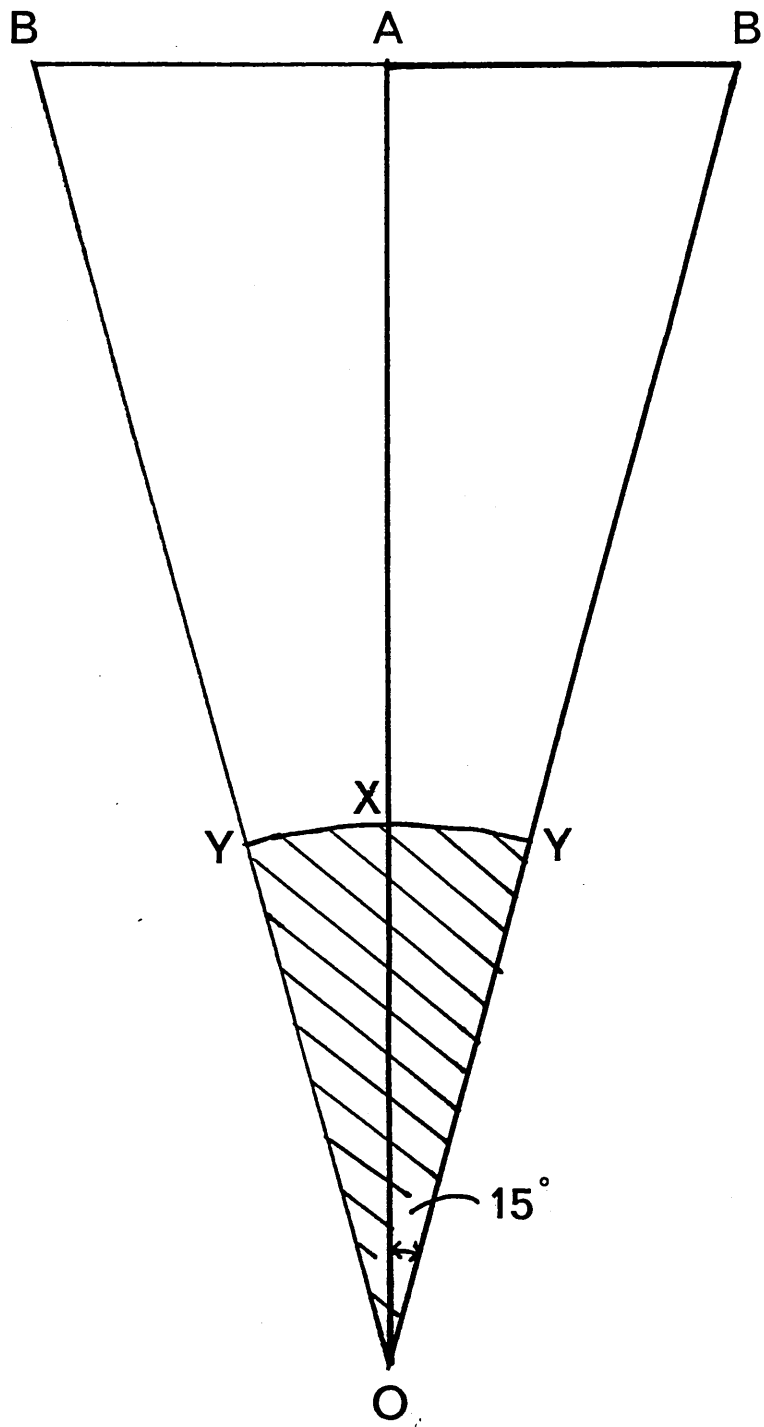


Figure 9. Representative unit cell for fibre having twelve nearest neighbours

Figure 10. Temperature distribution: cooling of the top surface from 190°C to 20°C over 2 hours. Given at the end of cooling, time  $t = 7200$  seconds - model MATH (single mesh)  
(original in colour)

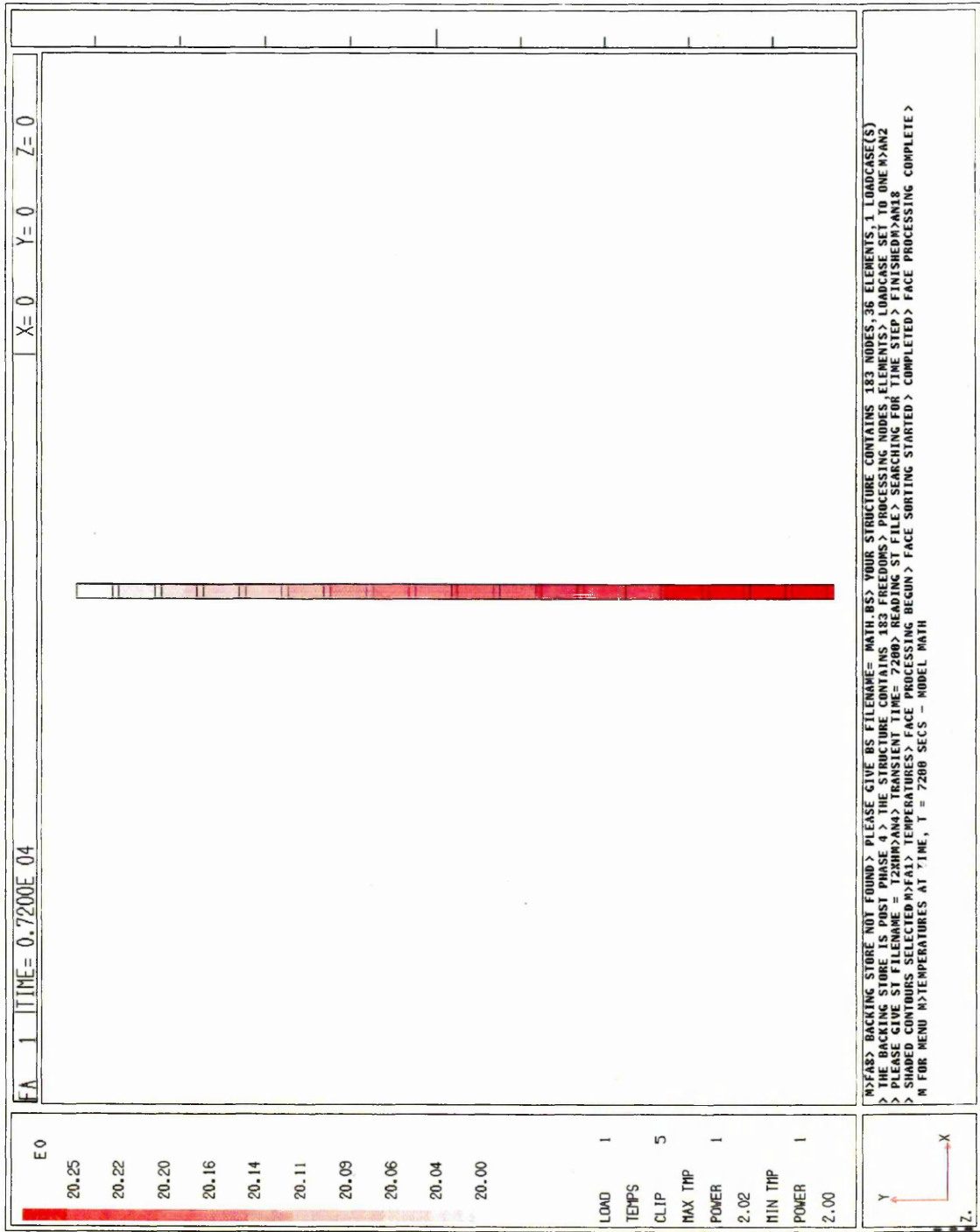
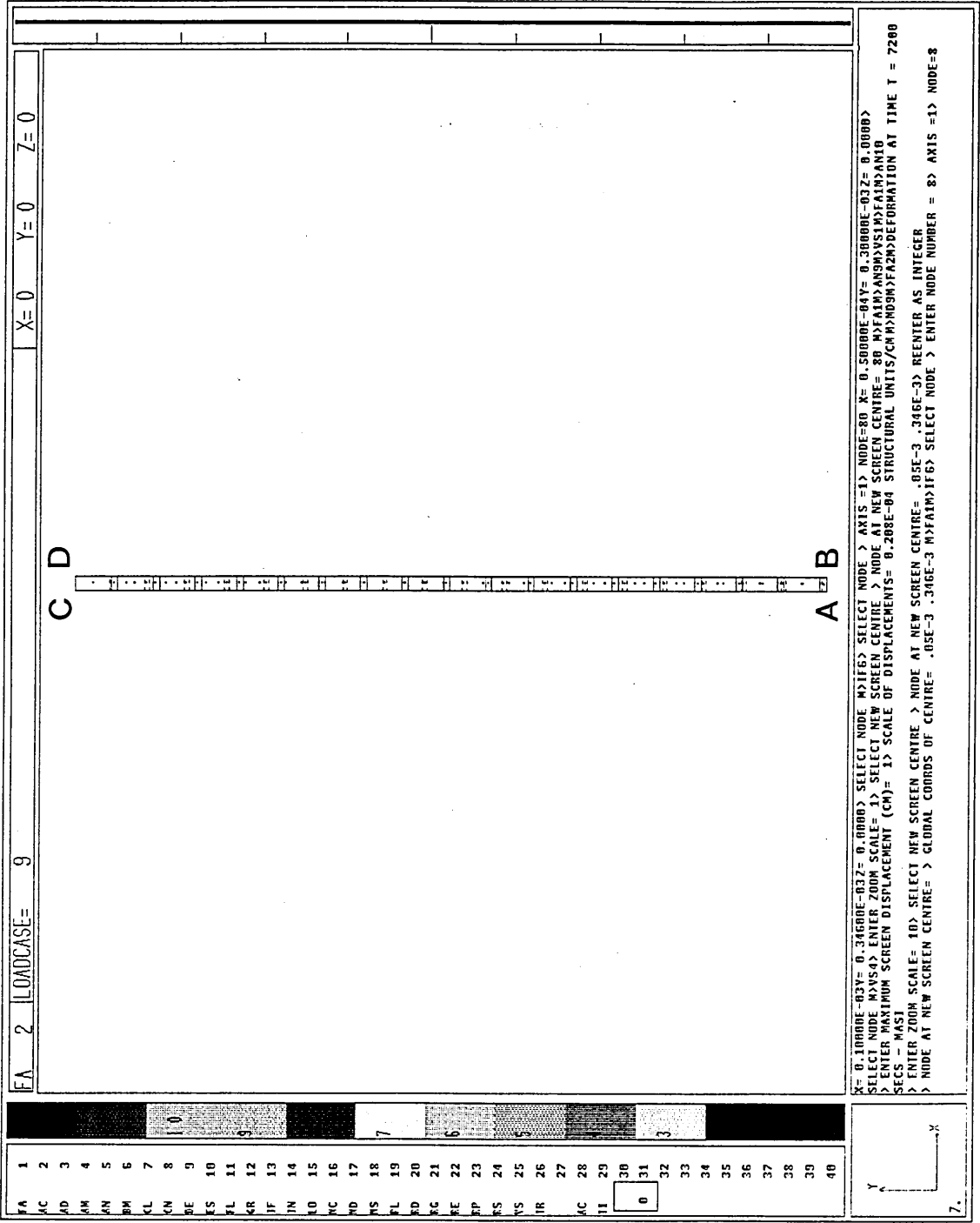


Figure 11. Deformation: cooling of the top surface through 170°C over 2 hours. Given at the end of cooling, time  $t = 7200$  seconds - model MASI (single mesh)



FA 2 LOADCASE= 9

FA	1	2	3	4	5	6	7	8	9	10	11	12	13	14	15	16	17	18	19	20	21	22	23	24	25	26	27	28	29	30	31	32	33	34	35	36	37	38	39	40
----	---	---	---	---	---	---	---	---	---	----	----	----	----	----	----	----	----	----	----	----	----	----	----	----	----	----	----	----	----	----	----	----	----	----	----	----	----	----	----	----

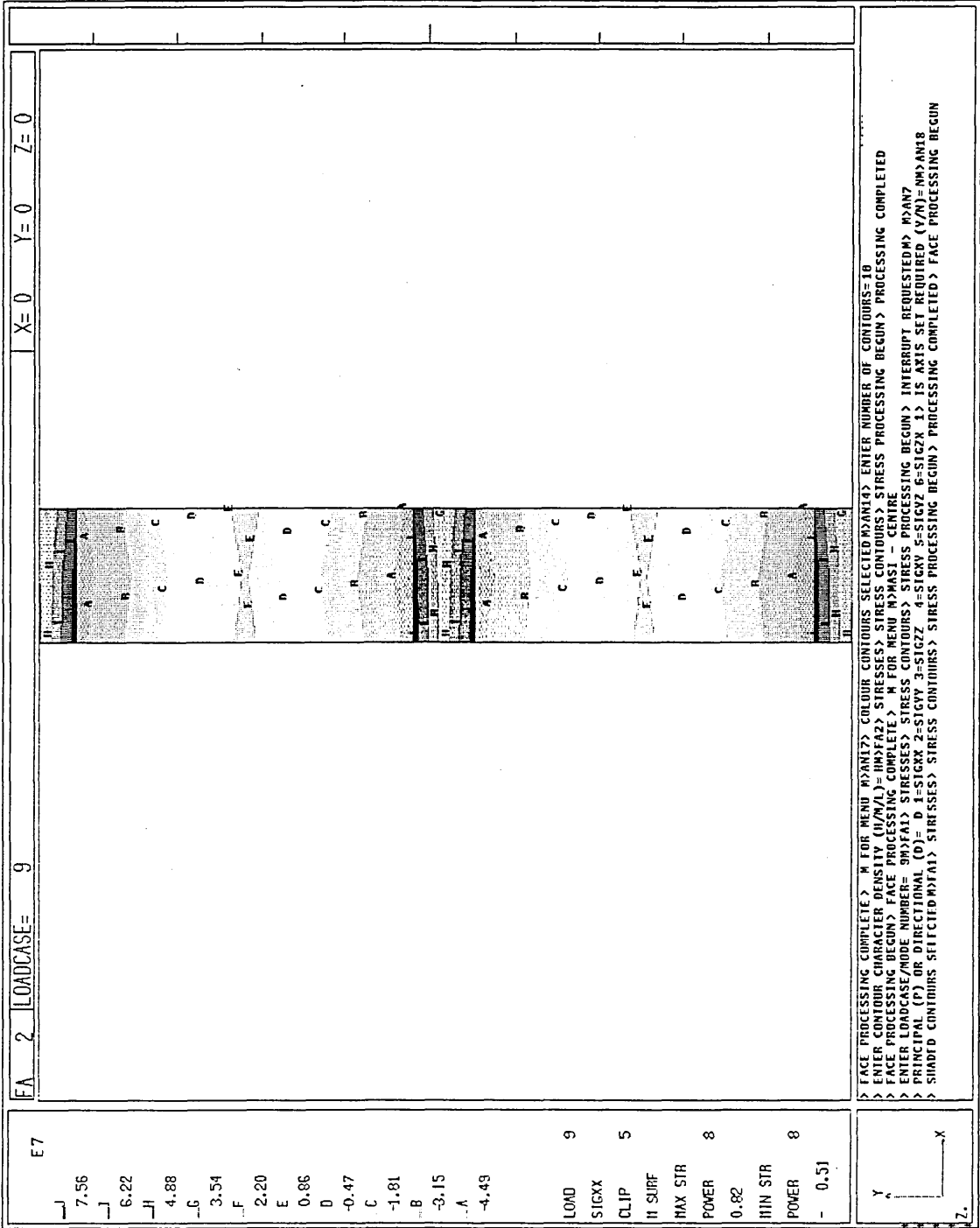
X= 0.1000E-03 Y= 0.34600E-03 Z= 0.0000E-00 X= 0.50000E-04 Y= 0.30000E-03 Z= 0.0000E-00  
 SELECT NODE M>S4> ENTER ZOOM SCALE= 10> SELECT NEW SCREEN CENTRE > NODE AT NEW SCREEN CENTRE = 80 M>FA1M>ANSW>S1M>FA1M>A10  
 > ENTER MAXIMUM SCREEN DISPLACEMENT (CM)= 1> SCALE OF DISPLACEMENTS= 0.208E-04 STRUCTURAL UNITS/CM>M>NO0M>FA2M>DEFORMATION AT TIME T = 7200  
 SECS - MASI  
 > ENTER ZOOM SCALE= 10> SELECT NEW SCREEN CENTRE > NODE AT NEW SCREEN CENTRE = .05E-3 .346E-3 REENTER AS INTEGER  
 > NODE AT NEW SCREEN CENTRE=> GLOBAL COORDS OF CENTRE= .05E-3 .346E-3 M>FA1M>IF6> SELECT NODE > ENTER NODE NUMBER = 8> AXIS =1> NODE=8



Figure 12. Mesh, centre elements - model MASI (single mesh,  $t = 7200$   
seconds)

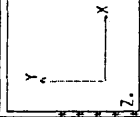


Figure 13.  $\sigma_{xx}$  stress, centre - model MASI (single mesh,  $t = 7200$   
seconds)



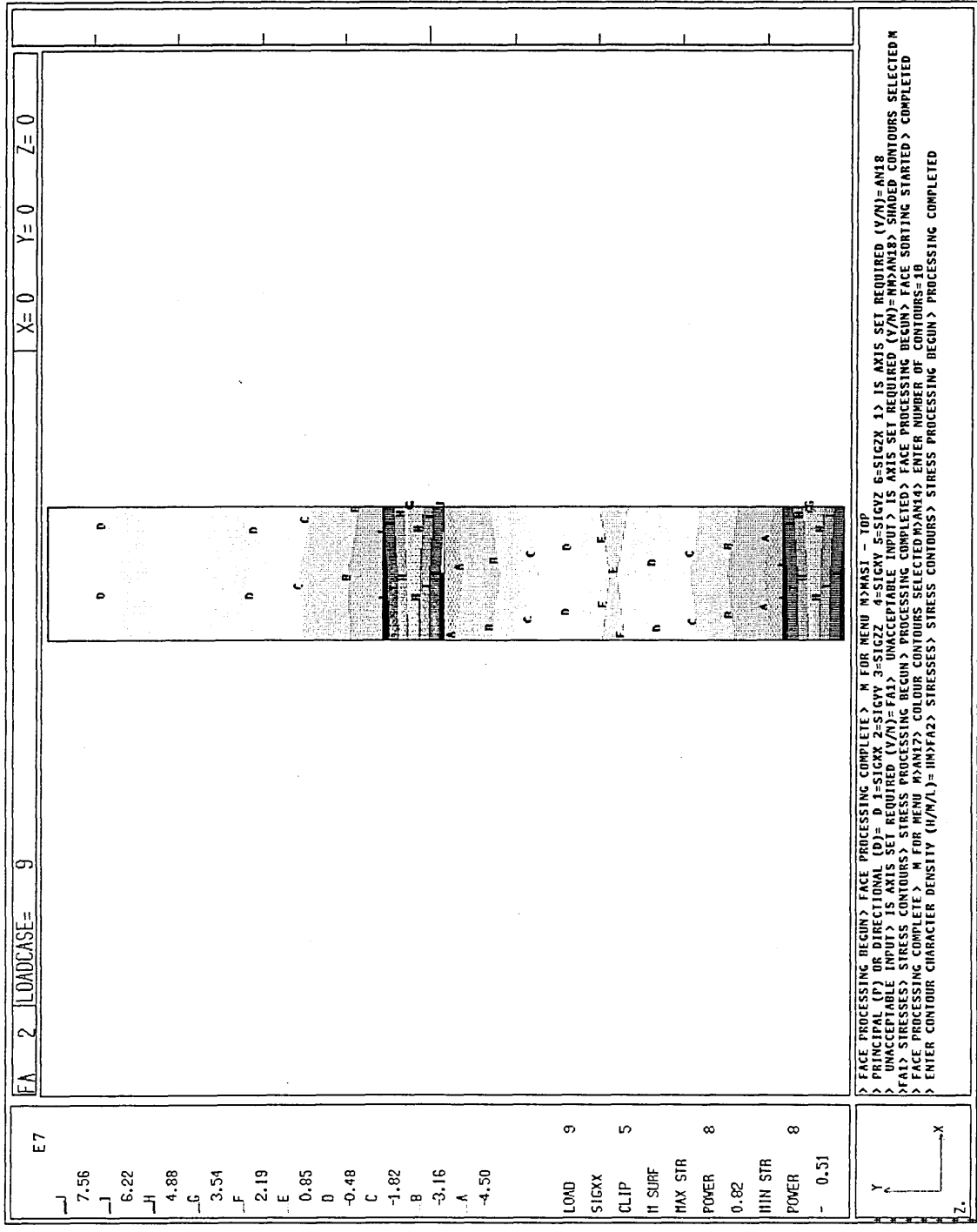
FA 2 LOADCASE= 9 X=0 Y=0 Z=0

E7  
 J 7.56  
 J 6.22  
 H 4.88  
 G 3.54  
 F 2.20  
 E 0.86  
 D -0.47  
 C -1.81  
 B -3.15  
 A -4.49  
 LOND 9  
 SIGXX 5  
 CLIP  
 II SURF  
 MAX STR 8  
 POWER 0.82  
 IIN STR 8  
 POWER - 0.51



> FACE PROCESSING COMPLETE > M FOR MENU M>ANI7 > COLOUR CONTOURS SELECTED M>ANI4 > ENTER NUMBER OF CONTOURS= 10  
 > ENTER CONTOUR CHARACTER DENSITY (H/M/L)= HM>FA2 > STRESSES > STRESS CONTOURS > STRESS PROCESSING BEGUN > PROCESSING COMPLETED  
 > FACE PROCESSING BEGUN > FACE PROCESSING COMPLETE > M FOR MENU M>ASI - CENTRE  
 > ENTER LOADCASE/MODE NUMBER= 9H>FA1 > STRESSES > STRESS CONTOURS > STRESS PROCESSING BEGUN > INTERRUPT REQUESTED M>AN7  
 > PRINCIPAL (P) OR DIRECTIONAL (D)= D I=SIGXX 2=SIGYY 3=SIGZZ 4=SIGXY 5=SIGYZ 6=SIGZX 1> IS AXIS SET REQUIRED (Y/N)= NM>ANI8  
 > SHADED CONTOURS SELECTED M>FA1 > STRESSES > STRESS CONTOURS > STRESS PROCESSING BEGUN > PROCESSING COMPLETED > FACE PROCESSING BEGUN

Figure 14.  $\sigma_{xx}$  stress, top - model MASI (single mesh, t = 7200  
seconds)



EA 2 LOADCASE= 9 X=0 Y=0 Z=0

E7  
 7.56  
 6.22  
 4.88  
 3.54  
 2.19  
 0.85  
 0  
 -0.48  
 -1.82  
 -3.16  
 -4.50  
 LOAD 9  
 SIGXX 5  
 CLIP 5  
 H SURF 8  
 MAX STR 8  
 POWER 0.82  
 MIN STR 8  
 POWER - 0.51

> FACE PROCESSING BEGUN > FACE PROCESSING COMPLETE > M FOR MENU > MASI - TOP  
 > PRINCIPAL (P) OR DIRECTIONAL (D) = D 1=SIGXX 2=SIGYY 3=SIGZZ 4=SIGVY 5=SIGVZ 6=SICZX 1> IS AXIS SET REQUIRED (Y/N)=AN18  
 > UNACCEPTABLE INPUT > IS AXIS SET REQUIRED (Y/N)=FA1> UNACCEPTABLE INPUT > IS AXIS SET REQUIRED (Y/N)=NM>AN18> SHADED CONTOURS SELECTED M  
 > FACE PROCESSING BEGUN > STRESS CONTOURS> STRESS PROCESSING BEGUN > FACE PROCESSING BEGUN > FACE SORTING STARTED > COMPLETED  
 > FACE PROCESSING COMPLETE > M FOR MENU > AN17> COLOUR CONTOURS SELECTED M>AN14> ENTER NUMBER OF CONTOURS=18  
 > ENTER CONTOUR CHARACTER DENSITY (H/N/L)= IM>FA2> STRESSES> STRESS CONTOURS> STRESS PROCESSING BEGUN > PROCESSING COMPLETED

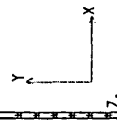


Figure 15.  $\sigma_{xx}$  stress, bottom - model MASI (single mesh,  $t = 7200$  seconds)

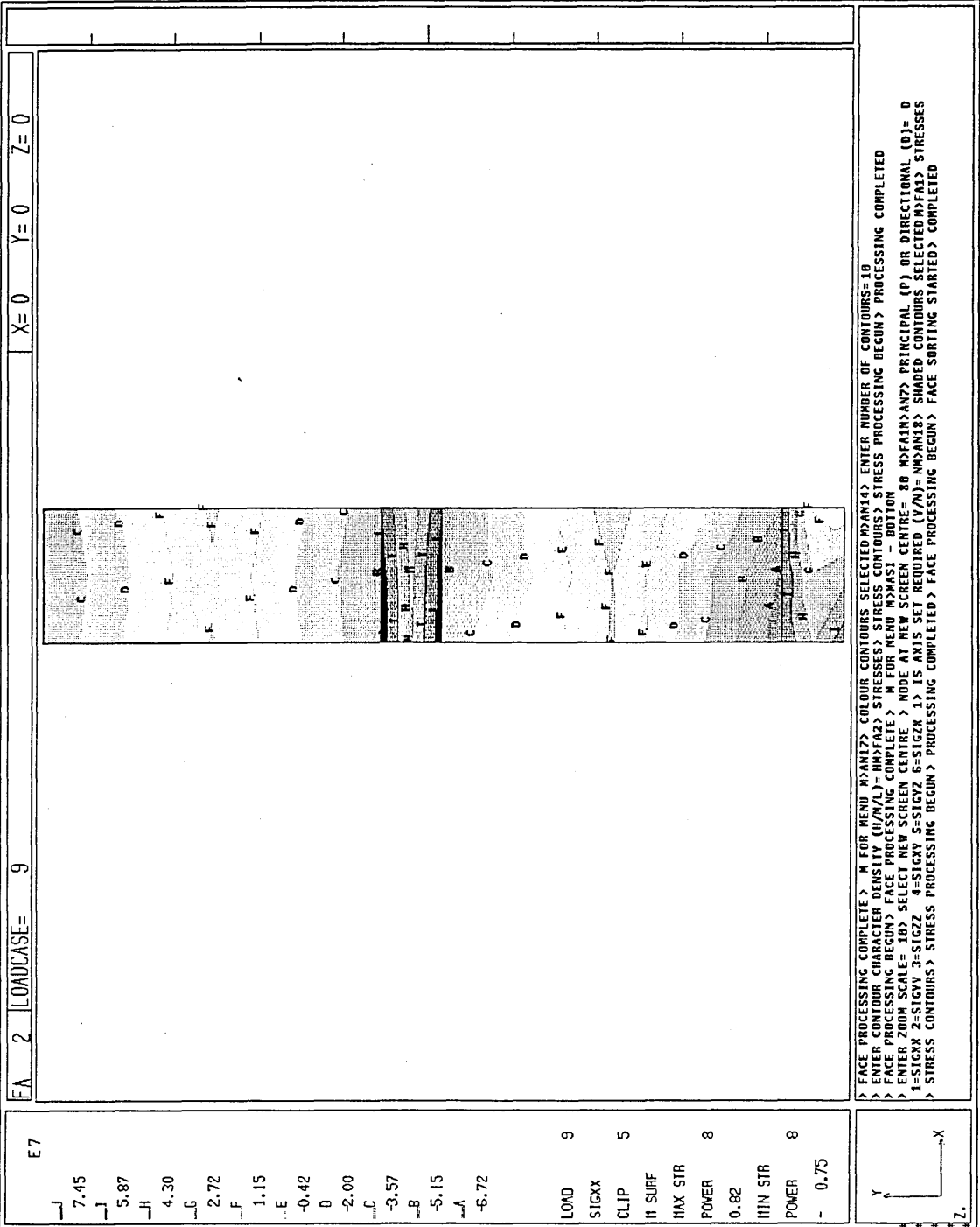
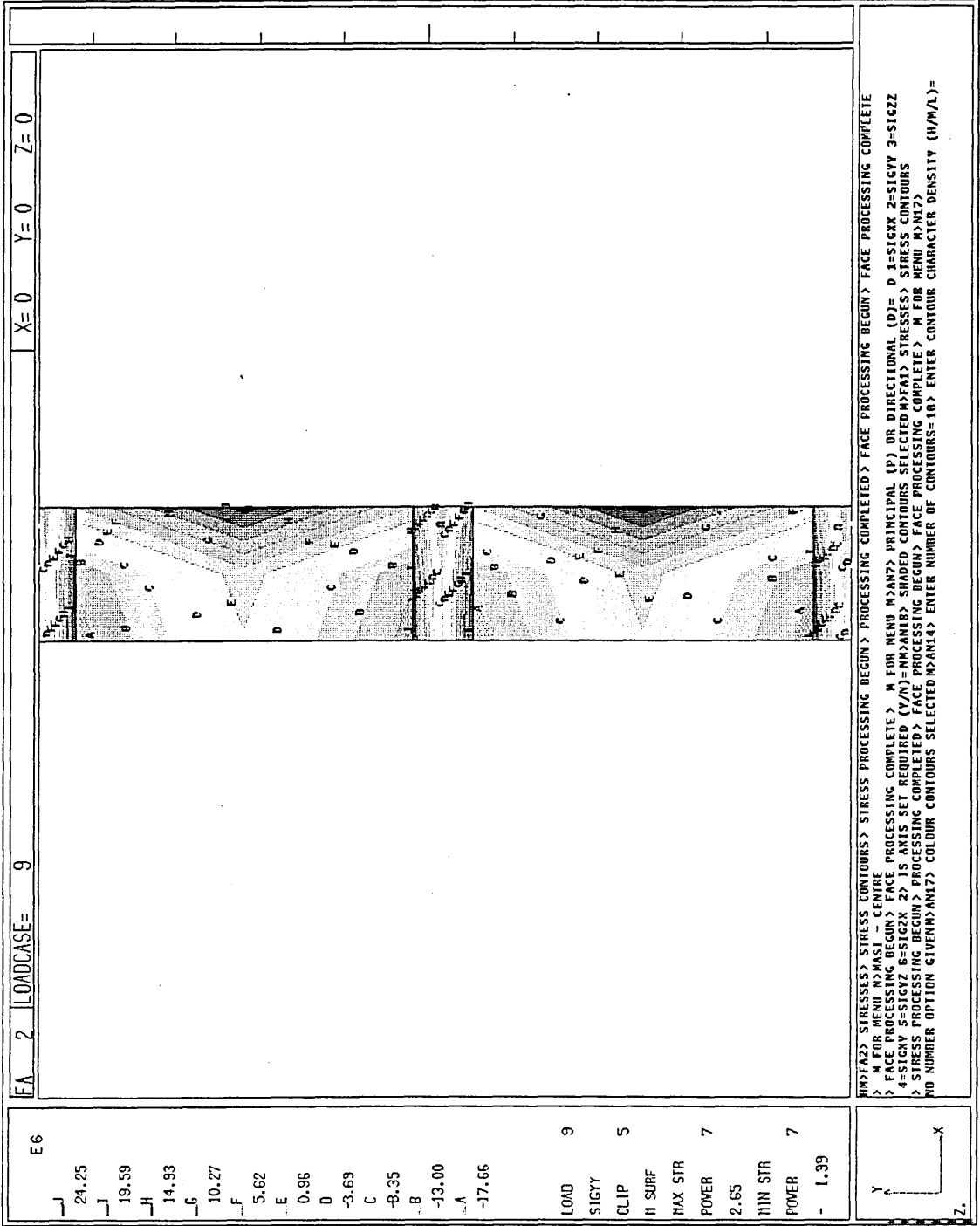


Figure 16.  $\sigma_{yy}$  stress, centre - model MASI (single mesh, t = 7200 seconds)

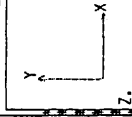


EA 2 LOADCASE= 9 X=0 Y=0 Z=0

E6

- J 24.25
- I 19.59
- H 14.93
- G 10.27
- F 5.62
- E 0.96
- D -3.69
- C -8.35
- B -13.00
- A -17.66

- LOAD 9
- SIGY 5
- CLIP 5
- H SURF
- MAX STR
- POWER 7
- 2.65
- MIN STR
- POWER 7
- 1.99



HM>FA2> STRESSES> STRESS CONTOURS> STRESS PROCESSING BEGUN > PROCESSING COMPLETED > FACE PROCESSING BEGUN > FACE PROCESSING COMPLETE  
 > M FOR MENU M>MAST - CENTRE  
 > FACE PROCESSING BEGUN > FACE PROCESSING COMPLETE > M FOR MENU M>AN7> PRINCIPAL (P) OR DIRECTIONAL (D)= D 1=SIGMX 2=SIGY 3=SIGZ  
 4=SIGX 5=SIGZ 6=SIGZ 2> IS AXIS SET REQUIRED (Y/N)=M>AN18> SHADED CONTOURS SELECTED M>FA1> STRESSES > STRESS CONTOURS  
 > STRESS PROCESSING BEGUN > PROCESSING COMPLETED > FACE PROCESSING BEGUN > FACE PROCESSING COMPLETE > M FOR MENU M>MI7>  
 NO NUMBER OPTION GIVEN M>AN14> COLOUR CONTOURS SELECTED M>AN14> ENTER NUMBER OF CONTOURS= 10 > ENTER CONTOUR CHARACTER DENSITY (H/M/A.)=

Figure 17.  $\sigma_{yy}$  stress, top - model MASI (single mesh,  $t = 7200$   
seconds)

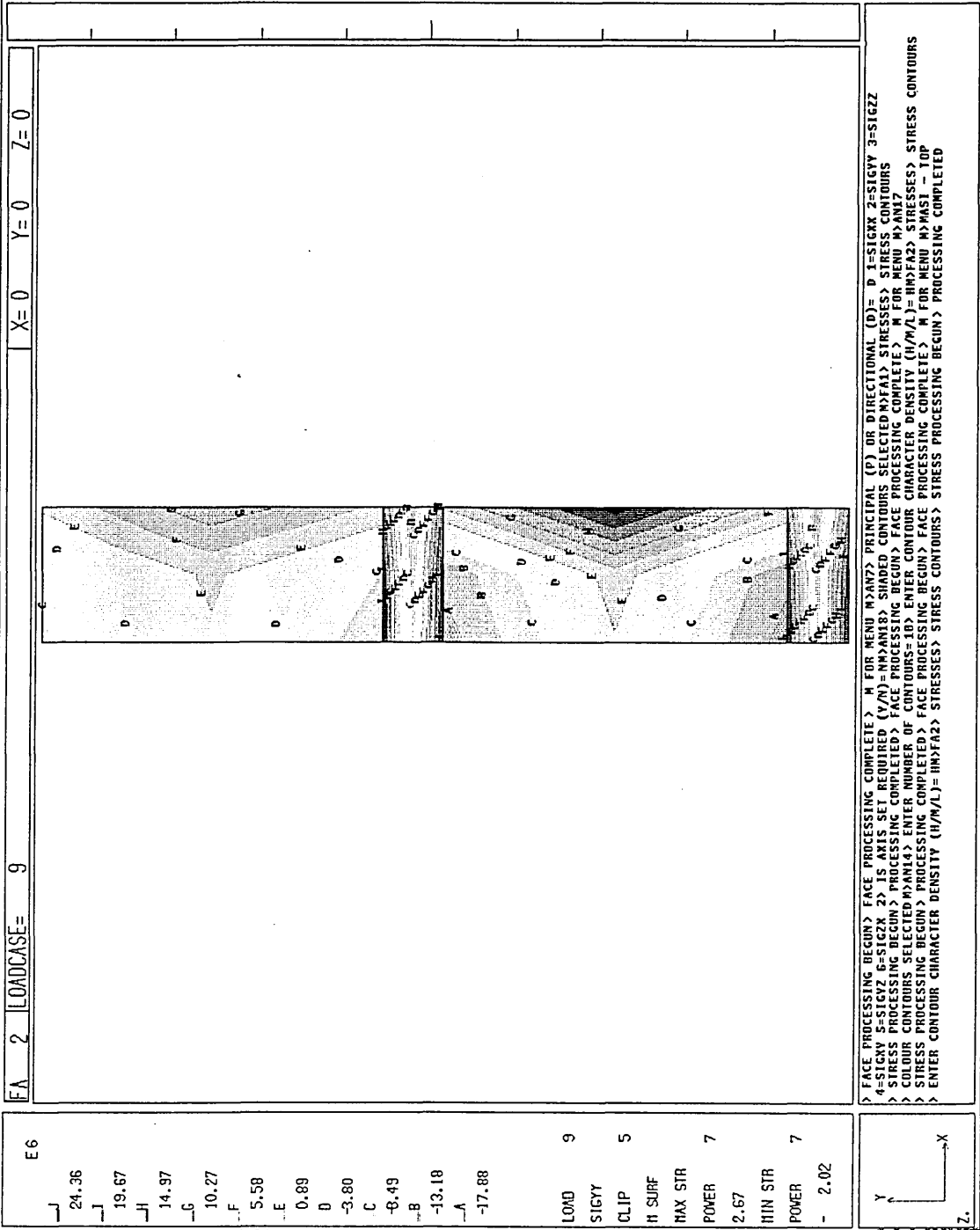


Figure 18.  $\sigma_{yy}$  stress, bottom - model MASI (single mesh,  $t = 7200$  seconds)

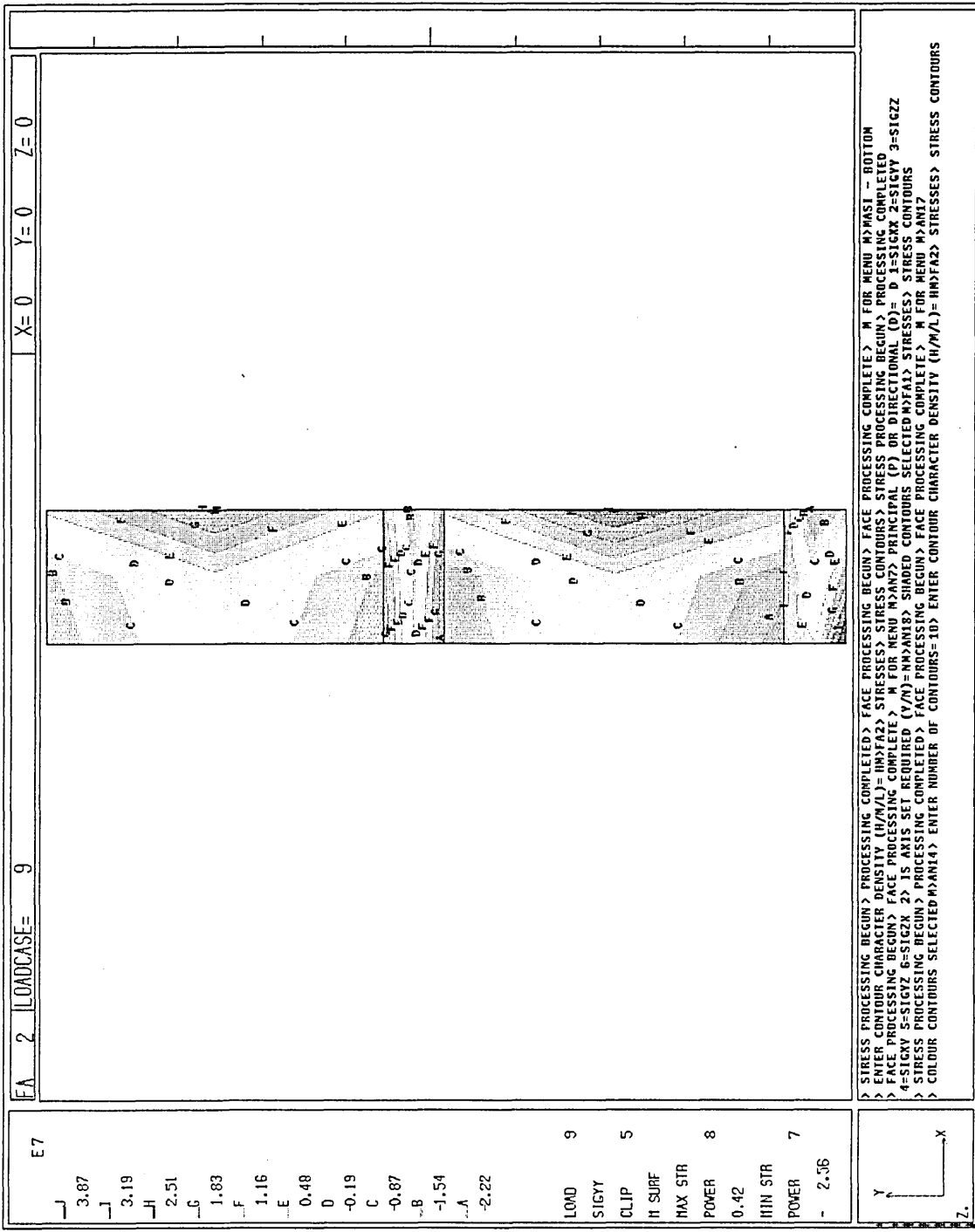


Figure 19.  $\sigma_{zz}$  stress, centre - model MASI (single mesh,  $t = 7200$  seconds)

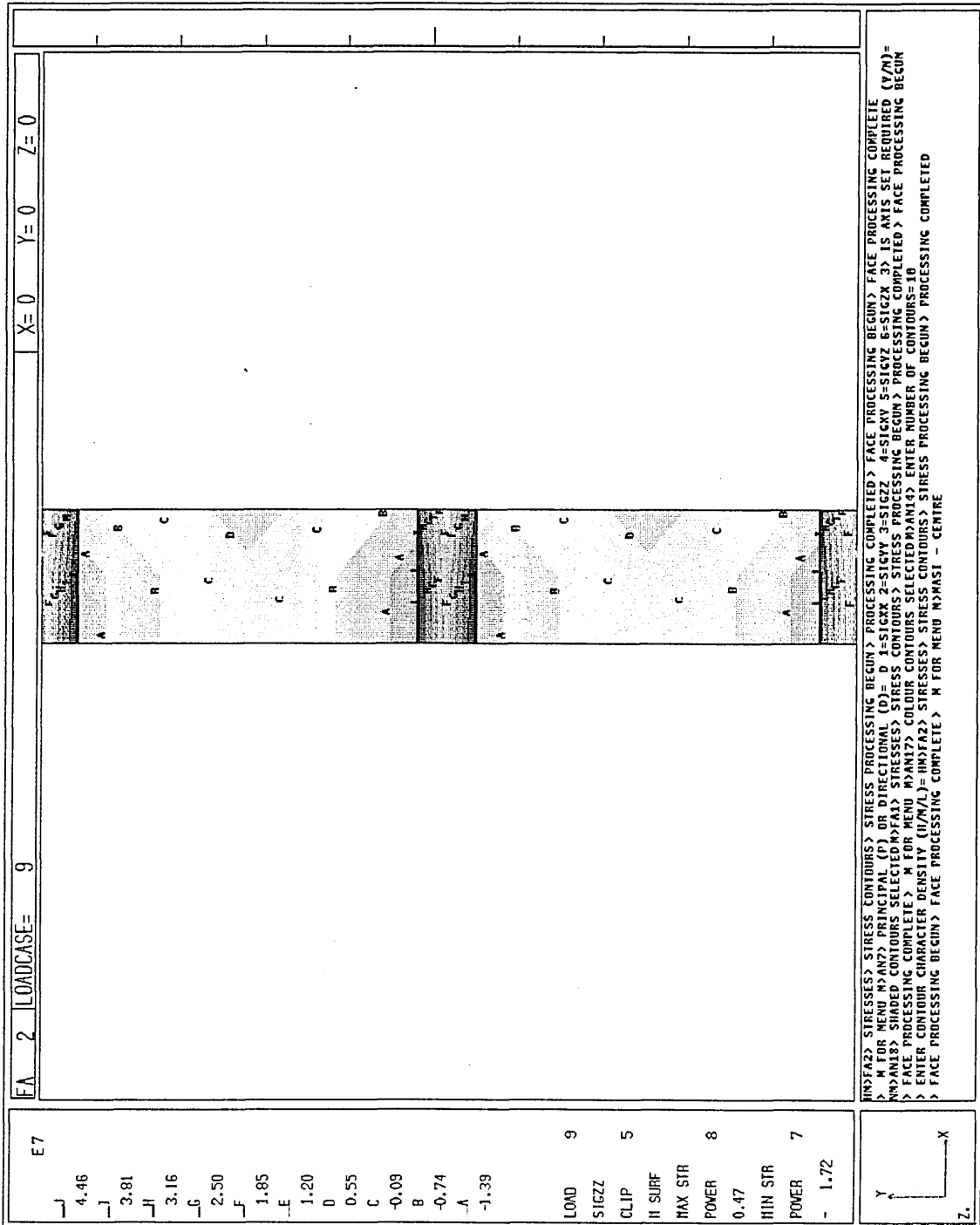


Figure 20.  $\sigma_{zz}$  stress, top - model MASI (single mesh,  $t = 7200$   
seconds)

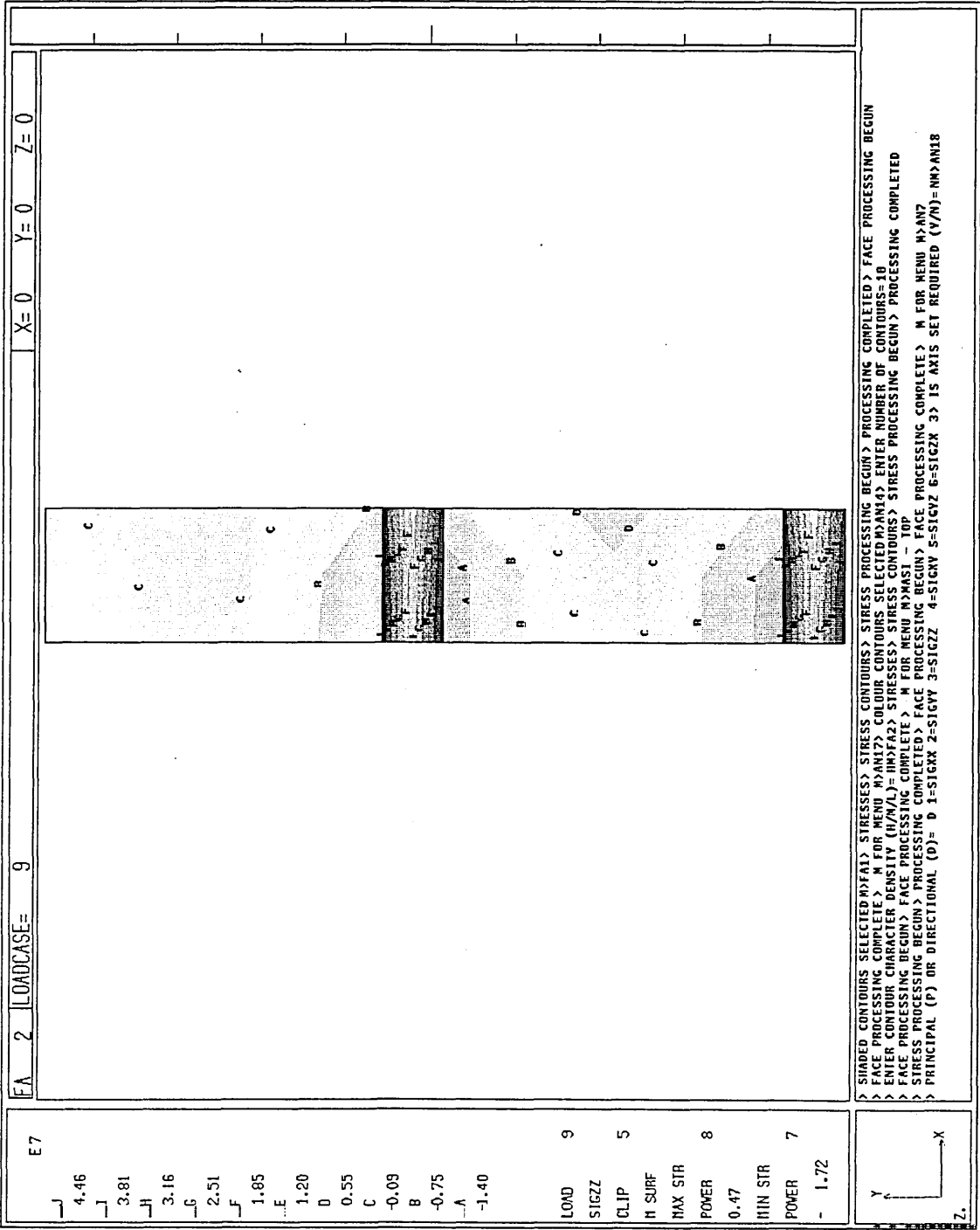
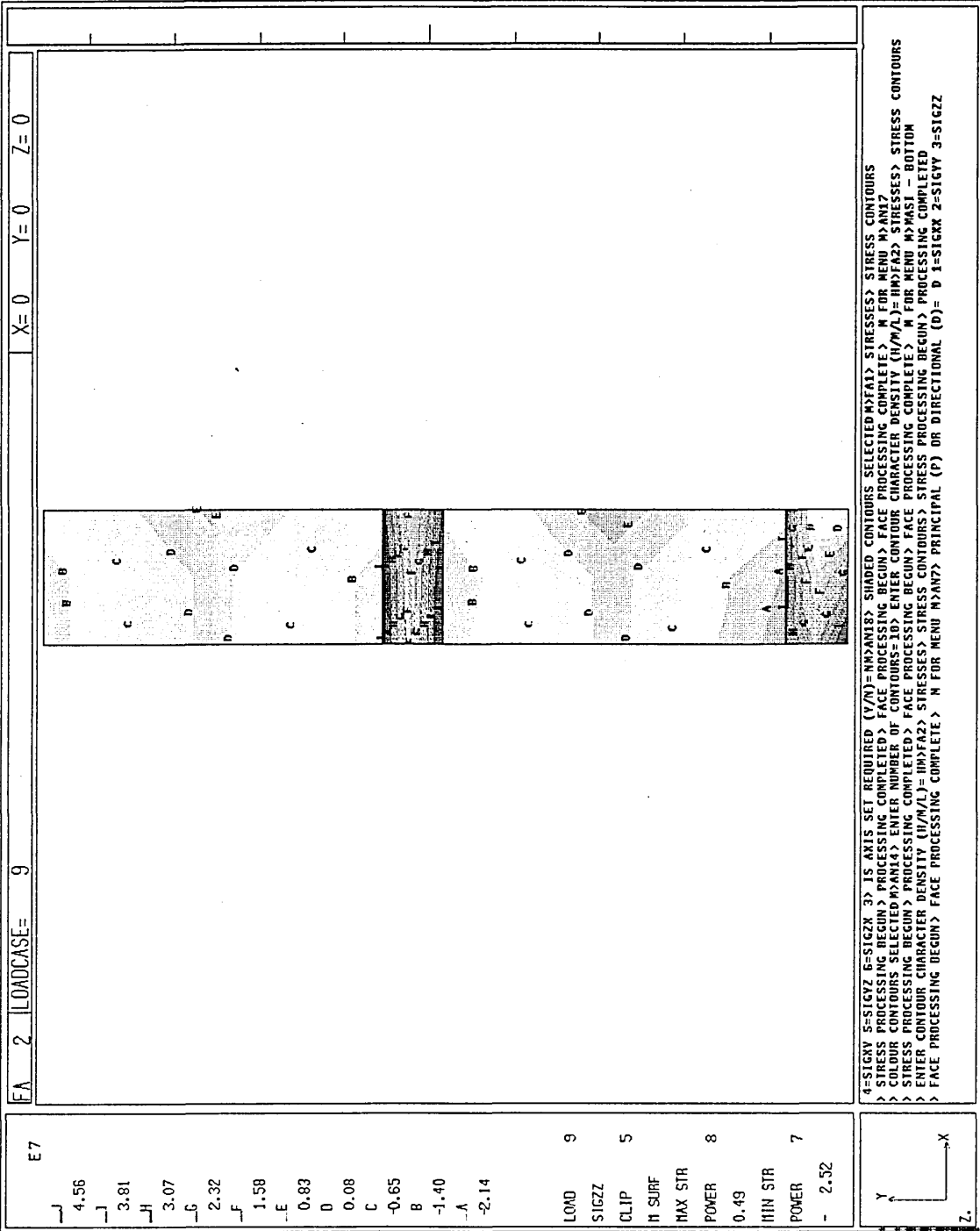
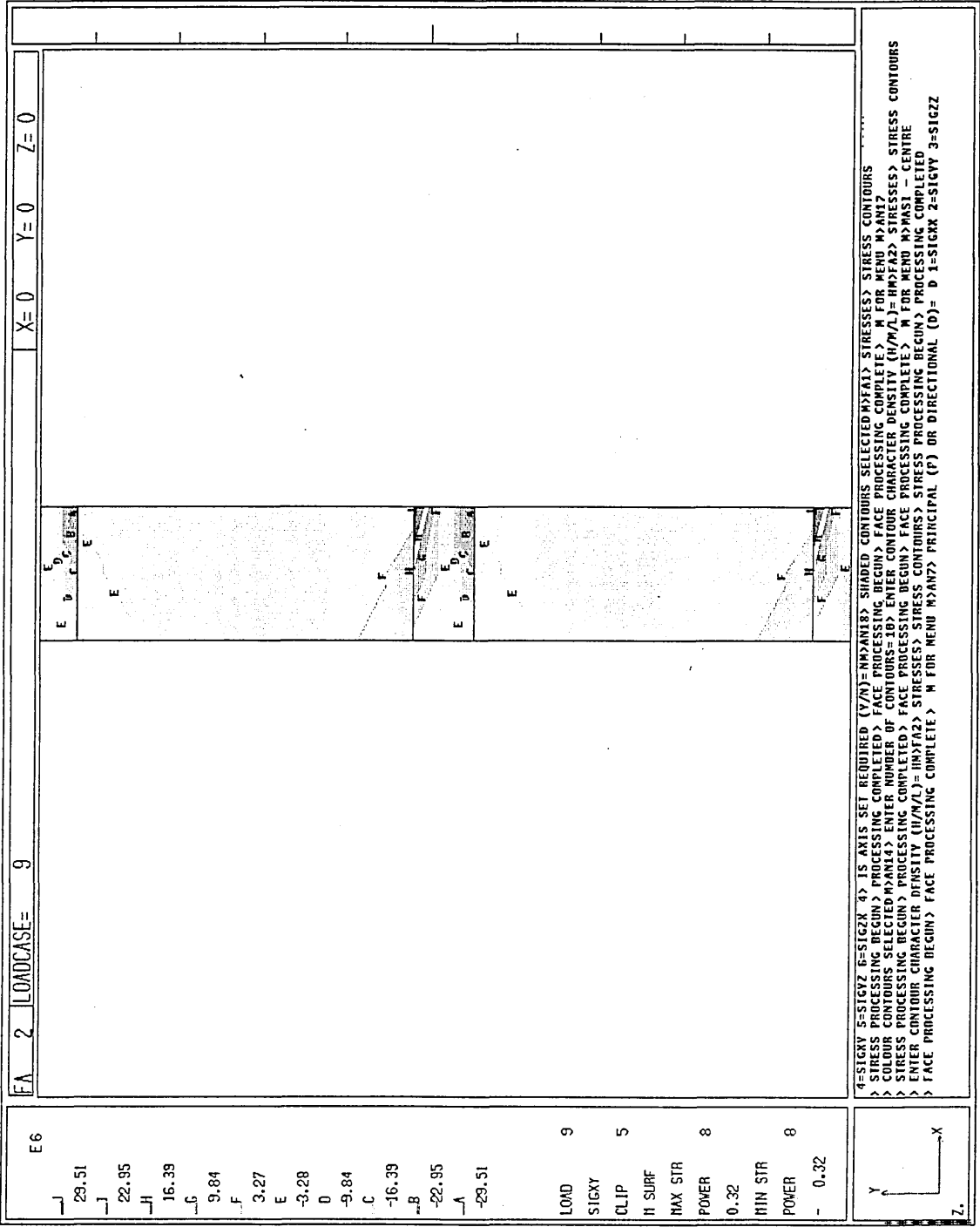


Figure 21.  $\sigma_{zz}$  stress, bottom - model MASI (single mesh,  $t = 7200$  seconds)



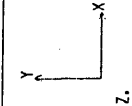


FA 2 LOADCASE= 9 X=0 Y=0 Z=0

E6

- J 29.51
- J 22.95
- H 16.39
- G 9.84
- F 3.27
- E -3.28
- D -9.84
- C -16.39
- B -22.95
- A -29.51

- LOAD 9
- SIGXY 5
- CLIP
- H SURF
- MAX STR
- POWER 8
- 0.32
- MIN STR
- POWER 8
- 0.32



4=SIGV 5=SIGZ 6=SIGX 4> IS AXIS SET REQUIRED (Y/N)=N>XAN18> SHADED CONTOURS SELECTED BY>A1> STRESSES> STRESS CONTOURS  
 > STRESS PROCESSING BEGUN> PROCESSING COMPLETED> FACE PROCESSING BEGUN> FACE PROCESSING COMPLETED> STRESS CONTOURS  
 > COLOUR CONTOURS SELECTED M>AN14> ENTER NUMBER OF CONTOURS=10> ENTER CONTOUR CHARACTER DENSITY (H/M/L)=H>M>L> STRESSES> STRESS CONTOURS  
 > STRESS PROCESSING BEGUN> PROCESSING COMPLETED> FACE PROCESSING BEGUN> FACE PROCESSING COMPLETED> M FOR MENU M>M18> CENTRE  
 > ENTER CONTOUR CHARACTER DENSITY (H/M/L)=H>M>L> STRESSES> STRESS PROCESSING BEGUN> STRESS PROCESSING COMPLETED  
 > FACE PROCESSING BEGUN> FACE PROCESSING COMPLETED> M FOR MENU M>AN7> PRINCIPAL (P) OR DIRECTIONAL (D)= D 1=SIGRX 2=SIGVY 3=SIGZZ

Figure 22.  $\sigma_{xy}$  stress, centre - model MASI (single mesh,  $t = 7200$  seconds)

Figure 23.  $\sigma_{xy}$  stress, top - model MASI (single mesh, t = 7200  
seconds)

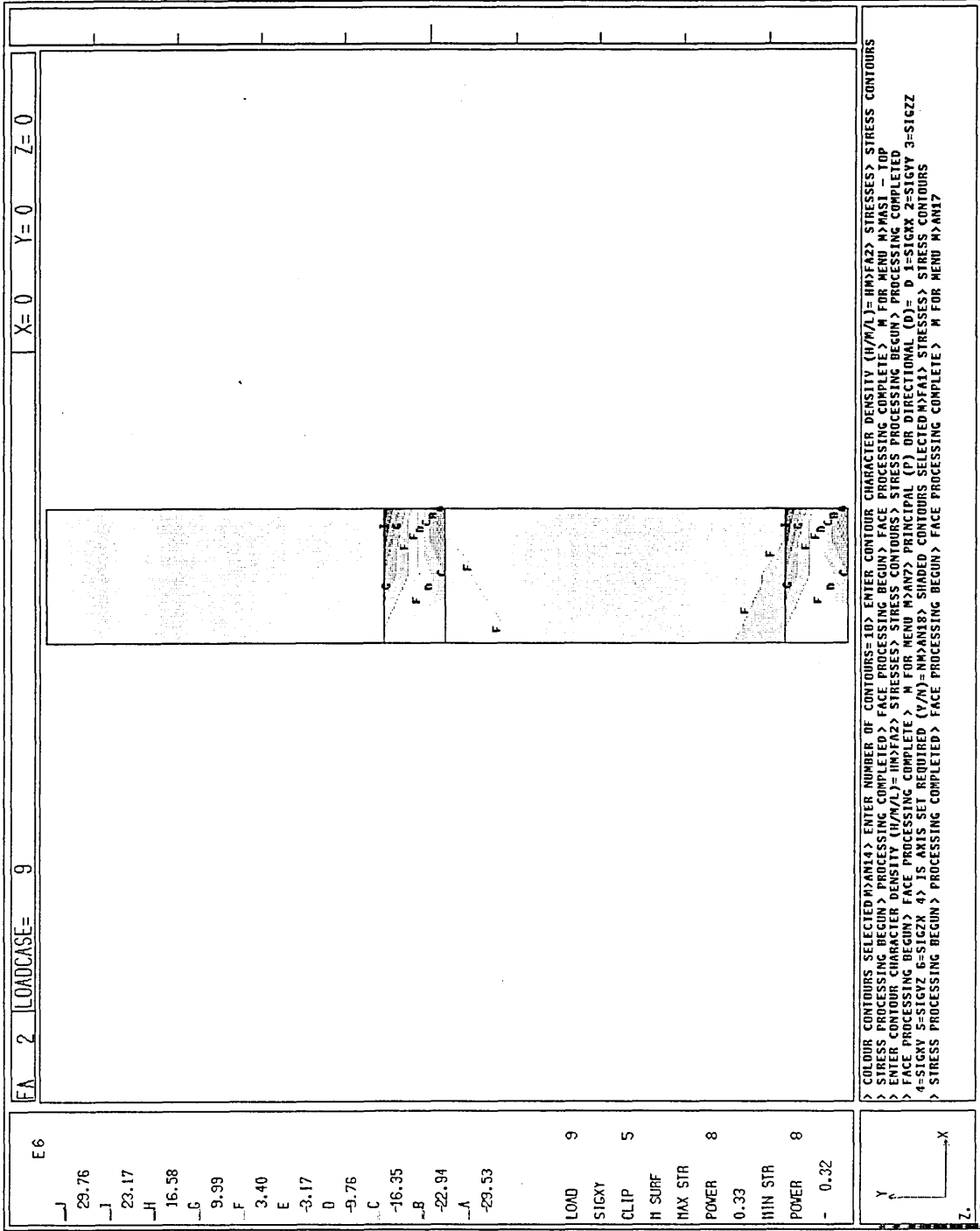


Figure 24.  $\sigma_{xy}$  stress, bottom - model MASI (single mesh,  $t = 7200$  seconds)

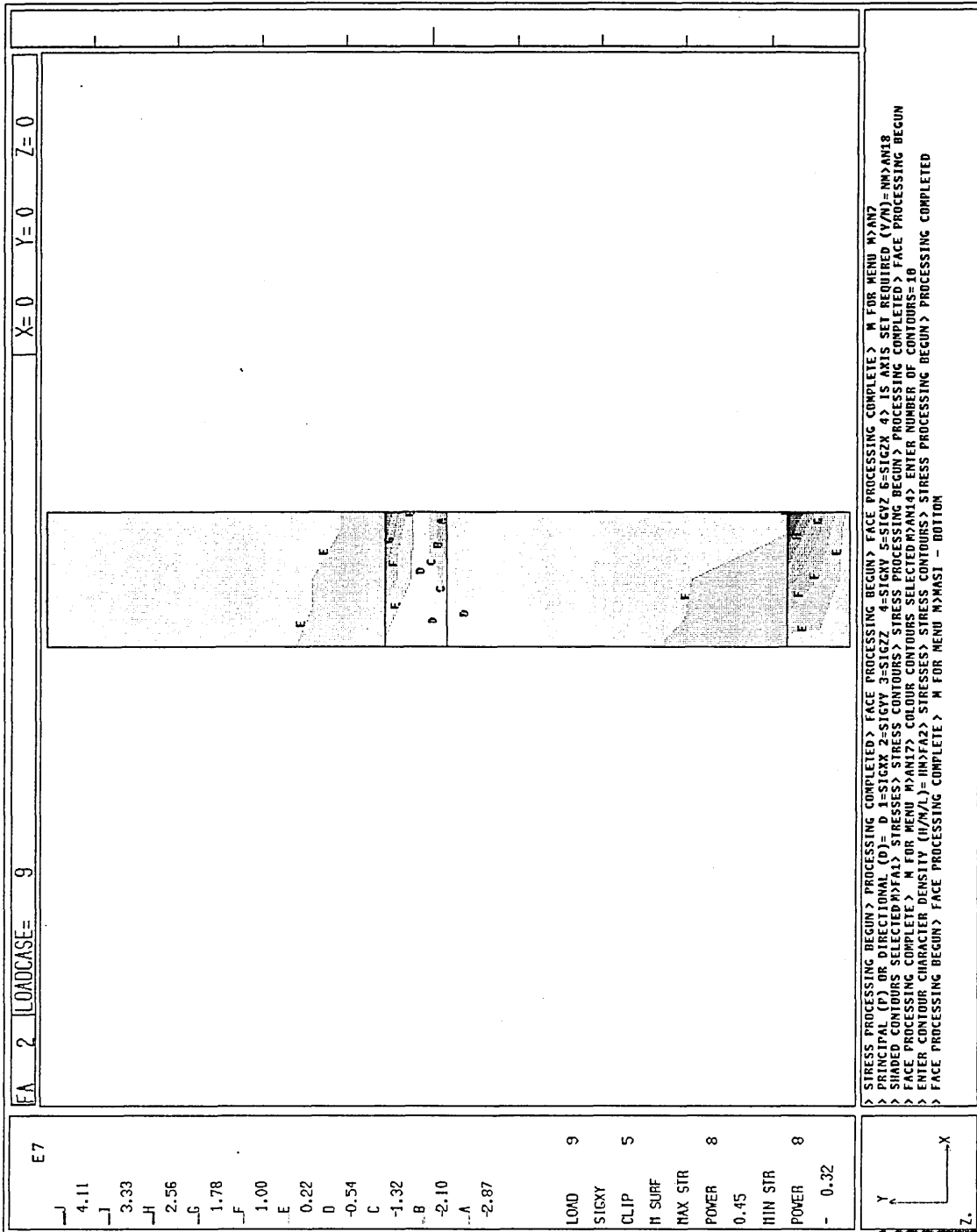


Figure 25.  $\sigma_{yz}$  stress, centre - model MASI (single mesh,  $t = 7200$  seconds)

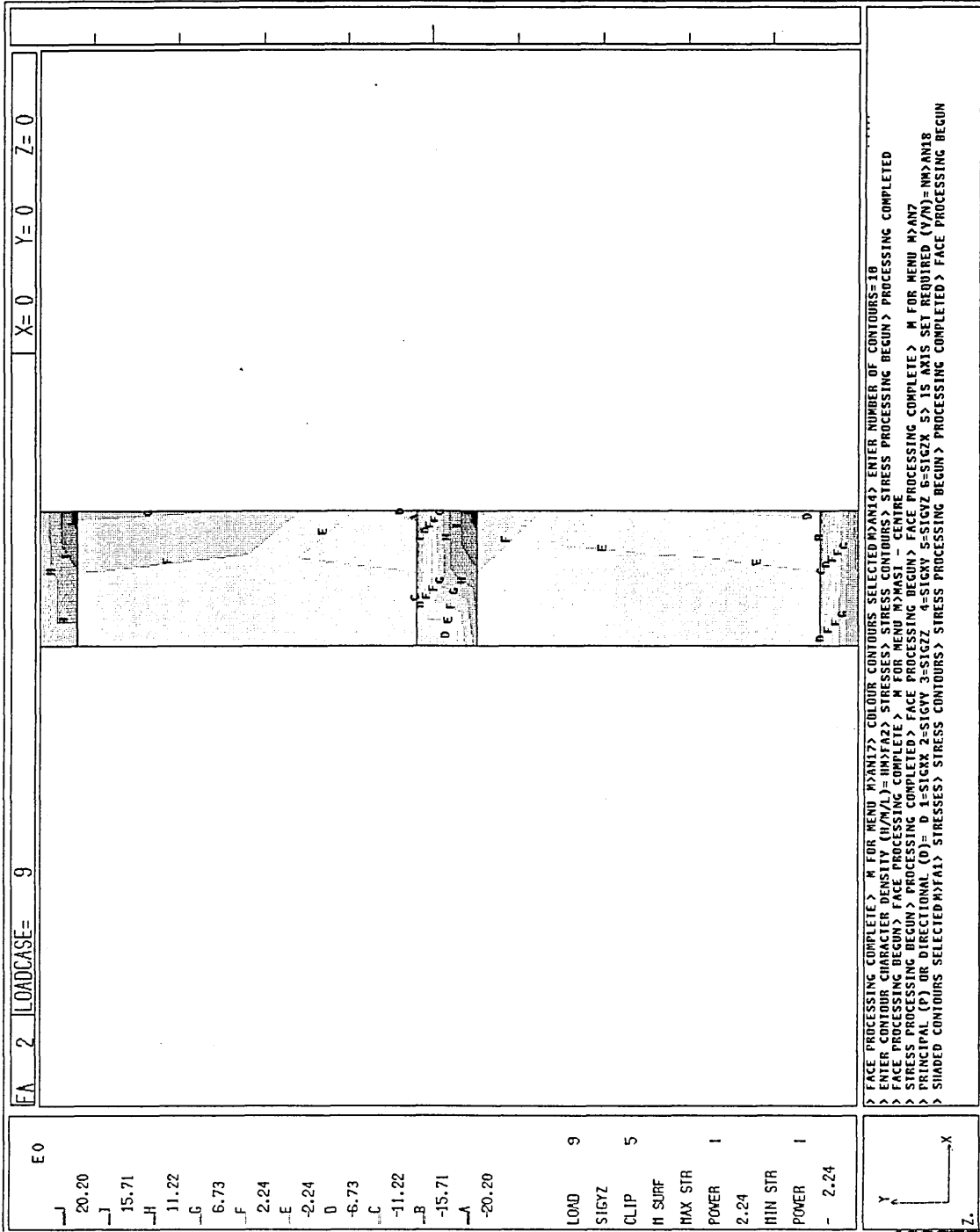


Figure 26.  $\sigma_{zx}$  stress, centre - model MASI (single mesh, t = 7200  
seconds)

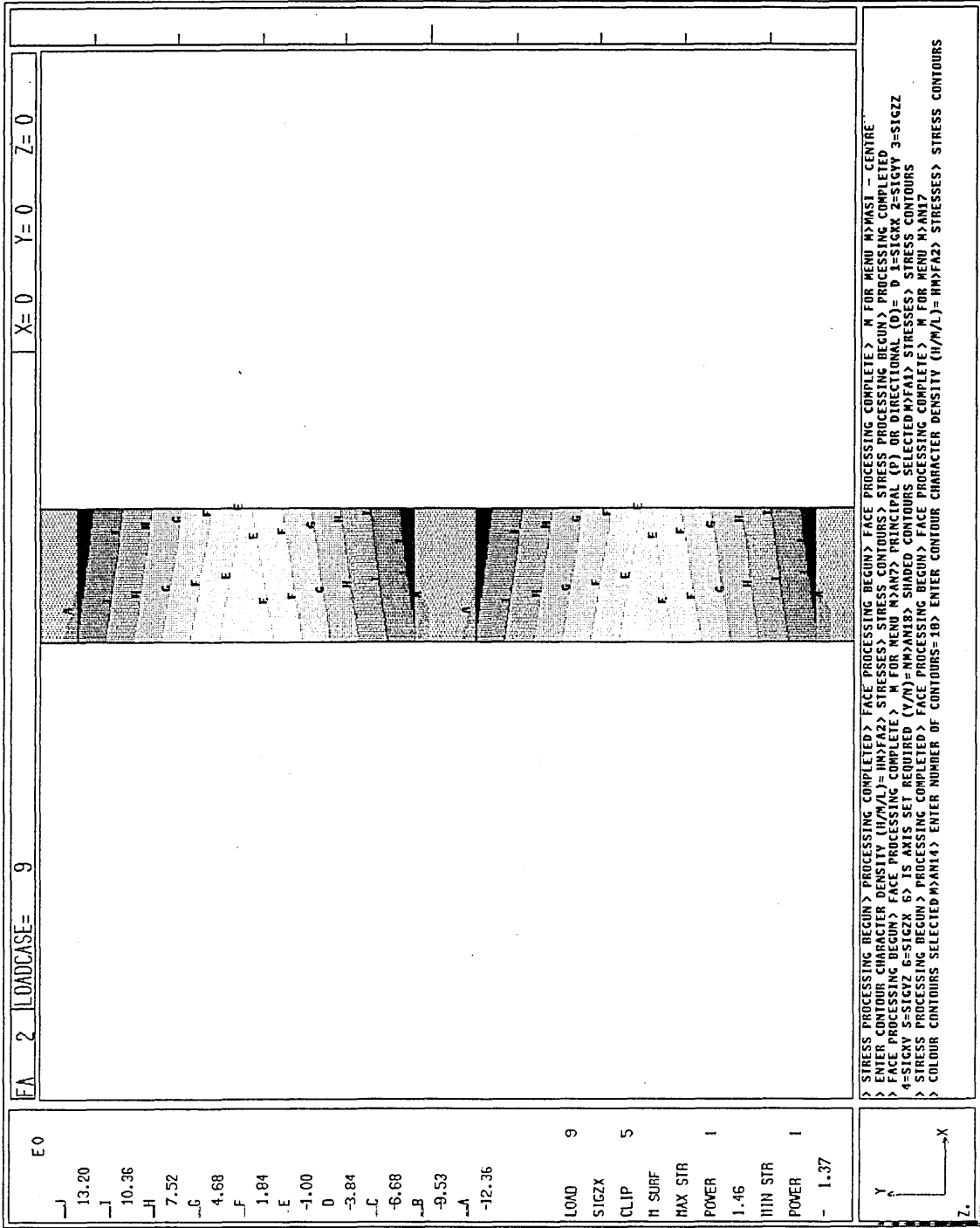


Figure 27. Maximum principal stress, centre - model MASI (single mesh,  
t = 7200 seconds)

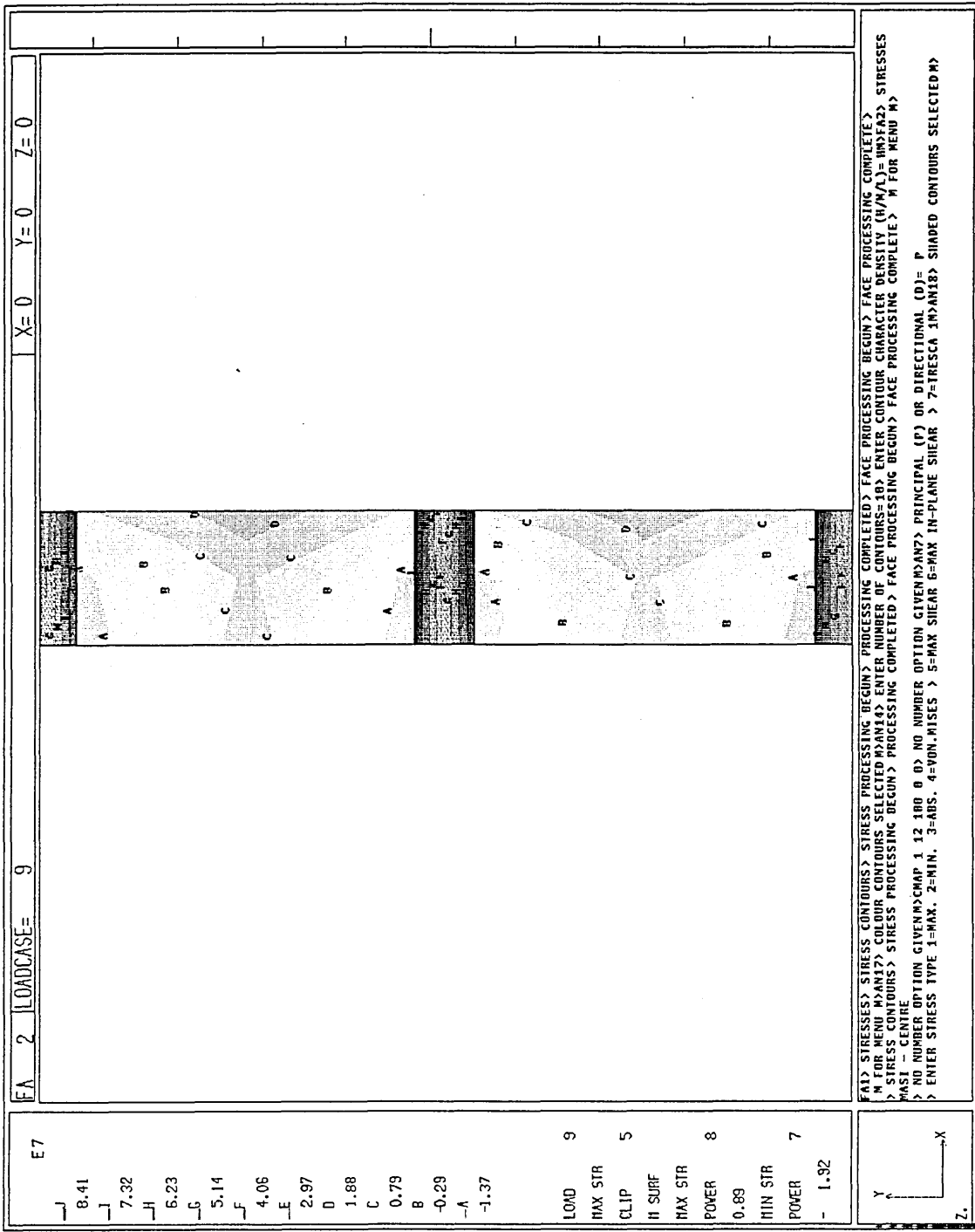


Figure 28. Maximum principal stress vectors, centre - model MASI  
(single mesh,  $t = 7200$  seconds)

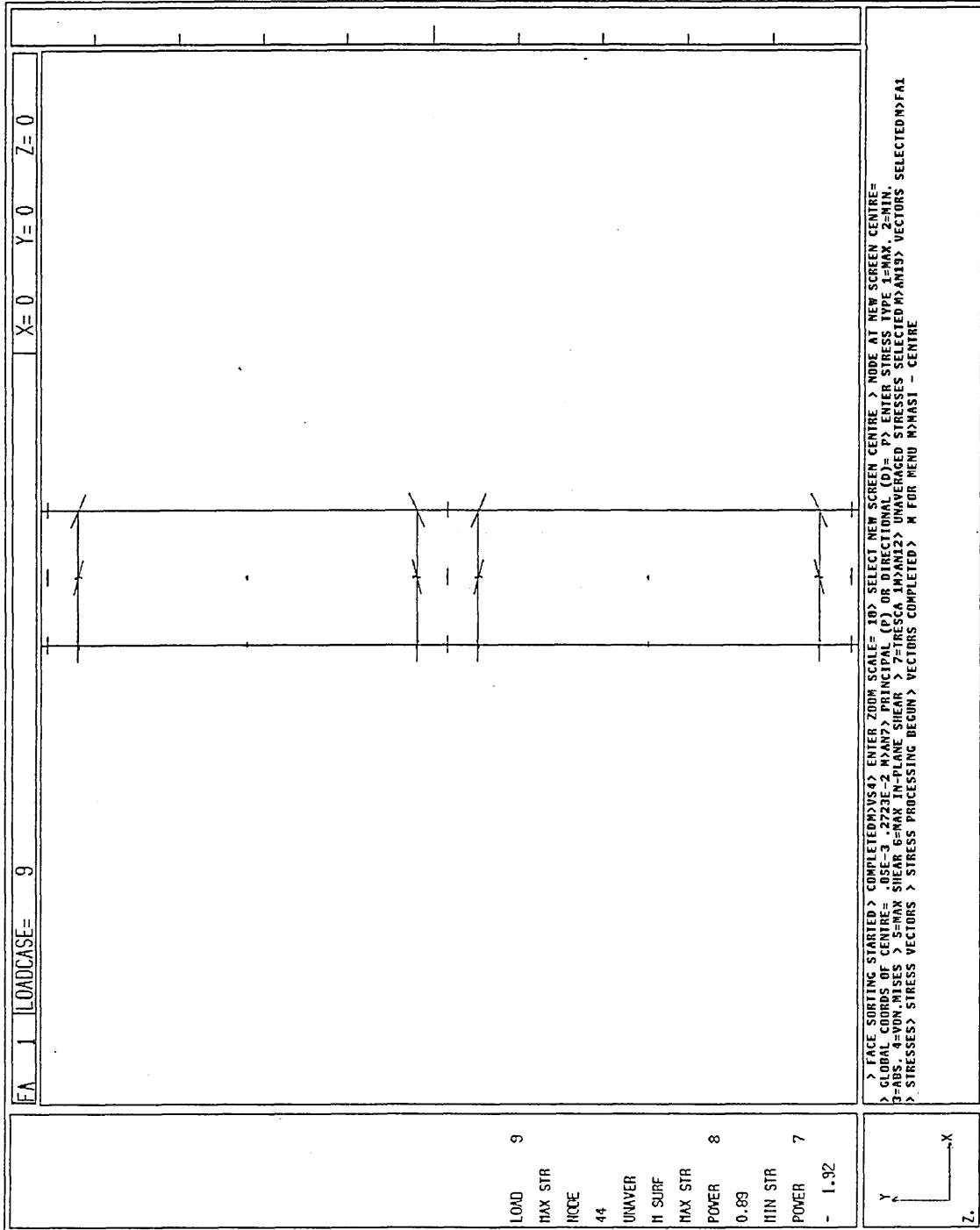


Figure 29. Maximum principal stress, top - model MASI (single mesh,  
t = 7200 seconds)

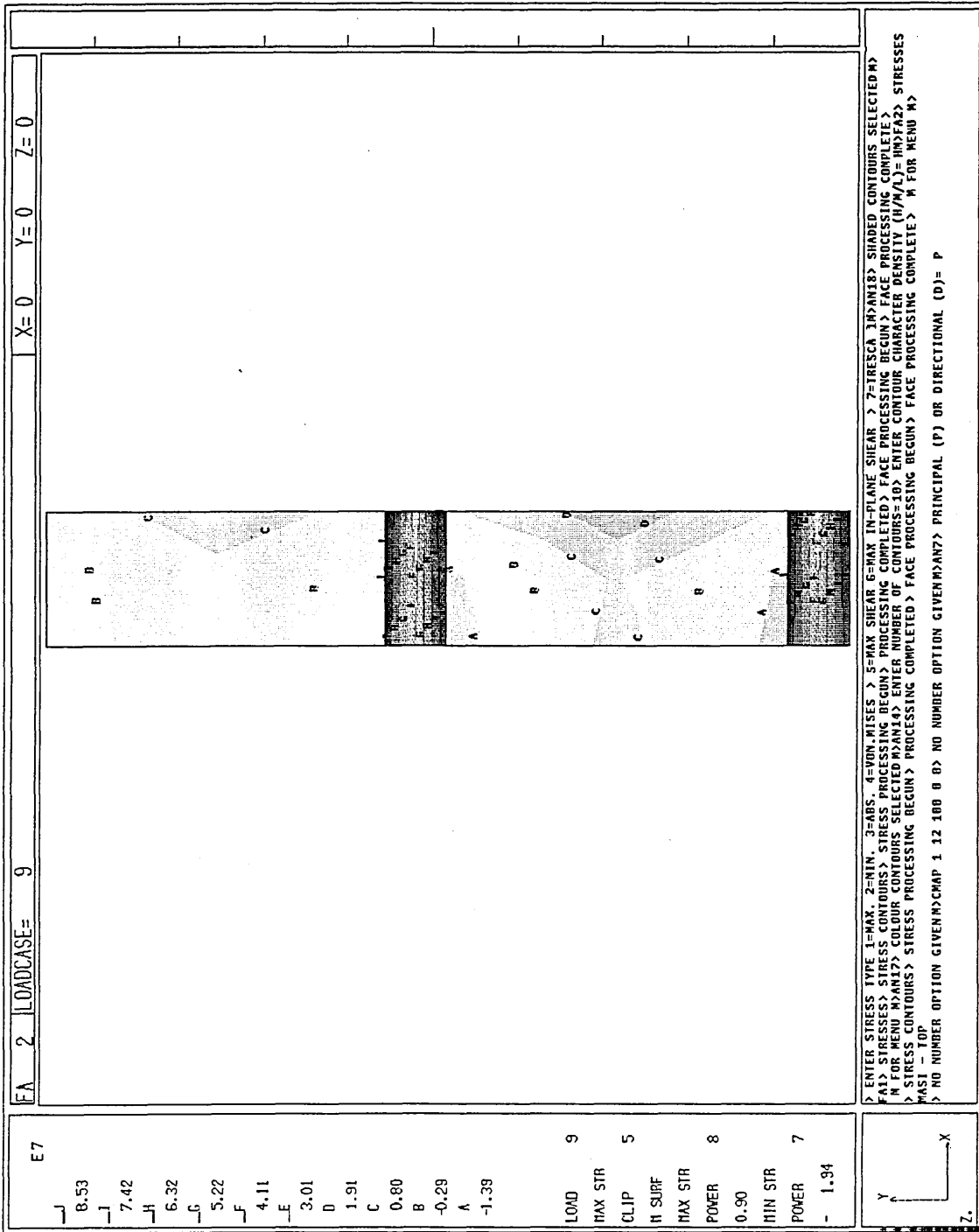


Figure 30. Maximum principal stress, bottom - model MASI (single mesh,  
t = 7200 seconds)

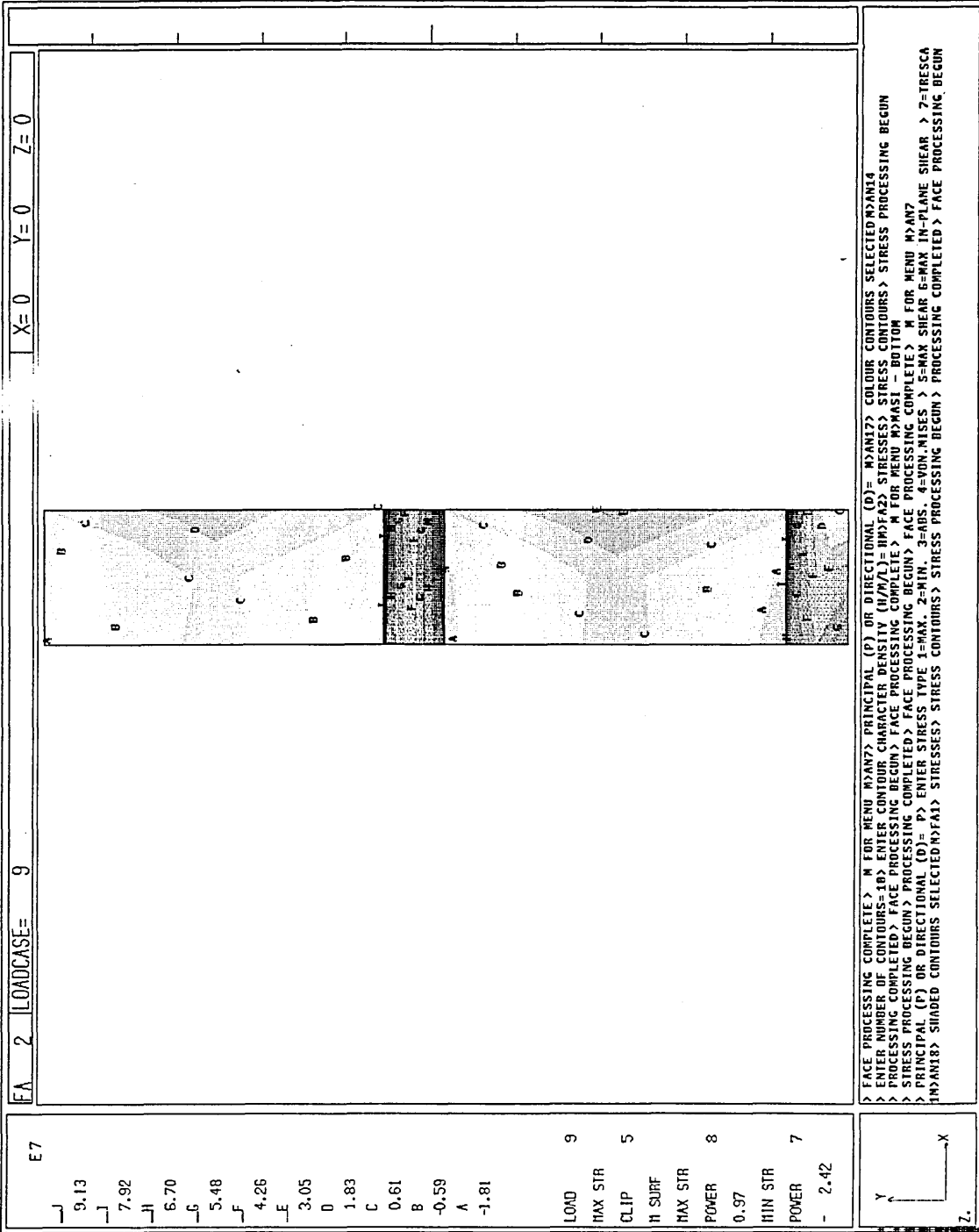


Figure 31. Minimum principal stress, centre - model MASI (single mesh,  
t = 7200 seconds)

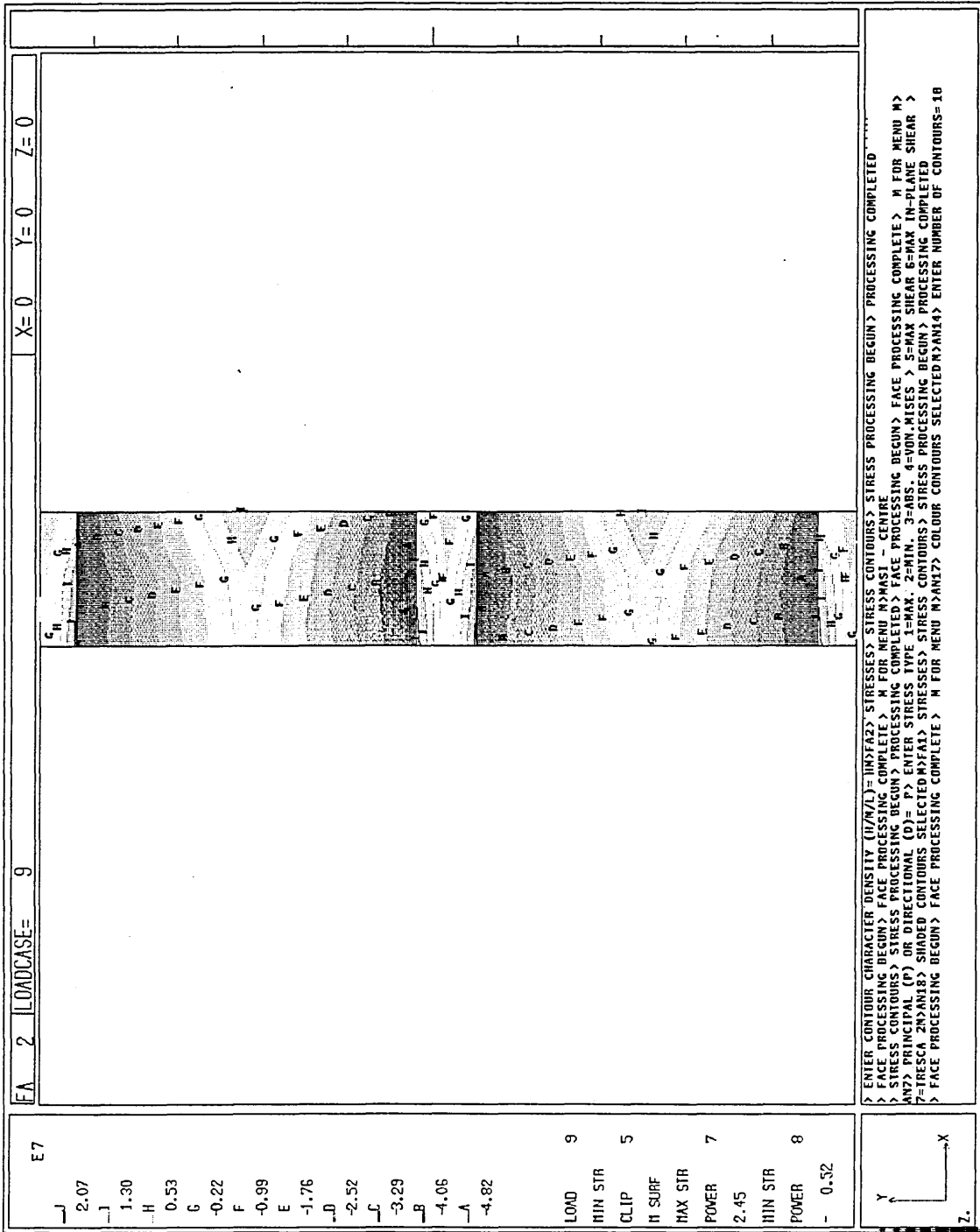


Figure 32. Minimum principal stress vectors, centre - model MASI  
(single mesh,  $t = 7200$  seconds)

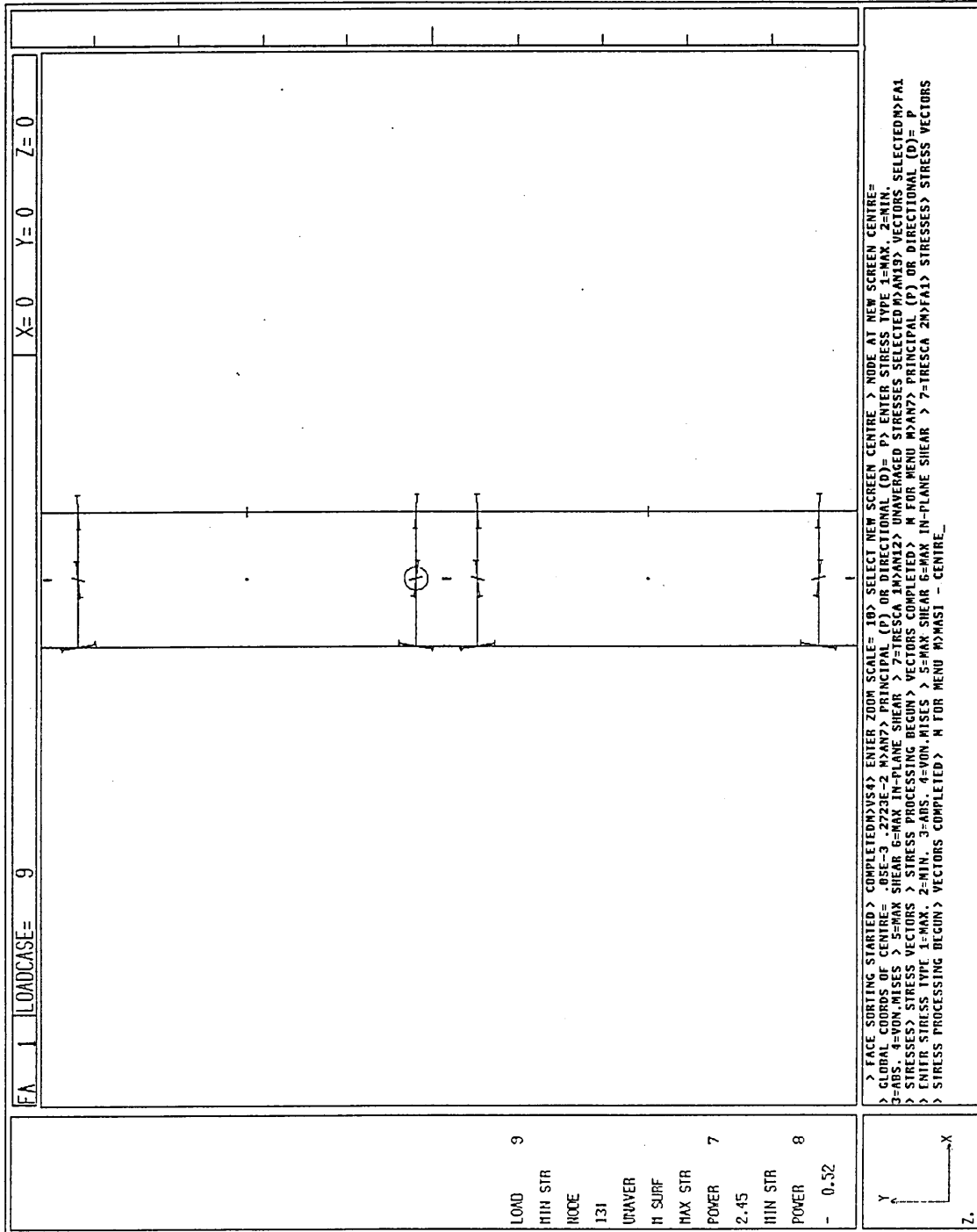


Figure 33. Minimum principal stress, top - model MASI (single mesh,  
t = 7200 seconds)

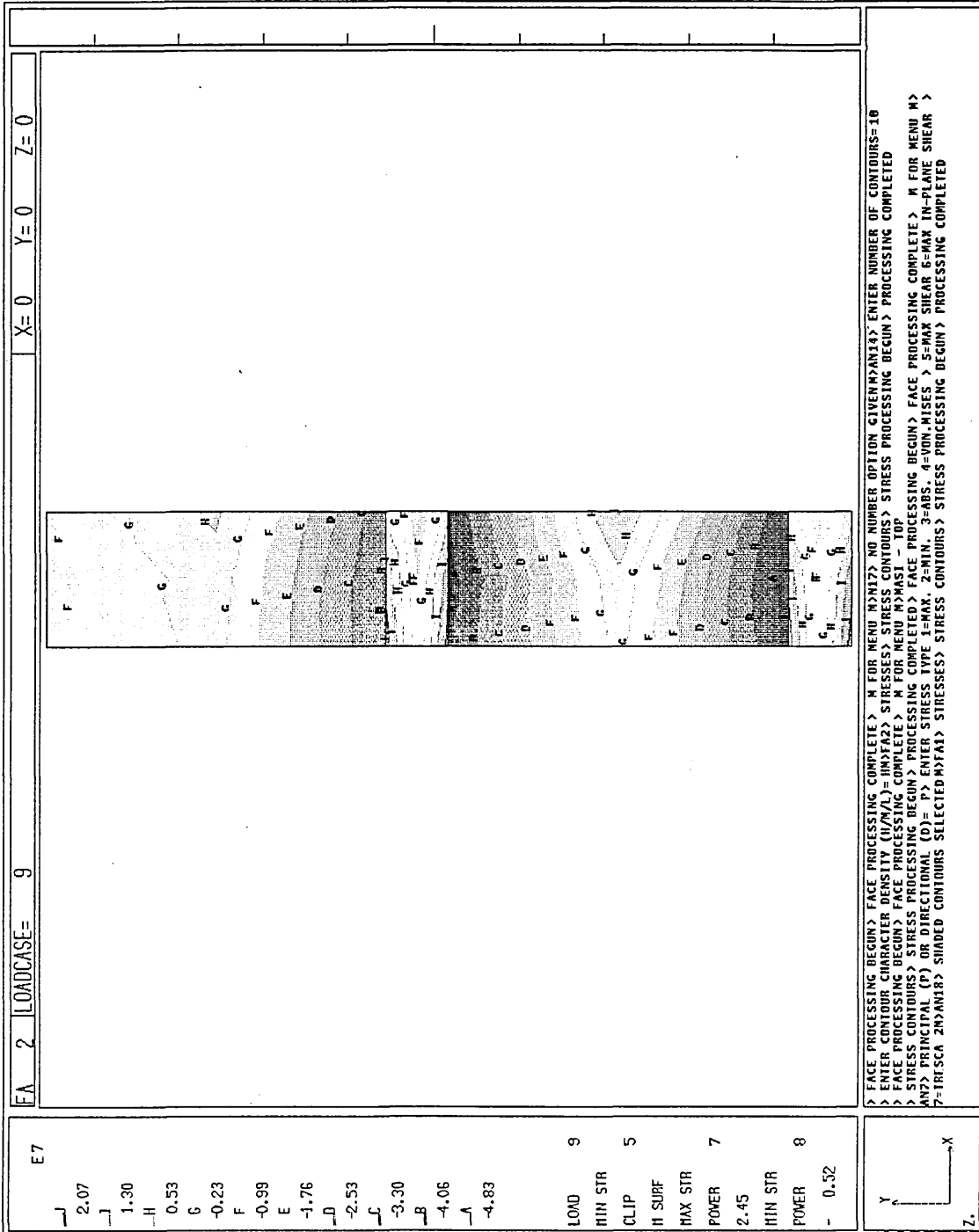


Figure 34. Minimum principal stress, bottom - model MASI (single mesh,  
t = 7200 seconds)

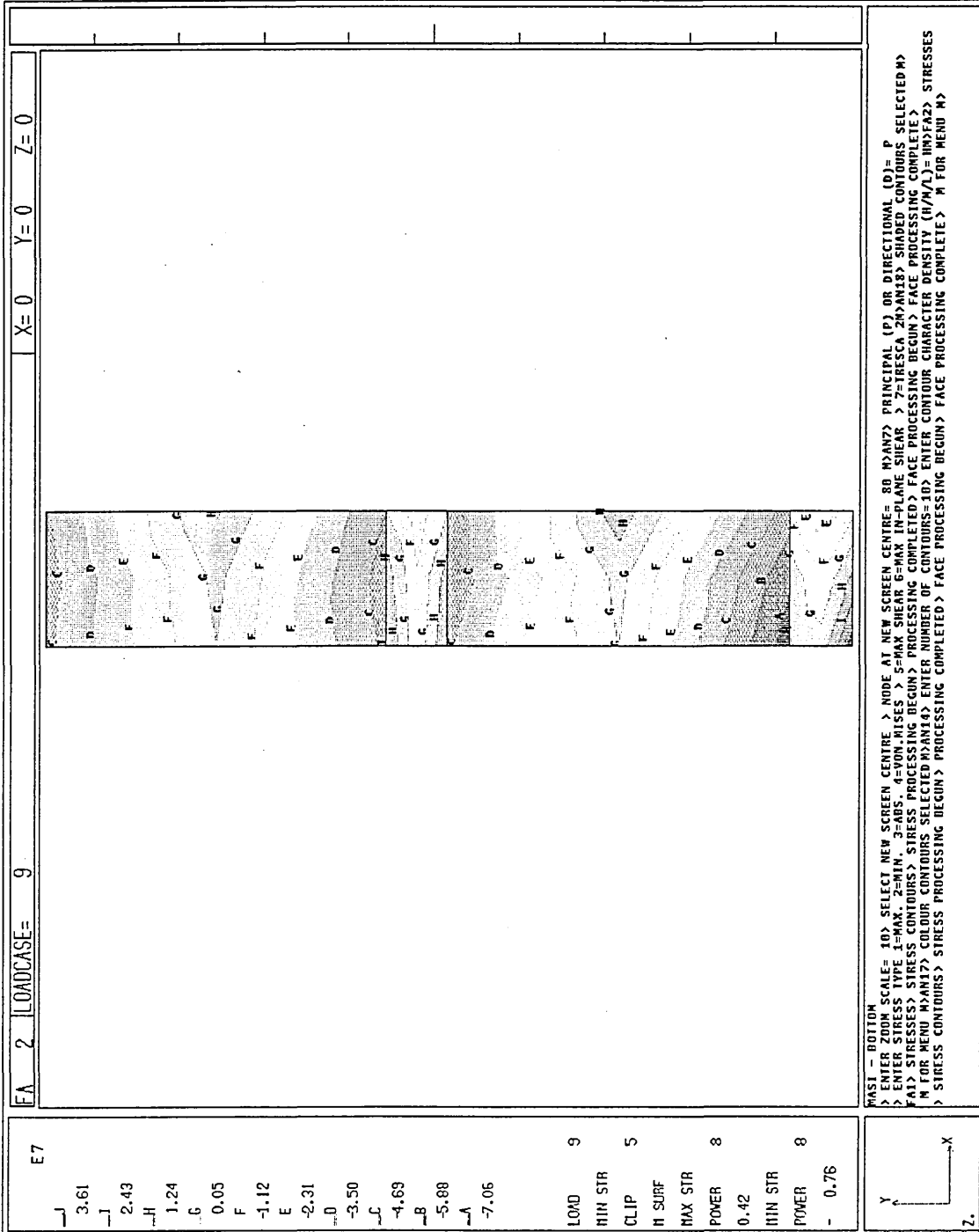


Figure 35. Von Mises stress, centre - model MASI (single mesh,  $t = 7200$  seconds)



Figure 36. Von Mises stress, top - model MASI (single mesh,  $t = 7200$  seconds)

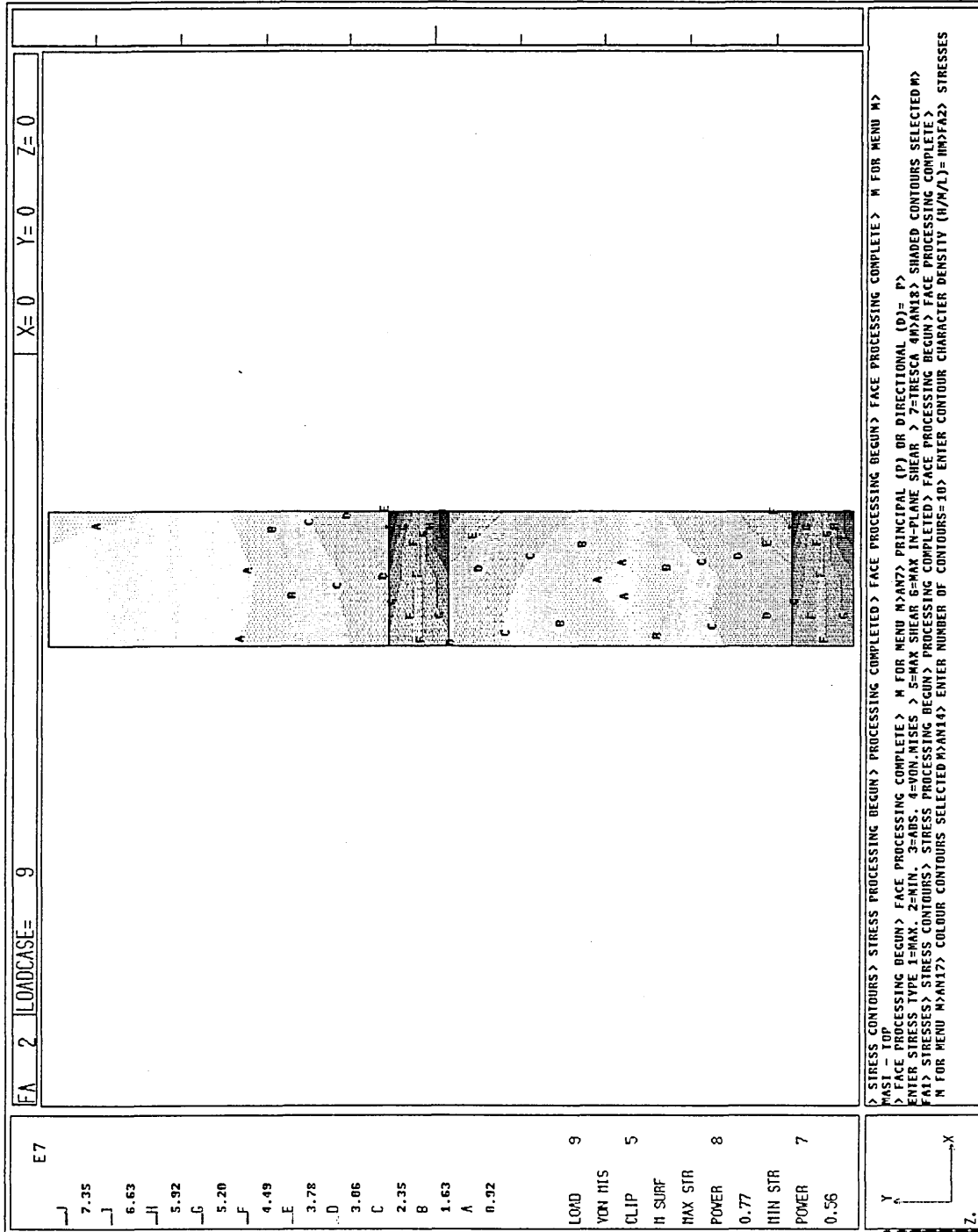


Figure 37. Von Mises stress, bottom - model MASI (single mesh, t = 7200 seconds)

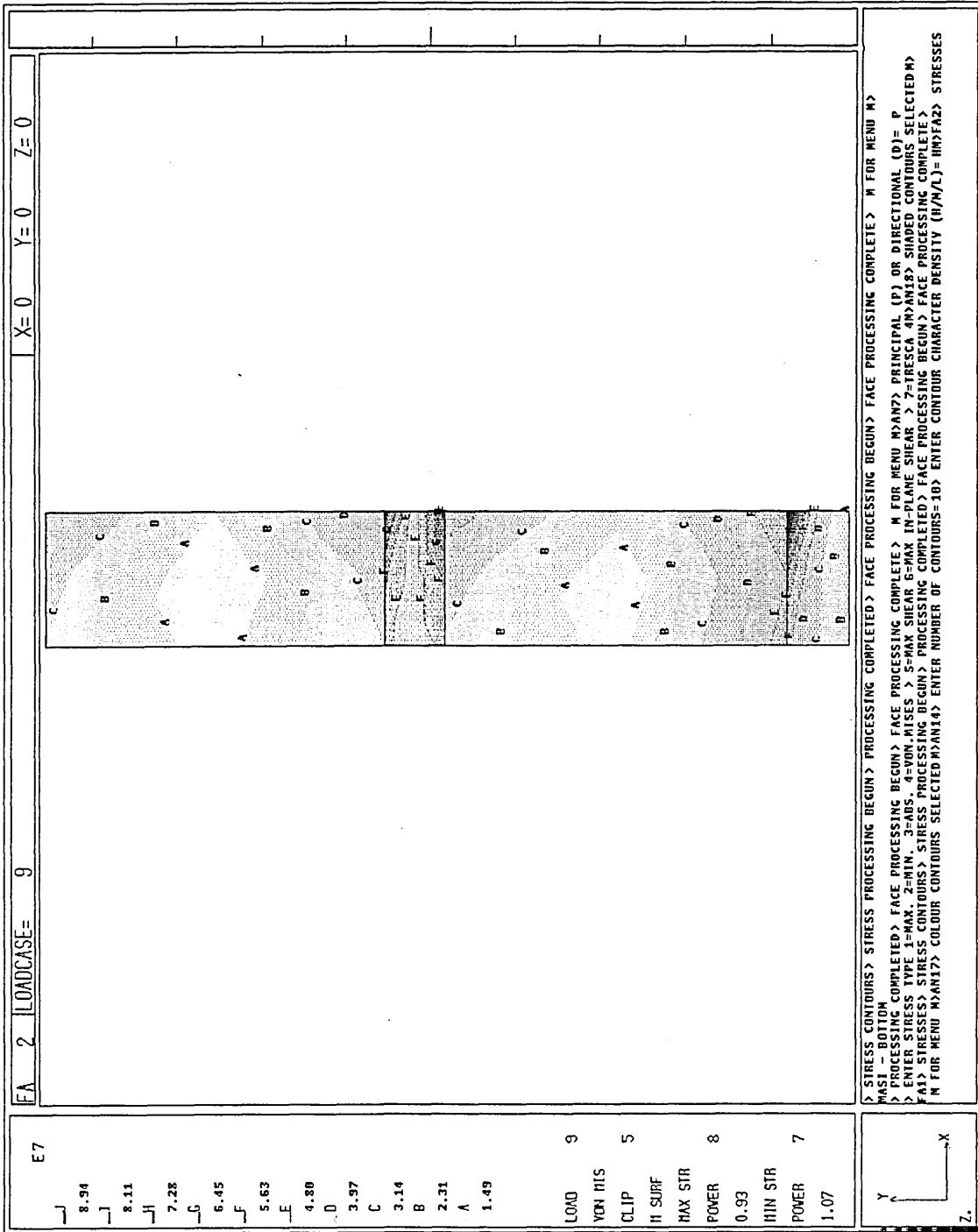


Figure 38. Maximum shear stress, centre - model MASI (single mesh, t = 7200 seconds)

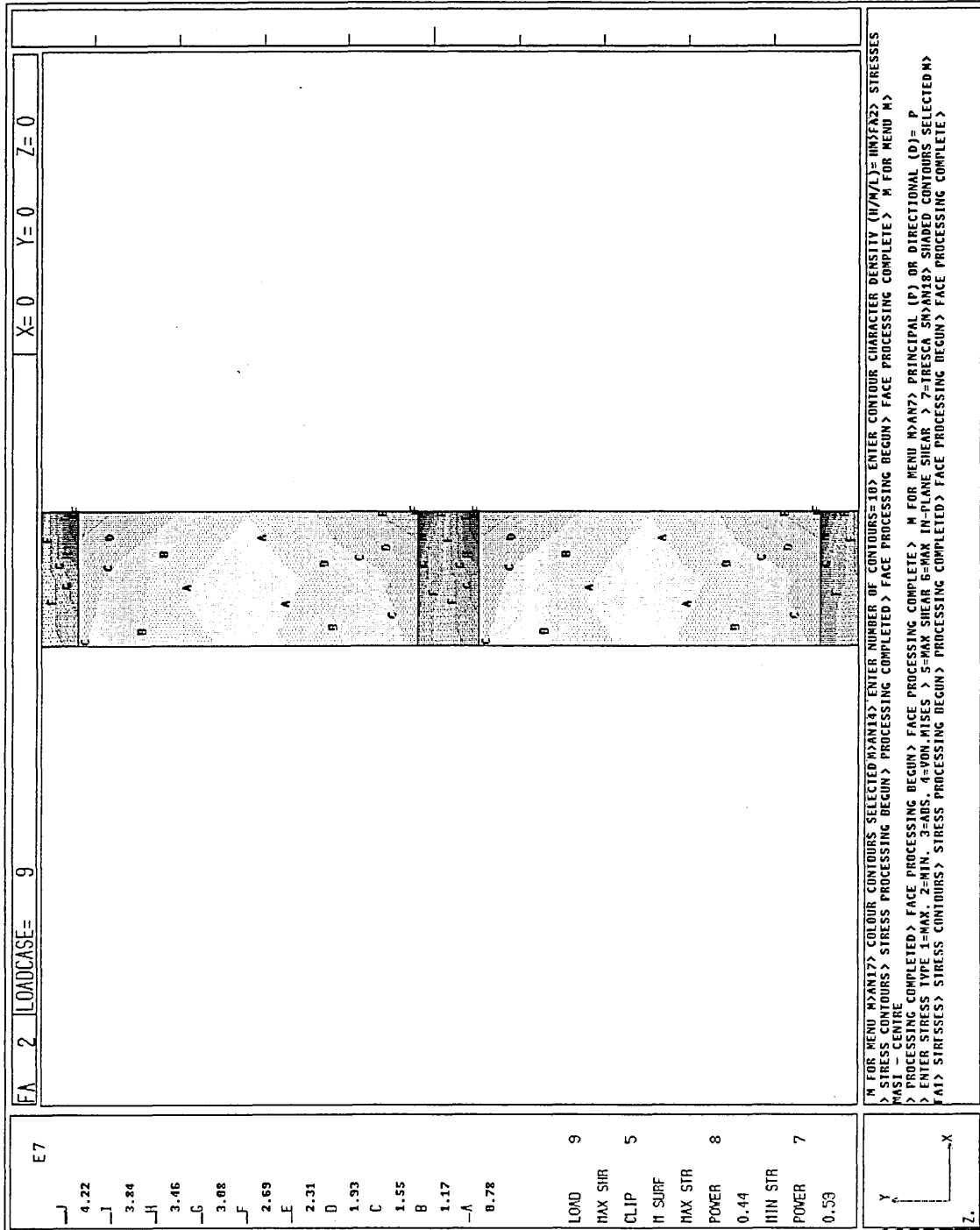


Figure 39. Tresca stress, centre - model MASI (single mesh,  $t = 7200$  seconds)

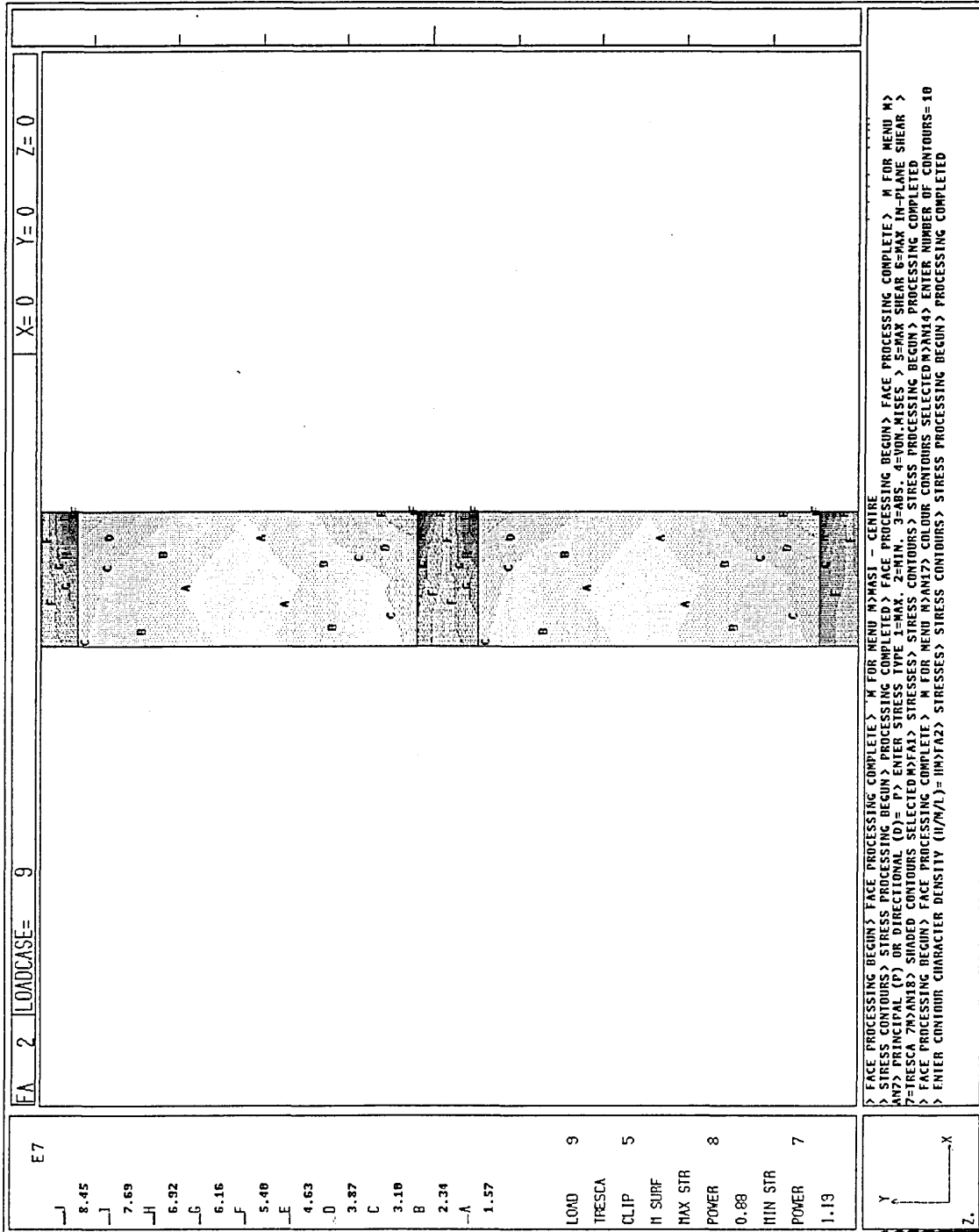
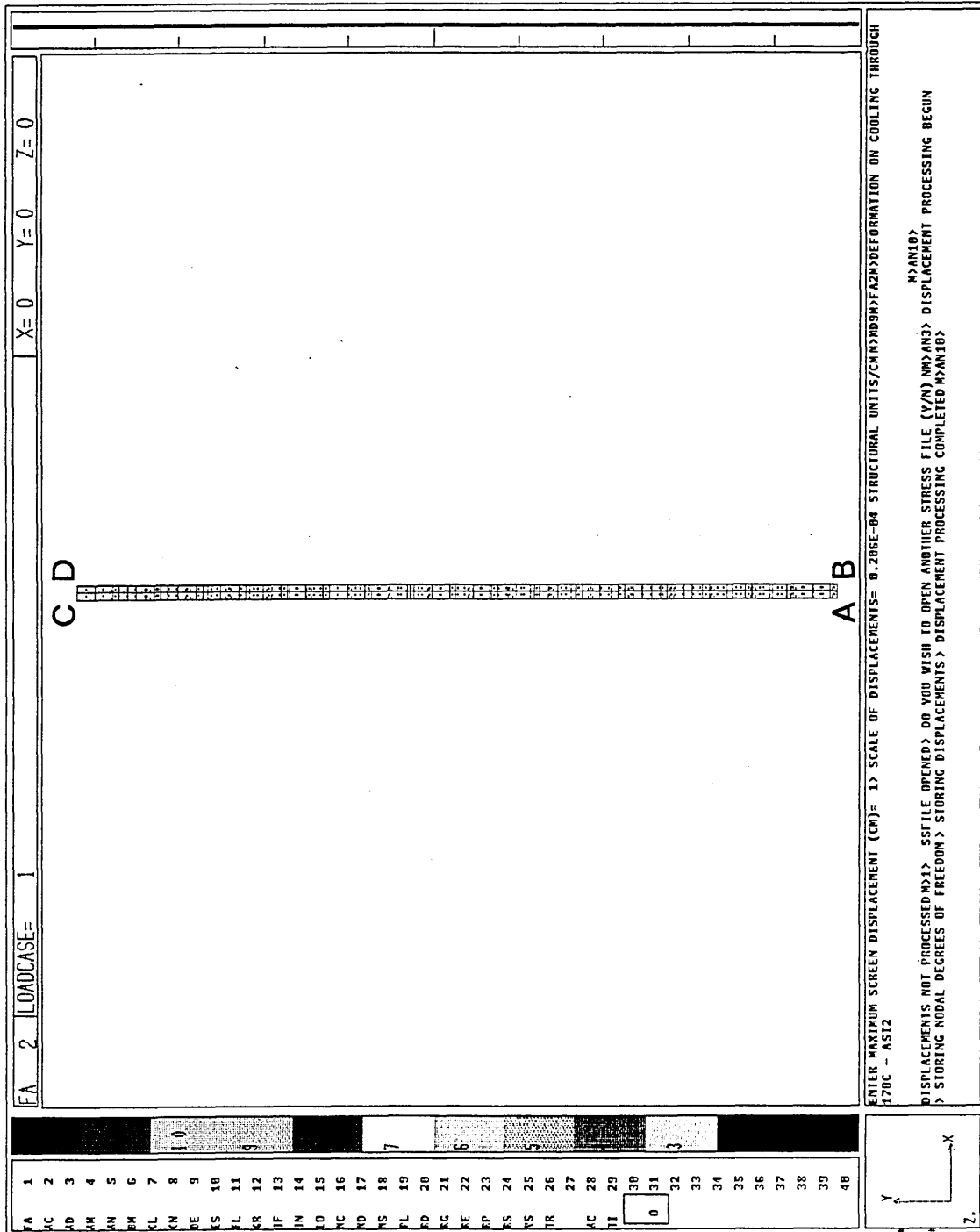


Figure 40. Deformation: uniform cooling through 170°C - model ASI2  
(double mesh)



FA 2 LOADCASE= 1

FA 1  
 AC 2  
 AD 3  
 AM 4  
 AN 5  
 AP 6  
 AL 7  
 KN 8  
 DE 9  
 KS 10  
 ZL 11  
 KR 12  
 IF 13  
 IN 14  
 LO 15  
 MC 16  
 ND 17  
 NS 18  
 FL 19  
 RD 20  
 SC 21  
 RE 22  
 RP 23  
 RS 24  
 TR 26  
 AC 28  
 TI 29  
 30  
 31  
 32  
 33  
 34  
 35  
 36  
 37  
 38  
 39  
 48

X=0 Y=0 Z=0

C D

A B

ENTER MAXIMUM SCREEN DISPLACEMENT (CM)= 1> SCALE OF DISPLACEMENTS= 0.206E-04 STRUCTURAL UNITS/CM N>M09M>FA2M>DEFORMATION ON COOLING THROUGH  
 170C - AS12  
 M>AN10>  
 DISPLACEMENTS NOT PROCESSED M>1> SSFILE OPENED> DO YOU WISH TO OPEN ANOTHER STRESS FILE (Y/N) NM>AN3> DISPLACEMENT PROCESSING BEGUN  
 > STORING NODAL DEGREES OF FREEDOM > STORING DISPLACEMENTS > DISPLACEMENT PROCESSING COMPLETED M>AN10>



Figure 41. Mesh, centre elements - model ASI2 (double mesh)

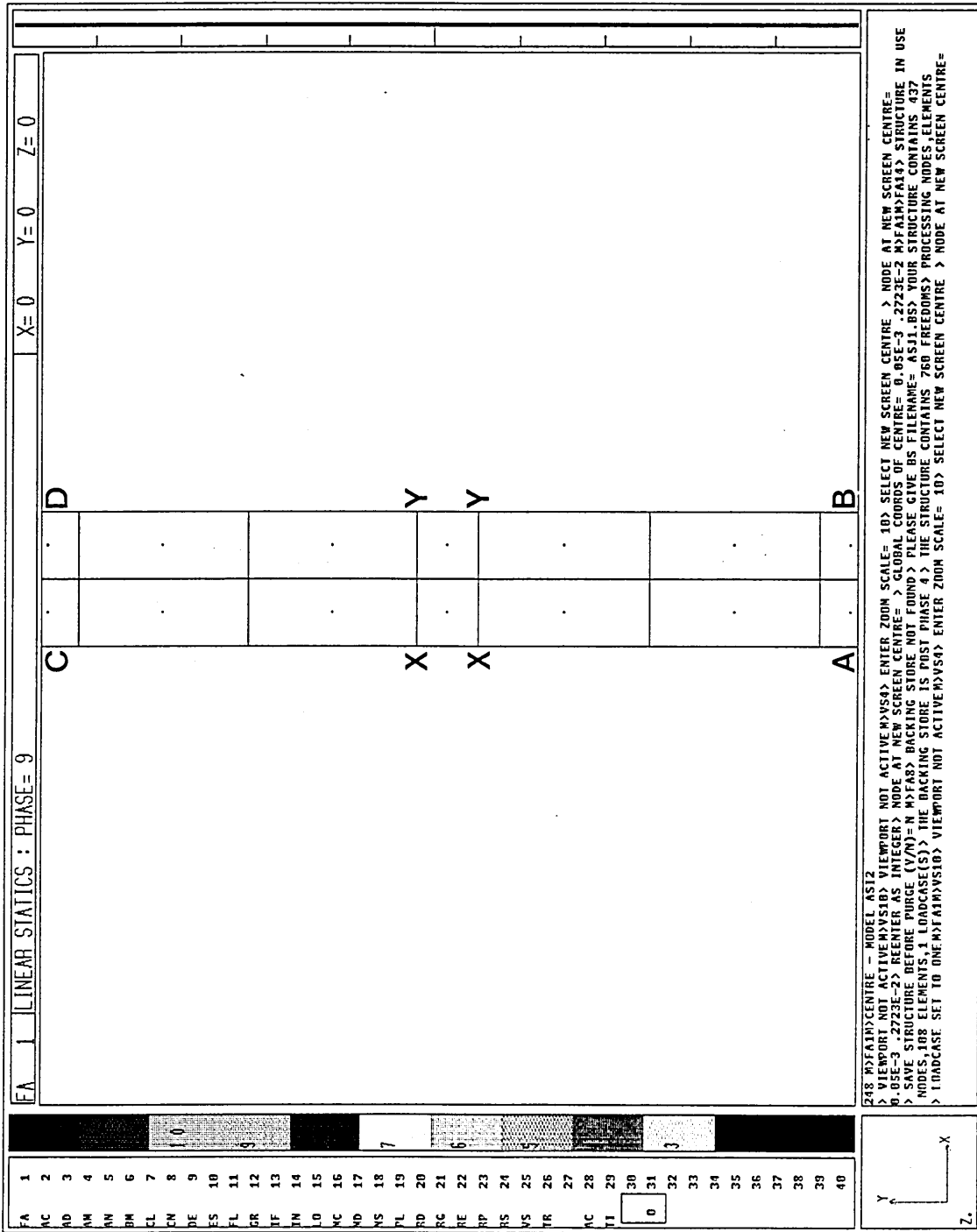


Figure 42.  $\sigma_{xx}$  stress, centre - model ASI2 (double mesh)

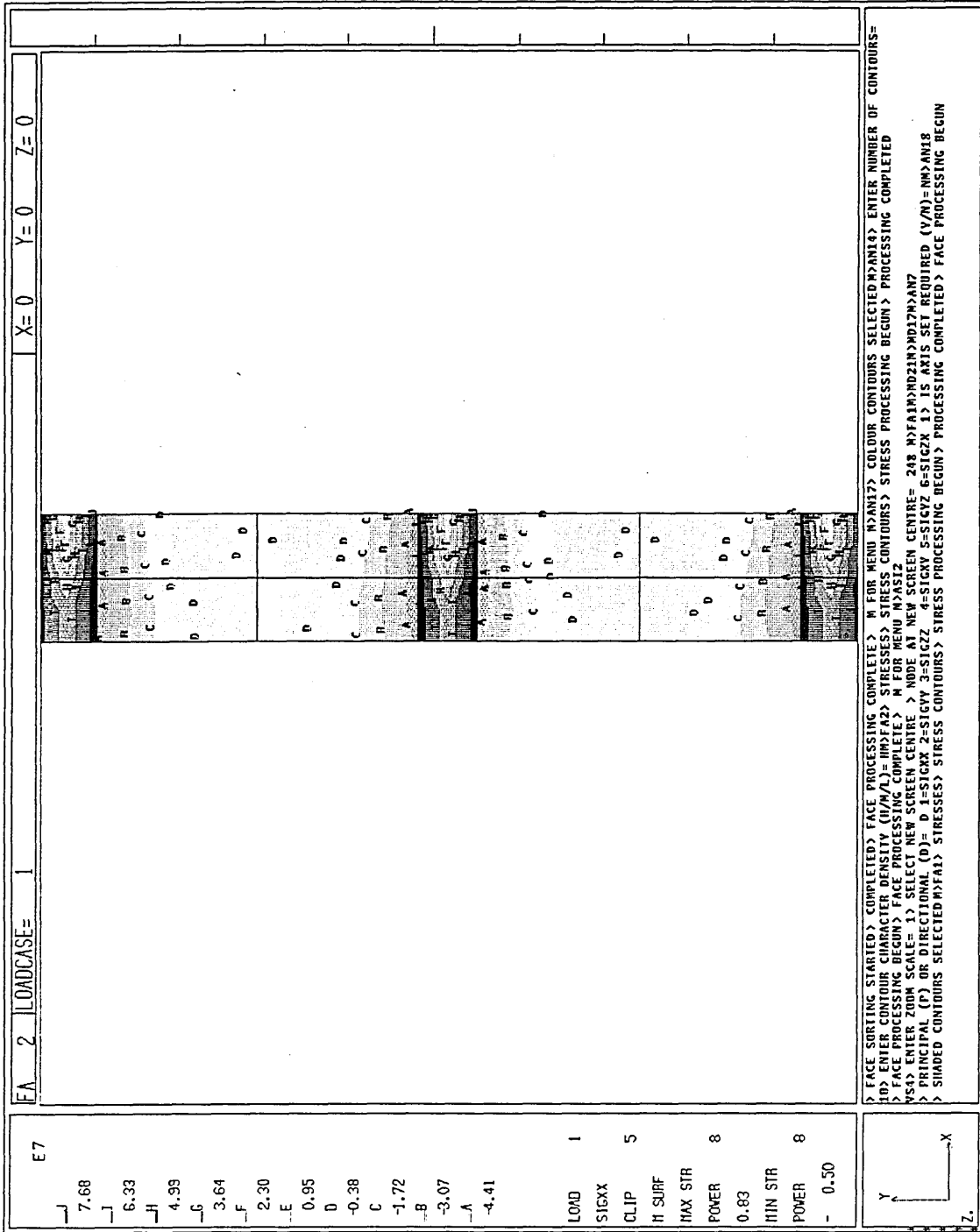


Figure 43.  $\sigma_{xx}$  stress, unaveraged, centre - model ASI2 (double mesh)



Figure 44.  $\sigma_{xx}$  stress, top - model ASI2 (double mesh)

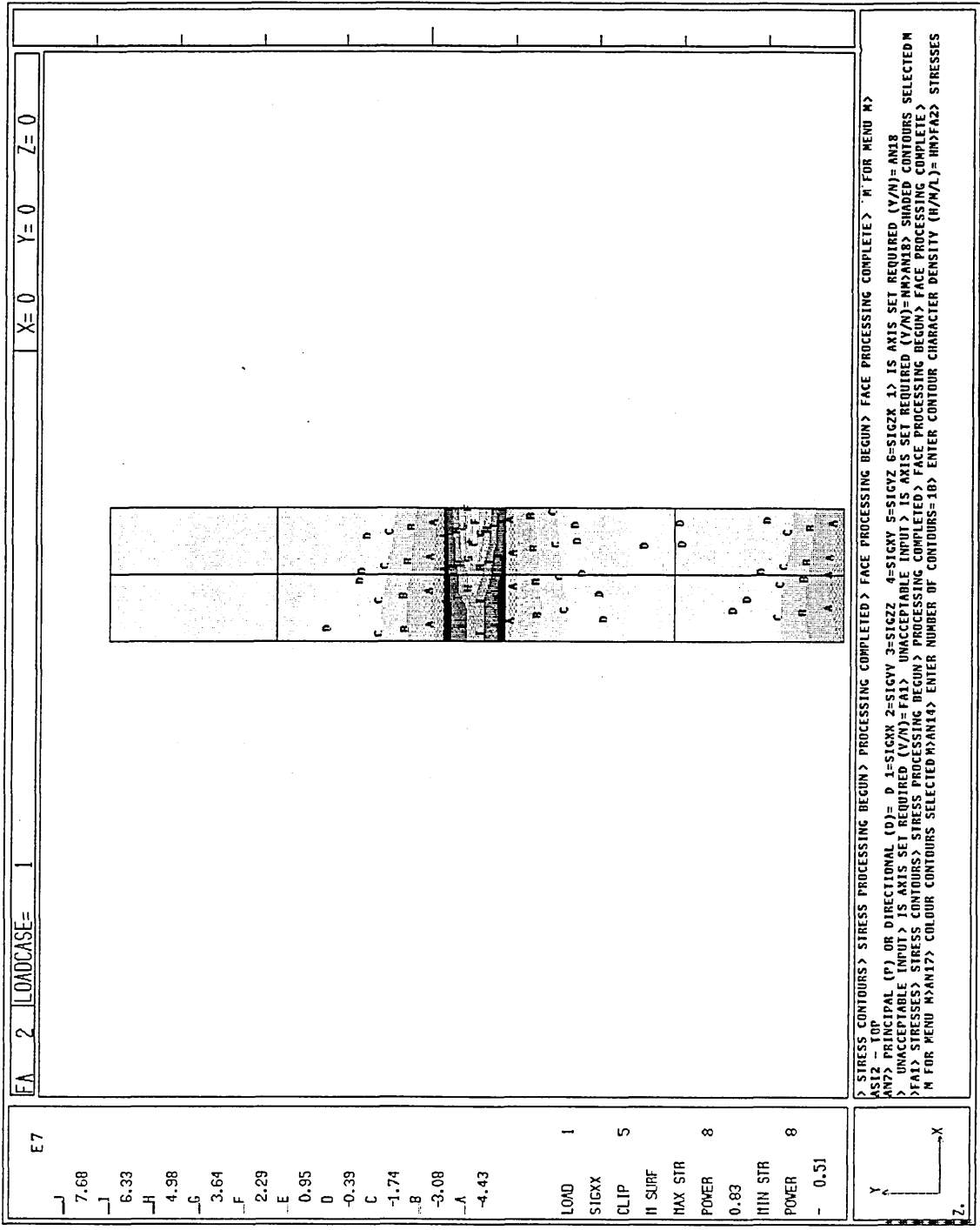


Figure 45.  $\sigma_{xx}$  stress, bottom - model ASI2 (double mesh)

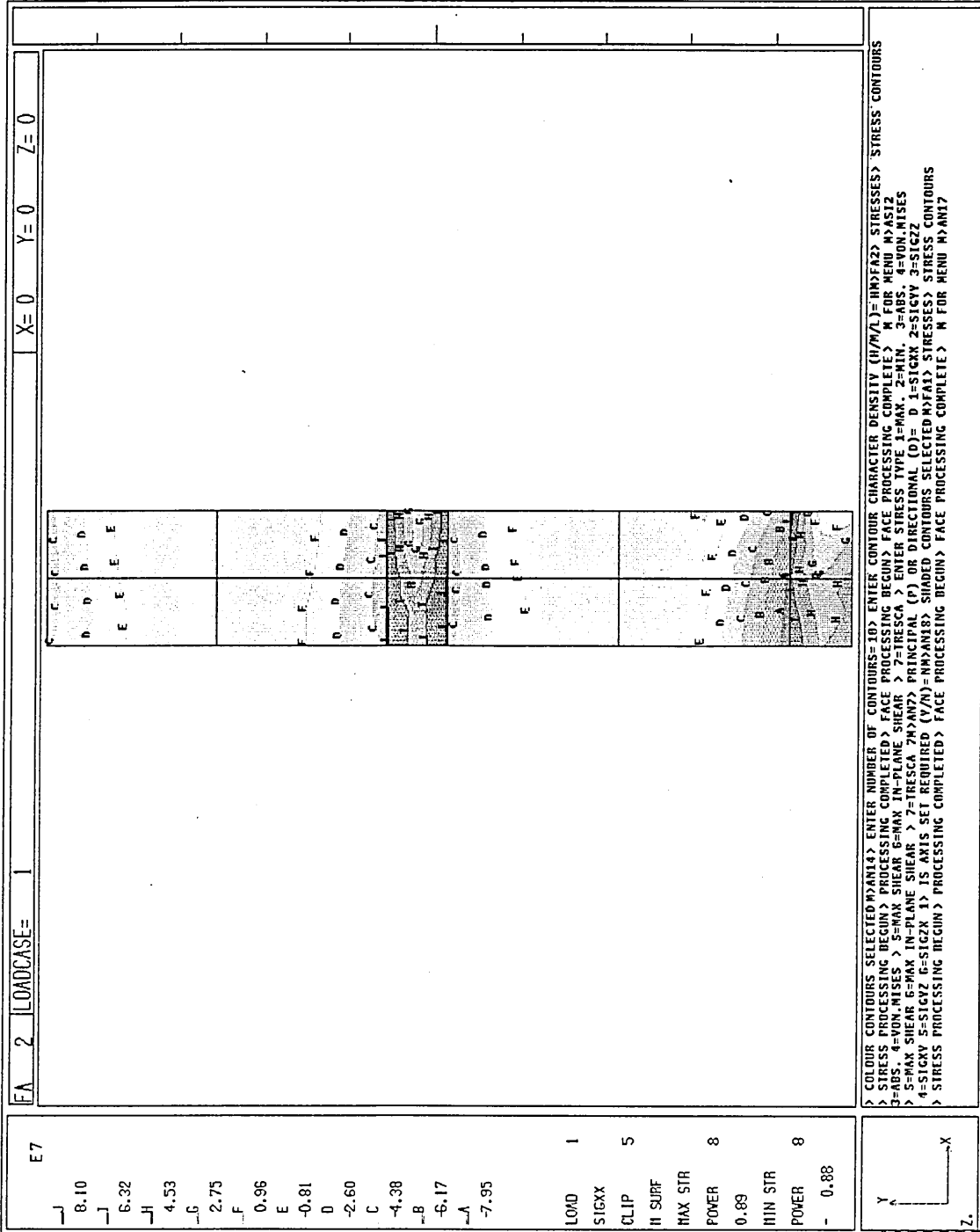


Figure 46.  $\sigma_{yy}$  stress, centre - model ASI2 (double mesh)

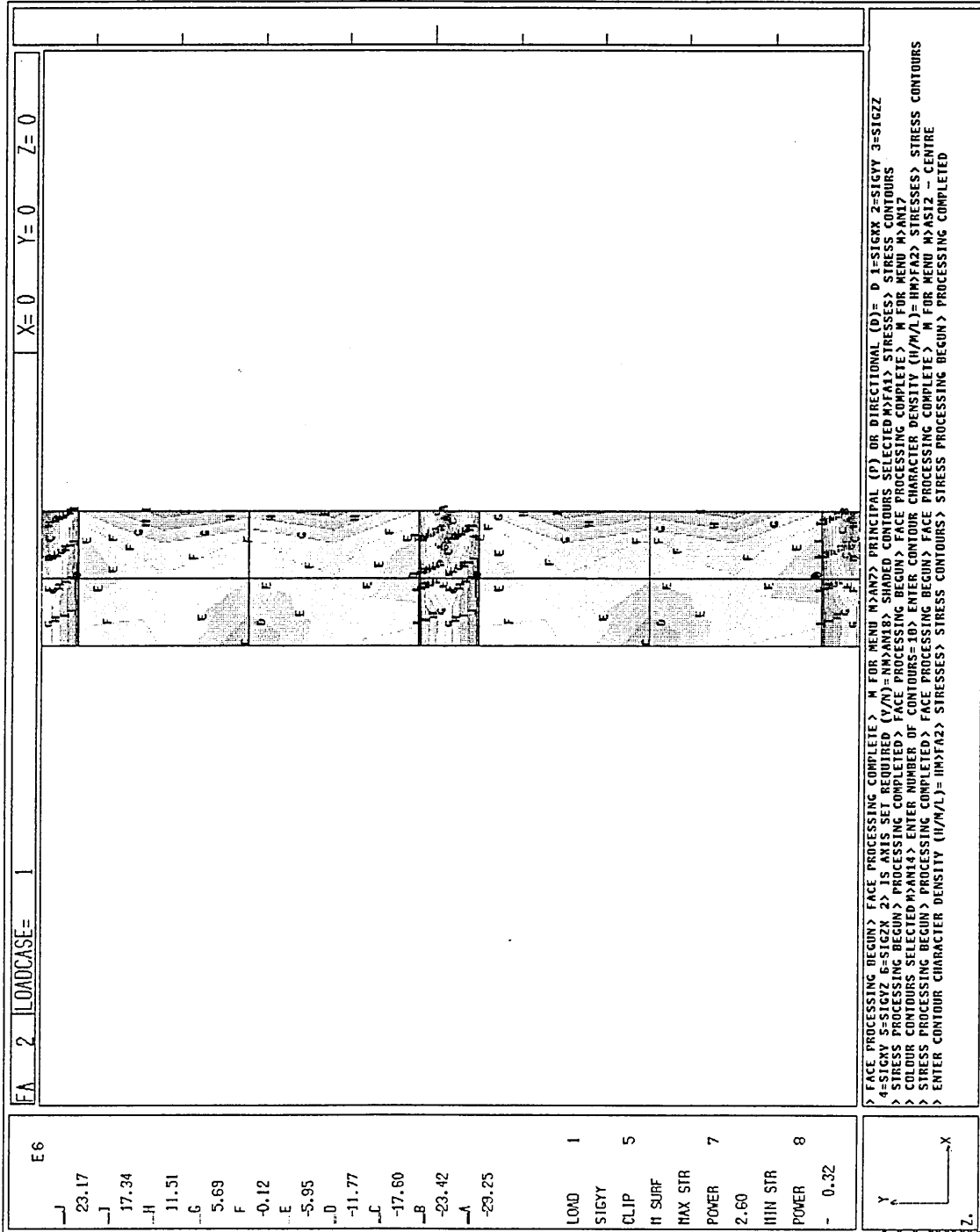
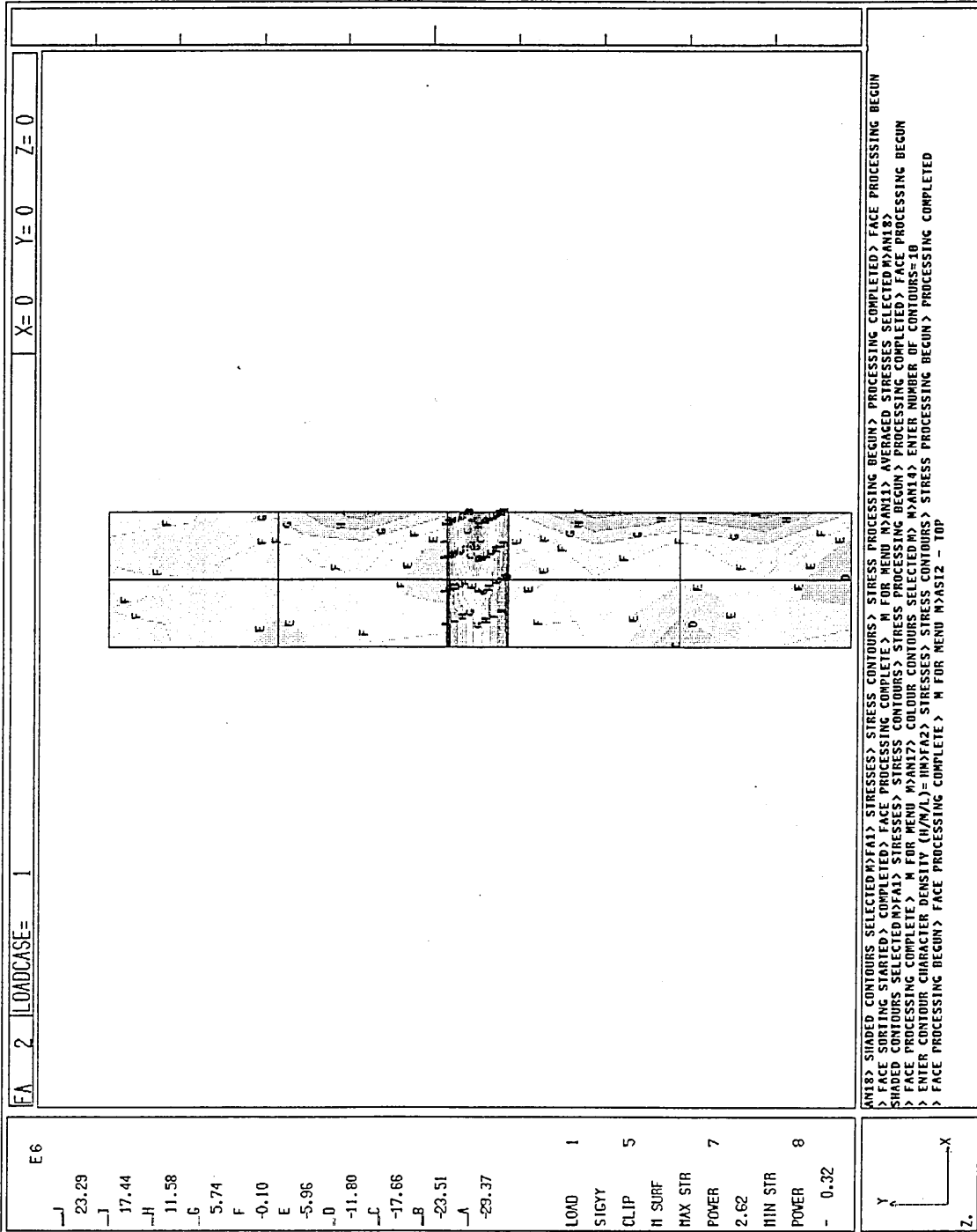


Figure 47.  $\sigma_{yy}$  stress, unaveraged, centre - model ASI2 (double mesh)



Figure 48.  $\sigma_{yy}$  stress, top - model ASI2 (double mesh)



ANIS> SHADED CONTOURS SELECTED (NFA1) STRESSES STRESS CONTOURS STRESS PROCESSING BEGUN STRESS PROCESSING COMPLETED > FACE PROCESSING BEGUN  
 > FACE SORTING STARTED COMPLETED (A) STRESSES STRESS CONTOURS STRESS PROCESSING BEGUN AVERAGED STRESSES SELECTED (NAN18)  
 SHADED CONTOURS SELECTED (NFA1) STRESSES STRESS CONTOURS STRESS PROCESSING BEGUN STRESS CONTOURS STRESS PROCESSING COMPLETED > FACE PROCESSING BEGUN  
 > FACE PROCESSING COMPLETE > M FOR MENU (NAN17) COLOR CONTOURS SELECTED (NFA1) STRESSES STRESS CONTOURS STRESS PROCESSING BEGUN  
 > ENTER CONTOUR CHARACTER DENSITY (H/W/A)= (H/W/A)= (H/W/A)= STRESSES STRESS CONTOURS STRESS PROCESSING BEGUN STRESS PROCESSING COMPLETED  
 > FACE PROCESSING BEGUN > FACE PROCESSING COMPLETE > M FOR MENU (NAN12) - 10P

Figure 49.  $\sigma_{yy}$  stress, bottom - model ASI2 (double mesh)

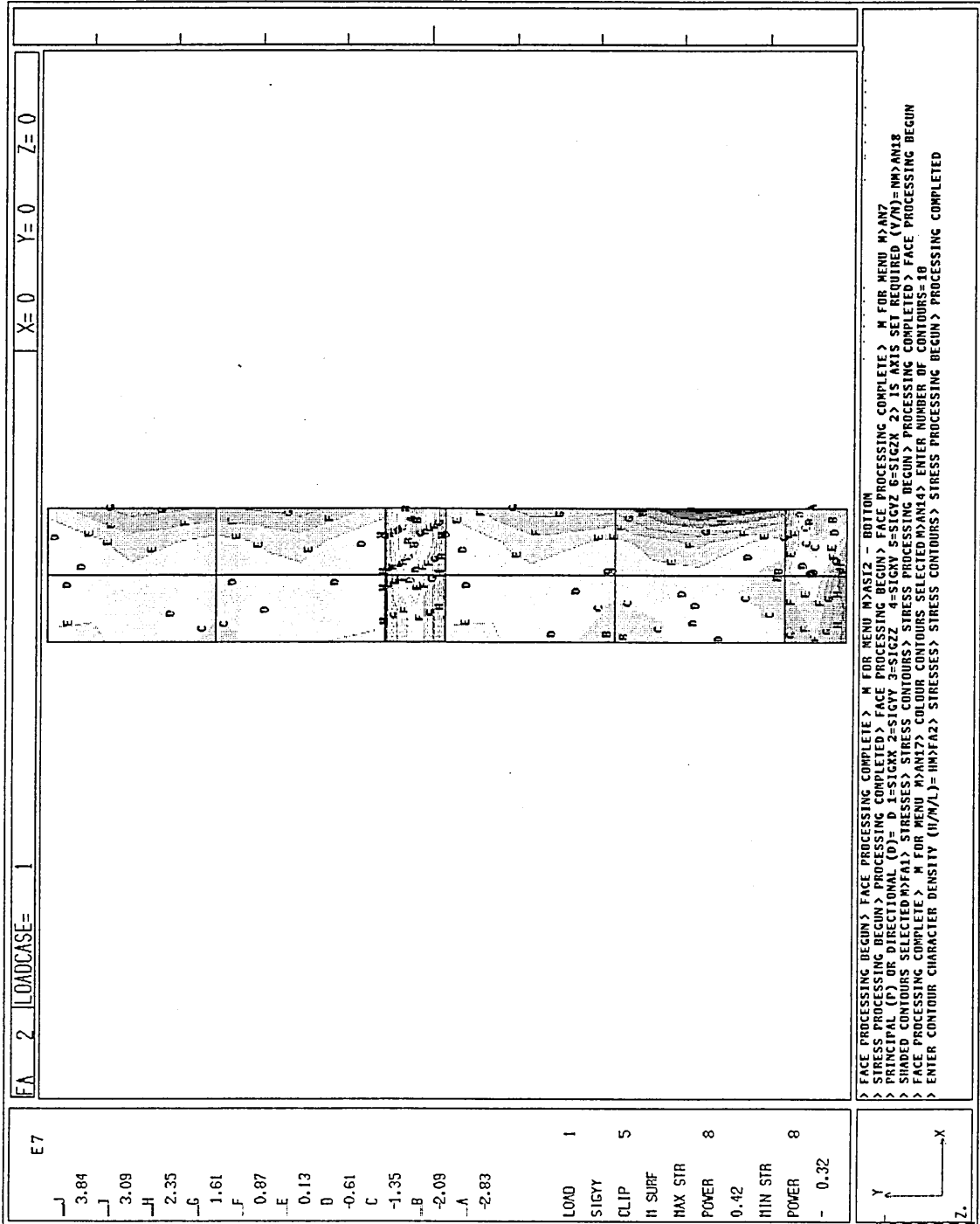
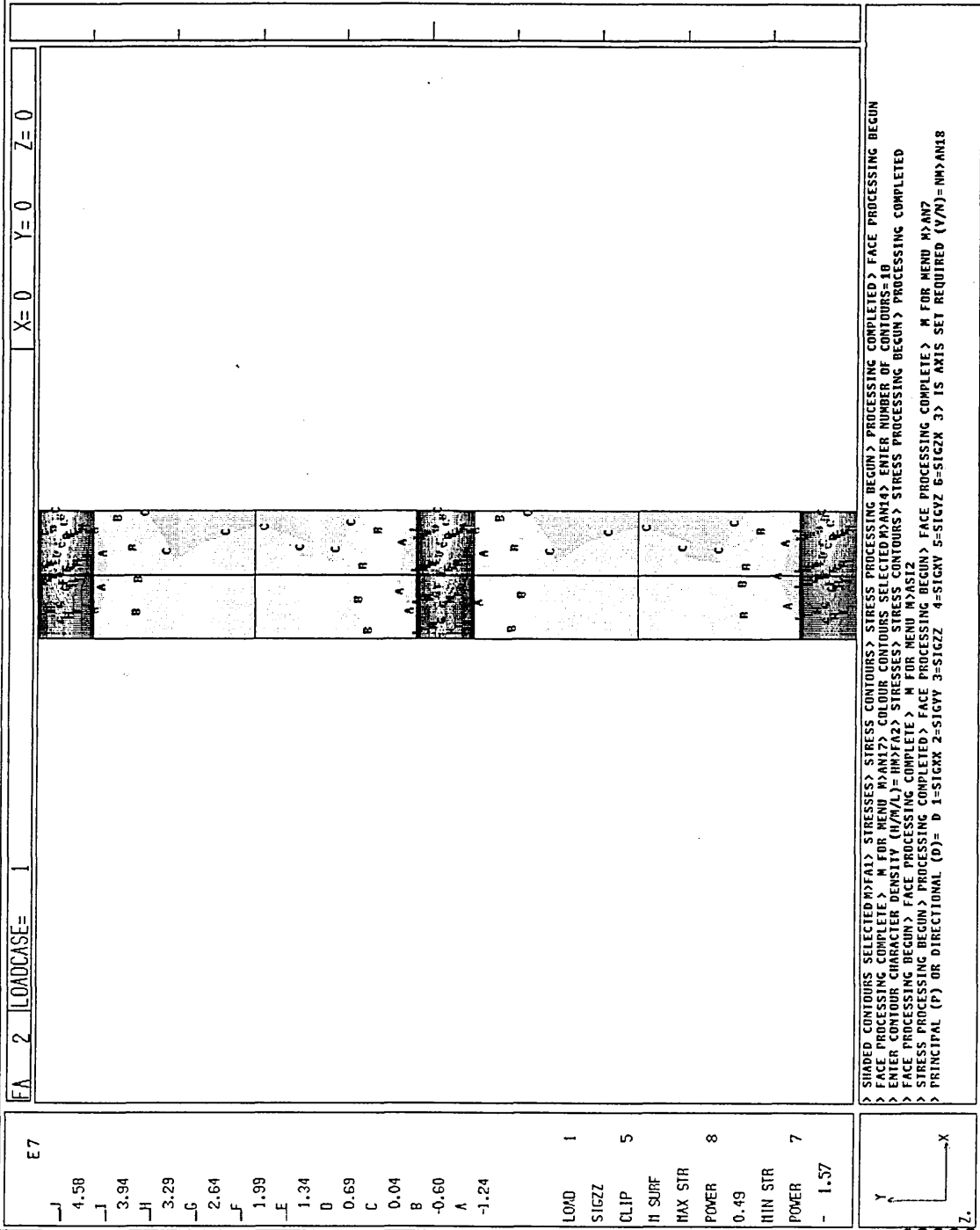


Figure 50.  $\sigma_{zz}$  stress, centre - model ASI2 (double mesh)



E7

_J	4.58
_I	3.94
_H	3.29
_G	2.64
_F	1.99
_E	1.34
D	0.69
C	0.04
B	-0.60
A	-1.24

LOAD	1
SIGZZ	5
CLIP	
H SURF	
MAX STR	8
POWER	0.49
MIN STR	
POWER	7
-	1.57

> SHADED CONTOURS SELECTED (M)FA1 > STRESSES > STRESS CONTOURS > STRESS PROCESSING BEGUN > PROCESSING COMPLETED > FACE PROCESSING BEGUN  
 > FACE PROCESSING COMPLETE > M FOR MENU (M)A12 > COLOUR CONTOURS SELECTED (M)A14 > ENTER NUMBER OF CONTOURS= 10  
 > ENTER CONTOUR CHARACTER DENSITY (H/W/L)= (H)M(F)A2 > STRESSES > STRESS CONTOURS > STRESS PROCESSING BEGUN > PROCESSING COMPLETED  
 > FACE PROCESSING BEGUN > FACE PROCESSING COMPLETE > M FOR MENU (M)A12  
 > STRESS PROCESSING BEGUN > PROCESSING COMPLETED > FACE PROCESSING COMPLETE > M FOR MENU (M)A7  
 > PRINCIPAL (P) OR DIRECTIONAL (D)= D 1=SIGXX 2=SIGYY 3=SIGZZ 4=SIGNV 5=SIGVZ 6=SIGZX 3> IS AXIS SET REQUIRED (Y/N)= (Y/N)A18

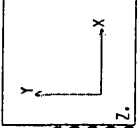


Figure 51.  $\sigma_{zz}$  stress, unaveraged, centre - model ASI2 (double mesh)

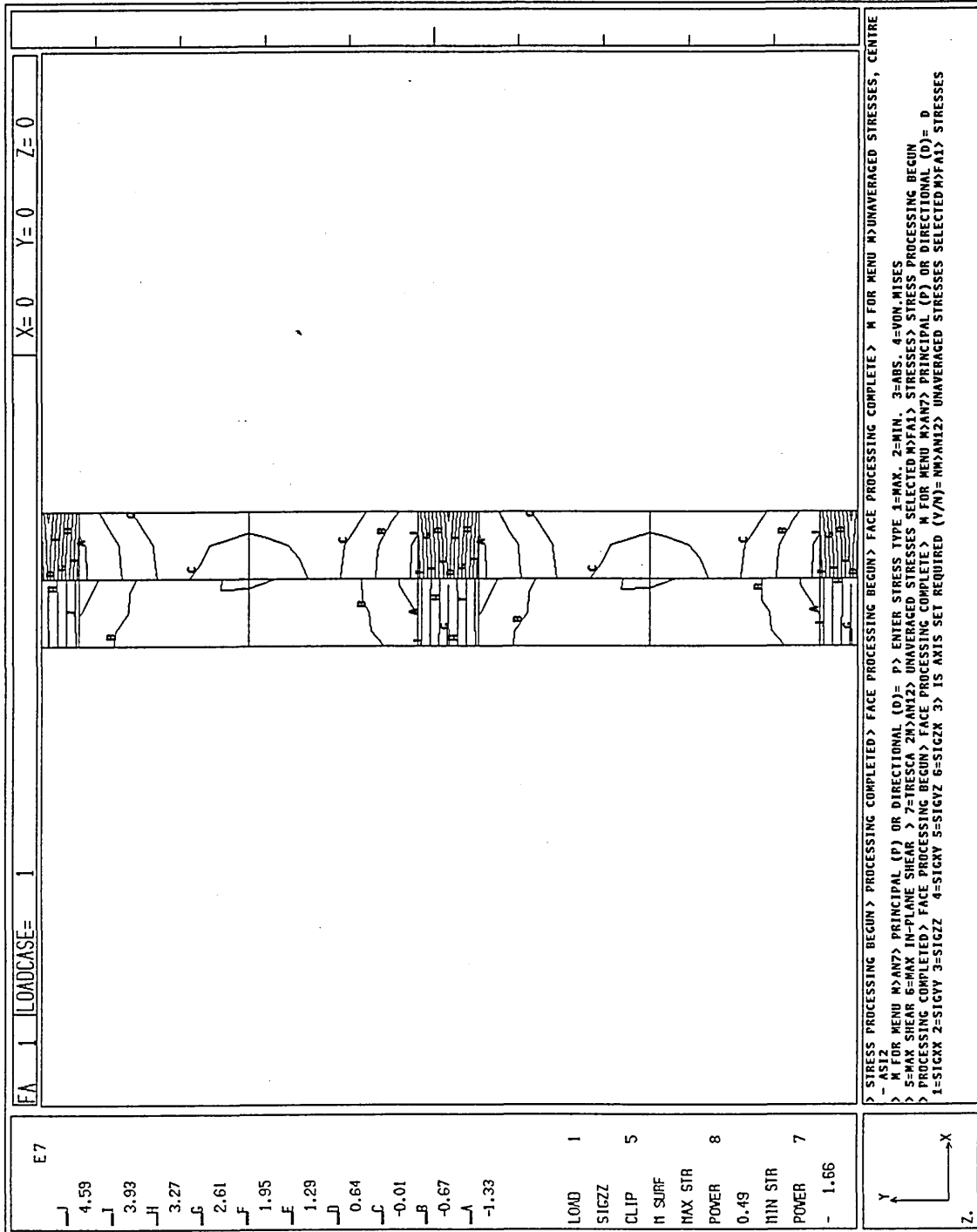


Figure 52.  $\sigma_{zz}$  stress, top - model ASI2 (double mesh)

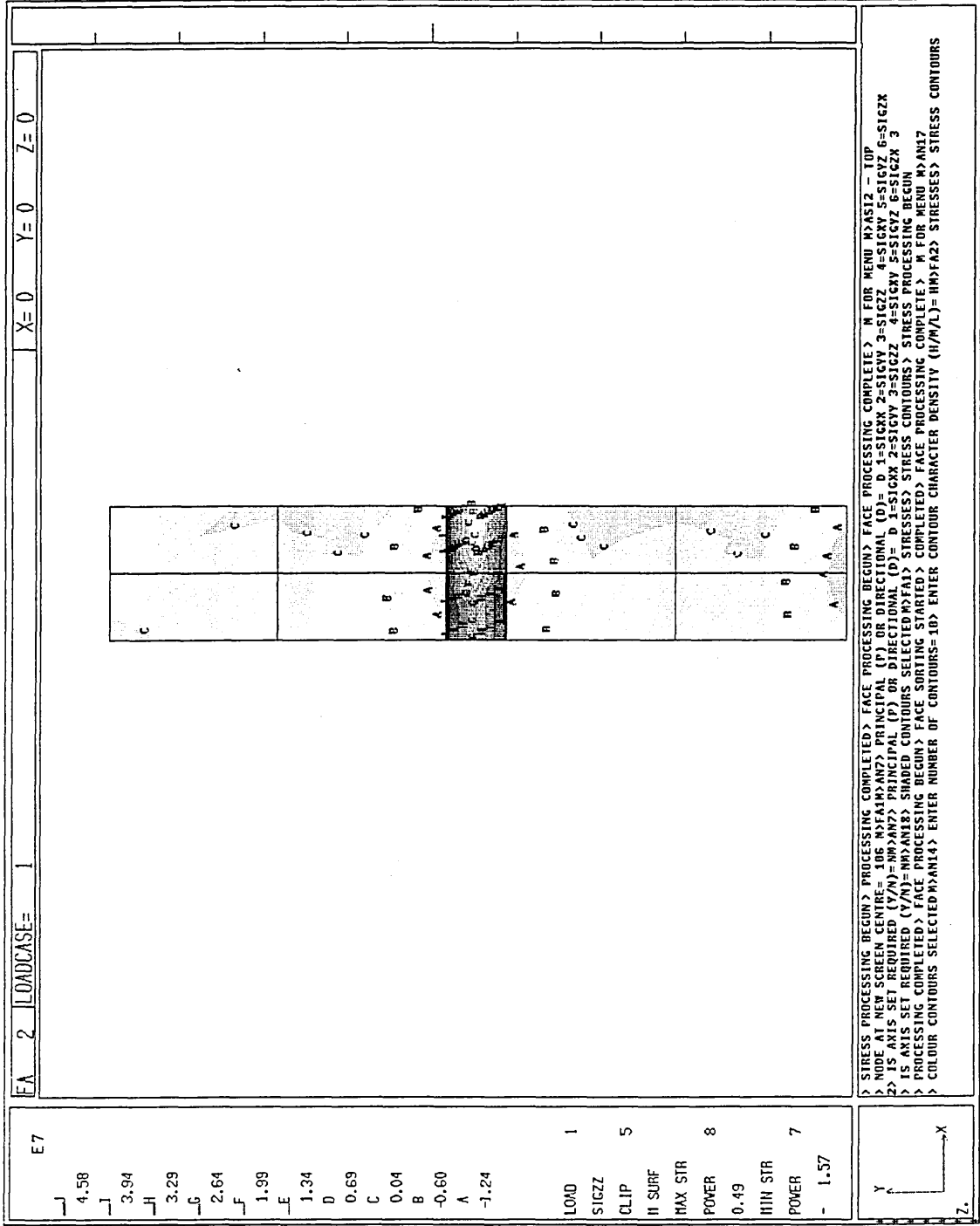


Figure 53.  $\sigma_{zz}$  stress, bottom - model ASI2 (double mesh)

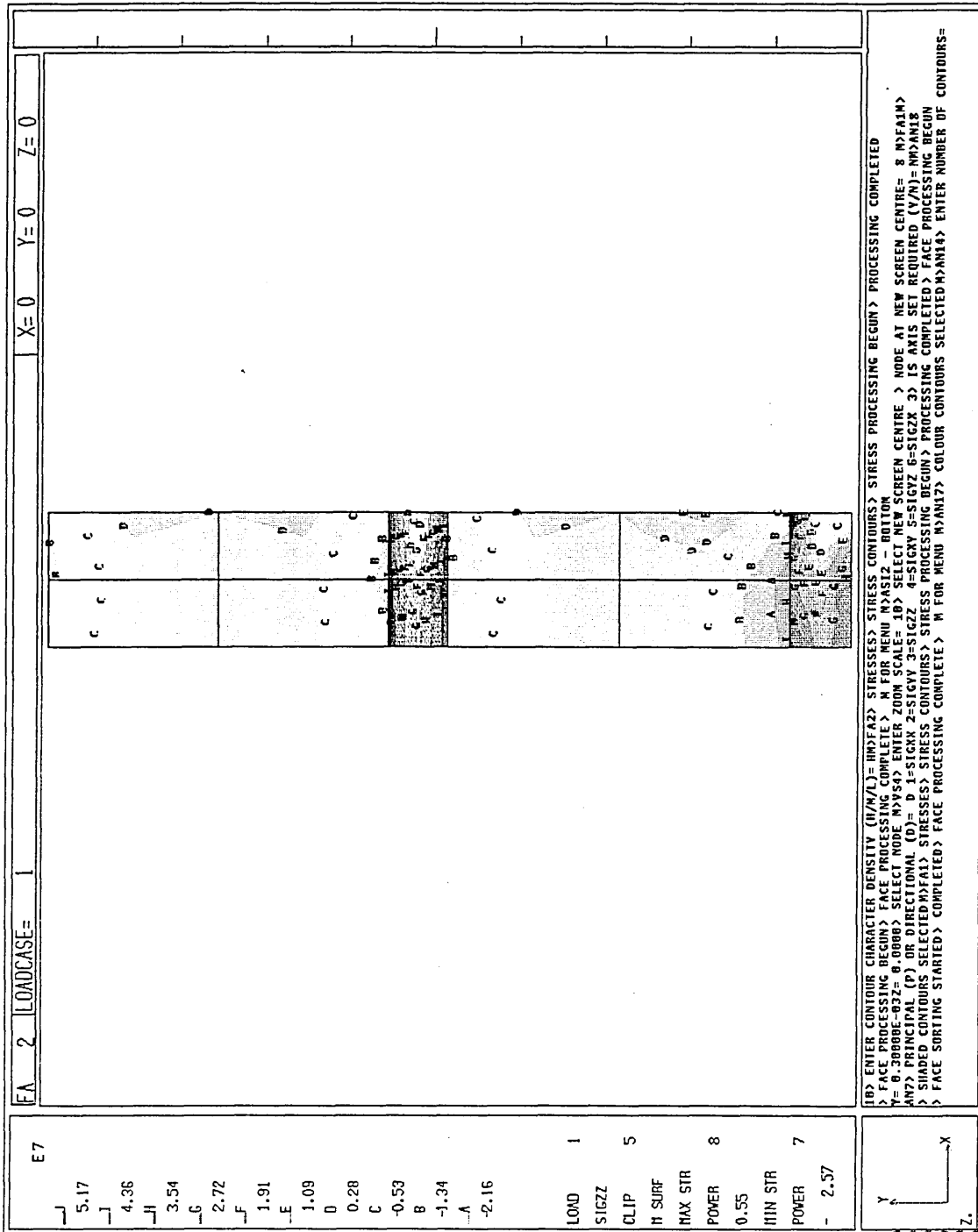


Figure 54.  $\sigma_{xy}$  stress, centre - model ASI2 (double mesh)

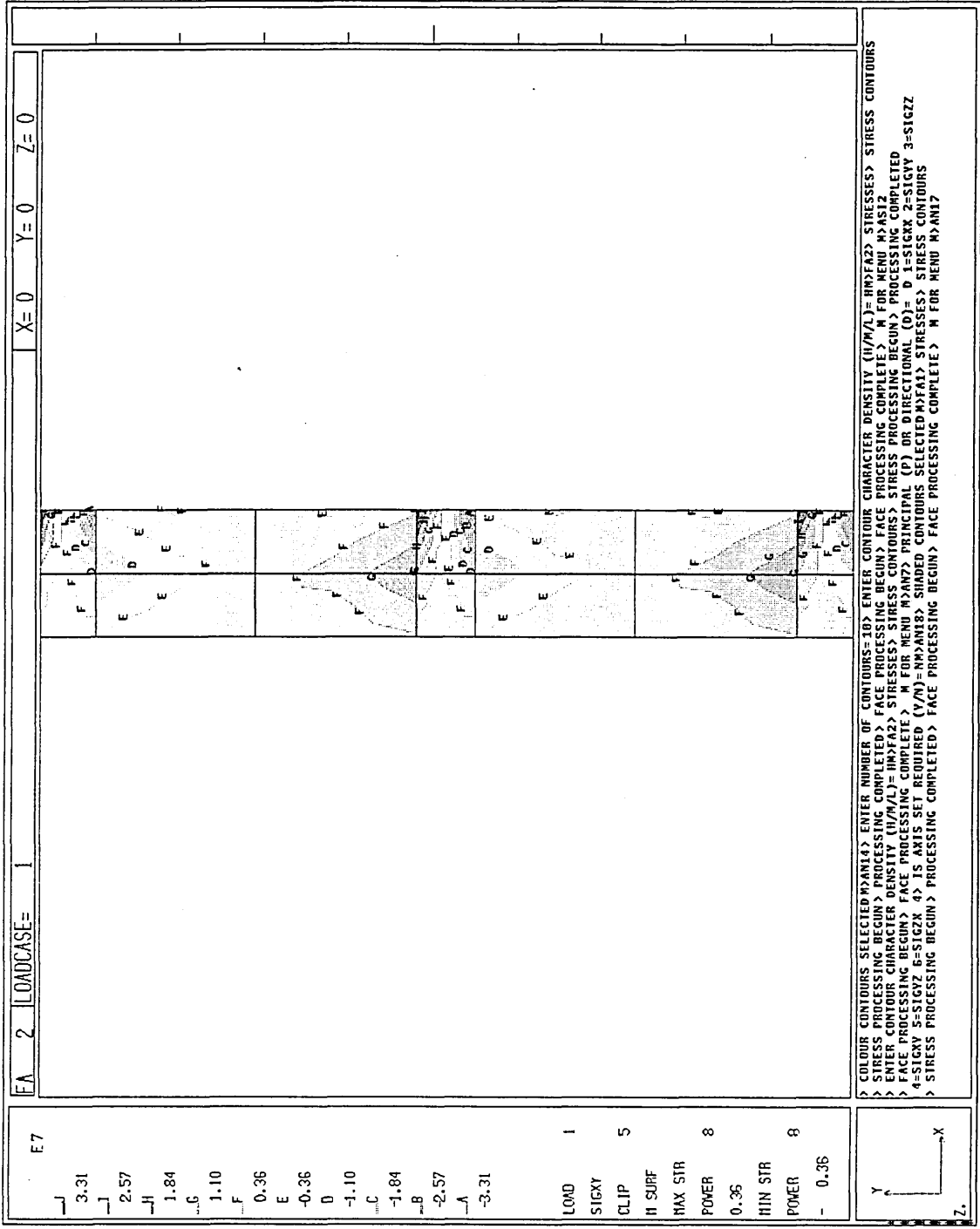


Figure 55.  $\sigma_{xy}$  stress, unaveraged, centre - model ASI2 (double mesh)

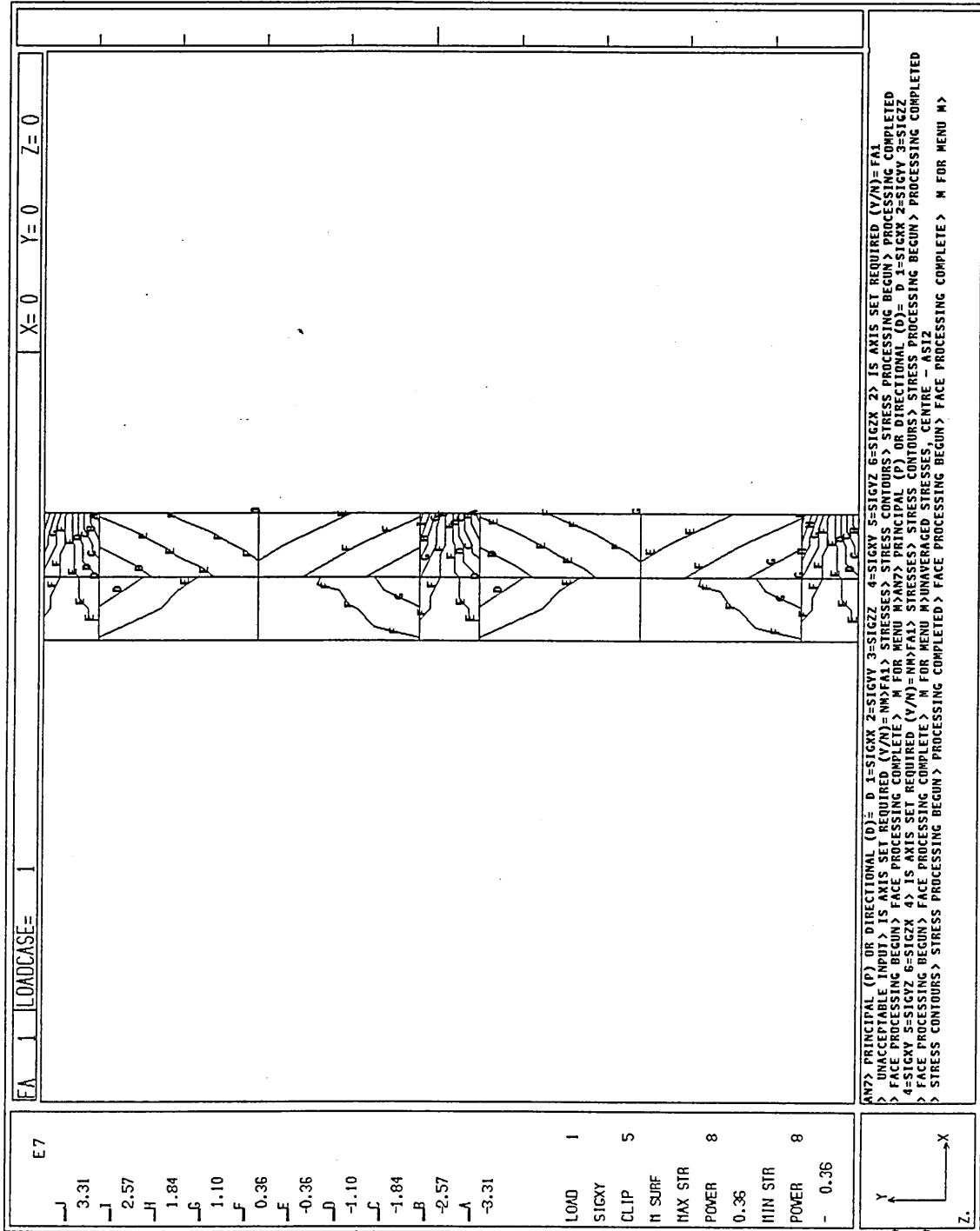


Figure 56.  $\sigma_{xy}$  stress, top - model ASI2 (double mesh)

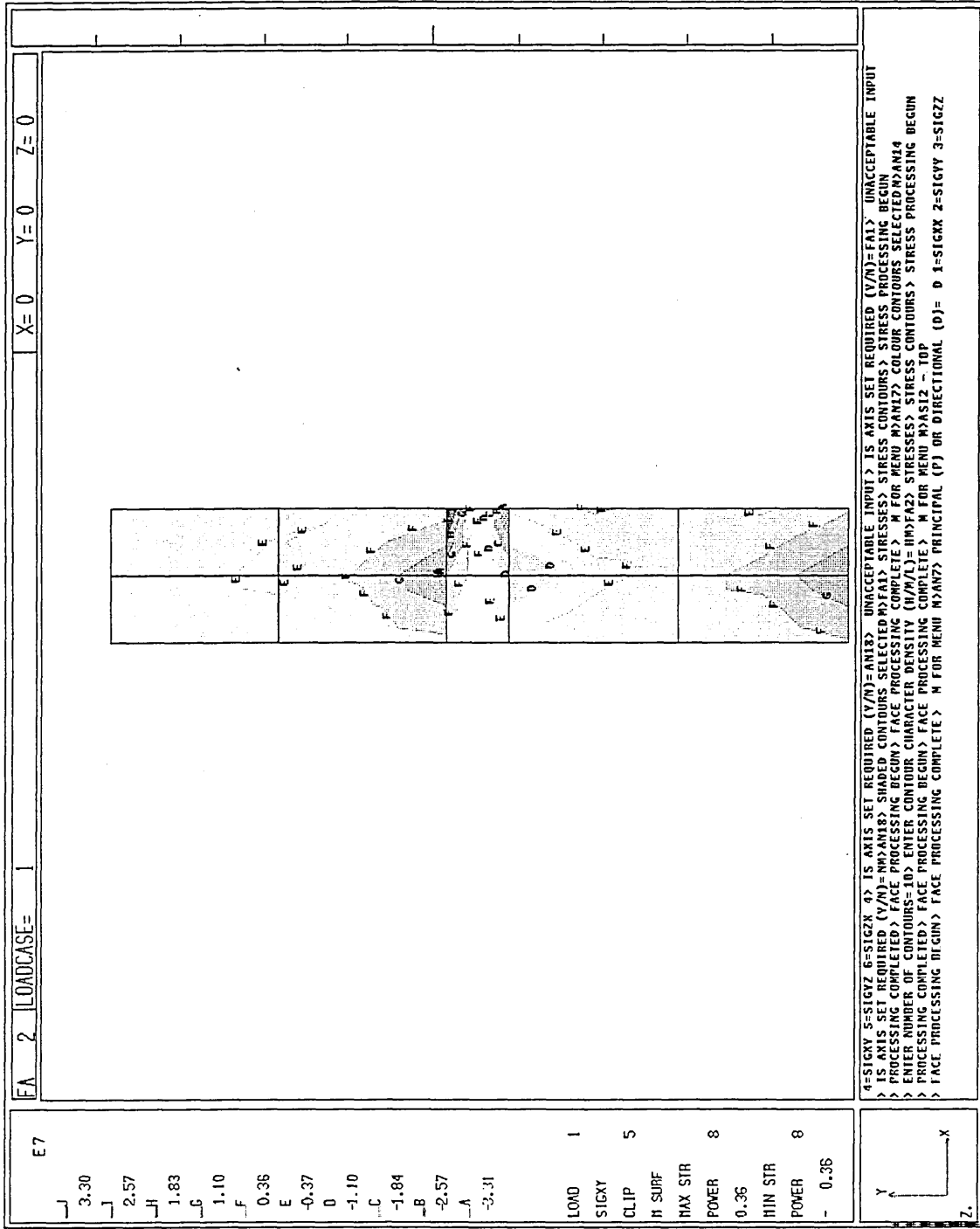


Figure 57.  $\sigma_{xy}$  stress, bottom - model ASI2 (double mesh)

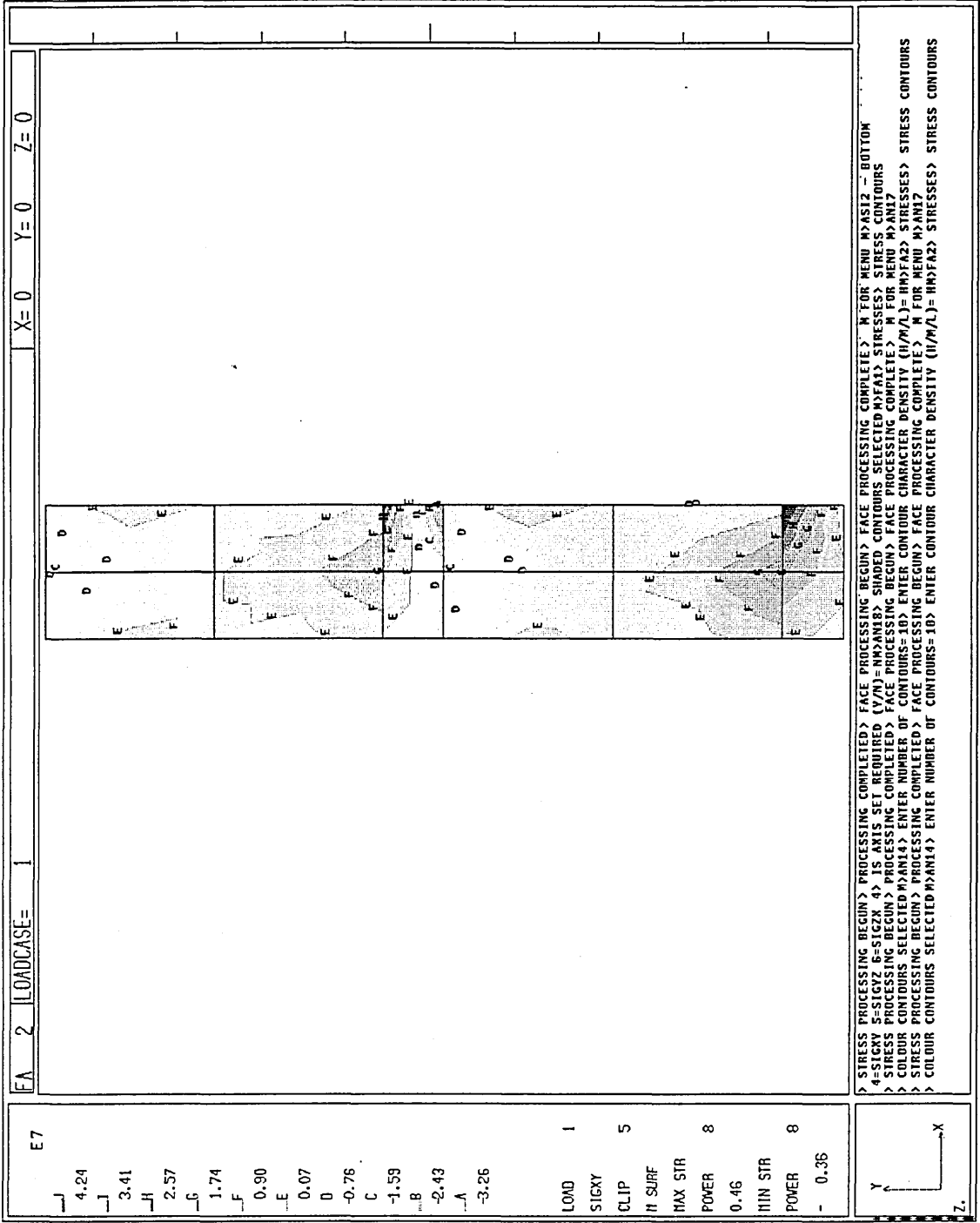


Figure 58.  $\sigma_{yz}$  stress, centre - model ASI2 (double mesh)



Figure 59.  $\sigma_{zx}$  stress, centre - model ASI2 (double mesh)

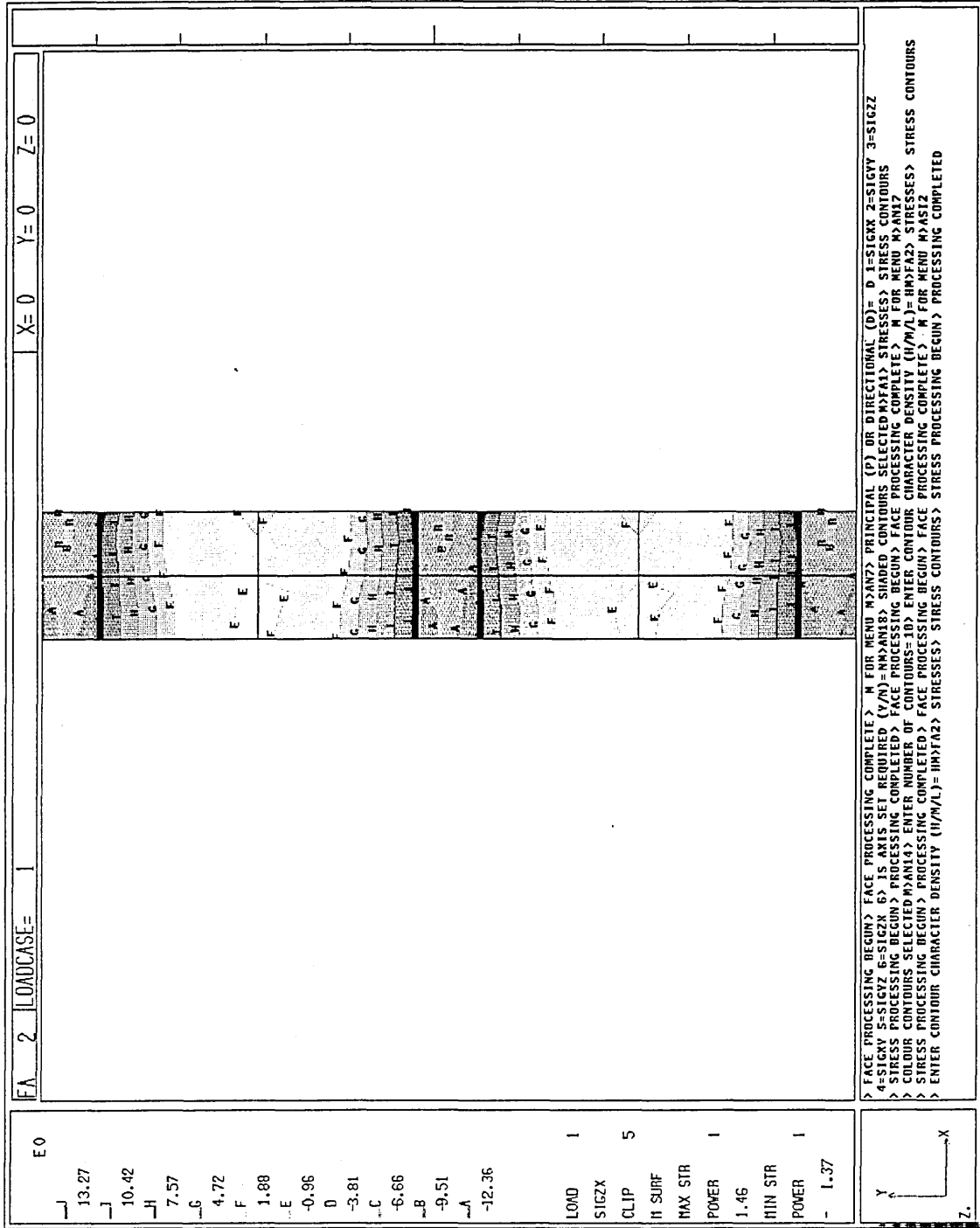
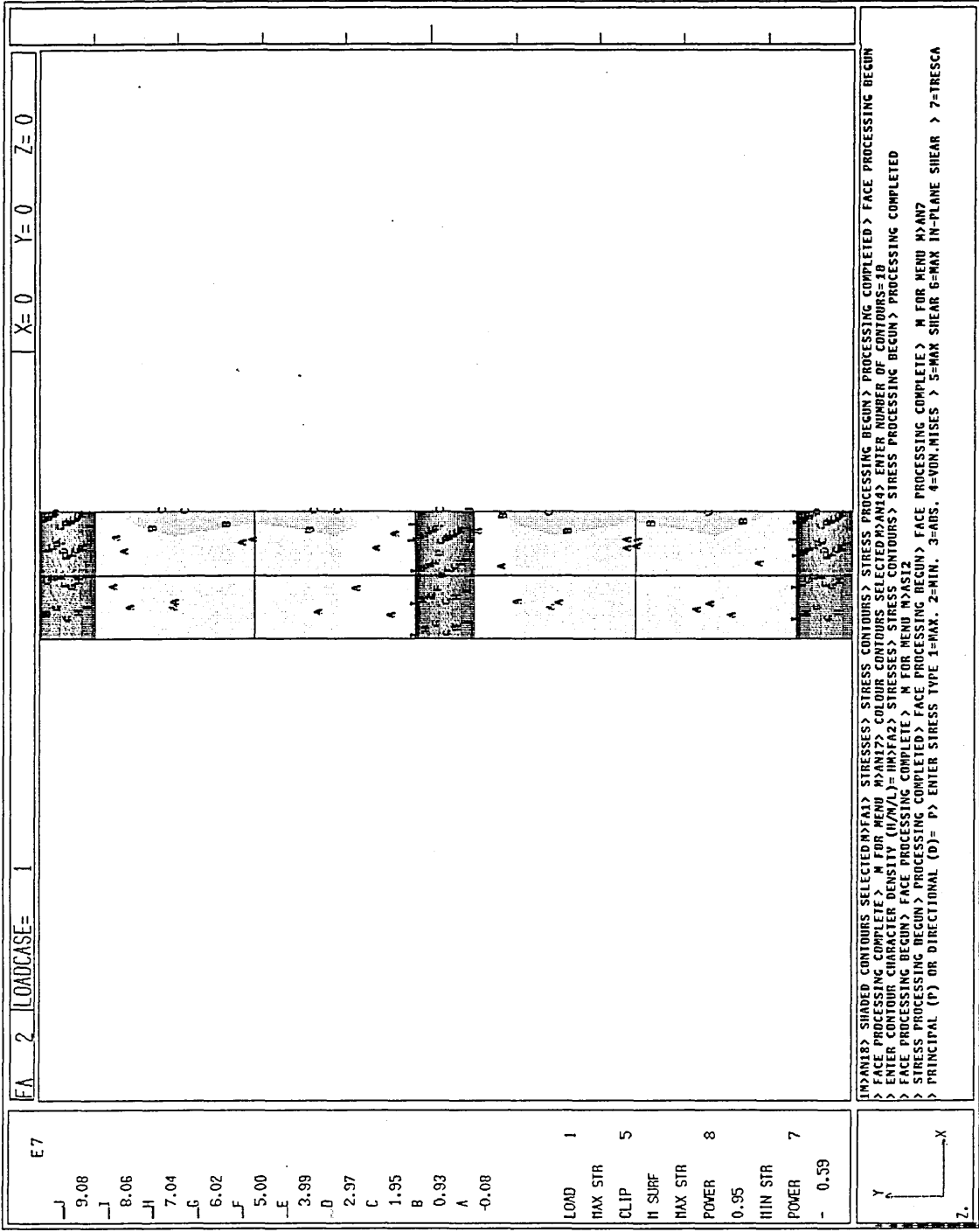


Figure 60. Maximum principal stress, centre - model ASI2 (double mesh)



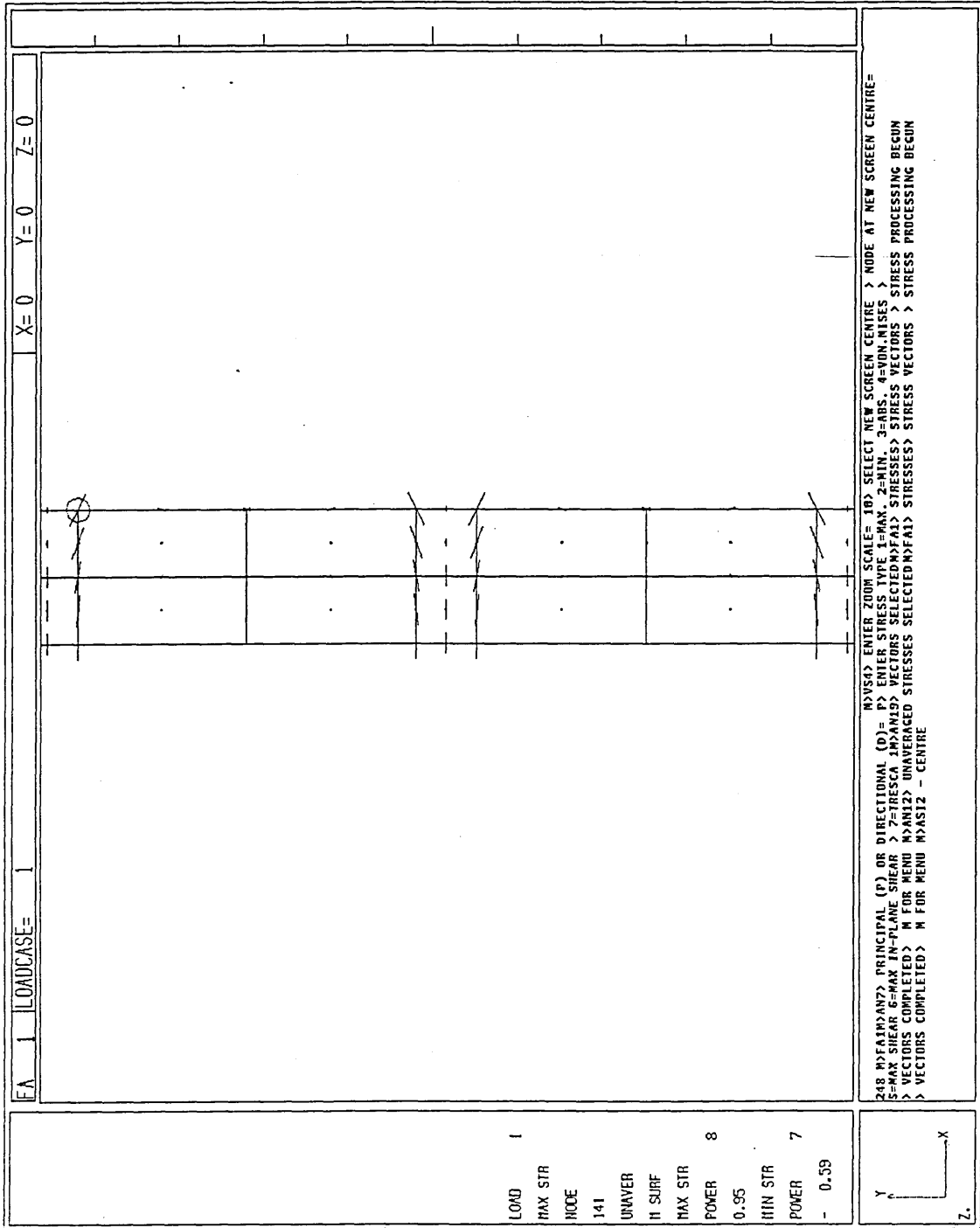


Figure 62. Maximum principal stress, unaveraged, centre - model ASI2  
(double mesh)

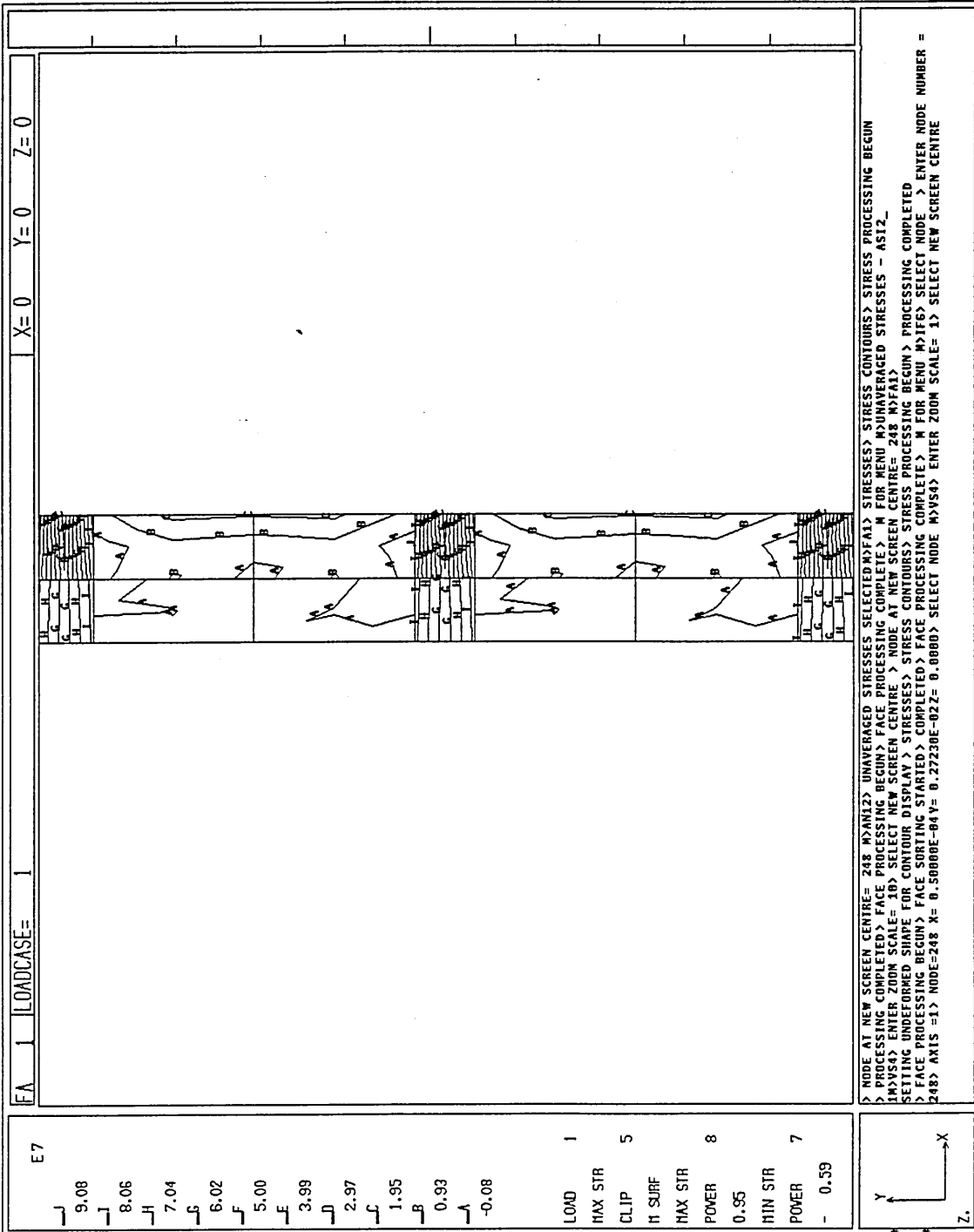


Figure 63. Maximum principal stress, top - model ASI2 (double mesh)

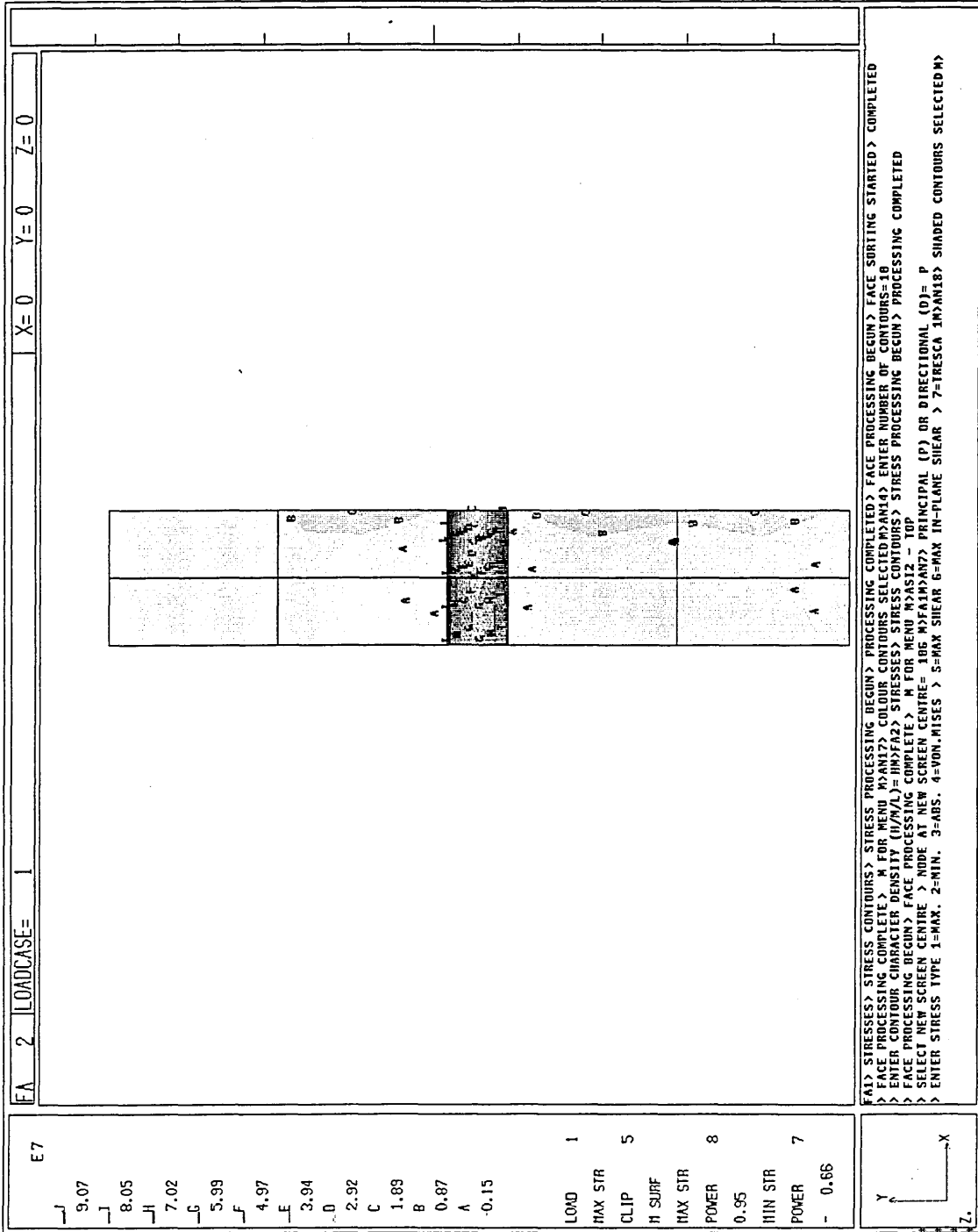


Figure 64. Maximum principal stress, bottom - model ASI2 (double mesh)

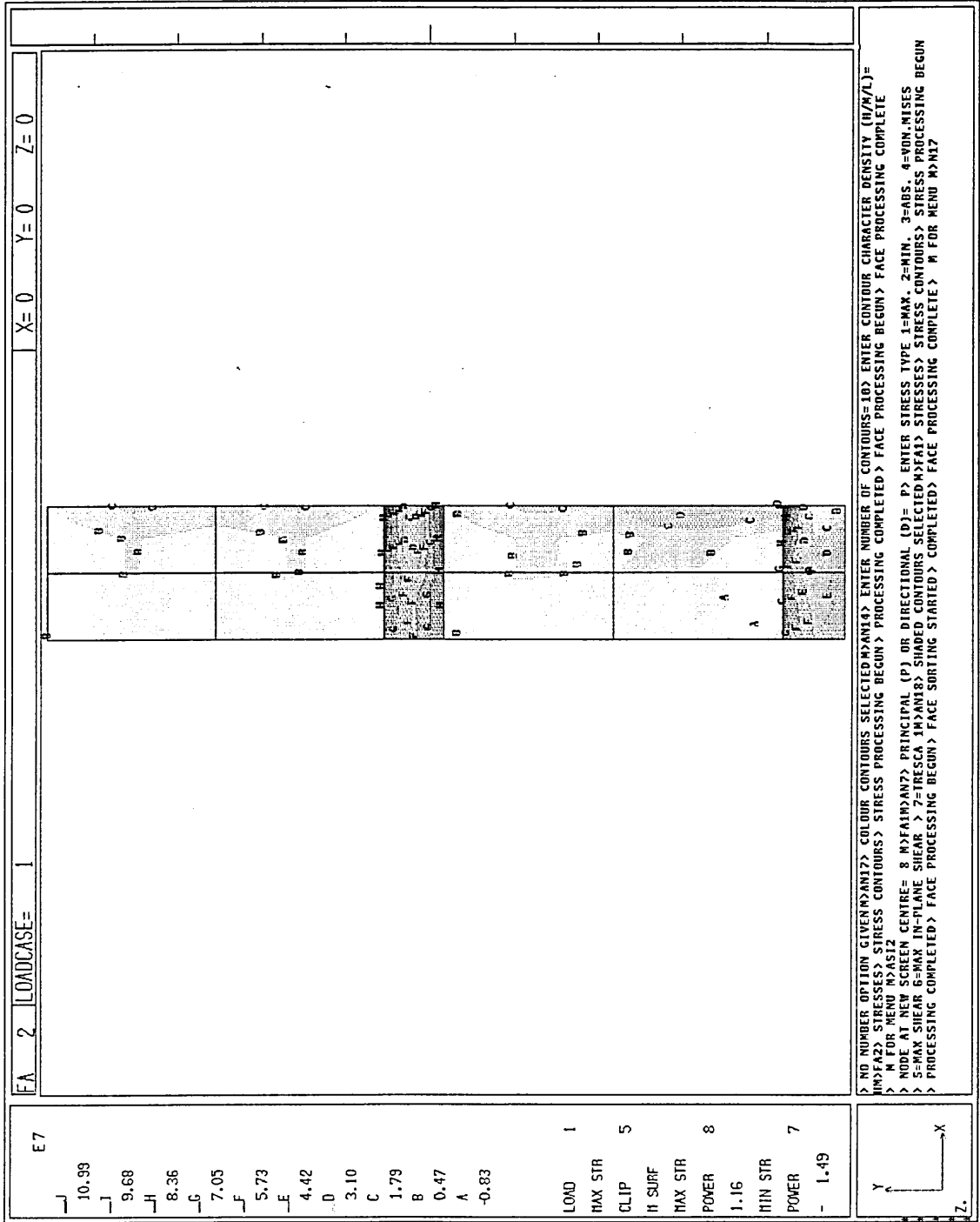


Figure 65. Minimum principal stress, centre - model ASI2 (double mesh)

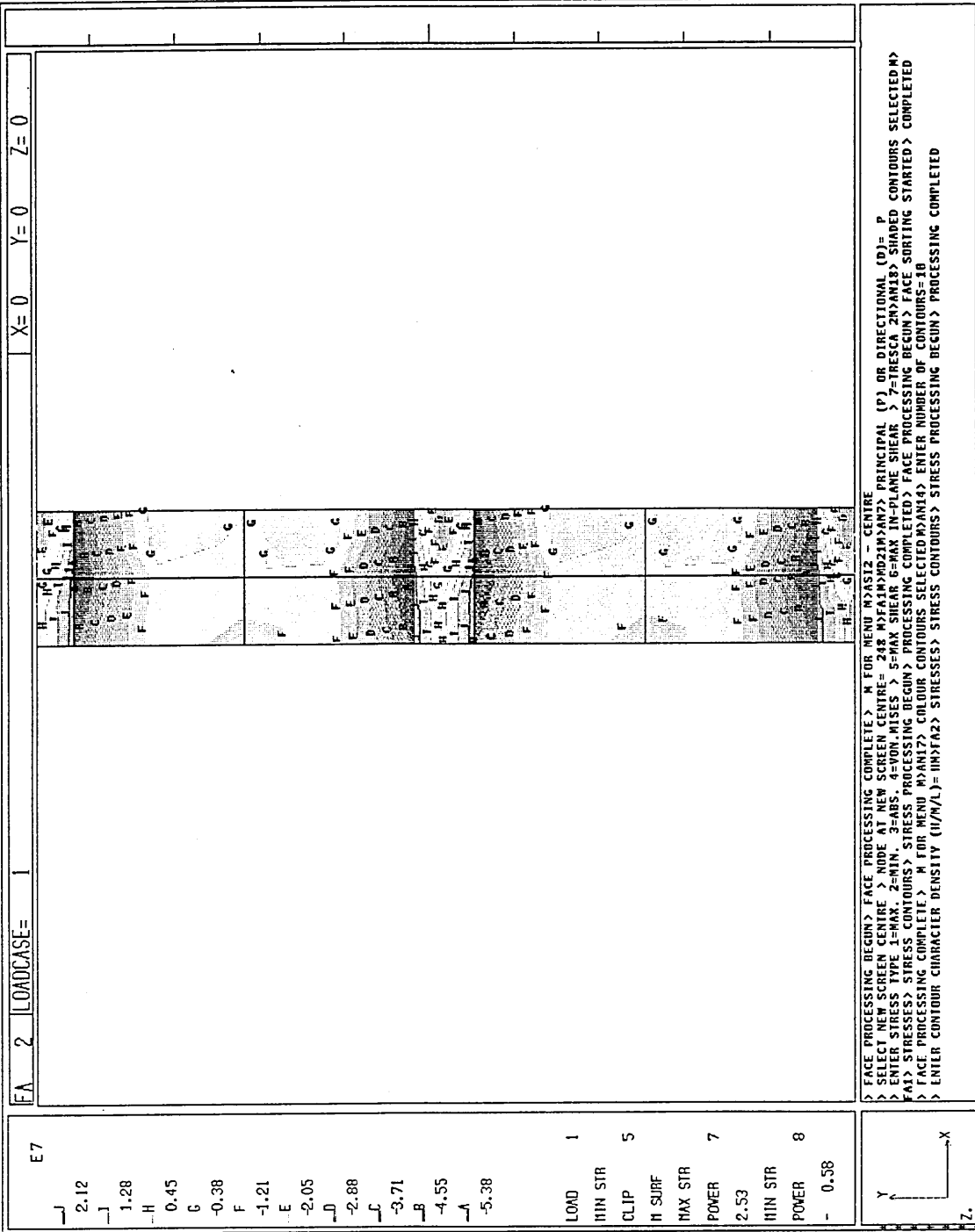


Figure 66. Minimum principal stress vectors, centre - model ASI2  
(double mesh)

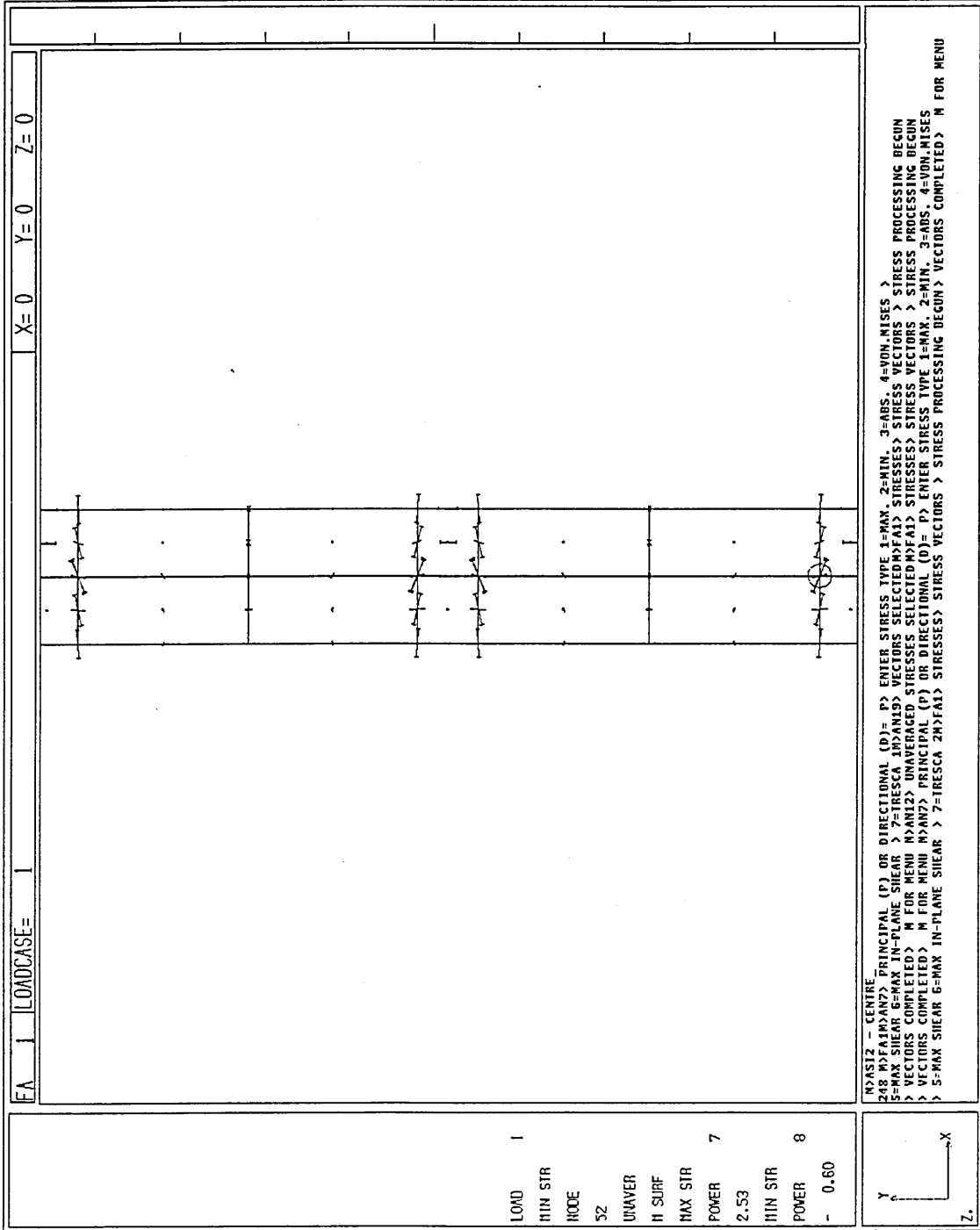


Figure 67. Minimum principal stress, unaveraged, centre - model ASI2  
(double mesh)

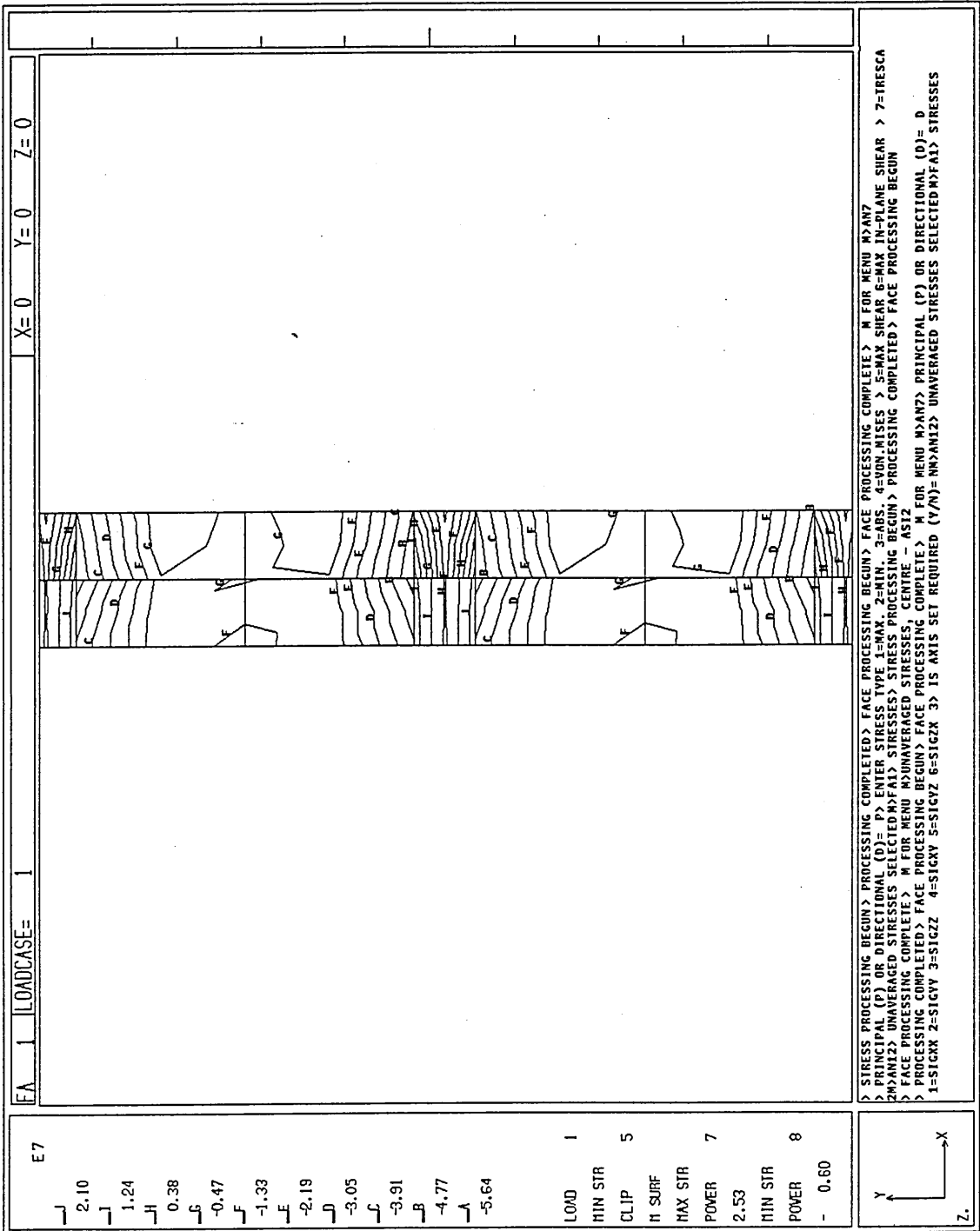


Figure 68. Minimum principal stress, top - model ASI2 (double mesh)

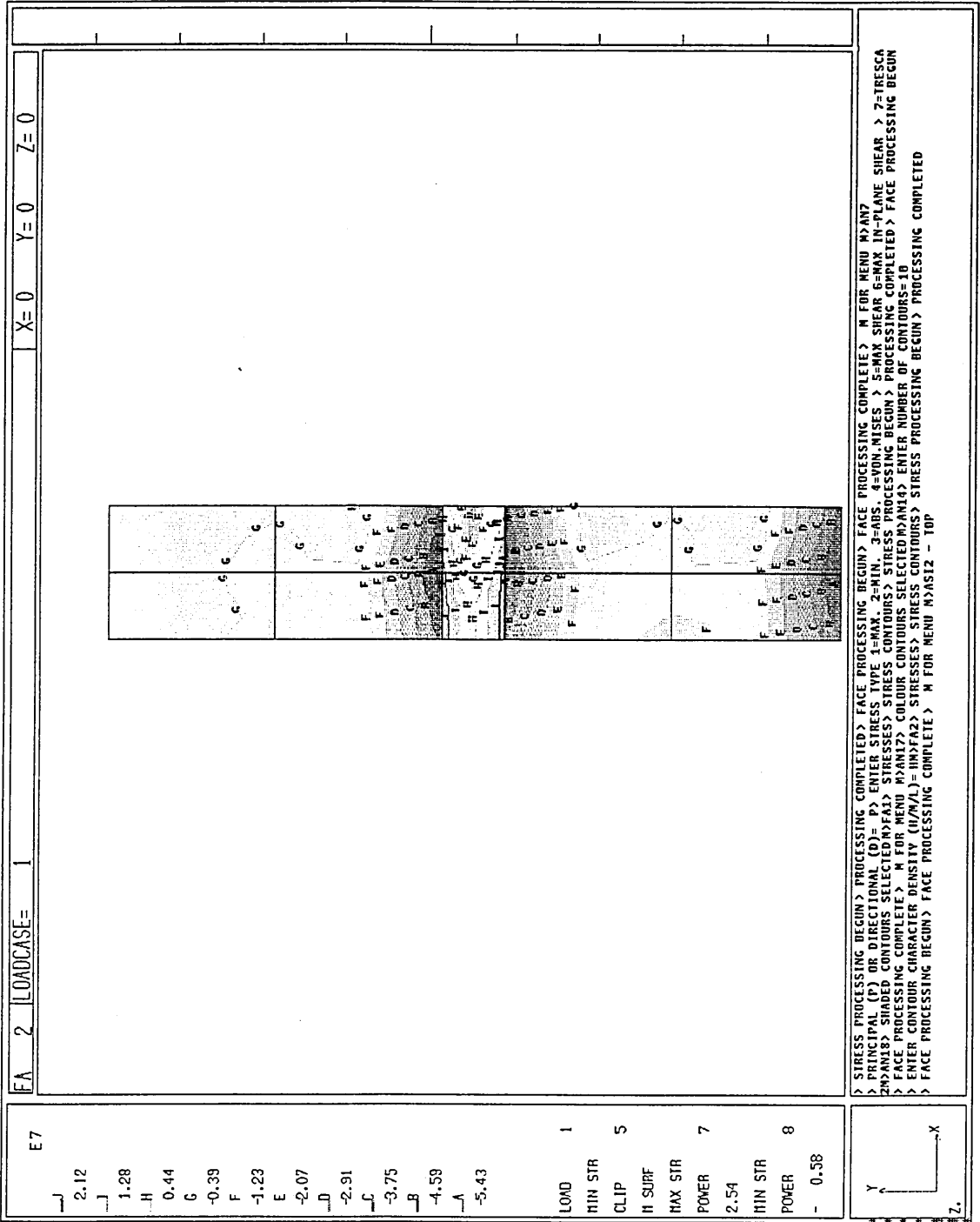


Figure 69. Minimum principal stress, bottom - model ASI2 (double mesh)



Figure 70. Von Mises stress, centre - model ASI2 (double mesh)

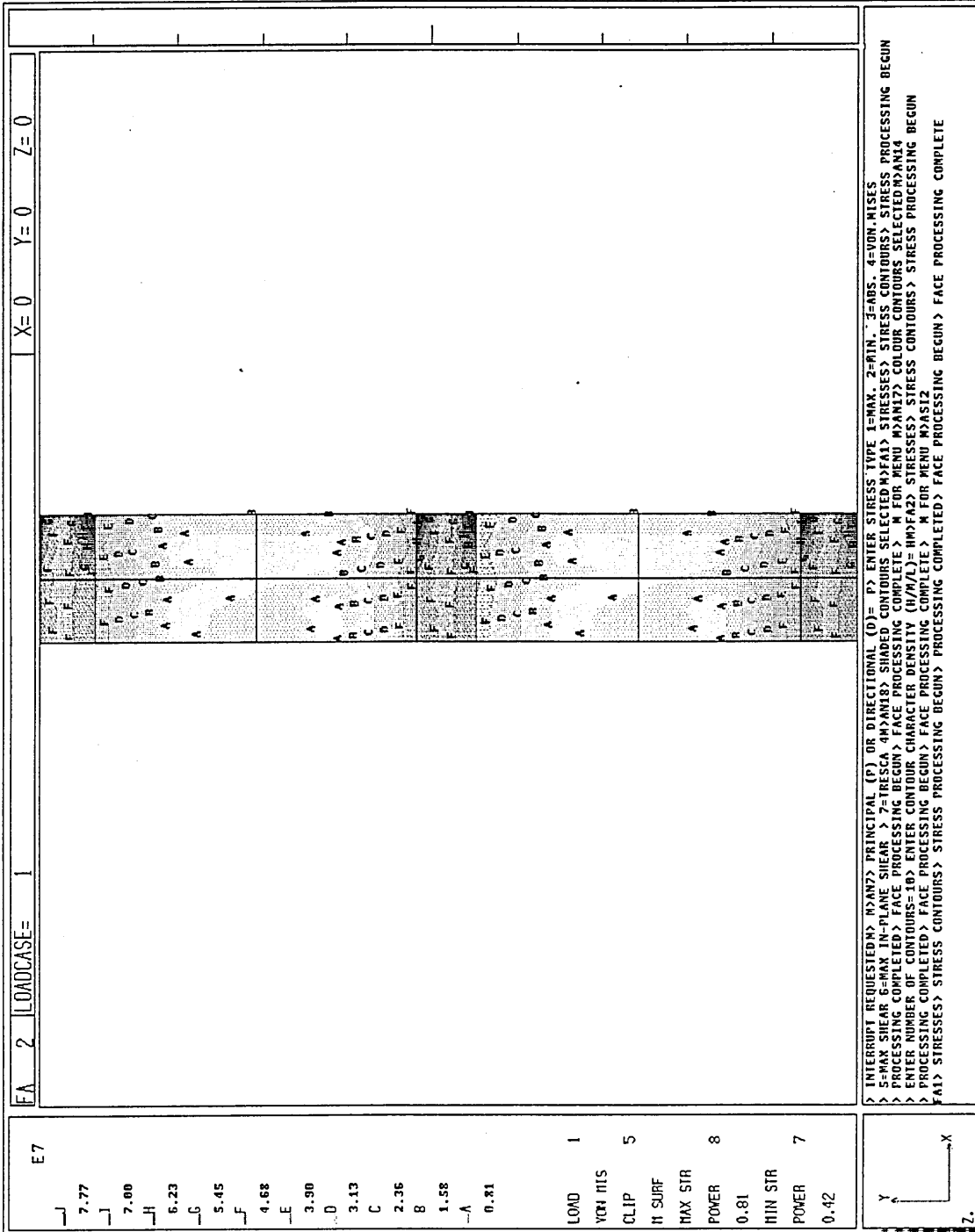


Figure 71. Von Mises stress, unaveraged, centre - model ASI2 (double mesh)

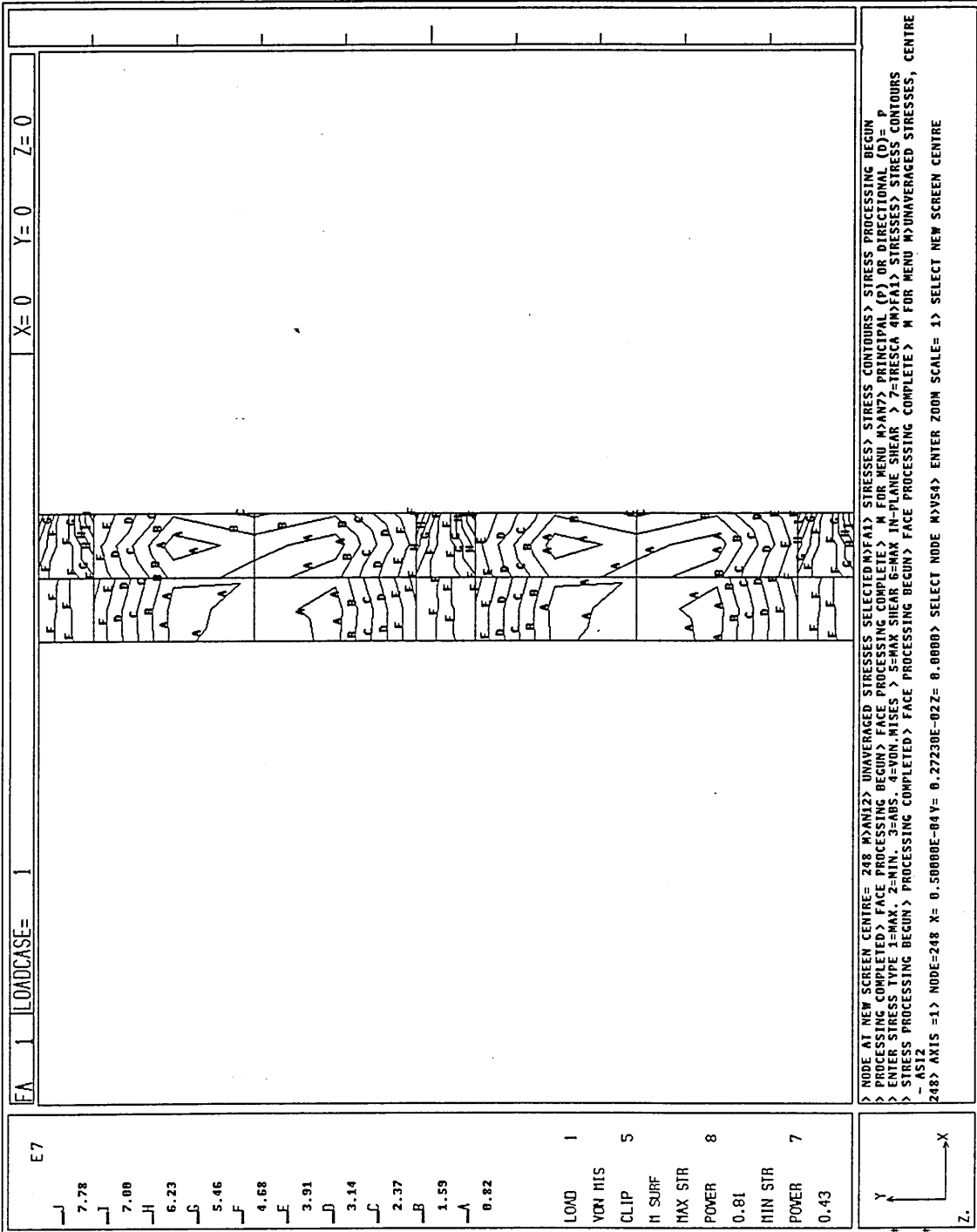


Figure 72. Von Mises stress, top - model ASI2 (double mesh)

Figure 75. Tresca stress, centre - model ASI2 (double mesh)

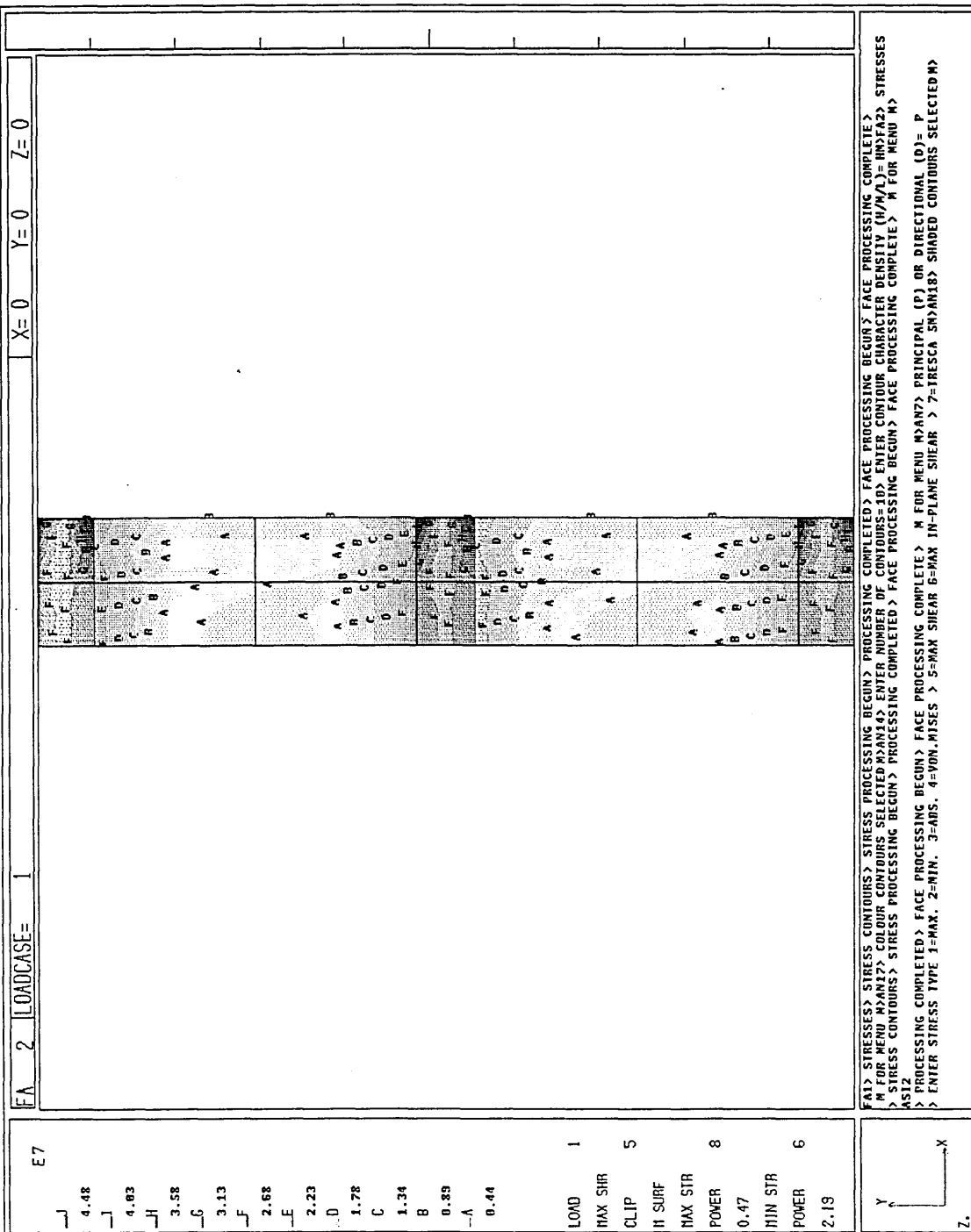


Figure 74. Maximum shear stress, centre - model ASI2 (double mesh)

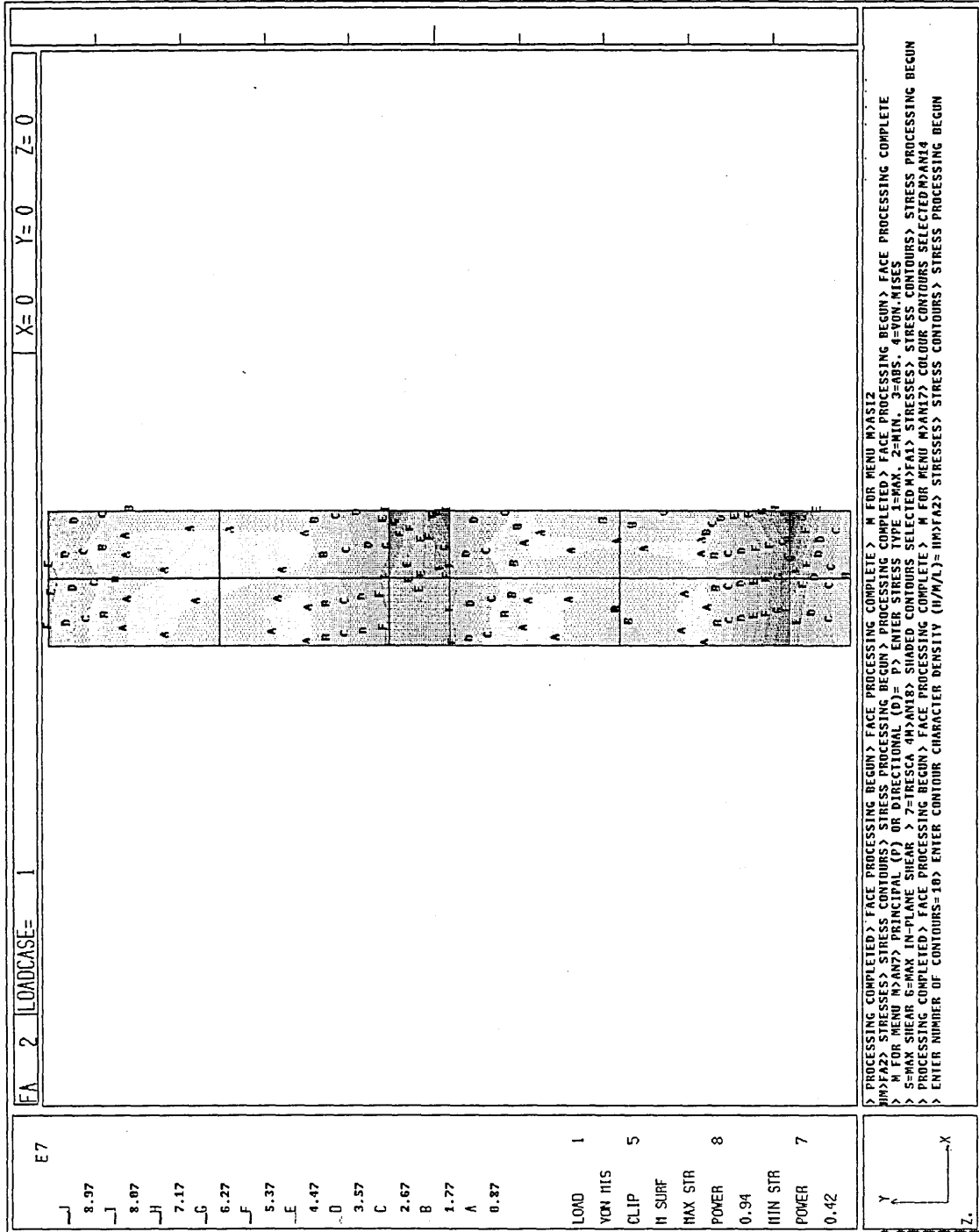


Figure 73. Von Mises stress, bottom - model ASI2 (double mesh)

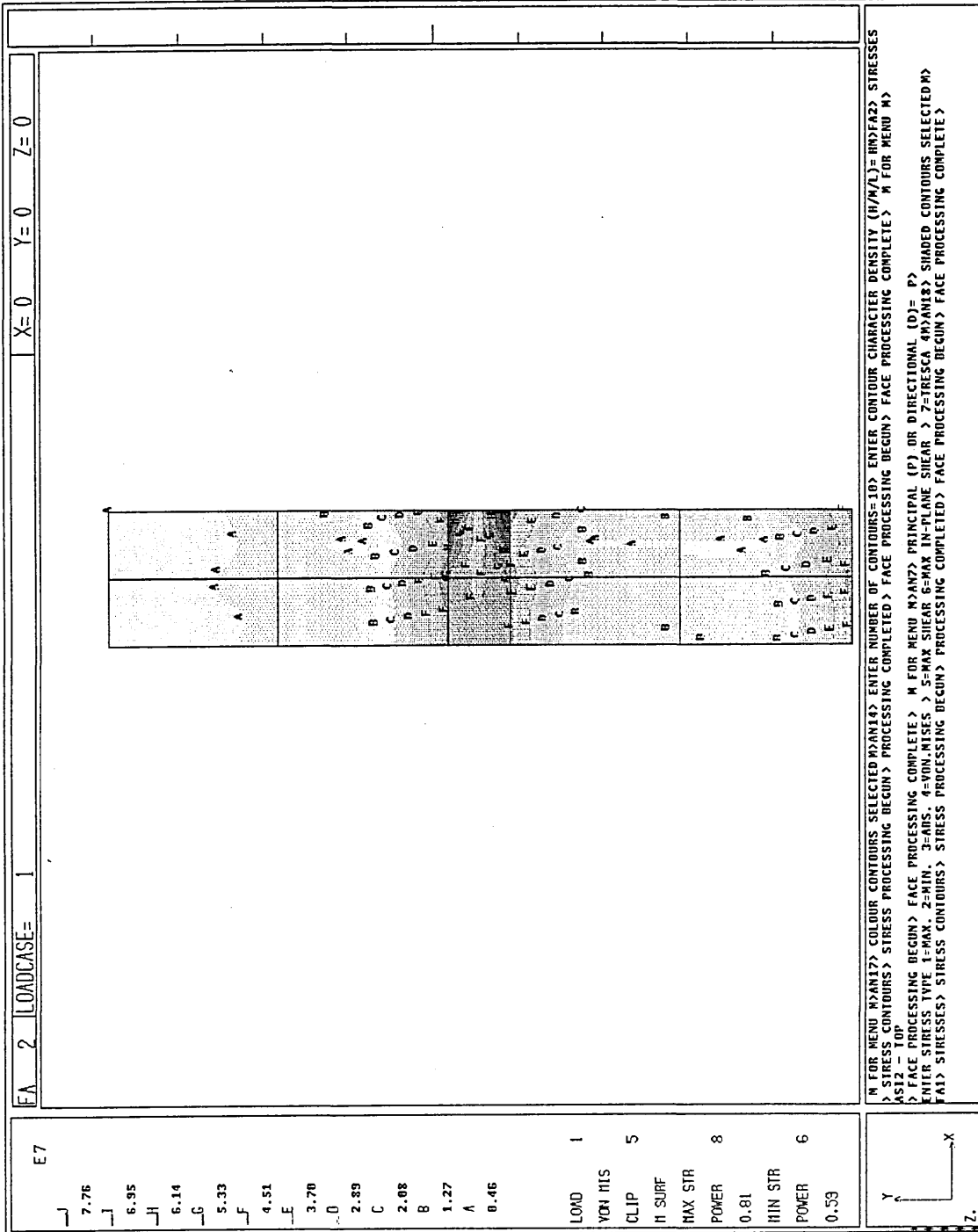


Figure 72. Von Mises stress, top - model ASI2 (double mesh)

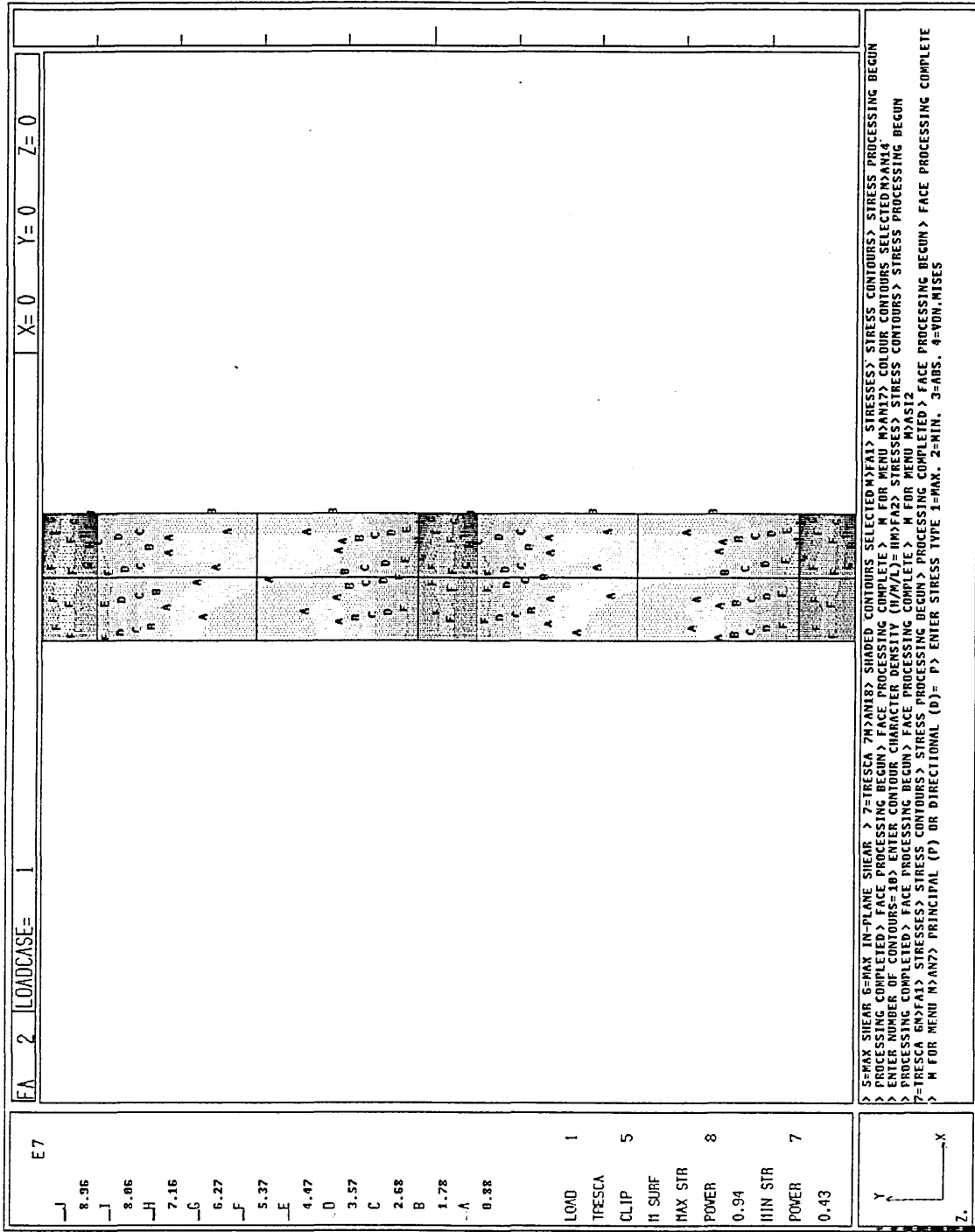


Figure 76. Deformation on cooling through 170°C - model ES04



Figure 77. Maximum principal stress - model ES04

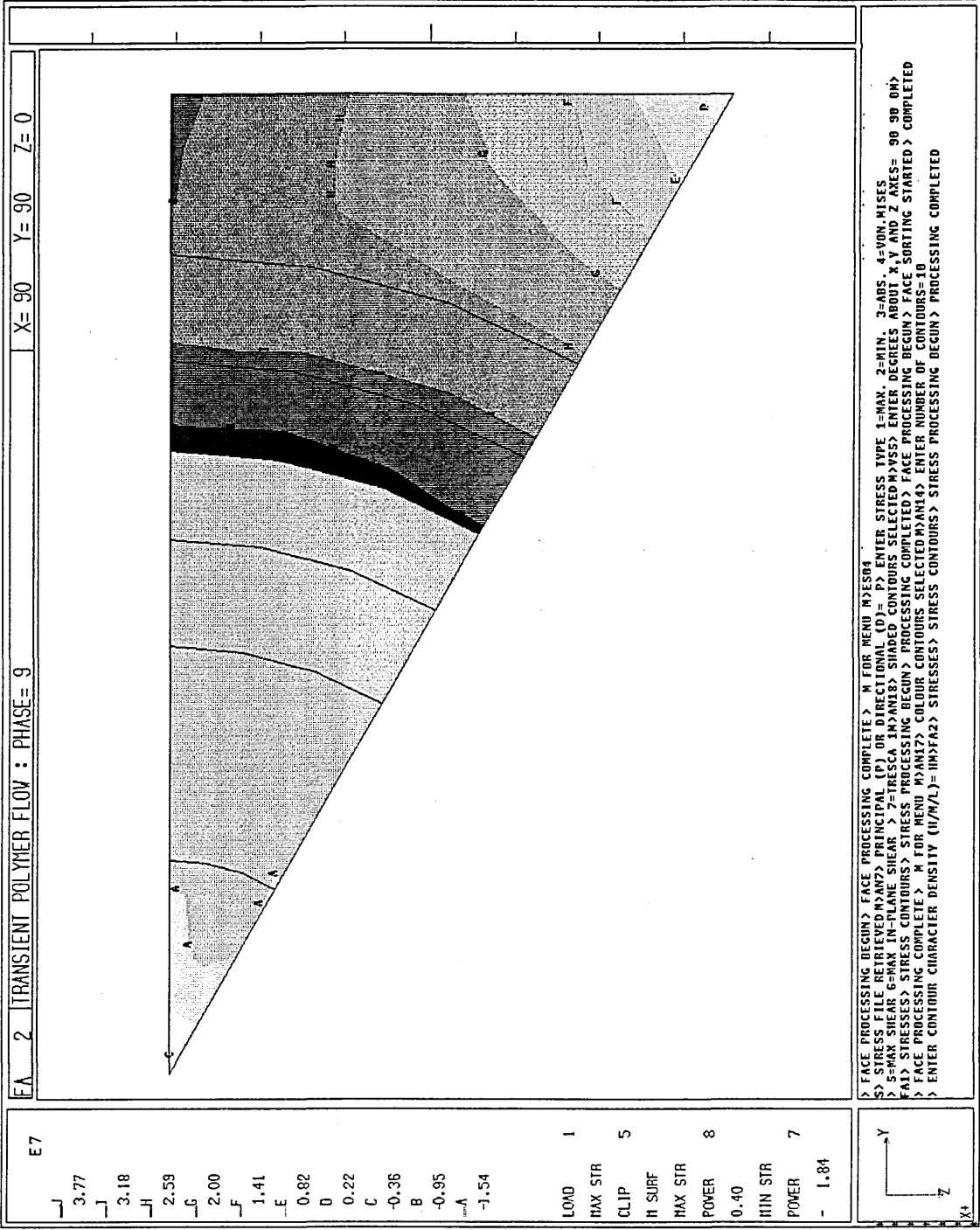


Figure 78. Maximum principal stress, vectors - model ES04



Figure 79. Maximum principal stress, unaveraged - model ES04

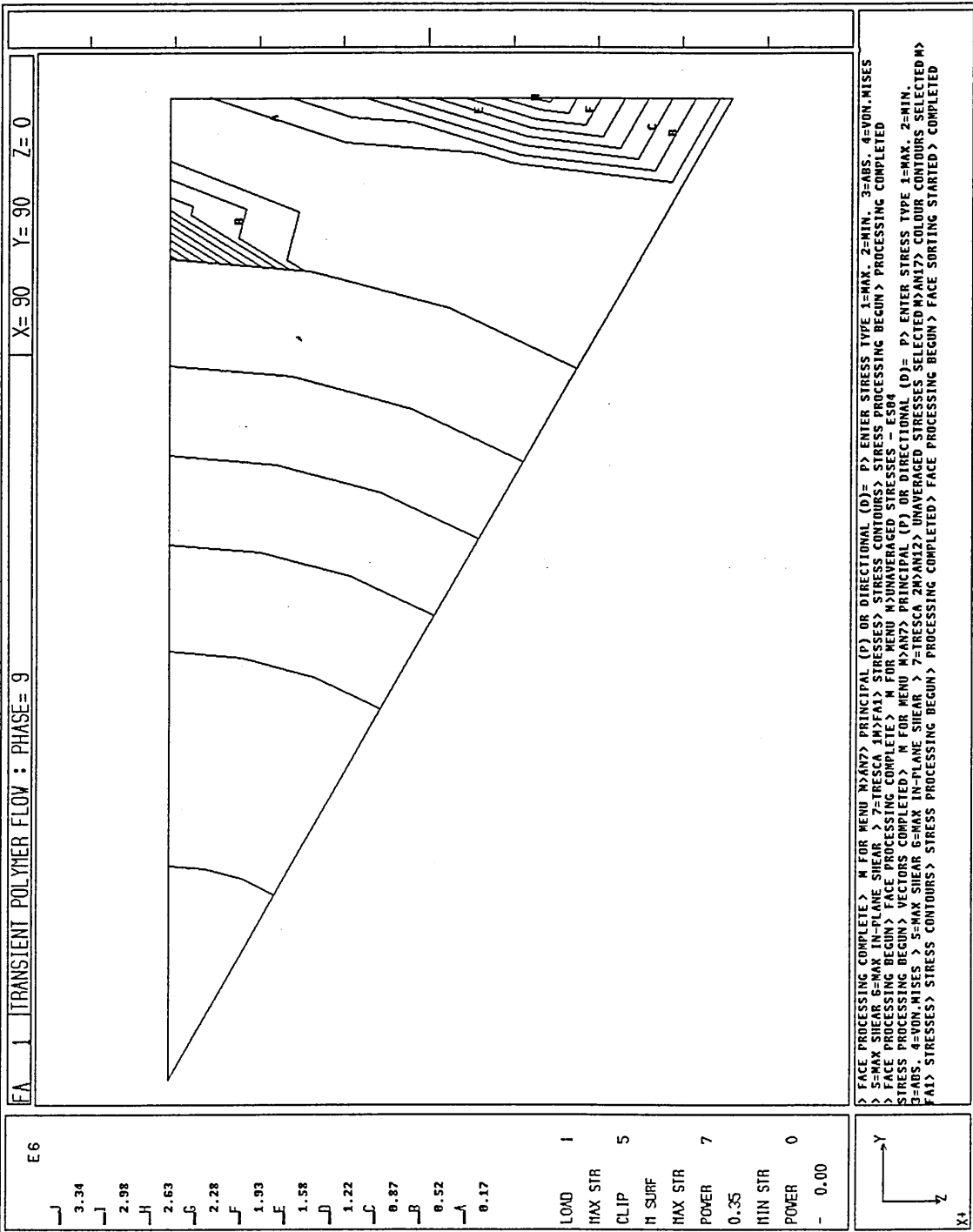


Figure 80. Minimum principal stress - model ES04



Figure 81. Minimum principal stress, vectors - model ES04

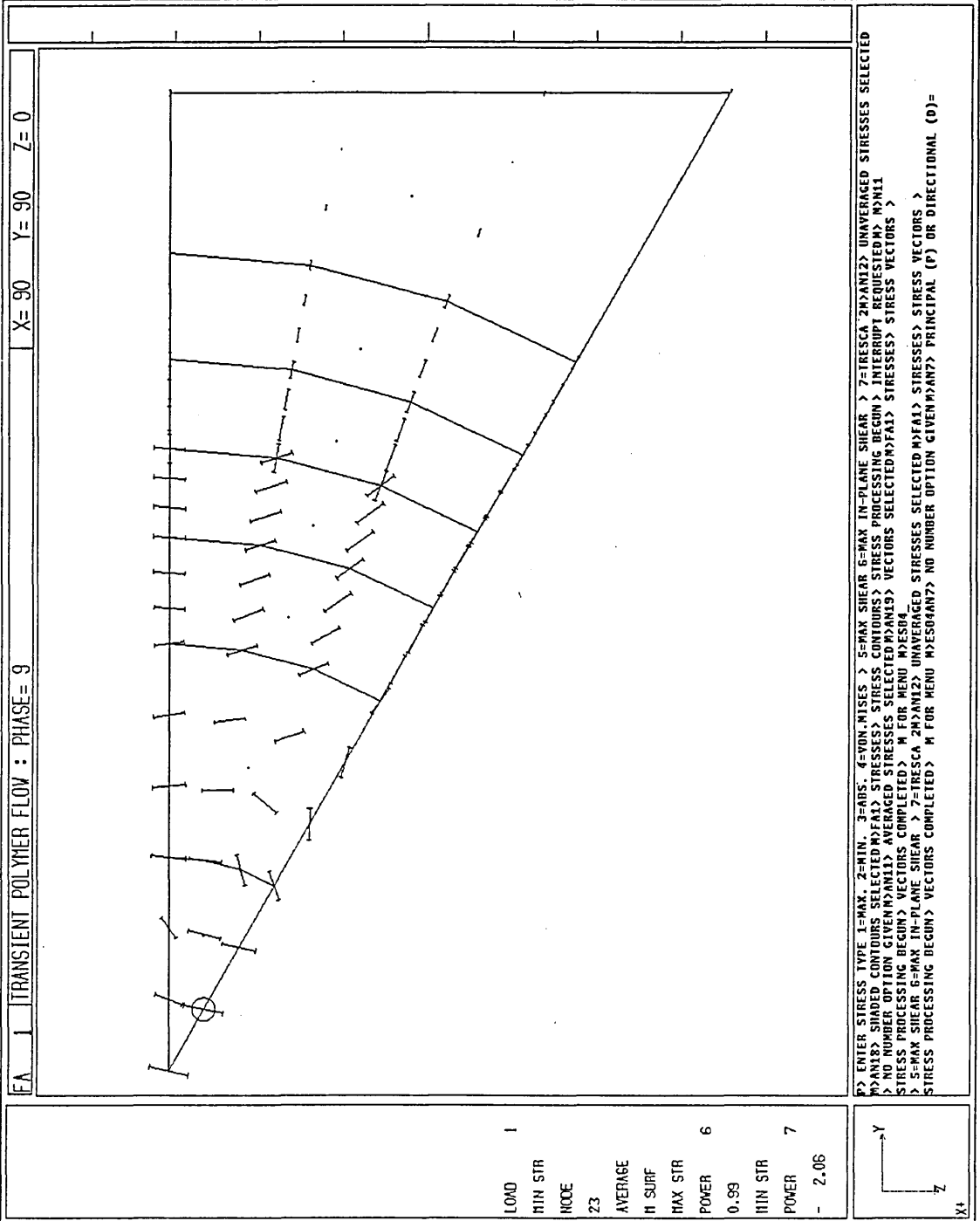
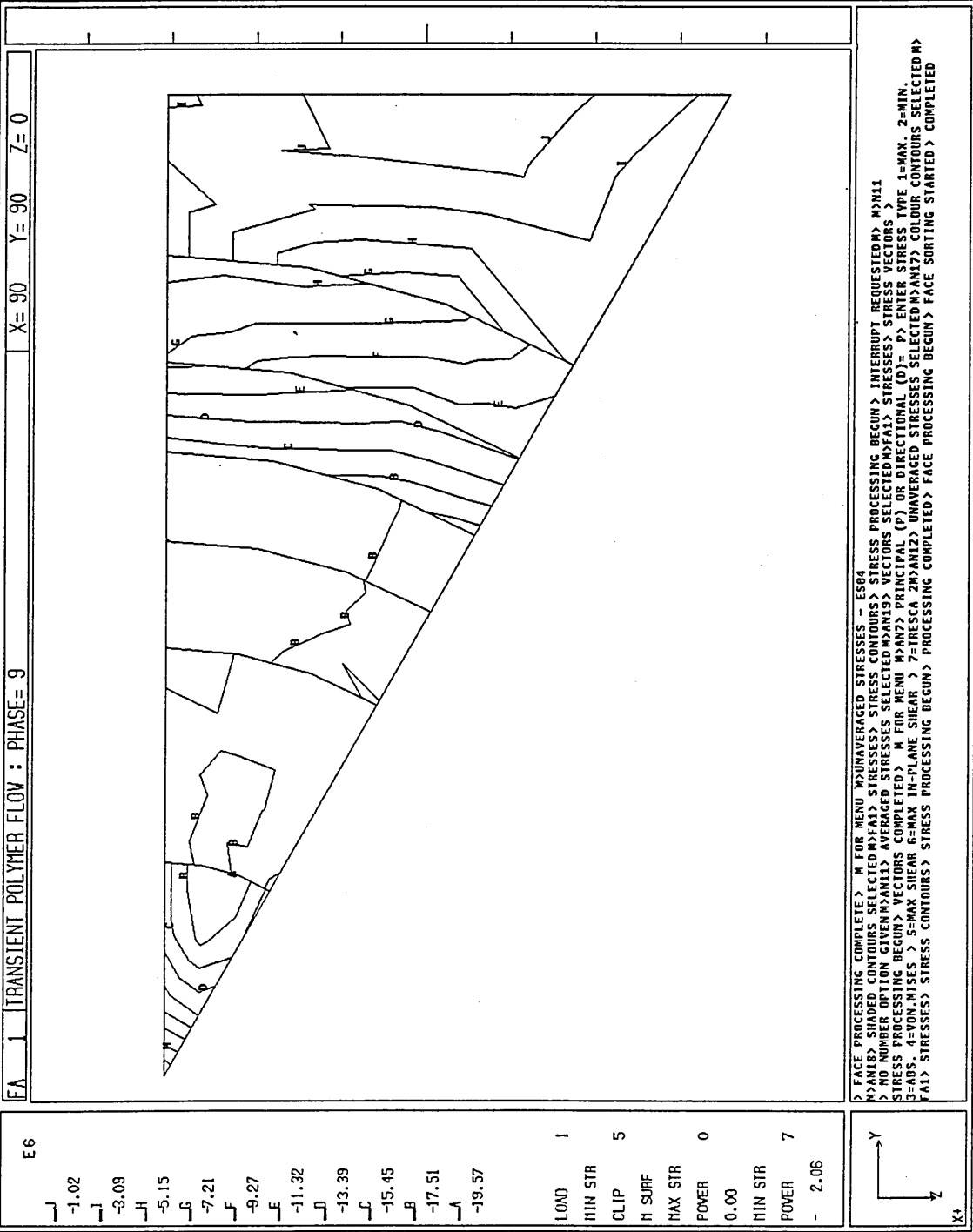


Figure 82. Minimum principal stress, unaveraged - model ES04



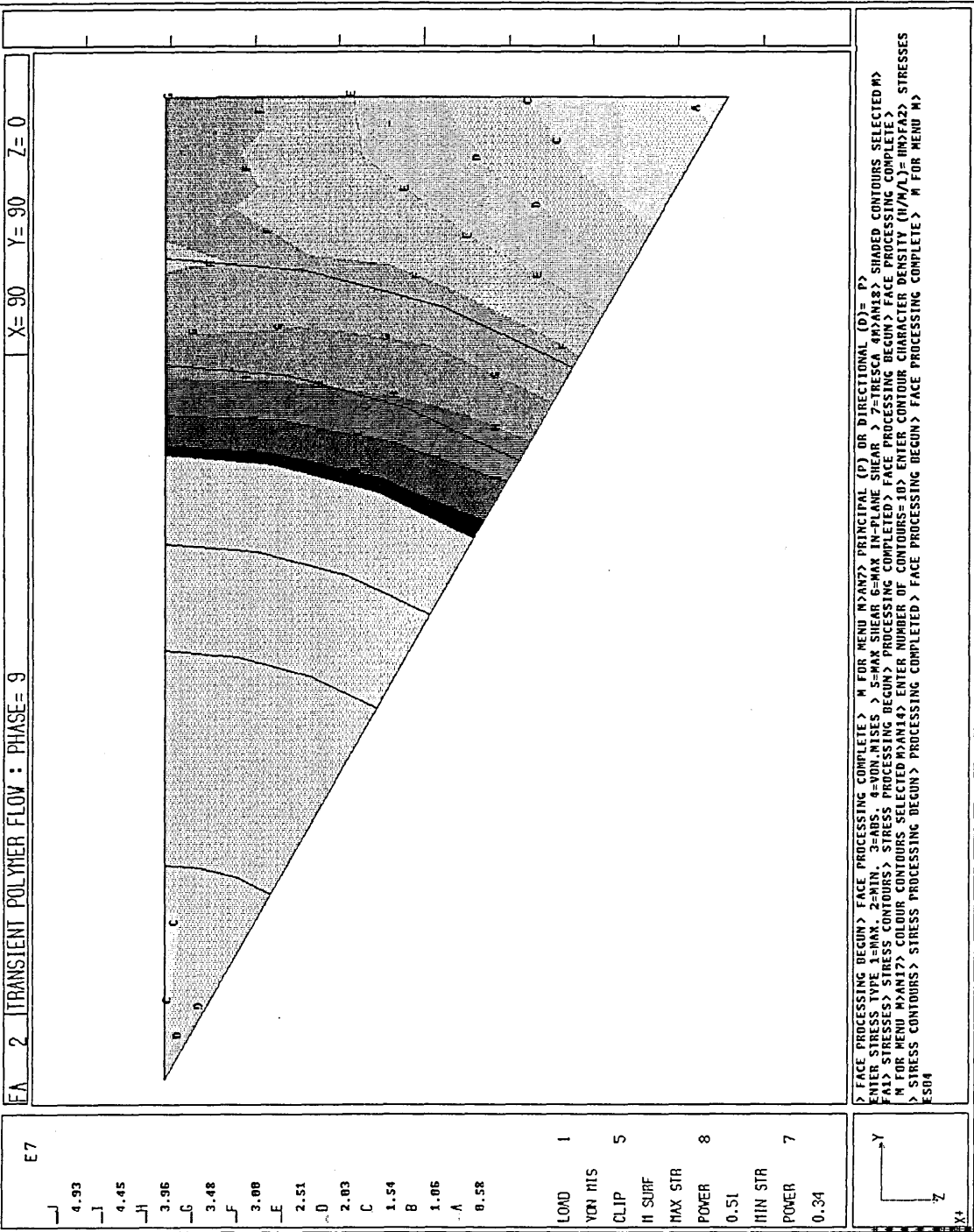
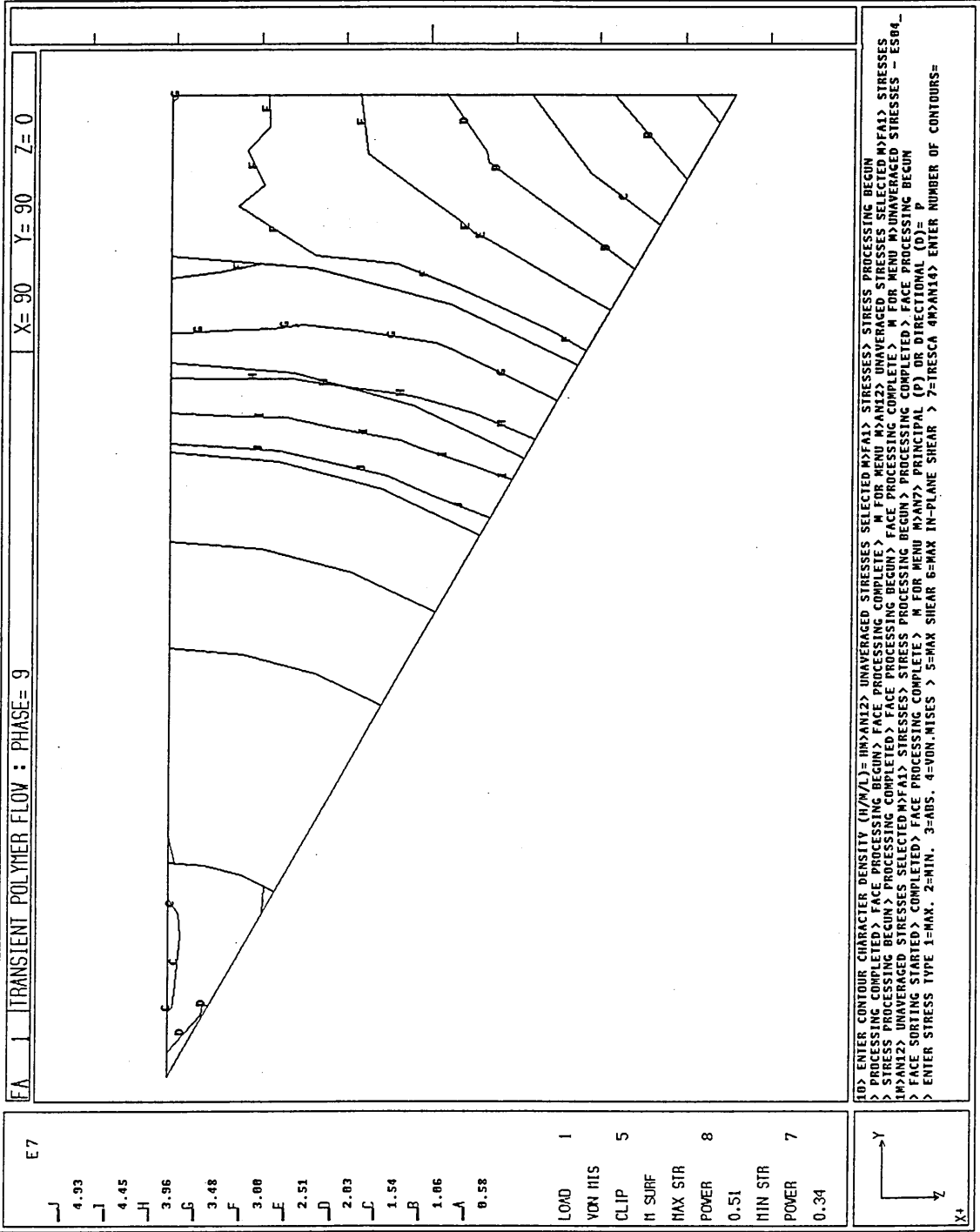
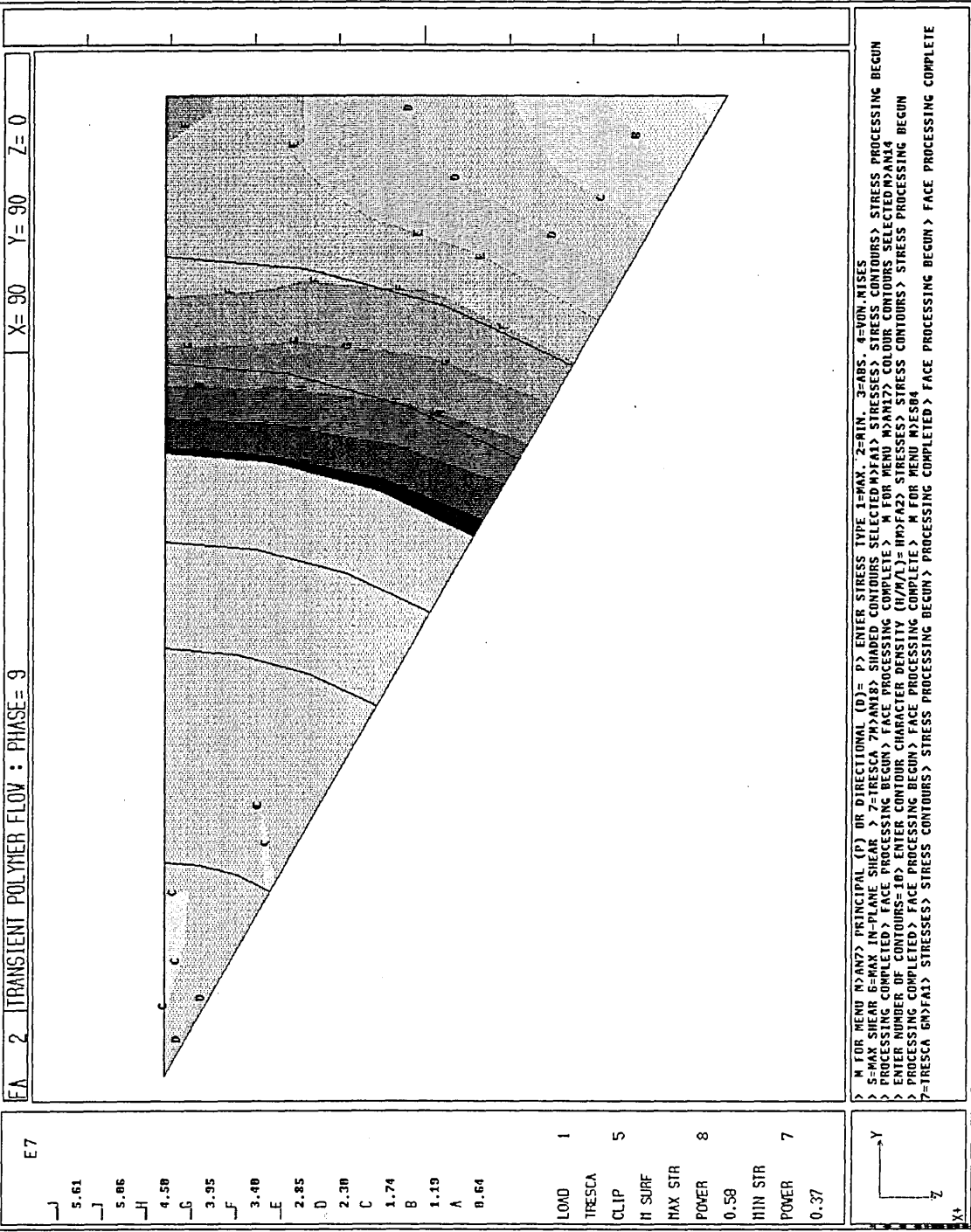
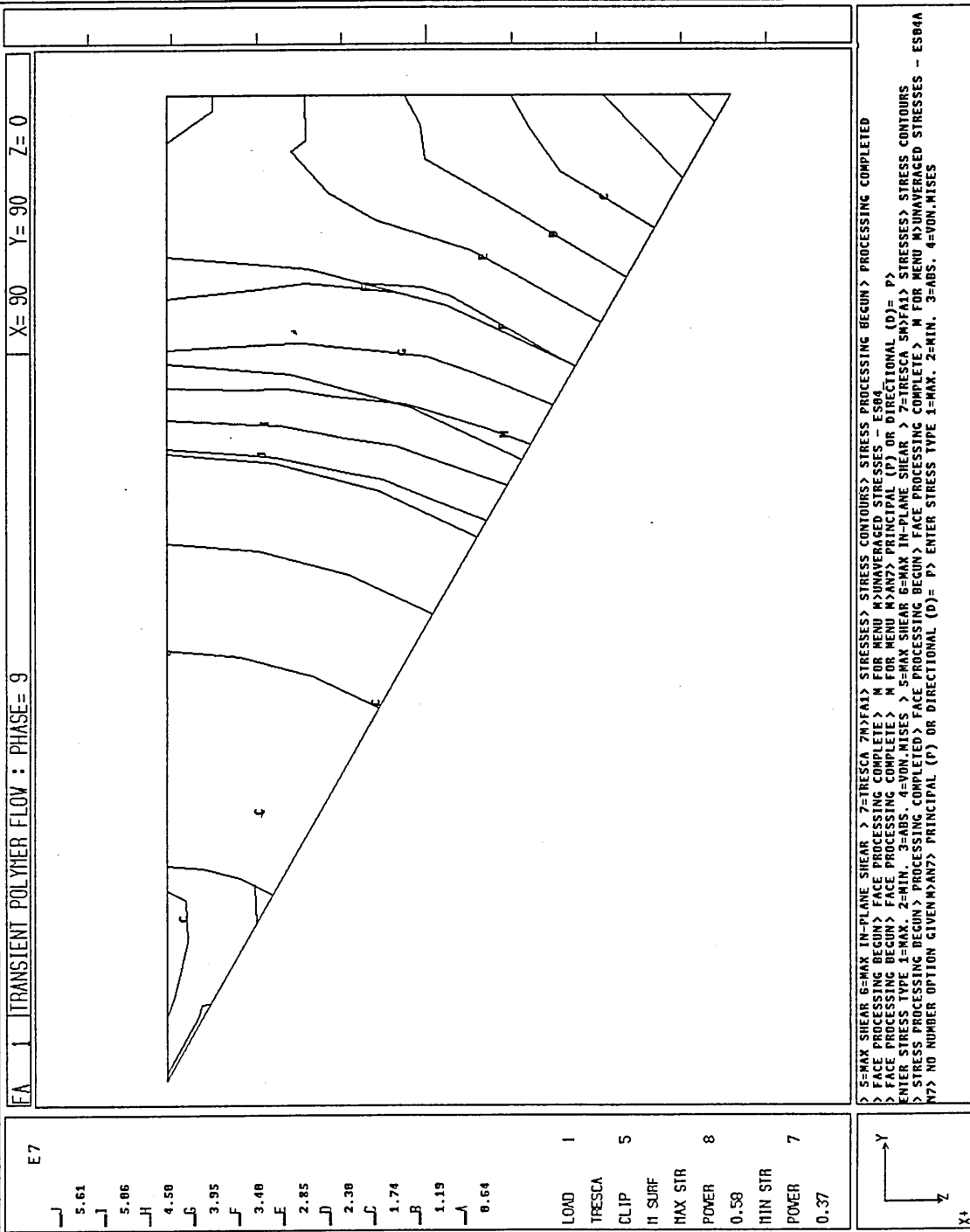


Figure 84. Von Mises stress, unaveraged - model ES04







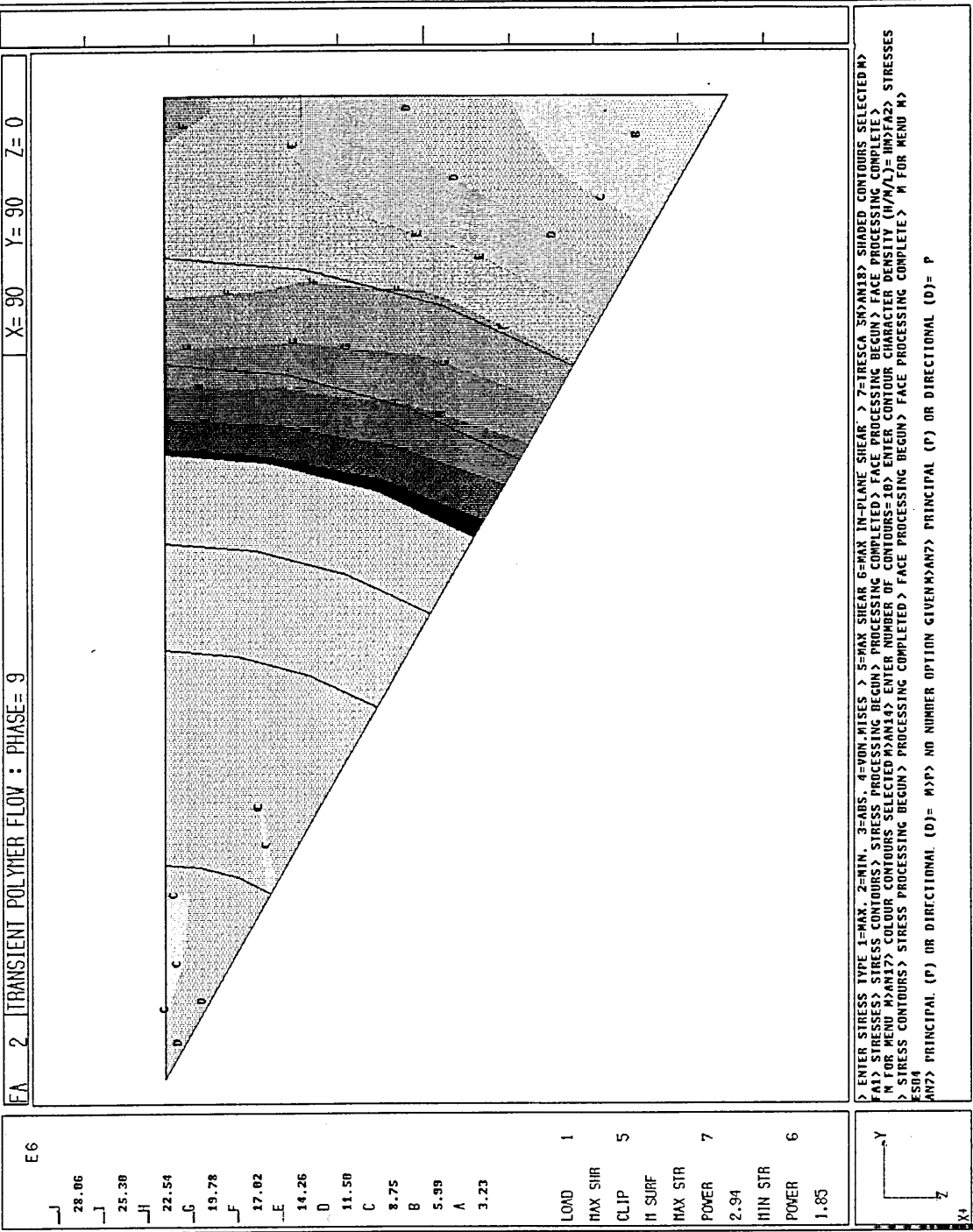




Figure 89. Deformation on cooling through 170°C - model D15C

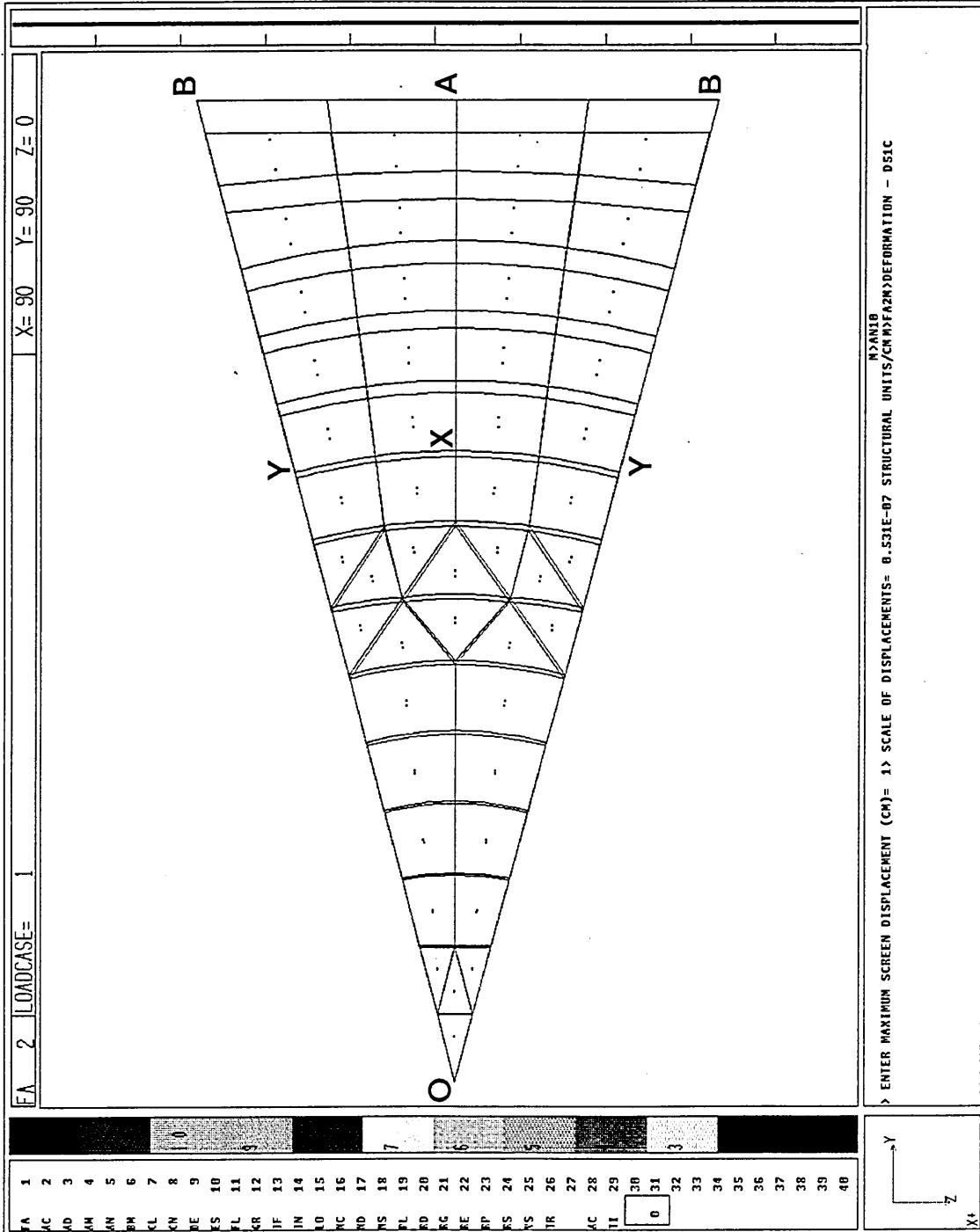


Figure 90. Maximum principal stress - model D15C  
(original in colour)

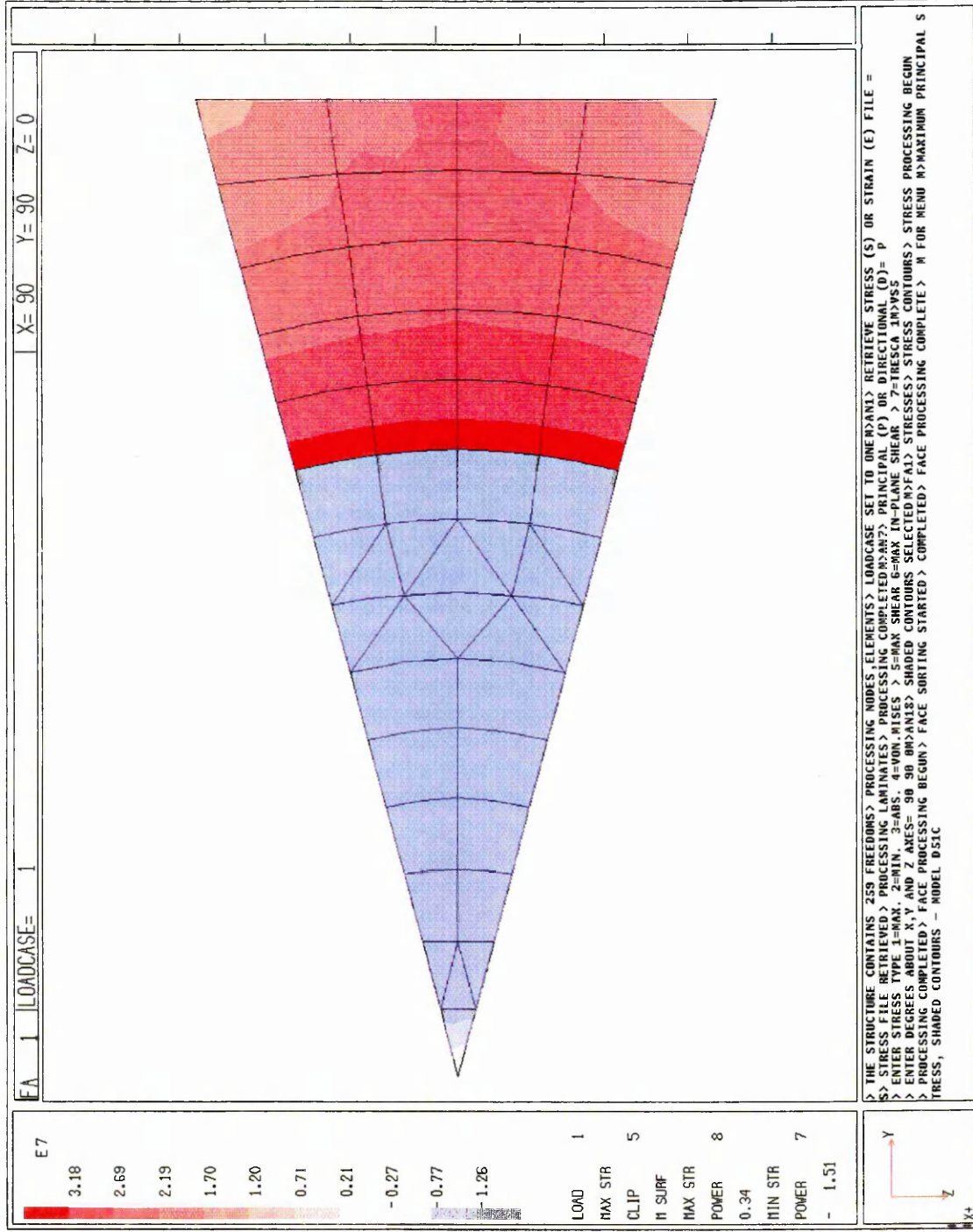


Figure 91. Maximum principal stress, vectors - model D15C

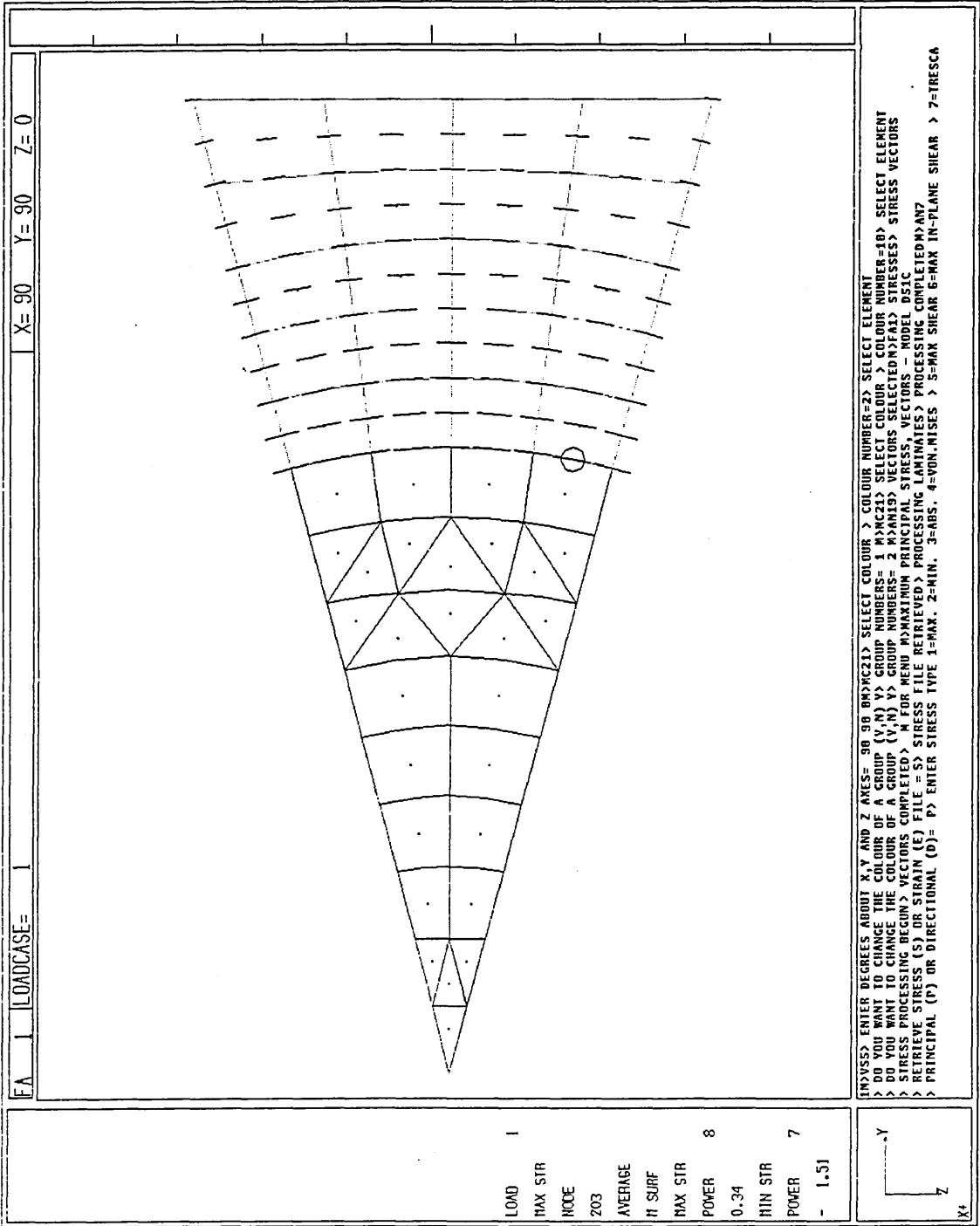


Figure 92. Von Mises stress - model D15C  
(original in colour)

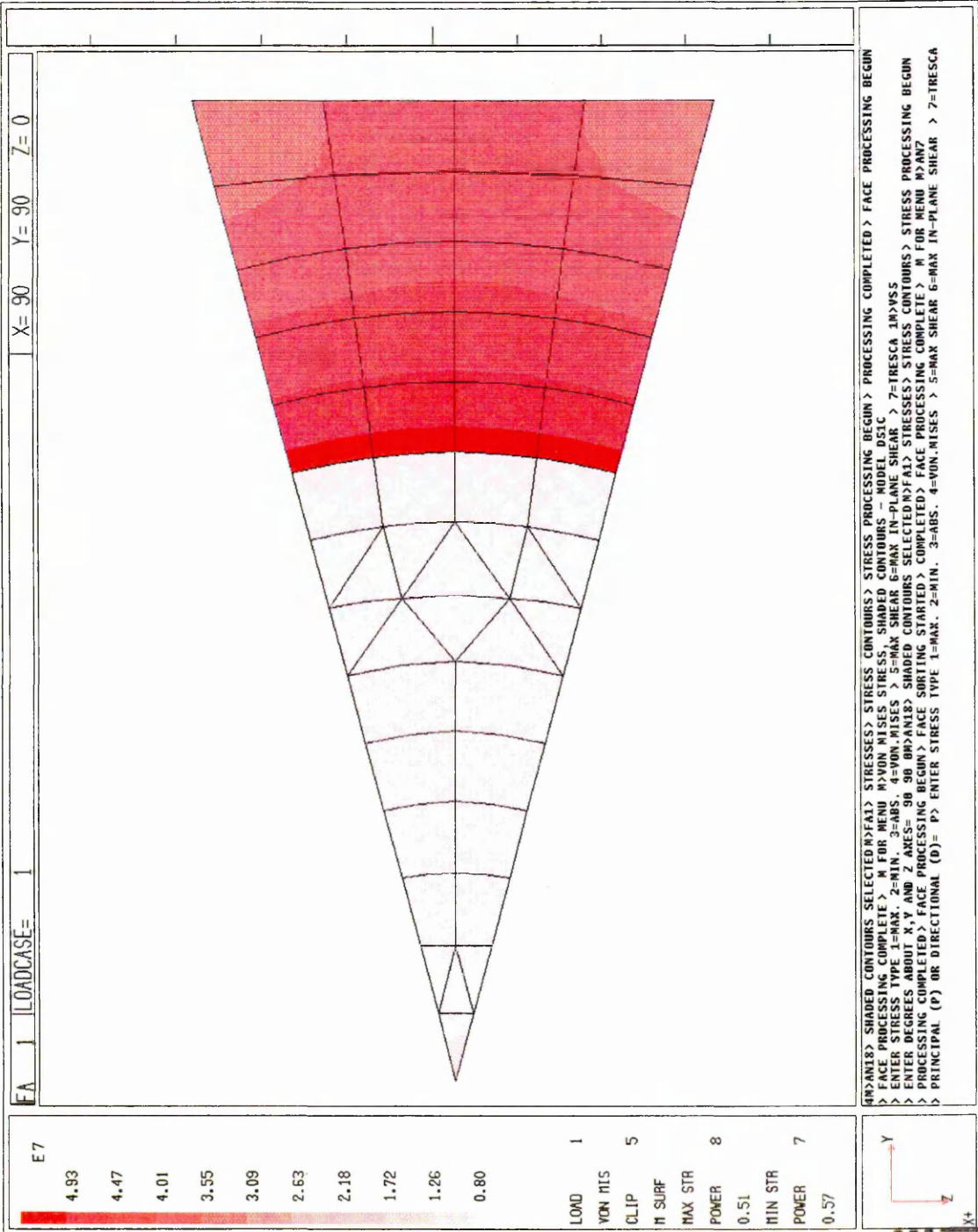
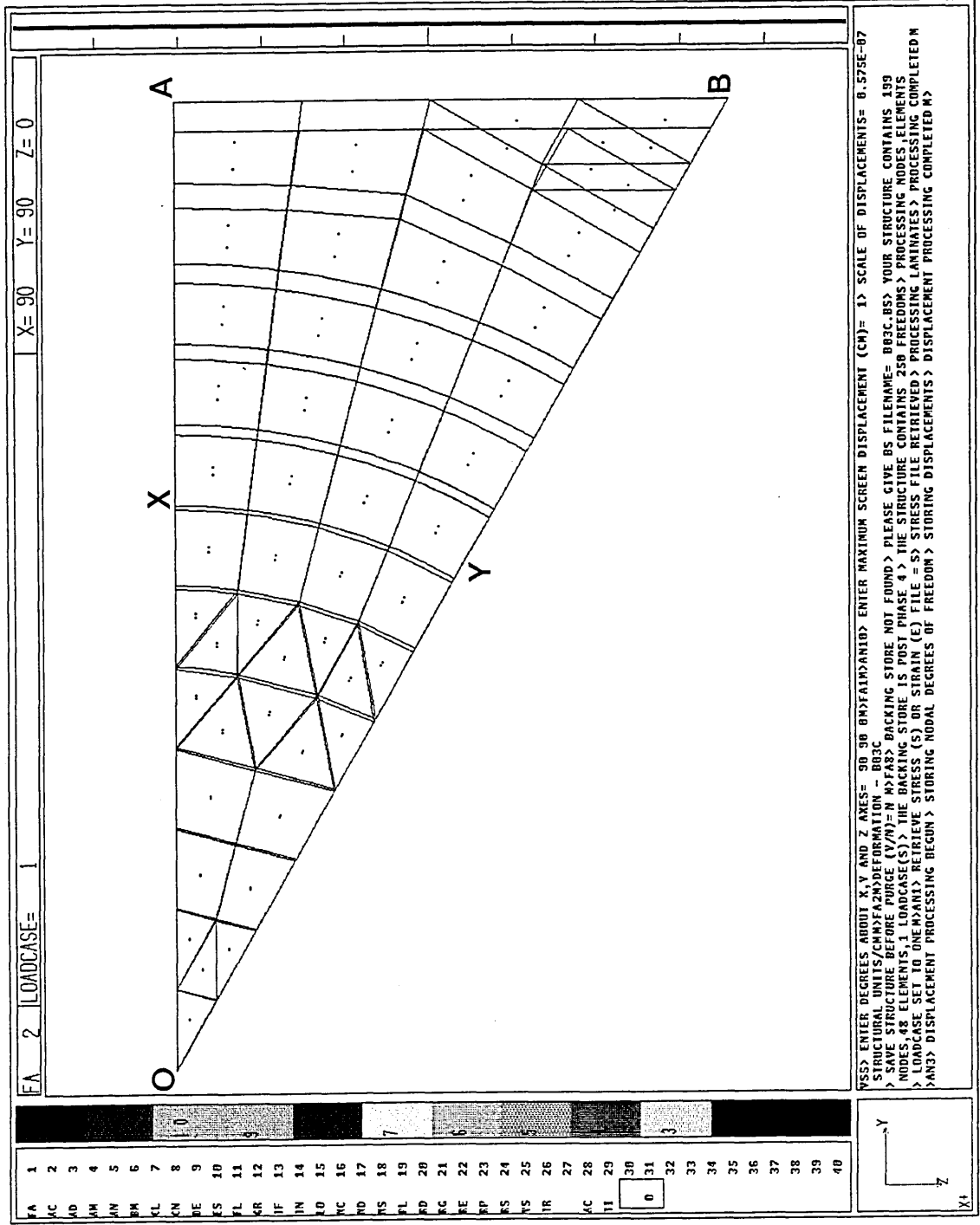


Figure 93. Deformation on cooling through 170°C - model B03C



EA 2 LOADCASE= 1 X= 90 Y= 90 Z= 0

WSS> ENTER DEGREES ABOUT X,Y AND Z AXES= 90 90 90 (MAYBE) ENTER MAXIMUM SCREEN DISPLACEMENT (CM)= 1> SCALE OF DISPLACEMENTS= 0.575E-07  
 STRUCTURAL UNITS/CM/FA2> DEFORMATION - DBSC BACKING STORE NOT FOUND > PLEASE GIVE BS FILENAME- DBSC.BS YOUR STRUCTURE CONTAINS 189  
 > SAVE STRUCTURE BEFORE PORGE (V/M)= N MAYBE> BACKING STORE IS POST PHASE 4> THE STRUCTURE CONTAINS 258 FREEDOM> PROCESSING NODES ELEMENTS  
 > NODES, 88 ELEMENTS, 1 LOADCASE(S)> THE BACKING STORE IS POST PHASE 4> THE STRUCTURE CONTAINS 258 FREEDOM> PROCESSING NODES ELEMENTS  
 > LOADCASE SET TO ONE> ANNY> RETRIEVE STRESS (S) OR STRAIN (E) FILE = S> STRESS FILE RETRIEVED > PROCESSING LAMINATES > PROCESSING COMPLETED M  
 > ANJ> DISPLACEMENT PROCESSING BEGUN > STORING MODAL DEGREES OF FREEDOM > STORING DISPLACEMENTS > DISPLACEMENT PROCESSING COMPLETED M

Figure 94. Maximum principal stress - model B03C  
(original in colour)

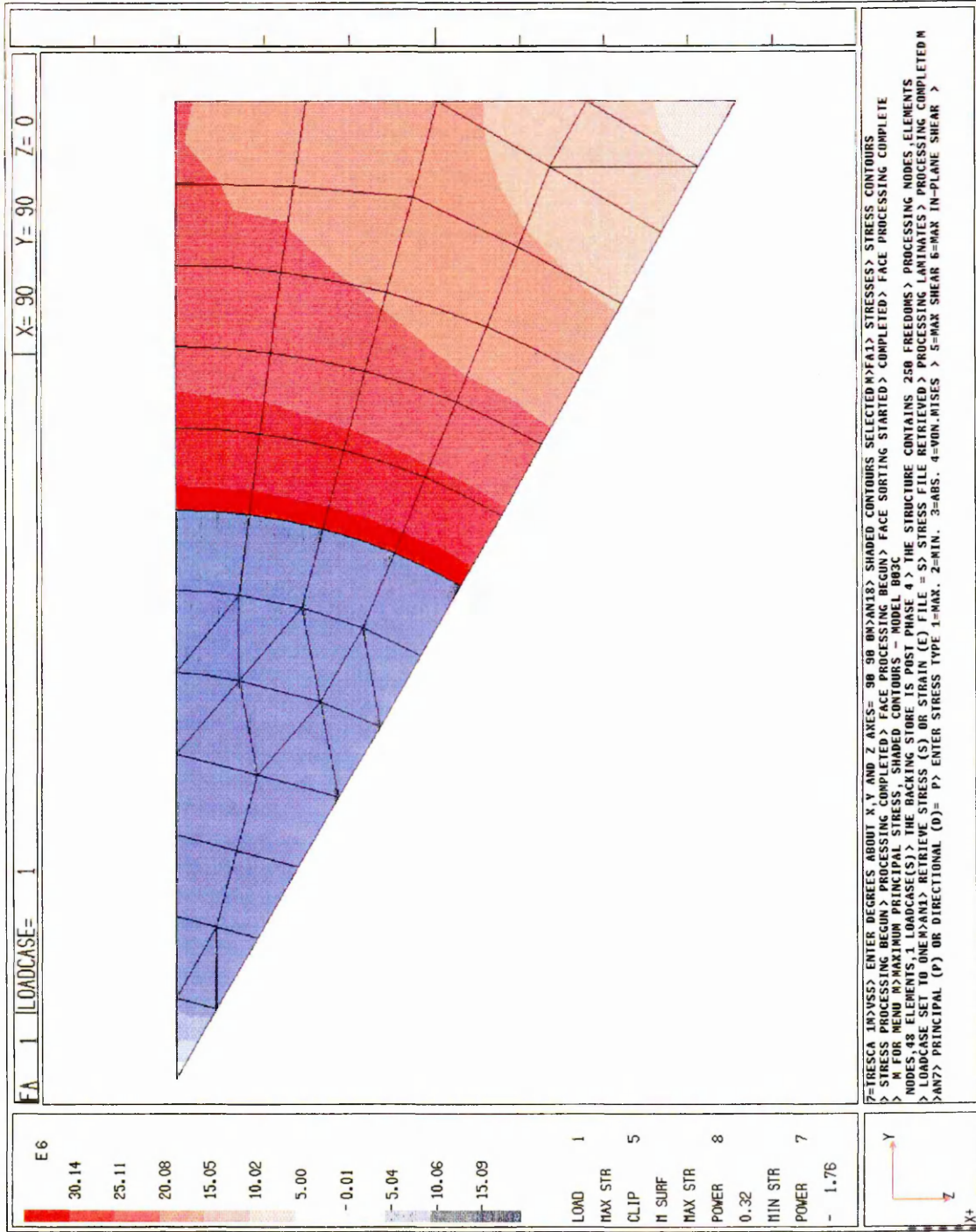


Figure 95. Maximum principal stress, vectors - model B03C

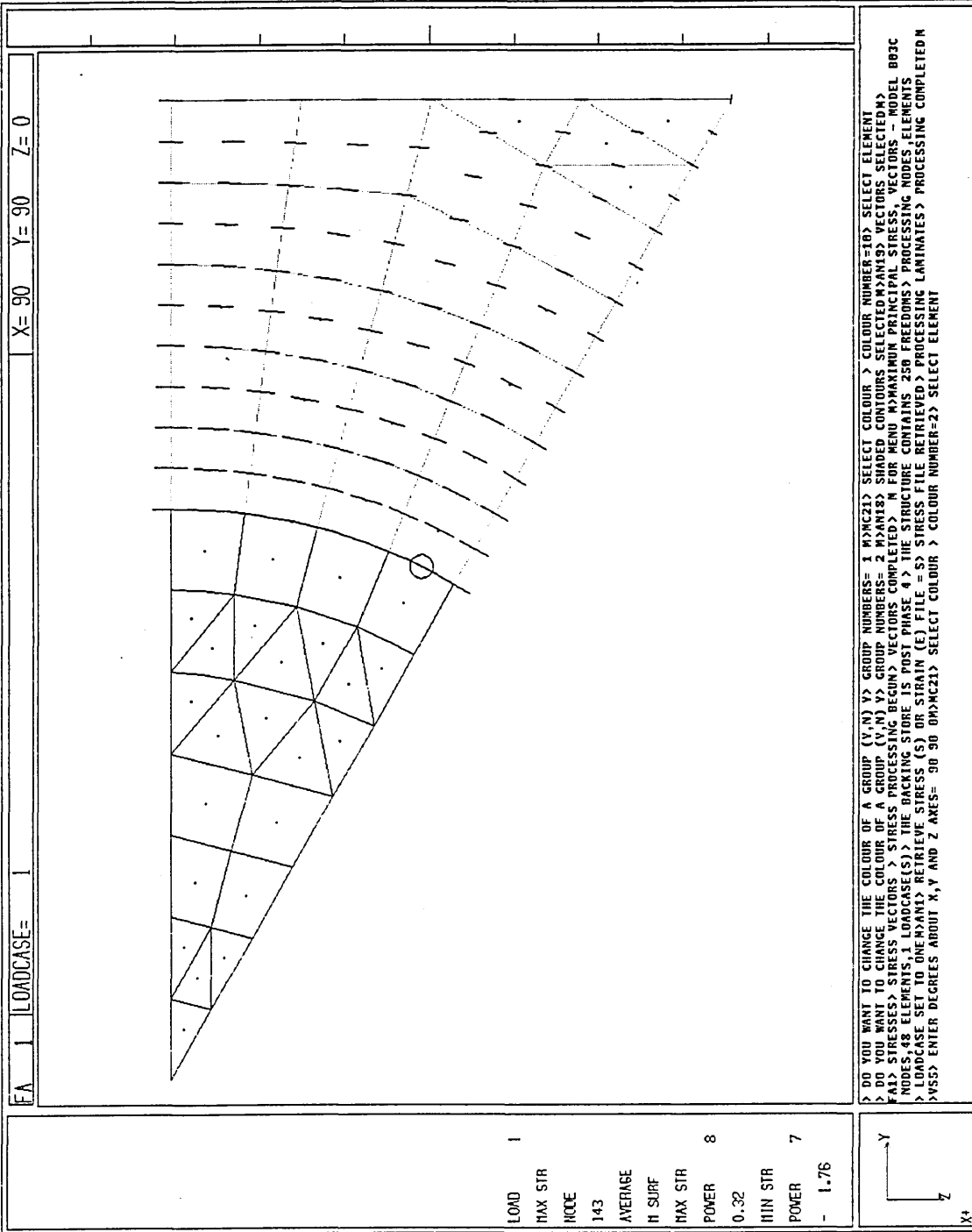


Figure 96. Von Mises stress - model B03C  
(original in colour)

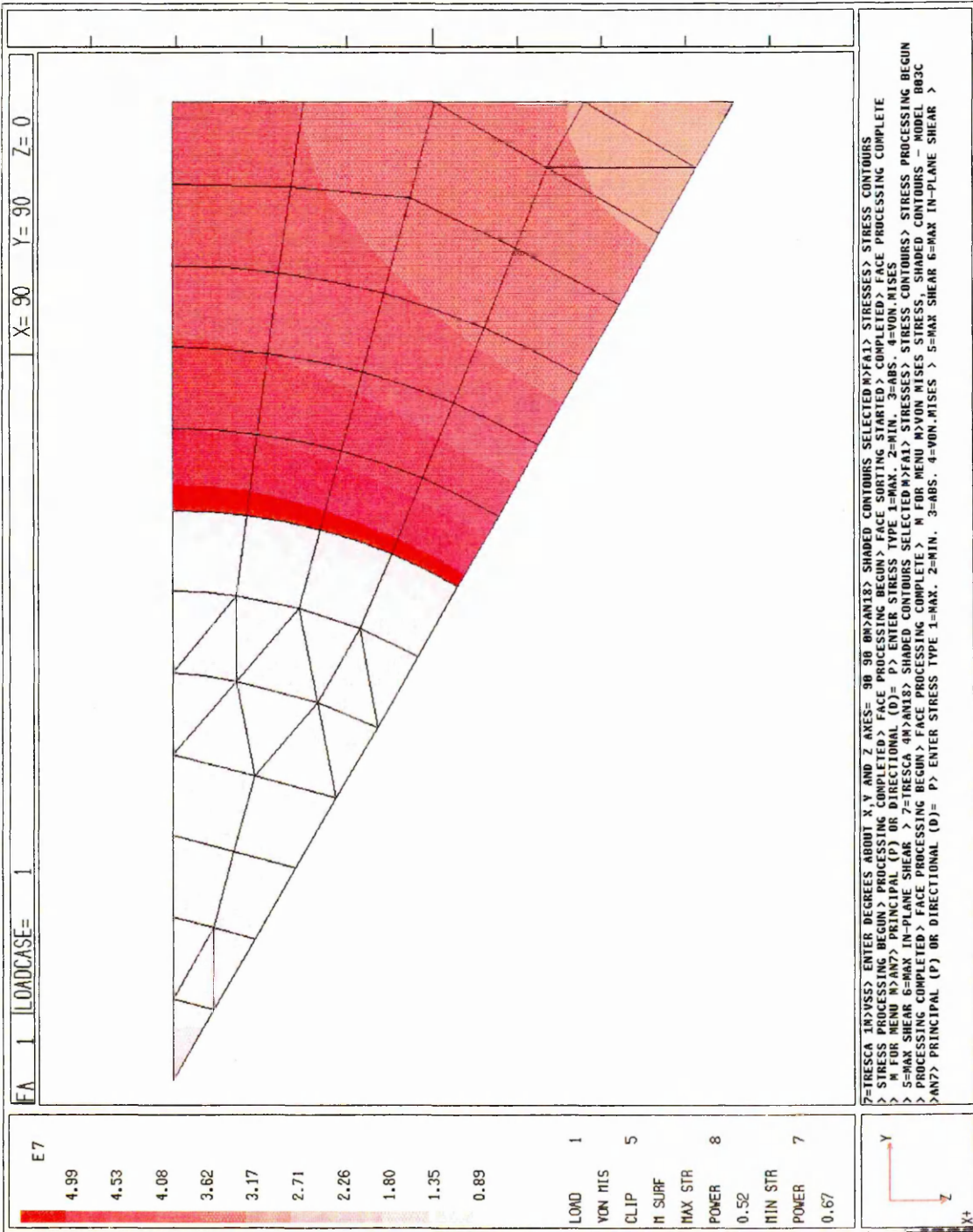


Figure 97. Deformation on cooling through 170°C - model F03B

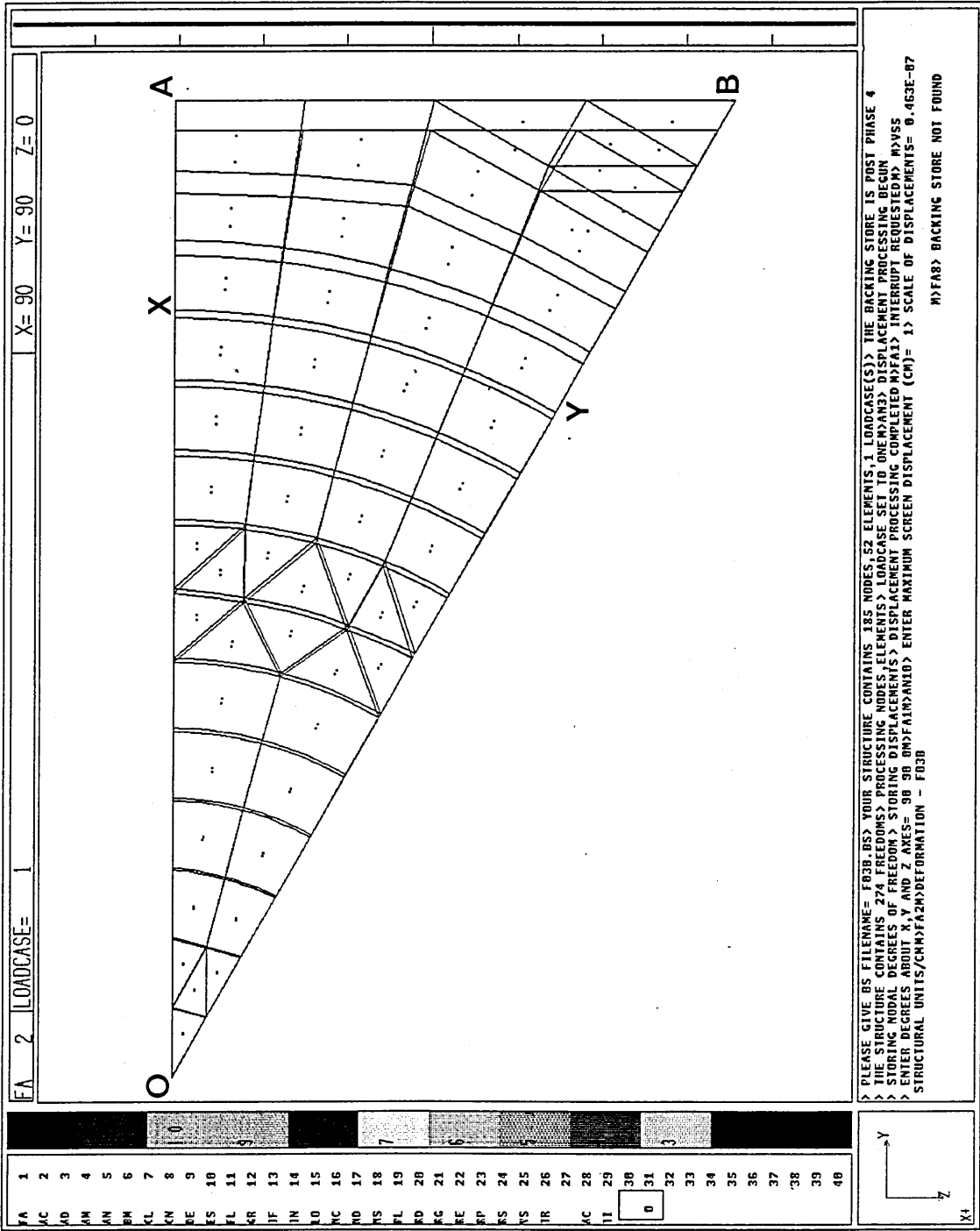


Figure 98. Maximum principal stress - model F03B  
(original in colour)

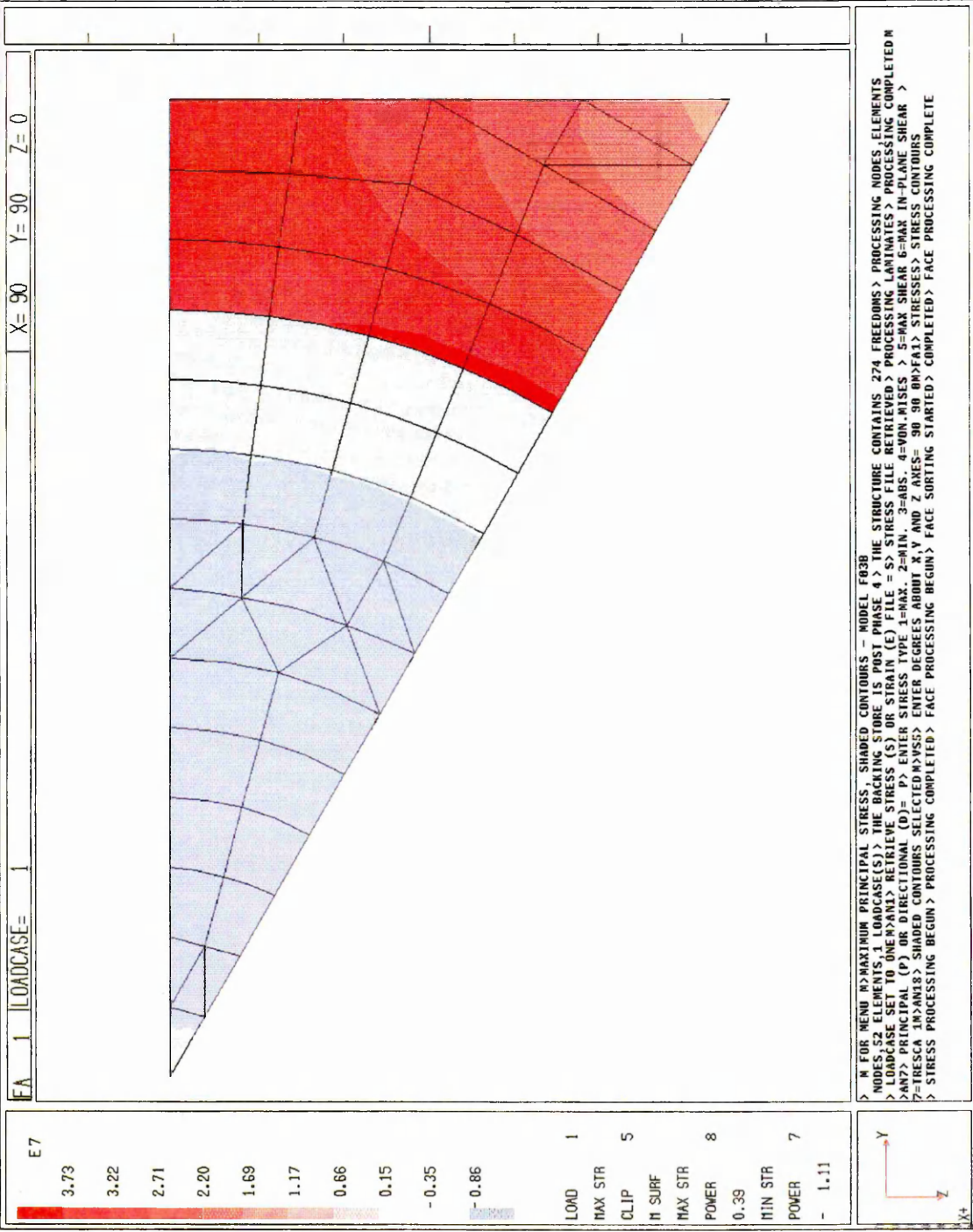


Figure 99. Maximum principal stress, vectors - model F03B

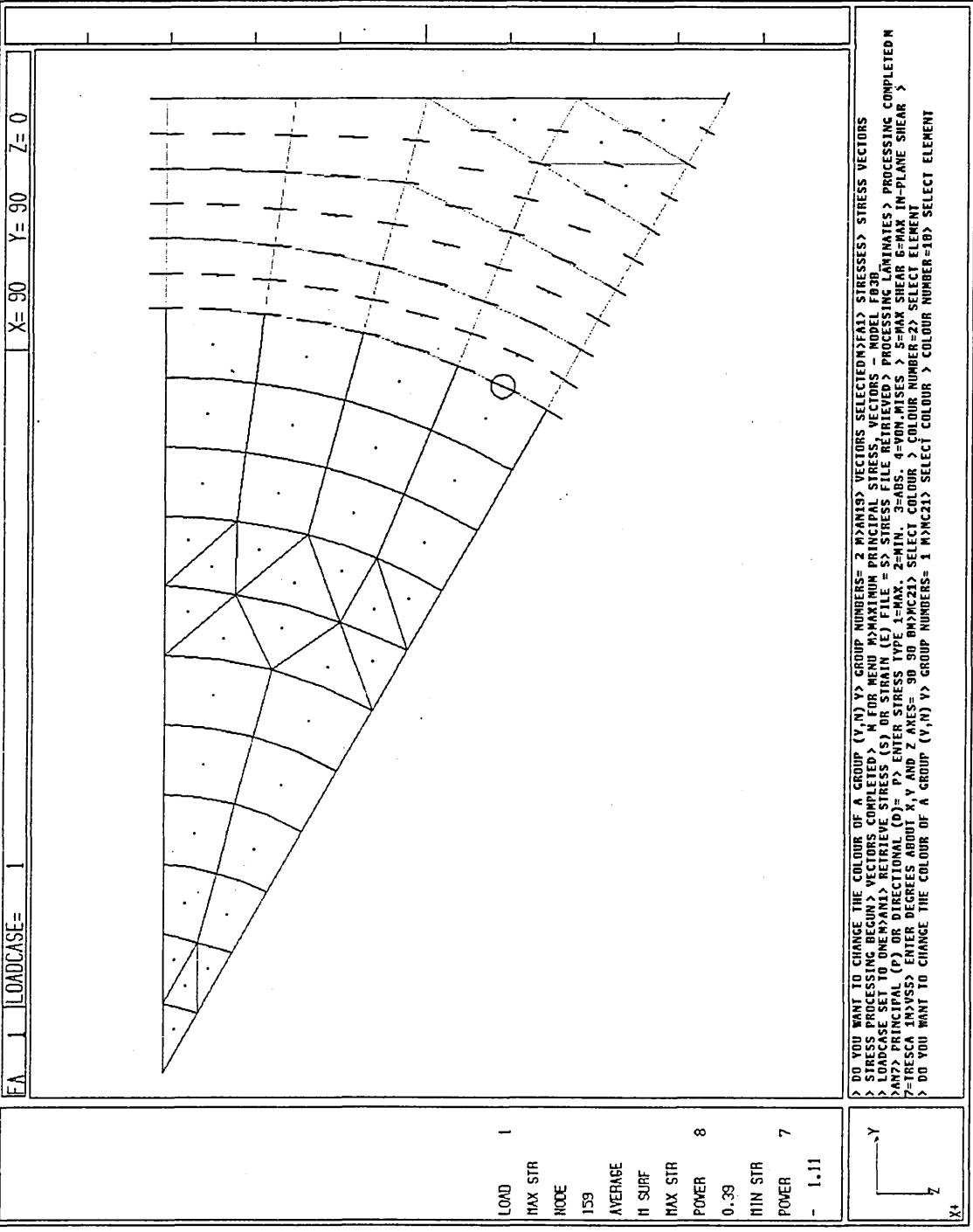


Figure 100. Von Mises stress - model F03B  
(original in colour)

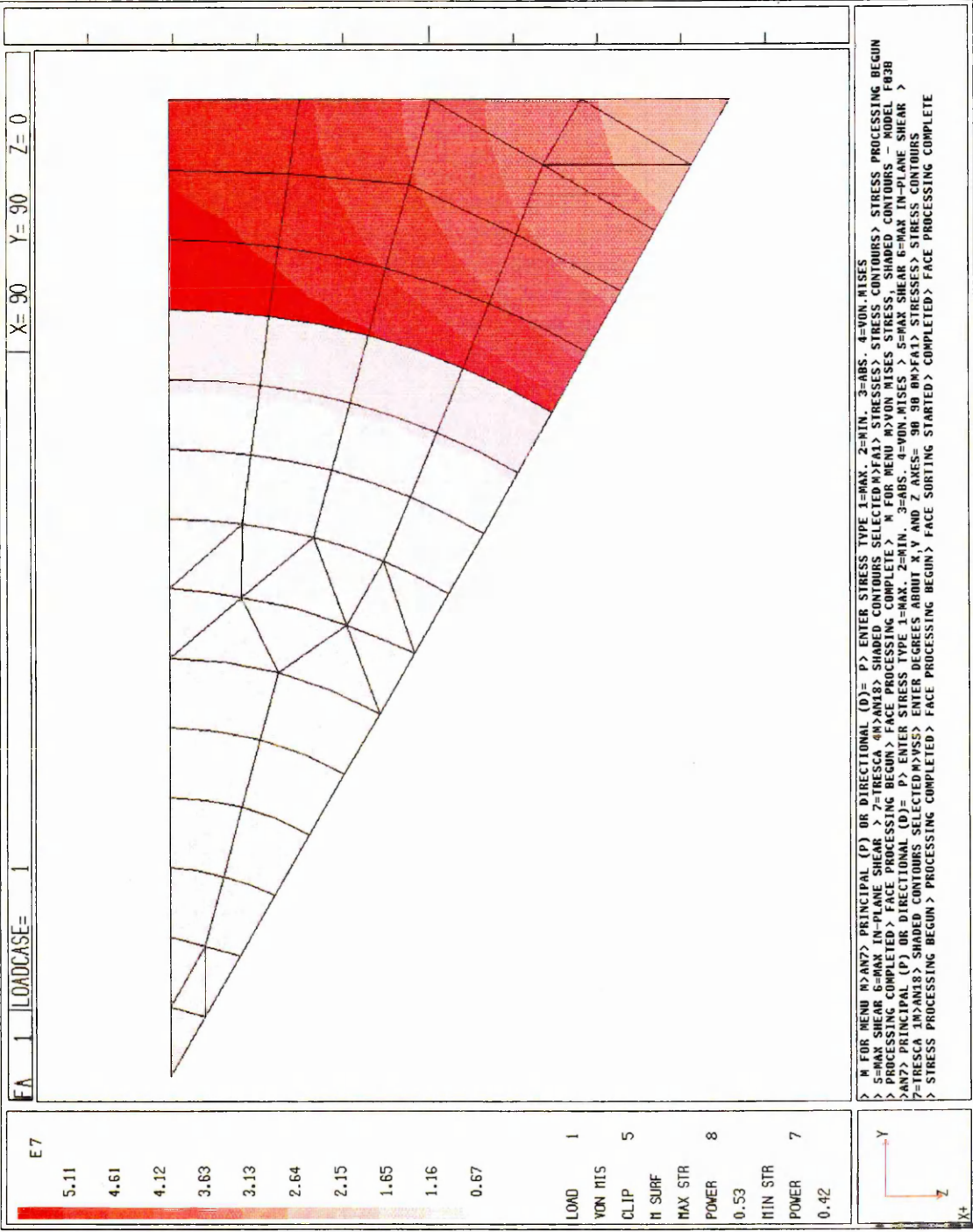


Figure 101. Deformation on cooling through 170°C - model C54C

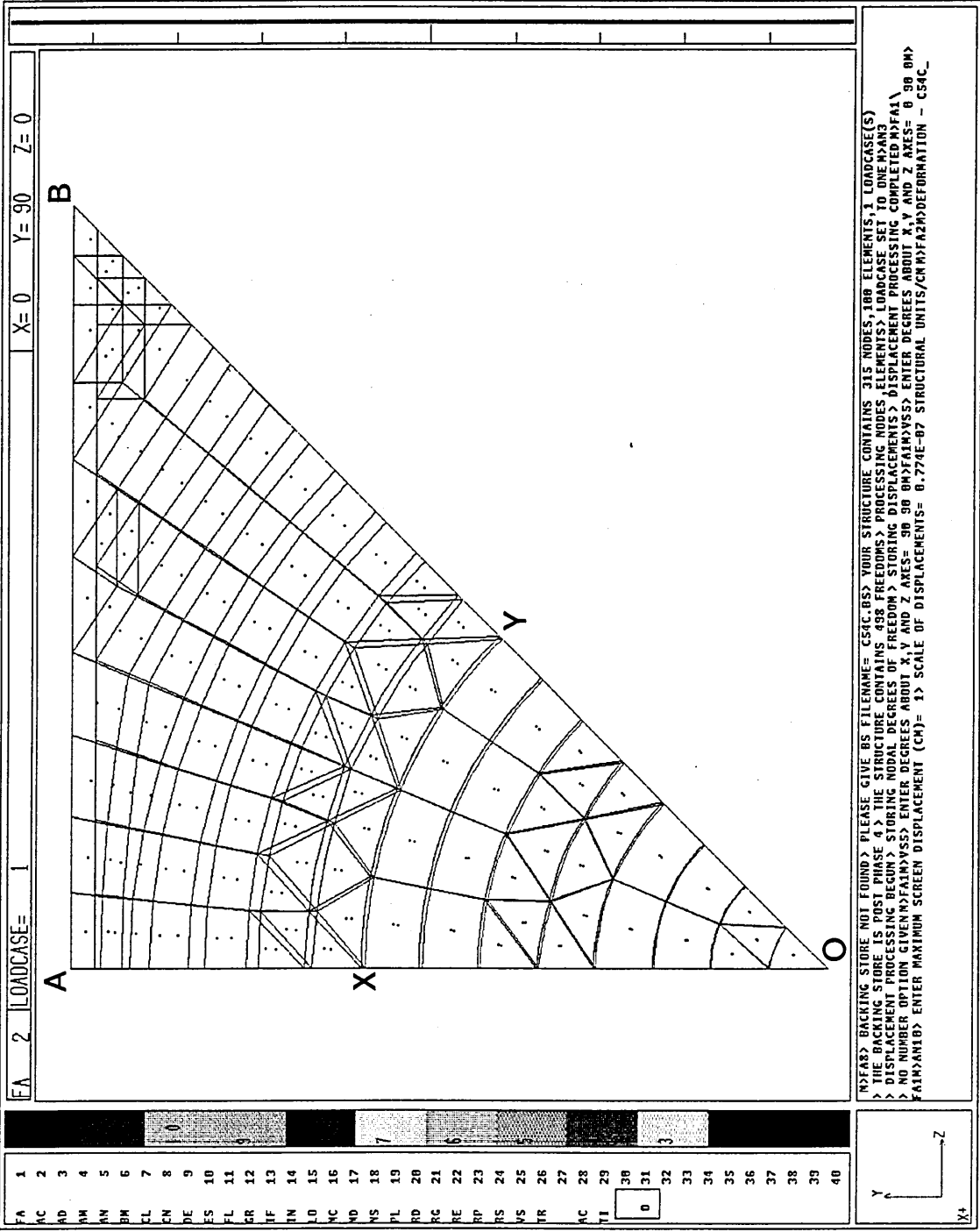


Figure 102. Maximum principal stress - model C54C  
(original in colour)



Figure 103. Maximum principal stress, vectors - model C54C

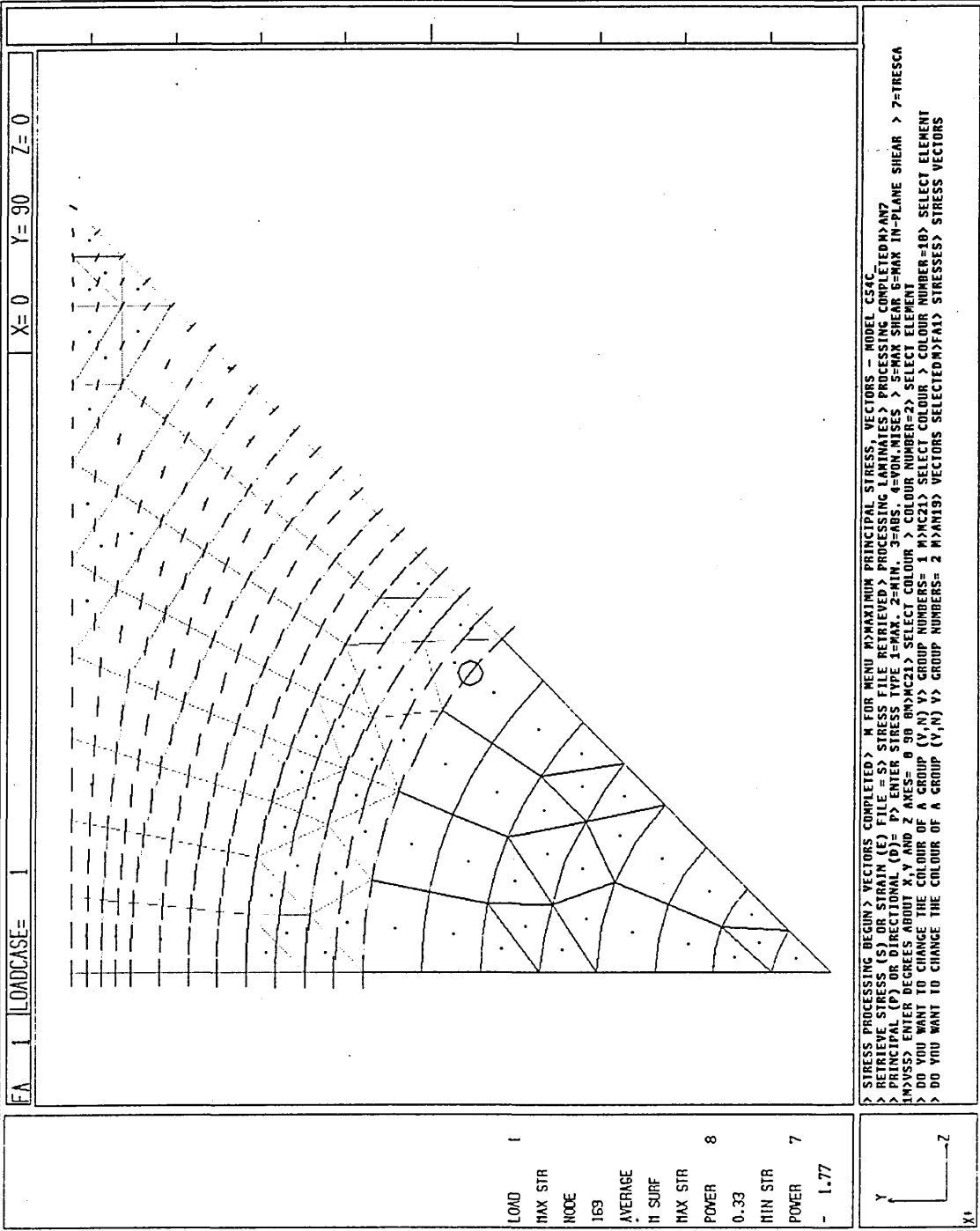


Figure 104. Von Mises stress - model C54C

(original in colour)

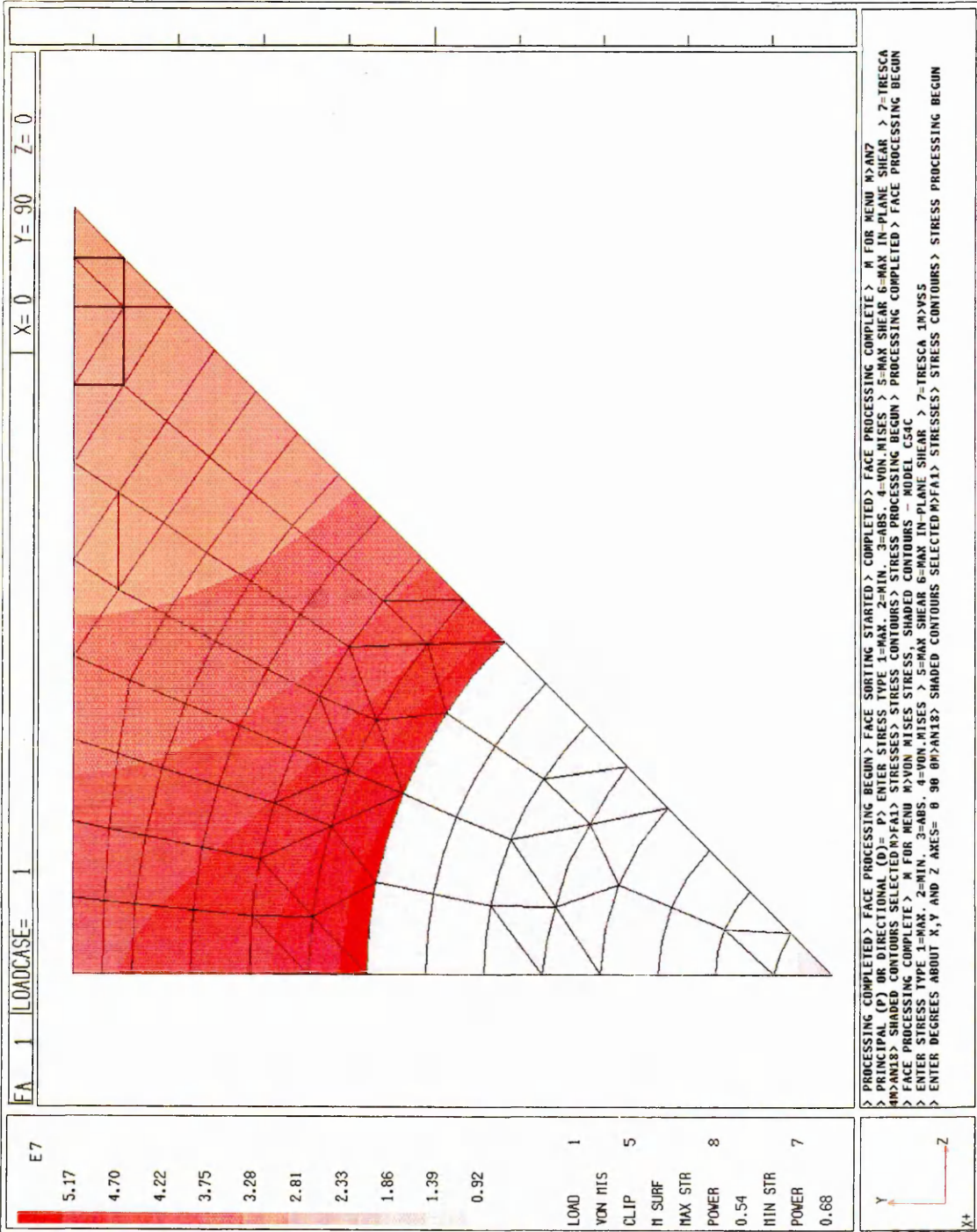


Figure 105. Deformation on cooling through 170°C - model E54A



Figure 106. Maximum principal stress - model E54A  
(original in colour)

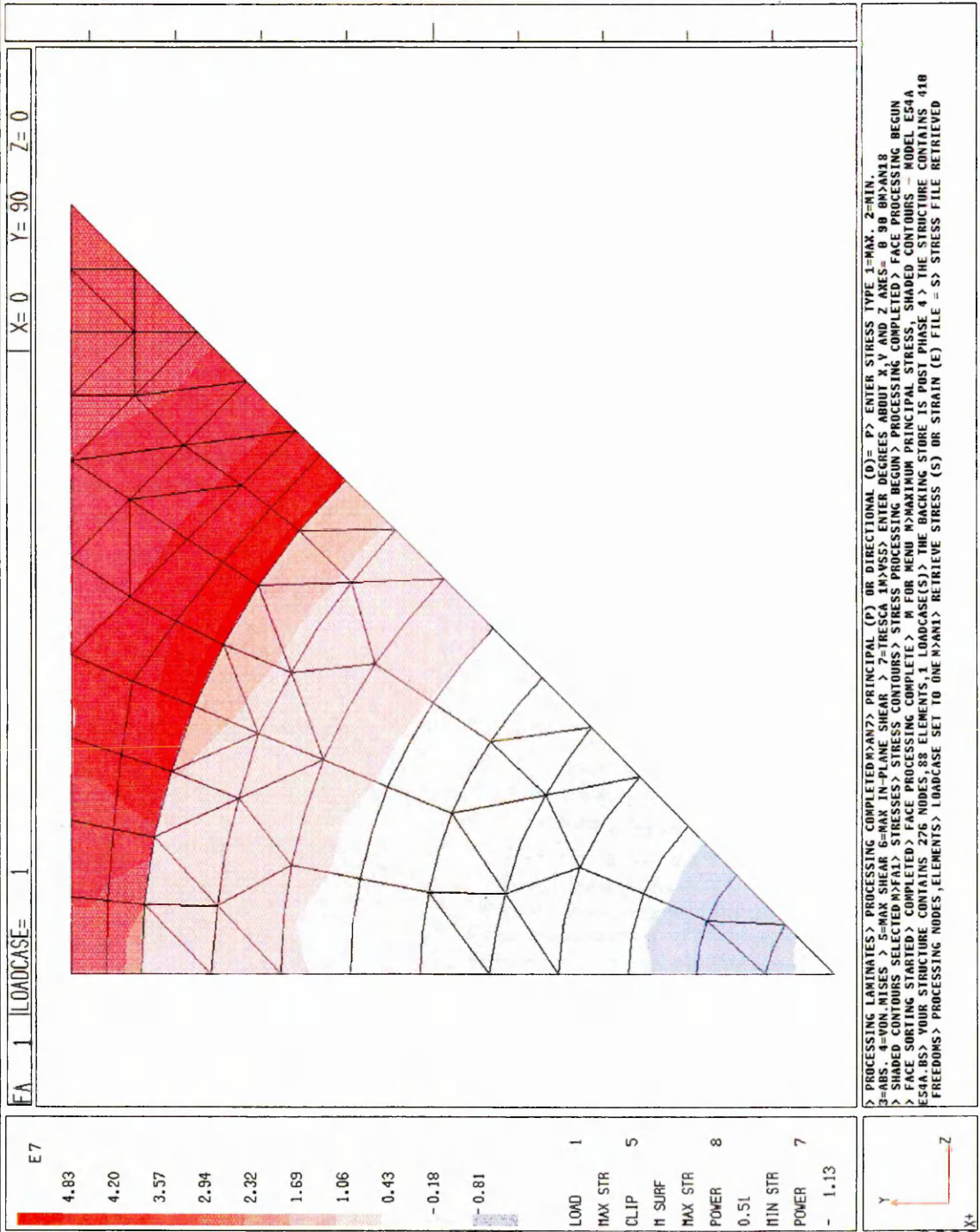


Figure 107. Maximum principal stress, vectors - model E54A



Figure 108. Von Mises stress - model E54A  
(original in colour)

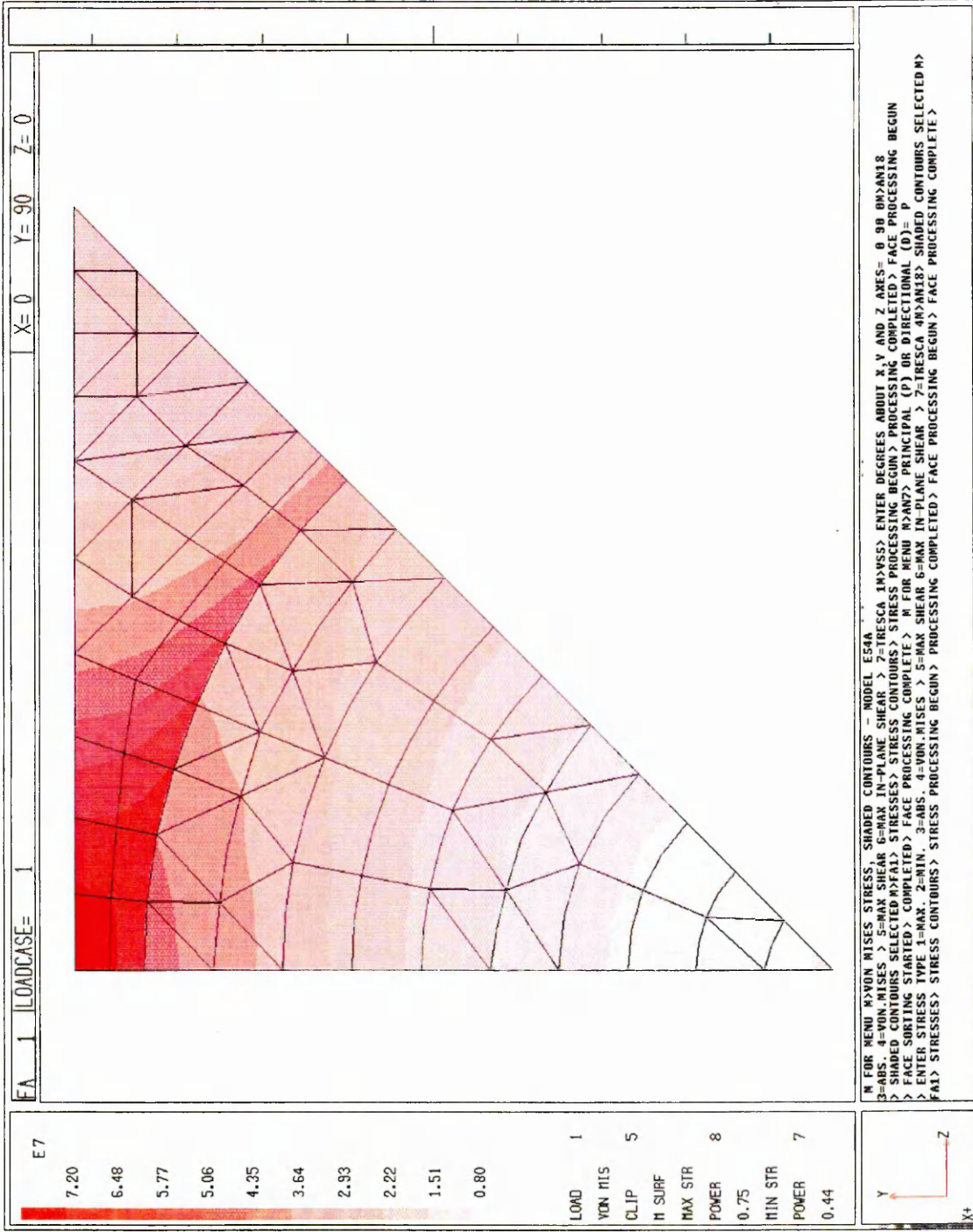
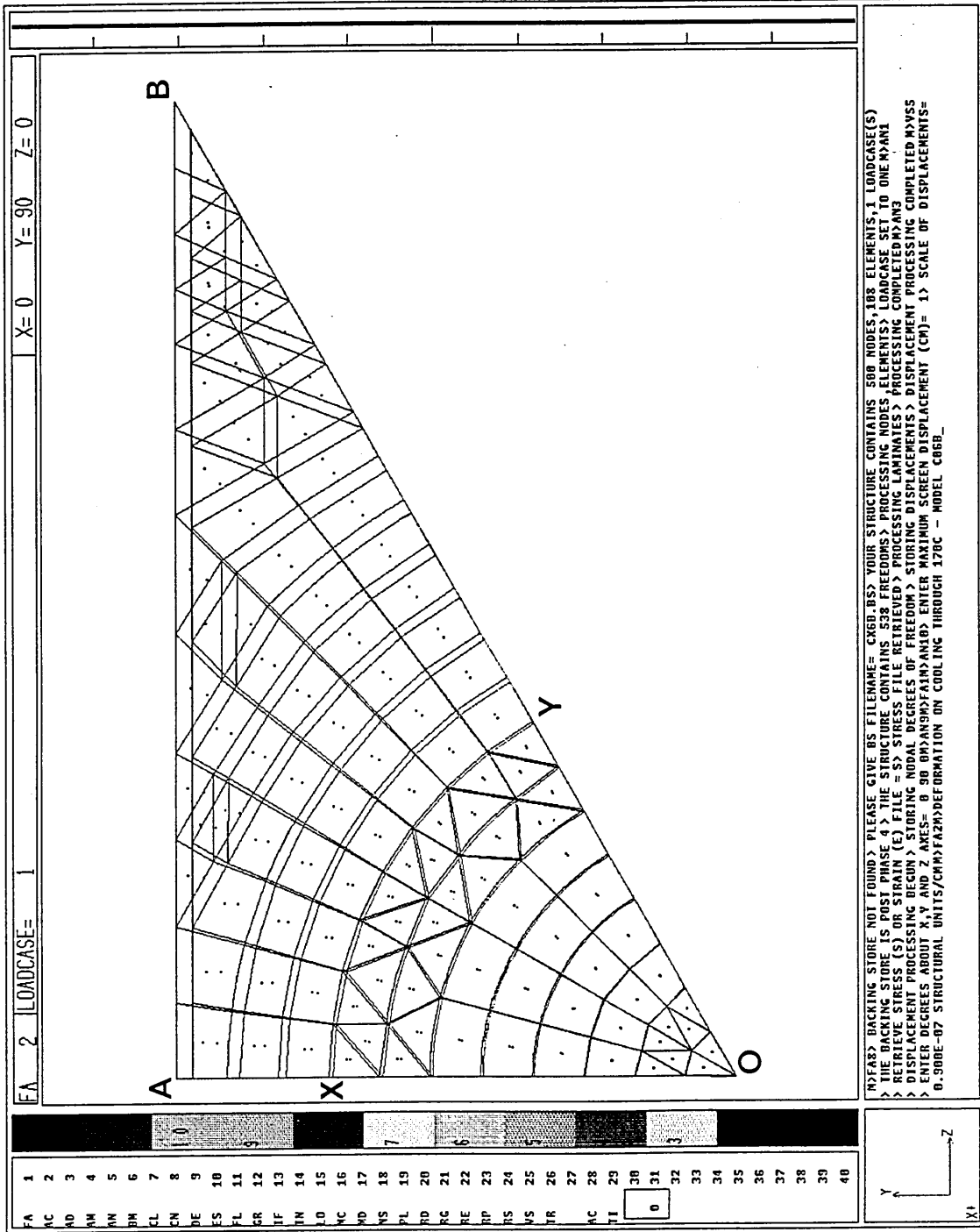


Figure 109. Deformation on cooling through 170°C - model C06B



FA 1  
 AC 2  
 AD 3  
 AM 4  
 AN 5  
 AO 6  
 AP 7  
 AQ 8  
 AR 9  
 AS 10  
 AT 11  
 AU 12  
 AV 13  
 AW 14  
 AX 15  
 AY 16  
 AZ 17  
 BA 18  
 BB 19  
 BC 20  
 BD 21  
 BE 22  
 BF 23  
 BG 24  
 BH 25  
 BI 26  
 BJ 27  
 BK 28  
 BL 29  
 BM 30  
 BN 31  
 BO 32  
 BP 33  
 BQ 34  
 BR 35  
 BS 36  
 BT 37  
 BU 38  
 BV 39  
 BW 40

R2FAB> BACKING STORE NOT FOUND> PLEASE GIVE BS FILENAME= CAGB.BS> YOUR STRUCTURE CONTAINS 500 NODES, 108 ELEMENTS, 1 LOADCASE(S)  
 > THE BACKING STORE IS POST PHASE 4> THE STRUCTURE CONTAINS 538 FREEDOMS> PROCESSING NODES, ELEMENTS, LOADCASE SET TO ONE, Y, ANI  
 > RETRIEVE STRESS (S) OR STRAIN (E) FILE = S> STRESS FILE RETRIEVED> PROCESSING LAMINATES, ELEMENTS, PROCESSING COMPLETED> ANI  
 > DISPLACEMENT PROCESSING BEGON> STORING NODAL DEGREES OF FREEDOM> STORING DISPLACEMENTS> PROCESSING COMPLETED> ANI  
 > ENTER DEGREES ABOUT X, Y, AND Z, ANGLE= 0, JO, OR ANI> FAI, ANI, JO> ENTER MAXIMUM SCREEN DISPLACEMENT (CM)= 1, SCALE OF DISPLACEMENTS=  
 0, 300E-07 STRUCTURAL UNITS/CM, FAI, FAI, DEFORMATION ON COOLING THROUGH 170C - MODEL C86B.

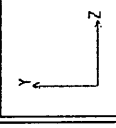


Figure 110. Maximum principal stress - model C06B

(original in colour)

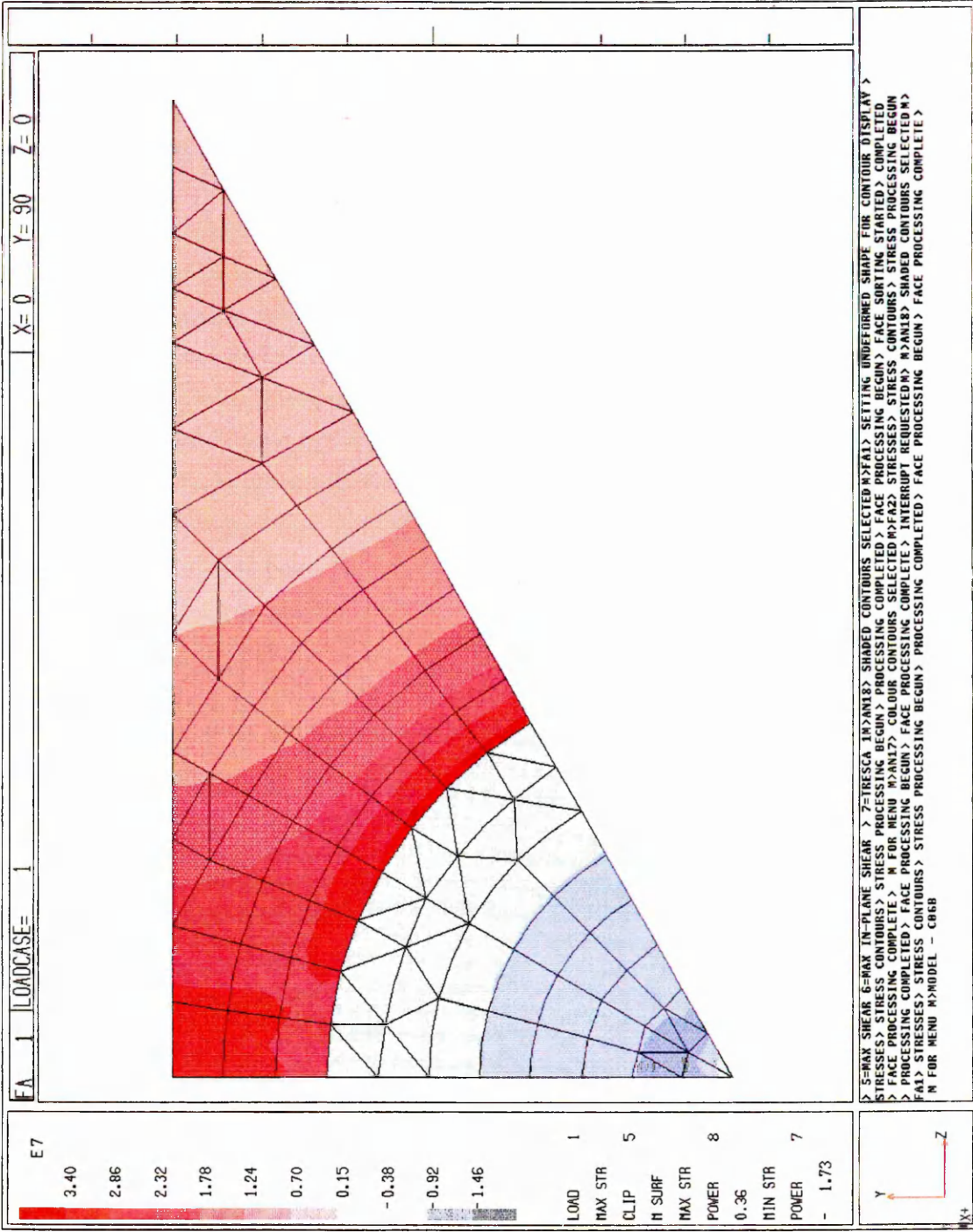


Figure 111. Maximum principal stress, vectors - model C06B

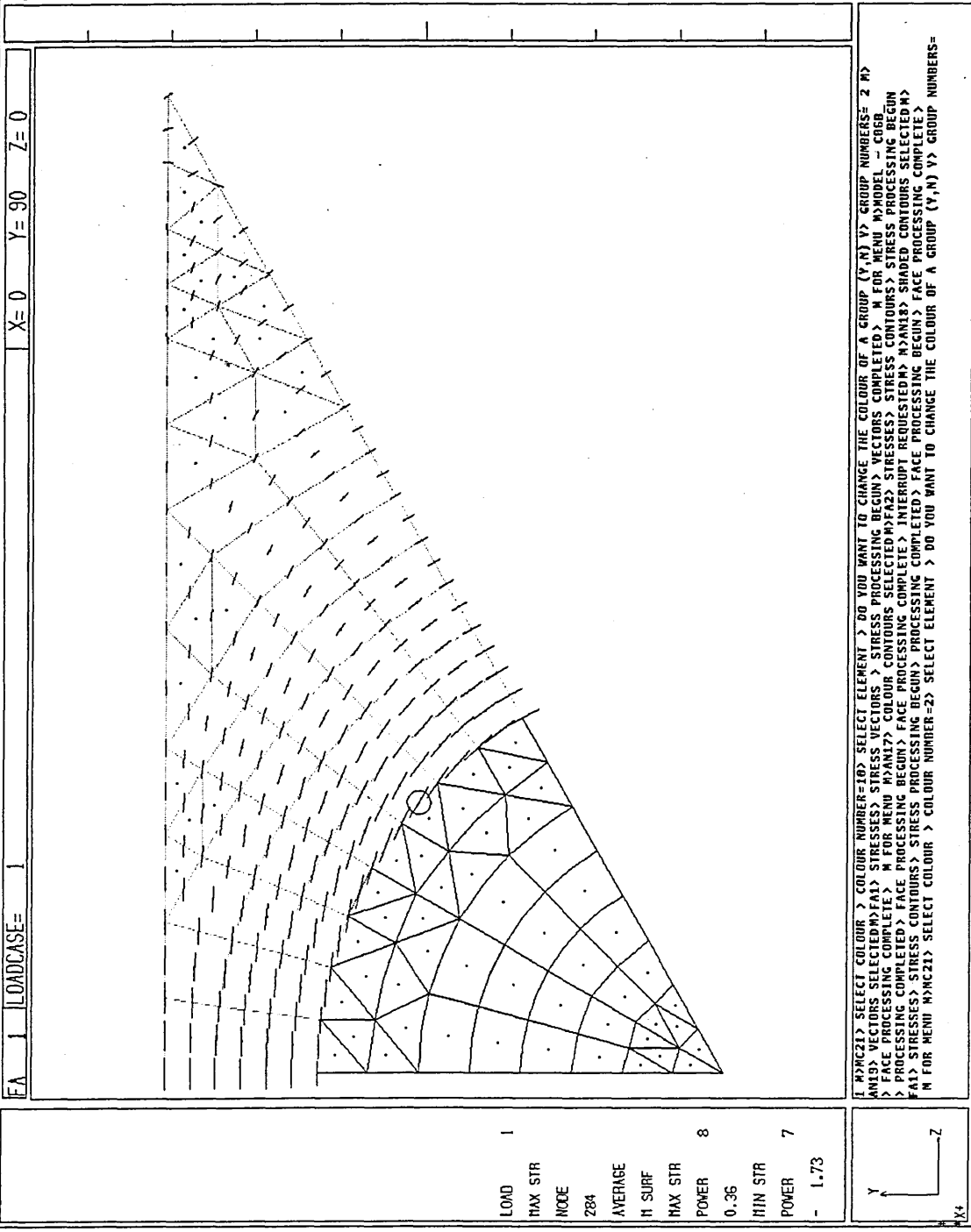


Figure 112. Von Mises stress - model C06B

(original in colour)

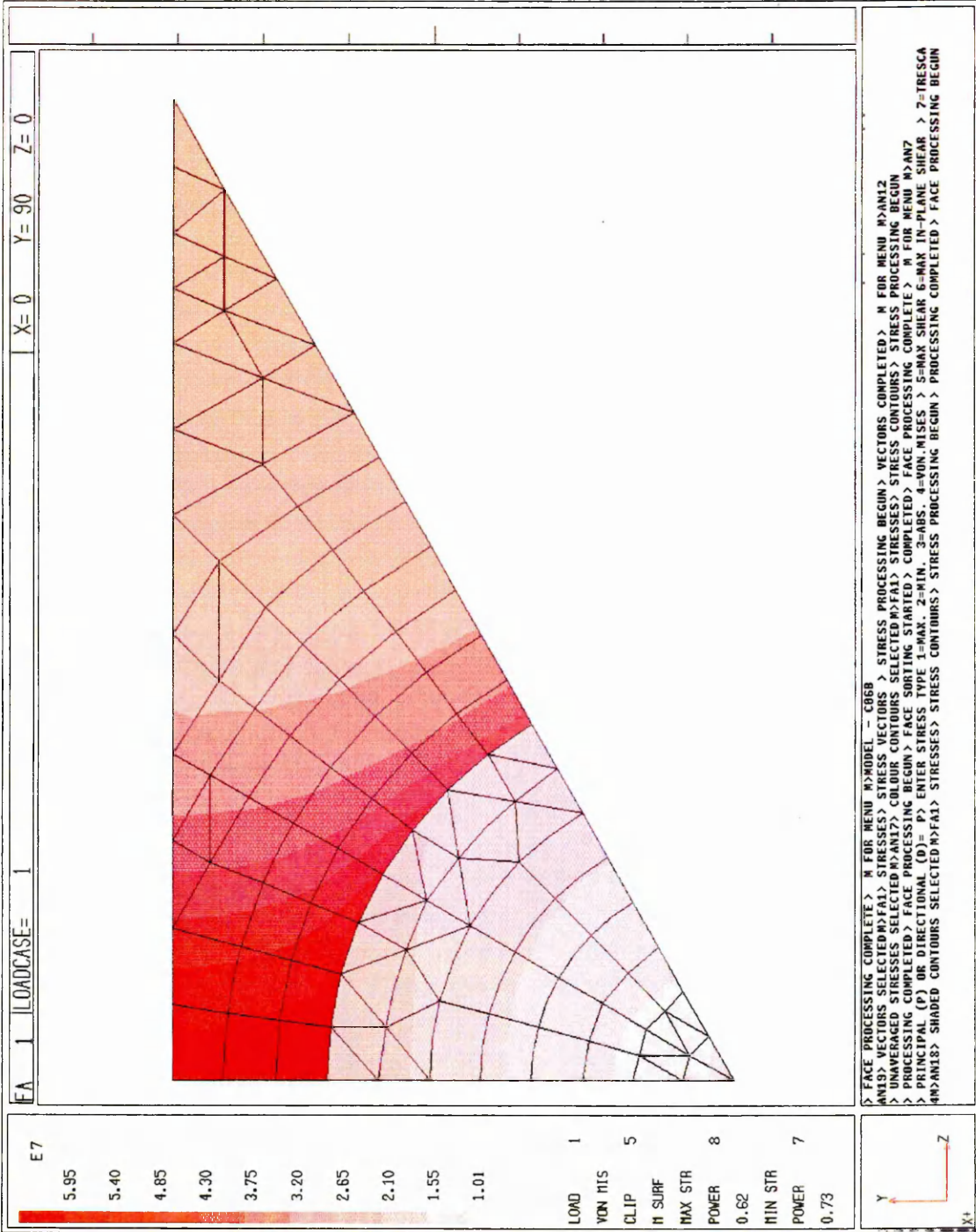
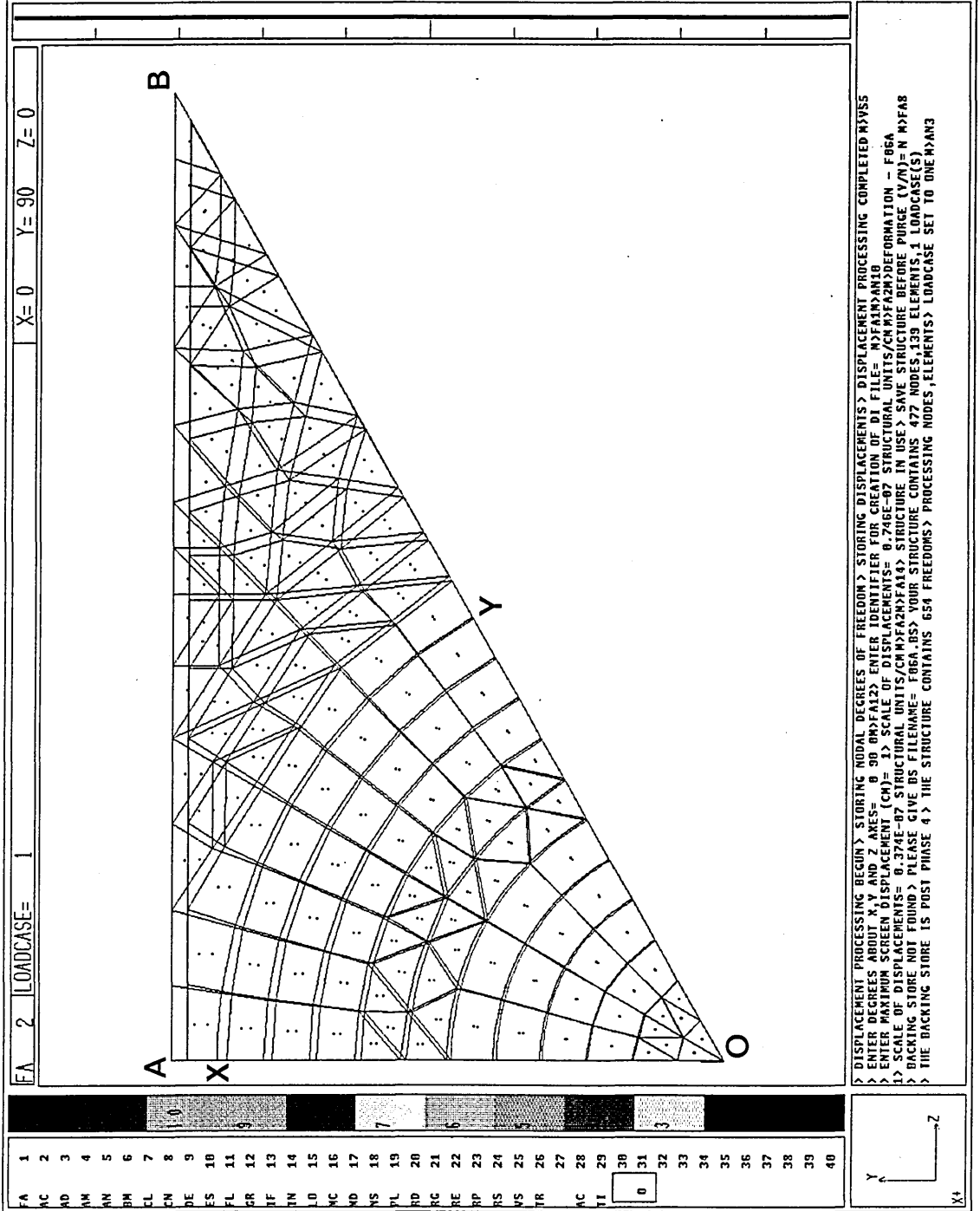


Figure 113. Deformation on cooling through Figure 170°C - model F06A



FA 2 LOADCASE= 1 X= 0 Y= 90 Z= 0

FA	1	2	3	4	5	6	7	8	9	10	11	12	13	14	15	16	17	18	19	20	21	22	23	24	25	26	27	28	29	30	31	32	33	34	35	36	37	38	39	40
----	---	---	---	---	---	---	---	---	---	----	----	----	----	----	----	----	----	----	----	----	----	----	----	----	----	----	----	----	----	----	----	----	----	----	----	----	----	----	----	----

> DISPLACEMENT PROCESSING BEGUN > STORING NODAL DEGREES OF FREEDOM > STORING DISPLACEMENTS > DISPLACEMENT PROCESSING COMPLETED MYSS  
 > ENTER DEGREES ABOUT X, Y AND Z AXES= 0 90 00 > ENTER IDENTIFIER FOR CREATION OF DI FILE= M>FAIM>AM18  
 > ENTER MAXIMUM SCREEN DISPLACEMENT (CM)= 1 > SCALE OF DISPLACEMENTS= 0.746E-07 STRUCTURAL UNITS/CM>FAZM>DEFORIMATION - F66A  
 > SCALE OF DISPLACEMENTS= 0.374E-07 STRUCTURAL UNITS/CM>M>FAZM>FA18 > STRUCTURE IN USE > SAVE STRUCTURE BEFORE PURGE (Y/N)= N >M>FAS  
 > BACKING STORE NOT FOUND > PLEASE GIVE DS FILENAME= F66A.DS > YOUR STRUCTURE CONTAINS 477 NODES, 139 ELEMENTS, 1 LOADCASE(S)  
 > THE BACKING STORE IS POST PHASE 4 > THE STRUCTURE CONTAINS 654 FREEDOMS > PROCESSING NODES, ELEMENTS > LOADCASE SET TO ONE >M>AN3

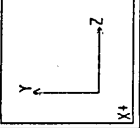


Figure 114. Maximum principal stress - model F06A  
(original in colour)



Figure 115. Maximum principal stress, vectors - model F06A



Figure 116. Von Mises stress - model F06A

(original in colour)

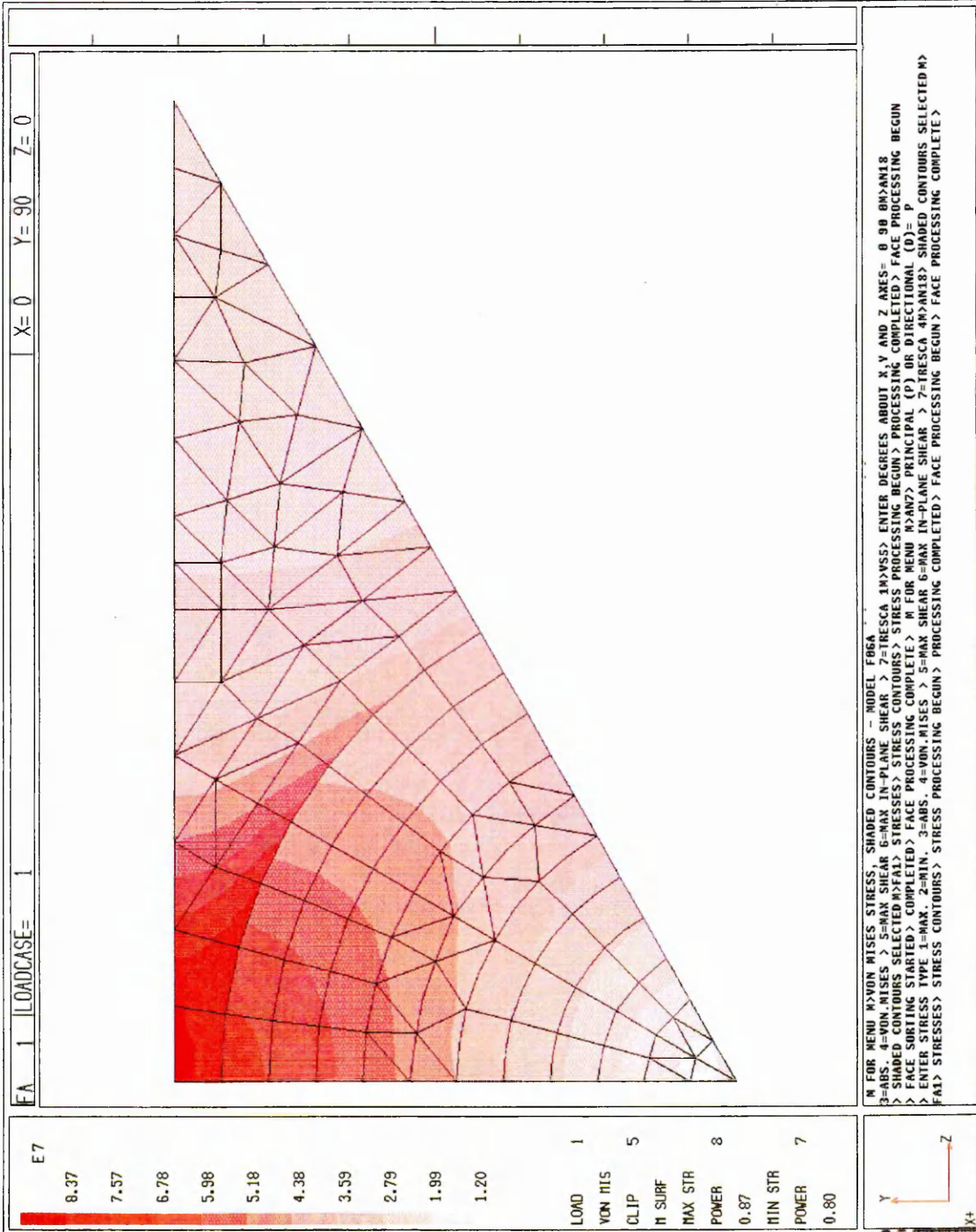


Figure 117. Deformation on cooling through 170°C - model B13C



Figure 118. Maximum principal stress - model B13C  
(original in colour)

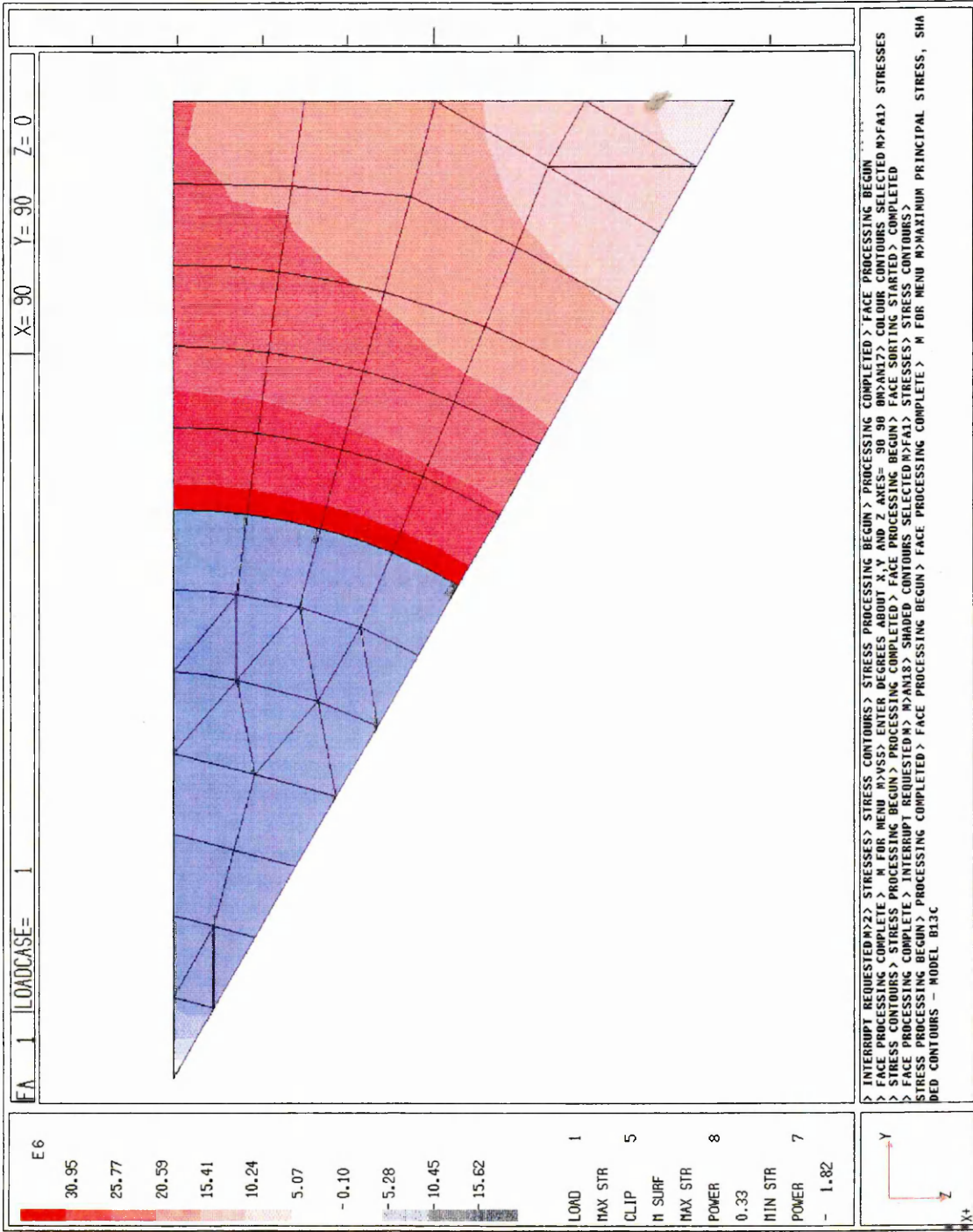


Figure 119. Maximum principal stress, vectors - model B13C



Figure 120. Von Mises stress - model B13C  
(original in colour)

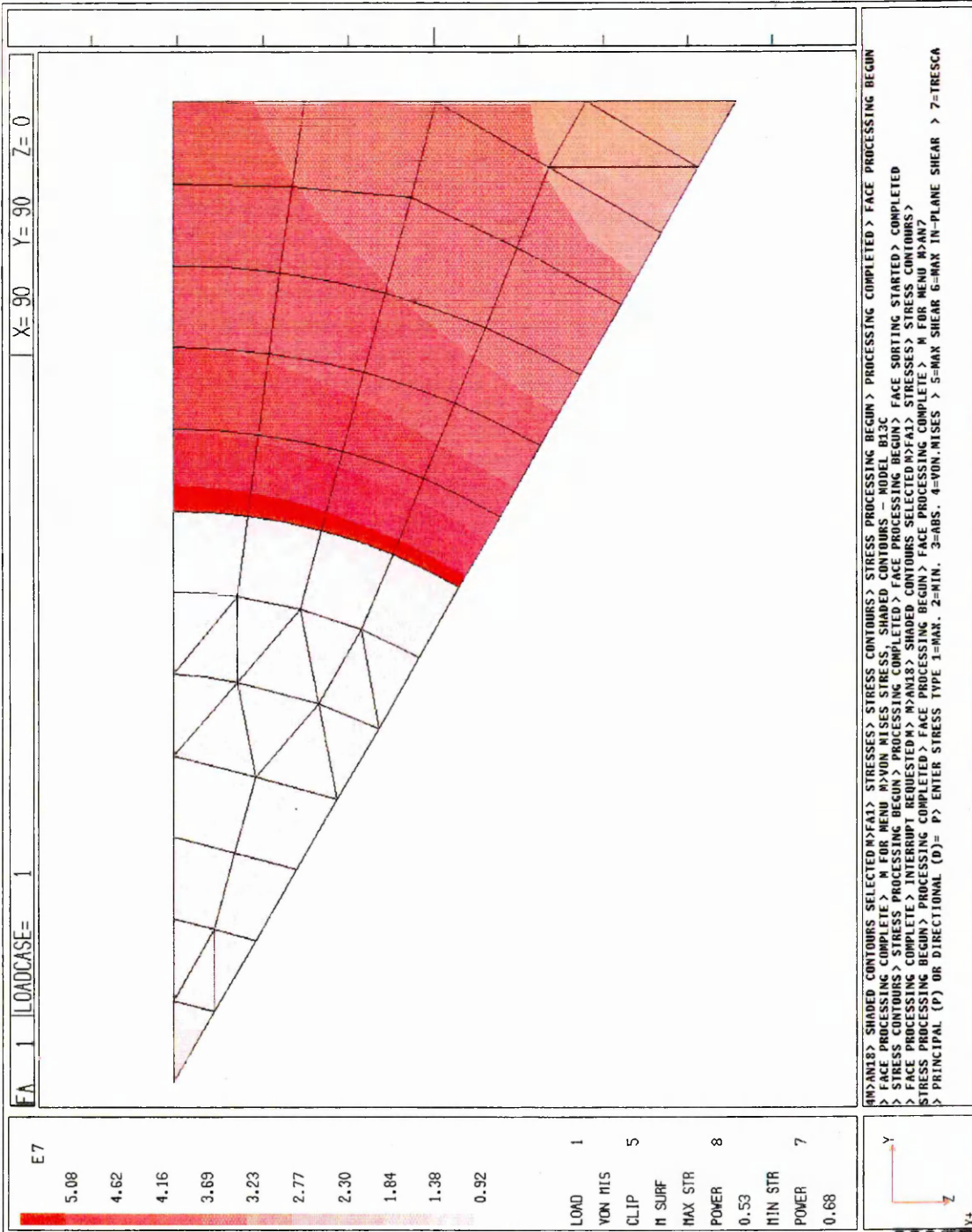


Figure 121. Deformation on cooling through 170°C - model V001

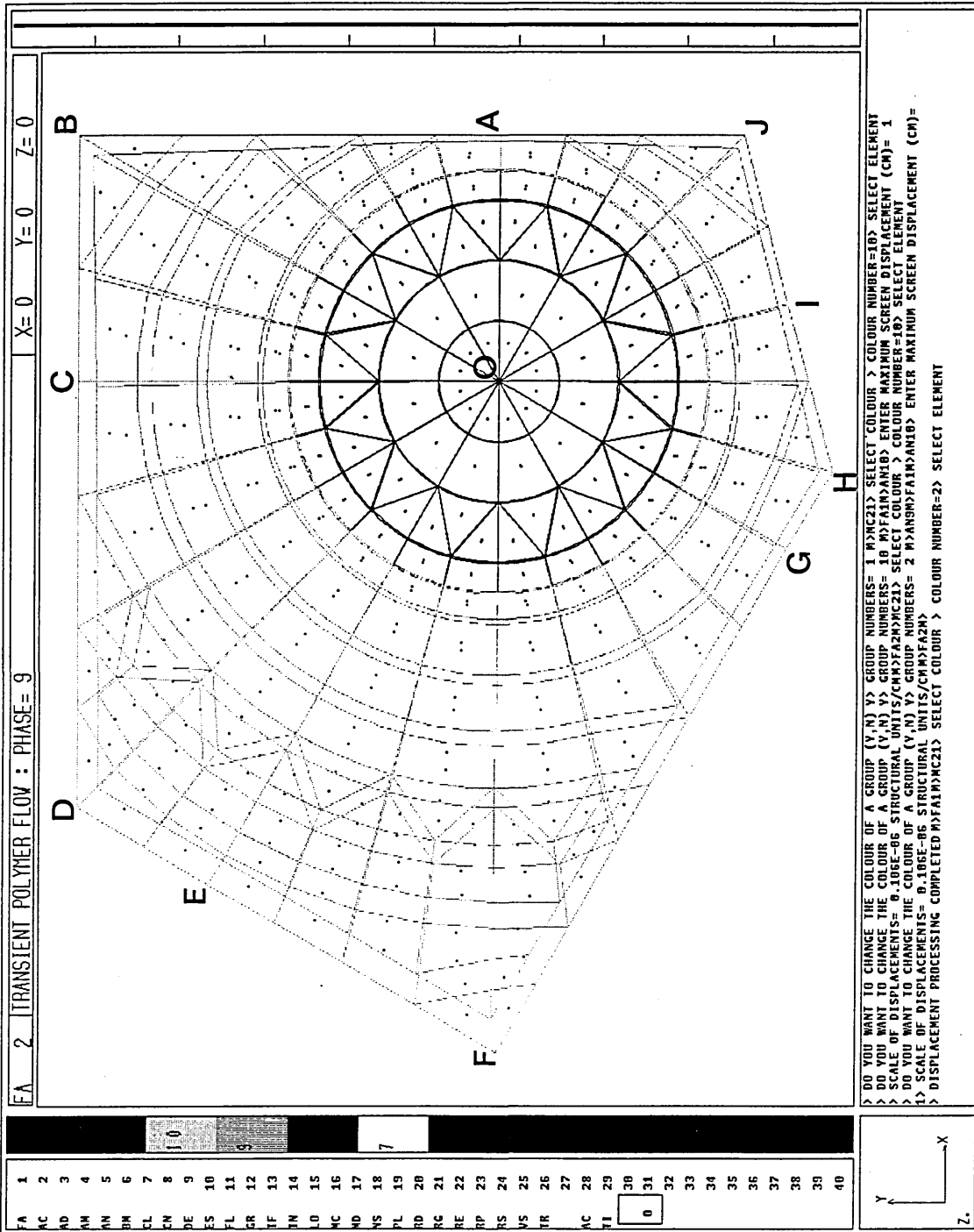
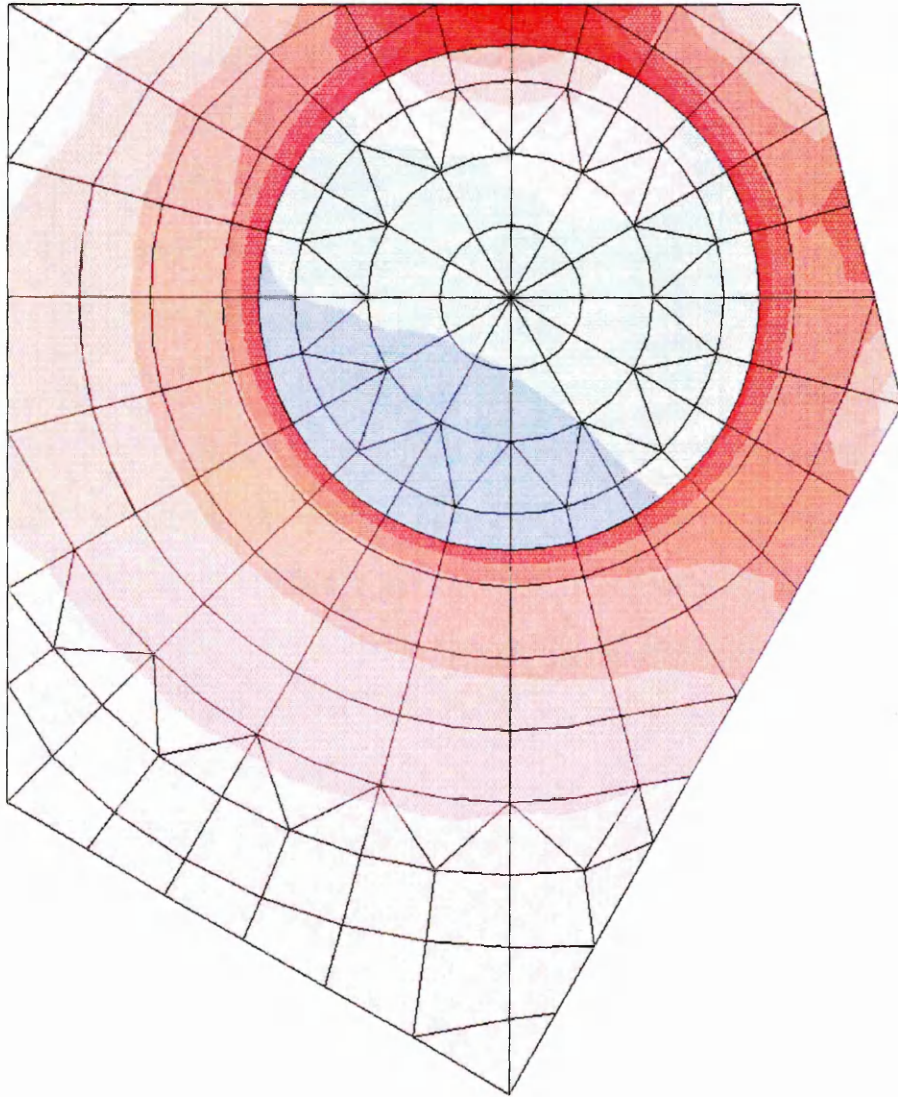


Figure 122. Maximum principal stress - model V001  
(original in colour)

EA 1 LOADCASE= 1 X= 0 Y= 0 Z= 0



E7

6.40  
5.54  
4.68  
3.82  
2.96  
2.10  
1.24  
0.38  
-0.47  
-1.33

LOAD 1  
MAX STR 5  
CLIP  
H SURF  
MAX STR 8  
POWER 0.68  
MIN STR  
POWER 7  
- 1.76



M>FA8> BACKING STORE NOT FOUND> PLEASE GIVE BS FILENAME= V081.BS> YOUR STRUCTURE CONTAINS 1169 NODES, 198 ELEMENTS, 1 LOADCASE(S)  
> THE BACKING STORE IS POST PHASE 4> THE STRUCTURE CONTAINS 1000 FREEDOMS> PROCESSING NODES ELEMENTS> LOADCASE SET TO ONE M>ANI  
> RETRIEVE STRESS (S) OR STRAIN (E) FILE = S> STRESS FILE RETRIEVED> PROCESSING LAMINATES> PROCESSING COMPLETED M>AN7  
> PRINCIPAL (P) OR DIRECTIONAL (D) = P> ENTER STRESS TYPE 1=MAX, 2=MIN, 3=ABS, 4=VON MISES > 5=MAX SHEAR 6=MAX IN-PLANE SHEAR > 7=TRESCA  
IM>ANI8> SHADED CONTOURS SELECTED M>FA1> STRESS CONTOURS> STRESS PROCESSING BEGUN> PROCESSING COMPLETED> FACE PROCESSING BEGUN  
> FACE SORTING STARTED> COMPLETED> FACE PROCESSING COMPLETE> M FOR MENU M>MAXIMUM PRINCIPAL STRESS, SHADED CONTOURS - MODEL V081

Figure 123. Maximum principal stress, vectors - model V001

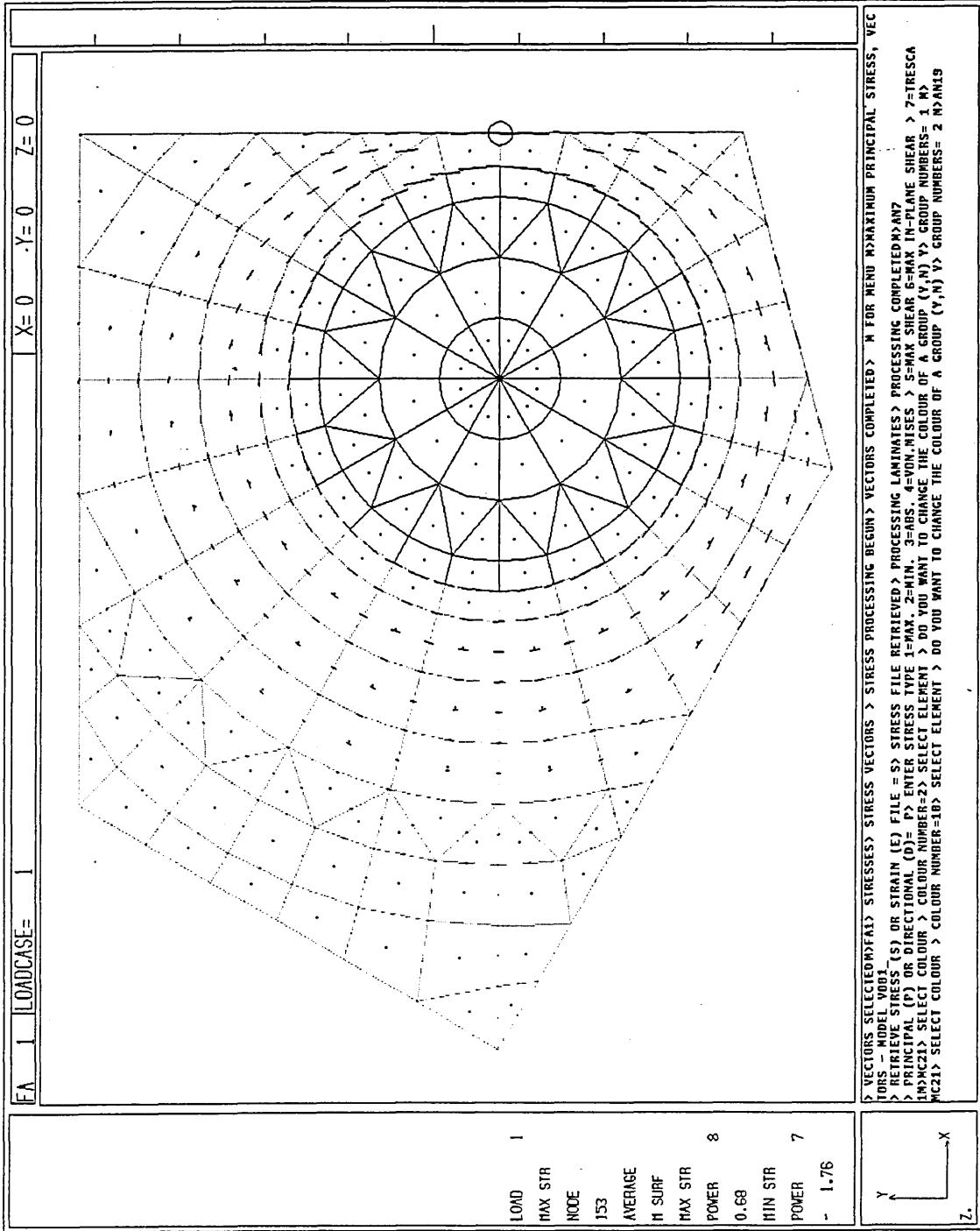
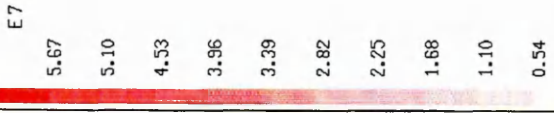
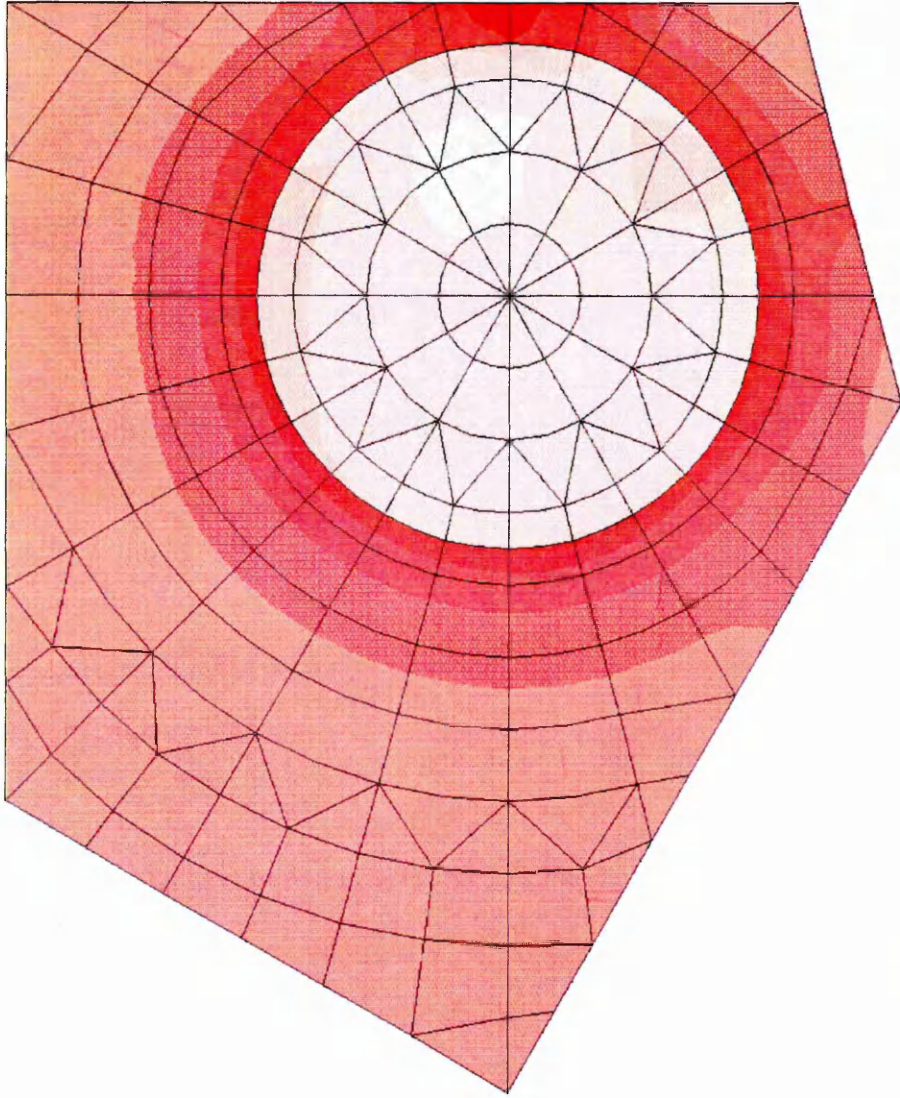


Figure 124. Von Mises stress - model V001

(original in colour)

EA 1 LOADCASE= 1 X= 0 Y= 0 Z= 0



- LOAD 1
- VON MISES 5
- CLIP
- M SURF
- MAX STR 8
- POWER 0.59
- MIN STR
- POWER 6
- 2.55

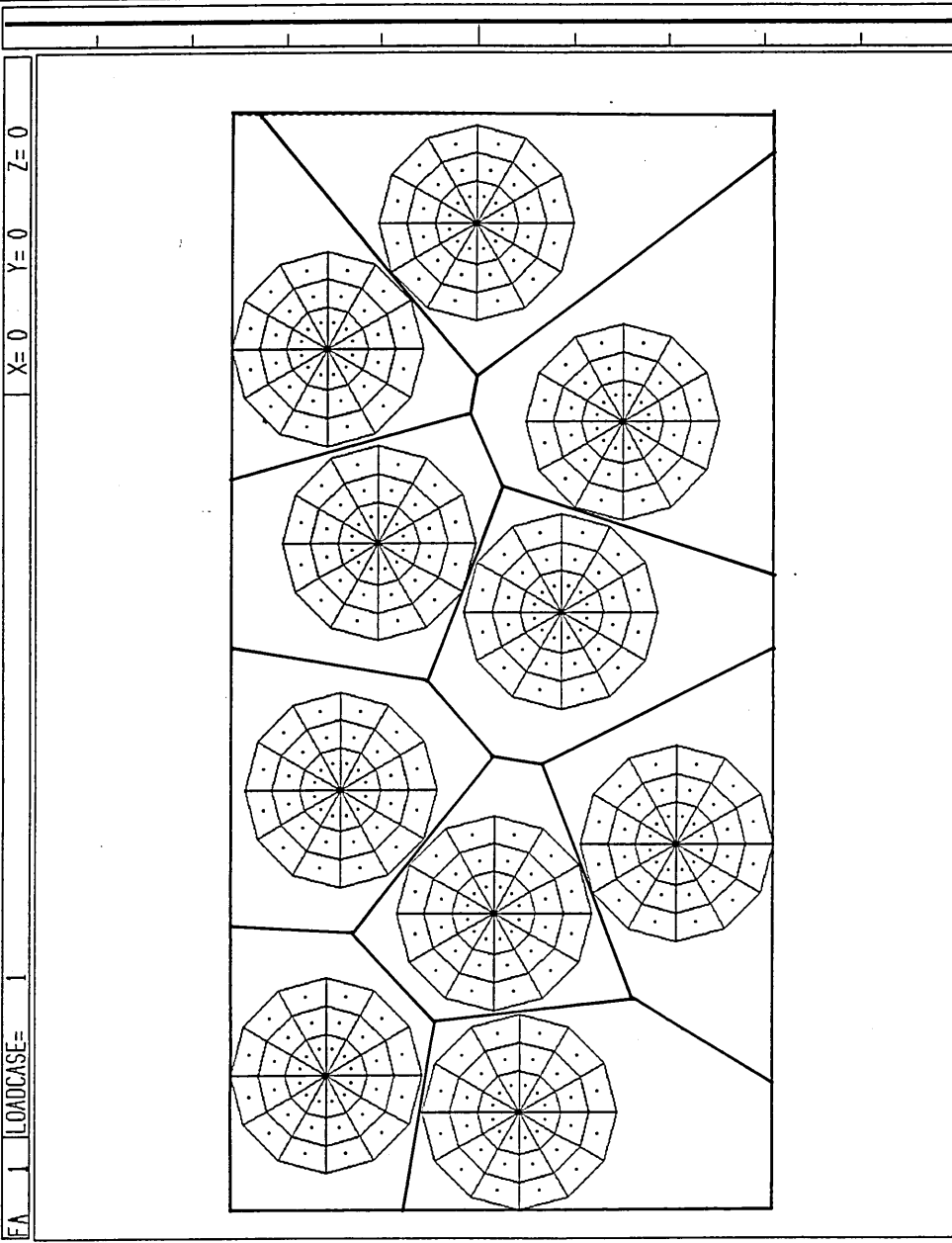


> ENTER STRESS TYPE 1=MAX, 2=MIN, 3=ABS, 4=VON MISES > 5=MAX SHEAR 6=MAX IN-PLANE SHEAR > 7=TRESCA 8=MAX IN-PLANE SHEAR > 9=MAX IN-PLANE SHEAR > 10=TRESCA  
> PRINCIPAL (P) OR DIRECTIONAL (D)= P > ENTER STRESS TYPE 1=MAX, 2=MIN, 3=ABS, 4=VON MISES > 5=MAX SHEAR 6=MAX IN-PLANE SHEAR > 7=TRESCA  
> FACE SORTING STARTED > COMPLETED > FACE PROCESSING COMPLETE > M FOR MENU M>AN7> PRINCIPAL (P) OR DIRECTIONAL (D)= P  
> FACE SORTING STARTED > COMPLETED > FACE PROCESSING COMPLETE > M FOR MENU M>AN7> PRINCIPAL (P) OR DIRECTIONAL (D)= P  
> ENTER STRESS TYPE 1=MAX, 2=MIN, 3=ABS, 4=VON MISES > 5=MAX SHEAR 6=MAX IN-PLANE SHEAR > 7=TRESCA 8=MAX IN-PLANE SHEAR > 9=MAX IN-PLANE SHEAR > 10=TRESCA  
> PRINCIPAL (P) OR DIRECTIONAL (D)= P > ENTER STRESS TYPE 1=MAX, 2=MIN, 3=ABS, 4=VON MISES > 5=MAX SHEAR 6=MAX IN-PLANE SHEAR > 7=TRESCA  
> FACE SORTING STARTED > COMPLETED > FACE PROCESSING COMPLETE > M FOR MENU M>AN7> PRINCIPAL (P) OR DIRECTIONAL (D)= P

Figure 125. 30% fibre volume fraction random fibre array



Figure 126. 50% fibre volume fraction random fibre array



EA 1 LOADCASE= 1 X=0 Y=0 Z=0

- EA 1
- AC 2
- AD 3
- AM 4
- AN 5
- BM 6
- CL 7
- CN 8
- DE 9
- ES 10
- FL 11
- FR 12
- IF 13
- JN 14
- LO 15
- MC 16
- ND 17
- NS 18
- PL 19
- RD 20
- RG 21
- RE 22
- FP 23
- RS 24
- VS 25
- TR 26
- AC 27
- TI 28
- TI 29
- TI 30
- TI 31
- TI 32
- TI 33
- TI 34
- TI 35
- TI 36
- TI 37
- TI 38
- TI 39
- TI 40

PLEASE GIVE DI FILENAME= RA38.D1> YOUR STRUCTURE CONTAINS 1277 NODES, 1 LOADCASE(S), THE HIGHEST NUMBERED ELEMENT IS 368M7ADZ7  
 > NO NUMBER OPTION GIVEN>NDZ7M3S1M3EA1M3EA14) SAVE DI FILE BEFORE PURGE (Y/N)=N M3FA11) PLEASE GIVE DI FILENAME= RA38.D1  
 > YOUR STRUCTURE CONTAINS 1385 NODES, 1 LOADCASE(S), THE HIGHEST NUMBERED ELEMENT IS 368M7ADZ7M3S1M3EA1M3EA14)RANDOM ARRAY OF FIBRES - FIBRE VOLU  
 ME FRACTION = 0.50

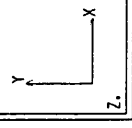


Figure 127. Deformation on cooling through 170°C - model V053



Figure 128. Maximum principal stress - model V053  
(original in colour)

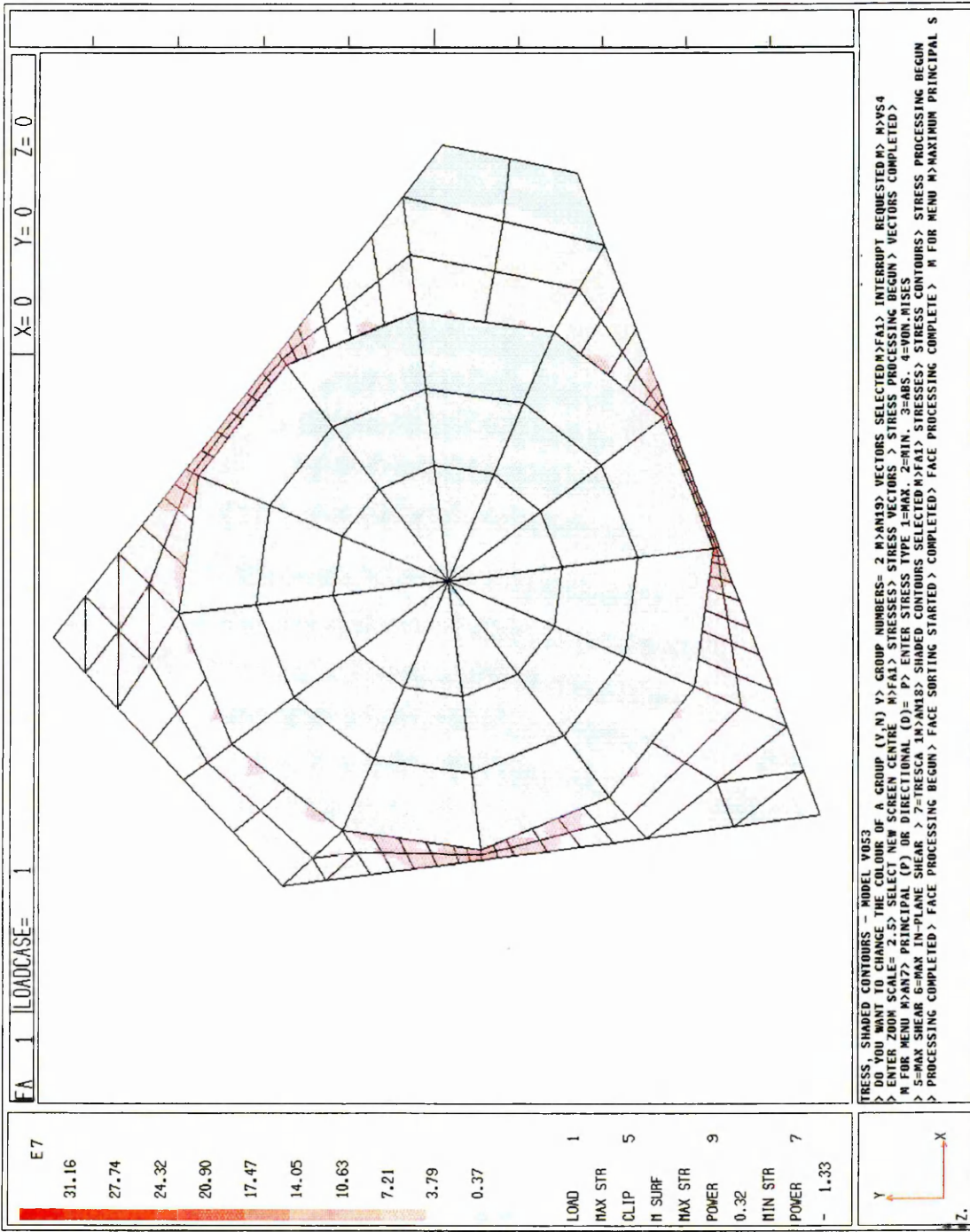


Figure 129. Maximum principal stress, vectors - model V053

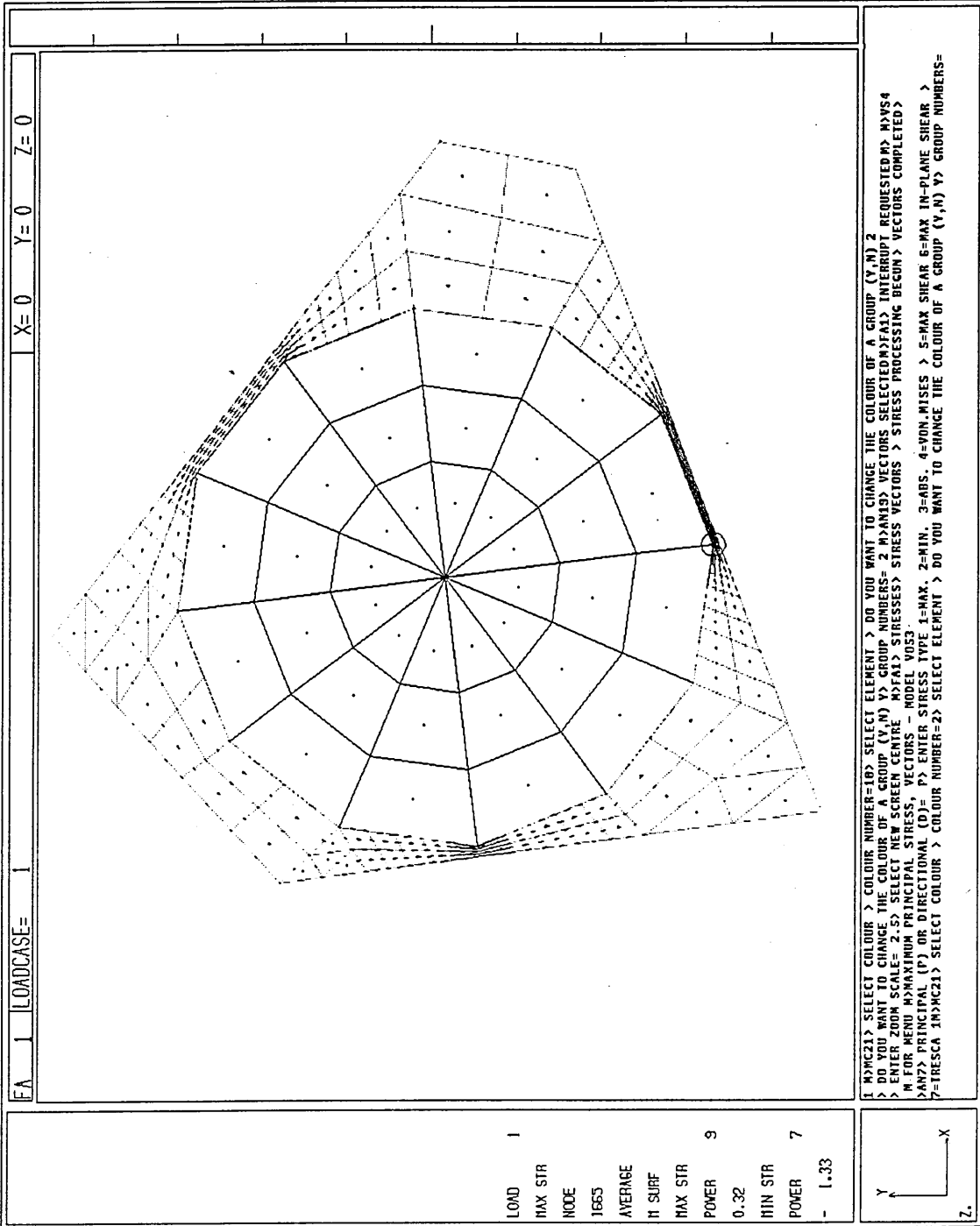


Figure 130. Von Mises stress, model V053  
(original in colour)

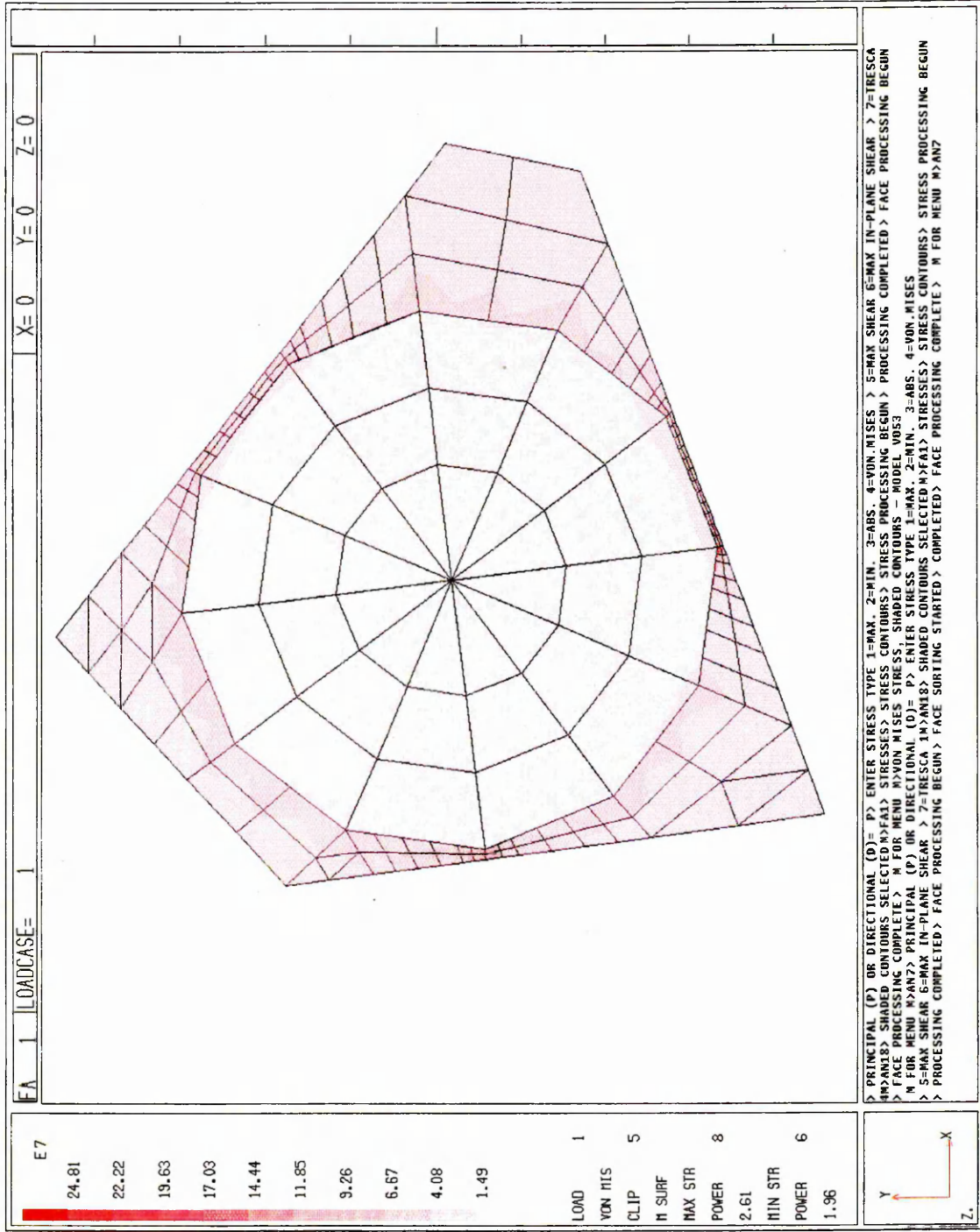


Figure 131. Maximum principal stress, high stress region - model V053  
(original in colour)

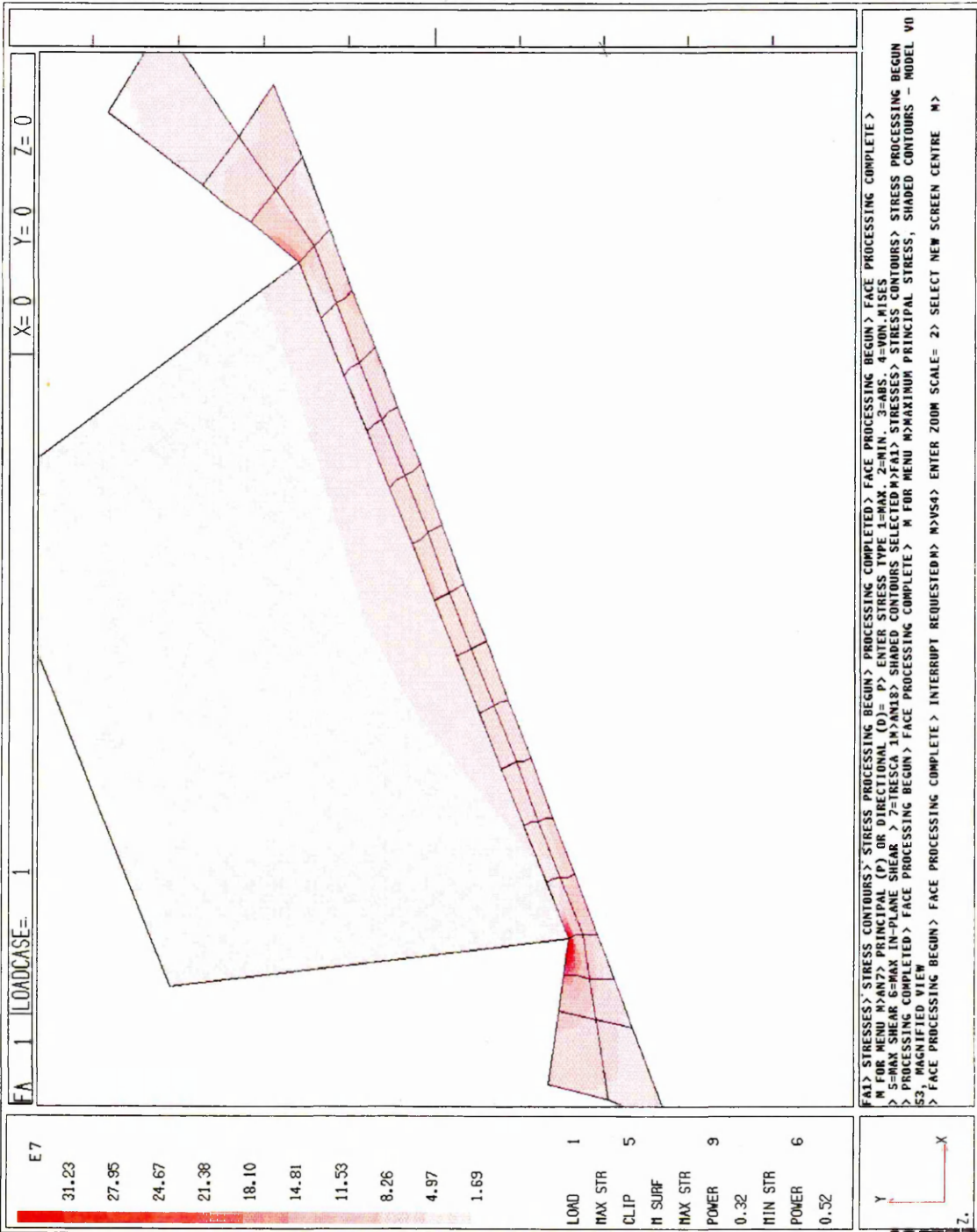


Figure 132. Maximum principal stress, high stress region, vectors -  
model V053



Figure 133. Von Mises stress, high stress region - model V053  
(original in colour)

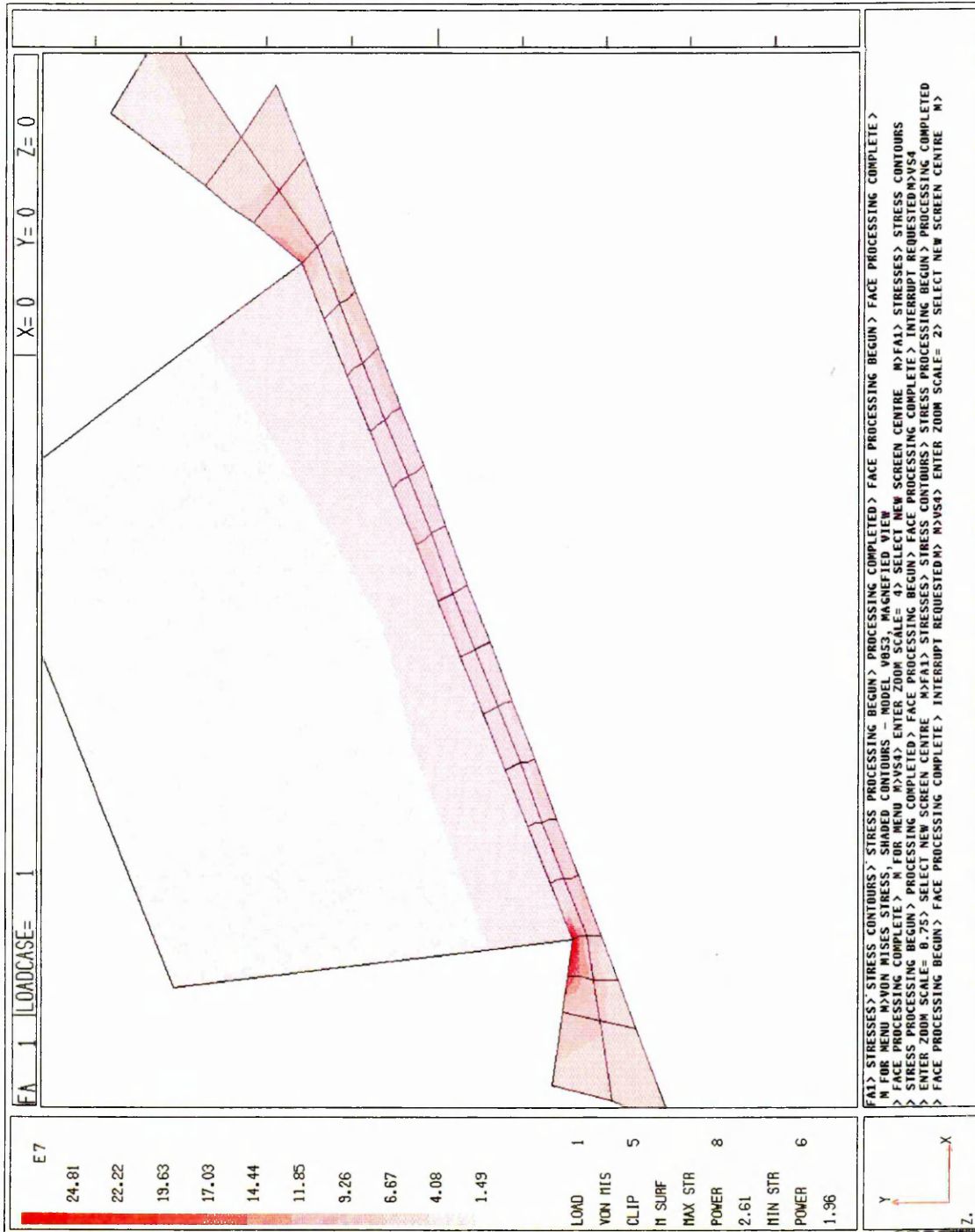
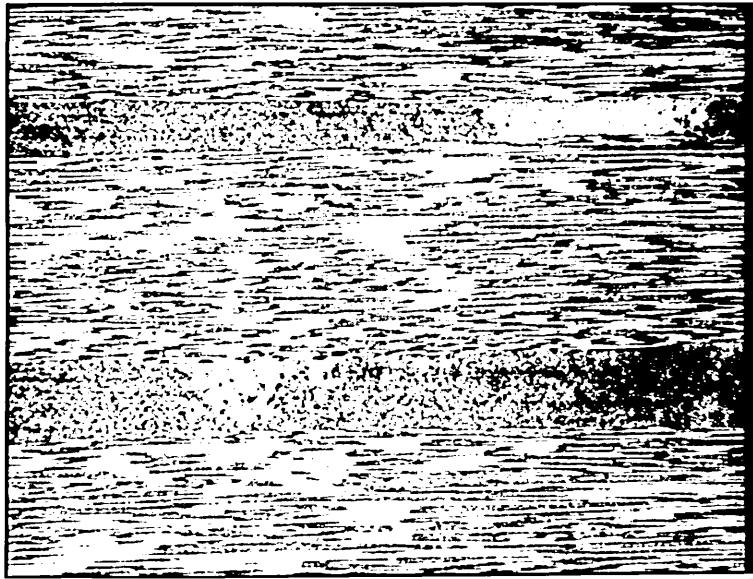


Figure 134. Centre plies of laminate sample - Mag x 60



SCHOOL OF ENGINEERING 10. 12. 91 MAGNIFICATION X60

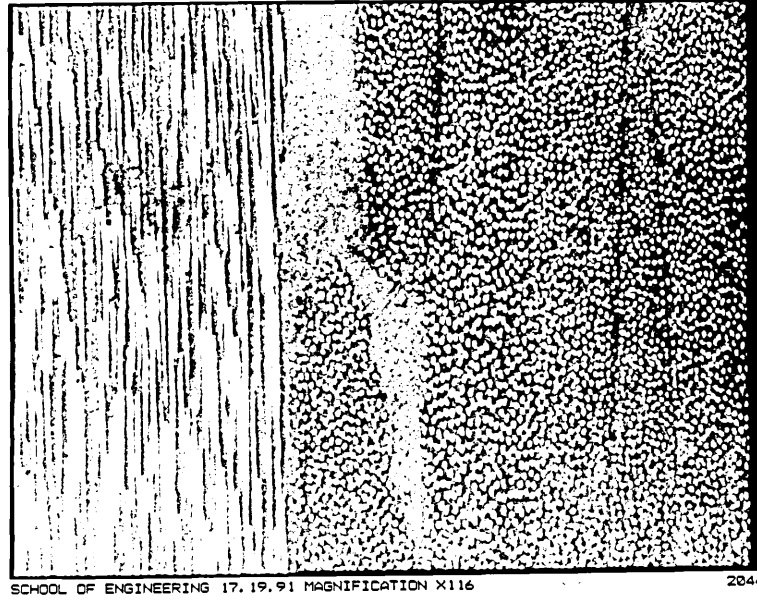
1863

Figure 135. Outer plies of laminate sample - Mag x 116:

a) View 1

b) View 2

a)



b)

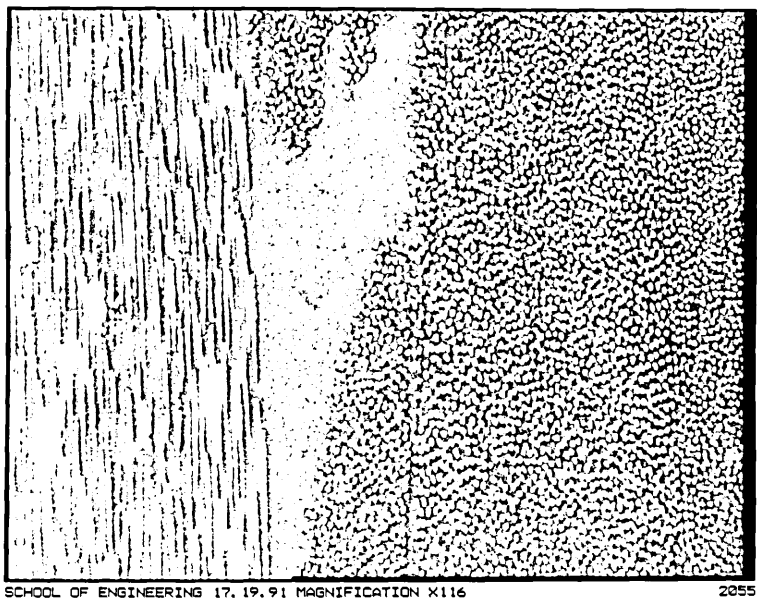
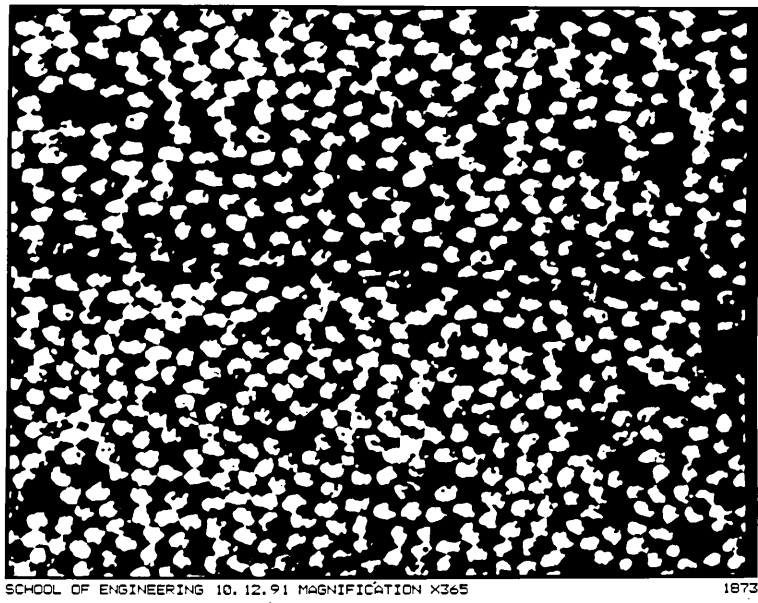


Figure 136. Cross sections through transverse layer - Mag x 365:

a) View 1

b) View 2

a)



b)

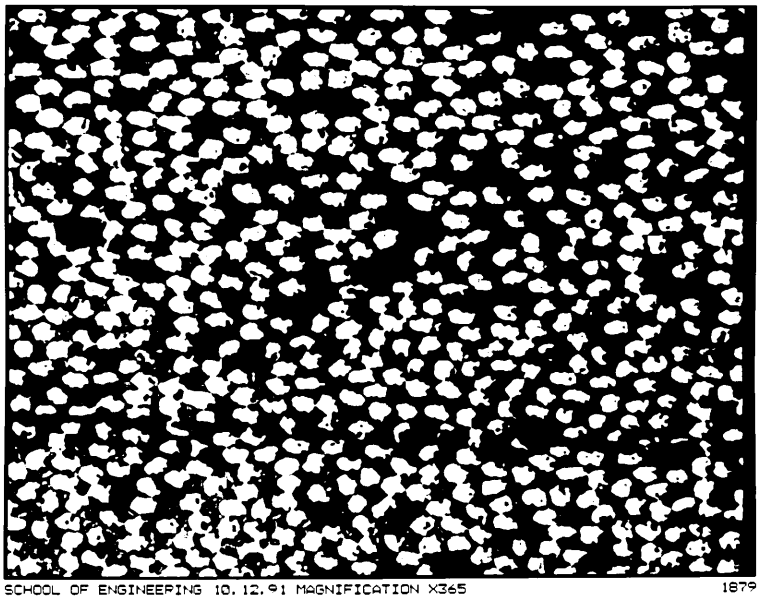
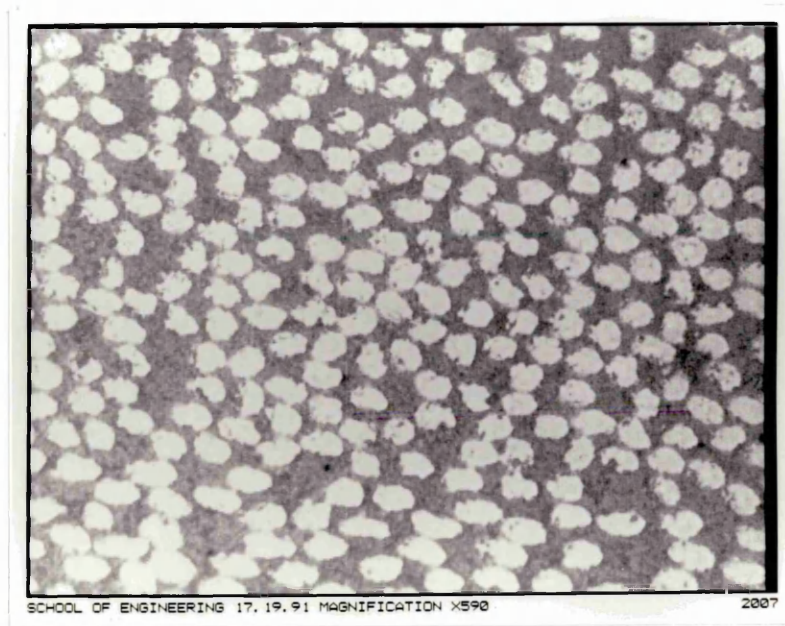


Figure 137. Cross sections through transverse layer - Mag x 590:

a) View 1

b) View 2

a)



b)

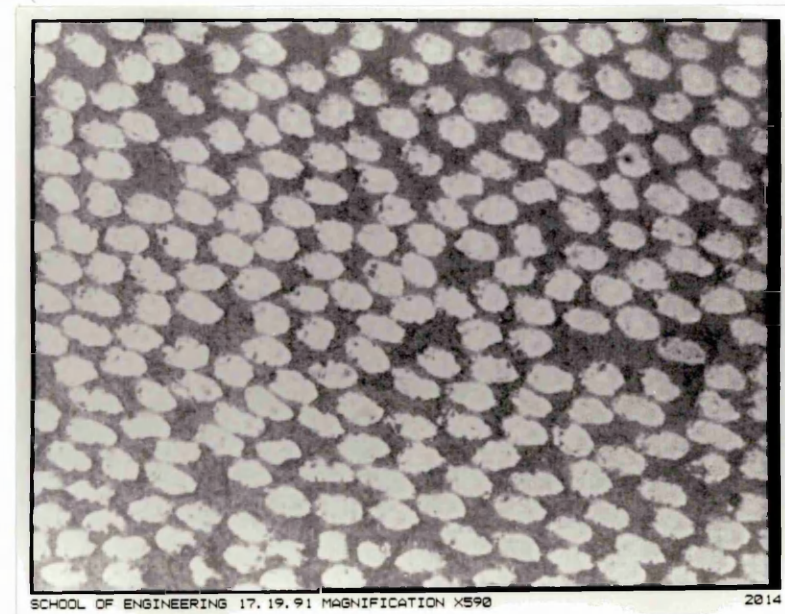
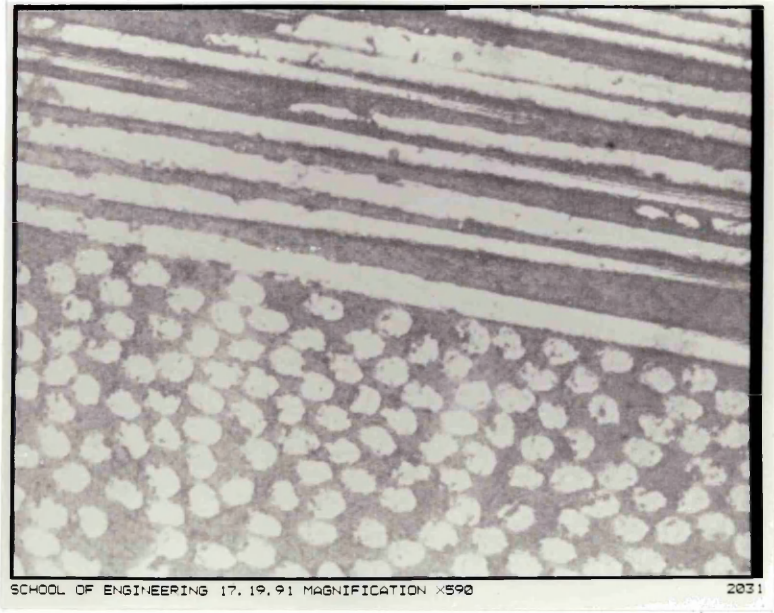


Figure 138. Ply interface - Mag x 590:

a) View 1 - no epoxy rich region

b) View 2 - with epoxy rich region

a)



b)

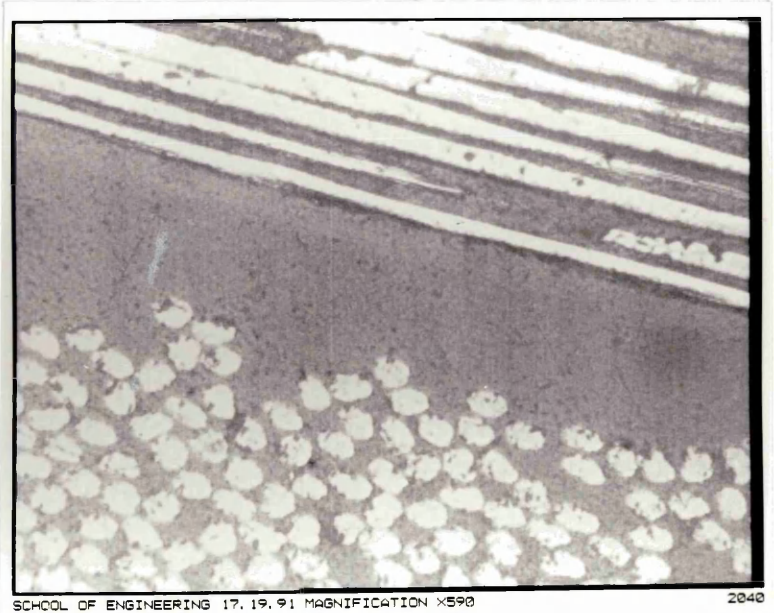
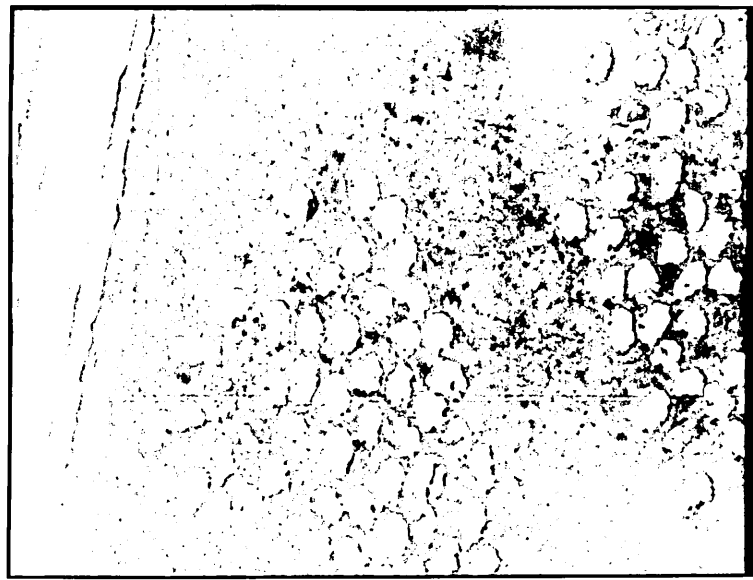


Figure 139. Epoxy rich regions between tows - Mag x 590:

a) View 1 -at ply interface

b) View 2 - in the centre of a transverse ply

a)



b)

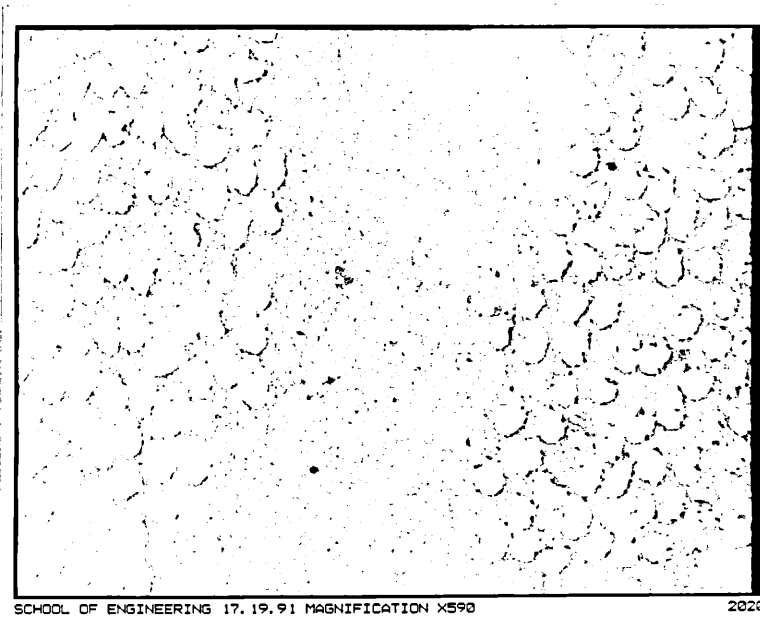
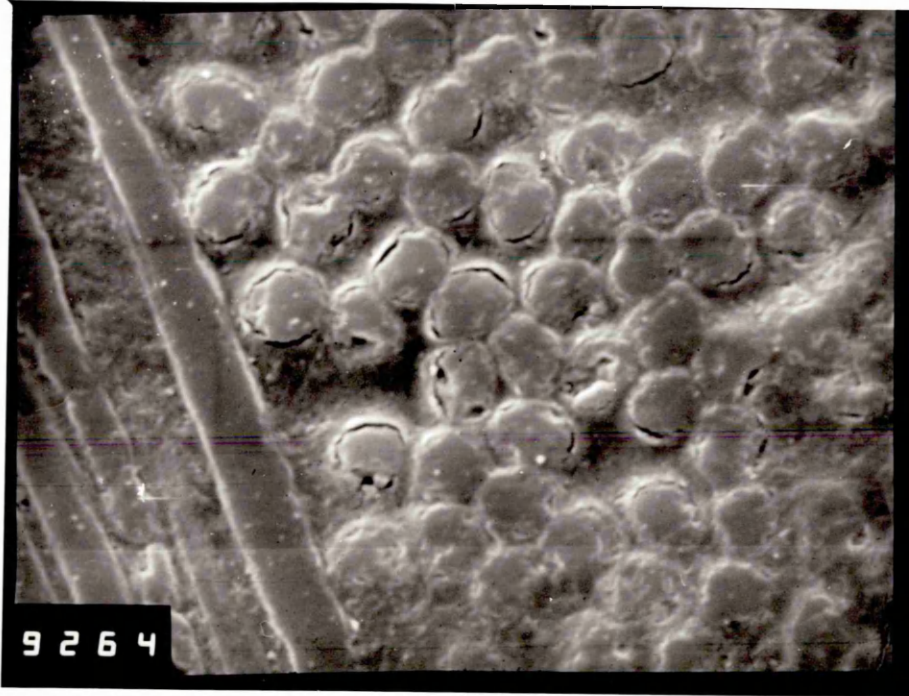


Figure 140. Cracking at fibre/matrix interface, view 1:

a) Mag x 1440

b) Mag x 2880

a)



b)

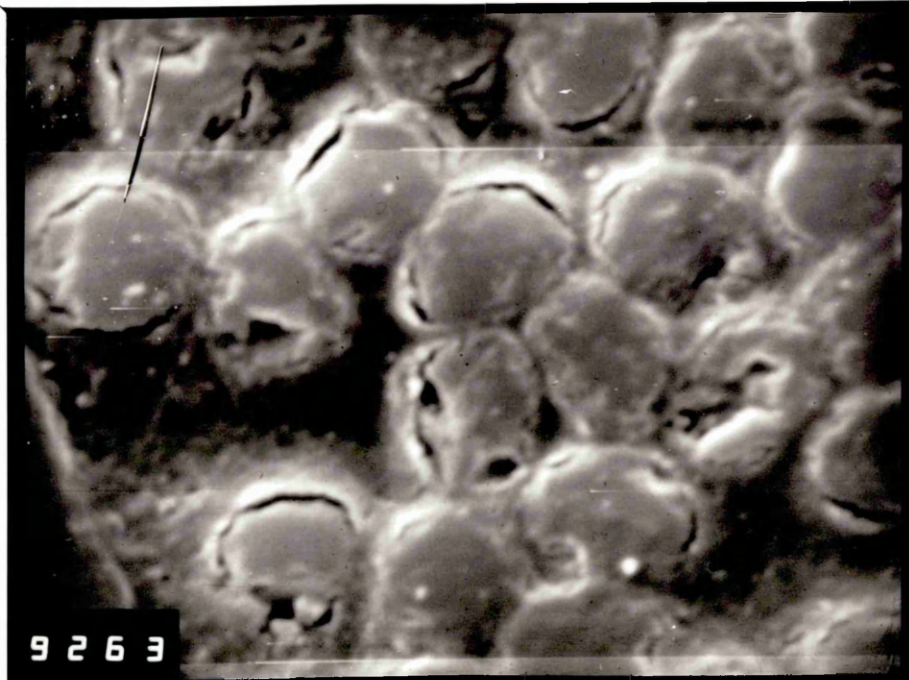
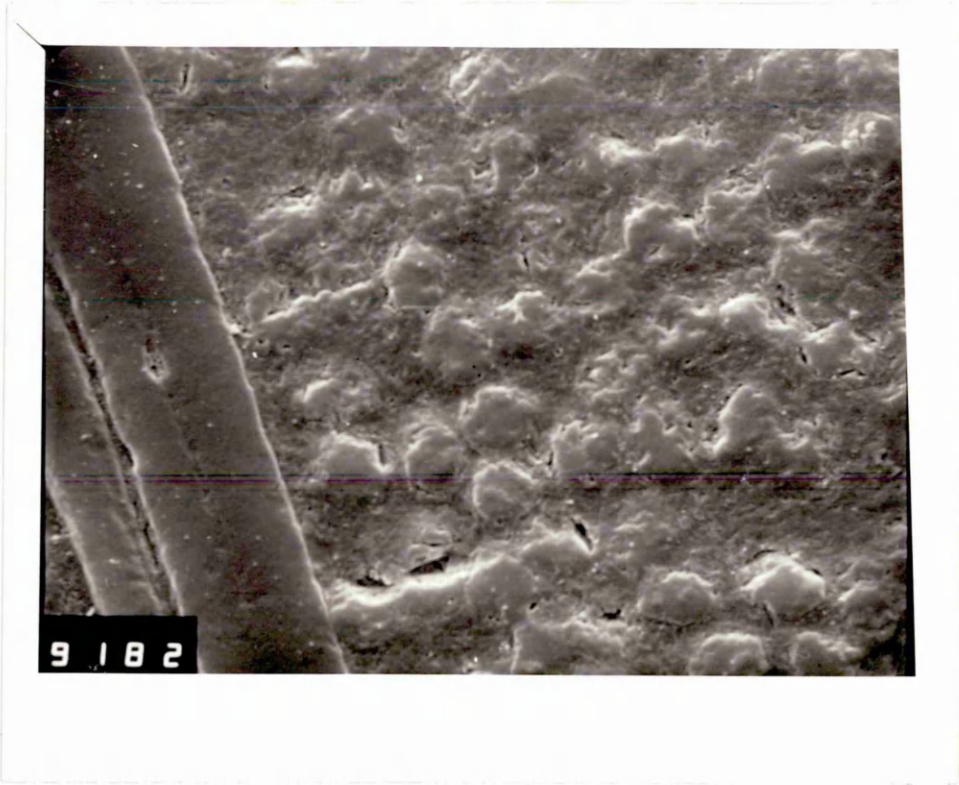


Figure 141. Cracking at fibre/matrix interface, view 2:

a) Mag x 1360

b) Mag x 2720, top

a)



b)



c)

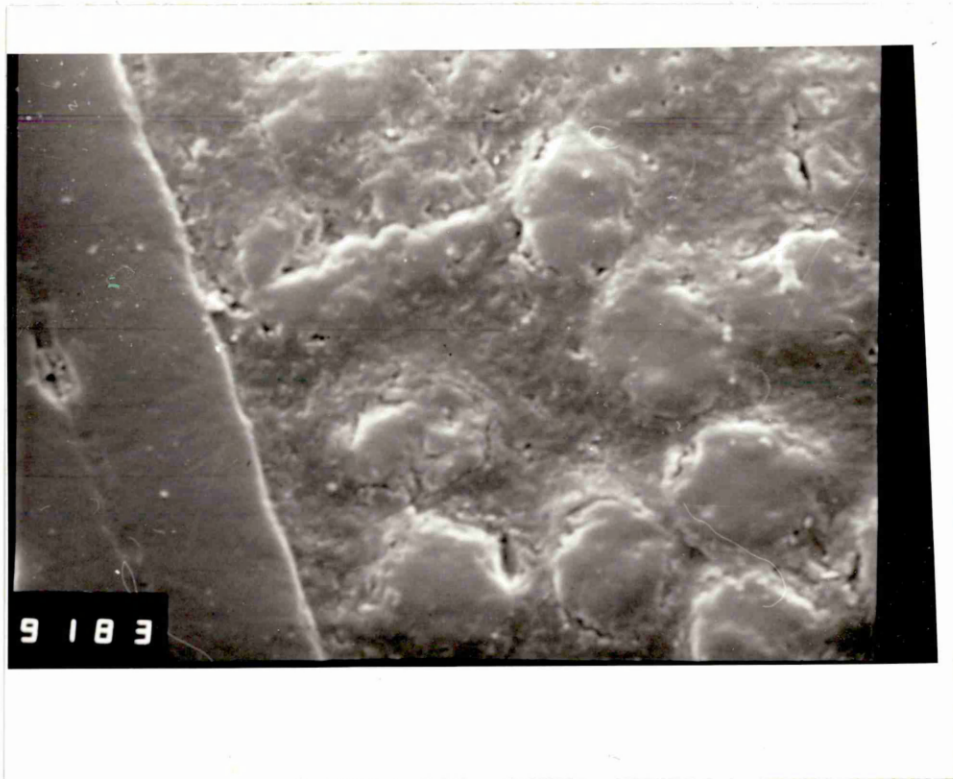
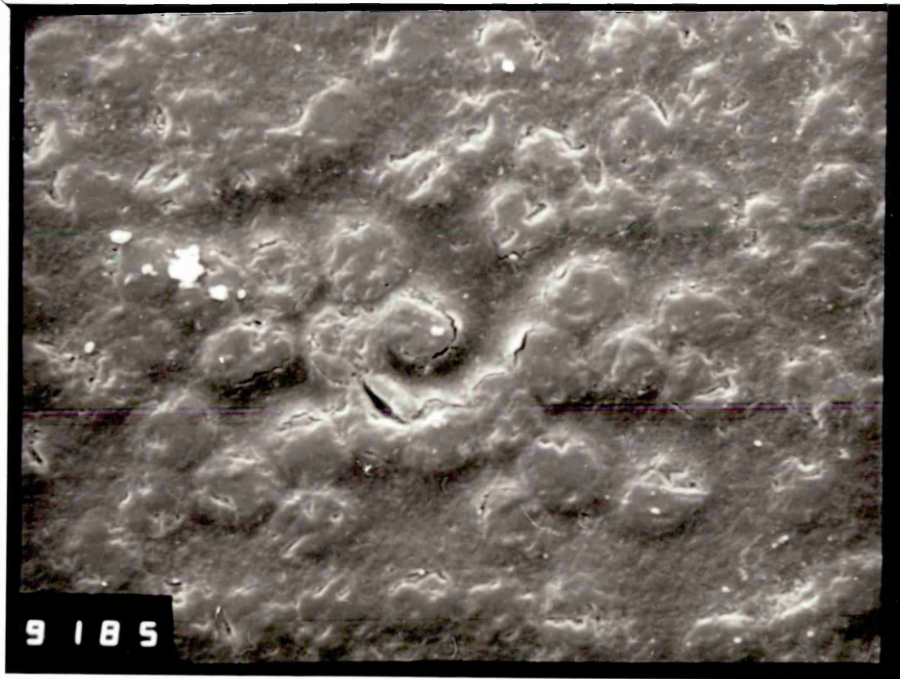


Figure 142. Cracking at fibre/matrix interface, view 3:

a) Mag x 1360

b) Mag x 2720

a)



b)

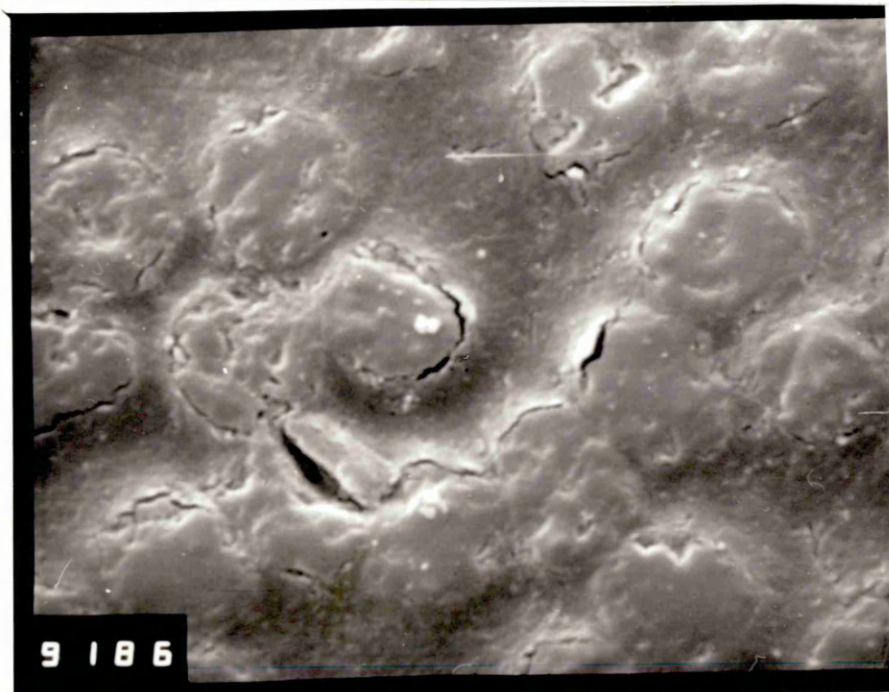


Figure 143. Cracking at fibre/matrix interface, view 4 - Mag x 2880

Figure 144. Cracking at fibre matrix interface, view 5 - Mag x 2880

Fig. 144 <sup>143</sup>

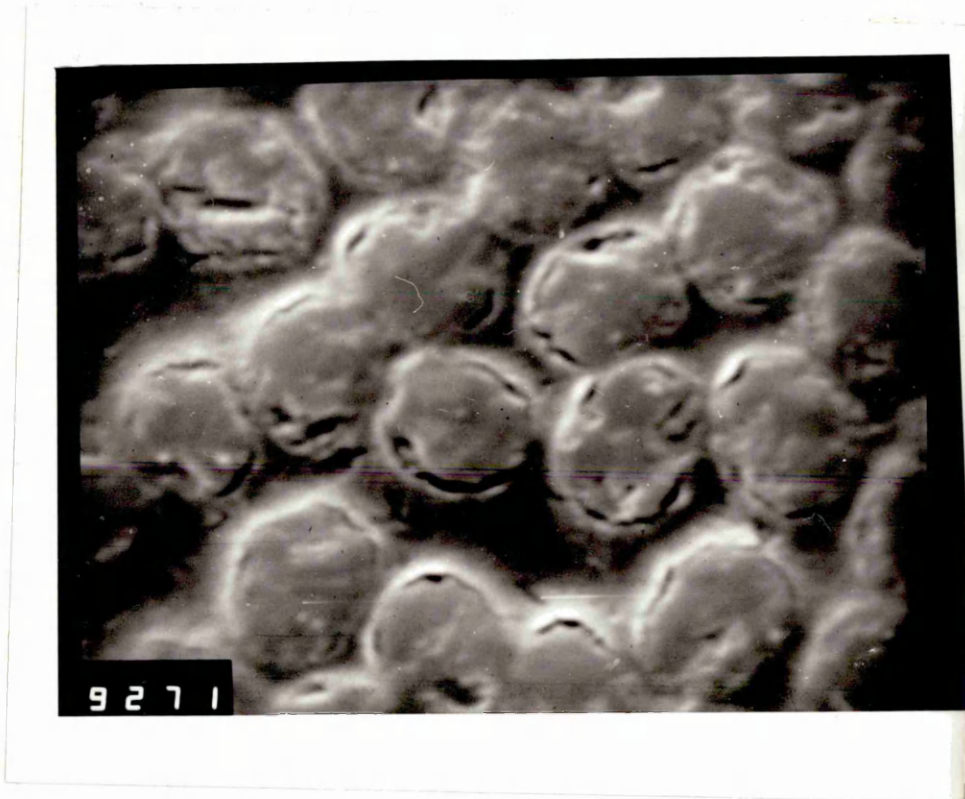


Fig. 145  
~~144~~



Figure 145. Sectioning artifact:

a) Mag x 720

b) Mag x 1440

a)



b)

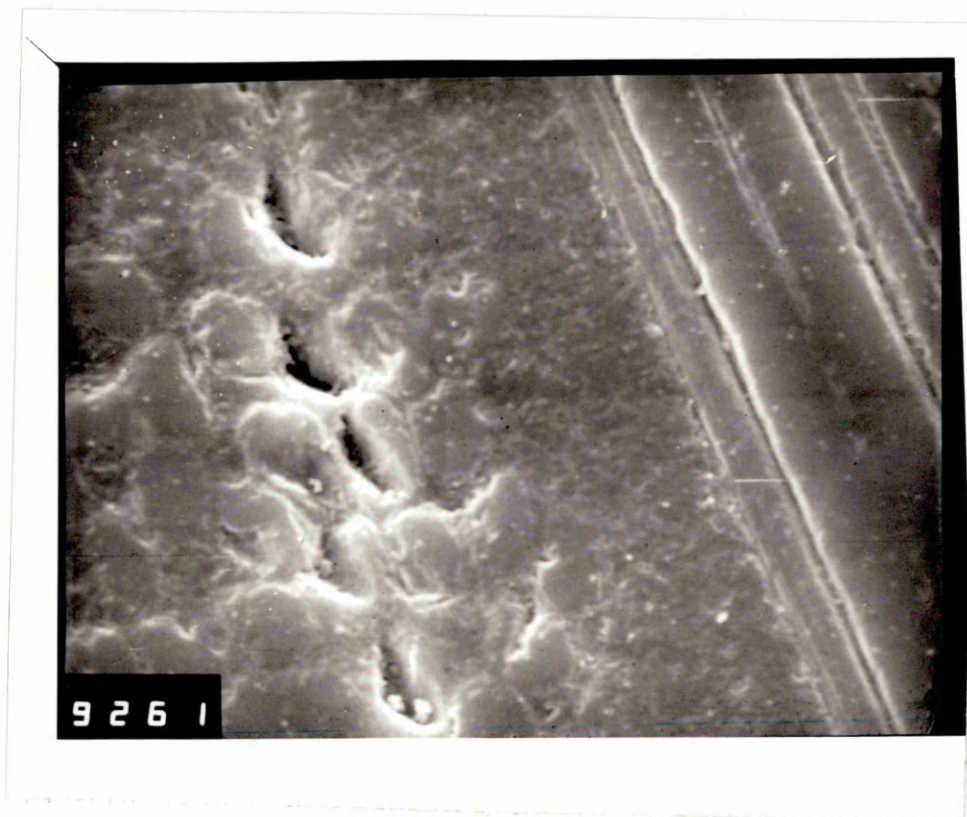
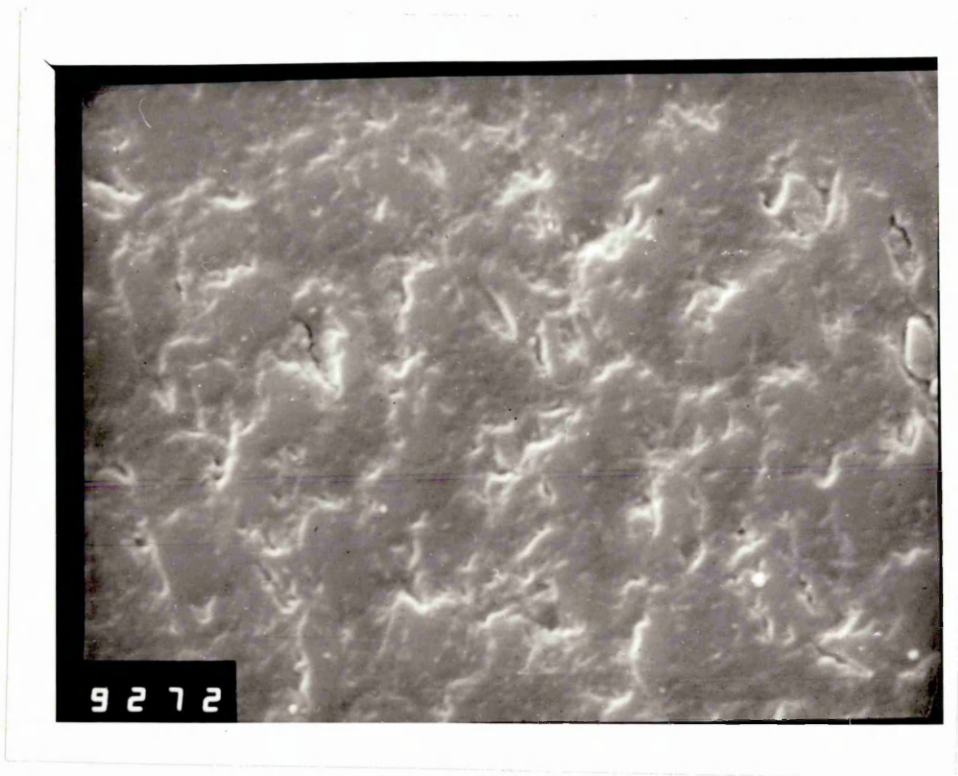


Figure 146. Polishing/sectioning artifacts:

a) View 1 - Mag x 1440

b) View 2 - Mag x 720

a)



b)



Figure 147. The greatest value of the maximum principal stress versus half-interfibre distance (XA) for varying co-ordination angle,  $\theta$

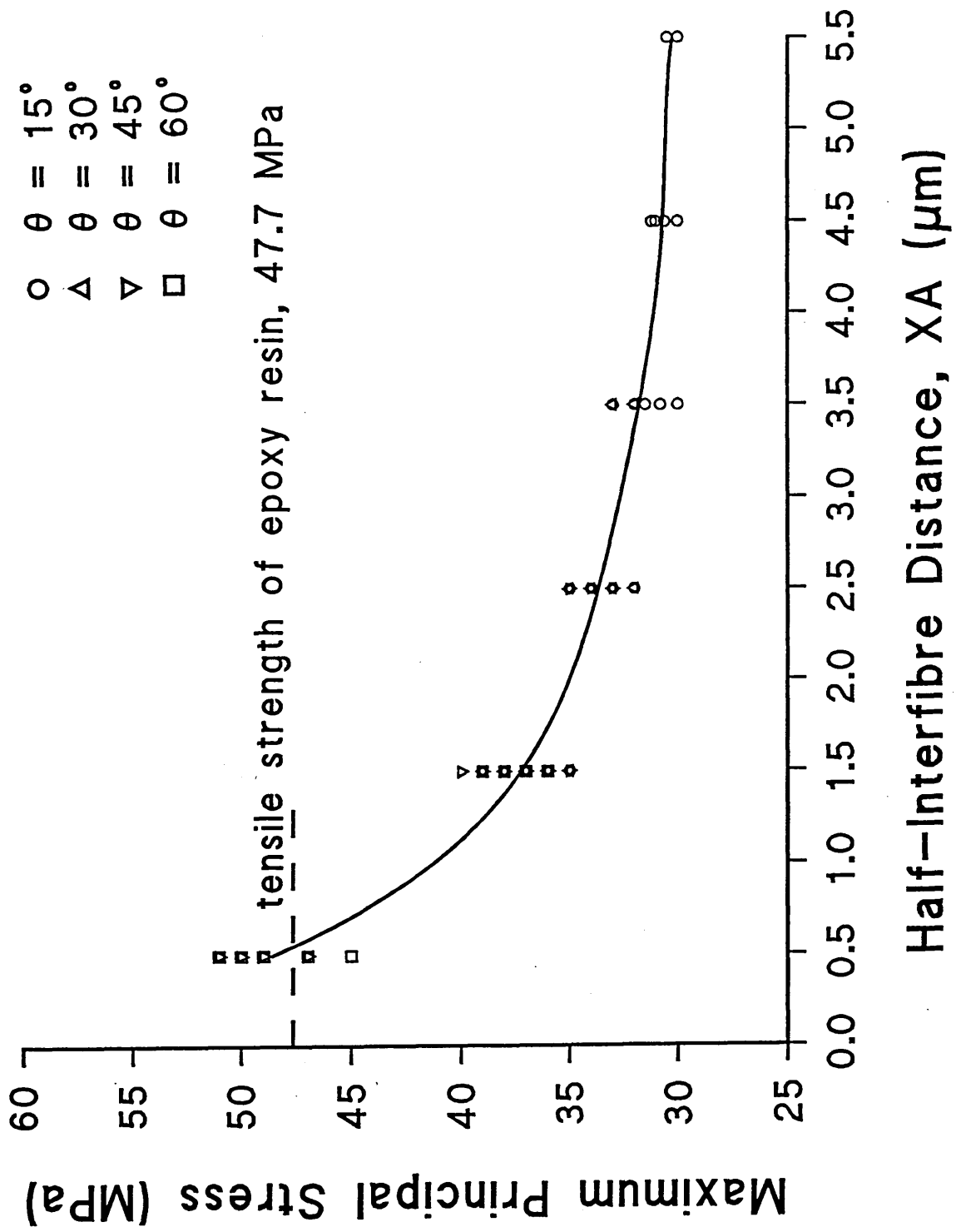


Figure 148. The greatest value of the maximum principal stress versus fibre radius showing the effect of variation in half-interfibre distance,  $XA$

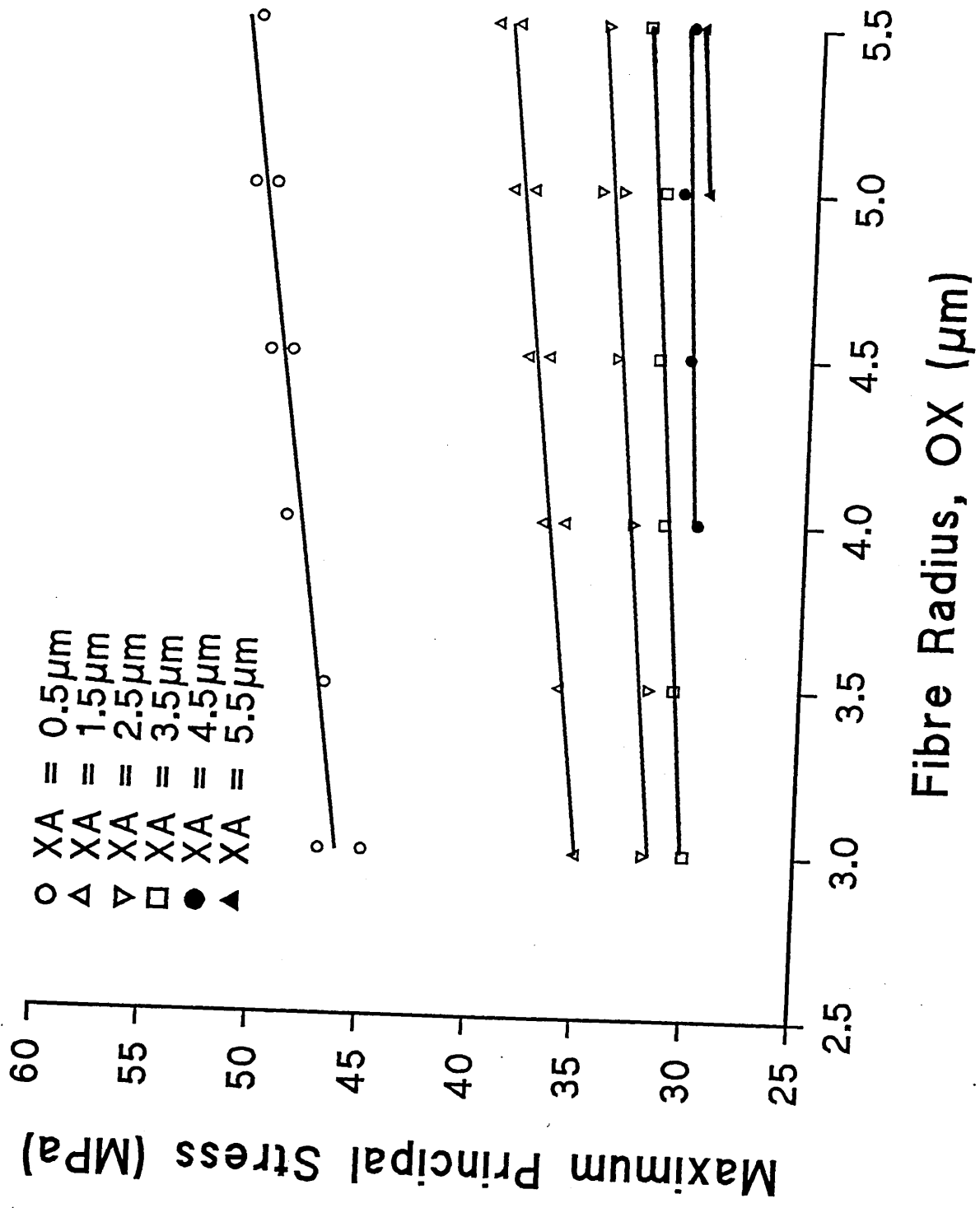


Figure 149. The greatest value of the maximum principal stress versus fibre volume fraction showing the effect of variation in co-ordination angle,  $\theta$

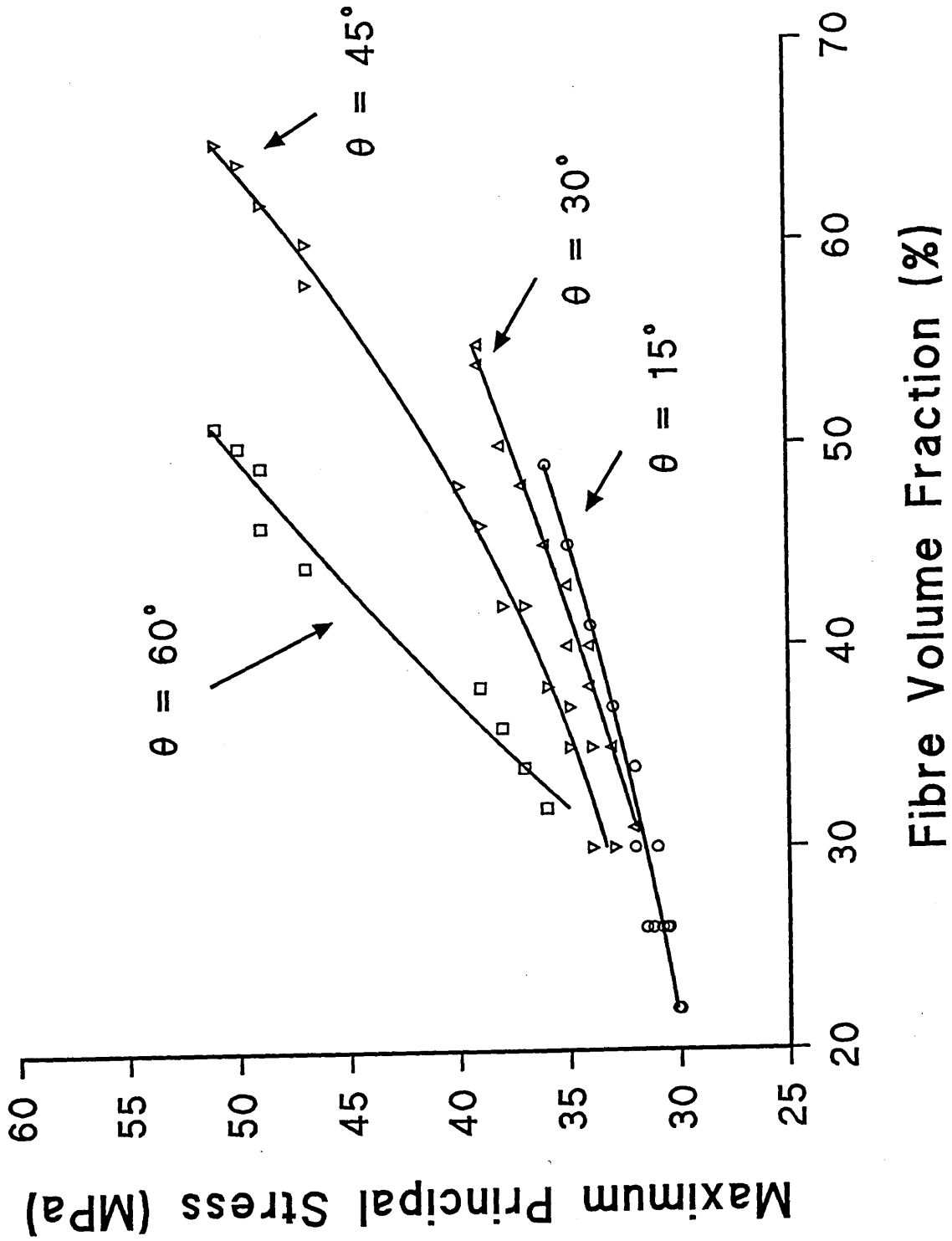
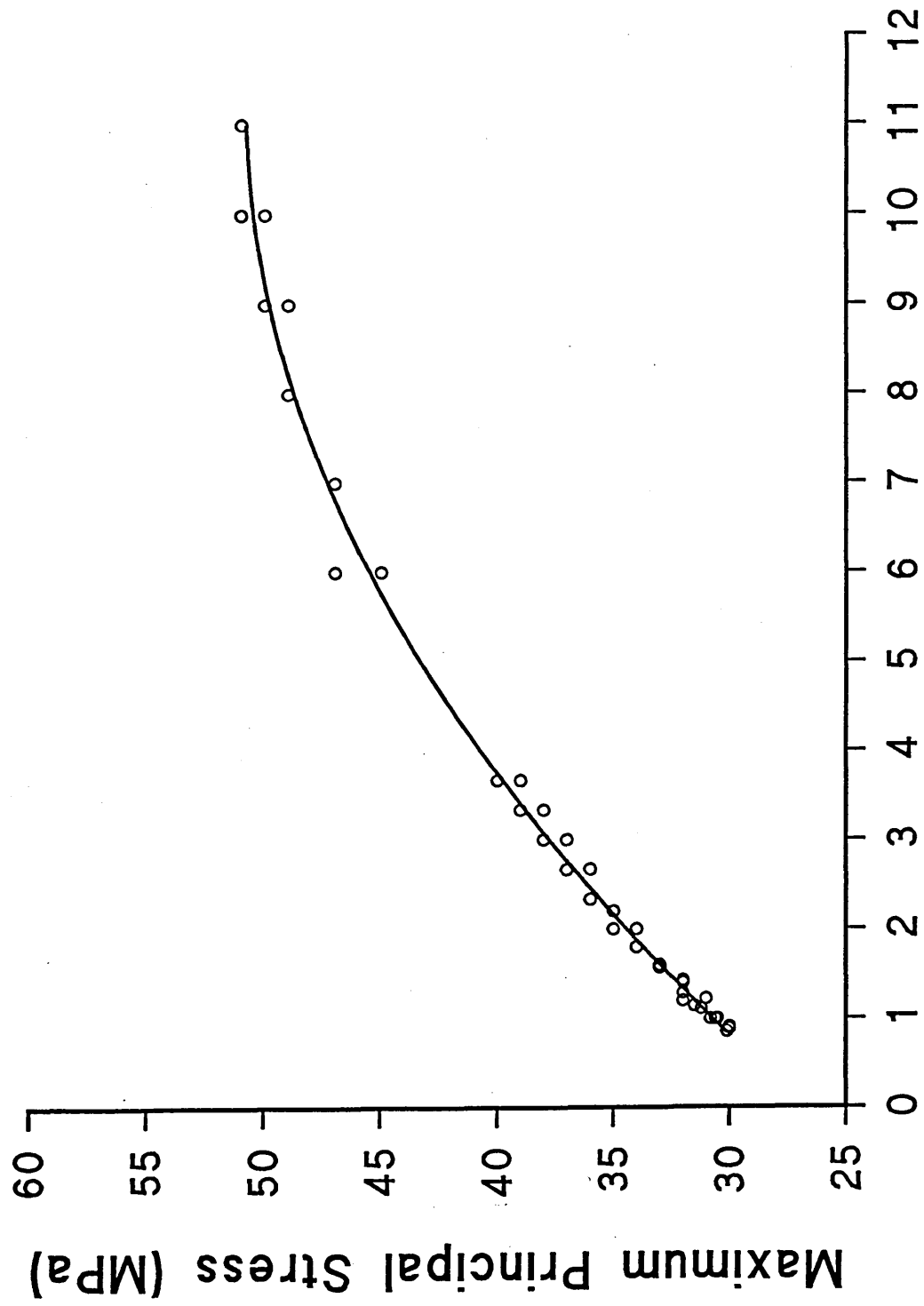


Figure 150. The greatest value of the maximum principal stress versus fibre radius to half-interfibre distance ratio,  $OX/XA$ .



Fibre Radius/Half-Interfibre Distance Ratio, OX/XA

APPENDIX 1 - FIBDIST Program

```
10 INPUT "NUMBER OF FIBRES";N
15 RANDOMIZE TIMER
20 INPUT "VOLUME FRACTION";F
30 DIM X(N):DIM Y(N)
40 SCREEN 2:CLS:WINDOW (0,0)-(1000,500)
50 R=SQR(500000!*F/(N*3.142))
60 FOR A=1 TO N:X(A)=RND*(1000-2*R)+R:Y(A)=RND*(500-2*R)+R
  :NEXT A
70 GOSUB 1000
75 H=0
80 FOR A=1 TO N
90 FOR B=1 TO N
100 IF A=B THEN 120
110 IF SQR((X(A)-X(B))^2+(Y(A)-Y(B))^2)*1.000001<2*R THEN
  GOSUB 2000
115 IF INKEY$<>" " THEN 150
120 NEXT B
130 NEXT A
140 IF H>0 THEN GOTO 70
150 INPUT "FILENAME FOR RESULTS ";F$
160 OPEN F$ FOR OUTPUT AS #1
165 PRINT #1,"FIBRE RADIUS ";R;" SCREEN 1000x500, VOLUME
  FRACTION ";F
170 FOR A=1 TO N:PRINT #1,X(A),Y(A):NEXT A
180 END
1000 CLS:FOR A=1 TO N:CIRCLE(X(A),Y(A)),R
1010 NEXT A:RETURN
2000 XD=(X(A)-X(B)):YD=(Y(A)-Y(B))
2005 CIRCLE (X(A),Y(A)),R,0
2006 CIRCLE (X(B),Y(B)),R,0
2010 C=SQR(XD^2+YD^2):YS=((2*R-C)*YD)/C)/2+3:XS=((2*R-C)
  *XD)/C)/2+3
2020 X(A)=X(A)+XS
2030 X(B)=X(B)-XS
2040 Y(A)=Y(A)+YS
2050 Y(B)=Y(B)-YS
2055 H=1
2060 IF X(A)>1000-R THEN X(A)=(1000-R)
2070 IF X(B)>1000-R THEN X(B)=(1000-R)
2080 IF X(A)<R THEN X(A)=R
2090 IF X(B)<R THEN X(B)=R
2100 IF Y(A)>500-R THEN Y(A)=(500-R)
2110 IF Y(B)>500-R THEN Y(B)=(500-R)
2120 IF Y(A)<R THEN Y(A)=R
2130 IF Y(B)<R THEN Y(B)=R
2135 CIRCLE (X(A),Y(A)),R
2136 CIRCLE (X(B),Y(B)),R
2140 H=1
2150 RETURN
```

## APPENDIX 2 - Modelling of Interlayer

Subsequent to the work presented in this thesis discussions at Rolls-Royce revealed observations to have been made of an interphase occurring in the carbon fibre/epoxy resin materials modelled. Analyses carried out had enabled predictions to be made concerning the properties of the interphase. Properties and interphase layer thickness were given as [1].

Young's modulus = 4.96 GPa      Poisson's ratio = 0.325

Thermal expansion coefficient =  $23.3 \times 10^{-6} \text{ } ^\circ\text{C}^{-1}$

Interphase thickness = 0.4-0.5  $\mu\text{m}$

When compared to the epoxy resin properties away from the interface (see section 3.5.1) it is interesting to note that the Young's modulus is higher whilst the thermal expansion coefficient and Poisson's ratio are lower. This is contrary to the prediction of a flexible interlayer. Rather it seems that the stresses at the interface are suppressed due to the lower thermal expansion coefficient of the interphase. No information was available concerning the temperature dependence of these properties.

It was a fairly simple procedure to incorporate these values into the finite element models and observe the effect on the results. The properties of the interlayer were assumed temperature independent, unlike the properties of the epoxy resin away from the interface. Models B03C and V001 were chosen producing models BI3C and VI01.

In addition the discussions revealed that measurements of the stress free temperature had shown this to occur at  $140^\circ\text{C}$ . Thus rather than a

170°C temperature drop it is more accurate to model a 120°C temperature drop. This was also incorporated into the models.

The results obtained for the deformation and the maximum principal stress are attached. The maximum deformations are smaller, 37.8  $\mu\text{m}$  (model BI3C) and 72.7  $\mu\text{m}$  (model VI01), than the original programs, 57.5  $\mu\text{m}$  (model B03C) and 106  $\mu\text{m}$  (model V001), as would be expected for the smaller temperature drop. It can be seen that the lower thermal expansion coefficient and lower Poisson's ratio of the interphase has the effect of suppressing the maximum principal stresses calculated at the interface. This is despite the higher value of the Young's modulus. In addition the smaller temperature drop lowers the overall stress level. The maximum value of the maximum principal stress occurs at the interlayer/matrix interface where it has lower values, 22.3 MPa and 53 MPa, compared to the original B03C and V001 models, 32 MPa and 68 MPa, respectively. The maximum principal stress in the interlayer is compressive having values between 3.53 MPa and 6.96 MPa, for model BI3C, and -2.1 MPa and 37.3 MPa for model VI3C. The maximum principal stress vectors show that these still act tangentially to the interface.

With the stresses displaced away from the fibre/matrix (interlayer) interface to the interlayer/matrix interface it is much less likely that the fibre/matrix (interlayer) interface will fail. Also, remembering that the overall stress levels are reduced by the presence of an interlayer and assuming good adhesion between the interlayer and the matrix (this seems very probable for such similar phases), it would be expected that failure of the interlayer/matrix interface, the interlayer and the matrix is less likely.

[1] private communication, Rolls-Royce (C. B. Allen).

Figure A1. Deformation on cooling through 120°C - model BI3C



Figure A2. Maximum principal stress - model BI3C  
(original in colour)

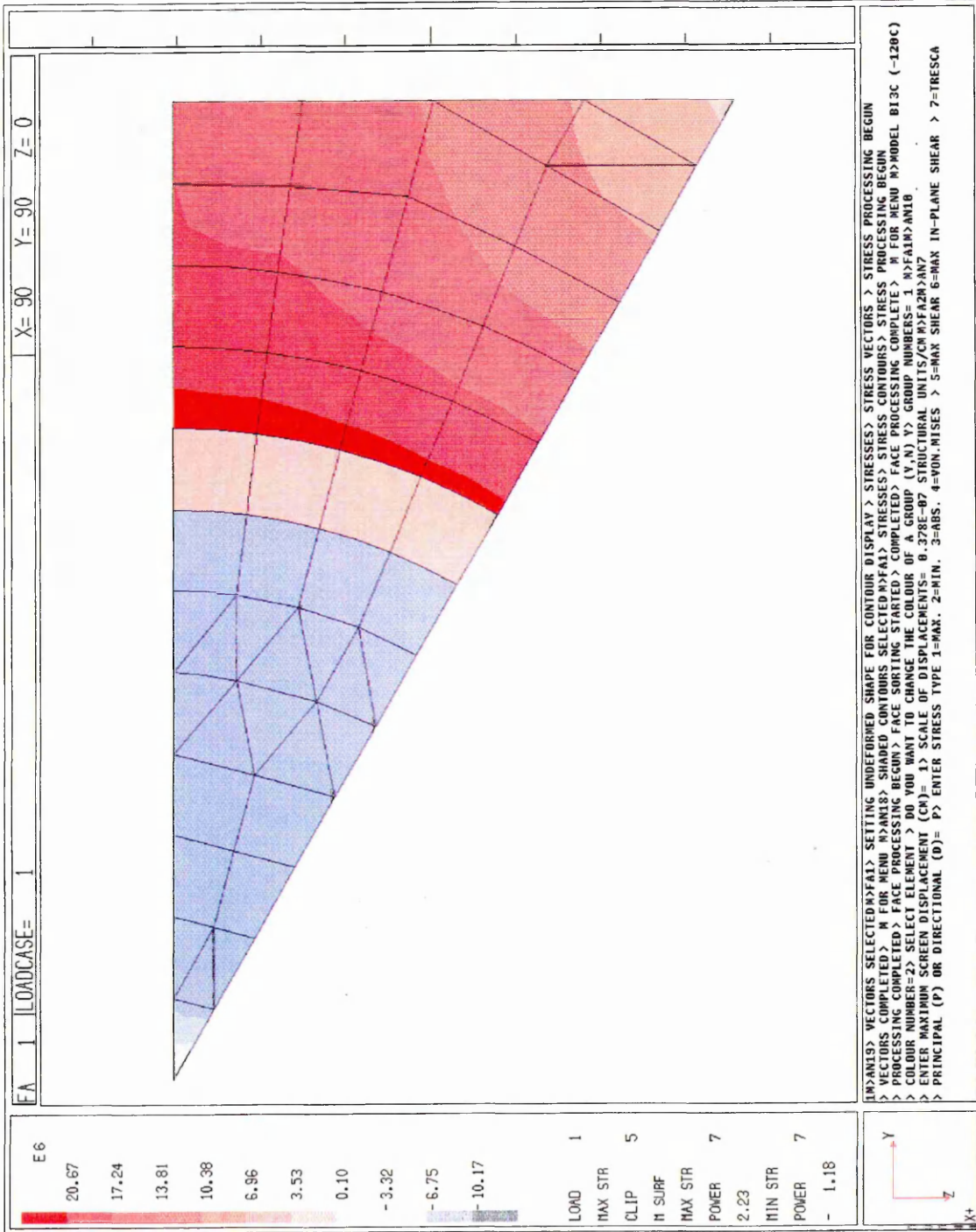


Figure A3. Maximum principal stress, vectors - model BI3C

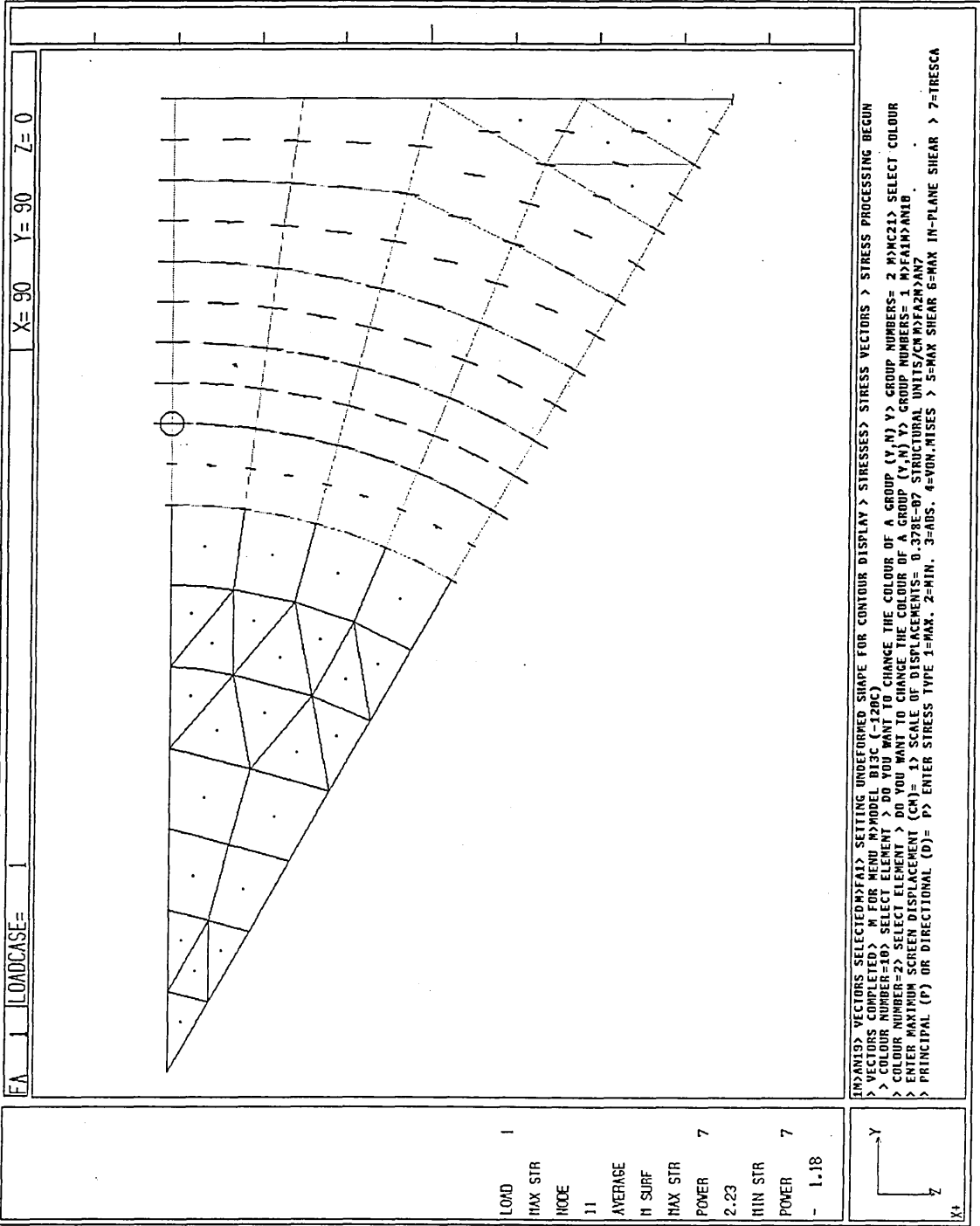


Figure A4. Deformation on cooling through 120°C - model VI01



Figure A5. Maximum principal stress - model VI01  
(original in colour)

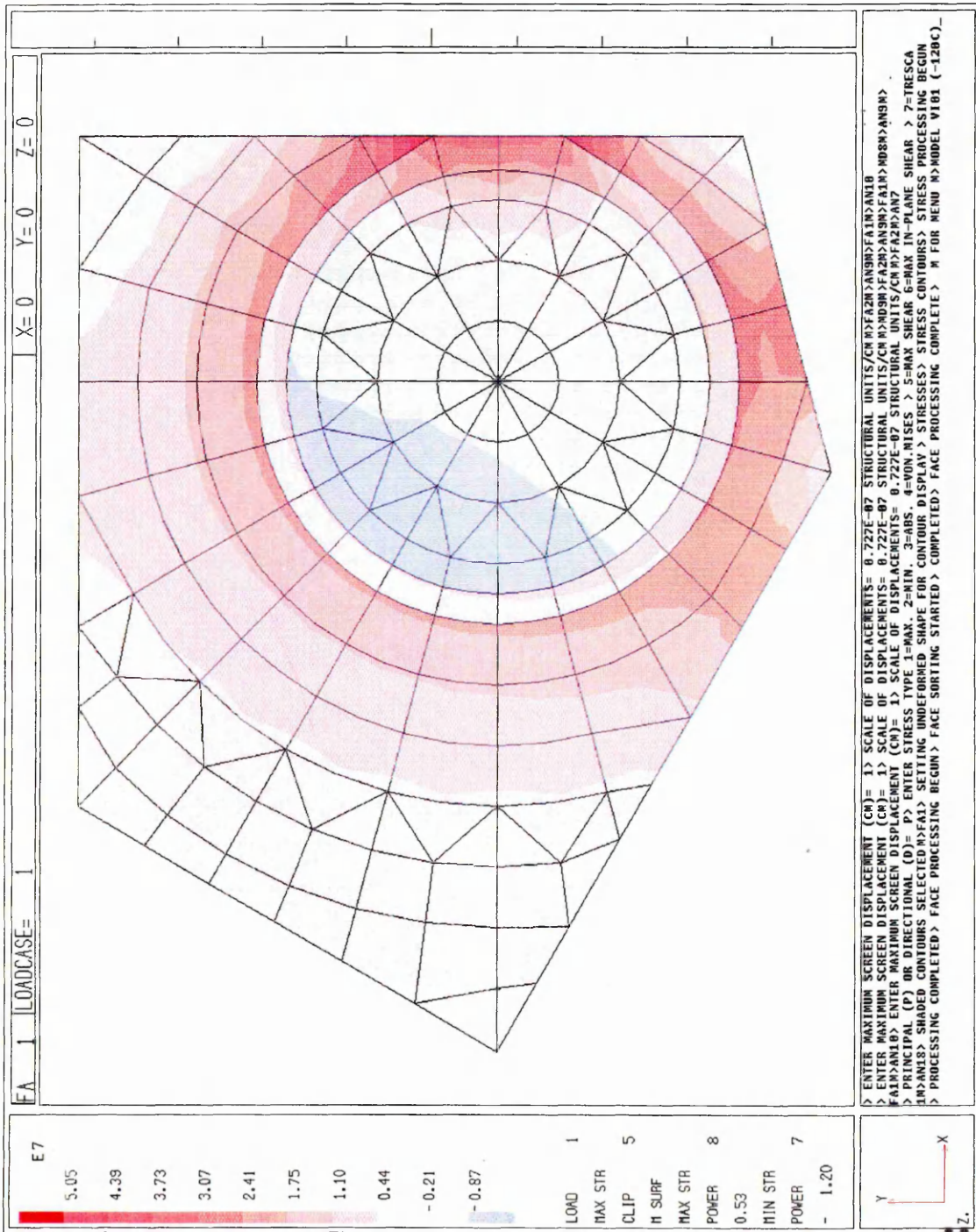


Figure A6. Maximum principal stress, vectors - model V001

